eman ta zabal zazu

Universidad del País Vasco
Euskal Herriko Unibertsitatea

Departamento de Ingeniería Mecánica / Ingeniaritza Mekanikoa Saila

In service behavior of components repaired by laser cladding - Process, microstructure and fatigue behavior relationships

Mario Renderos Cartagena

In service behavior of components repaired by laser cladding - Process, microstructure and fatigue behavior relationships

Ph.D. THESIS
presented to obtain the degree of
Doctor

Mario Renderos Cartagena

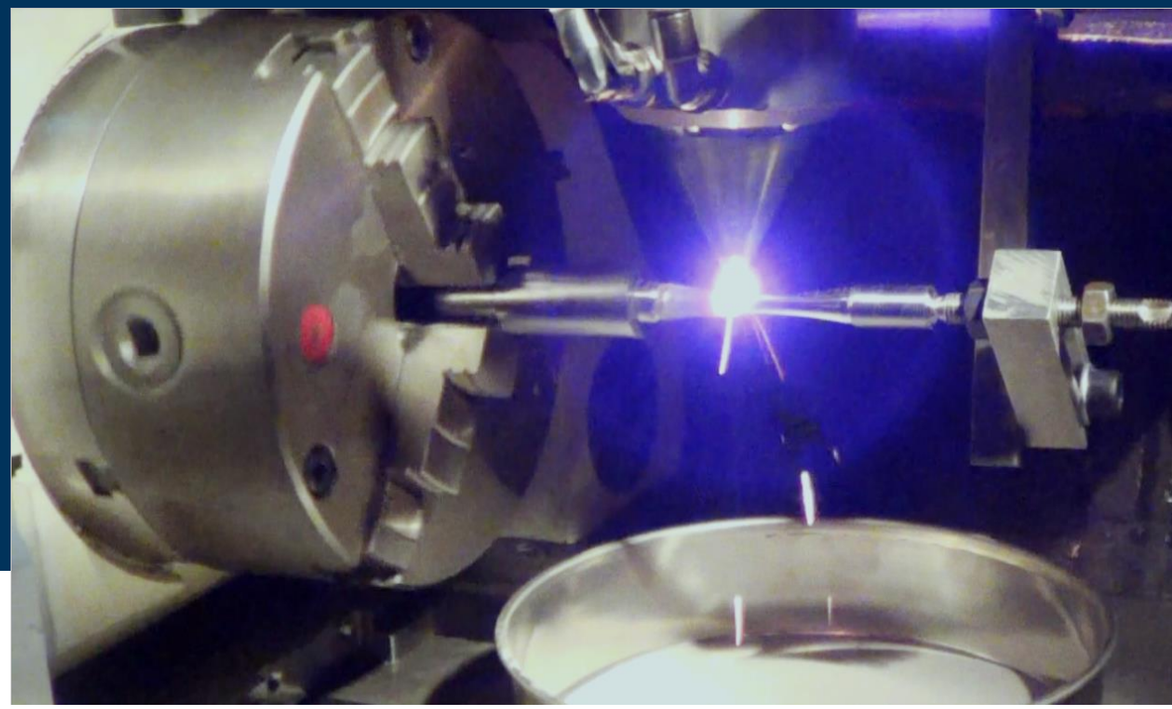

06/2021, Bilbao

THESIS ADVISOR
Pr. Franck Andrés Girot Mata, University of the Basque Country - UPV/EHU

eman ta zabal zazu

Universidad del País Vasco
Euskal Herriko Unibertsitatea

INGENIARITZA MEKANIKOA SAILA
DEPARTAMENTO DE INGENIERÍA MECÁNICA

eman ta zabal zazu

Universidad del País Vasco
Euskal Herriko Unibertsitatea

In service behavior of components repaired by laser cladding - Process, microstructure and fatigue behavior relationships

Mario Alfredo Renderos Cartagena, MSc.

Thesis submitted the University of Basque Country for the degree of Doctor

Department of Mechanical Engineering

Thesis Advisor

Pr. Franck Andrés Girot Mata

June 2021

PREFACE

This thesis is submitted for the degree of Doctor at the University of Basque Country-UPV/EHU. The research work was carried out under the supervision of Professor Franck Andrés Girot Mata (University of Basque Country - UPV/EHU) and Professor Nicolas Saintier (Arts et Métiers Science et Technologie), in the Department of Mechanical Engineering.

It is certified that the work presented in this thesis is original and suitable references are made to any work from the literature or carried out elsewhere.

The motivation for this research began with my desire to pursue a postgraduate degree outside of my country (El Salvador), and experience a higher level of education in first-hand. I like research, I like to develop innovation, I like to improve what already exists and above all I am very curious. I like the experience I have gained over the years through the people I have met.

I hope that the results of this research will be useful in solving problems related to additive manufacturing technology of Laser Cladding, a fascinating and multidisciplinary field of research, but one that is still too much to develop and understand.

This PhD has not only been an intellectual adventure, it has been a very satisfying experience as part of a group without which I would never have reached the success in the conclusion of this thesis. Here I have met people who have left their mark on my life, and to many of them I am truly grateful for their support and confidence in my work.

ACKNOWLEDGEMENTS

I would like to express my most sincere gratitude to my supervisors Professor Franck Andrés Girot Mata and Prof Nicolas Saintier for their guidance and immense support during the course of this research. The successful completion of this work would not have been achieved without their great assistance.

I would also like to express my gratitude to Dr. Eric Lacoste (IUT Bordeaux 1), Mohamed Elmay, Jeremie Bega and Jonathan Merzeau (Arts et Métiers Science et Technologie), for their invaluable comments and technical contributions during the experiments in the course of this research.

The authors thank for technical and human support provided by SGIker (UPV/EHU/ERDF, EU): Servicio General de rayos X de la UPV/EHU: unidad de moléculas y materiales, and Microscopía Electrónica y Microanálisis de Materiales.

And now more of this document in Spanish:

Quiero agradecer al Dr. Aitzol Lamikiz Mentxaka por su apoyo y ayuda cuando lo he necesitado, y por haberme recibido en el Grupo Láser.

También todo el apoyo que he recibido de mis compañeros de la Universidad del País Vasco a lo largo de estos años, sobre todo al grupo del Taller Mecánico y del Palomar, de quienes he aprendido muchísimo, y con quienes me he sentido aceptado (¡viva el café de las 11!). El personal de los Laboratorios y el Taller Mecánico me han ayudado a materializar mis ensayos, y sin su colaboración este trabajo no hubiera sido posible.

A mis amigos de la Cuadripanda Internacional, sobre todo a Iñigo, Paulina, Katherine, y Alberto por estar pendiente de mí, y otros como Iker y Elena que ha estado cuando he necesitado un consejo. Hay tantas personas a las que debo agradecer que me es difícil sintetizarlo en pocas palabras, pero que sepan cualquier ayuda que me hayan brindado la guardo cariñosamente.

Agradezco a mis padres (Papá Moris y Mamá Elma), mis hermanos (Moris, Silvia y Paty), sin su apoyo y ánimos no hubiera conseguido esta meta. Me siento orgulloso de todos ustedes, de cada uno, y de ser parte de esta familia.

Hay una persona a la que agradezco sobre todo su ayuda y apoyo, sin quien esto no hubiera concluido con éxito, hablo de la mujer que amo y respeto, mi esposa Denis Marisol Membreño Canales. Mi chelita ha sido mi fiel compañera en este extenso viaje a lo largo de los años, y es la persona a quién principalmente dedico este trabajo...

A DIOS por el privilegio de alcanzar este hito.

A todos y cada uno de ustedes desde el fondo de mi corazón ¡muchas gracias!

OBJECTIVE OF THIS THESIS

The objective of this thesis is:

- Establish the relationship between the process parameters and the mechanical properties in components rebuilt by Laser Cladding process applied to the superalloy Inconel 718.

ABSTRACT

The industry gradually incorporates Additive Manufacturing as part of its manufacturing processes. Laser Cladding is one of the most interesting Additive Manufacturing technologies.

Laser Cladding technology has been considered interesting because it is very versatile, allowing not only the manufacturing of small series of parts, but also the repair and maintenance of components (via the addition of a cladding). To extend the service life of high value-added components, the addition of a hard coating is desirable, or in certain cases, to repair pieces when errors have occurred during manufacturing. One of the most important drawbacks for the full acceptance of this AM technology is the lack of data relating process parameters to mechanical properties. A study of the process parameters, the microstructure that is generated and finally how this microstructure relates to the static and dynamic mechanical properties by means of appropriate descriptors, among other things, is necessary. This research was divided into 4 sections:

1. This research started with the study of the process parameters of the Additive Manufacturing technology of Laser Cladding on an alloy commonly used in the aeronautical industry, the super-alloy INCO718. The objective of this part of the research was to establish a general methodology for finding an optimal set of values for process parameter. Extensive use of Design of Experiments, and Multiple Linear Regression with Optimization was made.
2. Next, using the aforementioned optimal process parameters were fabricated series of specimens that allowed to manufacturing samples with very few amount of defects. The raw material used for the fabrication of that specimens (new and reconditioned metal powder), and the resulting microstructural characteristics of the fabricated parts were investigated. Material characterization was performed by optical microscopy, scanning electron microscopy (with chemical microanalysis) and X-ray diffraction, in addition to standardized uniaxial tension tests with different raw materials (new and reconditioned metal powder).
3. Subsequently, mathematical models were developed for the Laser Cladding process and the Crystallization Process (related to the grain morphology) for the alloy used in this research. For the Crystallization Model, a methodology was developed for the deduction of the constants necessary for its use.
4. For the establishment of the microstructure-mechanical properties relationships, the use of self-developed coated specimens compatible with those of standardized type was proposed, since there is no standard for coated probes. The effect of the texture generated by the Laser Cladding process was investigated by means of Uniaxial Tension tests and it was tried to establish some relation with the Fatigue Strength in specimens of similar

dimension. Hardness and Residual Tension tests were carried out on the fabricated material. For the relationship between microstructure and mechanical properties was used the Dang Van Criterion in combination with Fractal Theory and Multiple Linear Regression models with Optimization (with hypothesis testing).

As results for each section of this research are mentioned:

- Section 1: The use of values calculated with the Process Parameter Optimization Method allowed the fabrication of samples for mechanical properties testing of very high quality. The aforementioned was necessary to characterize the manufactured alloy. The novel use of polynomial descriptors to describe the geometry of the cladding beads of the Laser Cladding process was proposed with very good results, besides the mathematical demonstration of the existence of optimal values for certain parameters of the above mentioned process. Finally, the transfer of the methodology for the solution of an industrial problem to a company was achieved.
- Section 2: The feasibility of the reconditioning of metallic powder was determined as a method to take advantage of the raw material and as a way to avoid an excessive waste of the INCO718 alloy powder. It was demonstrated that the chemical composition of the fabricated material remains homogeneous when using optimized parameters in addition to avoiding the appearance of undesirable phases of inter-metallic type. It was observed that the texture and some phases generated by an additive manufacturing process are different from those produced by traditional manufacturing of the INCO718 alloy (especially in the distribution of Laves phase). The number of times that the metal powder can be reconditioned without a decrease in the mechanical properties in Uniaxial Tension test is two, and then the increase of porosity and oxygen content within the alloy gives rise to a significant decrease in the quality of the material manufactured by Laser Cladding process.
- Section 3: The development of Laser Cladding Model allowed to understand in depth the effect of the variation of process parameters on the resulting crystalline microstructure (including the dependence of alloy properties as function of temperature). As the previous model is semi-analytical, its implementation is relatively straightforward. The Crystallization Model allowed using the power of a statistical probability distribution (Gumbel) as a tool to predict the behaviour of the columnar-equiaxial transition for the INCO718 alloy, in addition to allowing the use of the information contained in Solidification Maps of a given alloy and transforming it to an easy to implement equation.
- Section 4: The proposed design of specimens for Tension and Fatigue life tests, both of uniaxial type, allows distinguishing between the apparent and real properties of the coating manufactured by the Laser Cladding process. Another

advantage is the possibility to compare the results with the existing literature on mechanical properties. It was demonstrated that there is no relationship between the performance in the Uniaxial Tension test and the Fatigue Strength tests for a material manufactured by Laser Cladding process. The combination of Dang Van's criterion for fatigue with Fractal theory was shown to be a suitable way to relate microstructure to mechanical properties, which was the ultimate goal of this research.

GENERAL CONTENTS

LIST OF FIGURES

GENERAL INTRODUCTION: LITERATURE REVIEW ON ADDITIVE MANUFACTURING AND THE CONTEXT OF THE LASER CLADDING AM PROCESS

CHAPTER II: MICROSTRUCTURE CHARACTERIZATION OF NEW AND RECYCLED IN718 POWDER AND RESULTING LASER CLADDING MATERIAL

LIST OF TABLES

GENERAL INTRODUCTION: LITERATURE REVIEW ON ADDITIVE MANUFACTURING AND THE CONTEXT OF THE LASER CLADDING AM PROCESS

GENERAL INTRODUCTION: LITERATURE REVIEW ON ADDITIVE MANUFACTURING AND THE CONTEXT OF THE LASER CLADDING AM PROCESS

0 Nomenclature and Abbreviations

AM:	Additive Manufacturing
ASTM:	American Society for Testing and Materials
BPP:	Beam Parameter Product
CAD:	Computer-Aided Design
CAM:	Computer-Aided Manufacturing
CNC:	Computer Numerical Control
CW:	Continuous Wave
DC:	Direct Current
DfAM:	Design for Additive Manufacturing
DLD:	Direct Laser Deposition
EBM:	Electron Beam Melting
FDM:	Fused Deposition Modelling
GA:	Gas Atomization
LMD:	Laser Metal Deposition
PA:	Plasma Atomization
PREP:	Plasma Rotating Electrode Process
RA:	Rotary Atomization
RF:	Radio Frequency
RP:	Rapid Prototyping
RT:	Rapid Tooling
SLA:	Stereolithography
SLM:	Selective Laser Melting
SLS:	Selective Laser Sintering
G_L:	Temperature Gradient in liquid isotherm ($K.m^{-1}$)
m':	Powder feed rate ($Kg.s^{-1}$)
v:	Scanning speed of laser beam ($m.s^{-1}$)
V:	Solidification grow rate ($m.s^{-1}$)

1 General Introduction to Additive Manufacturing

1.1 Additive Manufacturing

ASTM has defined Additive Manufacturing as: a process of joining materials to make objects from 3D model data, usually layer upon layer, as opposed to subtractive manufacturing methodologies. Synonyms: additive fabrication, additive processes, additive techniques, additive layer manufacturing, layer manufacturing, and freeform fabrication (Frazier, 2014).

The origins of AM are based on the development of technology for rapid prototyping, whose original objective was not the creation of functional parts, but simply for the "solid visualization" of ideas (Wong and Hernandez, 2012). Subsequently, the evolution of technology was aimed not only at visualizing the parts, but also at their functional construction.

According to (Ngo et al., 2018), this technology was developed by Charles Hull in 1986, through the process known as Stereolithography (SLA). Stereolithography has been followed by other developments such as powder bed fusion methods or fused deposition modelling (FDM).

The concept of Additive Manufacturing does not include any restriction on the type of material that can be used during built-up. It is equally applicable to metals, ceramics, polymers, or even biological materials (and even a combination of all the materials previously mentioned).

Fundamentally when we speak of Additive Manufacturing, we are talking about an inverse process to the typical "subtractive" type of manufacturing. In this process, manufacturing is done layer by layer, and this distinguishes AM from other traditional manufacturing processes such as casting. Another concept that sets AM apart is its versatility. Another concept that distinguishes AM is its versatility. Versatility is defined as the ability to quickly adapt to the needs of a certain sector, e.g. industrial production (where different prototypes need to be created quickly).

1.2 General Applications of Additive Manufacturing.

According to (Wong and Hernandez, 2012), some general applications of additive manufacturing are:

- Creating lightweight, functional machine parts: the main markets are automotive and aerospace industry. AM is able to create "organic" parts (e.g. honeycomb sections) or other features such as in-situ construction of channels for parts requiring cooling.
- A One field of wide application is medical: the possibility of rapid prototyping of patient bone models for precise diagnostic and treatment strategies, the construction of customised prostheses, tissue manipulation for the printing of "living parts", are just some of the possibilities. The ability to create free-form (virtually unrestricted) shapes gives clinicians the freedom to create implants with controlled porosity, maximising biocompatibility (Tofail et al., 2018). Other possibilities include the use of printed tissues at the molecular-electronic level for the development of biochips and biosensors.
- Architecture and construction: The application range of AM can be from the architectural model construction, to the automated construction of buildings (Ngo et al., 2018). Currently this field of application is very poorly developed. The use of additive manufacturing can potentially revolutionize the construction industry, reducing costs and even offering possibilities for making astronauts shelters in places like the moon (with the use of lunar regolith).
- Improvements in energy production: The deposition of materials in a precise way can be useful in the development and improvement of equipment such as fuel cells. In fuel cells it is necessary to uniformly deposit a thin platinum layer (necessary for oxidation and reduction reactions). Platinum acts as a catalyst, and it is important to use it efficiently because of its high cost. Another specific application is the repairment of turbine blades (for aeronautical and energy production), for more information, see section (General introduction, section 1.12.1).
- Art, entertainment and hobbies: additive manufacturing offers the possibility to create free shapes. One could mention, for example, its use in the field of fashion-related art (via SLS), as well as accessories for furniture, lighting and furnishings. Nowadays, it is also possible to buy additive machines for plastics (3D printers) at affordable prices, which enables the mass use of this technology.

In the work of (Tofail et al., 2018) a summary table with some applications of Additive Manufacturing was compiled, as shown in (Table 1).

Table 1: Some of the key applications of AM (Tofail et al., 2018).

Car Industry	• Integration of many parts in a unified composite part • Construction of production means • Production of spare parts and accessories • Fast standardization
Aerospace/ Aeronautics	• Production of accessories of complex geometry • Control of density, mechanical properties • Production of lighter accessories
Medicine/ Pharmaceutical Industry	• Planning of surgical operation with the use of accurate anatomic models that are based on the Computed Tomography (CT) or the Magnetic Resonance Imaging (MRI) • Development of adjustable orthopaedic implants and prosthetics • Use of printed simulated corpse for medical training in anatomy • Printing of biodegradable living tissues for tests during the development phase of the medicinal product
Sports Industry	• Production of accessories of complex geometry • Creation of adjusted protective equipment for better application and use • Creation of prototypes of multiple colours and composite materials for products testing
Construction industry	• Additive manufacturing of concretes for conventional building • Novel design of functional concretes such as self-cleaning concrete, high performance concrete • Building construction using materials found in the vicinity • Cement free building • Low cost, low energy building

Another interesting table was compiled by (Ngo et al., 2018). The table shows the average resolution data associated with each Additive Manufacturing process, where it is observed that the methods capable of producing functional parts generally have lower resolution, which is a great disadvantage for parts that require high precision, like those related with aeronautical applications (Table 2).

Table 2: A summary of materials, application, benefits and drawbacks of the main methods of Additive Manufacturing (Ngo et al., 2018).

Methods	Materials	Applications	Benefits	Drawbacks	Resolution range (μm)
Fused deposition modelling	Continues filaments of thermoplastic polymers Continuous fibre-reinforced polymers	Rapid prototyping Toys advanced composite parts	Low cost High speed Simplicity	Weak mechanical properties Limited materials (only thermoplastics) Layer-by-layer finish	50-200 μm
Powder bed fusion (SLS, SLM, 3DP)	Compacted fine powders Metals, alloys and limited polymers (SLS or SLM) ceramic and polymers (3DP)	Biomedical Electronics Aerospace Lightweight structures (lattices) Heat exchangers	Fine resolution High quality	Slow printing Expensive High porosity in the binder method (3DP)	80-250 μm
Inkjet printing and contour crafting	A concentrated dispersion of particles in a liquid (ink or paste) Ceramic, concrete and soil	Biomedical Large structures Buildings	Ability to print large structures Quick printing	Maintaining workability Coarse resolution Lack of adhesion between layers Layer-by-layer finish	Inkjet: 5–200 μm Contour crafting: 25–40 mm
Stereolithography	A resin with photo-active monomers Hybrid polymer-ceramics	Biomedical Prototyping	Fine resolution High quality	Very limited materials Slow printing Expensive	10 μm
Direct energy deposition	Metals and alloys in the form of powder or wire Ceramics and polymers	Aerospace Retrofitting Repair Cladding Biomedical	Reduced manufacturing time and cost Excellent mechanical properties Controlled microstructure Accurate composition control Excellent for repair and retrofitting	Low accuracy Low surface quality Need for a dense support structure Limitation in printing complex shapes with fine details	250 μm
Laminated object manufacturing	Polymer composites Ceramics Paper Metal-filled tapes Metal rolls	Paper manufacturing Foundry industries Electronics Smart structures	Reduced tooling and manufacturing time A vast range of materials Low cost Excellent for manufacturing of larger structures	Inferior surface quality and dimensional accuracy Limitation in manufacturing of complex shapes	Depends on the thickness of the laminates

One of the main markets for the use of Additive Manufacturing is the aeronautical sector. In the research by (Najmon et al., 2019), the use of AM in the manufacture of

multifunctional structures (those that can perform several functions simultaneously) is mentioned. Some examples of multifunctional structures would be structures with embedded electronics (in internal layers), structures with material hardness gradients, or those with thermal and/or acoustic insulation capabilities included in their own fabrication.

There are other applications in Additive Manufacturing which are related to the Materials Processing by means of laser (specifically Laser Cladding process). Laser Cladding and its applications will be studied in a separate section (General introduction, section 1.12.1).

1.3 Advantages and Drawbacks of Additive Manufacturing

1.3.1 Advantages of Additive Manufacturing

Among the advantages of additive manufacturing as a production method are (Ngo et al., 2018):

- The manufacturing of complex geometry parts with relatively high precision.
- Maximum material savings per manufactured part.
- Flexibility in part design (new ways to solve problems based on different designs).
- Customization according to the user's needs (for example, in the manufacture of medical implants).
- Ability to manufacture parts at various scales (depending on the material and the deposition technology).

In addition (Tofail et al., 2018) mentions other potential benefits:

- Direct transfer of the Design to the Component.
- Creation of hollow parts or pieces with a light and flexible structure.
- Reduction of the need for machining of parts (or directly elimination of machining), i.e. obtaining parts that are closer to their final functional shape.
- A way of approaching the objective of "zero waste", in terms of materials usage.
- Considerable reduction in time development from the concept of product to its implementation in the market.
- It is possible to establish a philosophy of “direct production” based on the demand for a certain product.

Related to AM, specifically Laser Materials Processing, as in the Laser Cladding manufacturing process, (Majumdar and Manna, 2011) mention some possible advantages of an energy source such as laser in manufacturing processes:

- The ability to produce novel microstructures in a non-equilibrium state, as well as to extend solubility in solids due to rapid cooling rates during material solidification.
- The possibility to focus an energy source with high precision, so that high flexibility and significant limitation of local thermal damage to the material being processed is possible.
- The ability to integrate laser processing technology with computer-aided design, robotics, machining, etc. is mentioned so that you can get an “all-in-one” solution.

The research of (Najmon et al., 2019) is related to the aeronautical sector. Specific AM advantages for the aeronautical sector are identified:

- Complex Part Consolidation: Traditionally, complex aerospace components contain multiple simple parts that are joined together using different types of fasteners (welds, bolts, and welds). These assemblies offer lower reliability and require higher inspection, tooling and maintenance costs compared to a single piece. Additionally, geometric errors and unwanted misalignments or deformations can exceed allowable tolerances in aerospace components. Consolidation of complex parts can be achieved using AM.
- High material economy: An important factor that contributes to the high manufacturing cost of aerospace components is the “buy to fly” ratio (which is defined as the ratio between the initial raw material weight and the final component weight). Aerospace components with large ratios (for example, thin-walled structures and turbine blades) have 20 ~ 40: 1 buy-to-fly ratios, which make planning of CNC tools very time consuming. In these cases, material usage and manufacturing cost can be significantly improved with AM's free-form manufacturing capabilities reducing the buy-to-flight ratio closer to 1: 1.
- Advantage for small series production and fast response time: AM is more profitable to produce custom parts and small production series (common in aerospace industry). Since aircraft have a useful life of more than 30 years, maintenance and replacement of legacy parts and tools can involve high

inventory costs. AM enables production of testing and replacement parts on demand for fast shipping and installation.

An example of use of AM in the aeronautical industry is shown in (Fig.1).

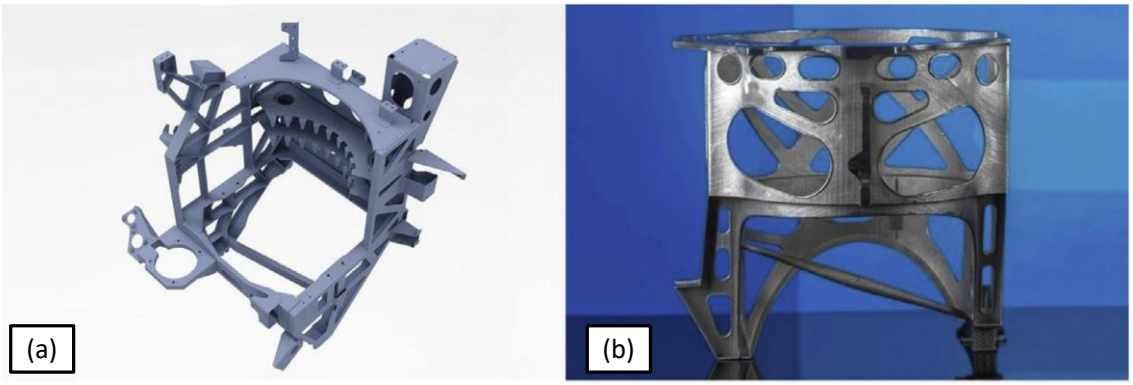

Figure 1. (a) AM hydraulic reservoir rack from Airbus consolidating 126 parts, (b) Consolidated design into one part AM (Najmon et al., 2019).

1.3.2 Drawbacks of Additive Manufacturing

Some of the disadvantages mentioned in the use of Additive Manufacturing technologies according to (Ngo et al., 2018) are:

- In the case of metals, there are problems in the manufacturing time per part (it can take a long time to manufacture a component compared to a traditional process, e.g. casting).
- High manufacturing cost, especially due to the complexity of the part and the use of expensive and difficult to process raw materials.
- Inferior quality in mechanical properties, as well as problems of anisotropy or lack of precision, especially for very small parts (due to low resolution, which in turn depends on the AM process used).
- Lack of diversity in terms of materials available for additive manufacturing (usually associated with lack of information on properties and process parameters necessary for the use of a given material in AM).

1.4 Challenges of Additive Manufacturing

According to research by (Tofail et al., 2018), the major challenge is to transfer these created "shapes" into functional structures (real objects), i.e. the main objective is to transfer AM technology from a level very close to the research level to the industrial application level. It should be noted that:

- As a “single object” it is possible to encompass a wide variety of shapes (from a slice of pizza to the wing of an airplane).
- The shape of the materials that can be used to create the objects (raw materials), layer by layer, is highly variable (for example, liquids, powdered metal, or wire).
- Given the variety of forms in which the raw material for the manufacture of the "object" can be presented, the handling of each type of raw material will be different, which in turn will limit the functional geometry of the "shapes" that each AM technology allows to produce.
- Related to the above, the "control" for the handling and deposition of raw materials to form the "object" layer by layer will be different, with each of the "controls" also having advantages and limitations.

According to (Frazier, 2014), some of the most important challenges are related to:

- Investigate the variability between the different results obtained from machine to machine (repeatability and consistency). It is proposed that the sensorization of the process (as an integrated part of the manufacturing), is a method of solving the previous mentioned variability/consistency.
- The concept of “qualification” must be redefined. It is proposed that methods, models, similarity between objects, and probabilistic type methods should be validated. The idea is to avoid the use of part-by-part type certifications to produce objects under the philosophy of “manufacture on demand”.
- The design concept must be redefined, and the possibilities offered by additive manufacturing methods must be integrated from the conceptualization of the part (the paradigms related to traditional machining must be changed).
- It is necessary to develop the basic science related to additive manufacturing. The physical models to be developed must relate microstructure, properties, and performance. The optimization of properties requires the development of new alloys, a deep understanding of the effect of fatigue on parts created by additive manufacturing methods, as well as the reduction of surface roughness.

Also, in the research of (Frazier, 2014), some other challenges identified by several authors and institutions are mentioned, among which are:

- Lack of knowledge related to the metallurgical transformations that materials undergo during an additive manufacturing process. Many additive manufacturing processes subject materials to complex thermal cycles.

- The development of material databases for use in additive manufacturing processes. There is not much development in terms of the performance of a given material for different additive manufacturing technologies with very few exceptions, such as Ti6Al4V and very few other alloys.

Referred to the aeronautical sector (Najmon et al., 2019) mention two specific challenges related to the fact that all Additive Manufacturing technologies have limitations in terms of resolution of the manufactured part, quality and consistency of the manufactured part, and especially deformations (among other defects). The specific challenges that this research has identified are:

- The need for post-processing: Aerospace applications will always require some post-processing. Additive manufacturing technologies that use powder as a raw material leave some residual porosity, and sometimes require an annealing process (for grain refinement) or a high quality surface finish machining. In complex parts such as those manufactured by AM, tooling capabilities and post-processing technology can limit the complexity of the parts, or at best delay their lead time, production, etc. The proposed solution is to improve capabilities through hybrid manufacturing systems.
- Development of standards and specifications: In this research (Najmon et al., 2019), it is mentioned that the use of AM for aerospace applications is not something new. However, there is a lot of research to be done regarding certifying a component or part, and consensus is often not reached on how this certification process should be done. There are some certifications regarding raw materials, defects, and inspection methods, but there are no specifications regarding how to achieve a correct surface finish or how to measure the component tolerance to damage.

A general idea of the advantages and drawbacks of various processing technologies for Additive Manufacturing can be seen in (Table 3). The processes compared ("SLM, EBM, powder-fed DED, wire-fed DED, Binder Jetting and Sheet Lamination"), are all applicable to manufacturing with metals (Sames et al., 2016).

Table 3: Comparison of defects and features across platforms (Sames et al., 2016).

Defect or feature	LM	EBM	DED – powder fed	DED – wire fed	Binder jetting	Sheet lamination
Feedstock	Powder	Powder	Powder	Wire	Powder	Sheets
Heat source	Laser	E-beam	Laser	Laser/E-beam	N/A; kiln	N/A; ultrasound
Atmosphere	Inert	Vacuum	Inert	Inert/vacuum	Open air	Open air
Part repair	No	No	Yes	Yes	No	No
New parts	Yes	Yes	Yes	Yes	Yes	Yes
Multi-material	No	No	Possible	Possible	Infiltration	Yes
Porosity	Low	Low	Low	Low	High	At sheet interfaces
Residual stress	Yes	Low	Yes	Yes	Unknown	Unknown
Substrate adherence	Yes	Material dependent	Yes	Yes	N/A	Yes
Cracking	Yes	Not typical	Yes	Yes	Fragile green bodies	No
Delamination	Yes	Yes	Yes	Yes	No	Yes
Rapid solidification	Yes	Yes	Yes	Yes	No	No
In situ aging	No	Yes	No	No	No	No
Overhangs	Yes	Yes	Limited	Limited	Yes	Limited
Mesh structures	Yes	Yes	No	No	Limited	No
Surface finish	Medium-rough	Rough	Medium-poor	Poor but smooth	Medium-rough	Machined
Build clean-up from process	Loose powder	Sintered powder	Some loose powder	N/A	Loose powder	Metal shavings

1.5 About the Design Methodology for AM and the use of Software

1.5.1 Design for AM

In the excellent work of (Wiberg et al., 2019), an exhaustive review of the available resources is made to establish a “Design Methodology” based on the special characteristics of additive manufacturing applied to metals. The idea of this Design Methodology is to optimize the structural design, so that aspects of topological optimization and AM are integrated as a whole. The methodology developed is called "Design for additive manufacturing (DfAM)", which includes aspects such as manufacturing methods, general guidelines for design and software available to carry out the entire process. The investigation is divided into 5 sections:

1. Method: describes the methodology under which the review of articles was carried out to establish the state of the art in MA Design.
2. State of the art and classification: the different existing DfAM classifications and processes are reviewed, where a new classification proposal is presented, as well as a new proposal for the design process.
3. Existing methods and software: it presents how to couple the different existing methods and software used for each step of the DfAM process that have been proposed in the previous section.
4. Automation of the design proposal in sections 2 and 3: An improved process that aims to automate the new proposal design system is discussed in this section.

5. Conclusion and further work: this is a chapter that summarizes and concludes, with suggestions, future research in the field of DfAM.

An example of a framework to automate a specific design methodology for AM is shown in (Fig.2). It is observed that the design validation process is an iterative process, which includes topology optimization, support structure(s) evaluation(s) and FEM modelling to calculate stresses in a combined mode within a multidisciplinary framework.

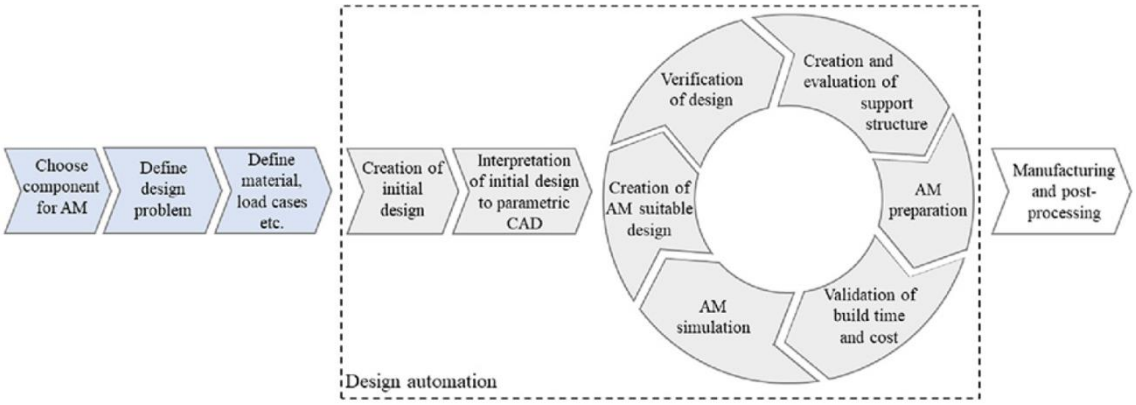

Figure 2. Proposed design automation framework (Wiberg et al., 2019).

1.5.2 The Role of Software in AM

Additive manufacturing is made possible by the advancement of other ancillary technologies, such as "Computer-aided design" (CAD), "Computer-aided manufacturing" (CAM) and "Computer numerical control" (CNC). The use of these previous three technologies together makes the creation of 3D objects possible. The need for CNC (basically referring to the machining of printed parts to their final size), is necessary because the precision of additively manufactured parts is not yet high enough, and it is generally necessary to give final machining to the objects created (Wong and Hernandez, 2012).

The software must fulfil an assistance and support function, in the sense that its good design can achieve a fluid communication with the end user of the process, as well as the coordination of all the subsystems integrated in the manufacturing of a module or product solution. Furthermore, it should allow high flexibility to enable advanced processes or sensorization of different configurations, and also the tracking or even modelling of the part manufacturing (including compensation of possible deviations), and finally the reduction of the total manufacturing time with the corresponding economic effect (Stavropoulos et al., 2018).

At the design level (in the case of powder bed technology), the software for additive manufacturing must meet the following requirements (3D SYSTEMS, 2018):

- Establish conditions for successful 3D printing: perform all the preparatory work necessary for additive manufacturing. For example, setting the correct orientation, modifying conditions for correct printing, creating supports, etc.
- Optimize the design: take full advantage of the characteristics of additive manufacturing; for example, reduce weight or improve functional properties.
- Minimize the complexity of the design to manufacture the part in the required time: streamline the preparation and optimization workflow.
- Reduce total cost of operations: minimize printing time, material consumption and post-processing work.

The intention is that good additive manufacturing software should be able to join the gap between the concept of the object (usually a 3D CAD model) and the set of instructions that will allow the part to be built on a generic AM machine. An example of a working diagram for comprehensive Additive Manufacturing software is shown in (Fig. 3).

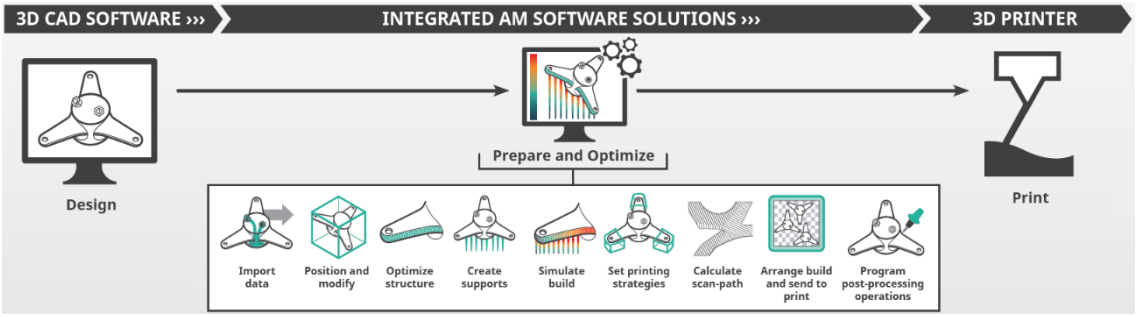

Figure 3. Scheme with the software-assisted workflow intermediate stages description (from the conception of a part, to its manufacture), in a generic machine (3D SYSTEMS, 2018).

In summary, a strong integration of automation, control and software within AM is necessary to achieve high repeatability, i.e. that the manufactured parts exhibit low variability in terms of mechanical properties. In addition, the design freedom achieved through the various methods in AM must be exploited and integrated from the beginning as part of the manufacturing process.

1.6 On Hybrid Machines and the Integration of AM in the Industry

According to (Sealy et al., 2018), AM hybrid processes are defined as: “the use of AM with one or more secondary processes or energy sources that are fully coupled and synergistically affect part quality, functionality, and/or process performance. Three key

features to this definition include: (a) fully coupled processes, (b) synergy, and (c) part and/or process improvement".

The research of (Sealy et al., 2018) focuses on exploring the possibilities of hybrid manufacturing, especially with regard to changing paradigms about design. To establish a reference framework, it is first necessary to define what is to be studied, and its scope. Therefore, in this research, a clarification of concepts is made about changing the conception that hybrid manufacturing is a sum of consecutive isolated processes, and moving to a concept where the processes "is at the service" material to turn it into something with much improved features.

The three key characteristics that define a hybrid manufacturing process are thoroughly discussed:

- All the processes involved must be fully integrated. It is not possible to call hybrid manufacturing, for example, a process that is sequential. A process that could be described as sequential is one in which a part of the piece is printed, say by the Laser Cladding process, and subsequently machined in a completely subsequent operation.
- The use of high synergy (it is related to the increase in the characteristics of the material that is manufactured by the combination of two or more processes): it seeks to obtain a part with characteristics that are more than the simple sum of the processes per separate (philosophy of the type 1 + 1 = 3).
- The process improvement (such as a study to carry out a paradigm shift through the use of hybrid manufacturing technology), transforming it in something capable of increasing desirable characteristics in the material (for example, hardness or ductility), compared to other traditional manufacturing methods.

In the research of (Merklein et al., 2016), the possibilities of integrating AM technologies in a process combined with traditional manufacturing technologies are analysed, exploiting the advantages of both worlds (traditional manufacturing with additive manufacturing). Emphasis is placed on the integration of additive manufacturing in CNC-type machining centres to generate a symbiosis for the production of "all-in-one" parts. In that research a study of several technologies that can be integrated in machining centres is made; and it is concluded that the main interest in the creation of hybrid solutions is the enormous freedom of design, process flexibility and high efficiency in the use of raw materials. Some limitations related to the increase in the number of

control parameters for the manufacturing process of the parts are also mentioned, in addition to the variability of mechanical properties in the products manufactured by AM, and the limited capacity of hybrid technologies for large-scale production. But, on the other hand, the ability of CNC + AM technologies to produce batches of small parts relatively inexpensively is taken as an advantage. In (Table 4) a summary of the traditional + additive manufacturing categories that the aforementioned author has investigated is presented.

Table 4: Categorization of additive manufacturing processes and the combination with conventional processes (Merklein et al., 2016).

Additive Process	Characteristic	Process Combination
Laser Beam Melting	+ high complex part geometry - limited on plane building platform - risk of powder dust by opening the machine	- integration in process chain only
Laser Metal Deposition	+ build up on any freeform substrate + multimaterial production - risk of powder dust by opening the machine	- integration in process chain - integration in CNC milling and turning centers for a sequential process
Metal Powder Application	+ small heat input - risk of powder dust by opening the machine - patented by Hermle	
Gas Metal Arc Welding	+ high build-up rate + well known process - inadequate accuracy	

The limitations for the industrial implementation of Additive Manufacturing technology are the main topic of the research of (Stavropoulos et al., 2018). Limitations such as: low work speed, limited work volumes and post-processing of the parts (secondary treatments) are analysed; as the main causes that prevent the full implementation of AM in the industry. It is mentioned that the main opportunity to integrate AM in the industry is its combination with traditional manufacturing technologies (as machining). As a proposed solution, the use of integral manufacturing cells with a high degree of automation is proposed. The necessary aspects to ensure consistency in product quality are also discussed; without sacrificing flexibility, productivity and economy. The use of integrated technologies in AM would be considered to produce mainly high value parts. The schematic description of the proposed integration of Additive Manufacturing in industry is shown in (Fig. 4).

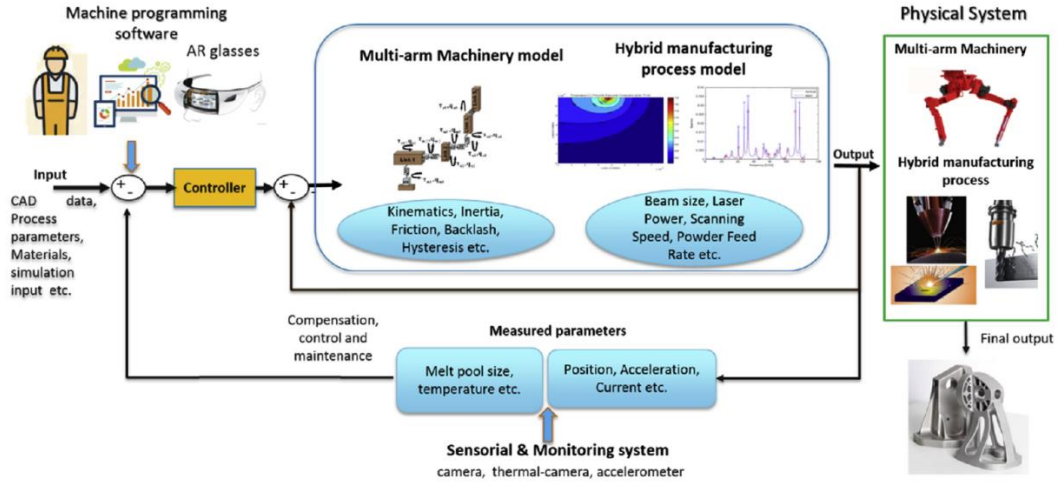

Figure 4. Schematic representation of the approach proposed using a set of subsystems (robotic positioning system, Directed Energy Deposition, milling centre, laser ablation, thermal camera, etc.), (Stavropoulos et al., 2018).

In the work of (Tofail et al., 2018), a representative table is presented with some of the representative brands and machines for the different additive manufacturing technologies for metals, observing a large dominance of manufacturers of European and North American origin (Table 5).

Table 5: General characteristics of AM of metals and manufacturers of AM machines (Tofail et al., 2018).

AM system and manufacturer		Build volume (mm × mm × mm)	Heat source and process	Country of manufacturing
Powder bed	ARCAM (A2)	$X = 200–300$	Electron beam melting (EBM)	Sweden
	EOS (M280)	$Y = 200–300$	Direct Metal Laser Sintering (DMLS)	Germany
	Concept Laser Cusing (M3)	$Z = 200–350$	Selective Laser Sintering/Melting (SLS/SLM)	Germany
	MTT (SLM 250)			Germany
	Phoenix system group (PXL)			France
	Renishaw (AM 250)			UK
	Realizer (SLM 250)			Germany
	Matsuura (Lunnex Advanced 25)			Japan
Powder feed	Optomec (LENS 850-R)	$X = 600–3200$	Laser engineered net shaping (LENS)	USA
	POM DMD (66R)	$Y = 1500–3500$	Direct Metal Deposition (DMD)	USA
	Accufusion Laser consolidation	$Z = 350–1000$	Laser consolidation (LC)	Canada
	Irepa laser (LF 6000)		Laser Deposition (LD)	France
	Trumpf			Germany
	Huffman (HC-205)			USA
Wire feed	Sciaky (NG1)	$X = 600–750$	Electron beam melting (EBM)	USA
	MER plasma FFF	$Y = 500–600$	Plasma arc melting	USA
	Honeywell ion fusion formation	$Z = 500–5000$	Plasma arc melting	USA

1.7 Economic Aspects of Additive Manufacturing.

According to (Tofail et al., 2018), the success of the Additive Manufacturing concept depends on how well these “parts” fulfil the task for which they were designed (direct use in the market). The desirability of AM (in terms of the flexibility of this technology), must be in line with the fact that it is necessary to "assure" the quality of the material from which the "objects" are created, i.e. how well the parts manufactured by additive technology meet predefined material standards; all the while trying to keep production

costs competitive. Much of the current excitement will depend on how well the problems related to the consistency of the mechanical properties of the manufactured materials are solved, so that additive manufacturing truly becomes an important field of industrial manufacturing.

At the level of a business plan, (Frazier, 2014) indicates that many factors must be taken into account. Among the most important are:

- The ratio of fixed costs / non-recurring manufacturing costs.
- The cost of certification of the manufacturing process and the components manufactured by it.
- Logistics costs (production orders will generally be on-demand).
- Cost of time (an additive manufacturing process will be slightly slower when a high volume of production is required).

In the same document (Frazier, 2014), some ideas on cost estimation techniques are included, in addition to a methodology to allocate these costs based on the stage of product development: (i) costs based on activities carried out, (ii) total life cycle costs, (iii) costs based on objectives and (iv) costs totals.

An interesting way to visualize the effect of the number of pieces on the profitability of an AM process is given by (Fig. 5), a theoretical graph where it is assumed that:

- The total cost is a linear function of the number "x" of pieces that are produced.
- Fixed costs for AM technology are one-tenth of those for conventional manufacturing.
- Recurring costs for an AM technology are higher by a factor of 1.5x and 2x (taken as two separate case studies).

The y-intercept on the graphs in (Fig. 5) represents the fixed cost, while the slope is the ratio of the recurring cost of the process divided by the recurrent cost of conventional manufacturing.

In general, conventional manufacturing (involving metal working, machining, etc.), has higher fixed costs, e.g. tools, dies, and fabrication space. However, its recurring costs are usually lower than those of AM, for example, in raw materials. This makes conventional manufacturing processes more competitive for large production runs. The crossover point (equivalent cost point) depends on the relationship between the recurring cost of AM and the recurring cost in conventional manufacturing. The breakeven point for a 2x recurring cost index is around 90 units, while it is 175 units for a 1.5x recurring index. For a 1x recurring cost ratio, AM costs would be lower for all production volumes. In this

research it is argued that the cost of raw materials (powder and wire) is a significant recurring cost factor for AM technologies, therefore, it is necessary to emphasize their price reduction.

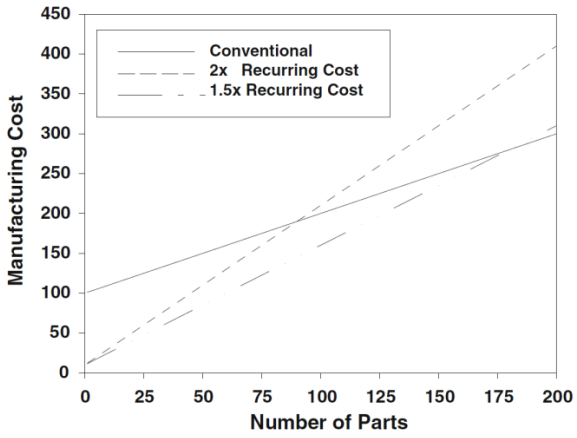

Figure 5. Low volume business case for AM vice conventional fabrication methods (Frazier, 2014).

The factors for and against the two approaches under study (Additive Manufacturing compared to Traditional Manufacturing), can be summarized in (Table 6).

Table 6: Factors favouring AM Vice conventional manufacturing (Frazier, 2014).

Favor AM	Favor conventional manufacturing
Low production volumes	Large production volumes
High material cost	Low material costs
High machining cost	Easily processed/machined materials
Capital investment	Centralized manufacturing
Logistics costs	
Transportation costs	
Prototyping	

One conclusion of this study is that Additive Manufacturing is profitable only for small production batches, where the high cost of raw materials is offset by the high fixed costs of conventional manufacturing methods. It is also possible to create business opportunities by offering certain large organisations (e.g. Defence), the ability to reduce the cost of inventory holding, logistics footprint or energy.

In the research by (Najmon et al., 2019), the focus is on the application of AM in the aerospace industry. However, market-related aspects are also studied, such as the use of additive technology for different types of industry (Fig. 6). The final conclusion of this study is that additive manufacturing is cost-effective in the aerospace maintenance industry as long as the repair time will be short and also the use of the technology will be focused on high value-added parts. It is concluded that most of the time spent on the

repair of high value-added parts is spent on the preparation of the part, and this is sometimes comparable to that spent on the manufacture of a new part.

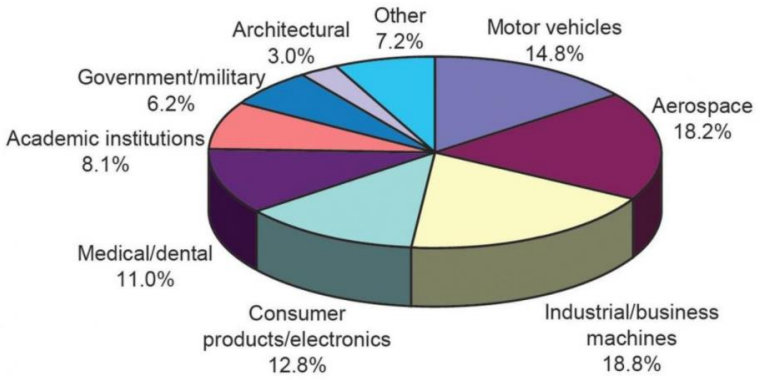

Figure 6. Additive manufacturing market share by industry (Najmon et al., 2019).

At the profitability level, according to (Tofail et al., 2018), the success of additive manufacturing lies in how well this manufactured "object" serves its intended use in the market. Translating the superiority and convenience of AM in creating forms and structures into useful products is essential for their adoption in the industrial matrix. Commercial success will also depend on how much it can be ensured that the properties of the materials, in the desired shape or structure, actually comply with the accepted and predefined standards while the cost of production is competitive. In other words, market acceptance of products manufactured through AM will occur when the parts produced through this technology meet the desired properties through appropriate measurement or metrology. This inter-relationship between market, manufacturing, materials and metrology is shown in (Fig. 7), (4M methodology). Related to (Fig. 7), the (Table 7) shows a summary table of the main key issues related to the 4M methodology.

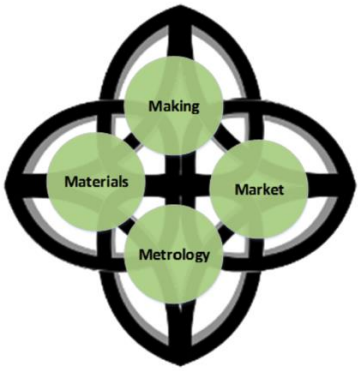

Figure 7. The four M's (4Ms) of additive manufacturing: Materials, Making, Metrology and Market.

Table 7: A summary of the issues related to the 4Ms of additive manufacturing (Tofail et al., 2018).

Making	- Evolution of the layer-by-layer fabrication technology with versatility, flexibility and customization - Wide range of materials including metallic, ceramic, polymers and their combinations in the form of composites, hybrid, or functionally graded materials (FGMs) - Development of self-contained, robust, user-friendly, safe, integrated system that would provide the required power, scan motion and speed, high feature-volume resolution with concomitant energy for part fabrication and dimensional control.
Material	- Manufacturing techniques, data communications and system changes within Industry 4.0 or Manufacturing 4.0 - Homogeneity prerequisite - Surface key properties - Extent of required finishing - Nanometers to micrometre feedstock material size
Metrology	- Need for real time in line quality assurance - Monitor and control towards optimization - High level of customization of the techniques for *in situ* measurements - High accuracy and measurement speed requirement
Market	- Factory 4.0 or Manufacturing 4.0 benefit from Digital Innovation Hubs - AM industries range from space to toy to food and represent a multi-billion dollar industry - Cheaper machines makes AM more accessible

Related to the supply chain, the work of (Szymczyk-Ziółkowska et al., 2019) shows that it is possible to establish production standards based on the particularities of Additive Manufacturing. A logistics methodology is also proposed that would enable (from the point of view of the supply chain network), the management of storage and packaging and delivery processes. The full introduction of AM-based production would minimise the costs and space required for logistics procedures. In the area of warehouse management, significant benefits were also identified, such as: lower material stock

levels, and an optimisation of all logistical aspects of the transition of assets from traditional manufacturing to additive manufacturing.

In conclusion, significant time and cost savings are possible. The packaging processes would remain similar to the ones used in traditional production. The summary of the proposed logistics methodology in this research is shown in (Fig. 8).

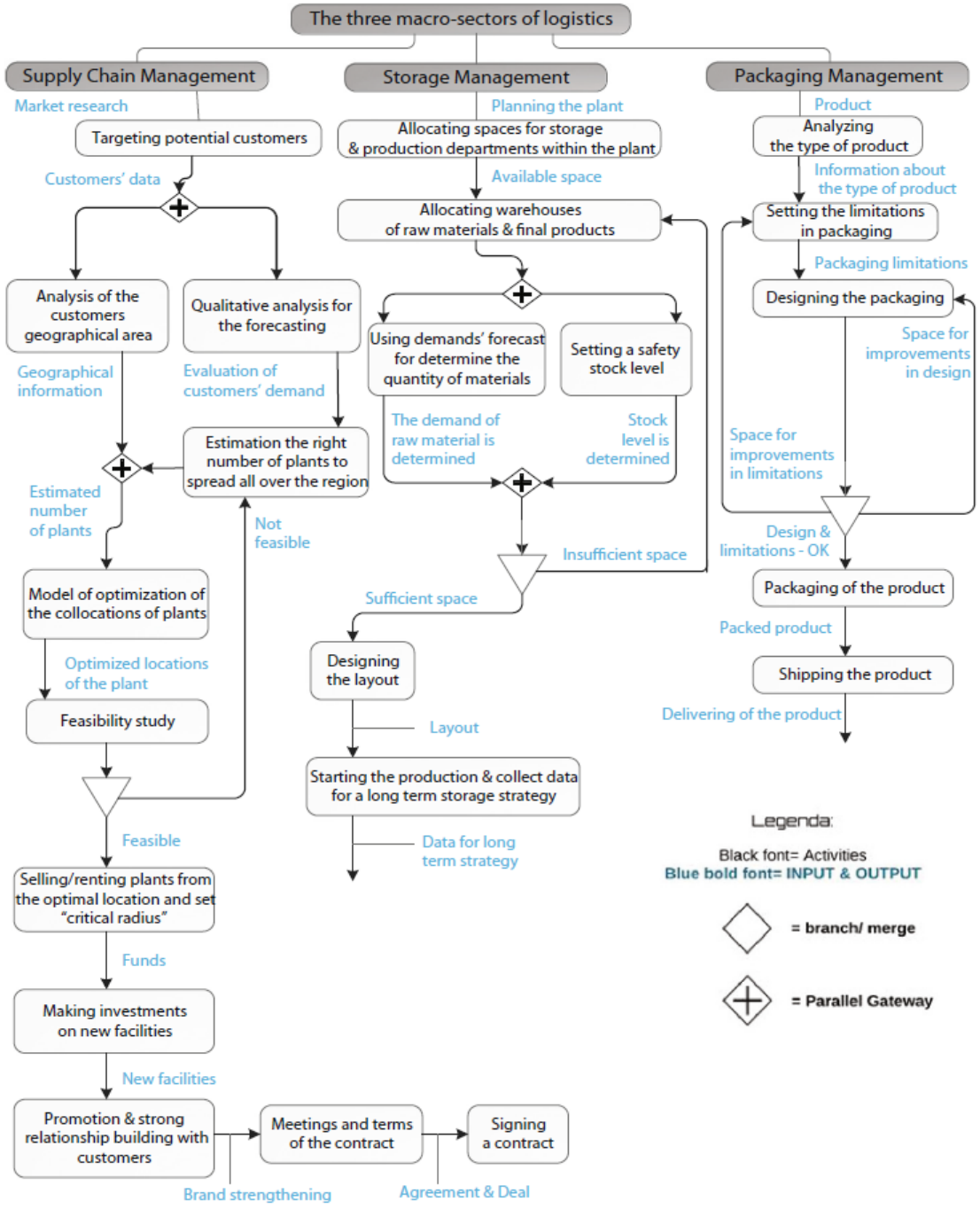

Figure 8. Processes, divided according to the three macro-sectors of logistics (supply chain management, storage management, packaging), to be carried out in case of manufacturing technology replacement (Szymczyk-Ziółkowska et al., 2019).

1.8 Several Classification Approaches to Additive Manufacturing

Regarding to standardization level, (Tofail et al., 2018) mentions that ISO and ASTM have classified Additive Manufacturing processes in the following seven categories:

1. Binder jetting (BJ).
2. Directed energy deposition (DED).
3. Material extrusion (ME).
4. Material jetting (MJ).
5. Powder bed fusion (PBF).
6. Sheet lamination (SL).
7. Vat photopolymerization (VP).

In (Fig. 9) a general map of the main industrial processes of Additive Manufacturing is shown. This first classification is a function of the material to be processed. Different raw materials are included such as: metals, plastics, composite materials, waxes, plaster, sand and paper.

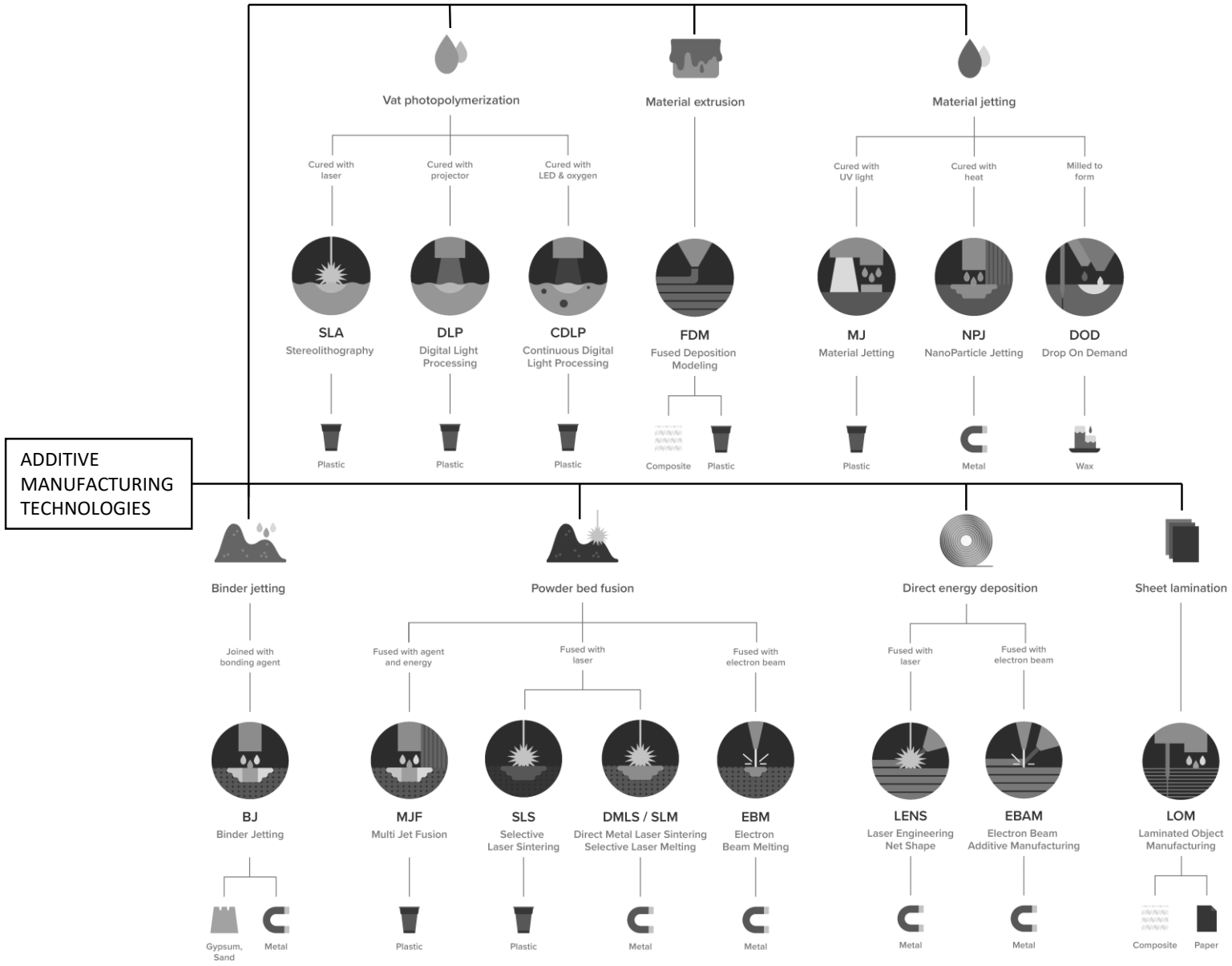

Figure 9. Overview of the most important additive manufacturing technologies in the industrial sector (Redwood, 2021).

A second classification can be made based on the temperature necessary for processing the raw material:

- Polymers and all associated products (such as those with a composite matrix) have relatively low melting points. In addition to low melting points, polymers have the advantage that they generally do not require special production environments (e.g. the use of protective atmospheres or vacuum). These polymers are relatively easy to cure and tend to bond easily.
- On the other hand, the fabrication of metal or ceramic parts in the context of AM is not easy due to the high melting points of the raw material. For this reason, lasers are a convenient means to use as an energy source for melting these high melting point materials, especially in the case of metals.

Another possible classification of additive manufacturing technologies is based on the physical state of the raw material, being it liquid, solid or powder (Fig. 10).

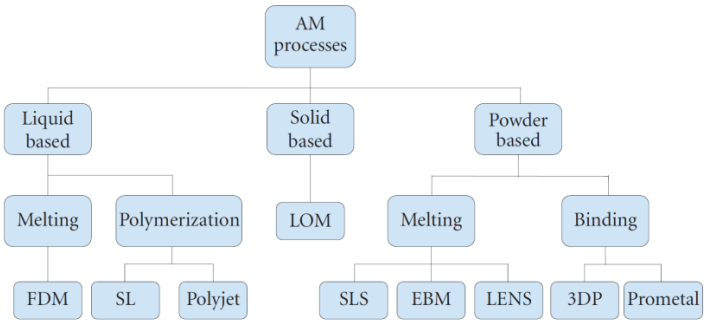

Figure 10. Three-dimensional printing processes (Wong and Hernandez, 2012).

For this research, a different categorisation will be used, based on the ability of a process (referring to a metallic material) to create parts with the characteristic of being solid and dense as a result of a single (one-step) manufacturing process.

According to (Azam et al., 2018), when a metal is used as a raw material in an Additive Manufacturing process, there will be a classification depending on the amount of post-processing of the cladded material.

- If the object has been manufactured without the need for post-treatment, it is said to be of "Direct Manufacture". An object manufactured from Direct Manufacturing is consolidated as a single piece from the beginning (the raw material solidifies to form the final part).
- If the object has been manufactured and needs some other treatment to consolidate the piece, it is said that the object is of type "Indirect Manufacture".

In an Indirect Manufacturing object, the metallic material is shaped by means of a binder, and post-processing generally makes use of a treatment that combines temperature and pressure to achieve the desired material density. The classification for these AM processes in metals is shown in (Fig. 11).

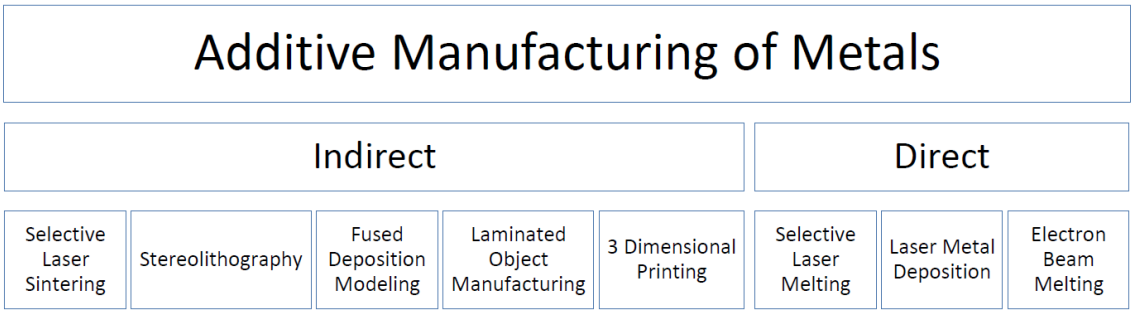

Figure 11. Classification of metal AM processes (Azam et al., 2018).

1.9 Metal Alloys used in Additive Manufacturing

The primary objective of an Additive Manufacturing process using metals will be to consolidate the raw material (powder, wire or sheets) into a dense and functional piece. The consolidation of the material through a melting-solidification process will make use of an energy source (laser, electron beam, electric arc as the most common).

For metallic materials (DebRoy et al., 2018) shows in (Table 8), a list of alloys commonly used in AM, along with their applications.

Table 8: Common additive manufacturing alloys and applications (DebRoy et al., 2018).

Alloys ⇨ Applications ⇩	Aluminum	Maraging steel	Stainless steel	Titanium	Cobalt chrome	Nickel super alloys	Precious metals
Aerospace	X		X	X	X	X	
Medical			X	X	X		X
Energy, oil and gas			X				
Automotive	X		X	X			
Marine			X	X		X	
Machinability and weldability	X		X	X		X	
Corrosion resistance			X	X	X	X	
High temperature			X	X		X	
Tools and molds		X	X				
Consumer products	X		X				X

1.9.1 Alloys and Material Properties

The properties of materials produced by additive manufacturing are very special. In the creation of metallic objects (depending on the technology), a small molten bath and the resulting rapid solidification process are characteristic.

The reasons for the special characteristics of a material manufactured by AM according to (Aumund-Kopp and Riou, 2019) are: (i) fine microstructure due to rapid solidification,

(ii) anisotropy in the build direction of the deposited material layers due to their overlapping (layers are built up in the Z-direction). In the XY directions it is possible to eliminate anisotropy with a suitable material deposition strategy. On the other hand, practically porosity-free material can be obtained with a suitable deposition strategy (with densities of about 99.9% as is common). In addition, additive manufacturing can be combined with a technique such as HIP to achieve full material density.

1.9.2 Nickel Base Alloys for Additive Manufacturing

Within the types of alloys available for additive manufacturing, this review will focus on nickel super alloys. In addition, of the common types of raw materials that can be used, the use of powder metal will be explored.

There are several Nickel-based alloys available for AM. According to (DebRoy et al., 2018), some of the most common nickel-based alloys in AM are also among the most common alloys used in the aircraft industry: Inconel 625, Inconel 718, as well as Invar 36. The measured mechanical properties for different AM technologies have been compiled in (Table 9).

Table 9: Summary of mechanical properties of Ni-base alloys fabricated by AM in literature, compared to traditionally processed counterparts, where HT=heat treated (DebRoy et al., 2018).

Alloy	P (W)	v (mm/s)	H (J/mm)		Orientation	E (GPa)	σ_y (MPa)	σ_{uts} (MPa)	Elongation (%)	HV
Powder bed fusion – laser heat source										
Invar 36	400	1800–4300	0.22	As-deposited	Long.		400	535	14	
					Transv.		340	455	30	
				HT	Long.		311	447	32	
Inconel 625	200	800–1200	0.25	HIP	Long.		380	900	58	347
					Transv.		360	880	58	296
Inconel 625	50	130	0.38	As-deposited	Long.	202.24 ± 4.12	800 ± 20	1030 ± 50	8–10	
					Transv.	140.66 ± 8.67	1070 ± 60	720 ± 30	8–10	
Haynes 230	200	450–1200	0.44	As-deposited	Long.	205 ± 4	798 ± 5	1102 ± 6	28 ± 1	
					Transv.	152 ± 1	656 ± 4	941 ± 2	32 ± 3	
Powder bed fusion – electron beam heat source										
Inconel 625	1800	10^4	0.18	As-deposited	Transv.		410	750	44	224
				HIP	Transv.		330	770	69	
Directed energy deposition – powder feedstock										
Inconel 718	–	–	–	As-deposited	Long.		650	1000	38% (Reduction in area)	
				HT	Long.		1257	1436	13% (Reduction in area)	
				HT+ HIP	Long.		1155	1380	20.4% (Reduction in area)	
Inconel 718	2350	8	294	As-deposited	Long.		590	845	11	
				HT	Long.		1133	1240	9	
					Long.		1170	1360	18	
Directed energy deposition – wire feedstock										
Inconel 625		5		As-deposited	Long.	180		722 ± 17	42.27 ± 2.4	240–270
					Transv.			684 ± 23	40.13 ± 3.7	
Inconel 718		5		As-deposited	Long.	154 ± 1	473 ± 6	828 ± 8	28 ± 2	
Inconel 718				As-deposited	Long.	163	666	1022	26.1	
				HT	Long.	24.1	947	1242	23.5	
				HT	Long.	25.8	932	942	22.2	
Traditionally processed										
Inconel 718	Cast - typical						915	1090	11	266 (max)
	Annealed and Aged - minimum						862	1034	20	318
Inconel 625	Cast - typical						350	710	48	266 (max)
	Annealed - typical						430	940	51.5	145 (min)
Invar 36	Cast - typical						265	483	44	–
	Annealed - typical						260	470	37	131

A different compilation of Nickel-based alloys used in AM is presented by (Graybill et al., 2018) in (Table 10). Some of the property data in the direction normal to the direction of the material built layers (Z direction) is included in (Table 10).

Table 10: Achievable room-temperature mechanical properties for various materials and AM processes (Graybill et al., 2018).

Achievable Properties (Room Temperature)									
		Yield Strength (MPa)		Ultimate Tensile Strength (MPa)		Elongation at Break (%)		Hardness	
Material	Process	XY	Z	XY	Z	XY	Z	XY	Z
Hastlloy X	SLM	-	815 [69]	-	937 [69]	-	36 [69]	277 ± 3.9 (HV0.5) [17]	-
Inconel 100	DED	-	956^ [39]	-	1050 - 1070^* [39]	-	9 [39]	-	-
Inconel 625	SLM	-	400^ [61]	-	930^ [61]	53*^ [60]	58*^ [60]	355-360 (HV0.5/30)^ [55]	-
	EBM	-	330 [39]	-	770 [39]	-	69 [39]	280 (HV0.1/10) [39]	250 (HV0.1/10) [39]
	DED	460 - 520* [33]	460-480* [33]	860- 920* [33]	860- 800* [33]	43-46* [33]	40-48* [33]	-	225 (HBW 2.5/62.5) [12]
	BJ	-	327^ [9]	-	612^ [9]	-	45^ [9]	237.4 ± 4.9 (HV0.1/10)^ [9]	-
Inconel 718	SLM	1186^ [62]	1180^ [62]	1440^ [62]	1400^ [62]	24.5 ± 1.1 [19]	21.5 ± 1.3 [19]	395.8 (HV0.1/10) [20]	338 ± 11 (HV10/10)^ [63]
	DED	1097.6^ [64]	-	1321.0^ [64]	-	-	-	456.6 (HV0.5/10)^ [31]	281 (HV0.5/10) [65]
Inconel 939	SLM	-	-	1000 - 1020^* [66]	1275 - 1300^* [66]	14.5^* [66]	25^* [66]	450 (HV0.5)^ [66]	-
K465	DED	917 [67]	-	1205 [67]	-	8.5 [67]	-	-	498 (HV0.5/15) [67]
Nimonic 263	SLM	843 ± 20^ [76]	709 ± 7^ [76]	1268 ± 7^ [76]	981 ± 4^ [76]	29 ± 3.0 [76]	70 ± 1 [76]	-	-
Rene 142	EBM	-	-	-	-	-	-	39 (HRC) [68]	-
^ denotes property was achieved through heat treatment. * denotes the value is approximated from research paper.									

In (Fig. 12) a selection of mechanical properties values for the uniaxial tensile test from different investigations compiled by (Graybill et al., 2018) is shown. The wide dispersion of two representative mechanical properties (the fracture strength and elongation at break) can be noticed for two of the most common aeronautical alloys: Inconel 625 and Inconel 718. The existence of a wide dispersion can be attributed to the lack of standards regarding the process parameter window for different types of Additive Manufacturing technologies.

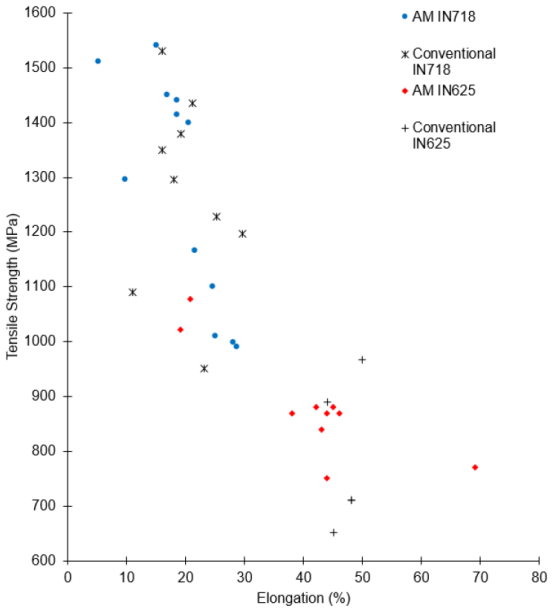

Figure 12. Tensile Strength and Elongation at break for conventionally and additively manufactured IN625 and IN718 (Graybill et al., 2018).

Regarding the ductility and anisotropy for the Tensile Strength Limits in the longitudinal and transverse directions of specimens made of Nickel based alloy through AM, (DebRoy et al., 2018) have created the graphs shown in (Fig.13). The conclusions on this latest research are: (i) regarding material anisotropy there is no clear trend, which is the result of lack of data and research to establish the relationship between process parameters, microstructure and mechanical properties. (ii) The same conclusion can be drawn with respect to ductility due to the lack of research and data, especially for nickel-based alloys manufactured by AM.

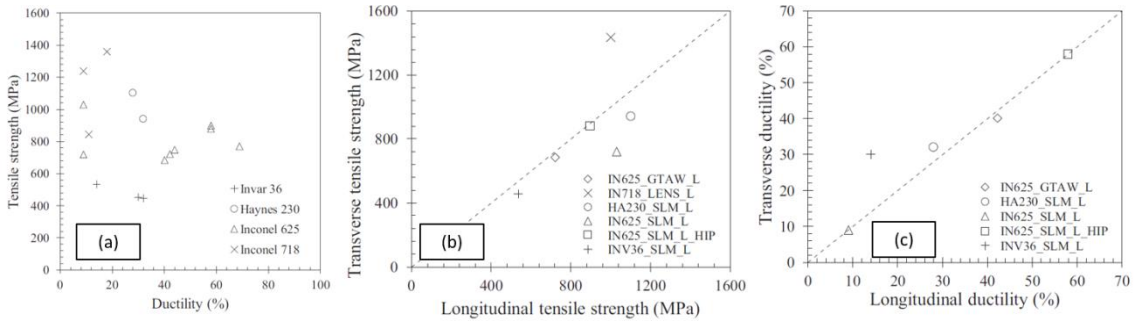

Figure 13. (a) Tensile strength versus uniaxial tension ductility for Ni-base alloys fabricated via AM. Determination of presence of mechanical anisotropy in additively manufactured Ni-based alloys with (b) transversal versus longitudinal tensile strength and (c) transversal versus longitudinal ductility (DebRoy et al., 2018).

The range of mechanical properties of an additively manufactured material ranges from being superior in quality to that of a cast material, but inferior to that of a forged material (Aumund-Kopp and Riou, 2019).

1.9.3 Use of Metal Powders in Additive Manufacturing

According to (DebRoy et al., 2018), the use of powders for Additive Manufacturing is a convenient method of adding the necessary material for part manufacture. It offers flexibility in the sense that metal objects with certain specific metallurgical characteristics can be constructed by simply mixing powders with different types of alloys. A disadvantage is that it is very difficult to produce high quality metal powder (it is very expensive). The characteristics that a high quality metal powder must have are as follows:

- Adequate shape (sphericity).
- Uniform size distribution.
- Surface morphology (smoothness is intended).
- Chemical composition according to alloy standard, without segregation.

- High fluidity.
- Low porosity (porosity can be transferred to the part during manufacture).

The quality of the powder is highly dependent on the manufacturing process. According to (Aumund-Kopp and Riou, 2019), the gas atomization process (GA), where a flow of liquid metal is atomized with the help of an inert gas at high pressure, is the most common process. The gas atomization process produces very spherical powder, which is beneficial for its fluidity. Other process uses water instead of a gas to atomize the metal, with the disadvantage that the powder produced is quite irregular.

Other common powder production techniques are according to (Sames et al., 2016): rotary atomisation (RA), plasma rotating electrode process (PREP), plasma atomisation (PA), and others. Some atomisation techniques produce irregular shapes (such as RA), some produce a large amount of satellites (such as GA), and some produce very spherical and smooth powder (such as PREP and PA).

A major problem is the porosity of the powder. The porosity of the powder is due to the manufacturing process, in the case of the gas atomisation (GA) method. This porosity is then trapped inside the part itself, due to the rapid solidification during the manufacturing of the object. The spherical shape of the cavities is a characteristic of the gas porosity, which makes them easy to recognise.

The (Fig. 14) shows the morphology of different types of metal powder and also the effect on the quality of the deposited material depending on the raw material.

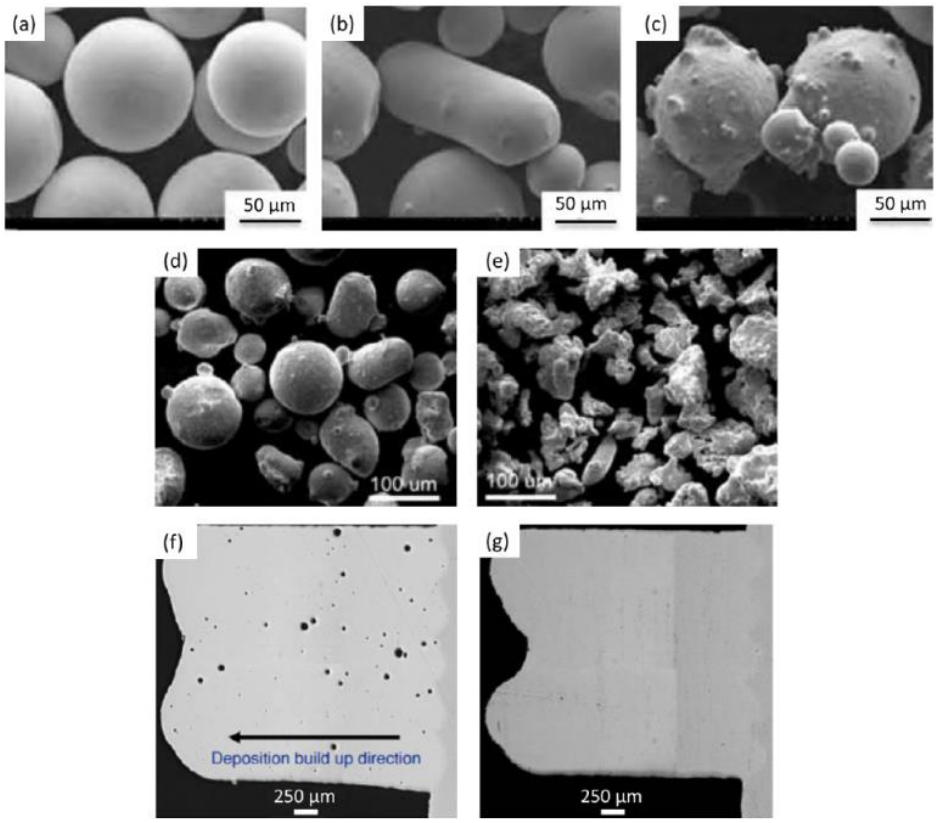

Figure 14. SEM image of alloy powders manufactured by (a) PREP (b) RA and (c) GA process. Comparison of shape of powders fabricated by (d) GA and (e) WA process. IN718 component fabricated using (f) GA and (g) PREP powder, (DebRoy et al., 2018).

The powder size to be used depends on the AM technology (Aumund-Kopp and Riou, 2019). For powder bed technology, the usual particle size will be between 10 and 20 µm, with a maximum of up to 50 µm. All powder particles smaller than 10 and even down to 10 µm should be discarded. Using too fine a powder will cause flowability problems (due to the high surface/volume ratio). For the Laser Cladding process (and for the EBM process), the typical powder size will be between 50 and 100 µm (EBM) and up to a maximum of 150 µm (for Laser Cladding).

The size distribution of the powder should be as uniform as possible. In addition to a uniform size, it is also important that the surface of the powder is as smooth as possible. The use of a good quality powder allows it to be concentrated in the focal plane (the working area), and in the case of a Laser Cladding process will help the deposition of material to be efficient. The reduced size of the powder allows this expensive raw material to be used more efficiently. In the case of Additive Manufacturing processes using powder bed technology, other sizing factors, such as the packing factor, must be considered. These aspects for powder bed processes will not be developed in this paper,

as that technology will not be used in this thesis. For more information, the reference of (DebRoy et al., 2018) can be reviewed.

Recycling of metal powder is only possible to a limited extent. For example, according to (Sames et al., 2016), with the reuse of previously collected powder, some of the sphericity of the powder is lost. It is mentioned that the flowability of the powder itself is not greatly affected by reusing the powder, because while its moisture is reduced, the percentage of powder with satellites is also reduced. In (Renderos et al., 2017), it is concluded that it is possible to recondition and reuse the metal powder for a Laser Cladding process a certain number of cycles before a noticeable decrease in mechanical properties is noticed.

1.9.3.1 About the Chemical Composition of Metal Powders

The composition of the metal powder must comply with the standards of the respective alloy. Just as important as the composition of the powder are the "interstices" within the raw material itself. Interstices can contain gases such as nitrogen, as well as carbon or sulphur, and other impurities (e.g. intermetallics), which can negatively affect the mechanical properties of the alloy. The use of gas atomisation powder production technology tends to generate a raw material with high oxygen content. The high oxygen concentration is due to the high surface area/specific area ratio of the powder. The variation in powder composition can affect the alloy's melting temperature, mechanical properties, weldability (understood as the ability to form a good quality metallurgical joint), thermal properties, etc. (Aumund-Kopp and Riou, 2019).

The composition of the metal powder can vary depending on the number of times it is reused. This is especially true for alloys that are very sensitive to the presence of oxygen, nitrogen or other gases, e.g. Ti6Al4V (Sames et al., 2016).

1.9.3.2 Regulations Applicable to Metal Powders

Apart from the nominal alloy composition, there are regulations for the quality control of the powder that include aspects such as: Fluidity, Apparent density, Angle of repose, granulometry and foreign matters content due to the manufacturing process. For more details see the references (Aumund-Kopp and Riou, 2019; DebRoy et al., 2018; Sames et al., 2016).

1.10 Laser Material Processing and Additive Manufacturing

The variety of processes in which a laser beam can be used is very wide and can range from basic scientific research and industrial processes to more mundane applications (Majumdar and Manna, 2011). In this context, all biomedical, spectroscopic, metrological, etc. processes will be excluded and the emphasis will be on the processing of metallic materials only.

At the material processing level, a laser is particularly interesting as a source of very high quality thermal energy. A laser beam makes it possible to work with a material through a heating process that can be very focused and fast.

According (Majumdar and Manna, 2011), it is possible to classify the use of lasers in materials processing into four different categories: Forming, Joining, Machining and Surface Engineering, all of which are laser assisted. It is also possible to divide laser material processing according to the amount of energy used in the process:

- "Low Energy" processes are those where the amount of energy used in the laser beam is limited, with very small changes at the level of microstructure and affected volume, absence of phase change (there is no perceptible change of state). Two examples of Low Energy processes are polymer curing and integrated circuit marking.
- “High Energy” processes are characterized by a high amount of energy used in the laser beam and generally require a change of state or phase transformation in the material being worked. Examples of this type of process are laser cutting, in addition to welding, tempering and the deposition always by laser (Laser Cladding).

1.10.1 The Laser and its use in the Industry

1.10.1.1 Definition of Laser.

Light amplification by stimulated emission of radiation (laser) is a coherent and monochromatic source of electromagnetic radiation that can propagate in a straight line with negligible divergence. In other words, a laser is simply a specific type of light that has been amplified giving energy to something called the active medium (stimulating this medium), creating in turn radiation and this radiation in turn stimulates the medium that generates it (Berkmanns and Faerber, 2010).

1.10.1.2 Principle of Operation of a Laser

The active medium will be simplified as a set of atomic nuclei surrounded by electrons. The form of excitation (the way in which the active medium is stimulated) is by means of electromagnetic radiation of energy E according to (Eq. 2).

The operational process of a laser can be described in four distinct stages (Berkmanns and Faerber, 2010):

- It start from an active medium in a low energy state (state E_1), as shown in (Fig. 15a), to which energy E is supplied.
- Atoms are excited to a state of higher energy, which is reflected as a transfer of electrons (e), towards layers that are also of higher energy (from state E_1 to state E_2), as shown in (Fig. 15 b).
- Atoms in the excited state begin to oscillate, making the "high-energy state" very unstable. To return to a "low-energy state", a process known as "spontaneous emission" takes place, as it is not triggered by any external agent. In general, the half-life of an excited state is very low, in the order of 10^{-8} s, but in certain cases a meta-stable state can be reached with duration of the “high energy state” on the order of 10^{-5} s. The photons emitted by spontaneous emission from an atom are neither monochromatic, nor directional, nor coherent (Toyserkani et al., 2005), as shown in (Fig. 15 c). The energy degradation can also take the form of heat or other energy pulse E. This process does not allow the emission of a beam with the characteristics of a laser by itself.
- To make the light emission monochromatic, directional and coherent, it is necessary to change the way the atoms return to the “low energy state”. The process consists of "irradiating" the active medium with radiation of a frequency lower than that of the active medium during the “high energy state”. When the active medium is stimulated while in “high energy state”, two photons will be released (the atom will no longer store energy). The two photons that will be emitted will be at the frequency of the light at which the active medium is radiated, as well as travelling in the same direction. The emission that is generated in the active medium in the previous manner is called “stimulated emission”. The stimulated emission process is an amplifier of the original incoming radiation. If the process is “fed” with sufficient energy, the emission of radiation will be brought to a state such that amplification with a “snowball” effect is generated, as shown in (Fig. 15 d).

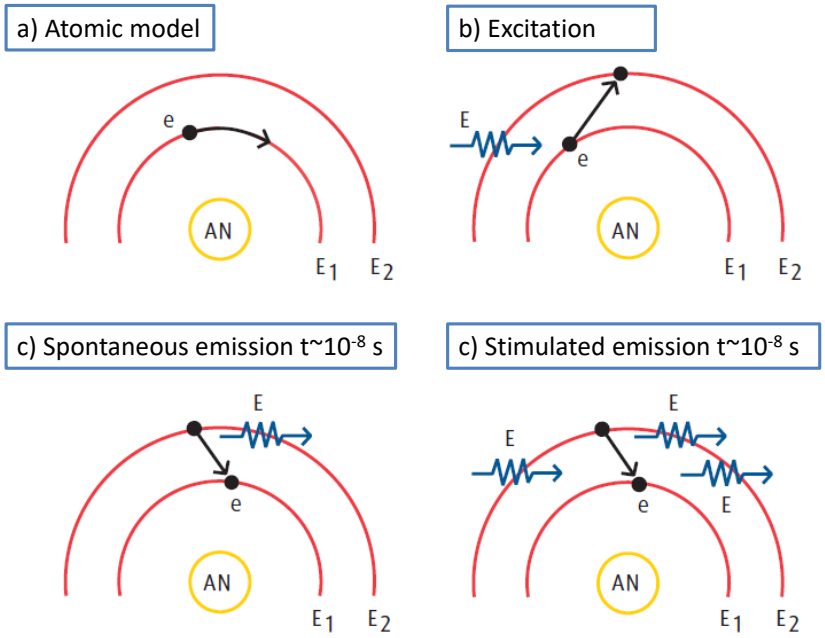

AN: atomic nucleus, e: electron, E: energy, E_1 and E_2: energy levels

Figure 15. Model for: atomic model, excitation, spontaneous emission, stimulated emission (Berkmanns and Faerber, 2010).

The stimulated emission process described in (Fig. 15) is for a single atom. However, in practice a laser requires the interaction of a large number of atoms. The number of atoms that can be found in an active medium in a "high energy state" at any given time can be described by (Eq. 1):

$$N_{\infty} = N_0 e^{-(E_1 - E_2)/\sigma T} \qquad \textit{Eq. 1}$$

Where:

N_{∞}: number of atoms in a high energy state within the active medium.

N_0: number of atoms in a low energy state within the active medium.

T: equilibrium thermal temperature.

σ: is the Boltzmann constant (~1.38065 × 10^{-23}) $J.K^{-1}$

1.10.1.3 Characteristics of a Laser Beam

The fundamental theory of laser was established by Einstein (Carpene et al., 2010), but it was not until 1960 that a practical laser was created due to the works of Maiman (a ruby-based laser). The monochromatic wavelength for lasers varies from the ultraviolet to infrared range, as shown in (Fig. 16), (Majumdar and Manna, 2011).

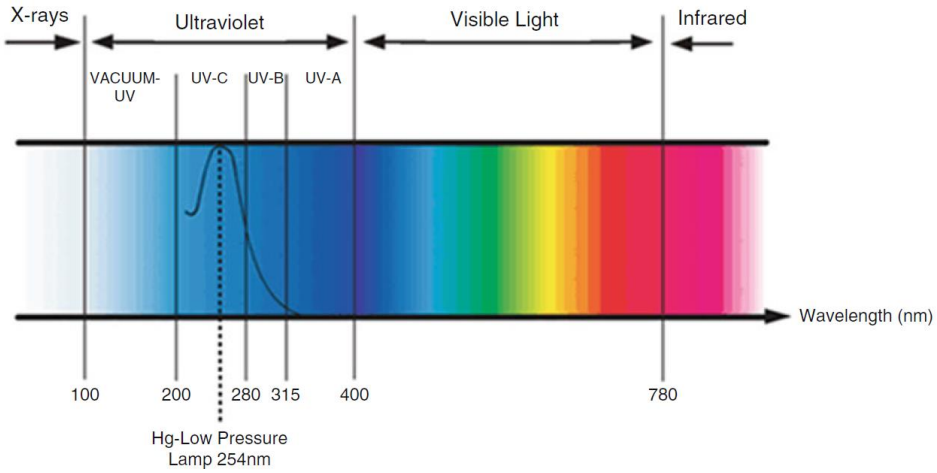

Figure 16. The regions of the electromagnetic spectrum, highlighting the optical spectrum which includes the visible and ultraviolet regions (Zwinkels, 2015).

The monochromatic wavelength of lasers is around the wave range of visible light, as shown in (Table 11).

Table 11: Regions of the electromagnetic spectrum (Zwinkels, 2015).

Wavelength range (nm)	Frequency range (s^{-1})	Description
<0.1 nm	10^{20}–10^{23}	Gamma rays
0.1–10 nm	10^{17}–10^{20}	X-rays
10–400 nm	10^{15}–10^{17}	Ultraviolet
400–700 nm	10^{14}–10^{15}	Visible
700 nm to 1 mm	10^{11}–10^{14}	Infrared
1 mm to 1 cm	10^{10}–10^{11}	Microwaves
1 cm to 100 km	10^{3}–10^{10}	Radio waves
100–1,000 km	10^{2}–10^{3}	Audio frequency

1.10.1.4 Main Components of a Laser Equipment

A laser consists of three main components: a gain medium (sometimes called “active medium”), a device for the excitation of the gain medium, and an optical device that allows the resonance/delivery of monochromatic light from the active medium to a suitable place for the work to be carried out (Majumdar and Manna, 2011).

Each of the basic components for the generation of a “practical” laser beam is described below (Berkmanns and Faerber, 2010):

- The active medium of the laser: this is the element responsible for emitting the energy stored inside it in various forms, generally in the form of laser radiation. Each active medium is capable of generating a specific wavelength, as shown in (Table 12), although there are some exceptions such as free electron laser type. In (Toyserkani et al., 2005), the following classification of laser types is

mentioned, related to the physical state of the active medium: Gas lasers, Excimer lasers, Solid state lasers, Semiconductor lasers, Liquid dye lasers and Fibre lasers. Each type of laser has different potential applications, as shown in (Table 12), but the emphasis in this document will be on those related to materials processing.

- The active medium exciter: to excite the active medium it is possible to use different forms of energy (electrical, photons, chemical reactions, flash lights and even a lower power laser). The way as active medium is excited limits the frequency of the pulses. For example, for a CO_2 laser, for excitation with direct current (DC of several kV of magnitude), the practical frequency of excitation used is in the order of 1 kilohertz. In the case of the use of electromagnetic radiation as a form of excitation of the active medium (CO_2), radio frequencies allow a practical range of excitation in the order of a few megahertz (with high instrumentation cost), (Fig. 17).
- The resonator: this is the set of elements necessary to feed back the laser radiation arranged as a single vessel. The simplest case (e.g., for a CO_2 gaseous active medium laser), will consist of two mirrors between which the radiation will be generated in a reciprocating path, as shown in (Fig. 17). Note that in (Fig. 17), the excitation of the gas (active medium), can be either direct current (DC) or radio frequency (RF).

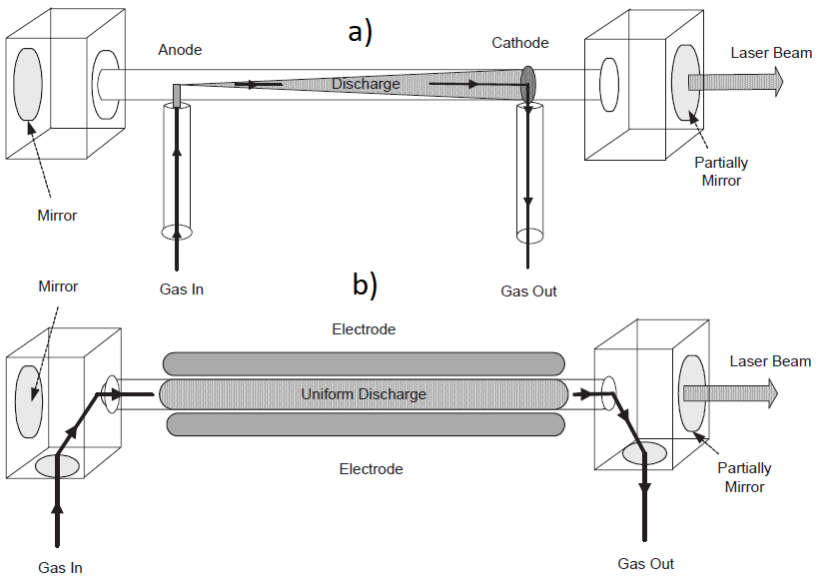

Figure 17. A schematic of a fast axial gas flow CO_2 laser with a) DC excitation, b) RF excitation (Toyserkani et al., 2005).

- The cooling of the active medium: most of the energy used in the excitation of the active medium is transformed into heat. Increasing the temperature of the active medium interferes with the generation of laser radiation. Different strategies can be used to cool the active medium. In the case of active medium of gaseous type, the circulation of the gas itself through a heat exchanger allows an adequate evacuation of excess thermal energy. In the case of solid active mediums there are different strategies. In Nd: YAG type lasers, cooling can only be used outdoors, which restricts the amount of heat that can be removed and the maximum performance of this type of laser. The Yt:YAG and Diode lasers can be mounted directly on a heat exchanger, and therefore be cooled efficiently (the performance of these equipment is improved). In the case of Fibber Lasers (made up of many optical fibbers), the power is distributed evenly within each fibber. By distributing power, the amount of energy dissipated by each individual fibber is small, and therefore the laser assembly is capable of handling powers of a few kW without the need for liquid cooling (Berkmanns and Faerber, 2010).

1.10.1.5 The use of Lasers for Different Types of Physical Processes

In general, the interaction of lasers with matter can be very complex, and can rarely be simplified to just a heat source. A laser can be used not only for heating, but also for evaporating material, forming plasma, creating laser-supported absorption waves (LSAW), creating Marangoni convection, studying Kelvin-Helmholtz instabilities, and so on. A laser beam interacting with a solid will mainly depend on the excitation of electrons from their equilibrium positions (equilibrium states) to other excited states through photon absorption (Carpene et al., 2010).

1.10.1.6 Principles of Laser Interaction with Matter

The type of interaction that a laser will carry out with a given material will be a function of the energy that the beam deposits on it.

The energy of a given light radiation is function of the frequency of the light, according to (Eq. 2):

$$E = h\nu \qquad \textit{Eq. 2}$$

Where:

E: individual energy of a photon.

h: is the Planck constant (~ 6.6261 × 10^{-34}) J.s

The way in which the power of a laser is delivered to a specific material has to do with an excitation/de-excitation process in an extremely short period of time only on the surface of the material.

The delivery of the energy of a laser beam can be in continuous wave (CW) mode, or in the form of pulses. The typical energy density of a laser is in the order of 10^{19} W.mm^{-2}, which allows the evaporation of the material, and can even start a nuclear fusion reaction. The power that can be obtained for the processing of a given material depends mainly on the geometry of the resonator, the mirrors and all the optics necessary to "carry" the beam to the desired work area. In general the quality of the focus will be better for the lower transverse magnetic radiation modes (e.g. TEM00 or Gaussian), (Carpene et al., 2010).

The conversion of electromagnetic energy into heat involves interactions of the type excitation of the valence electrons of the surface (or electrons of the conduction band), interactions of the excited electron/phonon type (in a time lapse of 10^{-11}~10^{-12} s), and interactions between electrons (including recombination of electrons by Auger effect with time lapses of the order of 10^{-9}~10^{-10} seconds), that is, the free charge carriers are always involved within the material (the electrons). Since the main path of energy absorption in metals is in turn the absorption of free charge carriers (the electron conduction band), the energy of the laser beam is transferred directly to the crystal lattice almost instantaneously. This is the reason why a laser beam is capable of locally heating a section of material almost instantaneously. Coupling of laser radiation with the crystal lattice, in the case of metals, occurs best in the range from infrared (10 µm) to ultraviolet (0.2 µm) approximately. Lasers for industrial use in metal treatment are generally not in the visible light range. In the case of semiconductors, the range from a wavelength of the order of 10 to 0.2 µm is the one that best interacts with the valence electrons (for conduction of energy and especially its transformation into heat), (Majumdar and Manna, 2011).

A simple way of relating the interaction of a laser with a solid is based on the change in the ratio of distribution between electrons (as free carriers of charge), and phonons (which are the quantization of the vibrations of the crystal lattice). The vibrations of the crystal lattice are due to the collisions between electrons and phonons, and these

collisions are the origin of the electronic temperature T_e. The variation of the electronic temperature T_e (Carpene et al., 2010) is given by (Eq. 3):

$$\frac{\partial T_e}{\partial t} = \frac{T_L - T_e}{\tau_{ep}} \qquad \textit{Eq. 3}$$

Where:

T_L: is the crystal lattice temperature.

τ_{ep}: is the coupling time of the electron-phonon pair. The time τ_{ep} is in turn dependent on other coupling constants.

1.10.1.7 Utility of Lasers for Industrial Material Processing

On an industrial level, the laser beam is especially useful because of its high coherence (spatially and temporally), where both the phase and the amplitude of the wave remain constant, as well as the tendency of the beam to a low divergence (high parallelism with respect to an optical axis). Another interesting feature is a high energy density (the energy can be concentrated in a very small and precise point).

Typical energy delivered to the surface is in the order of 10^{-3} to 0.1 J.mm^{-2}, which in effect results in surface temperature gradients (cooling rates) being on the order of 10^3 to 10^{10}) K.s^{-1} (depending on the material properties). The conditions under which the energy is delivered allow the processed material not to be affected too much internally (e.g. at the level of thermal affectation), yet it is possible to reach extreme surface working conditions (Chapter III.3.5). This document will focus on the use of laser as a heat source for processing materials at level of material interaction, it will not take into account the possible chemical reactions due to the high temperatures involved in the process. In addition, surface phenomena such as vaporization, recondensation, plasma formation, or absorption of waves supported by laser (where a self-induced reaction by the laser itself generates wave absorption through a phenomenon related to plasma formation), will not be taken into account (Carpene et al., 2010).

1.10.1.8 Types of Lasers commonly used in the Industry for the Processing of Materials

Not all types of lasers are suitable for processing materials commonly used in industry. The most common of laser on industrial use according to (Berkmanns and Faerber, 2010) are:

- Gas lasers (generally CO_2).
- Excimer lasers (excited dimer).
- Solid state lasers (YAG and Fibber type).

Each type of laser has different configuration, as shown in (Fig. 17) and (Fig. 18).

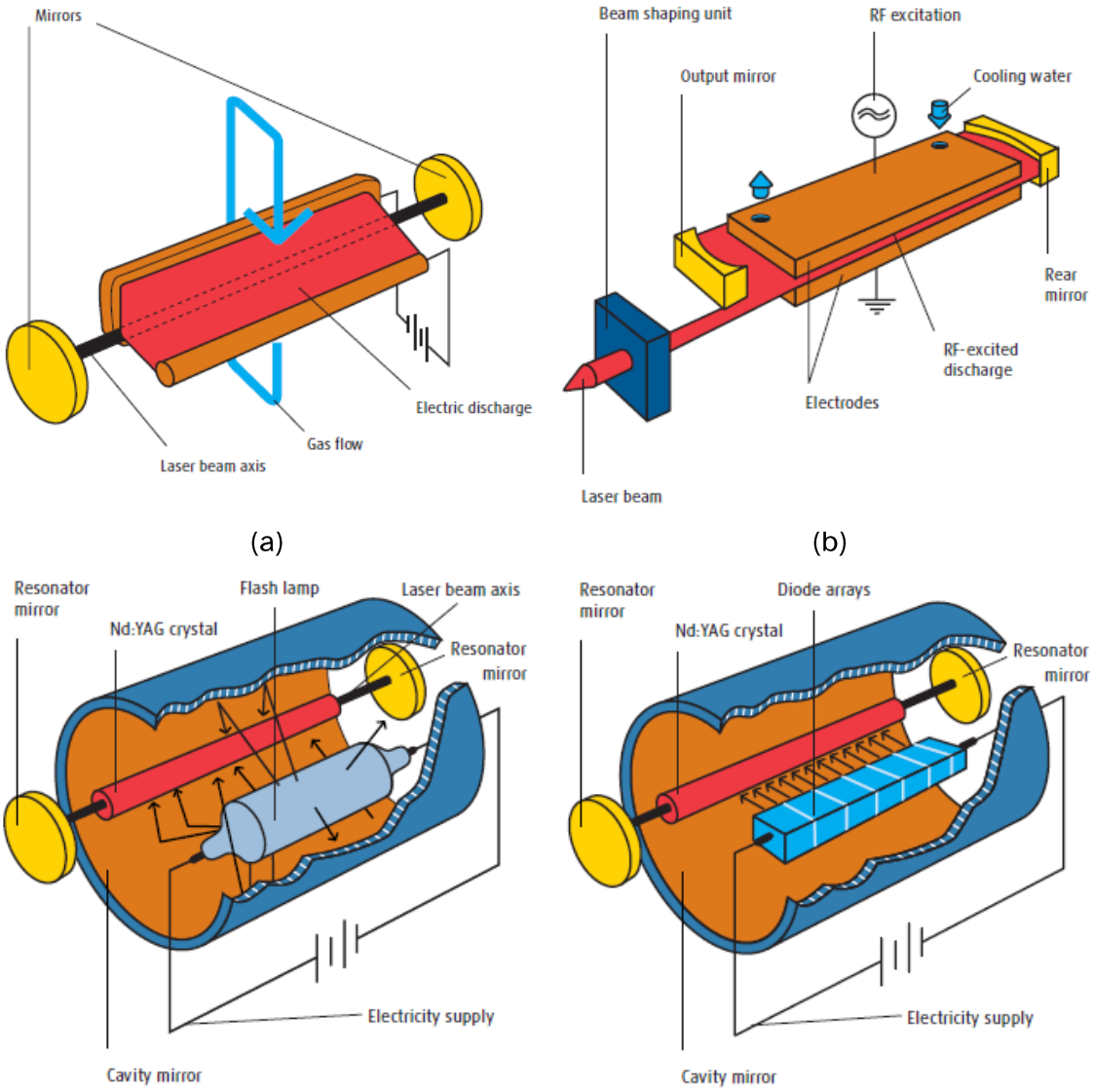

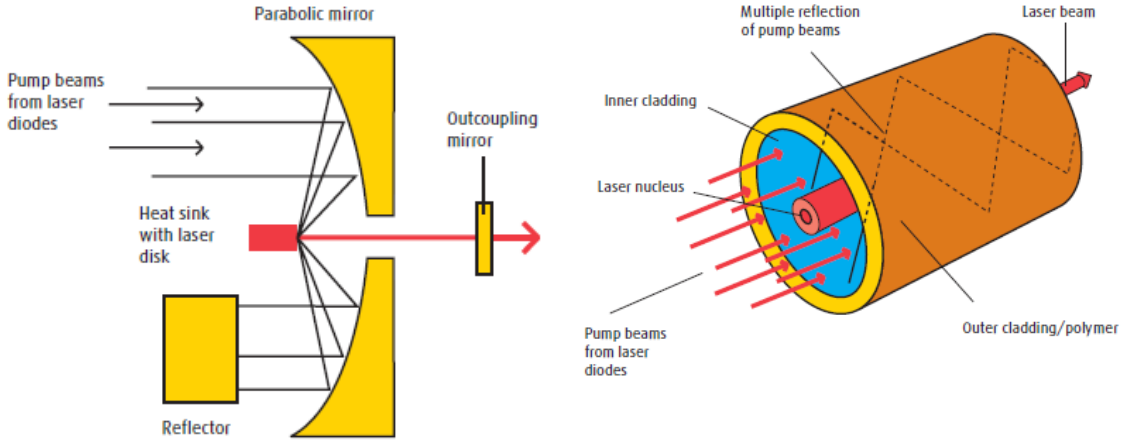

(e) (f)

Figure 18. Different types of lasers for industrial applications: (a) Transverse gas flow CO_2 laser, (b) Diffusion-cooled CO_2 laser, (c) Nd:YAG laser, lamp-pumped, (d) Nd:YAG laser, diode-pumped, (e) Yt:YAG laser (disk laser) and (f) Fibre laser (fibre diameter: 200 µm), (Berkmanns and Faerber, 2010).

For more details on each specific type of laser according to the active media used, consult the references (Berkmanns and Faerber, 2010; Toyserkani et al., 2005).

1.10.1.9 Available Powers and Wavelengths for Different Types of Lasers

The available power ranges found for lasers are in the range of a few mW to approximately 120 kW (IPG Photonics, 2019), in addition to various types of active media (medium that allows to generate monochromatic light in a resonance chamber), which gives rise to a wide range of applications as shown in (Table 12).

Table 12: Commercially available lasers and their industrial applications (Majumdar and Manna, 2011).

Laser	Discovery	Commercialisation	Wavelength/nm	Application
Ruby	1960	1963	628	Metrology, medical applications, inorganic material processing
Nd:glass	1961	1968	1060	Length and velocity measurement
Diode GaAs/GaAlAs	1962	1965	780–905	Semiconductor processing, biomedical applications, welding
He–Ne	1962		1152	Light pointers, length/velocity measurement, alignment devices
Carbon dioxide	1964	1966	10 200	Material processing – cutting/joining, atomic fusion
Nd:YAG	1964	1966	1064	Material processing, joining, analytical technique
Argon ion	1964	1966	480–515	Powerful light, medical applications
Dye (sodium fluorescein)	1966	1969	535–600	Pollution detection, isotope separation
Copper	1966	1989	511	Isotope separation
Excimer	1975	1976	300–350	Medical application, material processing, colouring
Free electron laser	1971	1997	2000–10 000	Medical surgery, surface modification of polymer

1.10.1.10 Quality Parameters of a Laser Beam

The productivity of a laser beam within materials processing technologies depends fundamentally on its power, although the “quality” of the beam is very important when precision operations are required, such as cutting or drilling.

There are many parameters to determine the "quality" of a laser beam. Among the most important are (Toyserkani et al., 2005):

- The beam parameter product (BPP): gives an indication of how focused a laser beam is (and quantitatively measure its focal depth). The BPP is defined by (Eq. 4). The geometric meaning of the BPP parameters is shown in (Fig. 19). In general, the higher the laser power, the higher the BPP of the beam and consequently the poorer the quality of the laser beam. Typical values for a laser cutting process in metal processing range from 3 to 30 mm.mrad.

$$BPP = \frac{r_{0l}\theta}{2} \qquad \textit{Eq. 4}$$

Where:

r_{0l}: is the beam spot radius in the waist of the laser beam.
θ: is the far-field full divergence angle (rad).

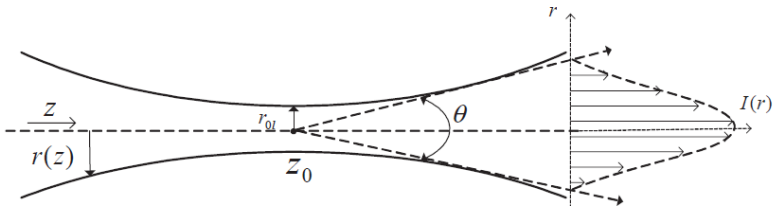

Figure 19. Laser beam geometry (Toyserkani et al., 2005).

- The quality parameters K and M^2: are mainly used for the laser cutting process. It allows quantifying and comparing different types of lasers in a simple way by means of a formula. Both parameters are related by K = 1 / M^2, and are related to the propagation and the ability of a device to focus a laser beam on a very small focal spot over a certain distance close to the beam (Eq. 5). Geometrically, the meaning of the parameters is shown in (Fig. 20).

$$K = \frac{2\lambda}{\pi}\frac{f}{D}\frac{1}{r_{0l}} \qquad \textit{Eq. 5}$$

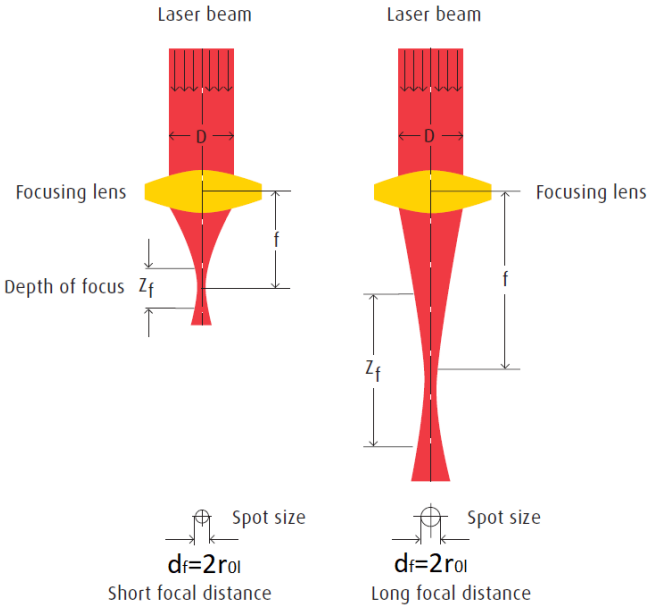

Figure 20. Geometric interpretation of the quality parameter K with the ability to focus a laser beam on a small diameter spot size over a certain focal depth (Berkmanns and Faerber, 2010).

Propagation is defined as the variation of r (z) from the minimum value r_{0l} along the direction of the laser beam axis, as expressed in (Eq. 6), and as shown in (Fig. 19).

$$r_l(z)^2 = r_{0l}^2 + 4\theta^2(z - z_0)^2 \qquad \textit{Eq. 6}$$

The ideal energy distribution would be the one where the laser beam has the smallest possible divergence when working in the TEM00 fundamental mode. This is only possible in Gaussian mode, that is, K = M^2= 1, (Toyserkani et al., 2005). For a real high-power CO_2 laser (on the order of kW), the K factor is on the order of 0.5 to 0.8, and for YAG-type lasers of the same power range the quality of the laser beam tends to be lower.

- Absorptivity/Reflectivity: these parameters are related to productivity in materials processing in terms of utilisation of the laser beam energy. For a cold metal, the radiation generated by a CO_2 laser is absorbed very little at the surface of the material, whereas radiation from diode and solid-state lasers is more absorbed (Fig. 21). The excess energy is reflected from the surface (reflectivity) and is considered as lost energy. Once the surface is sufficiently heated, the efficiency (in absorption) of the energy improves significantly.

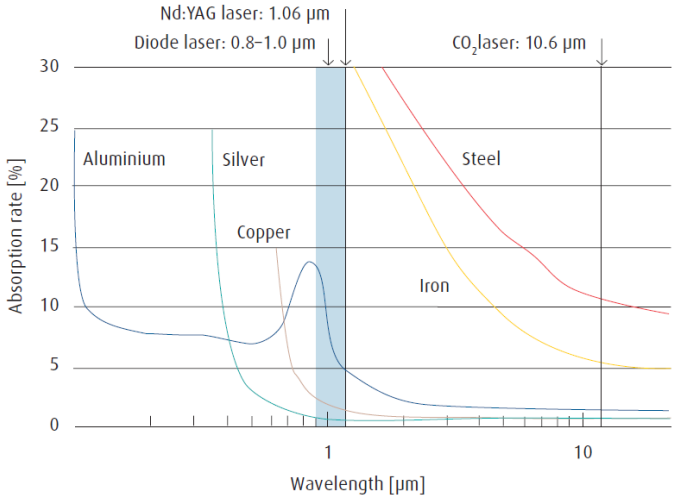

Figure 21. Absorption rate for laser radiation in cold metal (Berkmanns and Faerber, 2010).

The relationship between Absorptivity and Reflectivity is given by (Eq. 7), (Toyserkani et al., 2005).

$$R = \begin{cases} 1 - A & , for\ opaque\ materials \\ 1 - A - T, & for\ transparent\ materials \end{cases} \qquad Eq.\ 7$$

Where:

R: is Reflectivity.

A: is Absorptivity.

T: is Transmissivity.

It is possible to calculate the reflectivity of the clean flat surface of an opaque material in open air with respect to an angle of incidence normal to the surface itself based on indices of refraction appropriate to the wavelength generated by the laser, (Eq. 8).

$$R = \frac{(1-n)^2 + k^2}{(1+n)^2 + k^2} \qquad Eq.\ 8$$

Where:

n: is the refraction coefficient.

k: is the extinction coefficient of material.

The coefficients n and k are optical properties that are a function of the surface temperature of the material. In (Table 13) typical values of these coefficients are shown for a wavelength of 1.06 µm at room temperature.

Table 13: Optical properties of several materials for 1.06 mμ light wavelength at room temperature (Toyserkani et al., 2005).

Materials	k	n
Al	8.50	1.75
Cu	6.93	0.15
Fe	4.44	3.81
Ni	5.26	2.62
Pb	5.40	1.41
Ti	4.00	3.80
Zn	3.48	2.88
Glass	0.10	0.50

An example of the variation of Absorptivity as a function of temperature for a given material is presented in (Fig. 22), where it is also observed that the Absorption itself will even be a function of the surface finish of the material (in this case mild steel).

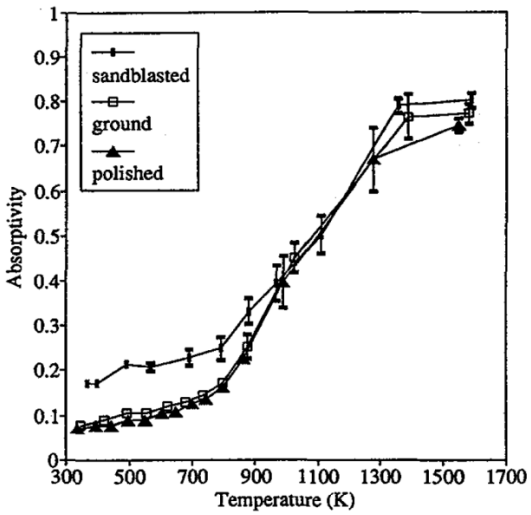

Figure 22. Absorptivity measured at 10.6 μm (CO2 laser), as a function of temperature for AISI 1045 steel (Sainte-Catherine et al., 1991).

For different types of material, different wavelengths should be used in order to improve the productivity in processing that material. As an example, (Table 14) describes the suitability of two types of lasers with different wavelengths for cutting different materials.

Table 14: Cutting suitability for different materials as function of laser wavelength (Berkmanns and Faerber, 2010).

Material	Wavelength (micrometer)	
	Nd:YAG laser: 1.06	CO_2 laser: 10.6
Construction steel	highly	highly
Stainless steel	highly	highly
Aluminium	well	well
Copper	well	difficult
Gold	well	not possible
Titanium	well	well
Ceramics	difficult	well
Perspex	meanly	highly
Polyethylene	meanly	highly
Polycarbonate	meanly	well
Plywood	meanly	highly

- The guidance system of the laser beam to the working area: In CO_2 lasers with a wavelength of 10.6 µm, the beam cannot be guided through the optical fibre, only mirrors and lenses can be used to condition the light until it reaches the point where it will work with it (work area). It is also necessary to use special shields to cover the entire path of the laser beam from the generator to the working area. Depending on the power, the mirrors must be cooled to avoid overheating and the confinement tubes that protecting the beam must be filled with a gas to create a protective atmosphere and other measures must be applied to avoid condensation or other disturbances that could interfere with the proper functioning of the optics. In YAG lasers, the laser beam can be delivered to the working area by the use of fibre optics, so that robots or other flexible guidance equipment can be used. The diameter of the fibres for guiding the laser beam is typically in the order of 100 to 1000 µm. The use of glass fibres allows greater flexibility in the handling of the laser beam, as the same fibre can be used to deliver the light to several workstations, as well as to send several lasers (of different wavelengths) through the same fibre (Fig.23).

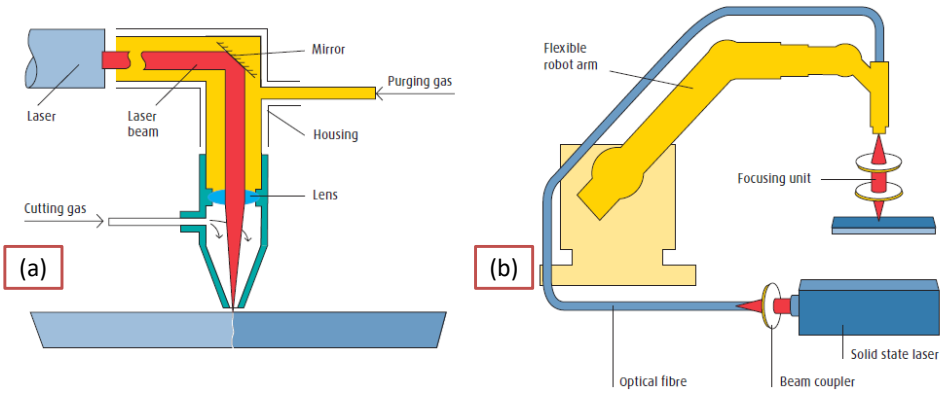

Figure 23. Example of Beam guidance system with: (a) mirrors for CO_2 laser system with processing head, (b) fibber optics (YAG laser), with a beam coupler and a focusing unit (Berkmanns and Faerber, 2010).

1.11 Direct type Additive Manufacturing Methods using Powder Bed Technology for Metals

A brief description of AM technologies by direct manufacturing to metals is presented for the Powder Bed type of technologies. The description of what is a direct manufacturing technology is detailed in (Fig. 10). The Laser Cladding process will be dealt with in a separate next section.

1.11.1 Selective Laser Melting method (SLM).

SLM is a method of Additive Manufacturing that involves the creation of a bed of powder of a very controlled thickness in a work area. Once the powder bed is uniformly deposited, an energy source (laser beam), programmed with precise movements, "draws" a layer of the part to be manufactured on the surface of the powder bed. The energy beam passing over the powder bed is sufficient to melt the entire layer of deposited raw material (metal powder), together with a part of the preceding material (previous layer), so that once all the melting of the material of the manufactured layer is completed, the substrate itself is lowered, and a new layer of raw material is deposited. The process is repeated consecutively until the desired part is built and shaped. The process has the ability to produce parts with very high resolution, and features such as internal passages, as well as very high control over the dimensions of the manufactured object (Frazier, 2014). A generic illustration of the process is shown in (Fig. 24).

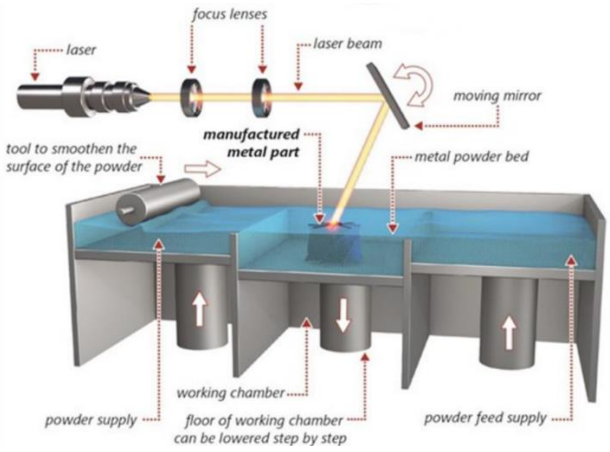

Figure 24. Selective Laser Melting (SLM) mechanism (Azam et al., 2018).

1.11.2 Electron Beam Melting (EBM).

It is a process similar to SLM. EBM is based on the fusion of metal powder particles using a high-speed electron beam instead of a laser beam. The generation of electrons

is done from a filament at high temperature. Later the electrons are accelerated by means of a strong electric field, and they are focused and directed to work area with the help of magnetic fields. The typical speed for the electrons in beam is c/2, where c is the speed of light. A disadvantage of this process is that it must be carried out under vacuum conditions, to avoid scattering of the electron beam in air. As in SLM, the part is manufactured by superimposing fused powders onto a substrate, as shown in (Fig. 25).

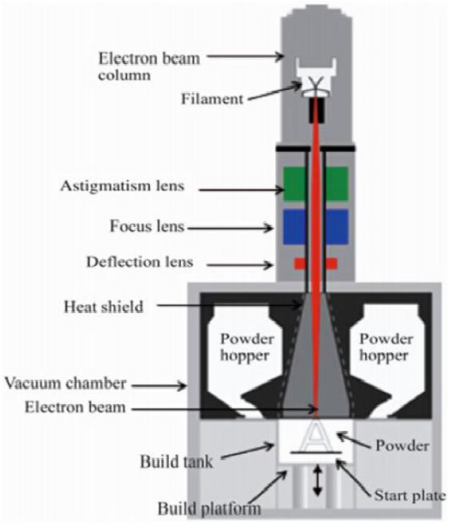

Figure 25. Electron Beam Melting (EBM) mechanism (Azam et al., 2018).

1.12 Additive Manufacturing by Laser Cladding Process

According to (Toyserkani et al., 2005), Laser Cladding is:

"An interdisciplinary technology utilizing laser technology, computer-aided design and manufacturing (CAD/CAM), robotics, sensors and control, and powder metallurgy", where "Laser cladding utilizes a laser heat source to deposit a thin layer of a desired metal on a moving substrate. The deposited material can be transferred to the substrate by several methods: powder injection, pre-placed powder on the substrate, or by wire feeding. Among these methods, laser cladding by powder injection has been demonstrated to be most effective. In this process, the laser beam melts the powder particles and a thin layer of the moving substrate to deposit a layer of the powder particles on the substrate". A schematic of the process is shown in (Fig.26).

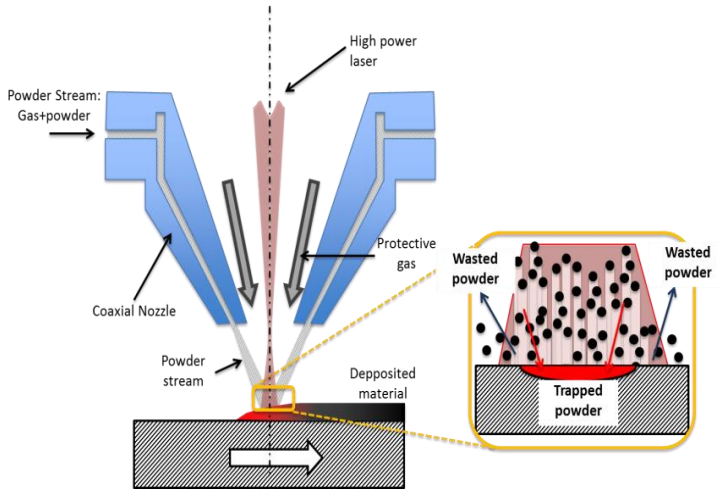

Figure 26. Typical configuration of a Laser Cladding system and detail of trapped and wasted powder.

In this thesis, this AM method will be used, transferring the filler material to the substrate in the form of metallic powder. The technology is known by several names according to: the institution that has worked with the technology, the amount of integration between different technologies for the objects manufacture, and even the geographical region.

A summary made by (Toyserkani et al., 2005) on the different names that have been given to the Laser Cladding technology is presented in (Table 15).

Table 15: Different names given to the additive manufacturing technology known as Laser Cladding, (Toyserkani et al., 2005).

Abbreviation	Name	Used by	Notes
ALPD	Automated Laser Powder Deposition	University of Waterloo	Automated laser cladding technology for coating and prototyping
DLF	Directed Light Fabrication	Los Alamos National Laboratory	To describe a process has been developed for free forming and prototyping
DMD	Direct Metal Deposition	University of Michigan in Ann Arbor, The University of Missouri at Rolla	This process incorporates features of laser cladding, CAD/CAM package, vision, and control system
LAM	Laser Additive Manufacture	AeroMet Corporation of Eden Prairie at Minnesota, fully owned subsidiary of MTS Systems Corporation	

LDC	Laser Direct Casting	University of Liverpool	To describe the process, in which a coaxial nozzle is utilized to produce 3D components
LENS	Laser Engineered Net Shaping	Sandia National Laboratories	
LMF	Laser Metal Forming	Laser Aided Manufacturing Processes Laboratory at the University of Missouri, at Rolla, and at Swiss Federal Institute of Technology	
LPD	Laser powder deposition	Used by several research groups in China and England	
LPF	Laser Powder Fusion	Used by some industries that are involved in turbine blade repair	
LRF	Laser Rapid Forming	Research group at Shanghai Jiaotong University	This name can be confused with another laser-based technology, laser bending, which is also called laser rapid forming
-	Laser Consolidation	The Integrated Manufacturing Technologies Institute (IMTI) of National Research Council of Canada (NRC)	
-	“Solid free-form fabrication” or “Shape deposition manufacturing”	Stanford University, Carnegie Mellon University, and Penn State University	

It is necessary to clarify that there are certain technologies analogous to the Laser Cladding process, known as Laser Alloying and Laser Glazing. The difference between them is a function of the amount of material added to the substrate.

- In "Laser Alloying" the amount of material added to the substrate (in the molten bath) is small. The result of this process is a homogeneous mixture in the resulting material throughout the fusion zone.
- In "Laser Glazing" again a very small amount of material is deposited on the substrate (with the help of a laser as a heat source), but under super-fast cooling conditions. The goal is to create a molten layer of material in a "metallic glass" state. The molten layer that is deposited is intended to be resistant to corrosion and wear (Kear et al., 1979).

Another important difference can be seen in the interaction times and in the specific energies associated with each AM process, as shown in (Fig. 33).

In (Fig. 27) the difference between the three processes is shown schematically through the difference in the microstructures generated when joining two materials of composition A and B. In the process of Laser Alloying the objective will be to create a hybrid composed of substrate material A and filler material B (compound A + B).

The objective of Laser Glazing is to create a very thin layer of vitreous material B, on substrate A. The microstructure of this "thin" layer is very different from that of the substrate (due to rapid cooling). The technology does not aim to change the chemical composition, only tries to improve the behaviour of the material via the modification of the microstructure.

In Laser Cladding, the technology deposits a material that is distinguishable as a well differentiated phase. If the substrate material is different from the cladding material, a very marked composition gradient will be generated, as indicated in (Fig. 27).

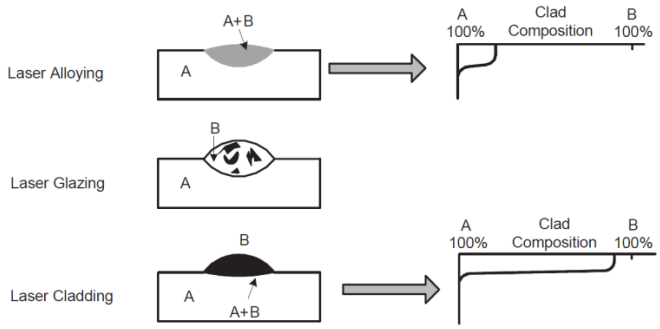

Figure 27. Different microstructures of laser alloying, glazing, and cladding (Toyserkani et al., 2005).

1.12.1 Applications of the Laser Cladding Process

The main characteristics of the Laser Cladding process are that it allows the creation of small parts with complex and intricate shapes. Some specific applications for this technology are:

- Prototyping and manufacturing of moulds using the additive process of Laser Cladding together with traditional machining techniques (Majumdar and Manna, 2011).
- Coatings: the deposition of a material (e.g. metal or ceramic), allows the substrate to acquire the characteristics of the added material rather than those of the base material. The coating can provide the substrate with characteristics such as corrosion resistance, wear resistance or high impact resistance (for use on power shafts, valve seals, tools, moulds, etc.). The limitation in this application is mainly due to the physical metallurgy of the materials being combined. An interesting application is the coating of turbine blades with high temperature resistant alloys that meet the requirements for the passage of very hot gases into the turbines (Toyserkani et al., 2005).
- Part maintenance and rebuilding: One of the most common applications is the repair of high value-added components, especially when errors have occurred during machining or manufacturing. The reason why Laser Cladding allows parts to be "recovered" that would otherwise be discarded is because the application of the laser beam as a heat source is much localised. If the amount of heat affecting the substrate is too high (or not localised enough), the repaired part is affected by metallurgical degradation due to excess heat, and is prone to cracking and reduced service life. In the specific case of aircraft turbine blades or repair within the power generation industry, the contribution of laser cladding has been recognised as a critical and essential technology. An example of the application of this technology is shown in (Fig.28).

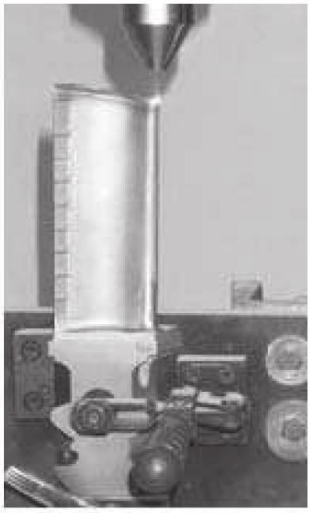

Figure 28. Application of laser cladding to repair a tip of rotor blade made of precipitation hardened CC-superalloy Inconel 738 (Toyserkani et al., 2005).

- The creation of prototypes and tools for the metal sector: The creation of rapid prototypes (RP, Rapid prototyping) and the creation of tools (RT, Rapid tooling), can be adapted to the Laser Cladding process. In general, it is desirable that the development of functional tools will be as fast as possible to take advantage of market opportunities. Additive manufacturing is well suited to the requirements for rapid prototyping. Within additive manufacturing processes, Laser Cladding also meets the requirement that parts manufactured for the tool sector can be functional (Toyserkani et al., 2005). In general, the development of very complex functional tools and prototypes requires the use of highly specialized CNC personnel, and it can sometimes lead to a delay in the implementation of a solution. An example is shown in (Fig. 29).

Figure 29. Fabrication of a blade by LENS(R), (Toyserkani et al., 2005).

1.12.2 Modelling and Simulation of the Laser Cladding Process

The importance of mathematical models is that they help to improve and understand the process and theory underlying a specific process. The models can be used in predicting process outcomes, as well as assisting in the design of the controller (automation), without performing any physical experiments. The latter is important to reduce the cost of system development in an automated laser cladding process.

According to (Toyserkani et al., 2005), the mechanisms and physical phenomena involved in the modelling of the Laser Cladding process are:

- The laser beam reaches the substrate, and a significant part of its energy is absorbed directly by the substrate. A small part of the laser energy is absorbed by powder particles. The energy absorbed by the substrate then develops a melt pool. Molten or semi-molten particles are added simultaneously to the melt mixture (Fig. 30, a). This process step is expressed solely by the heat conduction equation.

- The surface tension gradient drives the fluid flow within the molten pool. As the flow field penetrates the substrate, the energy transfer mechanism changes to a mass convection mechanism. During this phenomenon, the molten particles mix rapidly in the melt bath (Fig. 30, b). This step in the process must be expressed by the equations of momentum, heat transfer, and continuity.

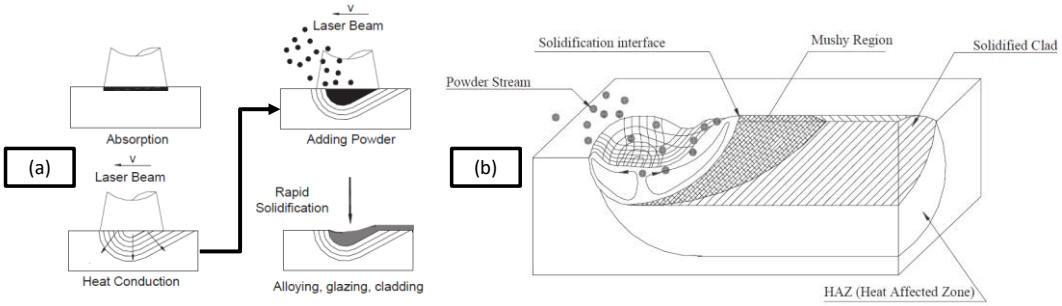

Figure 30. (a) Schematic of physical phenomena during different laser material processing techniques, (b) Schematic of the influence of convection during the laser cladding process (Toyserkani et al., 2005).

The equations corresponding to the Laser Cladding process are shown below (Toyserkani et al., 2005):

Equation of temperature distribution for the transient state within the substrate (Eq. 9):

$$\frac{\partial(\rho c_p T)}{\partial t} + \nabla.(\rho c_p \mathbf{v} T) - \nabla.(k \nabla T) = Q \qquad \textit{Eq. 9}$$

The equation of momentum conservation applied to fluid flow is another of the equations that govern the physical laws within the Laser Cladding process (Eq. 10), in conjunction with the continuity equation (Eq. 11).

$$\frac{\partial(\rho \mathbf{v})}{\partial t} + (\rho \mathbf{v} \nabla)\mathbf{v} = \rho \mathbf{g} - \nabla p + \mu \nabla.(\nabla \mathbf{v}) \qquad \textit{Eq. 10}$$

$$\nabla \mathbf{v} = 0 \qquad \textit{Eq. 11}$$

The boundary conditions necessary to solve analytically or numerically the (Eq. 9) to (Eq. 11) will be:

Boundary condition of the laser beam energy together with the boundary condition of the interaction of the powder flow on the substrate surface (surface heat source), (Eq. 12) as shown in (Fig. 31).

$$-k(\nabla T.\mathbf{n})|_{\Omega}=\begin{cases}\eta I(x,y,z,t)-h_c(T-T_0)-\varepsilon_t\sigma(T^4-T_0{}^4) \text{ if } \Omega\in\Gamma\\ -h_c(T-T_0)-\varepsilon_t\sigma(T^4-T_0{}^4) \text{ if } \Omega\notin\Gamma\end{cases} \quad \textit{Eq. 12}$$

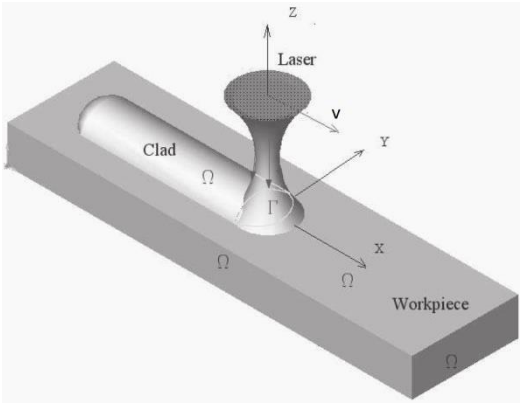

Figure 31. Scheme of the associated physical domains of the laser cladding process (Toyserkani et al., 2005).

The surface tension on the molten bath surface (melt pool), when $\mathbf{g}$ is vertical, is given by (Eq. 13). The (Eq. 14) indicates that the relative velocity of the substrate has no vertical component.

$$\Delta p+\rho\mathbf{g}z=\left(2\mu\frac{\partial\mathbf{v}}{\partial n}.\mathbf{n}\right)+\frac{\gamma_{suf}}{R_{melt}} \quad \textit{Eq. 13}$$

$$\mathbf{v}.\mathbf{n}=0 \quad \textit{Eq. 14}$$

For a pure element, it is necessary to establish an additional boundary condition such that it represents the shape of the solidification front during its hardening (Eq. 15), (Eq. 16) and (Eq. 17). In the case of alloys, it will be necessary to consider their solidification range.

$$f(x,y,z,t)=Const. \quad \textit{Eq. 15}$$

$$u_x=u_y=u_z=0 \quad \textit{Eq. 16}$$

$$T=T_{melt} \quad \textit{Eq. 17}$$

Finally, the temperature conditions at the beginning and at the end of the Laser Cladding process are expressed by (Eq. 18) and (Eq. 19).

$$T(x,y,z,0)=T_0 \quad \textit{Eq. 18}$$

$$T(x,y,z,\infty)=T_0 \quad \textit{Eq. 19}$$

The modelling of the Laser Cladding process is highly dependent on the configuration of the equipment to carry out the process. For example, there are several ways to deposit metal powder in the work area. The most common configurations are concentric nozzle and lateral nozzle, as shown in (Fig. 32).

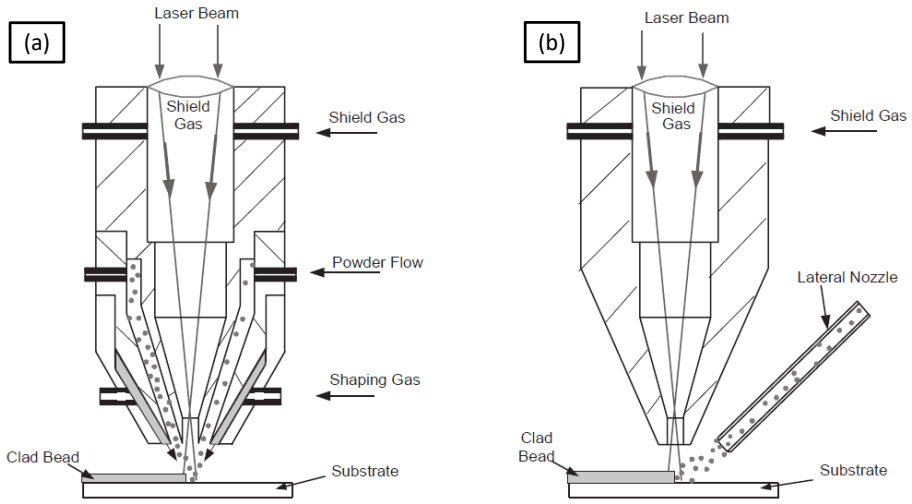

Figure 32. (a) Coaxial nozzle, (b) lateral nozzle, (Toyserkani et al., 2005).

In addition, there are different approaches with respect to the resolution of (Eq. 9) to (Eq. 19). For the model interactions, methods can be used that consider the transient (time-dependent) state, steady state or with different types of physical simplifications (thermo-mechanical coupling, non-linear, phase-shifting, etc.).

For this investigation, to resolve (Eq. 9) to (Eq. 19) the approach used were the steady state (not dependent on time), by means of a semi-analytical heat transfer equation with the use of a surface heat source in local coordinates of the laser beam (Eq. 20). The absorption and attenuation effect of the energy of the laser beam by the powder will be based on a negative enthalpy balance (Chapter III.3.7).

$$I(x,y,z) = I(r, z' = s_n), \forall\ r = \sqrt{x_0^{\,2} + y_0^{\,2}} \qquad \textit{Eq. 20}$$

As a complement, a statistical modelling method will be used to optimise the conditions of the deposition parameters of the INCO718, material used in this thesis. The usefulness of using statistical modelling is to obtain a solution adapted to the laser cladding process, without the complexity of solving the complete physical equations of the model describing the laser deposition phenomenon (Chapter I.2.2).

1.12.3 Laser Requirements for the AM Process with Laser Cladding

The laser cladding process requires certain special characteristics regarding the parameters of the light beam to ensure a successful material deposition:

- High power density: the main characteristic is the need for sufficient power to carry out the additive process. According to (Toyserkani et al., 2005), the Laser Cladding process requires at least a power density in the order of 70 to 100 W/mm^2, with interaction times close to 0.01 to 1 s. Equipment that does not meet this requirement of power to be delivered is not suitable to carry out the laser deposition process (Fig. 33).

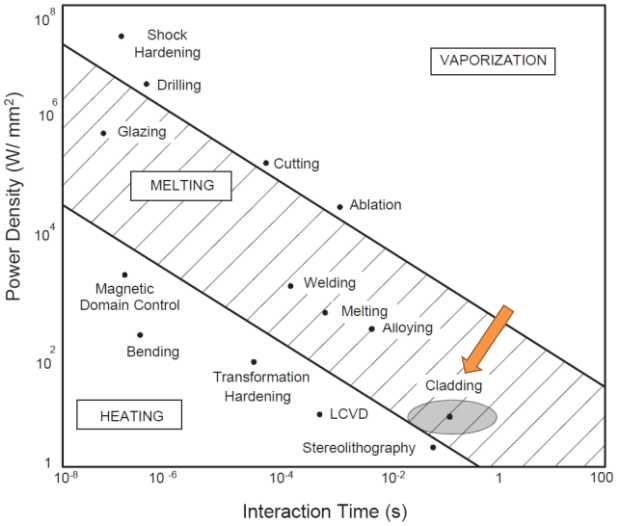

Figure 33. Power density and interaction time for various laser material processing (Toyserkani et al., 2005).

- High beam quality: As mentioned previously, there are many different types of laser equipment (CO_2, YAG, Fibre and Diode are the most common at industrial level). Regardless of the type of laser used, all of them must have a very high energy distribution (beam quality). The laser deposition process not only involves interaction with the substrate surface of the material to be processed, but also with the metal powder or wire that will provide the material to make the part. If the beam quality is poor, the material addition process is likely to result in a deposition with low mechanical properties. A Gaussian energy distribution is generally preferred, as it produces a weld bead with a more uniform and homogeneous microstructure (Toyserkani et al., 2005).
- High stability in energy delivery to the working area: in material deposition by Laser Cladding process, the way of delivering energy through the laser beam can

make use of a continuous wave (CW) or pulse working configuration, as shown in (Fig.34).

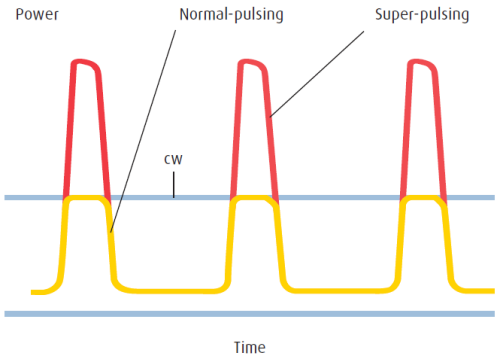

Figure 34. CW operation, pulsing and super-pulsing for laser (Berkmanns and Faerber, 2010).

In the pulse mode, special care must be taken in the use of peaks with very high-power delivery ("super-pulses" must be avoided). If the energy peaks are too high (even with low-medium power lasers), the laser beam may be able to vaporize the metal powder before reaching the surface for deposition (Toyserkani et al., 2005).

- Long focal length: when the focal length is long, it is possible to decrease the sensitivity by changing the propagation of the laser beam (Fig. 20). With a long focal length, it is also possible to better accommodate the nozzle containing the metal powder injection system, protect the optics from the gases generated during the deposition process, and even prevent the formation of plasma in the working area.

1.12.4 About of Laser Cladding Nozzles

The versatility of the Laser Cladding process is also a function of the nozzles used for material deposition, especially at the level of process stability. A nozzle consists of different body types, tips, adapters, powder delivery shapes and even monitoring within the device itself (all ensuring compatibility between the various components). There is no such thing as a "universal" nozzle, although the same nozzle can be used in various applications. The objectives of a good nozzle design should be: to maintain the same powder flow rate (uniform focal density on the working plane), with relative independence of orientation during the material deposition process; to efficiently utilise the raw material (high nozzle efficiency), to create an effective protective atmosphere during the manufacturing process and to allow high scalability to handle different types of powder at various feed rates, as needed in each specific application (Arrizubieta et al., 2014; Nowotny et al., 2003). In the Laser Cladding process, the versatility of the nozzle

allows to manufacture/repair parts of complex geometry with the help of a robot or other control mechanism (Fig. 35).

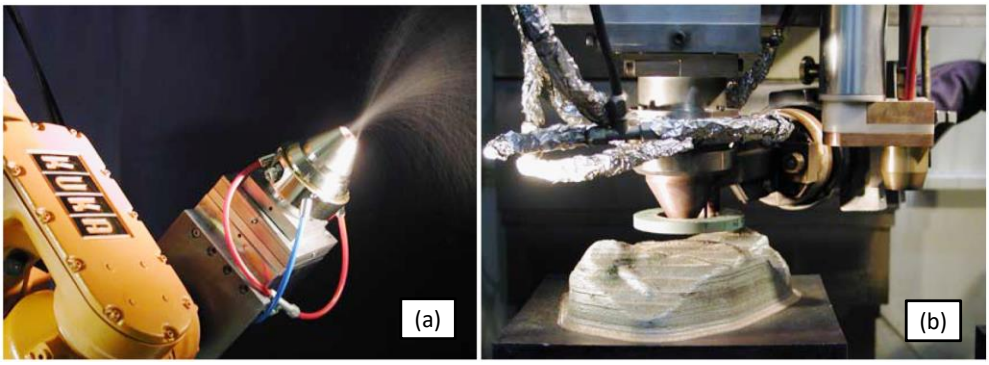

Figure 35. (a) COAX10 in a robot guided 3D cladding system, (b) High-speed generation of a tool section by induction assisted laser beam build-up welding (Nowotny et al., 2003).

1.12.5 Material Deposition Strategies for Laser Cladding

Related to the feasibility of the integration of Additive Manufacturing technologies in industry is the physical limitation of the available deposition strategies (trajectories in the nozzle workspace) used commonly. Emphasis will be placed on the study of the strategies used in AM technologies by powder or wire deposition with the use of a laser beam energy source, specifically for the method of Laser Cladding of deposition using metal powder as raw material.

In the case of Laser Cladding process, deposition strategies tend to be relatively simple compared to those used in powder bed technologies. The most common deposition strategies for a layer of material in the laser cladding method are shown in (Fig. 36). The feed ratio of deposited material (m'), and the speed at which the nozzle that deposits the powder moves relative to the substrate (v), play an important role in the number of defects found in the deposited material, and in the mechanical properties of the manufactured part (Sames et al., 2016).

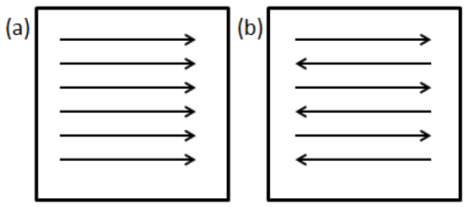

Figure 36. Scan strategies used to determine heat source path in metal AM as seen in the X-Y plane (perpendicular to the build direction): (a) unidirectional or concurrent fill, (b) bi-directional, snaking, or counter-current fill, (Sames et al., 2016).

There are other possible strategies of material deposition that will depend on the type of object to be built / repaired. An example is shown in (Fig. 37), where several strategies are shown for a simple infill layer that aims to create the same geometric shape (a square).

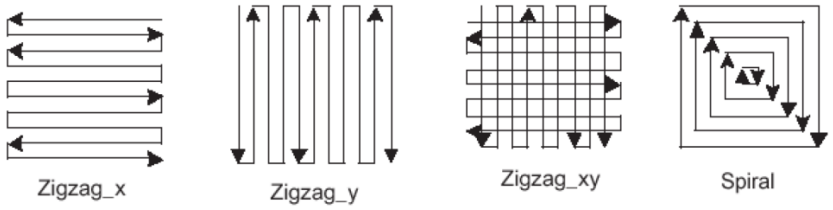

Figure 37. Different tool trajectory patterns used for fabrication of a cubic component (Toyserkani et al., 2005).

Strategies used in additive manufacturing methods using powder bed technology will not be discussed in this document. The reason is that the disposition and consolidation of the raw material for the manufacture of the object is very different. In powder bed technology the raw material is previously deposited in the work area, and it is not necessary to "carry" it to the manufacturing area (the laser source basically has a free movement). In contrast, with powder-deposition-type technologies, the amount of movement is limited by the ability of the powder or wire to be carried into the work area along with the laser source. Some common strategies for AM with powder bed technology are shown in (Fig. 38).

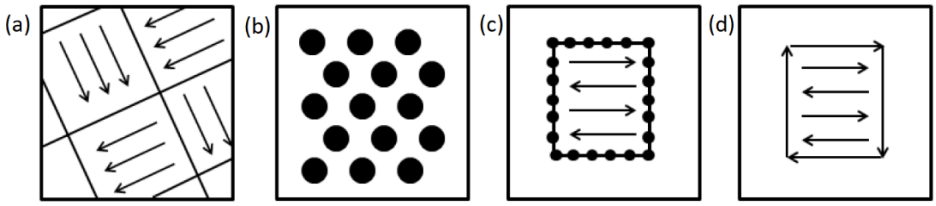

Figure 38. (a) Island scanning, (b) spot melting, (c) spot melting contours with snaking fill, and (d) line melting contours with snaking fill (Sames et al., 2016).

1.13 Important Differences between Direct Manufacturing Processes based on Metal Powder Technology

An important difference between the Laser Cladding process and those of SLM and EBM (also considered as a powder-based process), is that the raw material is not “pre-deposited” in the work area. In the Laser Cladding process, the powder is "injected" into the work area, by means of a gas that acts as a transport medium. The transport of the metallic powder to the work area is carried out by means of nozzles. In general, the work

area is locally protected by means of a protective atmosphere (an inert gas such as argon is introduced in the work area).

In Powder bed processes, it is always necessary to use a closed chamber that provides a protective atmosphere in the case of a SLM process, or a vacuum chamber in the case of EBM. The use of a chamber limits the size of the part that can be manufactured. To get an idea of the relative volumes of the pieces that can be manufactured by different AM processes of the Direct Manufacturing type, (Frazier, 2014) presented a comparative table of some commercial equipment available for the processes that were been mentioned in this section (Table 16).

Table 16: Representative AM equipment sources and specifications (Frazier, 2014).

System	Process	Build volume (mm)	Energy source
Powder bed			
ARCAM (A2)(a)	EBM	200 × 200 × 350	7 kW electron beam
EOS (M280)(b)	DMLS	250 × 250 × 325	200-400 W Yb-fiber laser
Concept laser cusing (M3)(b)	SLM	300 × 350 × 300	200 W fiber laser
MTT (SLM 250)(b)	SLM	250 × 250 × 300	100-400 W Yb-fiber laser
Phenix system group (PXL)(c)	SLM	250 × 250 × 300	500 W fiber laser
Renishaw (AM 250)(d)	SLM	245 × 245 × 360	200 or 400 W laser
Realizer (SLM 250)(b)	SLM	250 × 250 × 220	100, 200, or 400 W laser
Matsuura (Lumex Advanced 25)(e)	SLM	250 × 250 diameter	400 W Yb fiber laser; hybrid additive/subtractive system
Powder feed			
Optomec (LENS 850-R)(f)	LENS	900 × 1500 × 900	1 or 2 kW IPG fiber laser
POM DMD (66R)(f)	DMD	3,200° × 3°,670° × 360°	1-5 kW fiber diode or disk laser
Accufusion laser consolidation(g)	LC	1,000 × 1,000 × 1,000	Nd:YAG laser
Irepa laser (LF 6000)(c)	LD		Laser cladding
Trumpf(b)	LD	600 × 1,000 long	
Huffman (HC-205)(f)	LD		CO_2 laser clading
Wire feed			
Sciaky (NG1) EBFFF(f)	EBDM	762 × 483 × 508	>40 kW @ 60 kV welder
MER plasma transferred arc selected FFF(f)	PTAS FFF	610 × 610 × 5,182	Plasma transferred arc using two 350A DC power supplies
Honeywell ion fusion formation(f)	IFF		Plasma arc-based welding

Country of Manufacturer: (a) Sweden, (b) Germany, (c) France, (d) United Kingdom, (e) Japan, (f) United States, and (g) Canada

Another interesting table is the compilation of (DebRoy et al., 2018). In (Table 17), the two main additive manufacturing technologies for metals (powder bed process, and powder / metal wire deposition process) are compared. In the previous author's research, it is mentioned that one of the major difficulties in choosing between the various AM processes is the relationship between the cost of the raw material and the precision of the manufactured part. In the case of powder metal as raw material, higher precision, higher flexibility in terms of part complexity and reasonably good surface finish are obtained; but the raw material is very expensive. With wire or sheet metal as raw material, less precision and surface finish is obtained. However, the raw material is relatively cheaper.

Table 17: Comparison of two main categories of additive manufacturing processes for metallic components: directed energy deposition (DED) versus powder bed fusion (PBF), (DebRoy et al., 2018).

Process	DED			PBF	
Feedstock	Powder	Wire		Powder	
Heat source	Laser	E-beam	Electric arc	Laser	E-beam
Nomenclature	DED-L	DED-EB	DED-PA/DED-GMA	PBF-L	PBF-EB
Power (W)	100–3000	500–2000	1000–3000	50–1000	
Speed (mm/s)	5–20	1–10	5–15	10–1000	
Max. feed rate (g/s)	0.1–1.0	0.1–2.0	0.2–2.8	–	
Max. build size (mm × mm × mm)	2000 × 1500 × 750	2000 × 1500 × 750	5000 × 3000 × 1000	500 × 280 × 320	
Production time	High	Medium	Low	High	
Dimensional accuracy (mm)	0.5–1.0	1.0–1.5	Intricate features are not possible	0.04–0.2	
Surface roughness (μm)	4–10	8–15	Needs machining	7–20	
Post processing	HIP and surface grinding are seldom required	Surface grinding and machining is required to achieve better finish	Machining is essential to produce final parts	HIP is rarely required to reduce porosity	

1.14 Scope of this Thesis Work in Relation to AM

With everything written previously, the scope of this thesis can be clearly expressed: "In this research, using an Additive Manufacturing technology, a metallic material in powder shape (Nickel based and with high melting temperature) will be processed by the Laser Cladding process, with the help of a suitable high power laser source for the creation/repair of Direct Manufacturing type parts with post-processing (probes), in order to investigate the relationship between the generated microstructure and mechanical properties of the INCO718 alloy".

2 Nickel-based alloy Microstructures Generated by AM

2.1 Difference between Generated Microstructures for Powder Bed and Nozzle Powder Technology in AM Processes

It was been mentioned previously in this paper that "Direct Manufacturing" type processes for dense metal parts are divided into two types: powder bed based and powder nozzle injection technologies. While both additive manufacturing methods share some characteristics (use of metal powder, fast solidification, texture in the microstructure, etc.), they differ in some important aspects at the microstructure level (Nguejio et al., 2019):

- The grain recrystallization (dependent on the thermal cycle in the post-processing), originates grains of different size and orientation. In the investigation with the Nickel base alloy INCO625, the SLM process in

conjunction with annealing produces a complete recrystallization (no dendritic grains). For the LMD process, the annealing is not complete, which results in a more heterogeneous structure (mixture of columnar and equiaxed grains).

- Precipitates derived from recrystallization after the annealing process are more common at the grain boundaries for a DLD process than for a SLM process (despite the high temperature involved in heat treatments). The effect of the precipitates that are generated (if they are well distributed in the grain boundaries), is the reinforcement of the mechanical properties in the case of an AM process by means of DLD. A comparison of both types of microstructures is shown in (Fig. 39).

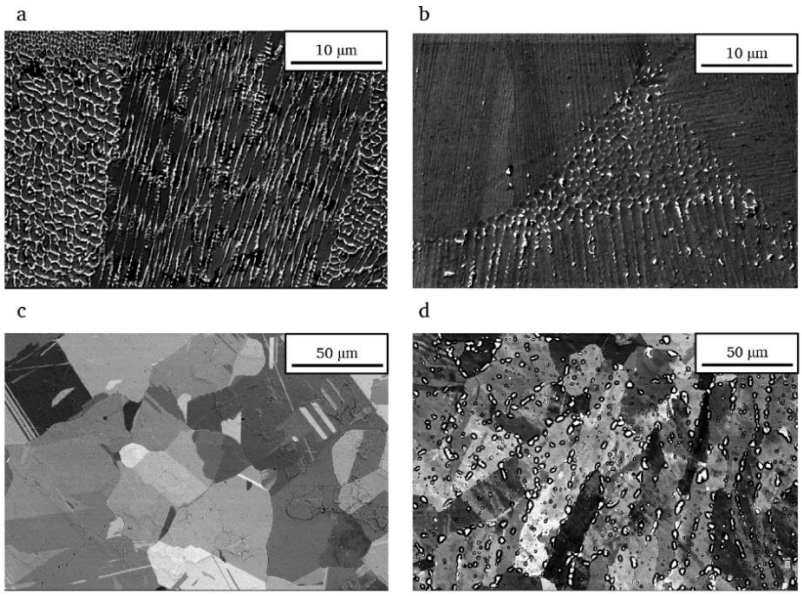

Figure 39. SEM images of the manufactured Inconel 625 samples annealed 1 h at different temperatures. (a) SLM at 700°C; (b) SLM at 900°C; (c) SLM at 1100 °C; (d) LMD at 1100°C, (Nguejio et al., 2019).

As the microstructures generated by both addictive manufacturing processes are slightly different, emphasis will be placed on the microstructural characteristics of the alloys manufactured by Laser Cladding (when possible), specifically for Nickel-based alloys.

2.2 Microstructural Characteristics of Nickel-based Alloys generated by AM

In the work of (DebRoy et al., 2018) an excellent summary of the microstructural characteristics of Nickel-based alloys manufactured with AM was made. Basically, Nickel-based alloys are very sensitive in terms of intermetallics that are formed during the manufacture itself and the post-treatment (Table 18).

Table 18: Microstructure of Nickel-based alloys by various AM processing conditions. AD: as deposited, ST: solution treatment, DA: double aging, TSRHT: thermal stress relief heat treatment γ: Ni (fcc) solid solution, γ': Ni3Al and Ni3Ti, cubic (ordered face-centered) Ll2 crystal structure, γ": Ni3Nb, metastable coherent in γ-matrix, body-centered tetragonal (bct) (DO22) crystal structure, δ: Ni3Nb, stable incoherent in γ-matrix, orthorhombic crystal structure, (DebRoy et al., 2018).

Alloy	Process	Condition	Microstructure
Inconel 625	DED-L	AD	γ-Ni (fcc) solid solution
		AN (700 °C/1 h/AC)	γ″ in γ-matrix
		AN (800 °C/1 h/AC)	δ in γ-matrix
		AN (1100 °C, 1200 °C/1 h/AC)	γ solid solution
Inconel 718	DED-L	AD	Laves phase in interdendritic region of γ-matrix
		AN (700 °C/1 h/AC)	γ′ + γ″ in γ-matrix
		AN (800 °C/1 h/AC)	γ′ + γ″ in γ-matrix
		AN (900 °C/1 h/AC)	γ′ + δ in γ-matrix
		AN (1000 °C, 1100 °C, 1200 °C/1 h/AC)	γ′ in γ-matrix
	DED-L	AD	Laves phase + γ′ with γ-matrix
	DED-L	AD	γ″ in interdendritic regions and close to laves phase and NbC in γ-matrix
	DED-L	HT (1080 °C/1.5 h/AC, 980 °C/1 h/AC, 720 °C/8 h/FC, 620 °C/8 h/AC)	Nb-rich MC type carbides along grain boundaries
Inconel 718	PBF-L	AD	Oblate spheroids/ellipsoids γ″ in γ-matrix
		AN (1160 °C/4 h/AC)	Spherical γ′ + δ in γ-matrix
	PBF-L	ST (980 °C/1 h/AC)	δ + Laves phase in γ-matrix
		DA (720 °C/8 h/FC, 620 °C/8 h/AC)	γ′ + γ″, δ + Laves phase in γ-matrix
Inconel 738	DED-L	AD	γ′ + γ, eutectic on the grain boundary
	PFB-L	AD	Small carbide precipitates
		HIP (1180 °C/4 h), 1120 °C/2 h, 850 °C/20 h	Duplex-size γ′ in γ-matrix
René 41	DED-L	AD	γ′ + γ, with γ′ larger in dendritic cores than in interdendritic zones
René 80	PBF-L	TSRHT (1082 °C/2 h heating and cooling/FC)	γ′ + γ
René 142	PBF-EB	AD	Cuboidal γ′ 59 vol%, γ 41 vol%
CMSX-4		AD	Cuboidal γ′ 72 ± 5 vol% with γ
IC221W (Ni_3Al based single crystal alloy)	DED-L	AD	Mainly Ni_3Al and some γ and Ni_5Zr

As explained in (Chapter II.2.2), the main hardening phase of the alloy INCO718 is created during post-treatment (tempering and aging), and the mechanical properties will be highly dependent on heat treatment. It is necessary to establish a careful heat treatment to achieve the mechanical properties required for the application of the manufactured part. For example, in the research of (Sames et al., 2016), various heat treatments are proposed according to the mechanical characteristic to be improved on the material, as shown in (Table 19).

Table 19: Common post-processing procedures for Ti–6Al–4V and Inconel 718 (Sames et al., 2016).

Treatment	Ti–6Al–4V	Inconel 718
Stress relief	2 hours, 700–730°C	0·5 hours at 982°C 1065 ± 15°C for 90 min (–5±15 min)
Hot isostatic pressing (HIP)	2 hours, 900°C, 900 MPa 180 ± 60 min, 895–955°C, >100 MPa	4 hours at 1120°C, 200 MPa
Solution treat (ST)	Not typical	1 hour at 980°C
Aging	Not typical	8 hours at 720°C Cool to 620°C Hold at 620°C for 18 hours total

An additional complication is the fact that AM processes of Direct Manufacturing type (for dense parts), generally involves a series of complex heating-cooling cycles, which can modify the evolution of the microstructure. In addition, the high cooling speeds produce strong grain size refinement. Other observations on the microstructure of Nickel-based parts manufactured by AM are (DebRoy et al., 2018):

- Different layers of the manufactured part have different phase proportions (γ, γ ', δ, etc.), depending on the number of thermal cycles to which the area is subjected, (Fig. 40). The previous explanation applies on certain occasions to grain growth (there may be more pronounced recrystallization in the lower part of the deposition than in the upper part of it).

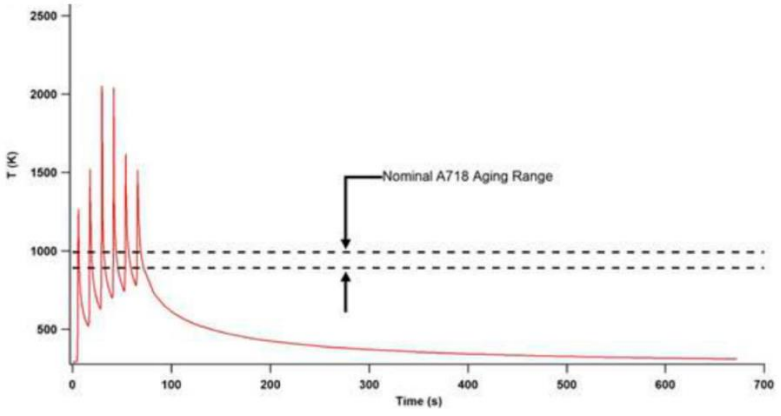

Figure 40. Thermal simulation of a point during powder-fed DED showing cyclic heating cycles, (Sames et al., 2016).

- The supersaturation and microsegregation during deposition in Laser Cladding process, can give rise to an important variation in the morphology of the dendritic microstructure (spatial heterogeneity). Spatial heterogeneity will give

rise to variability in mechanical properties. An example of the morphology variation during the Laser Cladding process is shown in (Fig. 41).

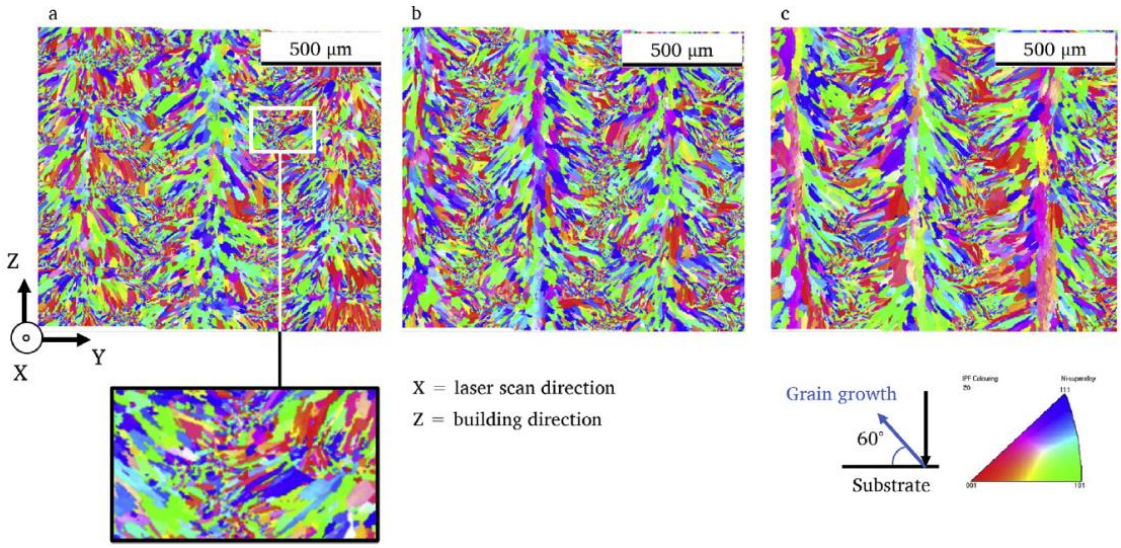

Figure 41. EBSD analyses of the LMD Inconel 625. Inverse pole figure (IPF) of the transverse section observations of samples printed at the same scan speed of 2500 mm. min^{-1} and different laser power. (a) 270W; (b) 300W; (c) 330W, (Nguejio et al., 2019).

- The formation of intermetallic during the AM process is a function of the solidification conditions. Intermetallics will form near the end of the alloy hardening process and will be largely controlled by the cooling rate. Solidification under high cooling rates and low G_L/V ratios is beneficial because they form discrete Laves phases.
- The vast majority of the drawbacks or defects of the microstructure can be solved via a suitable heat treatment.

2.3 Texture generated by the Laser Cladding Process

In the research by (DebRoy et al., 2018) is commented that the textures in the microstructure are the result of a compromise solution between the alignment of the easy-growing directions of a crystal during solidification, and the direction of the maximum temperature gradient within the melt pool. Grain growth will be favoured when the maximum direction of heat flow aligns with one of the easy-growing directions of the crystal system. A particular case is the “alternate type” textures, where the direction of heat flow (the direction of the laser beam) does not coincide with the direction of epitaxial grain growth of the previous layer. An example of alternating growth is shown in (Fig. 42), where the change of direction in the strategy of deposition (keeping all the

other parameters constant), gave rise to a change in the growing orientation of the dendrites from approximately 60° to 45°, (Dinda et al., 2012).

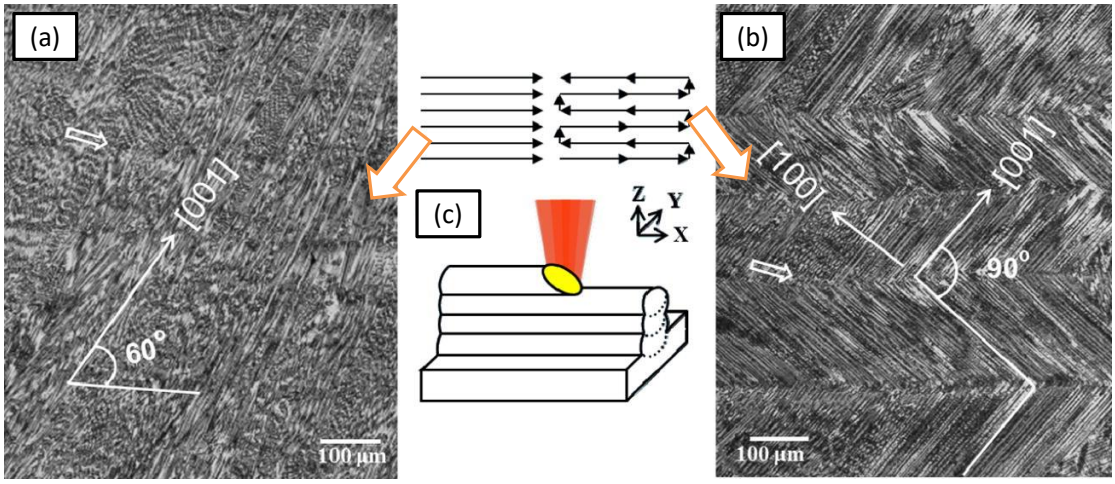

Figure 42. (a) and (b) Optical micrographs of the as-deposited IN718 samples produced with two different laser beam scanning patterns, as schematically shown in (c), (Dinda et al., 2012).

3 Context and Motivation for this Research

Summary:

- Additive manufacturing is an interesting technology, very versatile and has unique characteristics that other manufacturing processes do not have.
- Laser Cladding is an excellent application of additive manufacturing technology that has the potential to solve many problems in the industry; however, it has the problem that there is not enough information about the mechanical properties of cladded material that is added during the process (lack of knowledge is a problem to ensure reliability in the repair of a component).
- By other side, Inconel 718 alloy has many applications in the industry, is easily weldable (making it suitable for application in the laser cladding process), and is generally used for high value-added components, and is therefore a suitable material to investigate the relationship between microstructure and mechanical properties.

The motivation of my doctoral thesis will be to slightly close the information gap between a technology that is an excellent solution to industry problems (Laser Cladding), in a material that has applications in high value-added components and that is suitable for the laser cladding process (INCO718), but for which there is insufficient information

on its mechanical properties of the deposited material when used in processes where it must work in conjunction with the substrate in part repairment applications.

4 Organization of this Thesis

This thesis is organized in 6 sections:

- GENERAL INTRODUCTION: LITERATURE REVIEW ON ADDITIVE MANUFACTURING AND THE CONTEXT OF THE LASER CLADDING AM PROCESS
- CHAPTER I: PARAMETER OPTIMIZATION FOR THE LASER CLADDING PROCESS
- CHAPTER II: MICROSTRUCTURE CHARACTERIZATION OF NEW AND RECYCLED IN718 POWDER AND RESULTING LASER CLADDING MATERIAL
- CHAPTER III: MODELING OF LASER CLADDING PROCESS AND GRAIN MORPHOLOGY
- CHAPTER IV: APPLICATION TO THE REPAIR OF COATED PROBES TO OBTAIN MECHANICAL PROPERTIES IN CLADDING MATERIAL
- CHAPTER V: GENERAL CONCLUSIONS
- ANNEXES
- REFERENCES

Each chapter develops different topics of study and the objective is to separate the investigation into models that may be useful individually, but that together will serve to fulfil the objective of this thesis.

CHAPTER I: PARAMETER OPTIMIZATION FOR THE LASER CLADDING PROCESS

I.0 Nomenclature and Abbreviations

AM:	Additive Manufacturing
ANOVA:	Analysis of variance
CAM:	Computer aided manufacturing
CNC:	Computer numerical control
DOE:	Design of experiments
EBSD:	Electron backscatter diffraction
HAZ:	Heat affected zone
HRC:	Rockwell Hardness measured on the C scale
MRA:	Multiple regression analysis
RSM:	Response surface methodology

A:	Generic area (m^2)
a_1, a_2, a_3:	Constants for the polynomial equation of the shape of the laser cladding bead
A_c:	Transversal area of bead for the adhered material above the level of the substrate for a Laser Cladding process (m^2)
A_m:	Transversal area of the substrate material melted during laser cladding process and mixed together with the clad material (m^2)
$A_{\substack{spot \\ laser}}$:	Spot area of laser beam in work plane (m^2)
b_1, b_2, b_3:	Constants for the polynomial equation of the shape of the laser cladding melt zone in substrate
Dil:	Dilution in a single bead (-)
Dil_{ml}:	Dilution in a multiple bead (-)
H:	Height of a single cladding bead (m)
H_{Ac}:	Transversal height of bead for the adhered material above the level of the substrate for a Laser Cladding process (m^2)
H_{Am}:	Transversal height of the substrate material melted during laser cladding process and mixed together with the clad material (m^2)
L_{t_tr}:	Total width between the ridges of the clad layer (m)

m :	Schmid factor (-)
n_{ly} :	Number of layers in a multiple bead clad (-)
n_{tr} :	Number of tracks in a multiple bead clad (-)
$\%Off$:	Percentage of offset (-)
$\%Ove$:	Percentage of overlap (-)
$P_{\substack{laser \\ sv}}$:	Reduced composite variable of Laser beam power (-)
Por :	Porosity in a single bead (-)
Por_{ml} :	Porosity in a multiple bead (-)
P_{spe} :	Specific power ($W.m^{-2}$)
s_n :	Coordinate on the z' axis of the powder consolidation plane (m) (Chapter III.3.1)
t_{clad} :	Thickness of the cladding material (m)
v :	Scanning speed of laser beam ($m.s^{-1}$)
$Vc1$:	Auxiliary variable of the Scanning speed of laser beam ($m^{-0.5}.s^{0.5}$)
$Vc1_{sv}$:	Reduced composite variable of Auxiliary variable of the Scanning speed of laser beam (-)
v_{sv} :	Reduced composite variable of Scanning speed of laser beam (-)
W :	Width of a single cladding bead (m)
y_{Ac} :	y coordinate of the fourth degree polynomial equation for the shape of a clad bead (m)
y_{Am} :	y coordinate of the fourth degree polynomial equation for the shape of a laser melt zone in substrate (m)
α_c :	Wet angle for a single laser cladding bead measured from the centre thereof (°)
$\eta_{\substack{clad \\ deposition}}$:	Efficiency of the deposition of clad material on the substrate (-)
η_{clad_ml} :	Mass efficiency of powder feed deposition in a multiple bead clad (-)
σ :	Standard deviation (-)

I.1 Introduction

I.1.1 Characteristics of Laser Cladding Process

The Laser Cladding process consists of the addition of metallic material (usually in the form of powder or wire) into a melt pool generated by a high-power laser beam moving over a substrate (also metallic), with the objective of creating a high-density cladding. The addition of material is performed at a specific location called the focal plane.

The filler material is melted by the action of the laser beam and consolidated together with the base material by metallurgical bonding in a series of beads (similar to welding beads). For this research, the filler material will be a metal powder type.

The process has interesting characteristics such as (Fayazfar et al., 2018; Hofmann et al., 2014; Toyserkani et al., 2005):

- The possibility of adding material with low thermal affectation over the substrate.
- Rapid solidification rates, allowing large deviations in chemical composition from the alloy's equilibrium constitution (resulting in a substantial increase in solid solubility).
- The possibility of creating very small grain size microstructure and improving metallurgical uniformity.
- Metallurgical uniformity can be improved by eliminating the segregation defects typical of thick sections and by improving the response to heat treatment and cold working.
- In some cases, it is possible to improve the service life of components and, in special cases, to increase the cold working percentage of alloys on the basis of the higher ductility that has been achieved.
- It also allows the production of material combinations that would be impossible with other ingot-type processes, e.g. the creation of alloys with gradient-type compositions.

In addition, the Laser Cladding process allows the creation of free forms by adding and controlling the geometry of the bead cladding; in addition to the precise control of the generated microstructure by varying its process parameters (Chapter III.4).

In certain cases, the Laser Cladding process allows the elimination of redundant machining and most finishing operations, as the addition of material to the workpiece can be roughly adjusted to the final shape of the built object. This is especially advantageous for small series of products (in this case, the Laser Cladding process offers advantages at the production and prototyping level).

I.2 Modelling and Input Parameters of the Laser Cladding Process

A drawback of the laser cladding process is the difficulty of modelling a process that is complex. So-called "input parameters" (a number of variables characteristic of the process), can significantly modify the final properties in the deposited material.

The main input parameters include:

- Relative velocity of the laser beam compared to the substrate surface.
- Type and flow rate of gas used to entrain the metal powder particles to the melting zone (melt pool), to the substrate in the so-called working zone. To deliver the particles (metal powder), a noble gas is generally used to serve as protection against oxidation.
- Shape distribution and spatial density of the metal powder delivered to the substrate (the powder mass density in the working space depends in general on the geometry of the nozzle and the mass flow of the carrier gas).
- Geometry of the metal powder (generally characterised by its mean diameter and sphericity).
- Surface finish (roughness) of the powder and substrate surface as well as its opacity change due to oxidation. The effect on the change of opacity on surfaces is perceived as a variation in the spectral absorptivity of the laser beam.
- Laser beam power density, geometry and volumes of the beads deposited on the preliminary layers.
- CAM path trajectories according to the desired application (the trajectory strategy in which the coating beads are deposited allows for anisotropies in certain mechanical properties). All the previous factors are regardless of thermal material properties (which are temperature dependent).

An example diagram with a summary of the parameters for the laser cladding process following the sequence methodology: inputs, processes and outputs is shown in (Fig. I.1) (Toyserkani et al., 2005).

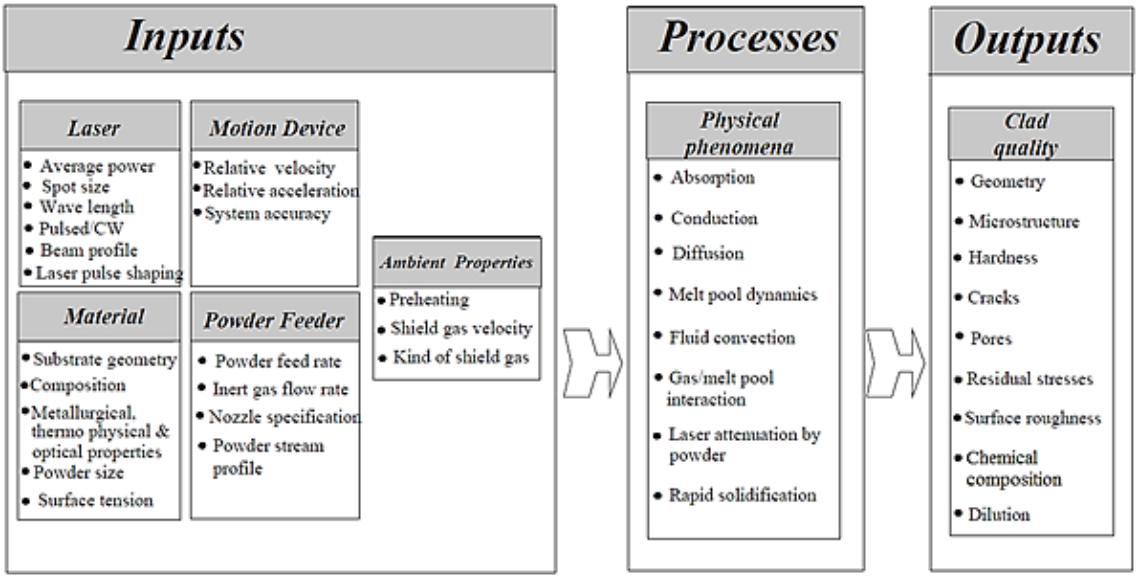

Figure I.1. Summary diagram of parameters for the Laser Cladding process (Toyserkani et al., 2005). Note the variety of parameters that can influence the previous mentioned process.

The number of input parameters is very large, and not all of them are of equal importance in generating "quality" deposited material. However, it is first necessary to define what quality for cladding material is.

An example list is presented by (Ghosal et al., 2018) with a summary of the main characteristics for the Laser Cladding process that must be taken into account to define “quality”:

- Precision on deposition of material and surface finish.
- The porosity.
- The surface hardness.
- Mechanical properties.
- Texture at the microstructure of the deposited material.
- Residual stress and distortion.

It is therefore not possible to define the term "quality" on the basis of a single criterion, which may in principle lead to the existence of a compromise solution.

In (Mondal et al., 2011) another extensive study was conducted on the effect of process parameters, and the cause-effect relationships were expressed by means of an Ishikawa diagram (Fig. I.2). In this case, the division by factors influencing the process is by branches related to the following aspects:

- Material properties.
- Local conditions in the cladded area.
- Characteristics of the cladding material itself and kinematic conditions (tool path strategy).
- Characteristics of the energy source (laser beam).

The usefulness of the following diagram is that it gives an idea of the influence of how the different "physical components" in the equipment (machine configuration), influence the process parameters. For example, in the case of the "Laser branch", the "amount" of energy is controlled by varying the characteristics of the laser beam.

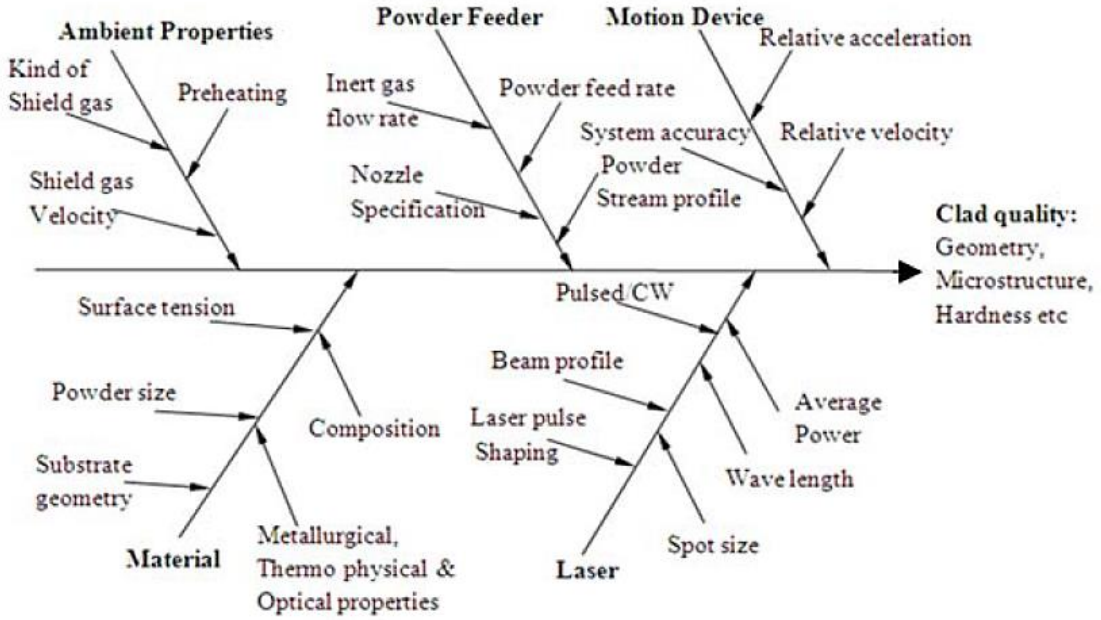

Figure I.2. Ishikawa diagram for performance characteristics in laser cladding process (Mondal et al., 2011).

I.2.1 Premises to use for this Research

It was necessary to establish a series of premises to enable the development of a methodology to address the optimisation of the Laser Cladding process. The aim of the premises was to obtain a high quality deposited material. These premises were:

- At a basic level, a single bead on a flat substrate is the minimum amount of coating material that can be added to the substrate by the laser cladding process. It is assumed that the "quality" of the coating (for a given volume of added material and for a specific application), is the sum of consecutive single beads. Therefore, it is first necessary to establish an optimisation of a bead as the basic coating unit.
- Because there is a large number of possible combinations of input and output parameters in Laser Cladding process, it is necessary to establish a basic set of them applied to the simplest amount of material addition (that is, a simple bead), so that a single high quality cladding can be obtained by modifying a minimum number of input process parameters. In other words, only the minimum necessary number of parameters will be used (not all parameters are equally important).
- Based on the previous paragraph, an optimisation of a set of coating beads to form layers (understood as "layer" as a sum of individual beads), must retain the same quality of the basic unit of coating material for the formation of aggregate material volumes (due to the successive build-up of layers). In other words, the transfer of the "good characteristics" of the optimised coating bead to the whole bead assembly should be sought in order to meet the "quality" requirements.

It is now necessary to define the "quality" of a laser cladding coating, i.e. a set of parameters to be considered as observable and measurable "output" of the process. As a basis we will take the work of (Toyserkani et al., 2005), which shows a list of the most important aspects to be taken into account in order to quantify the quality of the deposited material. Each aspect is related to a property that should be taken into account regarding the quality of the deposited material. The property "to be taken into account" for the quality of the material is shown in brackets:

- Geometry (related to the stability of the process).
- Microstructure (associated with the intrinsic properties of the material).
- Cracks and porosities (affect the structural integrity of the material, as they are origin of stress concentration).

- Surface roughness (related to the consolidation of consecutive layers of cladded material).
- Residual stresses (increased sensitivity to failures in static strength, but especially in dynamic strength, such as fatigue).
- Alloy segregation (undesirable separation and recombination of the original constituents of an alloy resulting in inhomogeneous metallurgy).
- High Dilution (excessive thermal damage to the substrate).

I.2.2 State of Art. The Use of Statistical Models in the Laser Cladding Process

Statistical models are useful for finding an optimised set of process parameters to achieve a high quality deposited material when applied, but without the inconvenience of physically modelling the Laser Cladding process.

For a specific application, it is very useful to avoid the complexity of modelling the Laser Cladding process using the statistical modelling tool. At this point is necessary a clarification on the term "specific application". It can be assumed that it will not be possible to use "the statistical model" in more than one case (i.e. only a very tight optimisation is possible, and without any flexibility). However, "specific application" in this case will mean processes with "similar" characteristics (e.g. use of the same filler material and the same type of substrate). This means that the process optimisation for by example flat geometry could be used for another with curvature on the surface, as long as both are using the same cladding material and substrate.

Sometimes, statistical parameter optimisation will not be directly applicable to a particular circumstance (e.g. extremely complex geometries). Even so (from the author's own experience), it was observed that the values obtained from a preliminary process optimisation are close to the new optimum for a particular case, thus saving a lot of resources (human, material and time).

Another usefulness of the statistical modelling approach comes from the fact that the number of process parameters chosen for the optimisation of the laser cladding process is significantly reduced. In other words, a tool is obtained that allows precise control of the process with few parameters (a great advantage for targeting the deposition of high quality material).

There are various approaches to the use of statistical methods. One of the most common is the use of RSM-type models in combination with an experiment design methodology such as Taguchi (Fatoba et al., 2017; Mondal et al., 2011). Another common method is the use of linear correlation analysis (Ansari et al., 2016; Nabhani et al., 2018), where combined parameters of type ($P_{laser}{}^{\alpha} v^{\beta} F^{\gamma}$) are used for each of the response systems (outputs). T These methods often rely on the use of an analysis of variance (ANOVA) to identify the sensitivity of parameters within the system response.

Another approach is to use neural networks to model the behaviour of the system (Mondal et al., 2014; Saqib et al., 2014; Toyserkani et al., 2005), used particularly related to the geometry of the bead deposited over the substrate and in multi-objective optimization.

For this research the use of Multiple Regression Analysis (MRA) is proposed, with certain primary set of process parameters that will be established later. It is also proposed (as a novelty) the use of polynomials to characterize the shape of the bead geometry. As will be seen later, the previous approach will avoid a number of ambiguities (subjectivities) that are common when characterising a laser cladding bead. The Henry's diagram test was used for the verification of the linear correlations, in combination with the study of the difference in error prediction of the correlations themselves (Pardoe, 2020).

I.3 Optimization of a Single Bead for the Laser Cladding Process

The first step will be to determine a suitable set of parameters to model the Laser Cladding process and its effect on the outputs (responses).

The same set of variables used by (Oliveira de et al., 2005; Pinkerton, 2014) will be taken as input parameters:

- Power of the laser beam (P_{laser}).
- Scanning speed (v).
- Powder flow (m').

These previous parameters were determined as the most influential for modelling the resulting geometrical characteristics of a single chord. From (Fig. I.1) it is obvious that there are many other parameters (but they will not be considered). It is important to limit the number of process parameters, because the combined effect of all of them in the

formulation of a statistical optimisation based on experimentation applied to the laser cladding process would excessively increase the complexity of the model.

Sometimes, it is possible to use the so-called combined parameters (the combination of two or more simple parameters), with the aim of reducing the number of variables considered. For example, instead of the raw laser power, it is possible to use the specific power (the power per unit area of the laser spot $P_{spe} = P_{laser} / A_{\substack{spot \\ laser}}$, where $A_{\substack{spot \\ laser}}$ is the area of the laser beam over the flat surface on the substrate. The advantage of combined parameters is the possibility of extending the applicability of the same (increasing the versatility of a parameter to be independent of a specific type of equipment). For example (if a given equipment can be configured for different power and point area values), the application of a certain set of optimal parameter values may not be possible to transfer easily in other equipment, simply because similar conditions cannot be established. However, it is more likely to achieve the transfer of optimal parameters by using combined ones (such as P_{spe}). The use of combined parameters is limited due to factors related, for example, to the energy density required to carry out a certain process. That is, other elements (such as the type of laser beam distribution) must be considered to ensure easy transfer of parameters to other equipment than the one used to obtain an optimal set of values. A laser beam can have different types of energy distribution: TEM01, uniform, Gaussian, etc., and it is not possible to standardize it simply applying the formula $P_{spe} = P_{laser} / A_{\substack{spot \\ laser}}$.

For a single bead, the Dilution (Eq. I.1) will be taken as the first output parameter. From (Ocelík et al., 2007) the Dilution (Dil) will be defined from the geometric measuring of the cross transversal section of a single bead as indicated in (Fig. I.3):

$$Dil = A_m / (A_c + A_m) \qquad \text{Eq. I.1}$$

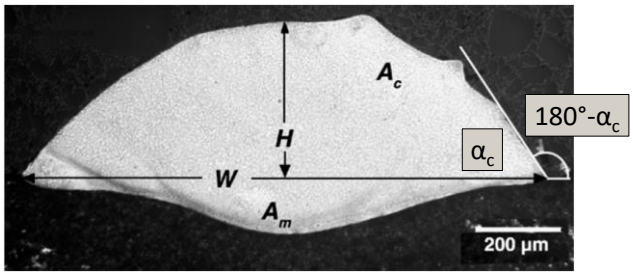

Figure I.3. Cross-section of a cladding bead using a Laser Cladding process with description of the main geometrical characteristics: clad height H, clad width W, clad angle α_c, clad area A_c and melted area A_m.

During the laser cladding process, dilution quantifies the relative amount of substrate area that has been melted and mixed in a cross-section of a cladding bead (as a reference usually taken from the original substrate surface), with added filler material. A_c and A_m shall be taken as absolute values, so it is a positive value.

The Dilution measurement, as expressed in (Eq. I.1) is only the geometrical quantification of the measured cross-sectional areas in the cladding bead. That is, a phenomenon of thermal affectation expressed as geometrical through clearly measurable areas. The precise measurement is possible because the solidification process during a coating process generates very clear differentiated crystalline microstructures (not only at the bead level, but also at the layer level).

The added material can then be observed after adequate metallographic etching preparation, which generally includes attack with a suitable chemical to reveal the difference in microstructures.

Dilution is an inherent characteristic of the process (Laser Cladding always requires a slight melting to ensure a good metallurgical bond), but it strongly depends on the material characteristics used in both the clad and the substrate (both can be different). Throughout this research, the INCONEL 718 alloy will be used as substrate and cladding material (in the shape of metallic powder). The physical characteristics of this Nickel-based product are described in (Chapter III.3.4).

I.3.1 General Objectives of Optimization for a Single Bead

Based on literature research for different materials (Ansari et al., 2016; Ocelík et al., 2007; Oliveira de et al., 2005; Tabernero et al., 2013), a set of optimal process parameters will be sought that meet the following requirements as far as possible. It will not always be possible to find an optimal solution; sometimes a compromise solution will be necessary:

- Maximize the clad area (A_c). This avoids wastage of filler material and helps the economic viability of the process (metal powders, as raw material, are generally very expensive to produce).
- Minimize the Dilution value (Dil). It is important to note that the value of this parameter should be kept as low as possible (non-zero), as a high value of this parameter indicates excessive addition of heat to the substrate (with risk of

segregation of alloying compounds in general), or may indicate low material deposition efficiency (when Dil is zero).

- Minimize the value of Porosity (Por). A porous material has poor mechanical properties. In general, porosity can be caused by the shielding gas trapped during the formation of the molten bath, and by the lack of fusion of the material supplied (beam power deficiency), (Wang et al., 2007). On the other hand, the use of too little shielding gas causes oxidation, and the use of too much energy can result in the formation of intermetallics (hard, but also brittle).

Once this first set of measurable output variables (A_m and A_c derived from Dilution, plus Porosity), has been defined, in addition to knowing the temperature-dependent properties of both the coating material and the substrate, it is necessary to establish a window (working range) of the chosen input variables:

- Power of the laser beam (P_{laser}).
- Scanning speed (v).
- Powder flow (m').

I.3.2 Initial Working Range for Design of Experiments

The initial working range for the three main input parameters is shown in (Table I.1). It is important to note that the working ranges for the input parameters also depend on the equipment available. It may be the case that they have "local optimum values" that are not valid on other Laser Cladding process machines because the machine is not able to overcome certain functional limitations in the parameters (e.g. laser beam power).

On the other hand, the optimisation procedure described in this chapter is of a general nature and can be used independently of the equipment available for a given application. In laser cladding processes, the use of certain units is common (e.g. speeds are generally expressed in mm/min instead of m/s). By convention, the usual units for this type of process will be used. Therefore, when making a change of units or using a combined variable, the necessary conversions shall be made to maintain the consistency of the unit system.

Table I.1: Initial input parameters for the working window of a laser cladding process for INCO718 alloy (single bead). In all cases, the beam profile has been of cylindrical type and the spot diameter remains constant at $\phi d_{laser} = 1\ \mathrm{mm}$.

	Minimum	Maximum	$\Delta Step$ between minimum and maximum value
v (mm/min)	200	600	200
m' (gr/min)	6.49	8.77	1.14
P_{laser} (W)	200	600	200

The previous range of parameters was established based on the author's experience. Other process parameters were kept constant during the course of the experiments:

- The focal working distance from the nozzle to the plane of maximum concentration of metallic powder (s_n).
- Spot diameter (laser beam) at focal distance (ϕd_{laser}).
- Continuous laser beam working mode (at constant frequency in the order of 10 kHz).
- Wavelength of the laser beam (in this case for a fibber laser it is 1063 nm).
- Flat substrate with uniform surface (all substrate samples were machined and sanded with 80 grit metal sandpaper to ensure a similar surface finish, presenting the same clean but opaque appearance).
- Similar powder particle size distribution (metallic powder was purchased from the same supplier under the same specifications).

I.3.3 Configuration of the Clad Bead Experiment on the Substrate

I.3.3.1 Constraints and Modelling of Simple Clad Beads

The next step is the physical deposition of the beads. It is important, when establishing the DOE configuration of the bead array, to take into account the following aspects for the sample set in order to obtain consistent data:

- Leave enough space between each of the beads to avoid overlapping of the heat-affected cross-sectional areas (in general a spacing of 4 times the average width of the bead, about 4 mm, has been left). In addition, a bead of sufficient length is necessary for the establishment of steady state in the process (approximately 20 times the width of the bead).

- The substrate must be large enough in mass to act as a good and robust heat reservoir. It must be of sufficient thickness to avoid thermal deformation during the addition of the material. Substrates with a thickness of less than 5 times the bead width are not recommended. As far as possible, substrates should be clamped to restrict their movement. If substrate deformation is not avoided, the focal length from the nozzle tip to the deposition base will change (s_n variable).
- After completing the series of experiments, the surface must be cleaned in a suitable way (for example, a wire brush or other available ways), to remove powder particles that are not adherent due to the risk of distorting the reading during the taking of the cross section area of the beads, (Fig. I.4).

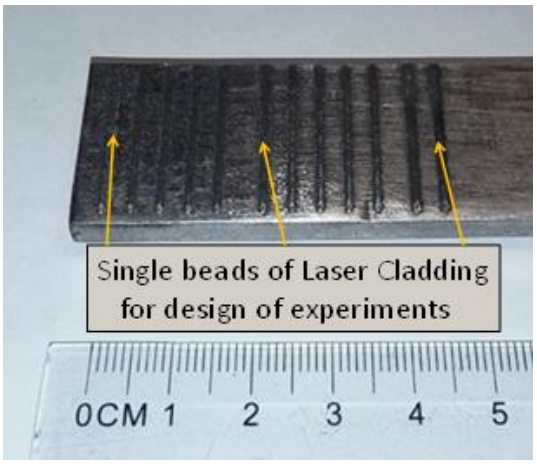

Figure I.4. General aspect of the beads made by the Laser Cladding method. The length of each bead is made in such a way that the geometric transversal section in steady state is measured.

I.3.4 Geometric Characterization of the Beads. Use of 4th degree Polynomials

The geometrical characterisation of the beads samples were carried out by cutting and metallographic preparation of the aforementioned samples. The series of beads were cut in the direction transverse to the deposition path. After encapsulation in phenolic resin, they were polished with sandpaper and diamond solution of different sizes until the surface irregularities were removed and then etching with a suitable reagent.

In this research, for the case of a nickel-based alloy, Kalling reagent #2 according to the procedure of (ASTM Subcommittee E04.01, 2015), is suitable. The appearance of a set of

beads and a specific detail one of them in optical microscope micrograph is shown in (Fig. I.5).

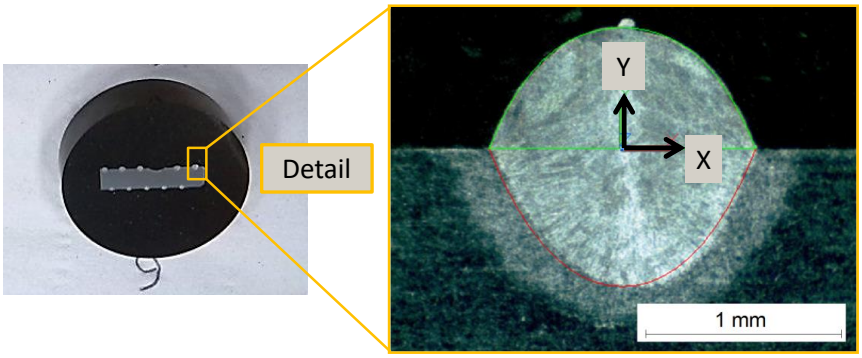

Figure I.5. Left, general appearance of a set of encapsulated tests cut perpendicular to the direction of deposition of the bead (the diameter of the capsule is 40 mm). Right, detail of the section of a bead delimited by the green and red lines (note the frame of reference in the centre of symmetry at the same height as the substrate surface).

The beads present, according to the parameters with which they are deposited, different geometric shapes in their transverse cross-section. In the literature, individual cross-sections of beads are fitted as circumferential sectors (Gong et al., 2013; Pinkerton and Li, 2004).

In the case of our experiments, it was observed that the shapes of beads obtained are, in some cases different from the geometry that can be modelled by a circumference sector. For the previous reason, a 4th degree polynomial function was chosen to model the shape of the transversal bead section above the level of the substrate according the associated frame of reference of (Fig. I.5, right). The use of a 4th degree symmetric polynomial $y_{Ac} = a_1 x^4 + a_2 x^2 + a_3$, rather than a sector of circumference, allows a greater flexibility in modelling the bead cross section shapes. It is possible to reduce the number of constants of the characteristic polynomial to only 3 (a_1, a_2 and a_3), and thus keep the mathematical complexity low with satisfactory results, at level of transversal bead section fitting.

Another advantage when using the derivative of the function $y_{Ac} = a_1 x^4 + a_2 x^2 + a_3$ for $y_{Ac} = 0$ was to calculate the slope (and therefore the wet angle α_c of (Fig. I.3)), in an objective way. In most cases, the calculation of the wet angle in beads is done by visual inspection dependent on the user's point of view.

In the melted area shown in (Fig. I.5, right), the previous methodology is applied to fitting the area with a 4th degree polynomial of the form $y_{Am} = b_1 x^4 + b_2 x^2 + b_3$ (with b_1, b_2 and b_3 as constants to be determined).

The methodology of 4th degree symmetric polynomial can be applied for the heat-affected zone (HAZ), although in this case it will not be done because it is unnecessary to determine at this moment this quality parameter for a single bead.

The next step (with the help of an image analysis software), consists of taking some measurements of the cross-sectional area for each input image (A_c and A_m), in order to deduce the appropriate constants for each characteristic polynomial, specifically the data of height (H) and width (W) (Fig. I.6).

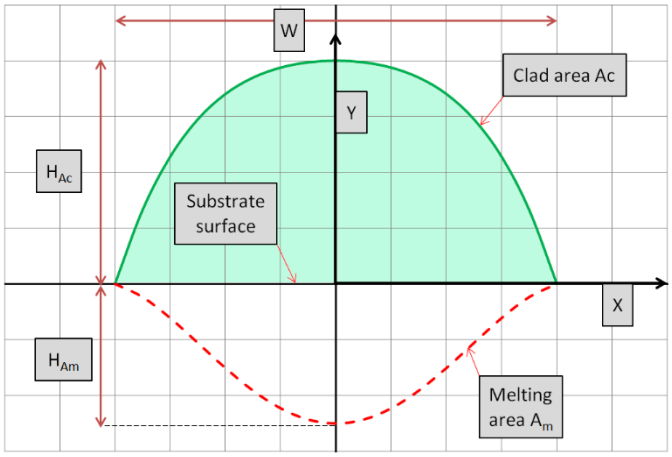

Figure I.6. Diagram showing the main dimensions of the cross-section of a cladding bead for data collection to model the clad area and the melted cross-sectional area.

Choosing for fitting and model the values such as A, H and W in the melted and added areas is not random. From the author's experience it has been observed the three previous geometrical parameters present a high dimensional reliability, they are easily measurable and with high precision, which in turn allows to obtain a good fit regarding the characteristic polynomials (y_{Ac} and y_{Am}), and therefore good Dil output parameter values.

To fully define a cladding bead (the part of the material added over the surface), it is necessary to know the following parameters: A_c, H_{Ac} and W. Any other geometric characteristic can be deduced from the previous three.

The calculations to obtain the coefficients for the modelling of each previously mentioned areas are then deduced from simple calculation. The sign for H_{Ac} (+) and

H_{Am} (-) must be taken into account. In the case of W, A_c and A_m only its absolute value is necessary. The calculations of coefficients are shown in (Eq. I.2) to (Eq. I.7):

$$a_1 = \frac{40(2H_{Ac}W - 3A_c)}{W^5} \quad \text{Eq. I.2}$$

$$a_2 = \frac{6(5A_c - 4H_{Ac}W)}{W^3} \quad \text{Eq. I.3}$$

$$a_3 = H_{Ac} \quad \text{Eq. I.4}$$

$$b_1 = \frac{40(2H_{Am}W + 3A_m)}{W^5} \quad \text{Eq. I.5}$$

$$b_2 = -\frac{6(5A_m + 4H_{Am}W)}{W^3} \quad \text{Eq. I.6}$$

$$b_3 = H_{Am} \quad \text{Eq. I.7}$$

The wetting angle α_c (whose measurement can now be done in an objective way), (Fig. I.3), is calculated from (Eq. I.8):

$$\alpha_c = -\text{atan}\left(\frac{W(W^2 a_1 + 2a_2)}{2}\right)\frac{180}{\pi}\,(°) \quad \text{Eq. I.8}$$

The deposition efficiency of the laser cladding process for a single bead is obtained from a mass balance (considered in steady state), between the deposited area A_c, and the powder flow m', (Eq. I.9):

$$\eta_{\substack{clad \\ deposition}} = \frac{\rho_p v A_c}{m'} \quad \text{Eq. I.9}$$

The use of 4th degree polynomials, allows to model a wide variety of shapes within the variation of parameters of the DOE, as the cladding area, the heat melted zone and the wetting angle α_c. An example of application is shown in (Fig. I.7).

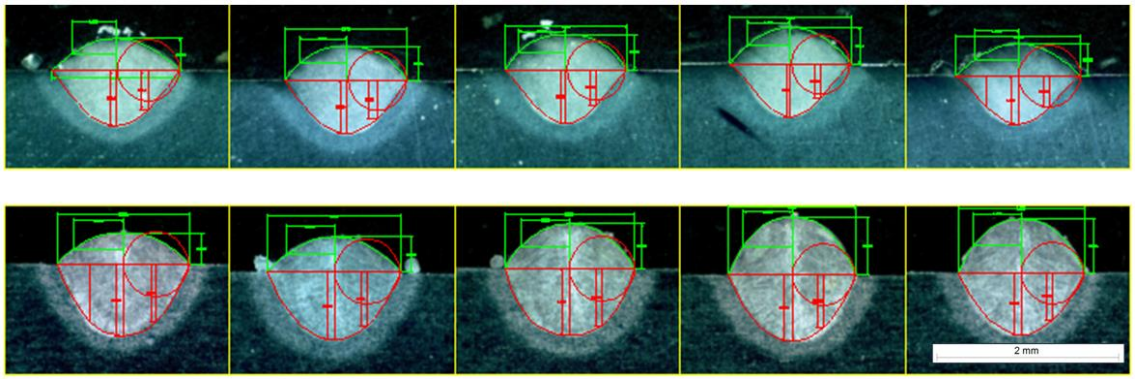

Figure I.7. Example of application by using fourth degree polynomials for the calculation of constants to estimate the cladding cross-sectional area and the melting area for a representative set of experiments.

I.3.5 Presentation of Preliminary Results. Limitations and Defects Observed in the Process Parameters Using 5D Graphics

During the development of the DOE, when using the data in (Table I.1), lack of fusion (poor union between the material supplied and the substrate), was observed for the experiments with a laser beam power of 200 W. It was suggested that the lack of adherence was due to the effect of the low power of the laser beam (without enough energy to create a proper melt pool).

As a correction, it was decided to increase the lower power value in the DOE window from a value of 200 W to 300 W, in addition to a significant variation in the working window of the variable "scanning speed" (v). This has been done in order to explore the effect on a combined variable defined below.

The linear energy density is defined according to (Eq. 1.10), at a constant power as:

$$\rho_{\substack{line \\ energy}} = \frac{P_{laser}}{v} \qquad \text{Eq. I.10}$$

When using the previous equation, care must be taken to convert the units of the numerator and denominator to consistencies.

The effect of varying the energy density by modifying the work speed in the process, allows quantifying the minimum threshold of the energy-speed combination necessary to establish a good metallurgical bond between the cladding material and the substrate in a single combined variable.

For the second variable in (Table I.1), i.e. m', it was decided to keep the amount of powder flow at a fixed value (the intermediate value in the original work window was chosen, which is considered a compromise solution). This can be justified because the magnitude of the attenuation due to the effect of powder shadow on the substrate which is relatively small (Tabernero et al., 2012).

The change in the parameter window values for the low beam power values in the DOE is presented in (Table I.2).

Table I.2: Variation in the lower value of power of the window of parameters in the DOE for the optimization of a bead clad. The beam profile and beam diameter parameters remain similar to those of (Table I.1).

	Minimum	Maximum	$\Delta Step$ between minimum and maximum value
v (mm/min)	200	700	100
m' (gr/min)	constant=7.63		
P_{laser} (W)	constant=300		

For the corrected parameters of (Table I.1) and (Table I.2), the results are shown in (Table I.3):

Table I.3: Results of the calculations of the parameters "Clad Area", "Dilution", "Efficiency of deposition" and "Linear energy density" for the DOE on INCONEL 718 material according to (Table I.1) and (Table I.2).

# CLAD	Speed (v), mm/min	Powder flux (m'), g/min	Power (Plaser), W	Clad area (Ac), mm2	Dilution (Dil), %	$\eta_{\substack{clad \\ deposition}}$, (%)	ρline energy (J/mm)
1	200	7.63	200	0.145	39.0%	3.1%	60.0
2	300	7.63	200	0.095	47.3%	3.1%	40.0
3	400	7.63	200	0.065	54.6%	2.8%	30.0
4	200	7.63	400	0.179	73.0%	3.8%	120.0
5	300	7.63	400	0.122	78.5%	3.9%	80.0
6	400	7.63	400	0.085	81.2%	3.6%	60.0
7	200	7.63	600	0.202	79.3%	4.3%	180.0
8	300	7.63	600	0.144	82.1%	4.6%	120.0
9	400	7.63	600	0.125	83.2%	5.4%	90.0
10	200	6.49	200	0.122	43.3%	3.1%	60.0

11	300	6.49	200	0.088	57.4%	3.3%	40.0
12	400	6.49	200	0.05	62.9%	2.5%	30.0
13	200	6.49	400	0.162	74.3%	4.1%	120.0
14	300	6.49	400	0.112	80.4%	4.2%	80.0
15	400	6.49	400	0.071	84.1%	3.6%	60.0
16	200	6.49	600	0.175	83.0%	4.4%	180.0
17	300	6.49	600	0.122	85.6%	4.6%	120.0
18	400	6.49	600	0.109	85.5%	5.5%	90.0
19	200	8.78	200	0.198	31.0%	3.7%	60.0
20	300	8.78	200	0.101	45.2%	2.8%	40.0
21	400	8.78	200	0.073	53.5%	2.7%	30.0
22	200	8.78	400	0.224	68.5%	4.2%	120.0
23	300	8.78	400	0.155	71.6%	4.3%	80.0
24	400	8.78	400	0.095	79.1%	3.5%	60.0
25	200	8.78	600	0.248	78.1%	4.6%	180.0
26	300	8.78	600	0.178	78.5%	5.0%	120.0
27	400	8.78	600	0.182	80.0%	6.8%	90.0
28	200	7.63	300	0.191	64.7%	4.1%	90.0
29	300	7.63	300	0.115	70.1%	3.7%	60.0
30	400	7.63	300	0.08	66.3%	3.4%	45.0
31	500	7.63	300	0.084	74.6%	4.5%	36.0
32	600	7.63	300	0.053	75.4%	3.4%	30.0
33	700	7.63	300	0.054	75.9%	4.1%	25.7
34	500	7.63	600	0.1	84.7%	5.4%	72.0
35	600	7.63	600	0.067	86.8%	4.3%	60.0
36	700	7.63	600	0.058	88.4%	4.4%	51.4
37	100	8.78	600	0.692	64.7%	6.5%	360.0
38	350	8.78	600	0.165	78.2%	5.4%	102.9
39	700	8.78	600	0.086	80.3%	5.6%	51.4

The calculated value of the wetting angle α_c has not been included in this table. This is because this parameter will receive special treatment because it is directly related to the creation of multiline beads. In this section, emphasis will only be placed on optimizing a single cladding line.

Once these first results have been calculated (Table I.3), certain data will be represented graphically due to their special importance for displaying trends, specifically the values of "Clad Area" and "Dilution".

The computer program (XLSTAT (R)) will be used, which allows drawing a composite graph (5D). This representation is advantageous in that it shows in a simple way the relationship between the three main input parameters (P_{laser}, m' and v, each on the main coordinate axis of a 3D graph), and two of the responses (output) parameters. In the outputs parameters, Dilution (Dil) is represented as a colour scale (associated with a sphere-like object), together with the cladded area (A_c), expressed as the size of the sphere-like object for each coordinate point based on the input parameters for the experiment.

The (Fig. I.8) shows all the behavioural trends in the output parameters as a function of the input parameters for the DOE in (Table I.3). This graph will serve together with the data in the previous mentioned table as the basis for the next stage of optimization for the Laser Cladding process from a single INCONEL 718 alloy bead.

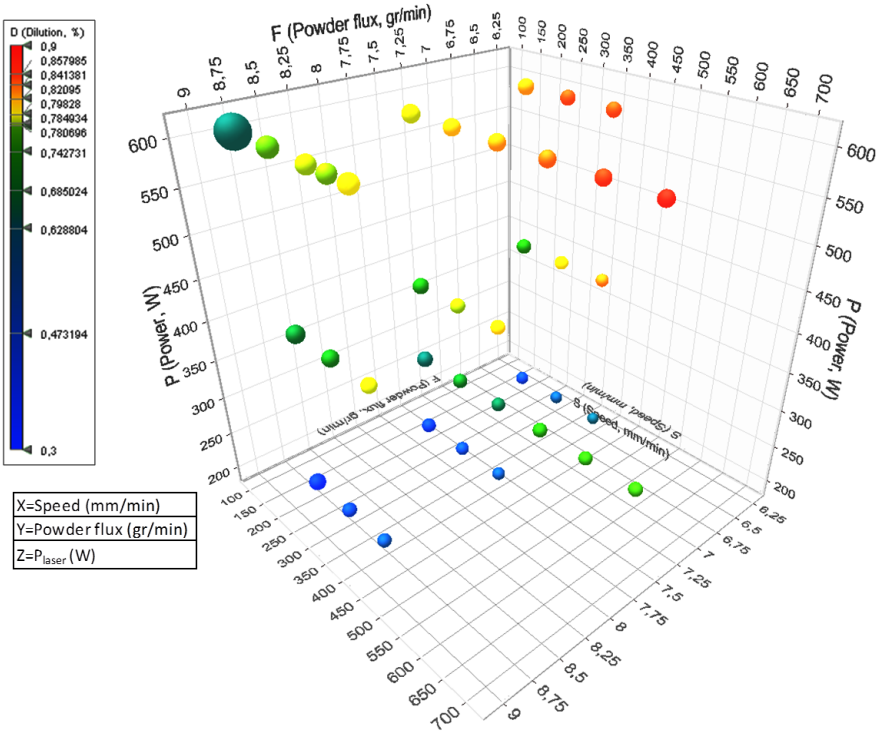

Figure I.8. 5D graph with the representation of the results of the calculations of "Clad area" (A_c) and "Dilution" (Dil) according to the input parameters "Power" (P_{laser}), "Scanning speed" (v) and "Powder flux" (m'). The input parameters are represented on the main coordinate axes, the "Clad area" by the sphere-object size and the "Dilution" by the colour scale.

I.3.6 Formation of Secondary Phases during Laser Cladding Process (Effect on Optimization)

It is necessary to mention that, in the early stages of optimization for the manufacturing of a single bead of a given material (in our case INCO718), it is important to put attention for the formation of secondary phases and to avoid from the beginning the conditions for the appearance of those. Secondary phase is defined as any compound or compounds formed from the same original elements of the alloy, but with a chemical composition different from it or outside the tolerance range from the original nominal composition of the alloy.

The origin of these secondary phases is because the Laser Cladding process involves high energy densities, in the order of $10^7 \sim 10^8\ W/m^2$ (Han et al., 2004). For the previous reason, despite the short local interaction time of the laser beam with the substrate, and depending on the input parameters used during the cladding process (Fig. I.1), it is possible to reach very high temperature values in the zone of convergence of the laser beam with the substrate (molten pool). This is sometimes sufficient for the chemical disaggregation of the alloying elements.

For example, if a high power laser beam is used to adhere a larger amount of material to the substrate surface (without changing other process parameters, which is a way to increase the efficiency of the process, according to (Eq. I.9)); the undesired effect of secondary phase formation can occur.

The consequence of the formation of the secondary phase (based on mass conservation), is an impoverishment of the necessary alloying elements in another volume within the bead (necessary for the hardening phases that would be expected as a result of the application of the heat treatment after the cladding process). The formation of secondary phases is easy to identify at the level of observation by optical microscopy for the alloy used in this research, INCO718.

The beads formed by Laser Cladding process of Inconel 718 (with a suitable protective atmosphere of 99.999% purity Argon), after a standard metallographic encapsulation process (ASTM Subcommittee E04.01, 2015); present a brilliant appearance (Fig. I.9, left inside of the bead).

However, the presence of secondary phases is revealed as areas of different colouration (from a shiny to a dull-dark appearance), that in the deposited material cannot be

attributed to a change in the microstructure. It was been observed that the secondary phase is generally located in the periphery zones of the coated area (on the surface or between the beads themselves when a complete layer is deposited by simultaneous beads), as shown in (Fig. I.9, top left of the "top").

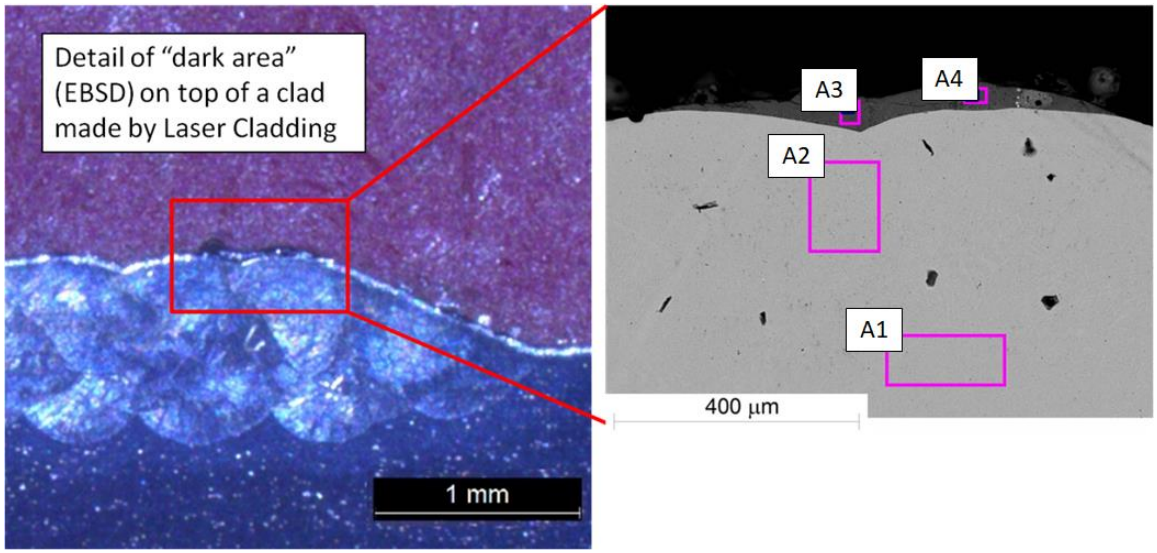

Figure I.9. Optical micrograph of INCO718 Laser Cladding beads, and scanning electron microscope detail highlighting rectangles in selected areas for compositional analysis using EDX.

The appearance of "strange" looking areas was the reason for a detailed examination. The quantitative composition of the dull-opaque areas was verified by EDX (Fig. I.9, right).

This chapter will not go into detail about the phases created during the Laser Cladding process with Inconel 718 alloy. The objective of this optimization chapter is to establish a criterion to quantify the absence of undesirable secondary phases and avoid their appearance, and thus use process parameters that allow an addition of material with a nominal composition similar to the original alloy. However, as a small guide, the results of qualitative composition in the areas indicated as A1 to A4 are shown in (Table I.4). The areas A3 and A4 (Table I.4), have a notoriously different composition from that of the initial material (INCONEL 718 raw powder); see (Chapter II.2.1.1). Areas A1 and A2 have the nominal composition of the original alloy. The “strange” phase type could not be accurately established, although it is suspected that it may be an intermetallic or an oxide.

Table I.4: Composition of areas selected A3 and A4 by means of an SEM-EDX analysis.

Spectrum	Al	Ti	Cr	Fe	Co	Ni	Nb	Mo
A3	1.32	1.3	42.3	29.6	0.22	13.45	7.97	3.87
A4	0.76	5.68	41.9	5.14		1.11	45.4	
All results in weight%								

For more details on the phases found in the material used for the fabrication of the different samples used in this research using the Laser Cladding process (INCO718), before and after heat treatment, see (Chapter II.2.2.2.2).

It was also observed that the hardness of the foreign phases is very high (a micro-hardness test sampling within the "opaque zone" (Fig. I.9), resulted in a value in the order of 70 HRC). The “strange” compounds found will be assumed to be intermetallic due to their hardness. The presence of hard particles can serve as stress concentrator and crack initiator. Regarding these (intermetallic) compounds, they are hard, brittle and have high melting points. With respect to the position that an intermetallic occupies within the alloy, the types of primitive unit cells that are formed will be a function of the interstitial positions (generally cubic or hexagonal in the base metal of the alloy), so that metals are located in positions in the cell and non-metals in the interstices (Merino Casals, 2012). Therefore, an intermetallic will not be incorporated into the cell structure easily, but will preferentially be located in the interstices between the crystalline cells.

For the initial optimisation tests, the process parameter combination limits will be taken as those at which the occurrence of secondary phases is not generated. It was been observed that a powder flow higher than m' = 8.78 g/min gives rise to undesired phases (regardless of P_{laser} and v). Therefore, this previous values of value m' will be taken as an upper fixed limit with the aim of establishing a compromise between maximizing η_{clad} $_{deposition}$ (and thus improving overall efficiency of the process), and also keep the beads generated free of segregations.

I.3.7 Modification of the Process Experiment Parameters

The (Table I.3) shows that very low deposition efficiencies (η_{clad} $_{deposition}$) were obtained, an average of 4.2%, indicating a possible process parameter selection problem, or an equipment problem.

The explanation was found in the poor quality of the cone formation of the powder concentration by the nozzle (Fig. I.10, left). As a correction, certain internal features

within the nozzle configuration were modified (specifically, the internal surface roughness was decreased), which resulted in a much better quality powder concentration (Fig. I.10, right).

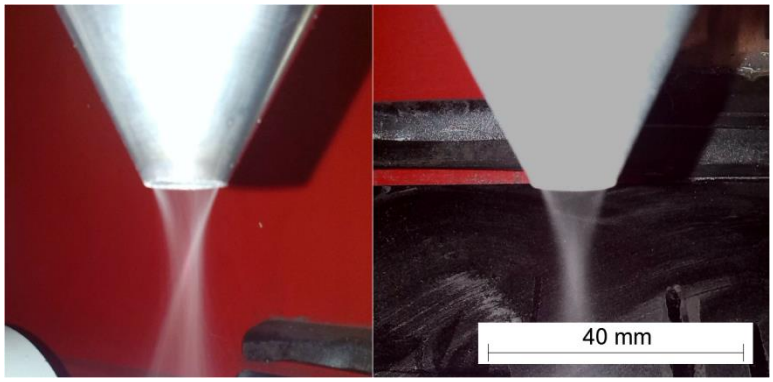

Figure I.10. Variation in the quality of the powder concentration in the work plane before (left), and after the modification of roughness in the internal surfaces of the nozzle (right).

The purpose of mentioning the above drawback was to show that a modelling and optimisation process is robust enough to observe general trends in system behaviour despite not being in optimal working condition, in this case due to a physical defect in the equipment.

Once the mass flow was been set (for the reasons explained in the previous paragraphs), the way forward in the optimization process is to carefully explore the effect in the variation of the process parameters Power (P_{laser}) and Scanning Speed (v) over the values of measurable quantities of outputs that define the “quality" of the cladding. Therefore, the range of process parameters for experiments was repeated and expanded, as shown in (Table I.5). It was decided to increase the power range of this new Design of Experiments because in tentative tests, it was observed that at low powers ($P_{laser} \leq$ 436 W), the porosity due to lack of bond between the substrate and the powder increases. The powder mass flow rate was also kept at m' = 8.78 g / min as excessive dilution was observed for values lower than indicated above.

Table I.5: Extended values data table in DOE to model and optimise the process of a laser cladding bead for INCO718.

# CLAD	Power (P_{laser}), W	Speed (v), mm/min	Clad Area (A_c), mm^2	Dilution (Dil), %	$\eta_{clad\ deposition}$, (%)
1	436	325	0.503	57.3%	15.3%
2	436	375	0.517	45.1%	18.1%

3	436	425	0.438	34.3%	17.4%
4	436	475	0.441	37.5%	19.5%
5	436	525	0.340	32.1%	16.7%
6	504	325	0.542	52.0%	16.4%
7	504	375	0.524	36.2%	18.3%
8	504	425	0.484	33.0%	19.2%
9	504	475	0.513	35.7%	22.7%
10	504	525	0.536	39.4%	26.3%
11	571	325	0.727	58.7%	22.1%
12	571	375	0.637	42.6%	22.3%
13	571	425	0.619	36.1%	24.5%
14	571	475	0.603	40.7%	26.7%
15	571	525	0.676	50.7%	33.1%
16	631	325	0.838	51.3%	25.4%
17	631	375	0.814	42.5%	28.5%
18	631	425	0.826	42.6%	32.8%
19	631	475	0.843	46.4%	37.4%
20	631	525	0.757	47.0%	37.1%
21	705	325	1.020	63.5%	30.9%
22	705	375	0.960	48.1%	33.6%
23	705	425	0.933	47.3%	37.0%
24	705	475	0.850	48.2%	37.6%
25	705	525	0.881	48.5%	43.2%
26	504	580	0.458	62.2%	24.8%
27	504	635	0.433	58.6%	25.6%
28	504	690	0.411	56.5%	26.5%
29	504	745	0.387	56.2%	26.9%
30	504	800	0.368	57.5%	27.4%
31	631	580	0.671	68.7%	36.3%
32	631	635	0.635	66.0%	37.6%
33	631	690	0.651	60.6%	41.9%
34	631	745	0.597	52.6%	41.5%
35	631	800	0.543	52.5%	40.5%
36	705	580	0.776	68.7%	42.0%

37	705	635	0.721	58.6%	42.7%
38	705	690	0.817	62.4%	52.6%
39	436	800	0.326	62.5%	24.3%
40	436	745	0.308	61.1%	21.4%
41	436	690	0.341	56.8%	22.0%
42	436	635	0.353	60.1%	20.9%
43	436	580	0.327	57.5%	17.7%
44	571	580	0.574	64.5%	31.0%
45	571	635	0.580	68.0%	34.3%
46	571	690	0.541	65.1%	34.8%
47	571	745	0.536	64.0%	37.3%
48	571	800	0.514	62.0%	38.4%
49	393	800	0.252	58.4%	18.8%
50	393	745	0.262	57.3%	18.2%
51	393	690	0.262	56.7%	16.8%
52	393	635	0.292	55.8%	17.3%
53	393	580	0.292	57.1%	15.8%
54	350	580	0.187	53.2%	10.1%
55	350	635	0.182	52.9%	10.8%
56	350	690	0.217	59.4%	14.0%
57	350	745	0.232	56.6%	16.1%
58	350	800	0.207	57.4%	15.5%
59	350	325	0.330	52.0%	10.0%
60	350	375	0.331	51.8%	11.6%
61	350	425	0.373	55.7%	14.8%
62	350	475	0.318	56.1%	14.1%
63	350	525	0.278	54.1%	13.6%
64	393	325	0.625	58.4%	18.9%
65	393	375	0.687	70.8%	24.0%
66	393	425	0.340	34.0%	13.5%
67	393	475	0.317	29.2%	14.0%
68	393	525	0.389	34.4%	19.1%
69	700	745	0.394	37.9%	27.4%
70	700	800	0.378	47.3%	28.2%

Again, a 5D composite chart was drawn to visualize graphically the best trends for input process parameters. The order of the axes is as follows: X axis is laser beam power (P_{laser} ,W), Y axis is scanning speed of laser beam respect the surface of substrate (v , mm/min), Z axis is cladding area (A_c, mm^2), Sphere Size for each coordinate (X, Y, Z) represents dilution (Dil ,%) and Sphere Colour represents material deposition efficiency ($\eta_{clad\ deposition}$,%), (Fig. I.11).

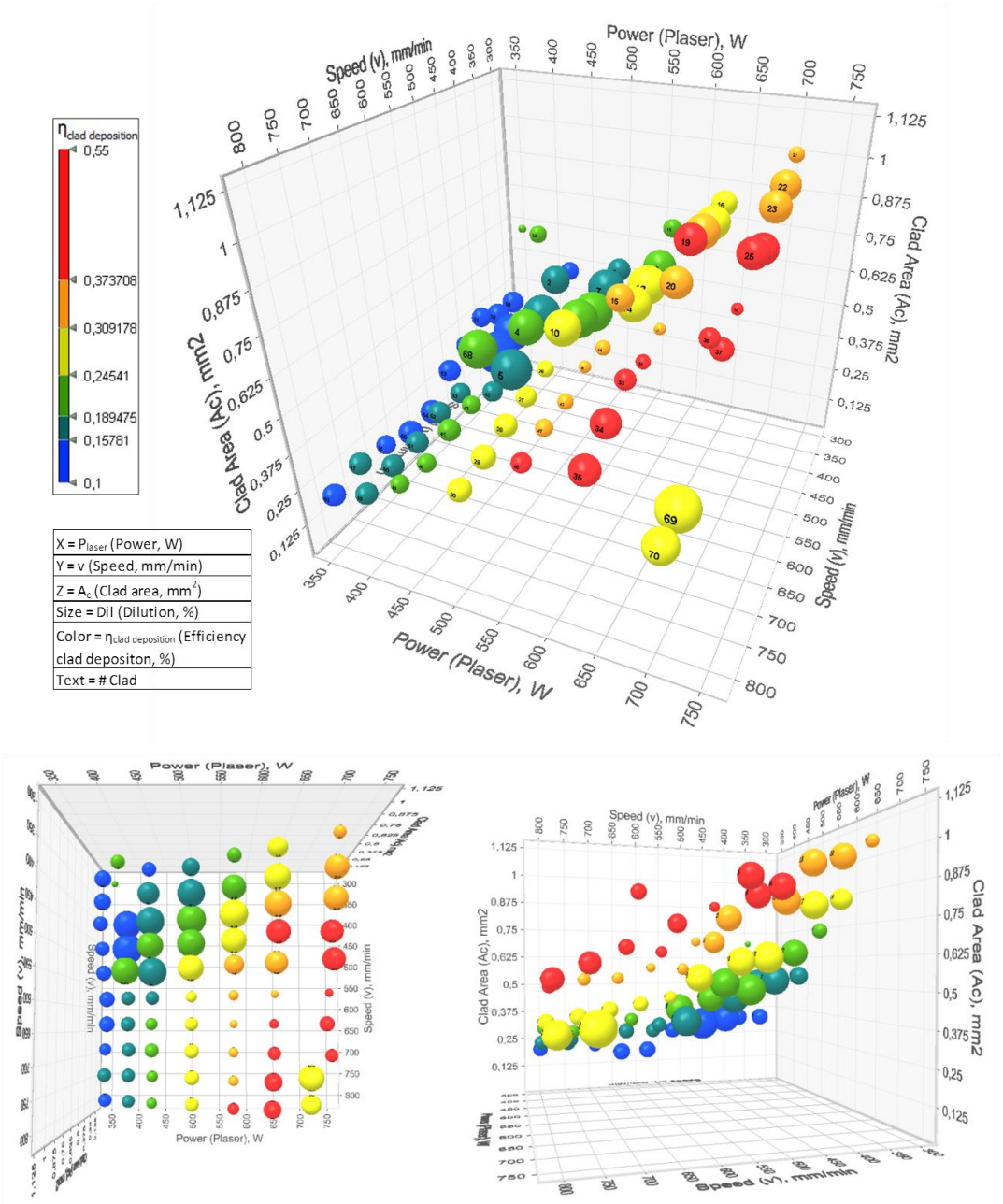

Figure I.11. 5D graph to visualize the behaviour of the deposition efficiency versus dilution for a range of power and speed variation with m' = constant. The graph allows observing for trends such as the largest cladded area that is obtained in combination with minimum dilution and maximum deposition efficiency.

Analysis of the graph in (Fig. I.11), shows that the region where the laser beam power is in the order of 400 W to 600 W and speeds between 300 to 600 mm/min offer the best conditions for the input process parameters. It is important to have an "idea" of the optimal parameter range, as it allows efforts to be focused within a given range of values to find the best set of final parameters. The usefulness of the previous 5D plots is justified in the sense that they save time and resources by not doing too many experiments in a process parameter range that is not optimal.

I.3.8 Optimal Cladding Process Parameters for a Single Bead, Statistical Modelling

A database of experiments will be considered as "sufficient" when useful information can be extracted from it on the entire dominion of parameters on which it was been defined. The database in (Table I.5) is considered suitable because in combination with the 5D type graph in (Fig. I.11), it allows to visualise the trend in the values to determine the optimum in the parameters for a laser cladding process.

When a sufficient database has been established to model the most important output parameters for a single bead (in this case the thermally melted area (A_m), and the deposited area (A_c)), it is convenient to use an optimization and compromise software.

The 5D chart or other type of visual aid is useful in order to verify by more than one method whether the results of an optimization have physical "sense", but they do not allow to directly obtaining the sought "optimal" values.

The Software Lumière (Logiciel à Usage de Modélisation Industrielle Et de Recherche Expérimentale) was used to search for “optimal” process parameters values. LUMIERE is a computer statistics program used in Research for:

- Development, improvement, optimization of products and processes,
- Analysis and control: repeatability, reproducibility, calibration, comparison of control methods,
- Manufacturing: statistical production control (statistical process control), capacity studies, centring, analysis of the effects of factors on responses, modelling, optimization and commitment.

From previous analysis, it has been established that the mass flow of powder will remain constant. Then the relationships to look for will only be a function of v and P_{laser}. It is

very appropriate to take advantage of the fact that by reducing the number of input variables to only two, it is possible to represent the behaviour of each measurable output parameter (Clad area, Dilution and Efficiency), using a 3D graph. (Fig. I.12) shows the surfaces generated from the database in (Table I.5).

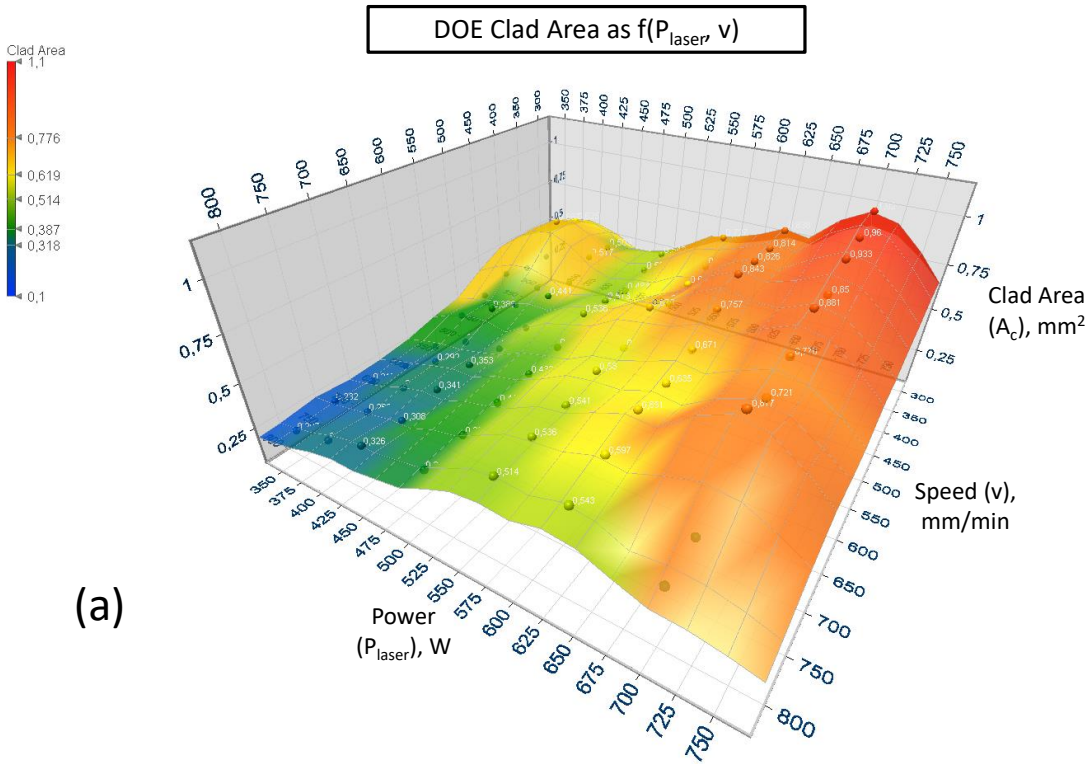

(a)

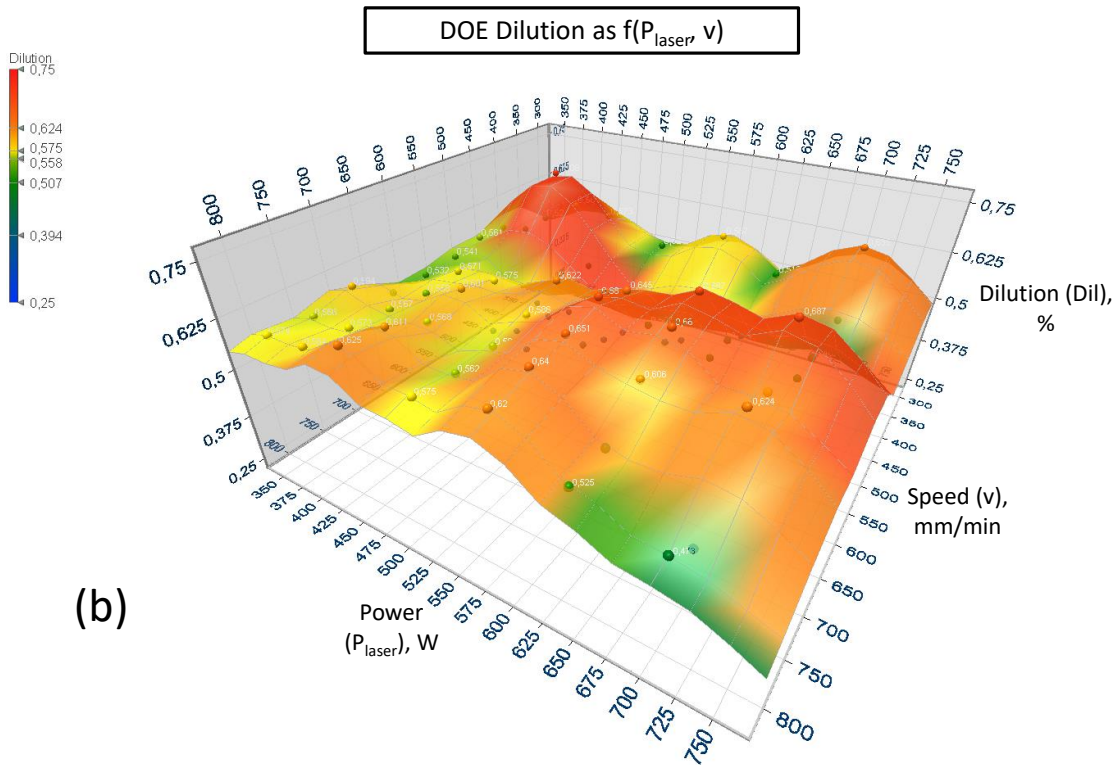

(b)

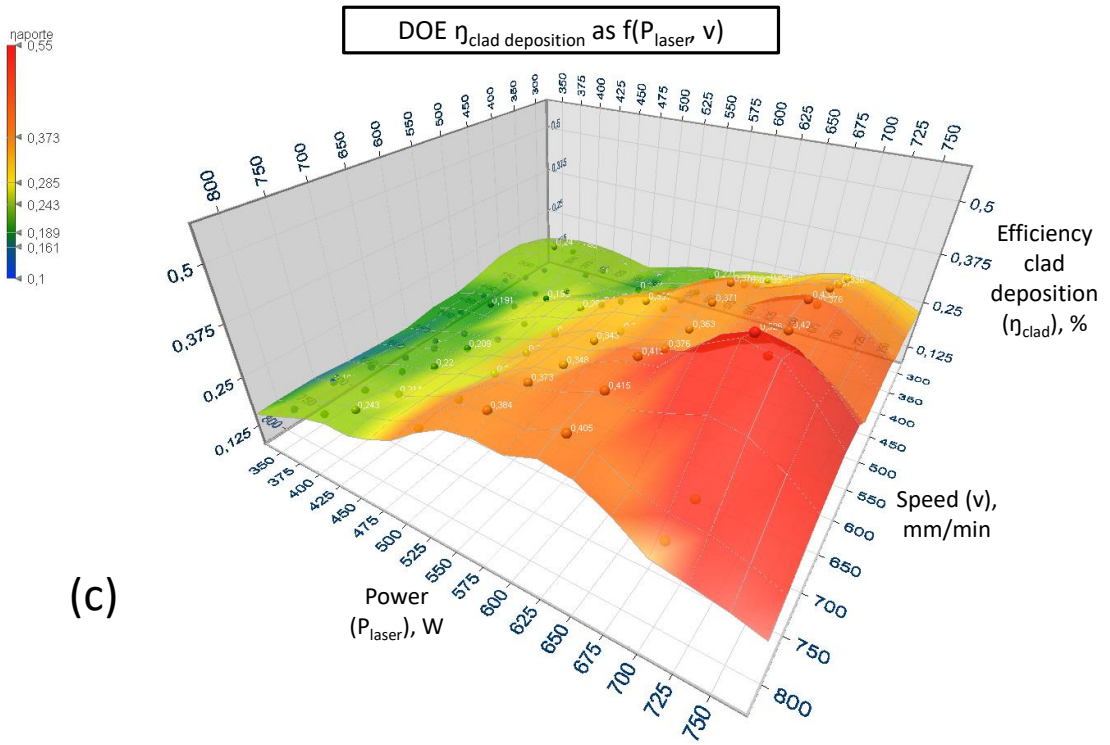

Figure I.12. Surface graphs to visualize the response values that define the cladding quality: (a) Clad Area, (b) Dilution and (c) Cladding deposition efficiency as a function of f (P_{laser} , v).

Some variables are more stable as a way for characterizing the geometry of a bead. Later (in the modelling details by means of statistical descriptors), it will be demonstrated from the data in (Table I.5), that the variable Dil tends to be less stable than A_m as a process parameter to model the amount of material that was been melted below the substrate level. It is easy to deduce that if Dil is known (and of course A_c), the value of A_m is derivable, since both quantities express different but related quantities.

To compare data from different samples or populations, or in this case of magnitudes with a wide range of values, the data in (Table I.5) will be transformed into reduced variables (DeVore, 2011). This allows reformulating the data with null mean and a standard deviation equal to one and allows all the input variables to have the same statistical dispersion (sometimes called standard score). It is important to remember that the reduced variables are dimensionless, and therefore during the transformation of data all units must be consistent.

It is was been observed that different authors use compound variables to facilitate data management in the modelling of the input-response parameters (Ansari et al., 2016; Ocelík et al., 2007; Oliveira de et al., 2005). In this research, we will use the compound

variable of (Eq. I.11). This variable will be used for the data in (Table I.5) for our statistical modelling:

$$Vc1 = 1/\sqrt{v} \qquad \textit{Eq. I.11}$$

The reduced compound variables for the correlations of H_{Ac}, W, A_c and A_m will therefore be (Eq. I.12) to (Eq. I.14):

$$P_{\underset{sv}{laser}} = \frac{P_{laser} - \bar{P}_{laser}}{sd(P_{laser})} \qquad \textit{Eq. I.12}$$

$$v_{sv} = \frac{v - \bar{v}}{sd(v)} \qquad \textit{Eq. I.13}$$

$$Vc1_{sv} = \frac{Vc1 - \bar{Vc1}}{sd(Vc1)} \qquad \textit{Eq. I.14}$$

The use of two reduced compound variables related to the same parameter is highlighted: v_{sv} and $Vc1_{sv}$ (which could seem redundant), but it was been observed that the correlations obtained are more complex than simply the combination by Linear Multiple Regression of the simple variables P_{laser} and v. Later it will be shown that, for example, for the variable H_{Ac}, one of the correlations is of the shape: $H_{Ac} = f(P_{\underset{sv}{laser}}, v_{sv}, Vc1_{sv})$ without any redundancy. The results for the application of the previous equations are shown in the (Table I.6).

Table I.6: Data for statistical modelling from the application of the equations for compound variables to the data in (Table I.5) for the DOE to single beads.

# CLAD	$P_{\underset{sv}{laser}}$, (-)	v_{sv}, (-)	$Vc1_{sv}$, (-)	H_{Ac}, (mm)	W, (mm)	A_c, (mm²)	Dil, (%)	$\eta_{\underset{deposition}{clad}}$, (%)
1	-0.635	-1.519	1.853	0.657	1.255	0.503	42.7%	15.3%
2	-0.635	-1.193	1.253	0.577	1.231	0.517	54.9%	18.1%
3	-0.635	-0.866	0.762	0.508	1.270	0.438	65.7%	17.4%
4	-0.635	-0.539	0.351	0.491	1.271	0.441	62.5%	19.5%
5	-0.635	-0.212	0.000	0.440	1.241	0.340	67.9%	16.7%
6	-0.072	-1.519	1.853	0.713	1.376	0.542	48.0%	16.4%
7	-0.072	-1.193	1.253	0.608	1.393	0.524	63.8%	18.3%

8	-0.072	-0.866	0.762	0.561	1.319	0.484	67.0%	19.2%
9	-0.072	-0.539	0.351	0.573	1.319	0.513	64.3%	22.7%
10	-0.072	-0.212	0.000	0.584	1.319	0.536	60.6%	26.3%
11	0.482	-1.519	1.853	0.766	1.400	0.727	41.3%	22.1%
12	0.482	-1.193	1.253	0.693	1.318	0.637	57.4%	22.3%
13	0.482	-0.866	0.762	0.605	1.428	0.619	63.9%	24.5%
14	0.482	-0.539	0.351	0.634	1.463	0.603	59.3%	26.7%
15	0.482	-0.212	0.000	0.662	1.468	0.676	49.3%	33.1%
16	0.979	-1.519	1.853	0.803	1.469	0.838	48.7%	25.4%
17	0.979	-1.193	1.253	0.771	1.521	0.814	57.5%	28.5%
18	0.979	-0.866	0.762	0.790	1.602	0.826	57.4%	32.8%
19	0.979	-0.539	0.351	0.761	1.535	0.843	53.6%	37.4%
20	0.979	-0.212	0.000	0.705	1.554	0.757	53.0%	37.1%
21	1.591	-1.519	1.853	0.918	1.509	1.020	36.5%	30.9%
22	1.591	-1.193	1.253	0.865	1.519	0.960	51.9%	33.6%
23	1.591	-0.866	0.762	0.818	1.561	0.933	52.7%	37.0%
24	1.591	-0.539	0.351	0.775	1.552	0.850	51.8%	37.6%
25	1.591	-0.212	0.000	0.768	1.585	0.881	51.5%	43.2%
26	-0.072	0.147	-0.332	0.558	1.296	0.458	37.8%	24.8%
27	-0.072	0.506	-0.620	0.539	1.238	0.433	41.4%	25.6%
28	-0.072	0.866	-0.873	0.547	1.242	0.411	43.5%	26.5%
29	-0.072	1.225	-1.097	0.535	1.225	0.387	43.8%	26.9%
30	-0.072	1.585	-1.298	0.494	1.264	0.368	42.5%	27.4%
31	0.979	0.147	-0.332	0.719	1.337	0.671	31.3%	36.3%
32	0.979	0.506	-0.620	0.677	1.344	0.635	34.0%	37.6%
33	0.979	0.866	-0.873	0.672	1.317	0.651	39.4%	41.9%
34	0.979	1.225	-1.097	0.666	1.289	0.597	47.4%	41.5%
35	0.979	1.585	-1.298	0.630	1.282	0.543	47.5%	40.5%
36	1.591	0.147	-0.332	0.775	1.401	0.776	31.3%	42.0%
37	1.591	0.506	-0.620	0.753	1.356	0.721	41.4%	42.7%
38	1.591	0.866	-0.873	0.744	1.465	0.817	37.6%	52.6%
39	-0.635	1.585	-1.298	0.432	1.184	0.326	37.5%	24.3%
40	-0.635	1.225	-1.097	0.462	1.121	0.308	38.9%	21.4%
41	-0.635	0.866	-0.873	0.465	1.215	0.341	43.2%	22.0%

42	-0.635	0.506	-0.620	0.472	1.228	0.353	39.9%	20.9%
43	-0.635	0.147	-0.332	0.463	1.227	0.327	42.5%	17.7%
44	0.482	0.147	-0.332	0.650	1.331	0.574	35.5%	31.0%
45	0.482	0.506	-0.620	0.685	1.320	0.580	32.0%	34.3%
46	0.482	0.866	-0.873	0.643	1.287	0.541	34.9%	34.8%
47	0.482	1.225	-1.097	0.599	1.258	0.536	36.0%	37.3%
48	0.482	1.585	-1.298	0.607	1.264	0.514	38.0%	38.4%
49	-0.991	1.585	-1.298	0.355	1.126	0.252	41.6%	18.8%
50	-0.991	1.225	-1.097	0.380	1.195	0.262	42.7%	18.2%
51	-0.991	0.866	-0.873	0.387	1.165	0.262	43.3%	16.8%
52	-0.991	0.506	-0.620	0.399	1.179	0.292	44.2%	17.3%
53	-0.991	0.147	-0.332	0.411	1.162	0.292	42.9%	15.8%
54	-1.347	0.147	-0.332	0.276	1.083	0.187	46.8%	10.1%
55	-1.347	0.506	-0.620	0.274	1.010	0.182	47.1%	10.8%
56	-1.347	0.866	-0.873	0.296	1.086	0.217	40.6%	14.0%
57	-1.347	1.225	-1.097	0.298	1.122	0.232	43.4%	16.1%
58	-1.347	1.585	-1.298	0.317	1.066	0.207	42.6%	15.5%
59	-1.347	-1.519	1.853	0.477	1.054	0.330	48.0%	10.0%
60	-1.347	-1.193	1.253	0.474	1.076	0.331	48.2%	11.6%
61	-1.347	-0.866	0.762	0.501	1.119	0.373	44.3%	14.8%
62	-1.347	-0.539	0.351	0.455	1.177	0.318	43.9%	14.1%
63	-1.347	-0.212	0.000	0.396	1.072	0.278	45.9%	13.6%
64	-0.991	-1.519	1.853	0.662	1.295	0.625	41.6%	18.9%
65	-0.991	-1.193	1.253	0.694	1.369	0.687	29.2%	24.0%
66	-0.991	-0.866	0.762	0.438	1.161	0.340	66.0%	13.5%
67	-0.991	-0.539	0.351	0.432	1.203	0.317	70.8%	14.0%
68	-0.991	-0.212	0.000	0.496	1.203	0.389	65.6%	19.1%
69	1.550	1.225	-1.097	0.515	1.217	0.394	62.1%	27.4%
70	1.550	1.585	-1.298	0.522	1.147	0.378	52.7%	28.2%

I.3.8.1 Confidence Levels and Global Restrictions for all Single Bead Models

Not all of the above compound variables (Eq. I.12) to (Eq. I.14) have the same weight in the statistical correlations to be calculated, some variables contribute more than others to the explanation of the results.

The restrictions to be fulfilled for the statistical modelling of H_{Ac}, W, A_c, Dil and $\eta_{clad\ deposition}$ are:

- The confidence level will be defined as 95%, with a minimum of 2.5% and a maximum of 97.5%.
- The maximum risk level for the coefficients will be 5%.
- The correlation coefficient will be established at a minimum value of 0.985

In addition, the previous restrictions will be indicated with coloured green highlights in (Table I.8), in which some of the variables have greater weight within the modelling. This will be observed in the “Analysis of Effects Contributions” section for each set of the input variables.

It should be noted that the confidence level for each of the Multiple Linear Regressions is near to the 100% value (see section “Decomposition of the sum of squares” for specific information of each of the modelled variables).

In the same previous section (“Decomposition of the sum of squares”), the level of residuals (literal “Residues”) is highlighted, where it will be observed that their quantity with respect to the total of the Regression is very low (around 1% for all correlations). Therefore, the fraction of experimental data that the model is not capable of explaining by modelling is very low. All these restrictions are intended to demonstrate the robustness of the statistical regressions.

I.3.9 Variable Correlation Matrices and Regression Models

The summary with the results of the modelling of process parameters is presented in the (Table I.7) and (Table I.8).

Table I.7: Correlation matrix for modelling the response variables of a single bead for the laser cladding process. The confidence level is specified in 95% with a range of [2.5% 97.5%] of the data.

Multiple Linear Regression

Defined Confidence Level: 95.00 %.

Correlation matrix

Significant correlations at 95.00 %
r = 0.2352 (70 - 2)

	P_laser_sv#	v_sv#	Vc1_sv#	P_laser_sv#*v_sv#	P_laser_sv#*Vc1_sv#	v_sv#*Vc1_sv#	P_laser_sv#*v_sv#*Vc1_sv	P_laser_sv#²	v_sv#²
P_laser_sv#	1.0000								
v_sv#	-0.0017	1.0000							
Vc1_sv#	0.0014	-0.9822	1.0000						
P_laser_sv#*v_sv#	-0.0053	-0.0012	0.0009	1.0000					
P_laser_sv#*Vc1_sv#	0.0045	0.0009	-0.0006	-0.9821	1.0000				
v_sv#*Vc1_sv#	0.0010	0.1135	-0.2982	0.0016	-0.0016	1.0000			
P_laser_sv#*v_sv#*Vc1_sv#	-0.7339	0.0023	-0.0021	0.0846	-0.2094	-0.0006	1.0000		
P_laser_sv#²	0.2326	-0.0063	0.0054	-0.0130	0.0111	0.0037	-0.1661	1.0000	
v_sv#²	-0.0014	0.0679	0.1172	-0.0020	0.0019	-0.9672	0.0012	-0.0053	1.0000

Range of variation of the Factors

Factors to consider	Minimum	Average	Maximum	Standard deviation
P_laser_sv	-1.3466	0.0000	1.5913	1.0000
v_sv	-1.5194	0.0000	1.5847	1.0000
Vc1_sv	-1.2983	0.0000	1.8534	1.0000

Table I.8: Regression matrices with statistical control parameters for each of the variables for the modelling process of a single laser cladding bead.

Regression of H_{Ac}

Summary of Coefficients

Table with the residual standard deviation.

Sr = 0.0515 - Nur = 62

Variable	Coefficient	Standard deviation	t Student	Confidence %	Risk %	Centring
P_laser_sv#	0.9223	0.3553	2.5957	98.82	1.18	No
v_sv#	-2.785	0.0565	-49.3351	100	0	No
Vc1_sv#	-2.8312	0.058	-48.8521	100	0	No
P_laser_sv#*v_sv#	3.6561	1.6754	2.1822	96.71	3.29	-
P_laser_sv#*Vc1_sv#	3.8095	1.744	2.1844	96.73	3.27	-
v_sv#*Vc1_sv#	-0.613	0.01	-61.2606	100	0	-
P_laser_sv#*v_sv#*Vc1_sv#	0.8179	0.367	2.2287	97.05	2.95	-
$P\_laser\_sv\#^2$	-0.0186	0.0076	-2.4508	98.29	1.71	-

Confidence Interval 95%

Variable	Coeff	Mini (2.50 %)	Maxi (97.50 %)
P_laser_sv#	0.9223	0.212	1.6326
v_sv#	-2.785	-2.8978	-2.6721

Vc1_sv#	-2.8312	-2.9471	-2.7154
P_laser_sv#*v_sv#	3.6561	0.307	7.0051
P_laser_sv#*Vc1_sv#	3.8095	0.3234	7.2956
v_sv#*Vc1_sv#	-0.613	-0.633	-0.593
P_laser_sv#*v_sv#*Vc1_sv#	0.8179	0.0843	1.5515
$P\_laser\_sv\#^2$	-0.0186	-0.0338	-0.0034

Decomposition of the sum of squares

Source	Sum of the squares	Ddl	Medium Square	Fisher	Confidence %	Risk %
Regression	24.6456	8	3.0807	1160.7193	100	0
Residues	0.1646	62	0.0027			
Total	24.8101	70	0.3544			
Correlation coefficient (R):	0.997					
Residual Standard deviation Sr :	0.0515	Ddl	62			

Analysis of Effects Contributions.

Effects	Contributions	%
P_laser_sv#	8.0871	32.6
v_sv#	12.8545	51.81
Vc1_sv#	-13.3968	-54
P_laser_sv#*v_sv#	-0.8095	-3.26

P_laser_sv#*Vc1_sv#	0.0826	0.33
v_sv#*Vc1_sv#	24.7691	99.83
P_laser_sv#*v_sv#*Vc1_sv#	-6.1865	-24.94
P_laser_sv#^{2}	-0.7548	-3.04
Residues	0.1646	0.66
Total	24.8101	100

Regression of W

Summary of Coefficients

Table with the residual standard deviation.

Sr = 0.1347 - Nur = 67

Variable	Coefficient	Standard deviation	t Student	Confidence %	Risk %	Centring
v_sv#	-6.2243	0.1149	-54.1773	100	0	No
Vc1_sv#	-6.4172	0.117	-54.8647	100	0	No
v_sv#*Vc1_sv#	-1.3316	0.0166	-80.0742	100	0	-

Confidence Interval 95%

Variable	Coeff	Mini (2.50 %)	Maxi (97.50 %)
v_sv#	-6.2243	-6.4536	-5.995

Vc1_sv#	-6.4172	-6.6506	-6.1837
v_sv#*Vc1_sv#	-1.3316	-1.3647	-1.2984

Decomposition of the sum of squares

Source	Sum of the squares	Ddl	Medium Square	Fisher	Confidence %	Risk %
Regression	116.6106	3	38.8702	2141.8466	100	0
Residues	1.2159	67	0.0181			
Total	117.8265	70	1.6832			
Correlation coefficient (R):	0.995					
Residual Standard deviation Sr :	0.1347	Ddl	67			

Analysis of Effects Contributions.

Effects	Contributions	%
v_sv#	24.7026	20.97
Vc1_sv#	-23.6045	-20.03
v_sv#*Vc1_sv#	115.5125	98.04
Residues	1.2159	1.03
Total	117.8265	100

Regression of A_c

Summary of Coefficients

Table with the residual standard deviation.

Sr = 0.0700 - Nur = 64

Variable	Coefficient	Standard deviation	t Student	Confidence %	Risk %	Centring
P_laser_sv#	0.2075	0.0127	16.2988	100	0	No
v_sv#	-2.4846	0.0597	-41.6323	100	0	No
Vc1_sv#	-2.4911	0.0608	-41	100	0	No
P_laser_sv#*Vc1_sv#	0.031	0.0089	3.4833	99.91	0.09	-
v_sv#*Vc1_sv#	-0.5286	0.0086	-61.1905	100	0	-
P_laser_sv#*v_sv#*Vc1_sv#	0.0332	0.0099	3.3522	99.87	0.13	-

Confidence Interval 95%

Variable	Coeff	Mini (2.50 %)	Maxi (97.50 %)
P_laser_sv#	0.2075	0.182	0.2329
v_sv#	-2.4846	-2.6038	-2.3654
Vc1_sv#	-2.4911	-2.6124	-2.3697
P_laser_sv#*Vc1_sv#	0.031	0.0132	0.0489
v_sv#*Vc1_sv#	-0.5286	-0.5458	-0.5113
P_laser_sv#*v_sv#*Vc1_sv#	0.0332	0.0134	0.0529

Decomposition of the sum of squares

Source	Sum of the squares	Ddl	Medium Square	Fisher	Confidence %	Risk %
Regression	21.1421	6	3.5237	719.5676	100	0
Residues	0.3134	64	0.0049			
Total	21.4555	70	0.3065			
Correlation coefficient (R):	0.993					
Residual Standard deviation Sr :	0.07	Ddl	64			

Analysis of Effects Contributions.

Effects	Contributions	%
P_laser_sv#	2.5152	11.72
v_sv#	15.7954	73.62
Vc1_sv#	-15.674	-73.05
P_laser_sv#*Vc1_sv#	0.0495	0.23
v_sv#*Vc1_sv#	18.8021	87.63
P_laser_sv#*v_sv#*Vc1_sv#	-0.346	-1.61
Residues	0.3134	1.46
Total	21.4555	100

Regression of Dil

Summary of Coefficients

Table with the residual standard deviation.

Sr = 0.0855 - Nur = 67

Variable	Coefficient	Standard deviation	t Student	Confidence %	Risk %	Centring
v_sv#	-2.3121	0.0715	-32.3208	100	0	No
Vc1_sv#	-2.2851	0.0717	-31.8801	100	0	No
$v\_sv\#^2$	0.4775	0.0102	46.733	100	0	-

Confidence Interval 95%

Variable	Coeff	Mini (2.50 %)	Maxi (97.50 %)
v_sv#	-2.3121	-2.4549	-2.1693
Vc1_sv#	-2.2851	-2.4282	-2.142
$v\_sv\#^2$	0.4775	0.4571	0.4979

Decomposition of the sum of squares

Source	Sum of the squares	Ddl	Medium Square	Fisher	Confidence %	Risk %
Regression	16.1249	3	5.375	734.601	100	0
Residues	0.4902	67	0.0073			
Total	16.6151	70	0.2374			

Correlation coefficient (R):	0.985		
Residual Standard deviation Sr :	0.0855	Ddl	67

Analysis of Effects Contributions.

Effects	Contributions	%
v_sv#	6.3065	37.96
Vc1_sv#	-5.4327	-32.7
$v\_sv\#^2$	15.2511	91.79
Residues	0.4902	2.95
Total	16.6151	100

Regression of η_{clad}

Summary of Coefficients

Table with the residual standard deviation.

Sr = 0.0367 - Nur = 63

Variable	Coefficient	Standard deviation	t Student	Confidence %	Risk %	Centring
P_laser_sv#	0.6709	0.2529	2.6533	98.99	1.01	No
v_sv#	-1.2181	0.0313	-38.9561	100	0	No

Vc1_sv#	-1.2928	0.0318	-40.6105	100	0	No
P_laser_sv#*v_sv#	2.6748	1.1923	2.2434	97.16	2.84	-
P_laser_sv#*Vc1_sv#	2.7784	1.2411	2.2387	97.13	2.87	-
v_sv#*Vc1_sv#	-0.2615	0.0045	-57.7744	100	0	-
P_laser_sv#*v_sv#*Vc1_sv#	0.6028	0.2612	2.3081	97.57	2.43	-

Confidence Interval 95%

Variable	Coeff	Mini (2.50 %)	Maxi (97.50 %)
P_laser_sv#	0.6709	0.1656	1.1762
v_sv#	-1.2181	-1.2806	-1.1556
Vc1_sv#	-1.2928	-1.3564	-1.2291
P_laser_sv#*v_sv#	2.6748	0.2922	5.0574
P_laser_sv#*Vc1_sv#	2.7784	0.2983	5.2586
v_sv#*Vc1_sv#	-0.2615	-0.2705	-0.2524
P_laser_sv#*v_sv#*Vc1_sv#	0.6028	0.0809	1.1247

Decomposition of the sum of squares

Source	Sum of the squares	Ddl	Medium Square	Fisher	Confidence %	Risk %
Regression	5.0919	7	0.7274	541.1352	100	0
Residues	0.0847	63	0.0013			
Total	5.1766	70	0.074			

Correlation coefficient (R):	0.992		
Residual Standard deviation Sr :	0.0367	Ddl	63

Analysis of Effects Contributions.

Effects	Contributions	%
P_laser_sv#	4.0443	78.13
v_sv#	-2.0852	-40.28
Vc1_sv#	2.3339	45.09
P_laser_sv#*v_sv#	1.213	23.43
P_laser_sv#*Vc1_sv#	-1.8347	-35.44
v_sv#*Vc1_sv#	4.2874	82.82
P_laser_sv#*v_sv#*Vc1_sv#	-2.8667	-55.38
Residues	0.0847	1.64
Total	5.1766	100

I.3.10 Validation of Correlations

A convenient way to check the validity of the previous correlations calculated is by means of Henry's plots (Thode, 2002). In these plots, the error between the value estimated by the MRA for each parameter studied and the actual value of that parameter (both reduced variables) were calculated and plotted. If the calculated error follows the trend of a statistical distribution (assumed to be Normal), then it can be concluded that the error distribution is random and, therefore, all the most significant parameters were considered during the modelling of each variable. Henry's graphs for the variables H_{Ac}, W, A_c, Dil and $\eta_{\substack{clad \\ deposition}}$ are presented in (Fig. I.13):

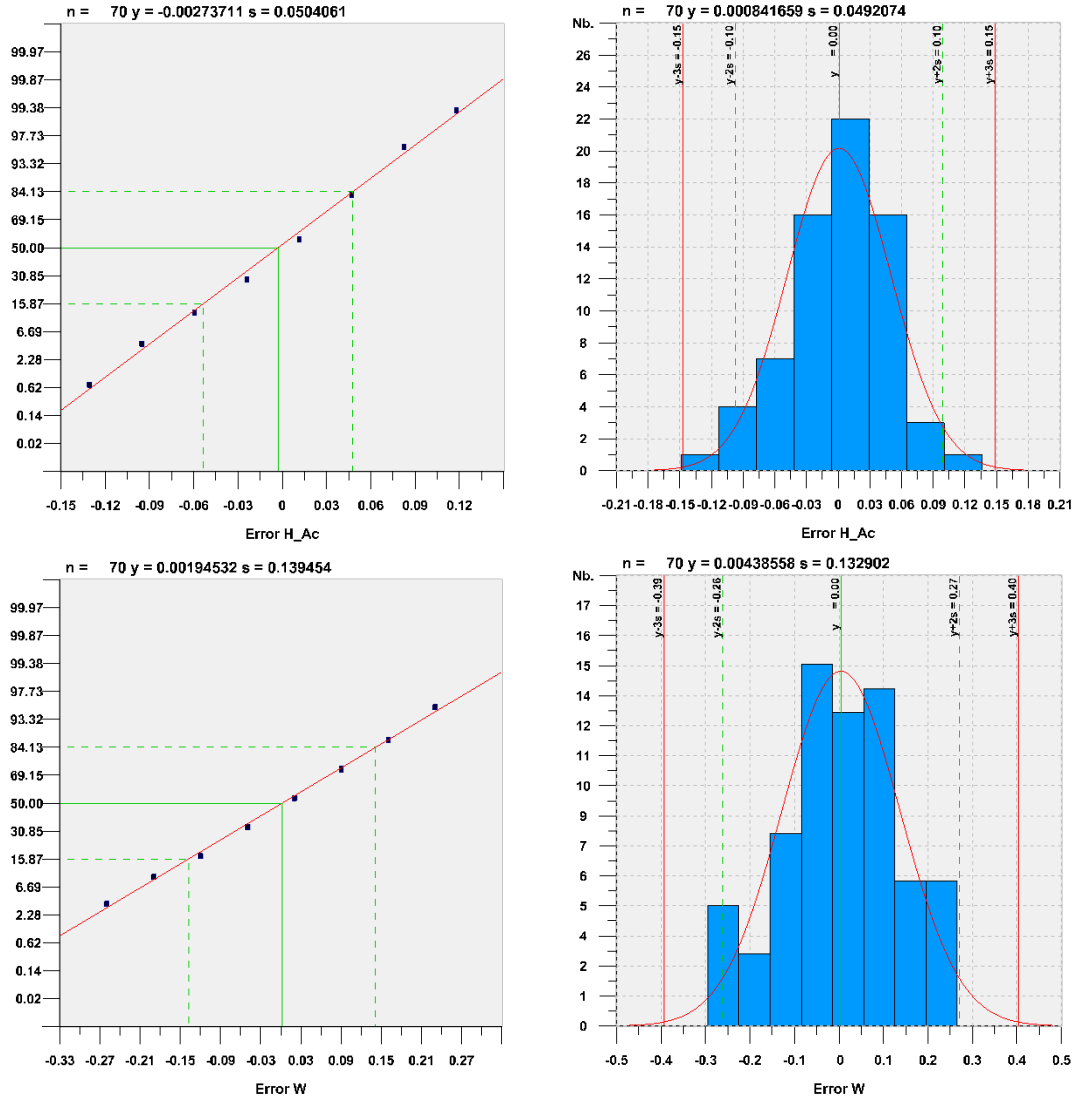

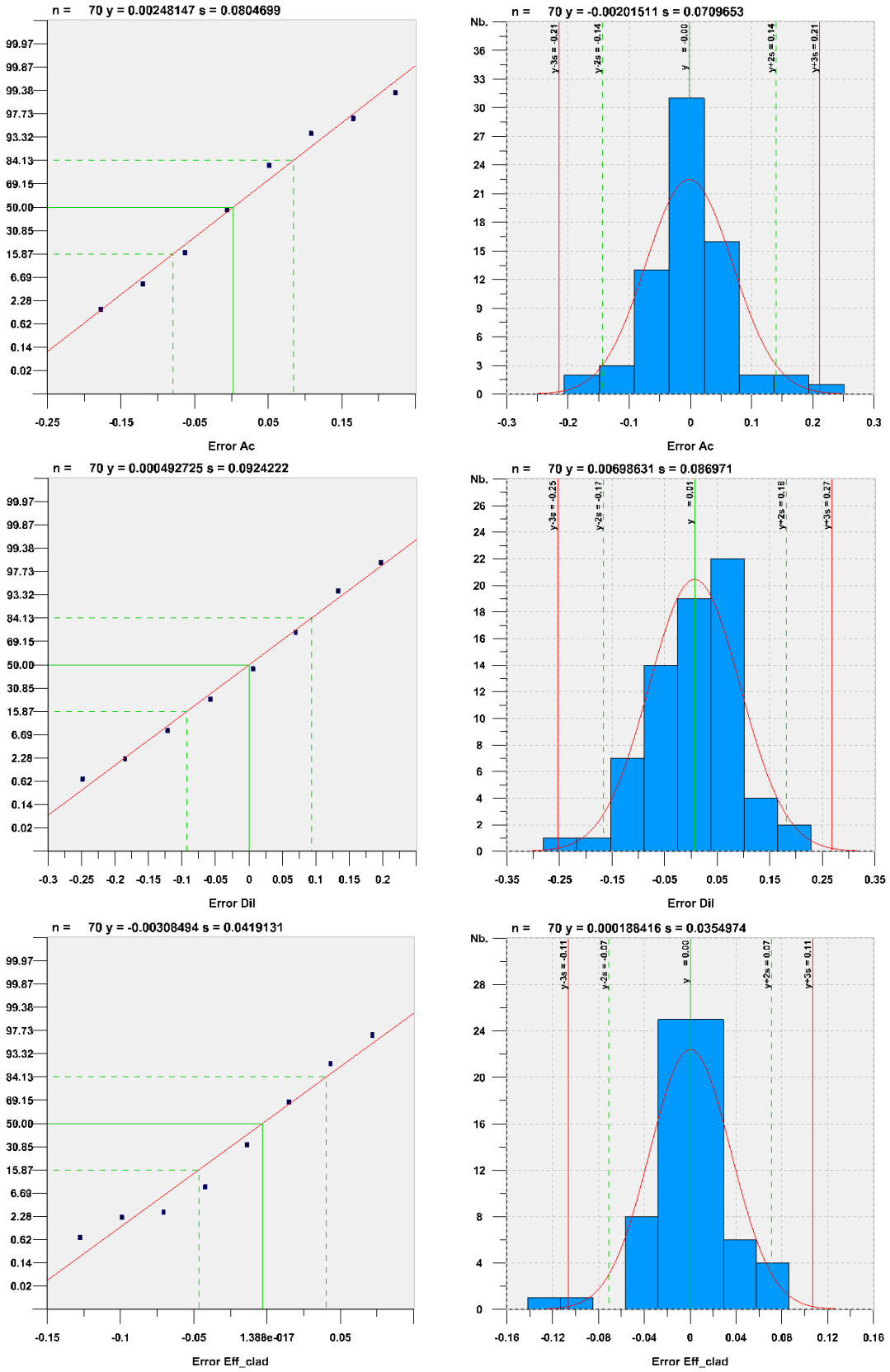

Figure I.13. Henry graphs to verify the normality on the error of the modelled variables H_{Ac}, W, A_c, Dil *and* $\eta_{clad}^{deposition}$ *compared with the real values obtained from experiments.*

For this Figure, n: sample size, y: average value of the data, s: standard deviation.

To check the normality of the previous calculated errors in a way that is not subjective (by simple visual inspection), a hypothesis test of normality was used. When the average and variance of data are unknown, a modification of the Kolmogorov-Smirnov test known as the Lilliefors test (specially developed to test normality) is used. The Kolmogorov-Smirnov test assumes that the population average and variance are known, which in most cases is impossible to know. This makes the test very conservative and underpowered.

The Lilliefors test assumes that the mean and variance are unknown (Lilliefors, 1967). The results for the test applied to the Error data between the values in (Table I.6) and the values obtained by the modelled variables in (Table I.8), are shown in (Table I.9).

Table I.9: Results of the hypothesis test for the Lilliefors test for the Error between the modelled variables of the (Table 1-8) and data from (Table 1-6).

Null hypothesis: the data in Error for the parameters H_{Ac}, W, A_c, Dil and $\eta_{\substack{clad \\ deposition}}$ comes from a distribution in the normal family (5% significance level).		
Parameter	Not rejects = 0 (p> 0.05)	Rejects = 1 (p<=0.05)
H_{Ac}:	p_{H_Ac} = 0.143	No
W:	p_W = 0.500	No
A_c:	p_{Ac} = 0.0661	No
Dil:	p_{Dil} = 0.267	No
$\eta_{\substack{clad \\ deposition}}$:	$p_{\eta clad}$ = 0.0588	No

Once the main response variables that define the geometry of the single bead for a Laser Cladding process were modelled, we will proceed to obtain the optimal values for those variables that will be considered as "important".

I.3.11 Multi-Objective Optimization for a Single Laser Cladding Bead

It is possible that the simultaneous optimization with more than one target objective results in an optimized value that cannot satisfy all the restrictions. In our case, this requires using a compromise solution.

The selection of the "important" response parameters was based on three of the main desirable characteristics of a single bead, and each one will be given the same weight. In general, it will be sought that:

- The Dilution (Dil) will be the less possible. It is desirable to thermally affect the less the substrate material if that is possible.
- The measured cross-sectional area (A_c) will be maximum, that is, the amount of material added will be the most that the process allows without compromising the chemical integrity of the alloy, and thus optimizing the time invested in the material deposition process.
- The deposition efficiency ($\eta_{\substack{clad \\ deposition}}$) will be maximum. Metal powder is an expensive and difficult raw material to treat (recycle), so the maximum amount to be adhered during the cladding process must be sought.

Three optimizations were done using the Grid Method (Ensor and Glynn, 1997), each for the previous mentioned three variables. Grid searching is a very traditional technique for implementing hyper-parameters. It is based on brute force applying all the combinations and restricting the responses for each one of them by restrictions of the other variables, see (Table I.10) to (Table I.12).

Table I.10: Optimization for the modelled variable "Dil" based on other parameters of the Laser Cladding process input variables.

Optimization of Dil# in the domain under constraints of other responses Number of constraints: 0		
Responses	Objectives	Calculated Values
H_Ac	0.2736 <= H_Ac<= 0.9183	0.5302
W	1.0102 <= W<= 1.6022	1.0027
Ac	0.1821 <= Ac<= 1.0198	0.4543
Dil	Minimize	0.3951
ŋ_clad	0.1002 <= ŋ_clad<= 0.5258	0.2514
Factors		Calculated Values
P_laser_sv		0.2385
v_sv		-0.2207
Vc1_sv		0.0606

Table I.11: Optimization for the modelled variable "Ac" based on other parameters of the input variables of Laser Cladding process.

Optimization of Ac# in the domain under constraints of other responses Number of constraints: 0		
Responses	Objectives	Calculated Values
H_Ac	0.2736 <= H_Ac<= 0.9183	0.6928
W	1.0102 <= W<= 1.6022	1.5337
Ac	Maximize	0.739
Dil	0.2924 <= Dil<= 0.7078	0.6001
ŋ_clad	0.1002 <= ŋ_clad<= 0.5258	0.3071
Factors		Calculated Values
P_laser_sv		0.6087
v_sv		-0.2531
Vc1_sv		0.0068

Table I.12: Optimization for the modelled variable $\eta_{clad\_deposition}$ based on other parameters of the input variables of Laser Cladding process.

Optimization of ŋ_clad# in the domain under constraints of other responses Number of constraints: 0		
Responses	Objectives	Calculated Values
H_Ac	0.2736 <= H_Ac<= 0.9183	0.6614
W	1.0102 <= W<= 1.6022	1.1396
Ac	0.1821 <= Ac<= 1.0198	0.5863
Dil	0.2924 <= Dil<= 0.7078	0.447
ŋ_clad	Maximize	0.3334
Factors		Calculated Values
P_laser_sv		0.6161
v_sv		-0.2252
Vc1_sv		0.0429

Each separate parameter for the optimization (A_c, Dil and $\eta_{clad\ deposition}$) converges to different numerical solutions. However, they are all in the same range of values, which indicates the existence of a possible optimal set of input process parameters, or at least that for these three optimised parameters all optimums are in the same range. A summary of the numerical values for each of the parameters is presented in (Table I.13), on the left in the form of a reduced variable, and on the right its corresponding transformation. The average of the calculated coefficient values for the three optimizations is also presented.

Table I.13: Optimal values for the coefficients of the parameters "Ac", "Dil" and "$\eta_{clad\_deposition}$" as a function of "P_{laser_sv}", "v_{sv}" and "$Vc1_{sv}$" in reduced variables and their transformations into standard variables. The average values of the coefficients for the real transformed variables are on the extreme right of this table.

	Reduced compound variables				Real value of parameter (optimal)			
Param. $_{stand\_val.}$	Ac	η_clad	Dil	Param. $_{real}$	Ac	η_clad	Dil	Average real value of parameter (optimal)
P_laser_sv	0.6087	0.6161	0.2385	P_laser (W)	586.3	587.2	541.5	571.7
v_sv	-0.2531	-0.2252	-0.2207	v (mm/min)	518.8	523.0	523.7	521.8
Vc1_sv	0.0068	0.0429	0.0606	Vc1 1/√(v) (1/√(mm/min))	0.0437	0.0439	0.0440	0.0439

From (Table I.13), it should be noted that the averaged compound variable $Vc1 = 1/\sqrt{v} =$ 0.0439 is equivalent to $v =$ 519.5 mm / min, which allows a double confirmation of the optimized values calculated with respect to $v_{\substack{average \\ optimal}} = 521.8$ mm / min. The value derived directly from the variable v_{sv} will be taken as the optimal one, since it differs by less than 0.5% from $Vc1_{sv}$ (both are approximately the same).

I.3.12 Optimization Results for a Simple clad Bead

Finally, the optimal values for a laser cladding process based on the DOE of (Table I.5) for a single bead are:

- m' = 8.78 g/min.
- v = 522 mm/min.
- P_{laser} = 571 W (for a spot diameter of ϕd_{laser} = 1mm, multimodal with cylindrical energy distribution).

I.4 Optimization of a Multiline/Multilayer Bead for Laser Cladding Process

I.4.1 Defects in Multiple Layer Beads

The optimization for multiple beads and layers aims to minimize / avoid the appearance of defects like those shown in (Fig. I.14).

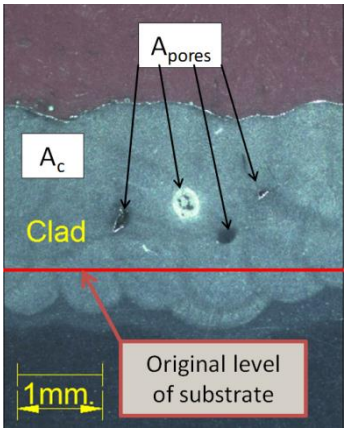

Figure I.14. Image with typical examples of various types of defects for multilayer laser cladding deposition.

The (Fig. I.14) shows the sum of the most important defects that are listed below:

- Multiline/Multilayer pores (it will be represented by the area Por_{ml}).
- Excessive Multiline/Multilayer dilution (it will be represented by Dil_{ml}), and its instability. The instability of Dil_{ml} can give rise to a lot of melting on the substrate or to its lack of fusion with the clad material, causing low quality on metallurgical bond.
- Excessive surface roughness after adding cladding material (too much instability in the laser cladding process leads to uneven deposition of the cladding material and deviation from the steady state conditions of the flat substrate).

I.4.2 Geometric Parameters for Multiple Beads and Initial Premises

Once the optimal conditions for a single clad bead are calculated, the next step is to replicate the process for multiple beads.

It will be assumed that in the formation of layers based on multiple single beads, a steady state is established that preserves the optimal calculated parameters (that is, the

optimal values of the parameters for a single bead are maintained for the entire volume of cladded material).

Since there are many ways to deposit single beads, it is necessary to limit the number of possible strategies (tool paths). For this investigation, strategies that add the material in the same direction will be used (zig-zig or zig-zag strategy according to the path followed when two attached beads are deposited following a repetitive pattern), (Fig. I.15).

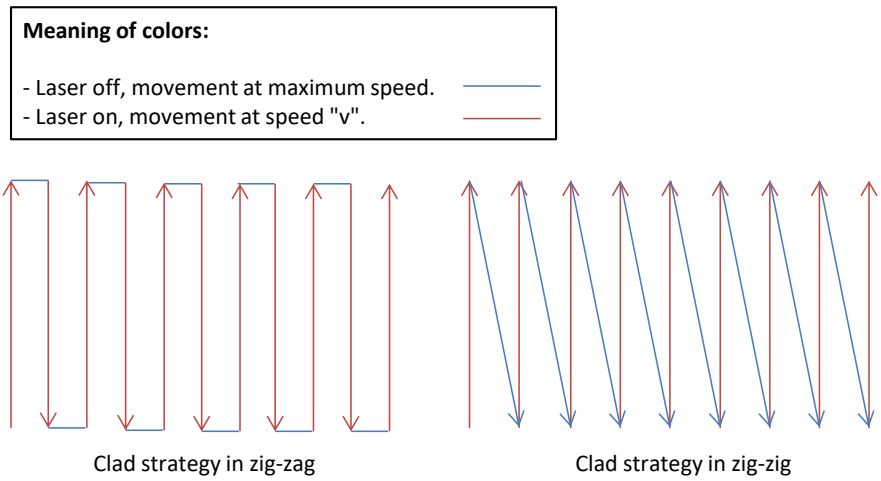

Figure I.15. Schemes of Zig-zig and zig-zag deposition strategies (tool paths).

As complexity in geometry increases, it is necessary to include two extra parameters in the description of multiple beads: $\%Ove$ and $\%Off$, (Fig. I.16).

Both new previous parameters will be a function of the width W of a simple bead, where $\%Ove$ will have a value between [0 and 1] * W and $\%Off$ one between [0 and 0.5] * W. The range for the case of $\%Off$ is less respect to $\%Ove$ because of its symmetry.

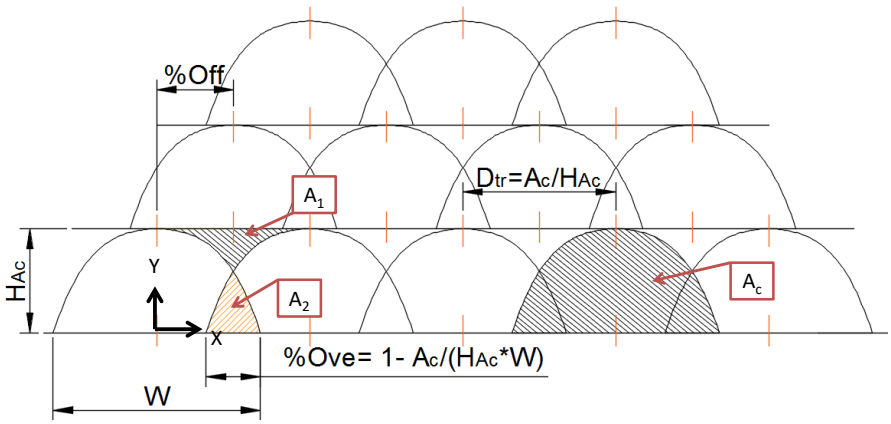

Figure I.16. Scheme of several consecutive single beads showing the geometric meaning of parameters $\%Ove$ and $\%Off$.

The objective of the $\%Ove$-parameter is to achieve an overlap between beads in such a way that when depositing a layer, the resulting surface after solidification is as flat (and parallel) as possible with respect to the previous one. The idea is that when the material is deposited (and melted due to the energy of the laser beam), an excess of it will fill the empty space of the overlap (by mass balance), i.e. the space between the ridges ($A_1 = A_2$) as shown in (Fig. I.17).

From (Fig. I.17), for a single cladding bead with a characteristic polynomial geometry $y_{Ac} = a_1x^4 + a_2x^2 + a_3$ and taking advantage of the symmetry between two consecutive beads, the mean areas A_1 and A_2 will be (Eq. I.15) to (Eq. I.16):

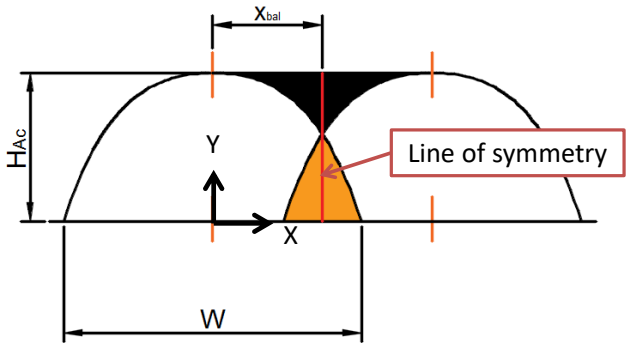

Figure I.17. Scheme of two consecutive bead clad for deduction of the coordinate x_{bal} for which A_1=A_2.

Where:

$$\frac{A_1}{2} = x_{bal} \cdot H_{Ac} - \int_0^{x_{bal}} (a_1x^4 + a_2x^2 + H_{Ac})dx = -\frac{x_{bal}^{\ 3}(3a_1x_{bal}^{\ 2} + 5a_2)}{15} \qquad \textit{Eq. I.15}$$

$$\frac{A_2}{2} = \int_{x_{bal}}^{W/2} (a_1x^4 + a_2x^2 + H_{Ac})dx = \left(\frac{W}{2} - x_{bal}\right) + \frac{a_1W^5}{160} + \frac{a_2W^3}{24} - \frac{a_1x_{bal}^{\ 5}}{5} - \frac{a_2x_{bal}^{\ 3}}{3} \qquad \textit{Eq. I.16}$$

Solving for x_{bal} (Eq. I.17):

$$x_{bal} = \frac{W(240H_{Ac} + 3a_1W^4 + 20a_2W^2)}{480H_{Ac}} \qquad \textit{Eq. I.17}$$

Because $a_1 = f(A_c, H_{Ac}, W)$ and $a_2 = f(A_c, H_{Ac}, W)$, $\%Ove$ (theoretical optimum), can be expressed as (Eq. I.18):

$$\%Ove = 1 - \frac{A_c}{H_{Ac} W} \qquad \textit{Eq. I.18}$$

For example, for the optimum process parameters which have been determined for a single bead (m' = 8.78 g/min., v = 522 mm/min., P_{laser} = 571 W), it could be obtained:

- a_1 =-1.454
- a_2 =-0.873
- $a_3 = H_{Ac}$ =0.659 mm.
- W =1.322 mm.
- A_c =0.629 mm^2.

And therefore:

- x_{bal} =0.478 mm.
- $\%Ove$ (theoretical optimum) = 0.278 = 27.8 %

The idea of an optimal value of $\%Ove$ is related to the stability of the process. It is desirable that the conditions throughout the deposition of the coating material remain constant. It has been mentioned before (as a premise), that the quality of a complex coating process is the sum of the individual qualities of all the beads involved. Therefore, when performing a DOE with the objective of finding the best conditions in the parameters for a single bead, one objective will be to maintain that "optimum" throughout the process for multiple beads.

If the growth per layer is not uniform (that is, the resulting surface after creating a layer is not “flat”), the following layers of cladding beads will not meet the same “flat” substrate at initial conditions, and therefore the following series of cladding beads “will grow” in conditions outside of those established as “optimal” (flat surface).

If the resulting geometry for a bead is modified, for example, by a temperature increase for a system without any automatic temperature control, it is easy to adjust the process conditions to a new optimal overlay looking for stability conditions by applying (Eq. I .17) and (Eq. I.18). It is important to remember that the above equations are applicable to individual bead profiles of the form: $y_{Ac} = a_1 x^4 + a_2 x^2 + a_3$.

Authors such as (Chen et al., 2018; Li and Ma, 1997; Ocelík et al., 2014), have deduced optimal overlap values for modelled bead geometries such as parabolas and circumference sections. The disadvantage of the previous approach is that cladding beads do not always fit geometry as close to these geometric shapes (parabolas and circumference sections), as is shown in (Fig. I.7), and therefore it is more difficult to establish a good model to describe and predict the geometry of the bead, as well as the molten area.

If there is the need to increase or decrease the $\%Ove$ from its optimal value of (Eq. I.18), that is, modifying the thickness of the layer deposited from H_{Ac}, a change in height per layer will be assumed as a function of the difference of area $\Delta A = A_2 - A_1$ (Fig. I.18).

If the overlap ($\%Ove$) is greater than the optimal value, there will be more growth per deposited layer; otherwise the opposite will be true. It is assumed that the change in height with respect to H_{Ac}, the variable (h') is given by the value of the area ΔA (delta area positive or negative), divided by the total width between the ridges of the clad layer (L_{t_tr}), as is shown in scheme of (Fig. I.18).

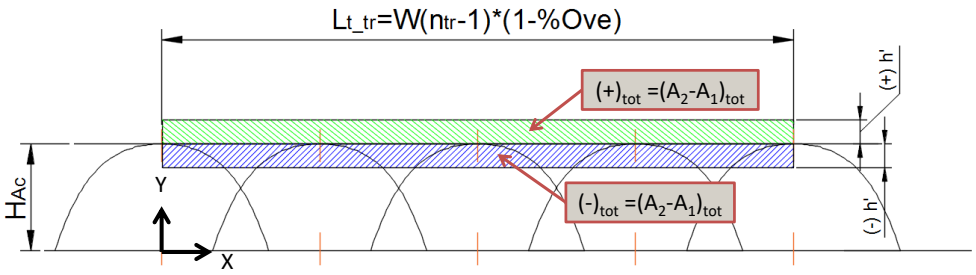

Figure I.18. Scheme to determine the value of the variable h' as function of the total difference of area ΔA (total), for overlapping on consecutive beads.

The height change (h') will be given by (Eq. I.19):

$$h' = \frac{\Delta A_{tot}}{L_{t\_tr}} \qquad \textit{Eq. I.19}$$

Where:

$$A_{tot} = \frac{W(n_{tr}-1)(240H_{Ac}\%Ove + 3a_1W^4 + 20a_2W^2)}{240} \text{ and } L_{t\_tr} = W(n_{tr}-1)(1-\%Ove)$$

The height H_{Ac_corr} for a layer of clad beads with any overlap ($\%Ove$) will be given by (Eq. I.20):

$$H_{Ac\_corr} = H_{Ac} + h' \qquad \textit{Eq. I.20}$$

The analogous parameters for quantifying the quality of multilayer/multilayer coatings (in the same way as for single beads) have the suffix "ml" (multilayer/multilayer), to distinguish them from those for single beads.

Substituting in (Eq. I.20) the (Eq. I.19), and multiplying by n-layers (n_{ly}), the theoretical total height (for a multilayer cladding), for a bead with height H_{Ac_corr} is given by (Eq. I.21):

$$H_{\substack{Ac\_ml \\ tot}} = \frac{n_{ly}(240H_{Ac} + W^2(3a_1W^2 + 20a_2))}{240(1-\%Ove)} \qquad \textit{Eq. I.21}$$

The total width of the cladding will be given by (Eq. I.22):

$$W_{tot} = W(\%Ove - n_{tr}(\%Ove - 1)) \qquad \textit{Eq. I.22}$$

No analytical mathematical solution for the optimal theoretical value of $\%Off$ was found.

Once the theoretical height for a multi-line, multi-layer coating was calculated from a series of single bead, a set of experiments were carried out under different conditions to verify to verify the theoretical calculation. In the tests on multilayer coatings, the optimal process parameter values for a single bead were used. In addition, tests were carried out under different conditions to verify the efficiency and stability of the optimisation solution.

In addition to the previous paragraph, it is desirable that the efficiency on the deposition of material will be as higher as possible (represented by η_{clad_ml}). The appearance of strange secondary phases is avoided using the optimal conditions for a single bead.

A series of test beads were deposited modifying some of the following parameters: v, P_{laser}, $\%Ove$ and $\%Off$.

DOE images from multilayer / multiline test are shown in (Fig. I.19). The areas are delimited by colours, green for the deposited material, and red to delimit the molten area. The numbers at the bottom of each test of cladding will serve as index.

After, cross sections corresponding to each test were cut. A metallographic etching was carried out, and the values corresponding to the cladded, melted and pore areas were measured through an image analysis software.

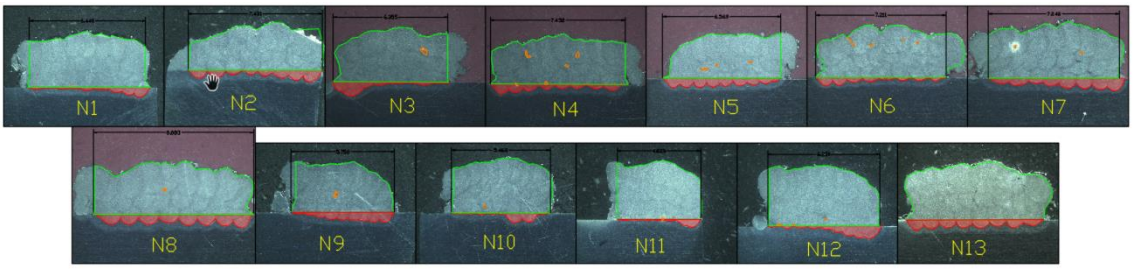

Figure I.19. DOE images for a multiline/multilayer series of trials for different Laser Cladding deposition parameters.

For each DOE, a trial was considered as steady state when a multilayer/multilayer test was formed by the deposition of 3 layers with 8 beads each.

The number of layers and beads for each multilayer / multiline trial for the DOE has not been increased because the quantification of, for example, the multilayer dilution (Dil_{ml}) is dependent of the number of layers cladded. That is because in (Eq. I.23) if the cladded area tends to be large, the ratio Dil_{ml} considering the total melted area tends to zero.

$$Dil_{ml} = \frac{A_{m\_ml}}{A_{c\_ml} + A_{m\_ml}} \qquad \textit{Eq. I.23}$$

Porosity and Efficiency (both multilayer) will be defined in (Eq. I.24) and (Eq. I.25):

$$Por_{ml} = \frac{A_{p\_ml}}{A_{c\_ml} + A_{p\_ml}} \qquad \textit{Eq. I.24}$$

$$\eta_{clad\_ml} = \frac{\rho_p v A_{c\_ml}}{m'(n_{ly} \cdot n_{tr})} \qquad \textit{Eq. I.25}$$

It is important to note that the data values concerning the measurements of the different areas, as shown in (Fig. I.19), do not fully describe the characteristics of the coating, as it is in the case of a single bead. Thus, for example, the coating named as N10 in (Fig. I.19), apparently presents a very low Dilution level (depending on its area A_{m_ml}), but the shape the melted area is distributed is very uneven, and can lead to metallurgical bond failure problems in the substrate/coating junction zone (and thus an

increase in porosity). Therefore, area data values without prior analysis are not sufficient and some kind of mathematical treatment needs to be applied.

The DOE for multiline / multilayer data is presented in (Table I.14). The experiment number (#$CLAD_{ml}$) matches the one shown at the bottom of each trial in (Fig. I.19).

Table I.14: Design of experiments to study the effect of the variables P_{laser}, v, $\%Ove$ and $\%Off$ on the responses expressed as a measure of the areas on a multiline/multilayer deposition (8 beads and 3 layers).

# $CLAD_{ml}$	P_{laser} (W)	v (mm)	$\%Ove$ (-)	$\%Off$ (-)	A_{c_ml} (mm²)	A_{m_ml} (mm²)	A_{p_ml} (mm²)	W_{ml} (mm)
1	436	475	0.36	0.25	17.74	1.07	3.80E-03	6.44
2	436	475	0.26	0.25	16.15	2.43	0.00E+00	7.43
3	436	522	0.36	0.25	16.14	1.57	9.18E-02	6.36
4	436	522	0.26	0.25	17.39	1.81	1.25E-01	7.45
5	393	475	0.36	0.25	13.57	2.24	5.94E-02	6.57
6	393	475	0.26	0.25	19.14	1.38	6.41E-02	7.21
7	571	522	0.36	0.25	19.95	3.04	2.53E-02	7.25
8	571	522	0.26	0.25	21.97	3.92	2.48E-02	8.88
9	436	475	0.5	0	13.14	1.90	4.88E-02	5.75
10	436	522	0.5	0	14.97	0.91	2.09E-02	5.46
11	393	475	0.5	0	13.55	0.53	1.61E-02	4.62
12	571	522	0.5	0	18.31	1.77	3.17E-02	6.23
13	436	475	0.26	0.375	21.51	2.69	4.40E-02	7.64

I.4.3 Characterization of the Stability of a Multiline/Multilayer Clad Bead

Characterizing the molten area is important. If the previous area is uniform and stable from the beginning of the cladding process, it means that the energy density towards the substrate has been kept approximately constant, and therefore the metallurgical bond should present better quality and uniformity.

In a previous paragraph it was mentioned that the measurement of areas (e.g. multiline/multilayer dilution) is not sufficient to adequately characterise the quality of a laser cladding coating.

To characterise the stability of the multilayer / multilayer coating, it is important not only to measure the areas that serve as control parameters for the process, but also the way in which these areas are distributed. It is proposed to use the measurement of the height of the coating bead ridges as a way to quantify the process stability.

A convenient statistical parameter was the standard deviation (σ). The standard deviation was applied to two sets of data: the height of the coating beads for the area above the substrate surface, and the height of the melted areas below the substrate surface. The procedure was as follows:

- The first was a sample of the data set corresponding to the height coordinates of the multiline / multilayer deposition, as shown in the example in (Fig. I.20, Left), red dots on the surface of the cladding. This sampling of points will be done with high density, in such a way that there is a representative statistical sample to characterize the final stability of the surface based on the distance (heights) with respect to a reference frame (in the substrate surface).
- The second was a sample of lower density coordinates on the molten area that gives rise to the dilution area, (Fig. I.20, Right), red dots at the bottom of the molten area). The lower number of data for the melted area is due to the desire to obtain values related to the period at the ridges of the fused area for the substrate. Thus, the spacing between beads of the laser beam was used to characterise the depth at which the source of heat fused the substrate.

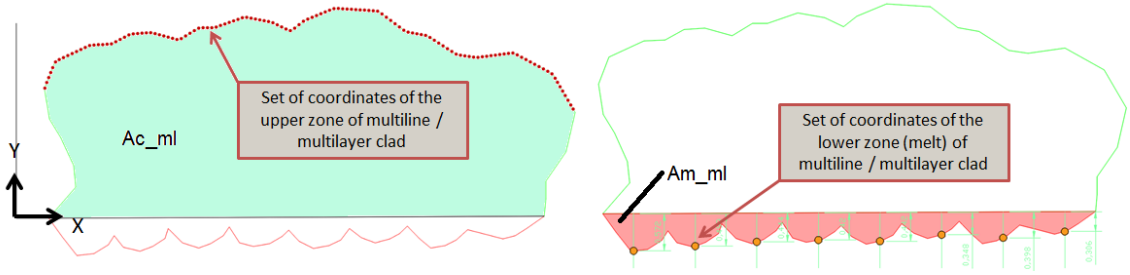

Figure I.20. Example of data collection to quantify the stability of a multi-line / multi-layer Laser Cladding deposition. Left, high point density to characterize the surface; right, low point density following the period of the molten area as a function of the overlap ($\%Ove$) of the beads.

The standard deviations of each set of coordinates were calculated as in the example of (Fig. I.20), as well as their normalization with respect to the smallest value (for comparison purposes the values were converted to natural scale).

Natural scale normalization is defined as (Eq. I.26):

$$\sigma_{sv} = \frac{\sigma_{i\_data}}{\min[\sigma_{(i=1\ldots n)}]_{data}} \qquad \textit{Eq. I.26}$$

The standard deviations for $H_{\substack{Ac\_ml \\ data}}$ and $H_{\substack{m\_ml \\ data}}$, their respective natural-scale normalizations (σ_a, σ_b) and the average of both normalizations are shown in (Table I.15).

Table I.15: Standard deviations in absolute value and in natural scale (with respect to the smallest value), of the data collection for the variables $H_{\substack{Ac\_ml \\ data}}$ y $H_{\substack{m\_ml \\ data}}$, from the tests for a multiline/multilayer deposition.

# $CLAD_{ml}$	$\sigma\left(H_{\substack{Ac\_ml \\ data}}\right)$ (mm)	$\sigma_a = \sigma_{sv}\left(H_{\substack{Ac\_ml \\ data}}\right)$	$\sigma\left(H_{\substack{m\_ml \\ data}}\right)$ (mm)	$\sigma_b = \sigma_{sv}\left(H_{\substack{m\_ml \\ data}}\right)$	$\sigma_{ab} = \frac{\sigma_a + \sigma_b}{2}$
1	0.190	1.00	0.171	2.05	1.53
2	0.348	1.83	0.142	1.70	1.77
3	0.335	1.76	0.259	3.12	2.44
4	0.248	1.30	0.155	1.87	1.59
5	0.705	3.70	0.118	1.42	2.57
6	0.332	1.75	0.133	1.60	1.68
7	0.297	1.56	0.165	1.98	1.77
8	0.277	1.45	0.119	1.44	1.45
9	0.558	2.93	0.160	1.92	2.43
10	0.367	1.93	0.175	2.11	2.02
11	0.446	2.35	0.161	1.94	2.14
12	0.515	2.70	0.244	2.93	2.82
13	0.355	1.87	0.083	1.00	1.44

Along with the previous table, other compound variable were calculated from the data in (Table I.14):

- $H_{\underset{real}{Ac\_ml}}$: total height of each set of filler beads test (its geometry is assumed as a rectangle of base W_{ml} and area A_{c_ml}), (Eq. I.27):

$$H_{\underset{real}{Ac\_ml}} = \frac{A_{c\_ml}}{W_{ml}} \qquad \textit{Eq. I.27}$$

- $P_{\underset{sv}{laser}}$ and v_{sv} according to (Eq. I.12) and (Eq. I.13), and the data values of the (Table I.14).
- $H_{Ac} = f(\text{Multiple linear correlation})$: height of a single bead according to the correlation model with the coefficients of (Table I.8).
- $W = f(\text{Multiple linear correlation})$: width of a single bead according to the correlation model with the coefficients of (Table I.8).
- $H_{\underset{tot}{Ac\_ml}}$: total theoretical height of a set of filler beads according to (Eq. I.21).
- W_{tot}: total theoretical width according to (Eq. I.22).
- η_{clad_ml}: according to (Eq. I.25), with m' = 8.78 g/min. The value of mass flow was the same as the optimum for a single clad bead.
- Dil_{ml}: according to (Eq. I.23).
- Por_{ml}: according to (Eq. I.24).

I.4.3.1 Error Estimation between Model for a Single Bead and Multiline/ Multilayer DOE Data as a Stability Criterion

To quantify the deviation between the values calculated by the different models, and those obtained from the experiments, the percentage error was used between the data sets. The values obtained from the DOE test experiment were assumed as the reference values.

The error $\%err$ is defined as (Eq. I.28):

$$\%err = \left(\frac{data_{real} - data_{\text{model}}}{data_{real}} \right) * 100\% \qquad \textit{Eq. I.28}$$

To express concisely the (Eq. I.28), the following nomenclature will be used: $\%err = \left(\frac{data_{real} - data_{\text{model}}}{data_{real}} \right) * 100\%$ equals $\%err\left(data_{real} \sim data_{\text{model}}\right)$

The percentage errors to calculate were the following:

- $\%err\left(H_{\substack{Ac\_ml \\ real}} \sim H_{\substack{Ac\_ml \\ teo}} \right)$: percentage error between the total height obtained from the set of filler beads test versus the theoretical height calculated from the (Eq. I.21).
- $\%err\left(W_{ml} \sim W_{tot}\right)$: percentage error between the total width obtained from the set of cladding beads test versus the theoretical width calculated from the (Eq. I.22).

Finally, to quantify the total error with a single parameter, the average of the absolute value of both previous errors were used, (Eq. I.29):

$$\overline{\%err} = \frac{abs\left[\%err\left(H_{\substack{Ac\_ml \\ real}} \sim H_{\substack{Ac\_ml \\ teo}} \right) \right] + abs\left[\%err\left(W_{ml} \sim W_{tot}\right) \right]}{2} \qquad \textit{Eq. I.29}$$

Absolute error values were used for the calculations because some of the data calculated for the same experiment were positive and some were negative, so that the sum of both can give a total error value close to zero if both data have approximately the same numerical value, but different signs.

The calculation values from the previous compound parameters are presented in (Table I.16).

Table I.16: Compound parameters calculated from DOE data in (Table I.14) to model the behaviour of multiline / multilayer Laser Cladding coating.

# CLAD	$H_{\substack{Ac\_ml \\ real}}$ (mm)	$P_{\substack{laser \\ sv}}$ (-)	v_{sv} (-)	H_{Ac} (mm)	W (mm)	$H_{\substack{Ac\_ml \\ tot}}$ (mm)	W_{tot} (mm)	η_{clad_ml} (%)	Dil_{ml} (%)	Por_{ml} x 10^3 (-)	%err($H_{\substack{Ac\_ml \\ real}}$ ~ $H_{\substack{Ac\_ml \\ teo}}$) (%)	%err(W_{ml} ~ W_{tot}) (%)	$\overline{\%err}$ (%)
1	2.75	-0.6349	-0.5391	0.530	1.354	1.489	7.418	32.9%	5.7%	0.214	-15.2%	45.9%	30.6%
2	2.17	-0.6349	-0.5391	0.530	1.354	1.288	8.366	29.9%	13.1%	0.000	-12.6%	40.8%	26.7%
3	2.54	-0.6349	-0.2124	0.490	1.320	1.403	7.232	33.1%	8.9%	5.655	-13.8%	44.8%	29.3%
4	2.33	-0.6349	-0.2124	0.490	1.320	1.214	8.156	35.6%	9.4%	7.132	-9.4%	48.0%	28.7%
5	2.07	-0.9907	-0.5391	0.472	1.354	1.227	7.418	25.1%	14.2%	4.359	-12.9%	40.6%	26.8%
6	2.65	-0.9907	-0.5391	0.472	1.354	1.062	8.366	35.5%	6.7%	3.337	-16.0%	60.0%	38.0%
7	2.75	0.4823	-0.2320	0.657	1.320	2.227	7.232	40.9%	13.2%	1.267	0.2%	19.1%	9.7%
8	2.47	0.4823	-0.2320	0.657	1.320	1.926	8.156	45.0%	15.2%	1.128	8.2%	22.1%	15.2%
9	2.28	-0.6349	-0.5391	0.530	1.354	1.906	6.092	24.3%	12.6%	3.701	-5.9%	16.6%	11.3%
10	2.74	-0.6349	-0.2320	0.490	1.320	1.796	5.939	30.7%	5.7%	1.395	-8.7%	34.4%	21.6%
11	2.93	-0.9907	-0.5391	0.472	1.354	1.571	6.092	25.1%	3.7%	1.187	-31.9%	46.4%	39.1%
12	2.94	0.4823	-0.2320	0.657	1.320	2.850	5.939	37.5%	8.8%	1.728	4.7%	3.1%	3.9%
13	2.82	-0.6349	-0.5391	0.530	1.354	1.288	8.366	39.9%	11.1%	2.041	-9.5%	54.3%	31.9%

I.4.4 Analysis of Results to meet the Overall Objectives of Multiline/Multilayer bead Optimisation

With the information in (Table I.15) and (Table I.16) it is possible to establish some trends. In order to clearly establish the optimisation objectives, the following aspects were taken into account:

1. Porosity must be minimal and if possible it should be absent.
2. The dilution for multi-line/multi-layer deposition should be as low as possible and above all uniform (to avoid adhesion problems of the bonded material to the substrate).
3. The stability of the multilayer/multilayer coating surface deposition must be maximised (so that the conditions for material deposition are as similar as possible to those optimal for a single bead).
4. The efficiency of material deposition must be maximised (economical use of raw material).

Considering the previous 4 literals, the following observations can be made from the data in the (Table I.15) and (Table I.16):

- All the porosities are low, as can be seen in column (Por_{ml}) of (Table I.16), with a maximum in experiment # 4 as the only value to highlight.
- The Dilution for multiple cladding beads (Dil_{ml}), remains low on average (9.87%) (Table I.16). However, this value does not have meaning by itself, since, as mentioned previously, it depends on the stability of the molten area across the entire cladding and the number of layers deposited. However, low values are generally beneficial, as it shows little thermal damage to the substrate for multi-line/multi-layer deposition.
- In addition to the Dilution, the values of the parameter of normalized standard deviation for the data of $H_{\underset{data}{Ac\_ml}}$ and $H_{\underset{data}{m\_ml}}$ expressed by the variable (σ_{ab}) in (Table I.15), should be closer to 1. A value close to 1 means that the stability conditions during the manufacturing of a multilayer/multilayer coating are maintained throughout the whole process. Noteworthy are cladding #1, 8 and 13 in the aforementioned table.

- The (Table I.16) shows that the best test for the variable η_{clad_ml} were #CLAD 7, 8 and 13, especially number 8 with a maximum of 45% in cladding deposition efficiency.
- Experiments # 8 and 13 in (Table I.15) and (Table I.16) excel in stability and material deposition efficiency parameters respectively.

The Lumière software (Logiciel à Usage de Modélisation Industrielle Et de Recherche Expérimentale) was used again to model three of the most important variables of the deposition process parameters for Multiline/Multilayer as a function of $f\left(\underset{sv}{P_{laser}}, v_{sv}, \%Ove, \%Off\right)$. The responses for the model were as follows:

- Dil_{ml} (%).
- Por_{ml} (%).
- η_{clad_ml} (%).

The restrictions to be fulfilled for the statistical modelling of Dil_{ml}, Por_{ml} y η_{clad_ml} were:

- The confidence level will be defined as 95%, with a minimum of 2.5% and a maximum of 97.5%.
- The maximum risk level for the coefficients will be 5%.
- The correlation coefficient was established at a minimum of 0.985.

I.4.5 Variable Correlation Matrices and Regression Models for Multiline/Multilayer

The results for the modelling are shown in (Table I.17) and (Table I.18).

Table I.17: Correlation matrix of the variables to be modelled. The confidence level is specified in 95% with a data range of [2.5% 97.5%].

Multiple Linear Regression

Defined Confidence Level: 95.00 %.

Correlation matrix

Significant correlations at 95.00 %
r = 0.5529 (13 - 2)

	Ove#	Off#	P_laser_sv#*v_sv#	P_laser_sv#*Off#	v_sv#*Ove#	v_sv#*Off#	Ove#*Off#
Ove#	1.0000						
Off#	-0.9122	1.0000					
P_laser_sv#*v_sv#	-0.0406	0.0588	1.0000				
P_laser_sv#*Off#	0.4463	-0.5051	-0.6725	1.0000			
v_sv#*Ove#	-0.4820	0.4135	-0.7360	0.1385	1.0000		
v_sv#*Off#	0.7419	-0.8401	-0.4318	0.7339	-0.0228	1.0000	
Ove#*Off#	-0.7874	0.9598	0.0424	-0.4692	0.3669	-0.7800	1.0000

Range of variation of the Factors

Factors to consider	Minimum	Average	Maximum	Standard deviation
P_laser_sv	-0.9907	-0.4592	0.4823	0.5570
v_sv	-0.5391	-0.3883	-0.2124	0.1695
Ove	0.2600	0.3646	0.5000	0.1033
Off	0.0000	0.1827	0.3750	0.1313

Control statistics for Multiple Linear Regressions are presented below. In all cases, the correlation coefficient (R) will be assumed to be valid for values> = 0.95, with risks for each variable less than 1% and without the use of "constants" in any of the linear correlations.

Table I.18: Regression matrices with statistical control parameters for each of the variables for the modelling process of a multiline / multilayer laser cladding deposition.

Regression of Dil_ml

Summary of Coefficients

Table with the residual standard deviation.
Sr = 0.0365 - Nur = 11

Variable	Coefficient	Standard deviation	t Student	Confidence %	Risk %	Centring
Ove#	0.1534	0.0356	4.3105	99.88	0.12	No
Off#	0.2301	0.0606	3.7997	99.71	0.29	No

Confidence Interval 95%

Variable	Coeff	Mini (2.50 %)	Maxi (97.50 %)
Ove#	0.1534	0.0751	0.2317
Off#	0.2301	0.0968	0.3634

Decomposition of the sum of squares

Source	Sum of the squares	Ddl	Medium Square	Fisher	Confidence %	Risk %
Regression	0.1282	2	0.0641	48.1116	100	0

Residues	0.0147	11	0.0013			
Total	0.1429	13	0.011			
Correlation coefficient (R):	0.95					
Residual Standard deviation Sr :	0.0365	Ddl	11			

Analysis of Effects Contributions.

Effects	Contributions	%
Ove#	0.069	48.28
Off#	0.0593	41.46
Residues	0.0147	10.26
Total	0.1429	100

Regression of Por_ml

Summary of Coefficients

Table with the residual standard deviation.

Sr = 0.0011 - Nur = 9

Variable	Coefficient	Standard deviation	t Student	Confidence %	Risk %	Centring
Off#	0.0271	0.004	6.7406	99.99	0.01	No
P_laser_sv#*Off#	-0.0201	0.0037	-5.4556	99.96	0.04	-

v_sv#*Ove#	-0.0092	0.0026	-3.5364	99.37	0.63	-
v_sv#*Off#	0.0746	0.0116	6.4196	99.99	0.01	-

Confidence Interval 95%

Variable	Coeff	Mini (2.50 %)	Maxi (97.50 %)
Off#	0.0271	0.018	0.0362
P_laser_sv#*Off#	-0.0201	-0.0284	-0.0117
v_sv#*Ove#	-0.0092	-0.015	-0.0033
v_sv#*Off#	0.0746	0.0483	0.1009

Decomposition of the sum of squares

Source	Sum of the squares	Ddl	Medium Square	Fisher	Confidence %	Risk %
Regression	1.29E-04	4	0	26.9865	99.99	0.01
Residues	1.08E-05	9	0			
Total	1.40E-04	13	0			
Correlation coefficient (R):	0.961					
Residual Standard deviation Sr :	1.10E-03	Ddl	9			

Analysis of Effects Contributions.

Effects	Contributions	%

Off#	0.0002	126.42				
P_laser_sv#*Off#	0.0001	59.65				
v_sv#*Ove#	0	27.94				
v_sv#*Off#	-0.0002	-121.7				
Residues	0	7.7				
Total	0.0001	100				

Regression of η_{clad_ml}

Summary of Coefficients

Table with the residual standard deviation.

Sr = 0.0341 - Nur = 9

Variable	Coefficient	Standard deviation	t Student	Confidence %	Risk %	Centring
Ove#	0.6856	0.0387	17.7199	100	0	No
Off#	1.8058	0.269	6.7131	99.99	0.01	No
P_laser_sv#*v_sv#	-0.2037	0.0415	-4.914	99.92	0.08	-
Ove#*Off#	-3.5797	0.8965	-3.9929	99.69	0.31	-

Confidence Interval 95%

Variable	Coeff	Mini (2.50 %)	Maxi (97.50 %)

Ove#	0.6856	0.598	0.7731
Off#	1.8058	1.1973	2.4143
P_laser_sv#*v_sv#	-0.2037	-0.2975	-0.1099
Ove#*Off#	-3.5797	-5.6078	-1.5516

Decomposition of the sum of squares

Source	Sum of the squares	Ddl	Medium Square	Fisher	Confidence %	Risk %
Regression	1.4974	4	0.3743	322.1021	100	0
Residues	0.0105	9	0.0012			
Total	1.5079	13	0.116			
Correlation coefficient (R):	0.997					
Residual Standard deviation Sr :	0.0341	Ddl	9			

Analysis of Effects Contributions.

Effects	Contributions	%
Ove#	1.06	70.3
Off#	1.5246	101.11
P_laser_sv#*v_sv#	-0.1834	-12.16
Ove#*Off#	-0.9038	-59.94
Residues	0.0105	0.69
Total	1.5079	100

I.4.6 Validation of Correlations

The verification of the correlation models (based on the values of DOE data) will be done through the Shapiro and Wilk Test (Mohd Razali and Yap, 2011), one of the test for normality considered most powerful. The results of tests to verify the normality between the error generated by the values calculated by the correlation model and the experimental data is shown in (Table I.19):

Table I.19: Results of the hypothesis evaluation for the Shapiro and Wilk test for the Error between the modelled variables in (Table I.18) and the data in (Table I.14).

Test of normality for residuals of multiline and multilayer for Porosity model, Dilution model and Efficiency model.

Adequacy to a Normal Law

CHARACTERISTICS OF THE SAMPLE Error_Por_ml#

Defined Confidence Level: 95.00%.

Number of observations:	Average:	Standard deviation:	D.D.L.:
13	0.0001	0.0009	12

Normality Test: SHAPIRO AND WILK

Calculated Statistics	Law	Confidence %	Risk (alpha)%
0.8712	Normal Distribution	94.7289	5.2711

The distribution is not significantly different from a normal distribution.

CHARACTERISTICS OF THE SAMPLE Error_Dil_ml#

Defined Confidence Level: 95.00%.

Number of observations:	Average:	Standard deviation:	D.D.L.:
13	0.0008	0.0349	12

Normality Test: SHAPIRO AND WILK			
Calculated Statistics	Law	Confidence %	Risk (alpha)%
0.9708	Normal Distribution	14.2253	85.7747
	The distribution is not significantly different from a normal distribution.		
	CHARACTERISTICS OF THE SAMPLE Error_Eff_ml#		
	Defined Confidence Level: 95.00%.		
Number of observations:	Average:	Standard deviation:	D.D.L.:
13	0.0007	0.0295	12
Normality Test: SHAPIRO AND WILK			
Calculated Statistics	Law	Confidence %	Risk (alpha)%
0.9395	Normal Distribution	57.4834	42.5166
	The distribution is not significantly different from a normal distribution.		

Once the validity of the model correlations was validated (since the error follows the trend towards a normal distribution, and therefore it means that all significant variables that affect the process were taken into account), optimisation proceeded with a process of finding compromise values in the model's responses based on previously established objectives (minimize Por_{ml} and Dil_{ml}, and maximize η_{clad_ml}).

The results of this optimization were not independent of the parameters applied to a single bead, therefore, an important restriction was applied, which was that all numerical solutions converge for values near $P_{\substack{laser \\ sv}}$ = 0.4823 and v_{sv} = -0.2320, that is, to the optimum of a single cladding bead, thus the non-appearance of undesirable metallurgical phases (intermetallic) was guaranteed.

Remember that the variables with subscript "sv" are reduced compound variables, as defined in (Eq. I.12) and (Eq. I.13). The (Table I.20) shows the search results for optimal solutions, where the variations were given by the changing the values of %Ove and %Off.

Table I.20: Optimization for Por_{ml}, Dil_{ml} and η_{clad_ml} based on input parameters for a multiline / multilayer cladding model.

Optimization of Dil_ml# in the domain under constraints of other responses
Number of constraints: 0

Responses	Objectives	Calculated Values
Dil_ml	Minimize	0.0489
Por_ml	0.0000 <= Por_ml<= 0.0071	0.0006
Eff_ml	0.2434 <= Eff_ml<= 0.4500	0.2392

Factors	Calculated Values
P_laser_sv	0.4823
v_sv	-0.2320
%Ove	0.287
%Off	0.0213

Optimization of Eff_ml# in the domain under constraints of other responses
Number of constraints: 0

Responses	Objectives	Calculated Values
Dil_ml	0.0370 <= Dil_ml<= 0.1515	0.1251
Por_ml	0.0000 <= Por_ml<= 0.0071	0.0002
Eff_ml	Maximize	0.5495

Factors	Calculated Values
P_laser_sv	0.4823
v_sv	-0.2320
%Ove	0.2419
%Off	0.3824

Optimization of Por_ml# in the domain under constraints of other responses
Number of constraints: 0

Responses	Objectives	Calculated Values
Dil_ml	0.0370 <= Dil_ml<= 0.1515	0.1496
Por_ml	Minimize	0.0001
Eff_ml	0.2434 <= Eff_ml<= 0.4500	0.4414

Factors	Calculated Values
P_laser_sv	0.4823
v_sv	-0.2320
%Ove	0.4026
%Off	0.3817

I.4.7 Obtaining a Compromise Solution for the Optimisation of Multiline/Multilayer Beads Model

As for a single bead, it was observed that each optimization of the previous section separately converges to different optimal values. However, in this, case it is noteworthy that the response values of $\%Ove$ and $\%Off$ are not in the same close range, unlike what happened in the optimization for a single bead. Therefore, an analysis of the various solutions was necessary to establish a compromise between them.

From (Table I.20), it is noteworthy that:

- When applying the different found solutions (regardless of the value of the optimized parameter), all the values for Por_{ml} were very low, therefore it can be assumed that the porosity will remain low regardless of which optimization solution was taken as valid. Therefore, compromises in the solutions were made on the basis of the two remaining parameters: η_{clad_ml} and Dil_{ml}.
- A weighted factor will be used as a criterion to quantify the optimum solution found for $\%Ove$ and $\%Off$ based on the remaining parameters (Dil_{ml} and η_{clad_ml}). The respective weights for the calculated responses were η_{clad_ml} = 0.67 and Dil_{ml} = 0.33, so that the sum of the weights is equal to one. The weighting of the cladding efficiency parameter as twice as important as the dilution was due to the fact that the former parameter in a multilayer deposition is an important value only for the first layer. On the other hand, the efficiency will be of higher importance (with a high probability), depending on the final height of the coating material.

Therefore, the compromise solution for $\%Ove$ and $\%Off$ were (Eq. I.30) and (Eq. I.31):

$$\%Ove_{comp} = (\%Ove * Wt)_{\min(Dil\_ml)} + (\%Ove * Wt)_{\max(\eta\_clad\_ml)} = 0.257 = 25.7\% \qquad Eq.\ I.30$$

$$\%Off_{comp} = (\%Off * Wt)_{\min(Dil\_ml)} + (\%Off * Wt)_{\max(\eta\_clad\_ml)} = 0.263 = 26.3\% \qquad Eq.\ I.31$$

With this compromise solution calculated on the basis of weighted parameters, the calculated porosity was (according to the Multiple Linear Regression (Table I.18)), Por_{ml} = 5.73E-04 = 0.0572%, which being practically zero is considered valid in terms of the objective of limiting porosity to a minimum. The values of the other parameters calculated with the compromise solution were: $P_{\underset{sv}{laser}}$ = 0.2843, v_{sv} = -0.232, equivalent in normal parameters to P_{laser} = 571 W and v = 522 mm / min respectively:

Finally, the values of the compromise solution were taken as suitable for the following reasons:

- The process parameters were maintained under conditions in which the undesirable phases (intermetallic) do not appear, as for the case of a single bead.
- When comparing the value of $\%Ove_{comp}$ (Eq. I.30), with the one mathematically deduced in (Eq. I.18), it was observed that both values are very close to the one obtained when applying the same parameters as for a pair of single beads (25.7% versus 27.8%). The previous results help to confirm that the solution obtained by mathematical deduction is accurate (a geometric optimum versus a statistical optimum gives approximately the same result).
- The values of the compromise solution that were most similar to those of the DOE in (Table I.14) were #CLAD 7 and 8.
- With respect to the stability of the process (characterized by the sum of the standard deviations in natural scale (Table I.15), where a lower value of (σ_{ab}) means greater stability), the #CLAD 7 and 8 were the best test results, together with the of experiment # CLAD 13. However, the #CLAD 13 presents a higher porosity and parameters of P_{laser} and v further away from the optimum for a single bead; as a result, it was not taken into account. In (Fig. I.21) the values of $\sigma_{ab} = \left[\sigma_{sv}\left(\underset{data}{H_{Ac\_ml}} \right) + \sigma_{sv}\left(\underset{data}{H_{m\_ml}} \right) \right] \Big/ 2$ and Por_{ml} were presented for comparison from the data of (Table I.15) and (Table I.16).

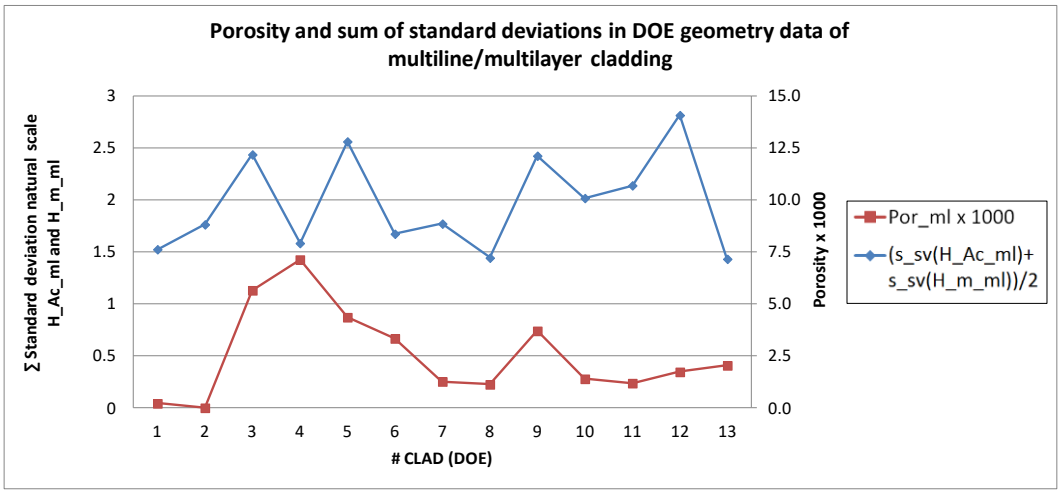

Figure I.21. Comparison of the sum values of the standard deviation for height and total width of a multiline / multiline cladding (σ_{ab}); and for the porosity (Por_{ml}) from the data of DOE in (Table I.14). For the sum of the standard deviations (σ_{ab}), values close to one are better. In the case of porosity values the lowest are better.

- The deposition efficiency for multiple beads (η_{clad_ml}), is maximum for experiments #CLAD 7 and 8. The disadvantage is that the amount of Dilution is one of the highest for both of the previous test. However, the test # 7 and 8 were very stable and ensures a good metallurgical union between the substrate and the cladding material, as well as between the successive layers of metal powder. The (Fig. I.22) shows the values of η_{clad_ml} and Dil_{ml} from the DOE data in (Table I.16).

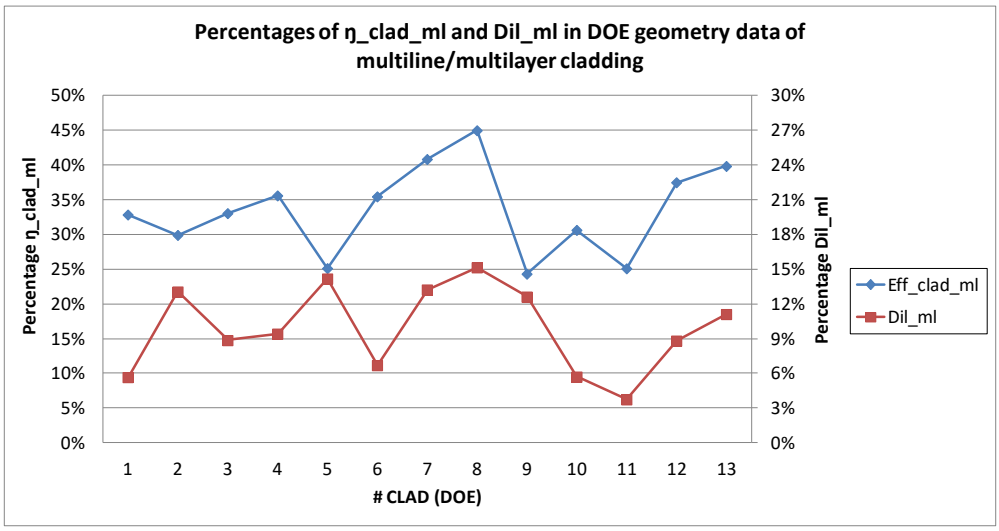

Figure I.22. Percentage of material deposition efficiency and Dilution from DOE data in (Table I.16). In the case of efficiency, a high values are better, in the case of Dilution, a lower values are preferable.

- For $\%Off$, no physical explanation has been found for the compromise value (as it is the average of two solutions). Separately, they can be interpreted as follows: When ($\%Off$) is calculated based on minimizing Dilution ($\%Off_{\min(Dil\_ml)}$), its value is in the order of 2.13%, that is, there will be no gap between consecutive layers of cladding, and therefore the previous layer serve as a "shield" for the laser beam to protect the material at its bottom. In the case of the substrate, this would explain the tendency for minimum dilution. On the other hand, if $\%Off$ is obtained based on maximizing efficiency ($\%Off_{\max(\eta\_clad\_ml)}$), the calculated value is 38.2%, that is, shifting the beads in such a way that the beginning of the next layer would be between the two ridges of the previous layer (in the gap between two beads). This would be an area where there would be a trend towards a greater efficiency of powder capture for growth than, for example, one of the edges, and this would explain the predisposition of that area to a greater efficiency in deposition.

Both phenomena are depicted in (Fig. I.23), where the crest of the first cladding bead on the left ($\%Off_{\min(Dil\_ml)}$) protects the previous ones (attenuation that allows low dilution), and instead the one in the centre ($\%Off_{\max(\eta\_clad\_ml)}$) would be deposited in a "hole between two ridges" (trapping more powder). As a compromise for both solutions, it has been decided to take the average of both compromise values (Fig. I.23, right side).

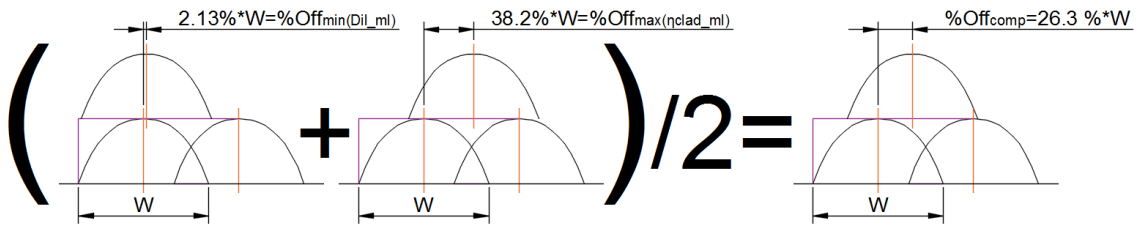

Figure I.23. Description of the compromise solution for the values of the variable $\%Off$ as an average of the solutions obtained to minimize dilution and maximize the efficiency of the multiline/multilayer cladding.

I.5 Optimal Process Parameters for a Multiline/Multilayer Beads for INCO718

Finally, the summary of the cladding process parameters for INCONEL 718 is presented in (Table I.21):

Table I.21: Summary of the optimal process parameters for multiline / multilayer laser deposition.

m':	8.78	g/min.
P_{laser}:	571	Watt (ϕd_{laser} =1 mm, Fibber Laser, Multimode).
v:	522	mm/min.
$\%Ove$:	26.75%	(-)
$\%Off$:	26.3%	(-)

I.6 Application of the Optimization Methodology of Process Parameters for the Laser Cladding Technology and Transfer of Research to Companies

The University of the Basque Country (through the Department of Mechanical Engineering, via the High Performance Manufacturing Group), has worked in consortium with private companies to develop projects, one of which was developed in consortium with IBARMIA INNOVATEK, S.L.U. (https://www.ibarmia.com/es/) a recognized machine tool manufacturer and TECNALIA technology centre (https://www.tecnalia.com/es/).

The objective of this collaboration was the development of a hybrid manufacturing machine (machining and deposition of metal material by the Laser Cladding process, with the name ADD + PROCESS), to be presented at the EMO machine tool fair held on 5 to October 10, 2015 in Milan.

A schematic of the contributors to the collaboration consortium is shown in (Fig. I.24).

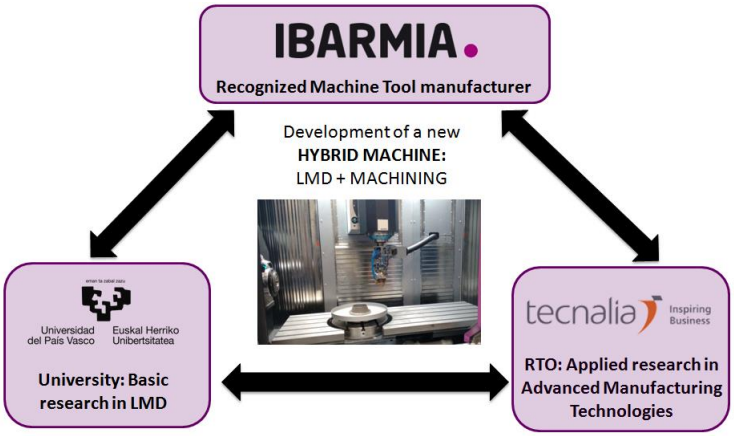

Figure I.24. EHU / UPV, IBARMIA and TECNALIA consortium established for the development of the hybrid manufacturing machine IBARMIA ADD + PROCESS. The picture in the centre shows the working area of the hybrid machine.

Part of the set up process (which was carried out by the Laser Group, part of the High Performance Manufacturing Group), consisted of obtaining the optimum process parameters for the manufacture of a prototype part that would be exhibited at the company's stand IBARMIA, in addition to those that would be produced "live" during the EMO machine tool fair itself. The material used was type 316 stainless steel.

The DOE and optimization method described this Chapter was used. The summary sequence of setting up is shown in (Fig. I.25).

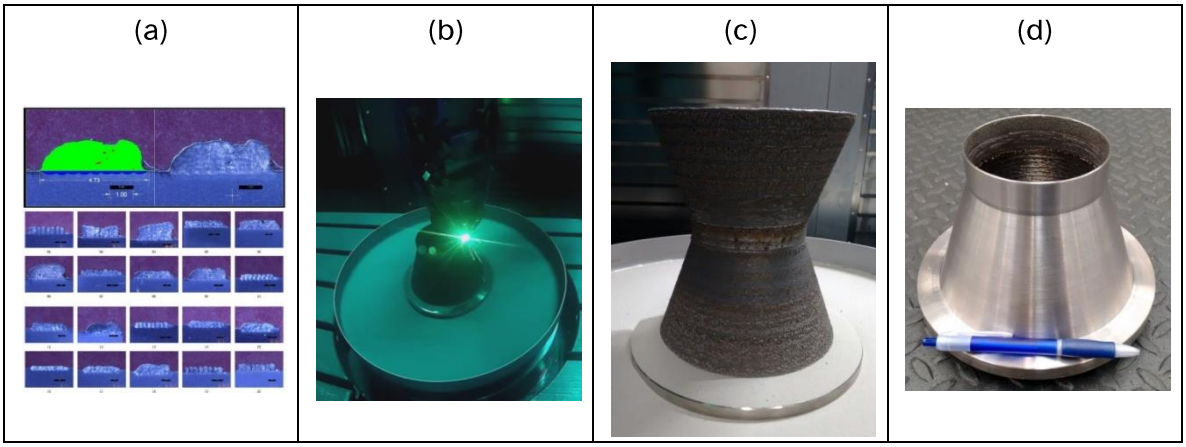

Figure I.25. Images of the set up sequence of a Laser Cladding process in the hybrid machine IBARMIA ADD + PROCESS, (a) design of experiments, (b) application of the optimal parameters to the manufacturing of demonstration piece, (c) a finished demonstration part, (d) machining the part manufactured by AM to verify the absence of pores and defects in the cladding material.

An independent (confidential) laboratory carried out an in depth metallurgical analysis of parts of the demonstration piece (Fig. I.26).

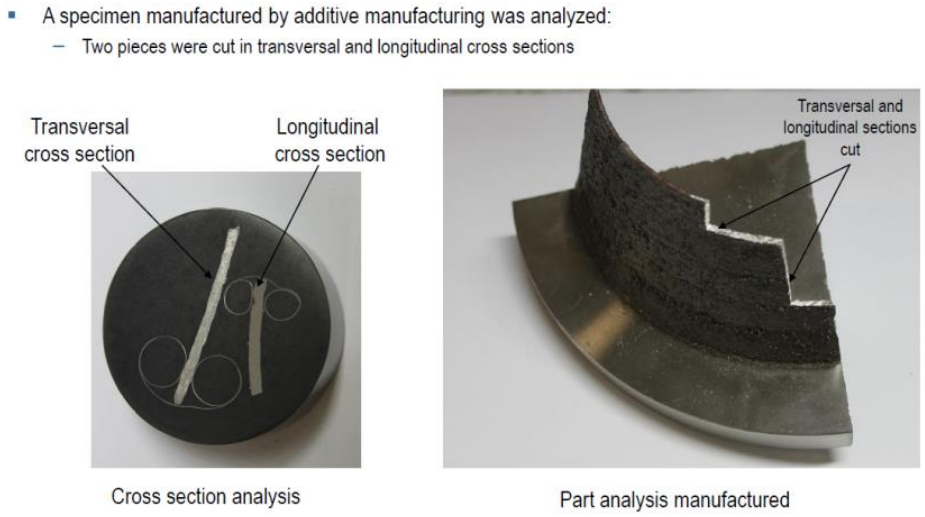

Figure I.26. Images from the report of an independent (confidential) laboratory, which analysed sections of the demonstration piece manufactured with the optimised process parameters based on DOE and the method described in this Chapter of the thesis report.

The results of the analysis shown that the composition of the material was homogeneous (a constitution analysis of the clad material was carried out by means of EDS / SEM), no segregations of the alloy were identified within the manufactured material and only very few pores were found (with a maximum diameter in the order of 10 μm).

From the above paragraph it is concluded that the optimisation method developed for the process parameters for Laser Cladding is versatile enough to be applied to an alloy other than INCO718 with good results.

CHAPTER II: MICROSTRUCTURE CHARACTERIZATION OF NEW AND RECYCLED IN718 POWDER AND RESULTING LASER CLADDING MATERIAL

II.0 Nomenclature and Abbreviations

AM:	Additive Manufacturing
CCT:	Continuous Cooling Transformation
CET:	Columnar to Equiaxed Transition
CP:	Cleaned Powders
CW:	Continuous Work Mode
DLD:	Direct Laser Deposition
DMLS:	Direct Metal Laser Sintering
EBM:	Electron Beam Melting
EBSD:	Electron backscatter diffraction
HIP:	Hot Isostatic Pressing
IMT:	Incipient Melting Temperature
LAM:	Laser Additive Manufacturing
LFC:	Low Cycle Fatigue
LMD:	Laser Metal Deposition
NbC:	Niobium Carbide
NP:	New Powder
QCW:	Quasi-Continuous Work Mode
RP:	Reacted Powder
SD:	Standard Deviation
SEM:	Scanning Electron Microscope
SLM:	Selective Laser Melting
STH:	Standard Heat Treatment
TCP:	Topologically Close-Packed Phases
TiN:	Titanium Nitrides
WAAM:	Wire Arc Additive Manufacturing
XDR:	X-rays Diffraction

II.1 Introduction

The Laser Cladding process consists of the addition of a metallic material (generally in the form of powder or wire) into a molten bath generated on a base material (also metallic), by means of a high power laser directed at the surface of the substrate in a specific area (focal plane). The cladding material is melt by the laser beam and consolidated together with the base material by means of metallurgical bonding in a series of beads (similar to the welding ones).

This chapter deals with the analysis and characterisation of a material deposited by the Laser Cladding process and the design of a procedure to collect and reuse the powder wasted during the cladding process itself for a nickel-based superalloy (INCO718).

The analysis and characterisation of the material deposited during the Laser Cladding additive manufacturing process is important to determine whether this manufacturing method changes the chemical composition of the alloy that is deposited, due to the characteristics of the process itself when the material is manufactured (rapid solidification, high temperature gradients, extended solubility, etc.).

The chemical composition of the alloy that was been used in this research (INCO718), should be investigated both at a general level (macro scale) and at the level of secondary phases (micro scale). The variation in the formation and distribution of secondary phases within INCO718 (depending on the manufacturing process of the material, as well as their transformations) are mainly a consequence of heat treatment.

Not all secondary phases have the same effect on the mechanical behaviour of the material. Some of the so-called "undesirable phases" can affect very differently depending on their location within the grain matrix within the alloy.

The additive manufacturing process by Laser Cladding generates very particular microstructures to those obtained from traditional methods such as the casting of ingots. The particular microstructure that is obtained prior to heat treatment changes much after the alloy has been subjected to heat treatment (Special Metals, 2007). After heat treatment there are phases that are very persistent and remain completely undiluted regardless of the alloy manufacturing method (e.g. Laves phases), but are distributed differently than in a traditionally manufactured INCO718 alloy. To compare the effect of the material manufacturing method ("traditional" or by additive

manufacturing), all heat treatments used shall be of the standard type whenever possible, as shown in (Fig. II.31).

This chapter will start with the study of superalloys (with special emphasis on INCO718 alloy), their phases and components, and the effect of these phases on the mechanical behaviour. Subsequently, a characterisation of the IN718 alloy powder will be carried out and a methodology for its reuse will be proposed.

II.2 State of Art

II.2.1 Super-Alloys and INCO718

INCO718 is one of the so-called nickel-based superalloys, nickel being the main alloying element. The combination of nickel with chromium provides the high oxidation resistance necessary for high temperature service. In addition, these INCONEL-type alloys do not become brittle at cryogenic temperatures and have excellent mechanical properties (Thomas, 2005). Most of these Nickel + Chrome-based alloys increase their resistance with the addition of other elements (Aluminium, Titanium, and Niobium). In the particular case of the INCO718, the amount of Iron is significant (close to 20% of total weight).

At a formal definition level, a superalloy is defined as (Akca and Gursel, 2015):

- An alloy that is rich in at least one of the following elements: Nickel, Cobalt, or Iron.
- An alloy that maintains its structural, superficial and mechanical properties at high temperatures, under high stresses and severe working conditions.

The characteristics that are described in the two previous literals fit with the main characteristics of INCO718 alloy, and therefore it is justifiable to call this material a super-alloy.

According to (Thomas, 2005), INCO718 is a relatively recent alloy, invented in 1959 and used at an industrial level since 1965.

The range of use of this alloy is close to 650°C, and its normal use is above 540°C for high temperature applications (Hassan and Corney, 2017).

The main use of this material is in gas turbines for power generation or maritime propulsion, aircraft turbines for both civil and military use, coal conversion plants,

chemical industry (mainly pressure vessels and heat exchangers), oil industry, submarines, and nuclear reactors or in any application where high resistance at high temperatures or corrosion is required. An interesting characteristic of super-alloys is that their working range is close to 70% of their incipient melting temperature, a fraction that very few alloys of any kind are capable of achieving.

In general, nickel-based alloys are some of the most complex materials developed by engineers, and for many metallurgists, superalloys are among the most interesting. According to (Akca and Gursel, 2015), they constitute more than 50% of the weight in advanced aircraft turbines.

The drawback of superalloys is that they are very expensive (because of the cost of nickel and the addition of rare elements, such as niobium, which is used in the alloy to solve problems such as the tendency to crack during welding). The use of alloying elements in superalloys leads to the fact that these materials are approximately 5 times more expensive than high quality turbine steel. In most superalloys, most of the dominant effects (mechanical properties) are due to the alloying elements, with the exception of iron.

II.2.2 Metallurgy of INCO718

The chemical composition of INCO718 can be seen in detail in (Table II.1). The main effect of the different alloying elements will be mentioned below, as well as the metallurgical phases (main and secondary) they will form:

- Nickel: it constitutes approximately 53% of the INCO718 alloy, and contributes to its resistance to corrosion. The amount of Nickel in this alloy is defined as a compromise solution between the Yield Strength and the Ductility of the material according to (Fig. II.1) (Keiser and Brown, 1976).

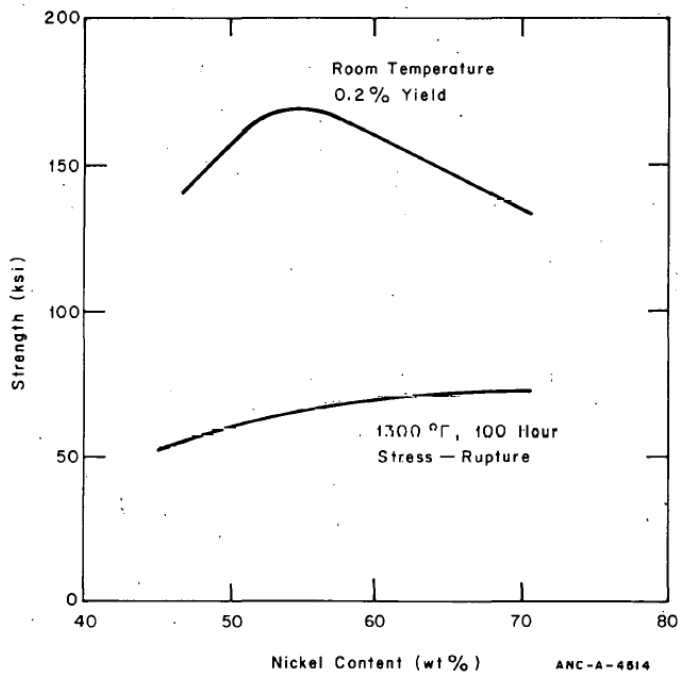

Figure II.1. The effect of nickel content on yield strength and stress rupture strength of Alloy 718 (Keiser and Brown, 1976).

- Chromium: it constitutes approximately 18% of the alloy; its effect is to contribute to the resistance to corrosion at high temperatures.
- Niobium: between 4.3 to 6% of the alloy. It is responsible for the main hardening phase of the INCO718 alloy due to the formation of γ'' precipitates. The amount of Niobium in the alloy is a compromise between the amount of hardening that is sought and the ductility of the material itself, as shown in (Fig. II.2). A value close to 5% in content of the element Niobium in the INCO718 alloy is assumed as optimal.
- Molybdenum: its effect is to increase the resistance in service at high temperature of INCO718 through the precipitation hardening mechanism. At moderate temperature, Molybdenum remains in the alloy as a solid solution. If too much of this element is used in the material, the hot workability of the alloy is affected, so the amount of Molybdenum is kept at a maximum value close to 3%.
- Titanium: fundamental element in the hardening of the INCO718 alloy through the mechanism of precipitates due to aging within the γ matrix of the alloy. The effect of Titanium is highly variable, especially in combination with Aluminium and Carbon (and also depends on the heat treatment to which the INCO718 alloy is subjected). The optimal amount of Titanium in the alloy in the INCO718 alloy is around 1%. Beyond a content of 1% of Ti, there is no perceptible increase in the value of the Rupture Strength of the material, but there is a significant reduction

in Ductility. Titanium together with Aluminium form γ' precipitates. The γ' precipitates play a less important role than γ'' precipitates for hardening the INCO718 alloy (Thomas, 2005).

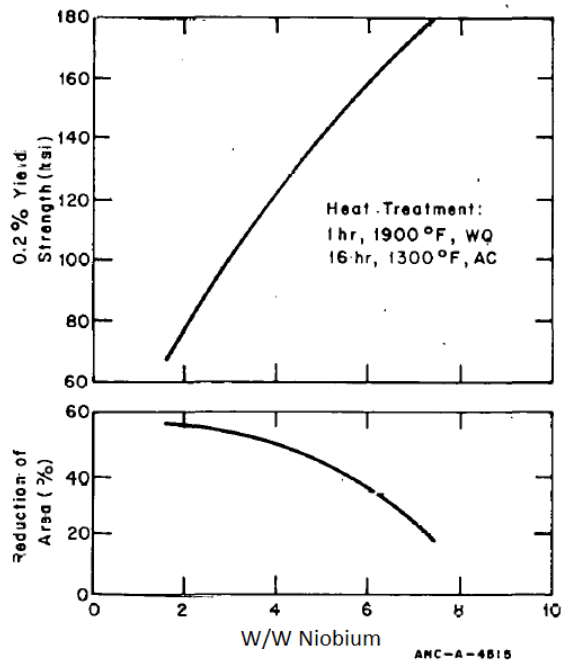

Figure II.2. The effect of columbium (Niobium) content on room temperature yield strength and ductility (Keiser and Brown, 1976).

- Aluminium: this element works in conjunction with Titanium and Carbon to modify the mechanical properties of the INCO718 alloy through the formation of hardening phases. As in the case of Titanium, the hardenability is highly dependent on the heat treatment that the INCO718 alloy has undergone. The optimal amount of Aluminium will be around 0.5%, according to (Keiser and Brown, 1976). Beyond the previous value there is a decrease in the Rupture Strength of the alloy.
- Carbon: Carbon shows a great tendency to react with Niobium to form NbC. The formation of Niobium carbides depletes this element to the hardening phases necessary for the γ' and γ'' precipitates, therefore, the content of C must be kept low, in the order of 0.05%. However, for a C content greater than 0.05%, the formation of Niobium carbides can help maintain the fine grain size under high temperature working conditions (again the amount of Carbon is a compromise solution).

Other elements:

- Boron: In small amounts it helps to improve the Fracture Strength value of the INCO718 alloy, with an optimal value close to 0.005% (the AMS5662M standard establishes the Boron value at a maximum of 0.006%).
- Nitrogen: This element has a tendency to form nitrides, and should be kept as low as possible. Titanium Nitrides are extremely hard (they can cause stress concentration points), in addition to generating an effect similar to Carbon in terms of depleting an element in a “useful” way in the alloy itself for the formation of hardening phases (Nitrogen "sequesters" Titanium).
- Silicon: This element is believed to brittle the solid solution matrix of the INCO718 alloy. In addition, it has been observed that this element reduces the amount of hot work that can be applied to the material and reduce the material's Rupture Strength value. It should be kept at a maximum value of 0.35% according to (SAE AMS5662M, 2009).

II.2.2.1 INCO718 Solidification and Dissolution Phase Sequence

The solidification sequence of the INCO718 alloy is described. A number of phases will be mentioned in which several of the chemical elements mentioned in the previous section will be involved. The details of each specific phase will be described later (γ, γ', γ'', δ, etc.). The solidification phases of INCO718 are well documented, and the purpose of mentioning them is to explain and clarify the morphology that is normally observed when making a detailed examination of the microstructure of the alloy.

According to (Ram et al., 2004), the solidification sequence of INCO718 is as follows:

Liquid Phase $\rightarrow \gamma \rightarrow (\gamma$ + Laves).

In detail, the process is as follows.

It begins with the solidification from a phase of primary liquid, towards a γ reaction. During the gamma reaction an enrichment of the interdendritic liquid of the alloying elements (Nb, Mo, Ti, C, etc.) is generated. Due to this enrichment, solidification takes on a eutectic morphology until is complete. A very small amount of the γ + NbC reaction is formed also on eutectic morphology (which is considered negligible).

The amount of γ + Laves eutectic is very important due to the low carbon content of the alloy. It is important to mention that there is no a single Laves phase composition, but that the compositions of the Laves phases will strongly depend on the local solidification

conditions. The variation in the composition of the Laves phases can be observed in data of (Table II.1), (Pautrat, 2013).

Table II.1: Measurement of chemical compositions of crystallographic phases of Inconel 718 (Pautrat, 2013).

	%Pds	Ni	Fe	Cr	Nb	Mo	Al	Ti	C	Si
Inconel Standard	Max	58,0	20,5	21,0	5,5	3,3	0,8	1,15	0,08	0,35
	min	46,0	16,5	17,0	4,8	2,8	0,2	0,70	0,02	0
γ	Max	58,4	25,5	22,0	9,6	4,0	1,44	1,6		0,6
	min	48,9	7,4	8,4	1,6	2,14	0,4	0,34		0,1
γ'	Max	68,8	2,2	0,86	10,4	0,40	10,8	9,40		0,35
	min		1,8	0,21	8,3	0,18	8,0	7,8		0,11
γ''	Max	70,0	2,3	1,53	25,1	1,36	5,6	8,5		0,13
	min		0,73	0,71	12,0	0,26	0,44	4,65		0,01
Laves	Max	49,5	15	15,3	29,0	10,2		1,6		4,9
	min	39,6	7,6	9,1	18,8	3,4	0,1	0,6		1,0
NbC TiC	Max	22,5	4,7	2,5	80,4	2,5	0,1	80,0		1,9
	min	1,5	0,5	0,73	12,5	0,0	0,0	5,1		0,0
delta		64,8	5,3	3,4	20,4	2,2	0,8	3,0		0,1

The heat treatment of INCO178 alloy requires a series of reheating steps. There is a temperature that is associated with the nucleation of undesirable phases, called the "incipient melting temperature (IMT)". The IMT lies in the range of 1160 to 1180 °C. In the specific case of the undesirable Laves-type phase, dissolution of the phase will be achieved at a temperature below the IMT (by back-diffusion of the solute atoms into the alloy matrix). The heat treatment is essential to achieve the homogenization of the INCO718 superalloy (Sohrabi et al., 2018), in such a way that it is possible to minimise or completely eliminate undesirable phases in the material and at the same time create the hardening phases of the alloy.

II.2.2.2 Common Phases on INCO718 Alloy

The metallurgical phases generally found in INCO718 super-alloy are as follows:

- Gamma matrix (γ): The basic matrix of the INCO718 alloy is formed by the Y phase (FCC type). The gamma phase is austenitic, with a high capacity to retain elements in solid solution (e.g. cobalt, chromium, molybdenum, etc.), when these previous elements are part of the alloy (Reed, 2007). The γ phase has the same structure as pure Nickel but with other chemical substitution elements. In the INCO718 alloy, the proportion of gamma phase is close to 98% under the

conditions obtained for the base material (“as-cast” condition). Then the γ phase ratio can drop to about 80% after heat treatment (it varies greatly depending on the heat treatment itself). The characteristic that the gamma phase is strongly alloyed results in a tendency to form dendritic growth in a columnar or equiaxial form. The dendritic growth during solidification of the alloy results in a large gradient in chemical composition within the same phase, especially of the chemical elements Nb and Mo (Pautrat, 2013). By itself in the solution annealed state, the gamma phase is relatively weak, with Yield Strength in the order of 275 to 415 MPa.

It is known that INCO718 is an alloy that obtains its strength properties after heat treatment by the formation of hardening phases and especially by the phase γ'' (Hassan and Corney, 2017; Ram et al., 2004). The main reason for the hardening of the INCO718 alloy is the precipitation of intermetallic compounds within the γ phase (matrix). The crystalline cell structure of the phase is shown in (Fig. II.3).

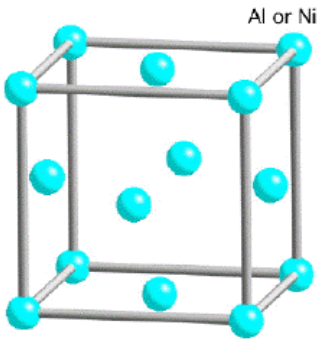

Figure II.3. Crystal structure of γ phase (Bhadeshia, 2020).

- Gamma prime phase (γ'): it is an intermetallic of the type $Ni_3(Ti, Al)$. The approximate chemical composition (in atomic percentage) is: 75% Ni, 15% Nb, 5% Ti and 5% Al. The structure of this phase is meta-stable with an FCC ($L1_2$) ordering. The structure of the γ'-phase crystalline cell is shown in (Fig. II.4).

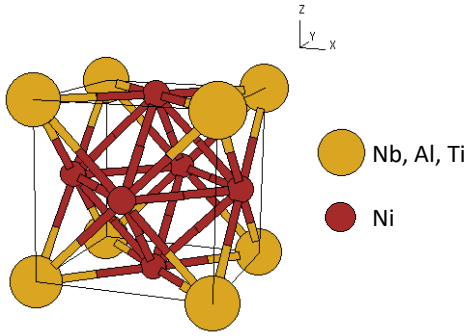

Figure II.4. Unit cell structure of gamma prime phase (Bhadeshia, 2020).

At level of microscopic observation, this phase appears as extremely small fine white dots within the γ matrix, and is coherent with the gamma matrix itself. The morphology of white dots is due to the fact that this phase tends to deposit as small spheres when is coherent with the matrix. The formation of the γ' phase begins at temperatures close to 650°C for periods of time close to one hour, with the highest speed within temperatures in the range of 732 to 760°C. It is estimated that the percentage of hardening contribution by the phase with respect to the total of INCO718 after heat treatment is in the order of 10 to 20%. The gamma prime phase plays an important role in the inhibition of "stacking fault mode of shear" (Keiser and Brown, 1976), to the point that this super-alloy is considered as not very susceptible to this failure mode still in hot deformation (Zhang et al., 2010).

- Double prime gamma phase (γ''): It is an intermetallic of the type Ni_3Nb, with a crystal structure of the kind centred on the tetragonal body, as shown in (Fig. II.5). The crystalline structure is of the DO_{22} class. The DO_{22} structure is a variation of the FCC structure, and can be described as two FCC structures stacked on top of each other.

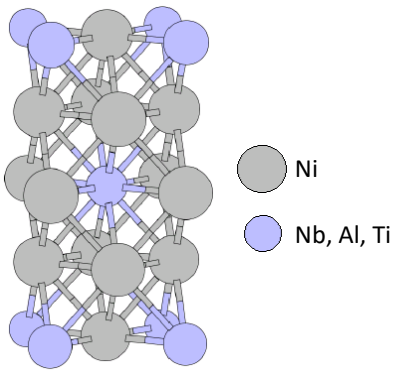

Figure II.5. Unit cell structure of gamma double prime (Bhadeshia, 2020).

At level of microstructure, the double prime gamma phase is deposited as disks with an arrangement on the planes (100) with respect to the austenitic matrix (gamma phase). At level of microscopic observation, they cannot be seen by optical microscopy, since the average size of this phase is in the order of 60 nm in diameter and with a thickness between 5 to 9 nm. The dimension of this phase is highly dependent on the heat treatment, since above 760 °C, it tends to thicken. In general, it is very stable in the temperature range between 500 and 900 °C (Sundararaman et al., 2001).

The phase is said to be metastable due to its tendency to decompose at temperatures greater than 650°C in δ phase.

- Delta phase (δ): It is produced by over-aging of the INCO718 alloy during the heat treatment from the transformation of the γ'' phase. At very high temperatures, the δ phase is generated directly from the matrix (γ phase) (Sundararaman et al., 2001). The crystalline structure of this phase is of the $D0_a$ class as shown in (Fig. II 6).

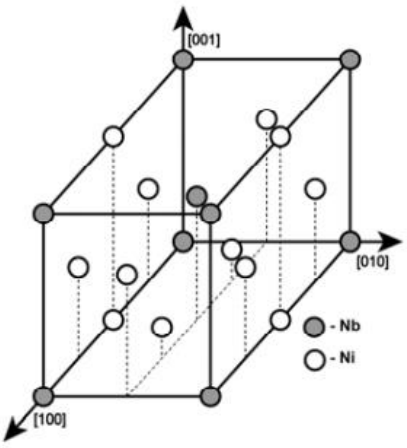

Figure II.6. The unit cell of Ni_3Nb - D0a structure of δ phase (Mahadevan et al., 2010).

The composition of delta phase according to (Keiser and Brown, 1976), has the formulation $Ni_3(Nb_{0.8}Ti_{0.2})$. The δ phase precipitates have an acicular or cuboid appearance (the latter shape is less common). The δ phase tends to germinate at the grain boundaries and has a composition very close to the double prime gamma hardening phase of the INCO718 alloy. The γ'' phase and the δ phase tend to be located in the same Niobium-rich spaces of the grain boundaries, and therefore compete for the latter element (Pautrat, 2013), however this competition apparently has no effect on the γ' phase. The δ phase is

particularly useful to control the grain size during the solidification of INCO718; however it is not consistent with the orientation of the γ matrix. According to (Sundararaman et al., 2001), the δ phase has the tendency to crystallize according to the orientations $(010)_\delta // \{111\}_\gamma$ and $[100]_\delta // <110>_\gamma$ with respect to the matrix. The delta phase nucleates at different times depending on the temperature to which the alloy is exposed. For example (Hassan and Corney, 2017) mention temperature ranges from 700 to 1020 °C (does not specify exposure time), and (Keiser and Brown, 1976) time ranges for the appearance of this phase from 15 minutes to 5 hours (at different temperatures). It is important to mention that this phase is very stable at high temperatures. At the level of mechanical properties, it does not contribute to the hardening of the alloy (because their orientation it is not consistent with the matrix). The effect of the δ phase on the behaviour of INCO 718 is mixed. On one hand it allows to control the grain size, and on the other it can reduce ductility (at room temperature). Depending on the desired material requirements, it may be necessary to avoid an excess of this phase.

- Laves phase: This phase belongs to the so-called TPC type phases (Topologically Close-Packed Phases). These intermetallic phases can be described as those in which the atoms are packed into very compact separate layers with relatively large inter-atomic distances between each layer. An example of this is shown in (Fig. II.7).

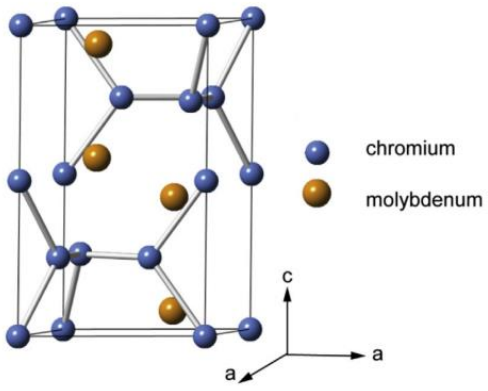

Figure II.7. C14 Laves phase crystalline structure (Krakow et al., 2017).

The phases σ and μ also belong to this group of phases (TCP). The constitution of the Laves phases is approximately 40 to 45% Ni, 25% Nb, 10% Fe, 10% Cr,

where the general composition follows the A_2B structure. The A atoms are Ni, Fe, and Cr, and the B atoms are Nb, Mo, and Ti.

Under the optical microscope the Laves phases of the INCO718 alloy appear as bright spots with a globular shape, often elongated, or as platelets in the case of long-term exposure to high temperature. The formation of Laves phases can occur during solidification or during heat treatment. During solidification, Laves phases tend to form in segregated areas of interdendritic zones at relatively low temperatures, in the range of 1149 to 1204 °C for INCO718 (Keiser and Brown, 1976).

Laves phases can be harmful for two main reasons: they “steal” elements necessary for the hardening phases (the γ' and γ'' phases), transforming the “stolen” elements into a less useful phase, and they can also act as crack initiators due to their brittle nature (Reed, 2007).

In general, it is desired to minimize the appearance of Laves phases. One way is to promote the formation of NbC, which limits the segregation of Nb in interdendritic spaces (Pautrat, 2013). Another way is by hot working at temperatures above 1093 °C (Keiser and Brown, 1976). Sometimes, homogenizing heat treatments are not capable of eliminating intermetallics, even applied over long periods of time.

According to (Pautrat, 2013), the amount of intermetallic Laves phase is determined by the solidification conditions, the cooling rate, the thermal gradient, and therefore the texture generated (columnar or equiaxial). The effect of Laves phases on mechanical properties is mainly a function of the distribution within the alloy matrix. For an equal fraction of Laves phases in a certain volume of alloy, it is much more advantageous to spread it finely within the interdendritic spaces, like a tissue. The worst case is continuous chains formed at the grain edges (sites prone to cracking).

The relationship between the δ phases, the Laves phases and the Y matrix is like a kind of sequential growth. Laves phases are generally surrounded by a series of δ phases. The germ of the δ phases will be a Laves phase. For a given Laves phase (which would serve as the nucleus), all δ-phases starting from it will have the same crystallographic orientation (both phases have the same origin). The germ of the Laves phase requires a large enough interdendritic space to

cause chemical segregation in the alloy; therefore, the Cooling Rate will determine the distribution of the Laves phase. The higher the cooling rate (V), the smaller the grain size and the less space there will be for the Laves phase and δ -phase nucleus to form, or at least both components will be reduced in size (Pautrat, 2013).

- Phases NbC and TiN : According to (Keiser and Brown, 1976), these phases do not have much effect on the in the mechanical properties behaviour on the INCO718 alloy, due to the low amount of them that are formed during solidification, but it will depend a lot on their distribution. For example (ASM Handbook, 1985) indicates that the function of carbides is beneficial if they are distributed at the grain boundaries in the form of a discontinuous chain. Another effect is to provide constitutional stability to the alloy during its service; however, if there is an excessive formation of carbides, these can degrade the content of C and reduce the resistance to creep, as well as the ductility in Nickel-based alloys. There are many different types of carbides: MC , $M_{23}C$, M_6C and M_7C_3, where M represents one or more metallic elements. The most commonly observed carbides in INCO718 are of the NbC kind, with an appearance under the optical microscope as a grey phase, roughly angular in shape. Compared to other phases, carbides are relatively large. They are very stable at high temperatures, but not as stable as TiN .
- Titanium Nitrides (TiN) are observed under the optical microscope as particles with an angular appearance, pink colour. They are the first intermetallic to form during the solidification of the INCO718 alloy; even before the γ matrix (TiN are stable at temperatures close to 1400 °C). In the case of the Laser Cladding process, it is important to mention that the amount of TiN will be a function of the amount of Nitrogen dissolved in the medium where the alloy solidifies. In the centre of the TiN -particles, it is common to find Al_2O_3-type oxide particles. Titanium Nitrides are generally considered to have little effect on the mechanical properties of the INCO718 superalloy, but consume Titanium which will not participate in the formation of the γ' hardening phase. In addition to previous information, the TiN particles tend to act as the germ of carbide formation (Pautrat, 2013).
- NbC particles have a tendency to “steal” Nb from the hardening phases, and therefore can lead to a reduction in the strength of the material.

Those NbC that can be observed in the raw INCO718 alloy (before any heat treatment), tend to dissolve during annealing at temperatures above 1038 °C. When the aging heat treatment is applied (between 704 and 982 °C), they tend to precipitate at the grain boundaries.

II.2.2.3 Effect on Mechanical Properties due to the Presence of Laves and δ Phases

Homogenization is important to eliminate (or at least significantly reduce), the amount of undesirable phases. During the reheating of INCO718 alloy, it has previously been mentioned that there is a temperature value known as incipient melting temperature (IMT), in the range of 1160 to 1180 °C (Sohrabi et al., 2018). The IMT temperature allows the back-diffusion of solute in the regions of the INCO718 alloy that are over-saturated (solute atoms), towards the matrix (γ), without a local melting of the alloy. The homogenization process is especially useful to eliminate the vast majority of Laves phases. As will be shown later, it is not always possible to eliminate the entire Laves phase, and therefore it is necessary to study its effect on the mechanical properties of the INCO718 alloy.

In (Schirra et al., 1991), Laves phases are reported to have a detrimental effect on mechanical properties. The mechanical properties that are affected according to this author are UTS and Ductility (reduction on both values), for the INCO718 alloy at room temperature. At higher temperatures, a reduction in ductility is also reported. The lack of ductility results in a decrease in the Fatigue Strength value for low cycle fatigue (LCF) rare, due to an increase in the rate of growth of cracks within the material. With respect to the welds, a reduction in Ductility and Toughness (energy accumulation in the elastic range of the material) is also reported. It is reported that the decrease of ductility in the material is mainly due to the brittleness of the Laves phases. Additionally, the Laves phases consume Nb in such a way that it will not be available for the formation of the useful hardening phases (γ' and γ'' phases). An important detail that is reported is that most of the decrease in mechanical properties is attributed to the formation of long continuous chains of Laves phases at the grain boundaries (Pautrat, 2013), which are even capable of forming segregated rich layers of this undesirable phase (Schirra et al., 1991). For a material produced by casting, the appearance of the Laves phases will be like that of globular particles, as mentioned above.

The δ phase influences the mechanical properties of INCO718, especially when the forged material. According to (Pautrat, 2013), the δ phase mainly influences the grain size and the mobility of the dislocations. The effect of the δ phase on the mechanical properties will not be taken into account for this study, since it was been observed that it was completely eliminated by the heat treatment (standard), for a material deposited by the Laser Cladding process (Fig. II.29).

II.2.2.3.1 Nucleation of the δ phase in the Laser Cladding Additive Manufacturing Process

According to the CCT diagrams for INCO718 from (Garcia et al., 1992; Zhao et al., 2020), such as the one shown in (Fig. II.8), the formation of the δ phase requires cooling rates less than approximately 15 K/s. The value of 15 K/s was established in the case of the work of (Zhao et al., 2020), as a critical value above which δ phase nucleation should not occur even in the case of additive manufacturing processes for the superalloy INCO718.

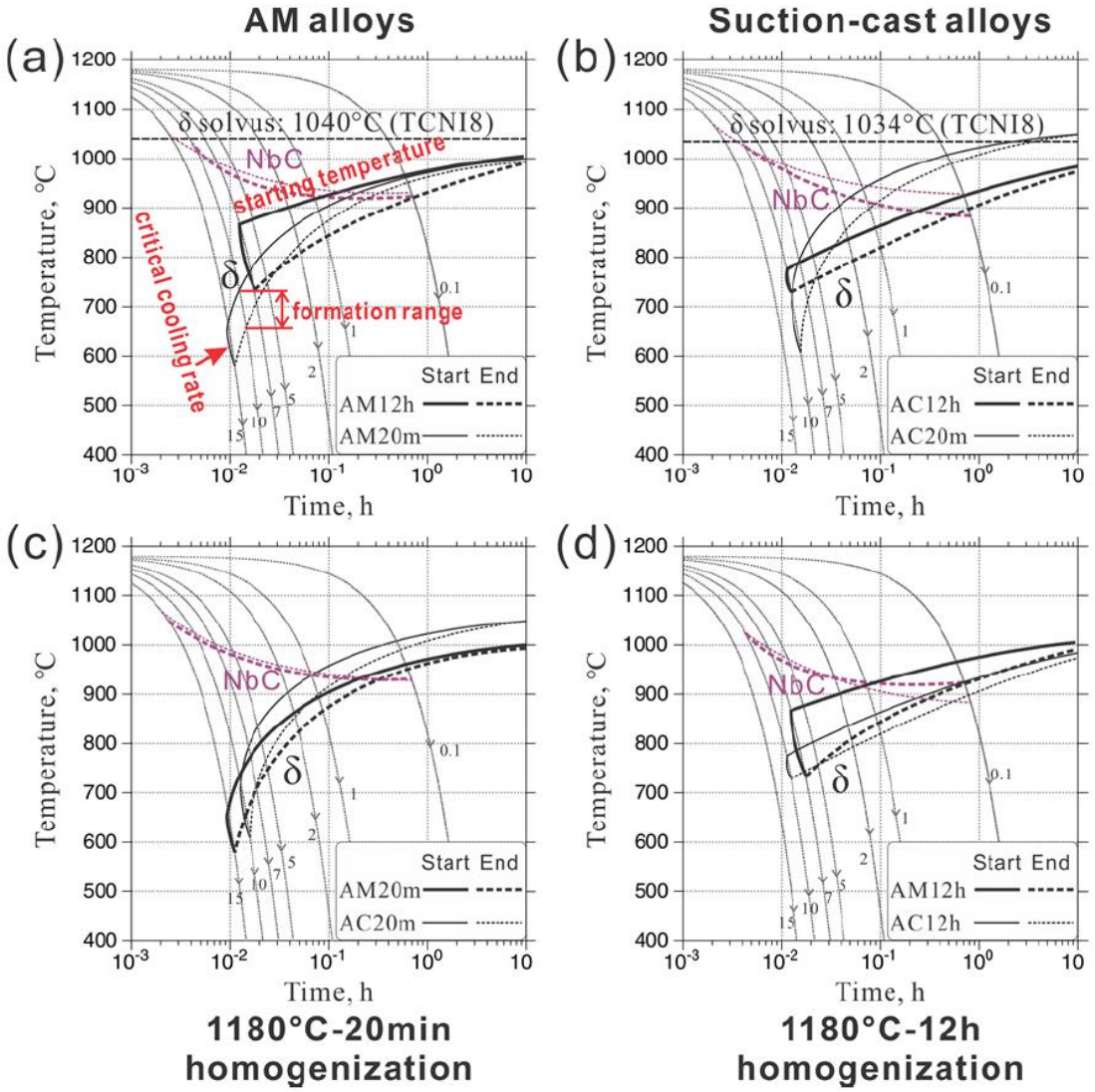

Figure II.8. CCT diagrams of Inconel 718 alloys measured in the work of (Zhao et al., 2020).

However (Fig. II.24) clearly shows the delta phase formation within the matrix material, despite the fact that the cooling rates in the Laser Cladding process are much higher than the critical value of 15 K/s mentioned above, see (Chapter III.3.5).

The explanation for this behaviour is given by the overheating that is generated due to the consecutive crosses of the laser beam typical of the Laser Cladding process, as described by (Ding et al., 2015), where it is reported that, during the deposition of material, sufficient temperature can be reached to activate the germination of the delta phase from the Laves phases (phenomenon observed in (Fig. II.25)). High temperatures are required to generate delta phase from the gamma phase directly (Sundararaman et al., 2001), which seems to be the case in our investigation.

Another phenomenon that requires explanation is the segregation of the δ phase within the gamma matrix of the alloy (intragranular segregation), since it has been mentioned previously that the delta phase is prone to germinate at the grain edges of the material (Keiser and Brown, 1976).

The explanation that has been found for the intragranular segregation of the δ phase within the matrix is a combination of phenomena as described below:

- The origin of the phases of intragranular Laves (which are the germ of the δ phases in our case), is the overheating by the successive crosses of the laser beam. It is proposed that these passes of the laser beam (in the layer immediately below which is deposited) are equivalent to a homogenization of the material at high temperature for long periods of time, which allows the supersaturation of Niobium in the matrix (Garcia et al., 1992), and the disappearance of supersaturation at the grain boundaries. If the cooling rates are too high, the formation of the δ phases will be suppressed.
- The passes of the laser beam in the innermost layers of the material will be sufficient to increase the temperature to the point where the cooling rates will be lower than the critical values for the formation of the Laves phases and the delta phase according to (Fig. II.8).
- Therefore, the formation of Laves phases and delta phases will be a sequential process depending on the successive passes of the laser beam, where: first the concentration of Nb will be diluted due to over-saturation at the high temperatures of the process and the high cooling rate (in the upper layers of the cladding), and then the germination of the secondary phases (Laves and δ) will result from the segregation according to the CCT diagram of INCO718 due to the lower “cooling rates” for the innermost layers of the material.

II.2.2.3.2 Review on the Decrease in Mechanical Properties Values due to the Distribution of Laves Phase within the INCO718 Alloy Matrix

The effect of the Laves phase on the mechanical properties is a function of how it is distributed within the INCO718 matrix alloy itself.

According to (Schirra et al., 1991), the decrease in Ductility values (at room temperature and elevated temperature), Ultimate Tensile Strength, as well as Impact Toughness are mainly the effect of the presence of Laves phases at the grain boundaries. The variation in the decrease of mechanical properties due to the presence of Laves phases seems to

be mainly dependent of: the alloy texture (average grain size in the case of a wrought material), and the composition in the case of a cast material.

When the amount of Laves phase deposited in the interdendritic matrix is considerable (i.e. not at the grain boundary), a reduction in the mechanical properties of the INCO718 alloy has been reported (Manikandan et al., 2015).

II.2.2.3.3 Laves Phases Formation in Additive Manufacturing Processes

Little information is available regarding the formation of Laves phases in additive manufacturing processes.

For the Laser Cladding process (Xiao et al., 2017) report that the formation of Laves phase can be substantially reduced by varying the laser's working mode (CW continuous mode, or QCW quasi-continuous mode). The quasi-continuous mode has an average energy of half that of the continuous mode. It is reported that the amount of Laves phases that formed in the material after the additive manufacturing process and heat treatment was lower when the energy density in the manufacture of the INCO 718 alloy was also low. In the article by (Xiao et al., 2017), no mention is made on the variation of the effect in the amount of Laves phase on the mechanical properties. The texture of the Laves phases generated for each type of working mode (CW and QCW) is shown in (Fig. II.9).

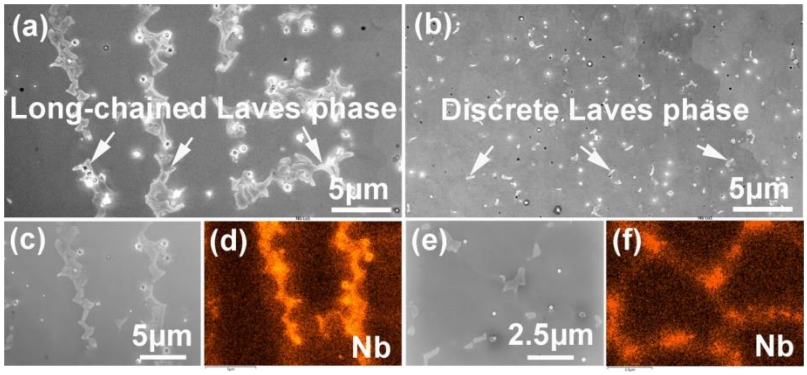

Figure II.9. SEM images showing the morphologies of Laves phase particles and Nb element distributions in the interdendritic regions: (a, c and d) CW sample and (b, e and f) QCW sample (Xiao et al., 2017).

As a reference image to the appearance of a typical microstructure of INCO718 alloy before and after standard heat treatment, a series of microphotographs of a material that was manufactured by a "traditional" process are shown, (Fig. II.10). A "traditional" process, as used in the research by (Ling et al., 2020), consists of melting INCO718 ingots under very controlled conditions, and then applying different heat treatments to

them. The morphology of the INCO718 alloy is shown for the case before and after standard heat treatment by means of optical photography. The (Fig. II.11) shows the morphology of a material manufactured in a traditional way (after standard heat treatment), but through an image obtained by scanning electron microscope (SEM).

Later in this research, a comparison will be made between morphologies in the microstructure generated by traditional manufacturing process (Fig. II.10) and by the Laser Cladding process (Fig. II.23) for the alloy INCO718. In the comparison to be made below, the differences in morphology that the two processes produce in the manufacture of IN718 alloy will be sought.

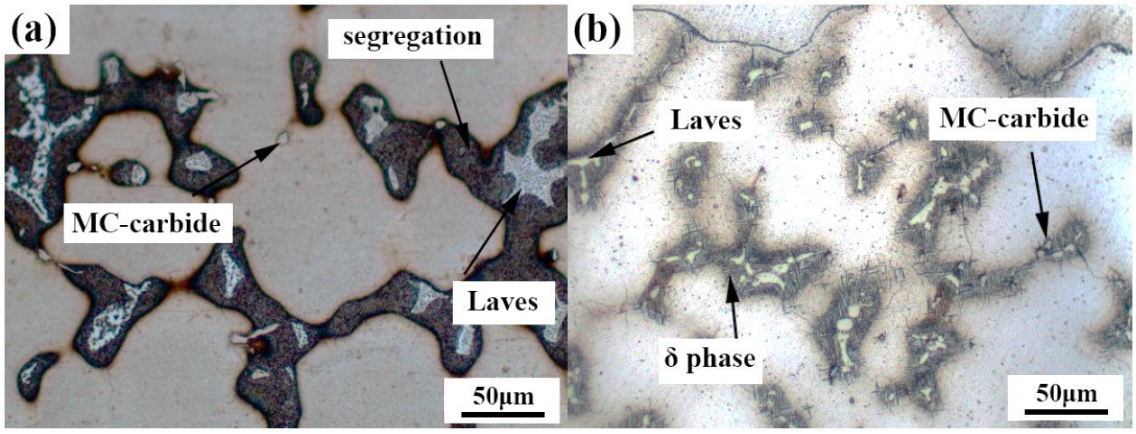

Figure II.10. The optical microstructures of the Inconel 718 superalloy after different heat treatments: (a) the cast case; (b) standard heat treatment (SHT), (Ling et al., 2020).

The use of the SEM technique allows observing in more detail the secondary phases that have been generated during the fabrication of the alloy mentioned above.

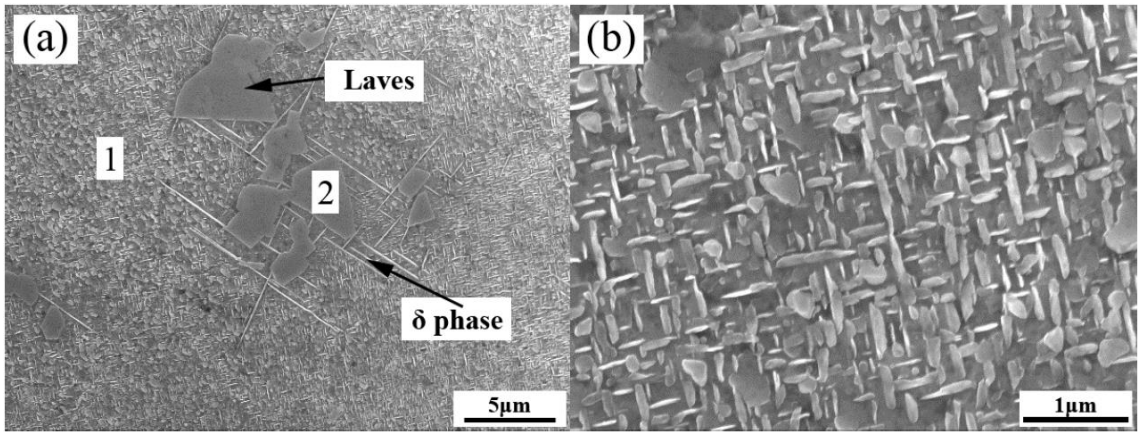

Figure II.11. SEM images of the Inconel 718 superalloy after different heat treatments: (a, b); standard heat treatment (SHT), (Ling et al., 2020).

The resulting microstructure shown (Fig. II.9) is significantly different from that of the INCO718 super-alloy manufactured in a "traditional" way, as shown in (Fig. II.10), in both

cases with standard heat treated material. In the case of a material manufactured in "traditional" way (Fig. II.10), it has not been possible to completely eliminate the δ phase (the phase with appearance in the shape of needles). The dilution of the δ phase was possible for INCO718 manufactured by means of additive manufacturing, as in the case of (Xiao et al., 2017), thus in (Fig. II.9) only the γ matrix and some possible nitrides and carbides are observed. The only well-defined secondary phases in the previous mentioned figure are some discrete Laves phases.

It is necessary to clarify that in the research of (Xiao et al., 2017), only SEM images of the microstructure after heat treatment are available, but not before heat treatment (therefore, it is difficult to compare the change in the secondary phases). Again, in the investigation of (Xiao et al., 2017), optical micrographs of the alloy in the state "as-cast" were presented. The microstructure generated depending on the amount of energy used during the manufacturing process (Fig. II.12). The optical micrographs in (Fig. II.12) do not allow observing the secondary phases that were formed, only the texture of the material itself.

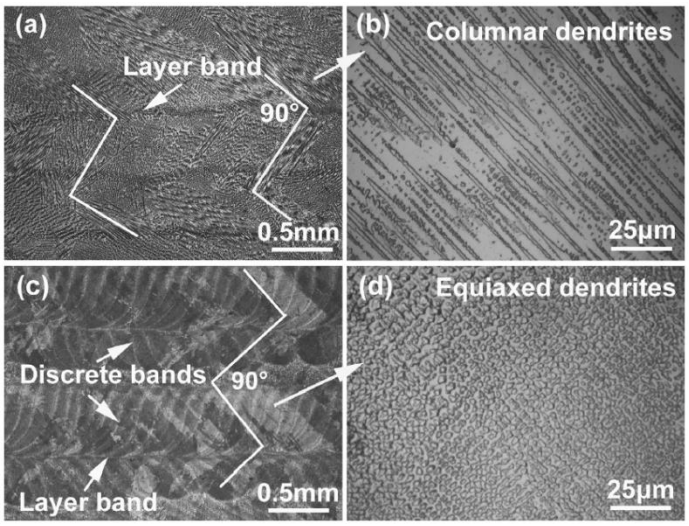

Figure II.12. Optical micrographs of the as-deposited Inconel 718 samples produced under two different laser modes: (a and b) CW sample and (c and d) QCW sample, (Xiao et al., 2017).

In the research of (Ding et al., 2015), emphasis is placed on the microstructure generated by the DLD additive manufacturing process (direct laser deposition). Not all the experimental conditions used in the manufacturing of the samples were specified, so it is difficult to compare results with the other works in this review regarding the formation of Laves phase. It was reported that two material deposition conditions were used, one with high power laser beam (low cooling rate) and other with low power (fast

cooling rate), corresponding to 550W and 350W respectively. The main objective of the research of (Ding et al., 2015), was to identify the main secondary phases in the deposited material. Regarding mechanical properties, the presence of a low amount of the $\gamma / Laves$ constituent at the grain boundary is mentioned as a possible cause of the degradation of mechanical properties (although it is not confirmed by any experimental test). It was also reported that the amount of secondary phases observed was not affected by the different cooling rates used to manufacture the material through the DLD process. The appearance of δ phases from the Laves phases was reported, possibly due to the repeated heating-cooling cycles typical of the additive manufacturing process of Laser Cladding.

On the other hand (Seow et al., 2019) used the WAAM (Wire + Arc Additive Manufacturing) process as an additive manufacturing method with INCO718 alloy. The results of the research by Seow et al. shown how a heat treatment different from the standard (Special Metals, 2007), is capable of profoundly modifying the dissolution of undesirable phases that were formed in the as-cast material (in this case Laves phases). The manufacturing method on this research is different from the Laser Cladding process, which may result in a different morphology of the deposited material. The usefulness of this research is that tests were carried out to evaluate the mechanical properties based on specimens obtained from the deposited material (INCO718), taking into account the effect of the Laves phases. From the data obtained in the unidirectional tensile tests on this research, it is concluded that a standard heat treatment (without homogenisation) was not capable of diluting the Laves phases in a material manufactured by additive manufacturing, at least for the WAAM process. It is reported that the use of a standard heat treatment with homogenization dissolves the Laves phases, but at the same time generates the precipitation of the δ phase at the grain boundaries (the Ductility obtained from experimental tests in the last case was the lowest of all samples subjected to heat treatment). Based on the results of this investigation tests, it was possible to conclude that the most damaging undesirable secondary phase in terms of ductility is the appearance of the acicular delta phase at the grain boundaries, and to a lesser effect the Laves phases.

II.2.3 Recyclability of Metal Powder for the Laser Cladding Process

One of the main drawbacks of the Laser Cladding process is the trapped powder efficiency. The powder needs to be injected into the melt pool, but high ratio of the

particles hits against unmelted area and directly bounces off the area for deposition of material. The efficiency ratio of trapped particles can drop 40% depending on the configuration of the nozzle and the laser spot size (Arrizubieta et al., 2014). Therefore, a relatively high amount of waste metallic particles is generated. A large part of these particles is not damaged and can be reused. On the other hand, a certain amount of the particles is affected by heat and may: (I) partially oxidise, (II) partially melt and/or (III) undergo variations of their chemical composition.

Many research in Laser Cladding has been mainly focused on process parameters, as overlap proportion (Cao et al., 2013; Kamara et al., 2014; Liu and Qi, 2014), laser power and/or feed rate (Tabernero et al., 2011) or metallurgical properties of the AM manufactured components (Lambarri et al., 2013). Few studies have been conducted to evaluate how the recycling of metal particles after the high power laser manufacturing process affects the properties and mechanical behaviour of the components. Considering the specific characteristics that the metal powder used in the LMD process must possess (such as spherical shape or flat grain surface), the cost of high quality powder is higher than other raw material geometries such as wire or foil, and it is therefore important to make efficient use of metallic powder raw material..

In the last years, researchers were interested by powder recyclability in Selective Laser Melting (SLM) (Strondl et al., 2015) and Electron Beam Melting (EBM) (Nandwana et al., 2016; Niñerola and Petrovic, 2015). The powder outside the melting area for the previous mentioned process can be recycled. The recycling contributes to economic viability and sustainability of these technologies. In each case, the powder characteristics and chemical composition are critical parameters to ensure repeatable process and suitable mechanical properties of metal components built. To ensure reliable and repeatable fabrication, the controls of powder stock properties as well as the variation in chemical composition limits are necessary. It is also important to understand how high power and high temperature during AM processes affect the characteristics of recycled powder.

Strondl et al. (Strondl et al., 2015) have reported that in the case of IN718 recycled powder that was screened and mixed with 5% new powder for the SLM process, resulted in: (I) no change in particle morphology or composition but the disappearance of smaller particles, (II) some oxygen uptake which may explain a slight increase in porosity in the fabricated part, (III) no change in the generated microstructure, Yield and Ultimate Tensile Strength and (IV) decrease in ductility and impact toughness probably associated with oxygen uptake.

Niñerola et al. (Niñerola and Petrovic, 2015) used only sieved Ti6Al4V powder for manufacturing by EBM process, and concluded after test that: (I) there is no change in powder composition, (II) a large oxygen absorption but hydrogen decreasing (III) no change in general morphology apart from occasional aggregates and (IV) a maximum of 12 cycles for reusing the powder as an optimal.

Nandwana et al. (Nandwana et al., 2016) for a powder bed process demonstrated that IN718 powders can withstand a large number of reuse cycles with no change in the chemical composition of the same. There are no significant changes in the flowability, morphology and size distributions of IN718 powders with the number of part build cycles. The initial powder chemistry and the alloying system under consideration are the key factors governing recyclability in powder bed systems, with oxygen uptake being the limiting factor.

Ardila et al. (Ardila et al., 2014) created a simple methodology based on sieving and drying of the IN718 powder for SLM process, and pointed out: (I) material use efficiency larger than 95%, (II) stable and sound properties obtained in all test samples irrespective of the iteration number. The IN718 powder morphology does not significantly change during its reuse: most of the particles remained spherical and particle size distribution after several production cycles was similar, with the exception of a small amount of particle aggregates that were detected with sizes between 50 and 100 μm. Alloy composition remained also unchanged.

LPW Technology (LPW TECHNOLOGY LTD, 2016) analysed the IN718 powder degradation during the SLM process. The wasted powder is sieved to remove coarse particles generated during the melting process and dried. After 25 builds, there was a significant increase in UTS, reduction in ductility from 20% to 13% and a little increase in oxygen with each reuse.

Carroll el al. (Carroll et al., 2006) presented a methodology to reuse Waspaloy^{tm} powder. The recycling methodology was similar to the above mentioned process, with filtering and drying of the wasted particles. Recycling the powder up to 10 times produces only minor changes in the composition, morphology, surface texture of the powder and in its size distribution.

Slotwinski et al. (Slotwinski et al., 2014) showed how virgin powder morphology changes after being exposed and recycled to one or more cycles of additive manufacturing process by Direct Metal Laser Sintering (DMLS), in the case of CoCr and 17-4 SS alloys.

The authors reported that recycling the raw material increases the size distribution of the powder with progressive builds-up. In the analysis of stainless steel powder from the residues of a sieve, melting and binding of metal powder particles was reported.

Rao et al (Rao et al., 2006) studied the behaviour of INCO718 powders with varied oxygen levels of 275, 180 and 140 ppm, and parts consolidated by hot isostatic pressing (HIP). Tensile test properties of the HIP parts + heat treated alloys have shown that Yield Strength (YS), Ultimate Tensile Strength (UTS) do not get influenced by the oxygen content, but the ductility was found to be deteriorated drastically with increasing the oxygen content within the alloy.

Powder reuse is a hot topic for SLM based processes since powder cost is significantly higher and the amount of wasted powder is also much higher than in the LMD process. Furthermore, the metallic powder is a hazardous and difficult to treat waste. It is also important to consider the typical powder size in LMD process ranges from 45 to 150 microns, and their associated health and safety issues (Benson, 2012).

II.3 Objectives for this Chapter

- Evaluate the recyclability of IN718 metal powder for the Laser Cladding process, since no data are available for this additive manufacturing process. The metallic powders were reused up to four times and corresponding builds were manufactured.
- Evaluation by means of metallurgical and mechanical tests on the evolution of the mechanical properties of the material added by the Laser Cladding process, and of the evolution of the texture of the material with the number of reuses.
- To characterise in depth the microstructure produced by the Laser Cladding process, and to investigate the effect of the secondary phases on the mechanical properties.

II.4 Materials and methodology

II 4.1 Materials

The material used was the nickel base alloy Inconel 718 in the form of metallic powder. An INCO718 build has been clad on a substrate material made of DIN C45E steel. The

final dimensions of the sample were 18 x 15 x 107 mm. The INCO718 metal powder used were an atomized alloy from Oerlikon Metco Company (Metcoclad 718 powder) with spherical shape and a particle size ranging from 45 to 106 microns. The chemical composition of the material is given in (Table II.2).

Table II.2: Chemical composition of Metcoclad™ 718 powder.

Element	Al	C	Co	Cr	Cu	Fe	Mn	Mo
Wt%	0.46	0.02	0.02	18.72	0.01	18.18	0.04	2.99
Range	0.20-0.80	0.08 max.	1.00 max.	17.00-21.00	0.30 max	Balance	0.35 max.	2.80-3.30
Element	Nb	Nb+Ta	Ni	P	S	Si	Ta	Ti
Wt%	4.96	4.97	53.6	<0.01	<0.01	0.04	0.01	0.80
Range		4.75-5.50	50.00-55.00	0.015 max.	0.015 max.	0.35 max.		0.65-1.15

The composition of this metallic powder is in the same range as the specifications for Inconel 718 alloy (SAE AMS5662M, 2009).

II.4.2 Equipment and Process Parameters

The processing for the different test-builds has been carried out with the following setup: a cladding cell Aktinos 500 with CNC control equipped with a coaxial LMD nozzle developed by the UPV/EHU University in previous works. A multi-mode Rofin FL 010 diode laser has been incorporated to the nozzle as well as an argon gas flux regulator system for protective and powder driving functions. The particles are stored in a hopper where the temperature can be adjusted to remove moisture (60°C). They are injected into the coaxial LMD nozzle, with its mass flow being controlled. In order to collect the wasted powder in a proper way, the laser machine has been equipped with a metallic tray located at the bottom of the substrate surrounded completely to avoid cross contamination. The values of the parameters used for the manufacturing of the samples (powder feed, scanning speed, laser power, spot diameter, offset and overlapping), has been taken from (Chapter I.5). The parameters have been kept the same during the building up of the clad builds (Table II.3).

Table II.3. Laser parameters used.

Power (W)	Scanning speed (mm/s)	Powder feed (gr./min)	Spot diameter (mm)	Overlap by track (%)	Offset by layer (%)
571	8.75	8.78	1	26	25

II.4.3 Recycling Procedure and Manufacturing of Test Samples

Visual inspections of the used powder showed the formation of new phases with magnetic properties in a very low fraction. This characteristic has been used to segregate them from the non-deposited and non-reacted metal powder. The production of the test samples and the recycling procedure of the non-deposited powder have been carried out following the scheme of (Fig. II.13).

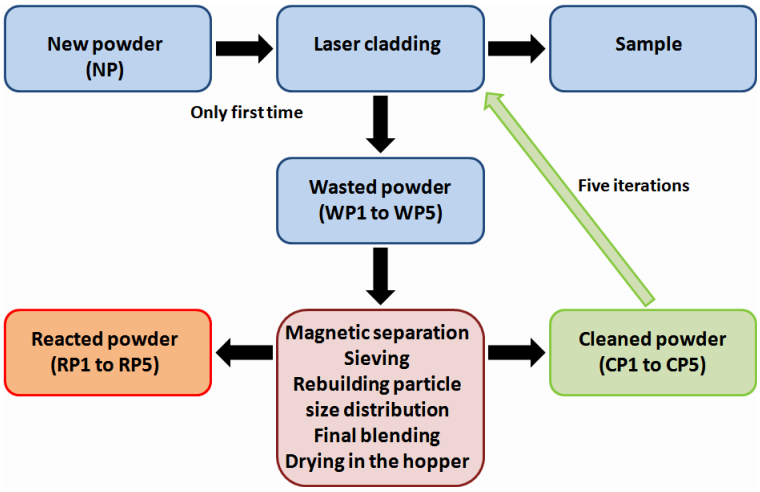

Figure II.13. Scheme of the recycling process.

Once the first test sample has been built with new metal powder, the wasted powder is collected from the tray and an EDX analysis is subsequently carried out. The wasted powder recycling has been done following this procedure.

1. The wasted powder slides first on an inclined magnetic tray (activated electromagnetically or by permanent magnets) which can be vibrated to facilitate the flowing of the particles. The unwanted phases are removed by adhering to the magnetic tray as the rest of the material slides into the sieve. The magnetic tray is cleaned regularly. The separation process can be repeated several times until no particles stick to the magnetic tray.
2. Once the magnetic fraction is removed, the cleaned fraction is sieved in order to check particle size distribution. When the particle size has been measured, all the clean fractions are blended again, trying to respect the Gaussian distribution curve of the initial particle sizes. The sizes of different sieves used meet those of the initial grain size of the new powder, namely: less than 53 µm, 53-63 µm, 63-71 µm, 71-90 µm, 90-105 µm, 105-150 µm and more than 150 µm. During the final blending of the

clean powder of the i-th iteration, we tried to always maintain the same proportion of each different size classes.

3. The cleaned powder was reintroduced in the hopper of the feeder system for manufacturing a new build. New powder is not added and all the used material comes from the recycled powder obtained following the procedure. Drying of the cleaned powder is achieved directly in the hopper.

This procedure has been repeated five times. At the end of each loop, five metallic builds designed to prepare samples for mechanical properties and microstructure observations are obtained. The build is cut from its substrate and heat treated as follows: precipitation hardening, 720°C during 8 hours and 620°C for 18 hours (Fig. II.31).

The tensile samples were then machined by wire EDM. The (Fig. II.14) shows one of the builds built in each recycling loop, as well as the test parts which have been obtained.

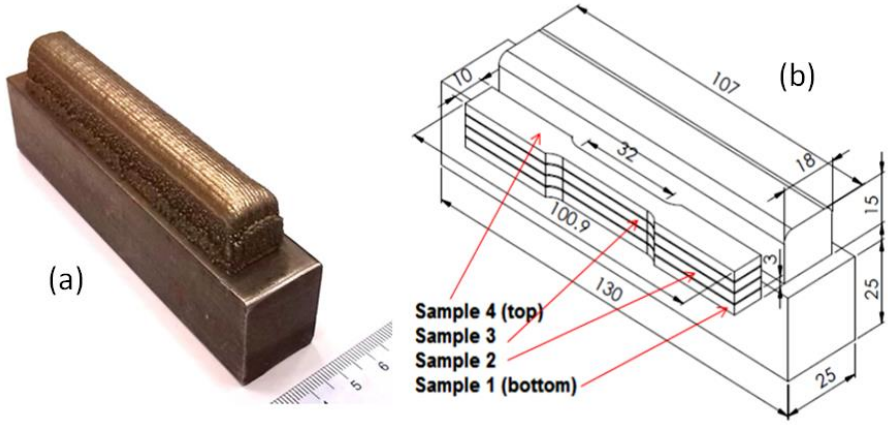

Figure II.14. a) Geometry of the clad part obtained on its steel support; b) Test part design and position of the samples within the clad part (dimensions on mm).

II.5 Results and Discussion

II.5.1 Chemical Analysis

The wasted powder was analysed by Energy-Dispersive X-ray Spectroscopy (EDX) in order to define the composition of the powder and X-rays Diffraction (XRD) for crystal information and structure using a Jeol JSM-6400 SEM equipment. Spectra obtained from the wasted powder (XRD and EDX) and analysed by PANalytical Xpert PRO, point out the presence of the base alloy INCO718 and a scarce amount of other phases.

There is no difference in the spectra of the NP new powder and those of CP1 and CP5 cleaned powders (Fig. II.15). The crystal structure is then the same whatever the number of uses.

Once magnetic segregation has been done, the spectra obtained from the reacted powder (RP1 to RP5) show the presence of other compounds than the base alloy (Fig. II.15). Moreover, it has been seen by XDR that magnetic fraction removed also contains a small amount of IN718 alloy powder (non-magnetic), surely trapped and pushed by the magnetic phase particles in the segregation process.

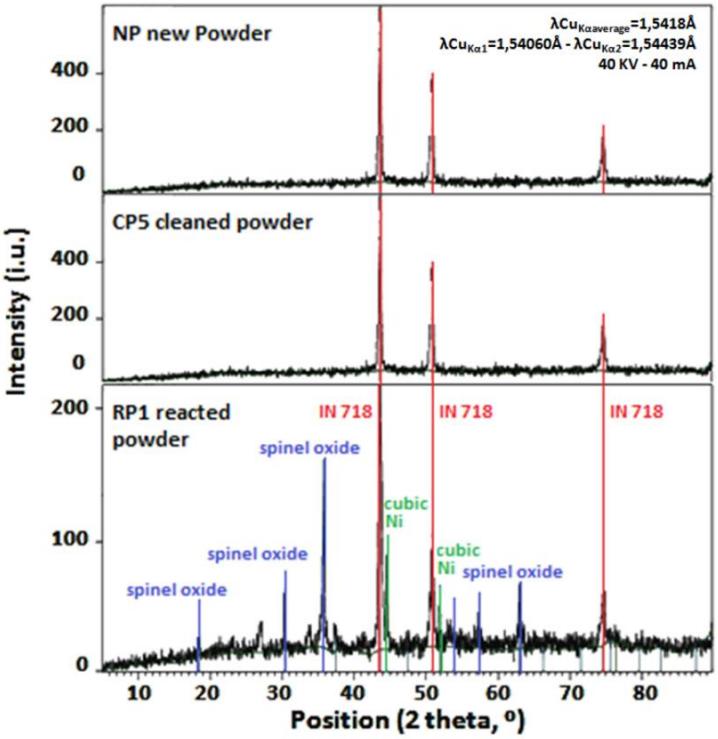

Figure II.15. Diffractogram of IN718 powder: NP new powder (top), CP5 cleaned powder (middle) and RP1 reacted powder (bottom).

These phases have been characterized by XRD and they have been identified as IN718 alloy, Ni cubic phase element and spinel type ferrous oxides (hexoctahedral phase such as $NiFe^{3+}{}_2O_4$ similar to Trevorite). Since all the undesirable detected phases present magnetic properties; this characteristic has been very useful to segregate them from the non-deposited and non-reacted metal powder. The ratio of undesirable phases has been estimated to be less than 2% by weighting the different fractions.

Oxygen content of the cleaned powder has been measured using a LECO ON736 Oxygen/Nitrogen Elemental Analyser (Fig. II.16a). Although the oxygen content remains quite low, it increases linearly with the number of reuses. This can be explained by a mild

oxidation of the particles outside the trapped zone but subjected to the high temperatures of the laser irradiation (particles located near to the thermal affecting zone but bouncing out of it) where the protective gas injected through the clad nozzle is not sufficiently effective. Some authors (LPW TECHNOLOGY LTD, 2016; Nandwana et al., 2016) have also pointed out that recycling increases the oxygen content of the powder with progressive builds (EBM or DMLS).

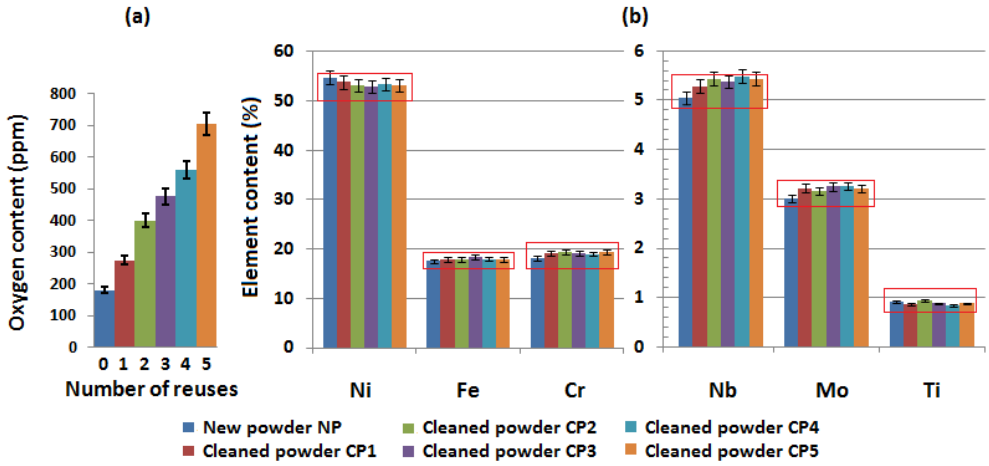

Figure II.16. (a) Oxygen content of the NP new powder and CP1 to CP5 cleaned powders after the different recycles; (b) Chemical composition of the NP new powder and CP1 to CP5 clean powders. In red, the compositional requirements range of IN718 (SAE AMS5662M, 2009).

The chemical composition of cleaned powders has been analysed after each iteration (Fig. II.16b). The variations in chemical composition agree with the extraction of the magnetic phases: nickel and iron percentages slightly decrease (as they are the main components of extracted magnetic phases) and the rest of elements increases, but without changing the chemical composition of the powder significantly. The (Fig. II.16b) shows also the ranges (marked with red rectangles) that comply with compositional requirements of IN718 standards (SAE AMS5662M, 2009). All the elements measured have a satisfactory proportion for the 5 iterations realized. Nevertheless, Niobium content increases in each loop and therefore it may be concluded that this element could define the limit of the recyclability in terms of chemical composition. The research of (Ardila et al., 2014) have pointed out a similar evolution of Nb in their recycled powders for SLM.

II.5.2 Powder Grain Size and Morphology

Powder grain size has been measured by sieving the powders at different steps, from new material or zero use up to the fifth use in the cladding process and also by image

analysis of SEM pictures of the different new and recycled powders. The (Fig. II.17) shows the distribution curve of the grain size for CP3, CP5 and NP powders. The change in particles size is effective after the first use. It seems that a near steady-state in mean grain size and standard deviation values exist.

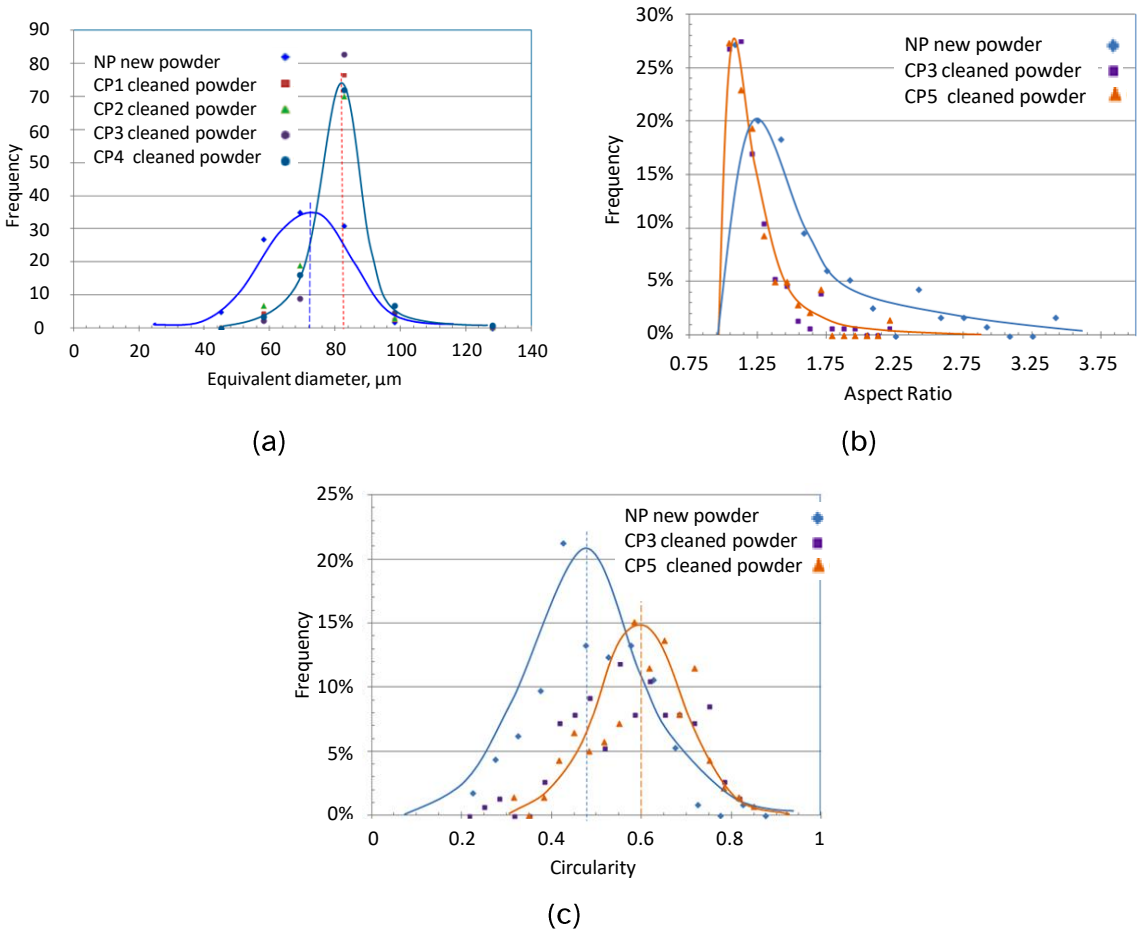

Figure II.17. Distribution curve of grain size (a), circularity (b) and aspect ratio (c) distribution of the NP new powder, CP3 and CP5 cleaned powders obtained after each iteration.

This mean size of the powder grains increases from 72 µm for the new powder to 83 µm for the cleaned powders when the standard deviation decreases from 15.5 µm to 12 µm. The recycled particles are a bit larger and more centred around their mean value than the new particles. The cleaned particles present a more homogenous size distribution than the new particles. This effect has been also reported by several authors (Ardila et al., 2014; Nandwana et al., 2016; Slotwinski et al., 2014; Strondl et al., 2015) in the case of EBM, SLM, LDMD or DMLS.

SEM observations and their posterior image analysis have pointed out an evolution in the morphology of the cleaned particles with a variation of circularity (Fig. II.17b) from

0.48 to 0.60 and of aspect ratio (Fig. II.17c) from 1.51 to 1.21, respectively for the new particles and for the clean powders. This means that after recycling the remaining particles are more spherical than the new ones (circularity and aspect ratio reaching the value 1). Backscattered SEM images (Fig. II.18) showed at the surface of the particles, dark zones mainly associated to a mild oxidation of the particles surface (Fig. II.18 b-d). The SEM analysis of the reacted particles (Fig. II.18 b-f) pointed out the presence of melted or partially melted particles with an acorn-shape made of spinel oxide cubic phase (similar to Trevorite $NiFe^{3+}{}_2O_4$).

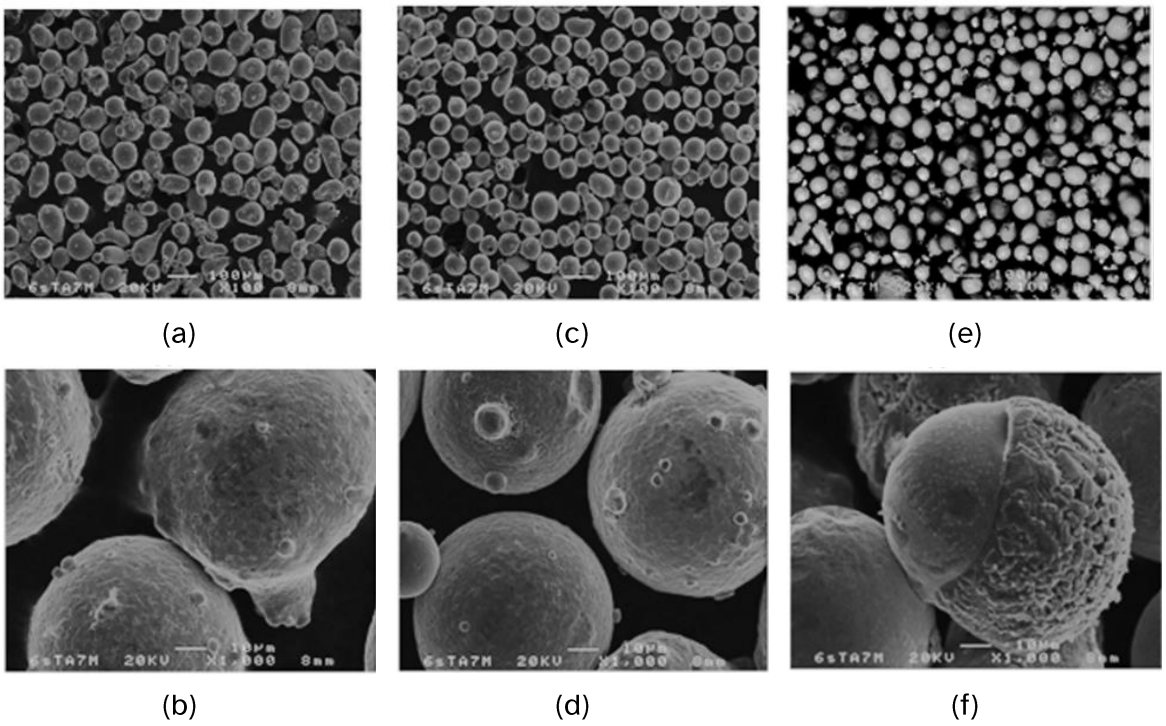

Figure II.18. Scanning Electron Microscope micrographs of the new powder NP (a) and (b), the cleaned powder of the 3th iteration CP3 (c) and (d), Bakscattered Scanning Electron Microscope micrographs of the reacted powders RP3 (e) and SEM details of the acorn-shaped particles of spinel oxide cubic phase (f).

The magnetic particles are not present in the cleaned powder which means that the magnetic separation process is effective. In the work of (Slotwinski et al., 2014) is showed that in the case of stainless steel powders in DMLS the sieve residue had characteristics of melting and particle joining.

II.5.3 Microstructure of Cladded Materials

II.5.3.1 Chemical Composition of the Cladding Builds

The chemical composition of the clad build was analysed by Energy-Dispersive X-ray Spectroscopy (EDX), through the thickness of each clad build. The results show that the contents of the different elements remain the same whatever the position in the clad build (top or bottom part) or the cleaned powder iteration number (new powder or one of the 5th iterations). After 5 iterations (Fig. II.16), the composition of the clad build remains in the limits of the IN718 standard (SAE AMS5662M, 2009).

II.5.3.2 Microstructure Analysis

The optical micrographs of the cladding samples shown in (Fig. II.19 a-b) reveal an almost directionally solidified dendritic microstructure. The columnar dendrites are aligned quasi parallel to the build direction. There is no great difference between the samples built with new powder and the recycled powder. These observations are consistent with previous work done on this material (Tian et al., 2014). The main difference between the top and the bottom of the build is the presence of some porosity. The porosity content seems to be higher in the top of the build than in the bottom whatever the number of reuses, and higher for the cleaned powder CP4 than for the new powder NP. Porosity has then been evaluated from optical micrographs using image analysis. The results point out an increase of the porosity with the number of reuses (Fig. II.19 c). In all the clad builds, porosity is higher at the top of the parts and lower in the middle or the bottom.

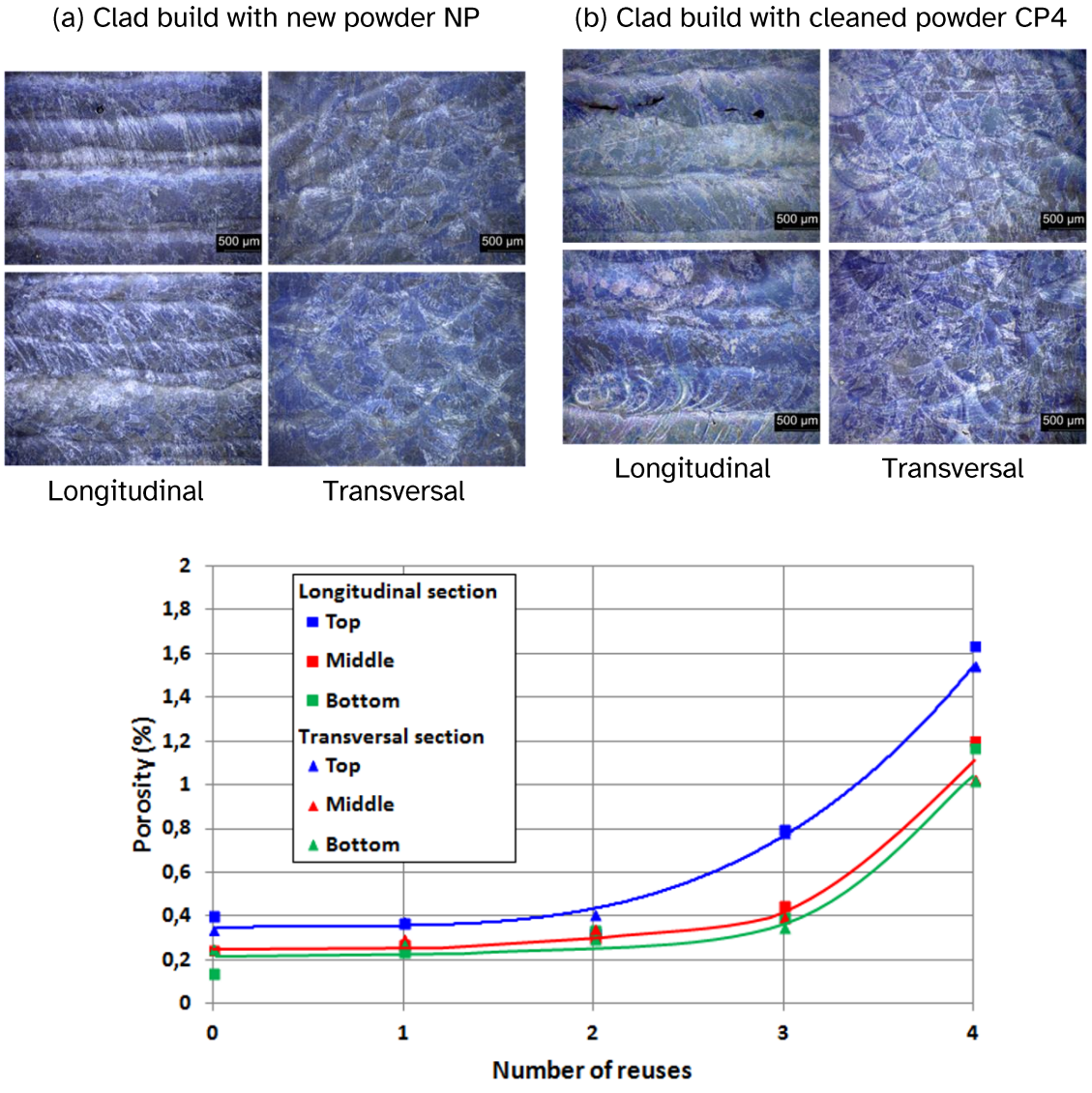

Figure. II.19. Optical micrographs of longitudinal section of clad builds (top and bottom parts) with NP powder (a), CP4 powder (b), and Evolution of the level of porosity in the clad builds with the number of powder reuses (c).

The present porosity is spherical which suggests that its origin is due to gas entrapment and the turbulences in the melt pool caused by the interaction between the powder particles and the laser. Excessive superheat increases the fluidity of the molten metal and the extent of gas entrapment in the build. The inter-pass temperature and the time for heat dissipation between passes also concentrate the heat in the melt pool explaining why the porosity is higher in the top of the clad build than in the bottom. Porosity is quasi constant up to the second reuse (CP2) and increases strongly for the 3rd and 4th reuses. The porosity is also slightly higher in the longitudinal than in the transverse direction, whatever the number of reuses. Strondl (Strondl et al., 2015) and

Ardila (Ardila et al., 2014) also pointed out an increase of porosity with the number of builds in the case of SLM.

A more detailed analysis of the microstructure has been made by EBSD (Fig. II.20). The grain orientation, size and aspect ratio have been analysed for the longitudinal as well as the transversal sections for the clad builds processed. For the NP new powder materials, the mean grain size is 53.4 µm with a mean standard deviation of 35.0 µm, for both directions (transverse or longitudinal) and whatever the position (top or bottom). For the CP4 cleaned powder, the mean grain size is 56.5 µm with a mean standard deviation of 37.2 µm, for both directions (transverse or longitudinal) and whatever the position (top or bottom). The grain is slightly larger for the clad build with recycled powder. The tendency is similar for the grain aspect ratio, with values, respectively for NP and CP4 builds, of 2.10±1.85 and 2.16±1.66, for both directions. The grains are slightly elongated for the build with recycled powder.

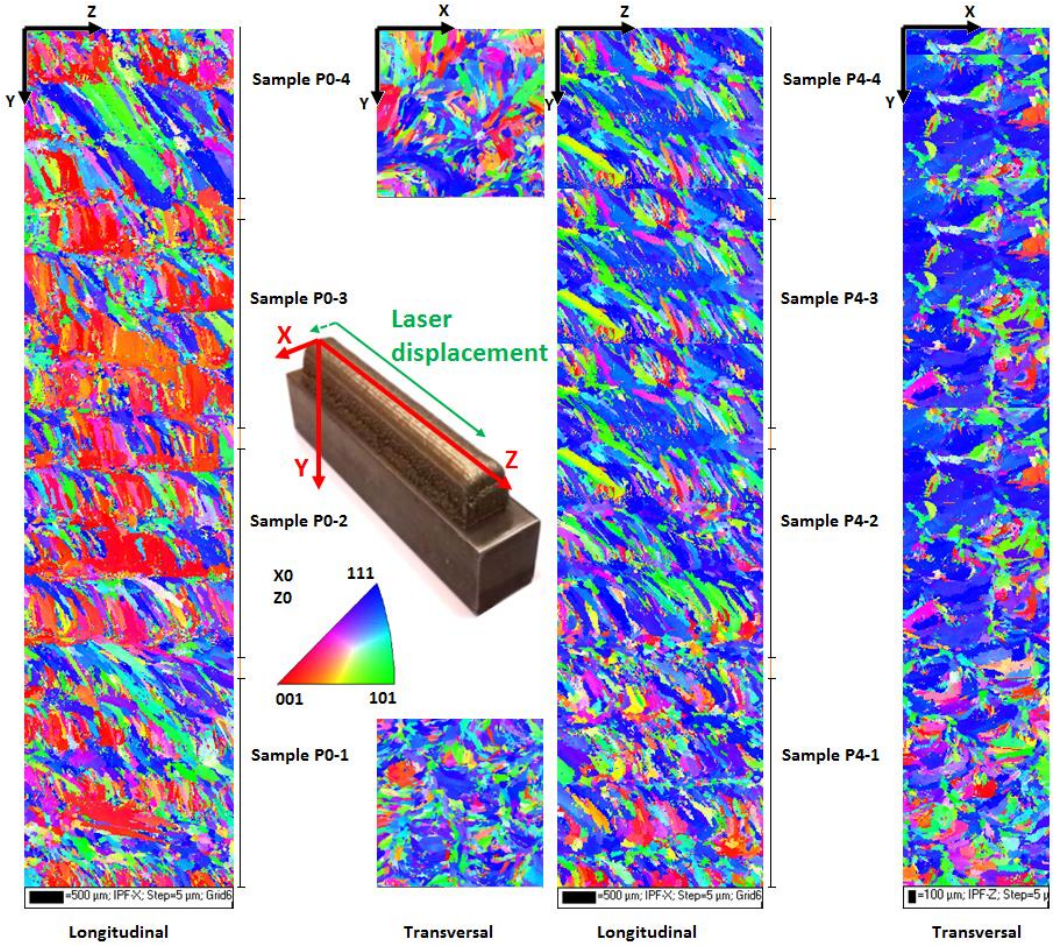

Figure II.20. EBSD analysis of samples 1 to 4 for NP (left) and CP4 (right) powders in both longitudinal and transversal sections.

For the grain orientation, the conclusions are different (Fig. II.21) and (Fig. II.22). For both NP and CP4 clad builds, there is not a preferential orientation of the grains in the X-Y section (Fig. II.21 b) while for the longitudinal X-Z section the results depend on the sample position in the build and the number of reuses of the powder (Fig. II.21 a). For samples 1 (bottom of the builds), the microstructure seems to be a mixture of equiaxed and columnar grains but with a strong proportion of columnar grains oriented at 125° with respect to the Z-axis. For sample 4 of the NP build, the microstructure is a mixture of equiaxed and columnar grains but with a slightly orientation at 125°.

Moreover, for the NP clad builds, there is not a particular crystallographic orientation of the grains, while for CP4 clad builds, a <111> crystal orientation clearly appears whatever the section (longitudinal or transversal) and the position of the sample (top or bottom) (Fig. II.20) and (Fig. II.22).

This crystallographic orientation of the grains is more pronounced for sample 4 (top) than for sample 1 (bottom). Even though the solidification rate of this process is quite high as to avoid the formation of laves and delta phase, a network of this brittle phase has been found.

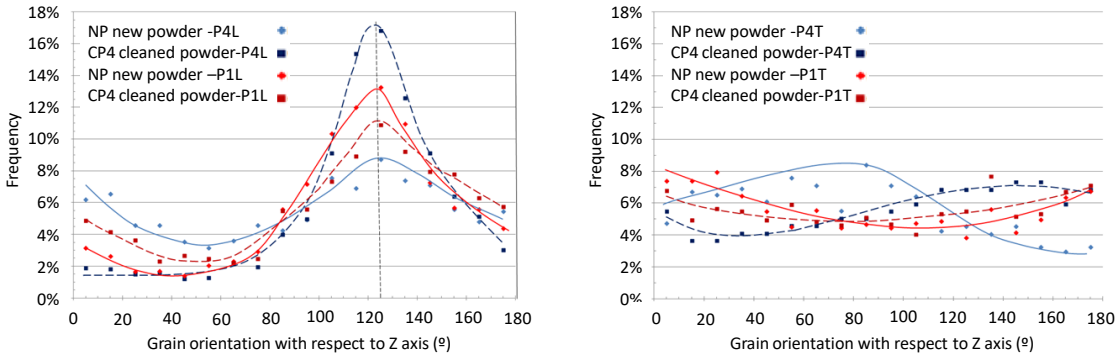

(a) (b)

Figure II.21. Grain orientation in the longitudinal (a) and transverse (b) sections of sample 1 (bottom of the build) and 4 (top) from clad builds NP (new powder) and CP4 (4 reuses)

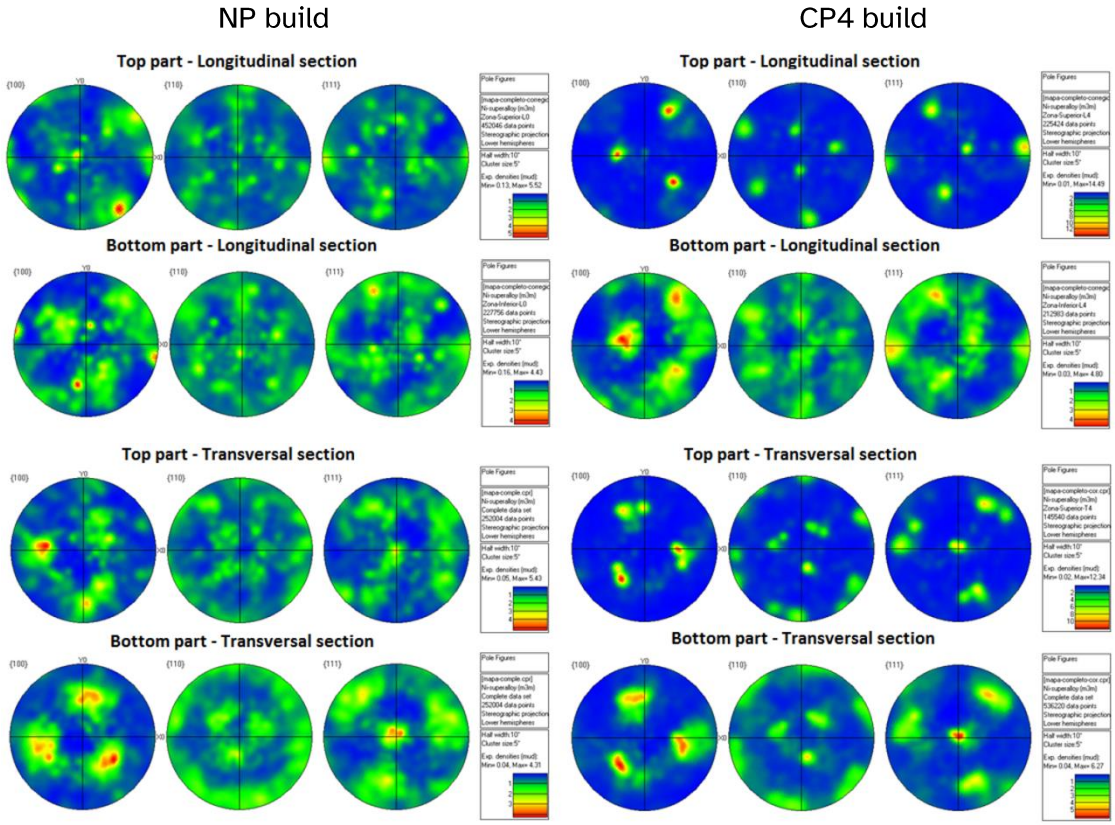

Figure II.22. Pole figures for NP and CP4 clad builds

II.5.3.2.1 SEM Analysis before Heat Treatment

According to (Keiser and Brown, 1976), "ideally" in a material in the age-hardened condition from the precipitation of the γ' and γ'' secondary phases, only the phases γ, the two hardening phases that were mentioned previously (phases γ' and γ''), and small amounts of NbC and TiN should exist within the super-alloy INCO718. Segregations within the alloy during fabrication, or continuous service at high temperatures will give rise to other secondary phases: Laves Phases, Ni_3Nb and carbides resistant to high temperatures.

For the INCO718 in real "as cast" state (without heat treatment), a significant number of phases will be formed (some of them undesirable), which can be mostly eliminated later with heat treatment. In addition, the same heat treatment will give rise to the hardening phases.

The initial microstructure of INCO718, manufactured using the Laser Cladding process, is observed as a γ matrix, with well-defined grain edges (Fig. II.23). Pre-heat treatment

δ phase precipitates have a needle-like appearance as previously mentioned. The δ phases are important because they constitute stress concentration zones.

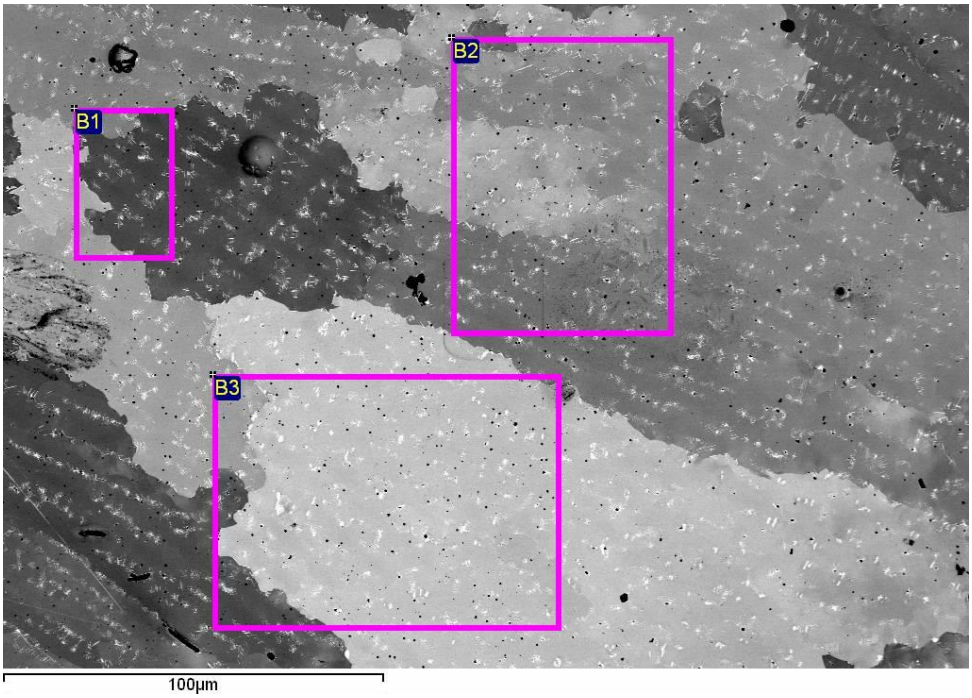

Figure II.23. SEM image of the microstructure of INCO718 in a state "as-cast" prior to heat treatment. The boxes that are shown are areas of analysis by means of the EDXq method (Energy-dispersive X-ray spectroscopy).

The configuration for taking SEM images like the one in (Fig. II.23) were determined by the collimation of the electron beam. To achieve better resolution, the acceleration of the electron beam has been done over a potential of 5kV instead of the traditional 20kV.

The chemical analysis (Section II.5.1) on the areas from B1 to B3 of (Fig. II.23) has been done on a relatively large region with the objective of macroscopically quantifying the composition of the super-alloy (and verifies if the Laser Cladding process has modified in any way the nominal composition of INCO718). The results by areas at the macroscopic level are shown in (Table II.4).

Table II.4: Chemical composition of the INCO718 alloy obtained from the analysis using the EDX method.

All results in weight%								
Spectrum	In stats.	Al	Cr	Fe	Ni	Nb	Mo	Total
B1	Yes	0.57	19.87	19.84	52.79	3.46	3.47	100.00
B2	Yes	0.55	19.85	19.27	53.56	4.08	2.71	100.00
B3	Yes	0.57	20.33	19.45	52.13	4.13	3.40	100.00

A SEM image (together with the EDX chemical analysis), at a level of zoom detail (10X magnification), allows obtaining data related to the segregated phases that were generated during the Laser Cladding manufacturing process (Fig. II.24).

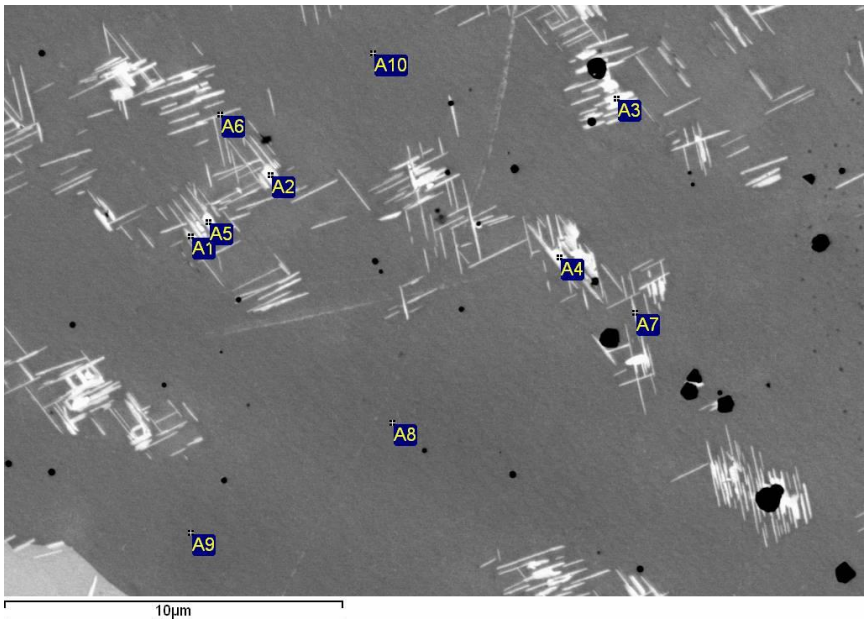

Figure II.24. SEM image of the microstructure of INCO718 in "as-cast" state prior to heat treatment (detail). EDX analyses have been carried out in specific areas to determine the approximate composition of the secondary phases that were generated during the additive manufacturing process.

The results of the compositional analysis at the detail level are shown in (Table II.5).

Table II.5: Chemical composition of the INCO718 alloy obtained from the analysis by means of the EDX method for image at the level of detail (shooting in specific areas).

All results in weight%								
Spectrum	In stats.	Al	Cr	Fe	Ni	Nb	Mo	Total
A1	Yes	0.24	12.51	12.56	56.50	15.44	2.76	100.00
A2	Yes	0.24	4.60	5.83	60.59	27.35	1.39	100.00
A3	Yes	0.29	12.70	12.38	56.75	14.88	3.00	100.00
A4	Yes	0.16	6.38	7.43	58.60	25.05	2.39	100.00
A5	Yes	0.11	4.95	5.84	60.45	27.21	1.43	100.00
A6	Yes	0.36	19.24	18.84	52.79	5.58	3.19	100.00
A7	Yes	0.28	10.99	10.32	57.49	18.60	2.31	100.00
A8	Yes	0.58	19.87	19.84	52.80	3.45	3.46	100.00
A9	Yes	0.55	19.84	19.27	53.55	4.08	2.70	100.00
A10	Yes	0.57	20.32	19.45	52.14	4.13	3.40	100.00

Points A8, A9 and A10 were purposely taken in the base material area (γ matrix), away from the areas of appearance of the secondary phases, as a calibration measure.

The points between A1 and A7 present a highly variable chemical composition, being the data of the numerals A2, A4 and A7 close to the composition of Laves phases reported by (Pautrat, 2013), as observed in (Table II.1).

On the other hand, A6 (whose objective was to take a sample of the chemical composition of a δ phase), is very close to the nominal base composition of the INCO718 alloy. A deviation of the quantity in Nb is noted related to the nominal values of the (Table II.1), but still within the nominal values reported in the previous table.

It is speculated that the data from tests A1, A3 and A5 correspond to those of Laves phases. It is proposed that the variation in the chemical composition with respect to the values reported in (Table II.1) is due to the fact that such phases are not completely isolated from each other (for example, the crystallographic orientation of the delta phase is coherent with that of the Laves phase).

To corroborate the correspondence between the appearance of the secondary phases observed via SEM (needles for the δ phase and globular forms for the Laves phase), and explain the variation in the composition of the aforementioned phases (it is proposed that the phases, despite presenting different appearance, are not completely chemically segregated), an inspection will be made at the level of zoom detail in a SEM image for a segregation of delta phases, and a phase of Laves will be assumed with a data collection step of 0.1 microns, and generation of a compositional map, as shown in (Fig. II.25). The size of the compositional map will be 12x8.5 microns.

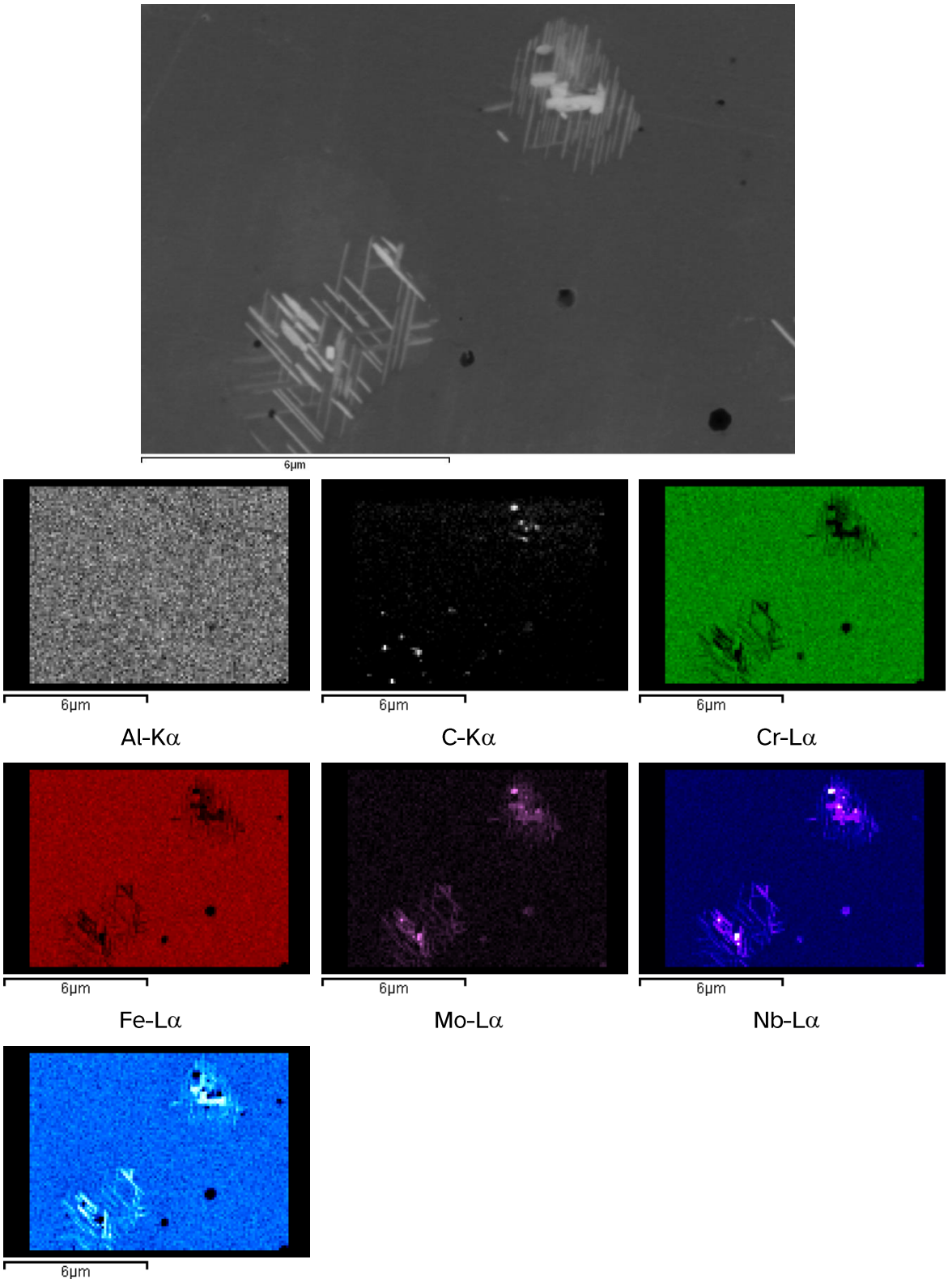

Figure II.25. Detailed chemical composition map of two sets of phases. In the upper image it is observed that the SEM image presents "only" two phases (δ and Laves phases). The map shows the existence of more secondary phases than can be seen with the single image at the top of this figure.

The following is observed:

- Al-Kα: Aluminium, per spectrum line Kα, is observed uniformly dispersed in the matrix.
- C-Kα: Carbon, the brightness indicates a high concentration, which is why the formation of carbides is deduced (as mentioned they are very stable). With the naked eye in the SEM image, it is very difficult to distinguish from the Laves phase. It is observed that carbides tend to form in the segregation zone of the same delta phases and Laves phases.
- Cr-Lα: Chromium- Lα, is substituted by Niobium in the Laves and δ phases.
- Fe-Lα: Iron-Lα, is substituted by Niobium in the Laves and δ phases.
- Mo-Lα: Mo is present, but its spectrum is not clear because it "overlaps" with the Niobium line.
- Nb-Lα: The Niobium that is observed substitutes inversely for Fe, Cr and Ni in the matrix, forming the Laves and δ phases. The pattern that is observed is apparently a Niobium carbide which always appears surrounded by acicular phases (δ phases), rich in Nb
- Ni-Lα: Very uniform in the matrix, but as previously mentioned it is substituted in carbides and rich in acicular phases (δ phases).

It seems that the thermal cycle generated by the cladding process to add new layers could be the responsible of the apparition of intragranular acicular delta phase (thermodynamically more stable), presumably as transformation of γ" phases during the thermal history. The work carried out by Tian (Tian et al., 2014) explains with detail the evolution of this microstructure.

These structures can also be found in wrought alloys after being treated at 750°C during 100h (Miller and Burke, 1991) but in this case is just the result of the cladding process.

The composition of the globular phases is consistent with that of "Laves Phases" (except for Ni content, but it is attributed to the difficulty of obtaining an accurate lecture due to the mixture of phases) and to the undesirable δ phases that should be eliminated with the thermal treatment, because as it has been commented previously, they brittle the material.

The Niobium content reveals the existence of a phase not considered at first (extremely rich in Nb). The colour scale in the corresponding diagram (white indicates 100%

content), makes us suspect that they are Niobium carbides. To confirm it, an analysis of a specific particle was made (Fig. II.26)

(a) (b)

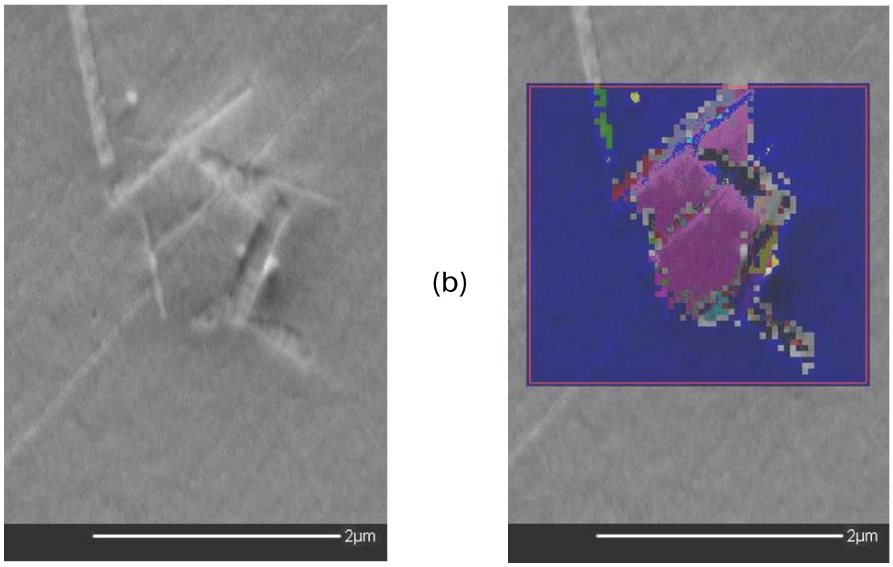

Figure II.26. Detail of particle analysis to confirm the chemical composition of the existence of Niobium carbides within a zone rich in δ and Laves phases.

The images of (Fig. II.26), together with its Spectrum (Fig. II.27), confirm that in general the internal "segregations" were Niobium carbides, within a matrix mainly constituted by Laves and δ phases.

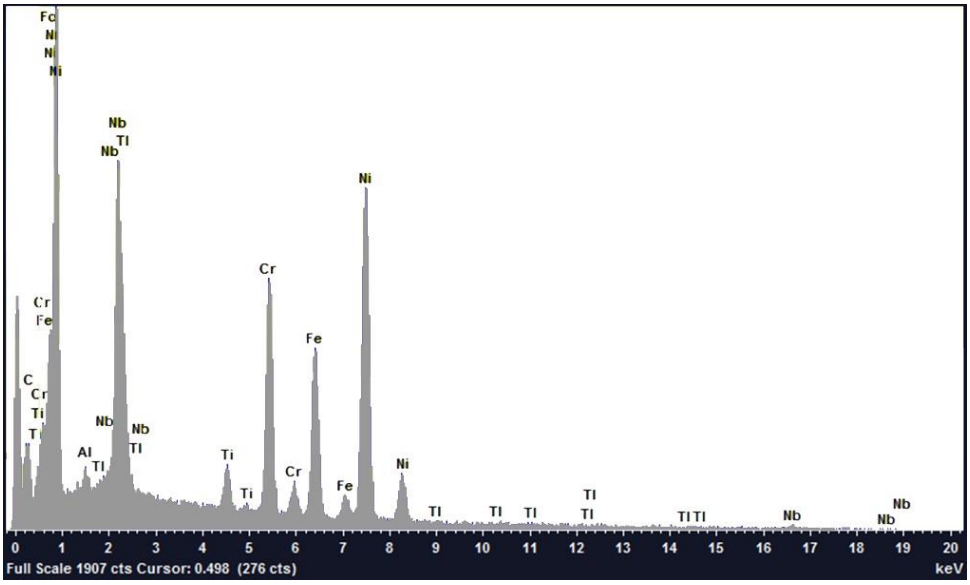

Figure II.27. Spectrum of the chemical composition of a "carbide-like" particle of (Fig. II.26), by means of the EDX analysis method (the analysed particle is attached to a δ phase).

In summary, it was observed that before heat treatment the phases present in a material manufactured by the Laser Cladding process are: standard matrix of INCO718 (γ phase),

Niobium carbides (in small quantity and difficult to distinguish only by SEM images), Laves phases and delta phase (the latter two are very mixed, although they are distinguishable by their own morphology).

II.5.3.2.2 SEM Analysis after Standard Heat Treatment

In (Fig. II.28) the morphology of two samples of material deposited by means of the Laser Cladding process is shown for two starting materials. The first material is new metal powder and the second is a 4 times reconditioned powder according to the procedure in section (Chapter II.4.3).

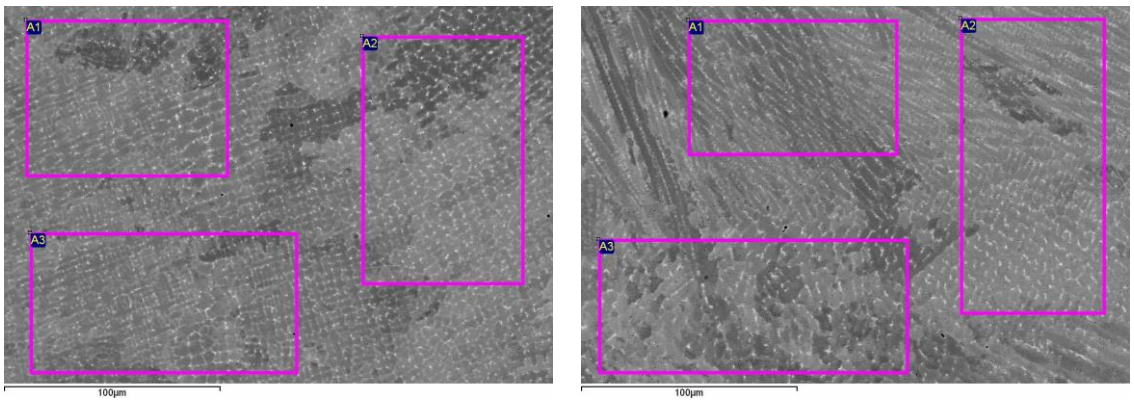

(a) (b)

Figure II.28. Aspect of the microstructure of a material manufactured by the Laser Cladding process for: (a) new metallic powder, (b) metallic powder reconditioned 4 times. The boxes in both images indicate areas of macro analysis via SEM to verify the chemical composition of the alloy.

Before heat treatment INCO718 does not have a good performance in terms of mechanical properties. For the heat treatment to be effective, it is necessary that the proportions of the chemical elements of the alloy are preserved. Heat treatment must also fulfil the function of eliminating all undesirable phases (or minimizing them), as far as possible.

Regarding of chemical composition, it was verified that the super-alloy composition is preserved after the Laser Cladding additive manufacturing process (via EDX chemical analysis), and the corresponding heat treatment (standard). To increase the precision of the chemical analysis to verify the chemical composition (boxes in (Fig. II.28)), the electron beam voltage was set at 20kV, which allows the quantification of lighter elements such as titanium (Table II.6).

Table II.6: Results of the chemical composition analysis for the INCO718 alloy manufactured by the Laser Cladding process after heat treatment starting from (a) new powder, (b) reconditioned powder according to (Fig. II.28).

(a) New Powder									
All results in weight%									
Spectrum	In stats.	Al	Ti	Cr	Fe	Ni	Nb	Mo	Total
A1	Yes	0.54	0.96	19.76	18.69	51.70	5.35	3.00	100.00
A2	Yes	0.56	0.94	19.72	18.70	51.65	5.21	3.22	100.00
A3	Yes	0.52	0.95	19.77	18.66	51.85	5.33	2.92	100.00
(b) Reconditioned powder, 4 times									
All results in weight%									
Spectrum	In stats.	Al	Ti	Cr	Fe	Ni	Nb	Mo	Total
A1	Yes	0.56	0.95	19.71	18.73	51.85	5.18	3.03	100.00
A2	Yes	0.56	0.91	19.67	18.45	51.92	5.27	3.22	100.00
A3	Yes	0.56	0.88	19.83	18.62	51.77	5.21	3.14	100.00

The chemical composition of the metal powder according to (Table II.6), is in accordance with the standard (SAE AMS5662M, 2009).

One of the consequences observed after heat treatment is the formation of intragranular Laves phases and the disappearance of the δ phases in the microstructure, as shown in the comparison of (Fig. II.25) and (Fig. II.29).

To verify the disappearance of the delta phase after the heat treatment, a detailed analysis of an area of an approximate size of (12 * 8.5) µm has been made in the form of chemical composition maps of a SEM image (Fig. II.29).

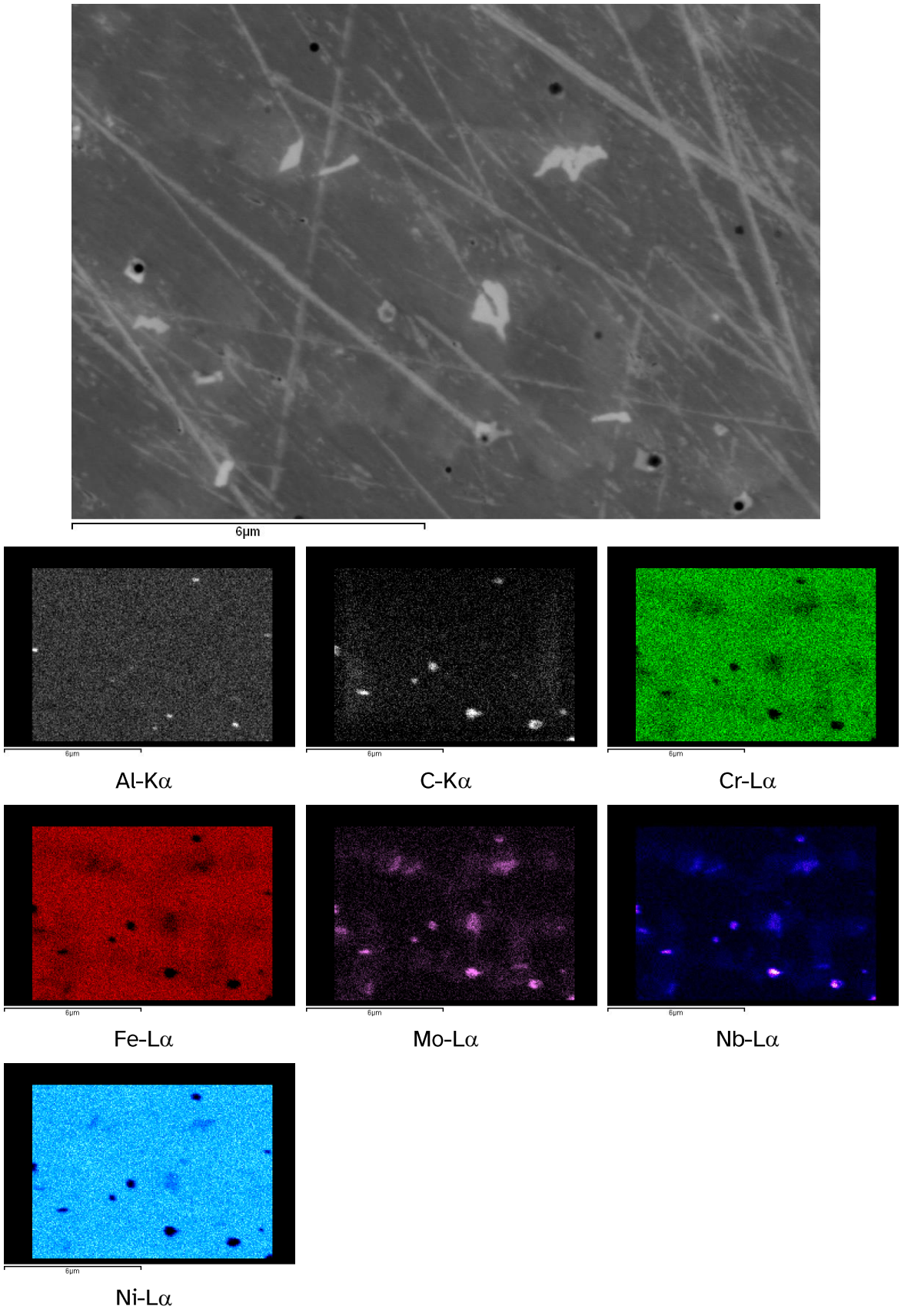

Figure II.29. SEM image at a detailed level with chemical composition maps for an INCO718 alloy manufactured by the Laser Cladding process with heat treatment from new metallic powder.

The “lines” observed in top of (Fig. II.29) correspond to scratches generated during the polishing process of the sample and should not be confused with some type of secondary phase. The δ phase was diluted in the matrix of the alloy, since the acicular morphology typical of the delta phase is not observed as in the maps $NiL\alpha$ and $CrL\alpha$ of the (Fig. II.25).

The content of Niobium and segregated Nickel (indicator of the presence of secondary phases such as Laves), has been notably diluted. The $NbL\alpha$ maps corresponding to (Fig. II.25) and (Fig. II.29) show a wide difference in the concentration of this last element. In (Fig. II.29), the presence of carbon-rich phases is strongly noted ($Ck\alpha$ map), possibly due to the presence of Niobium Carbides. The presence of Niobium Carbides is not strange in the final morphology of the INCO718 alloy, since carbides in general are very stable at high temperatures such as those used for the heat treatment of the alloy.

To quantify the composition of the resulting phases at the level of the SEM image of (Fig. II.29), a trajectory analysis has been performed, generating a relative intensity map of each element, as shown in (Fig. II.30).

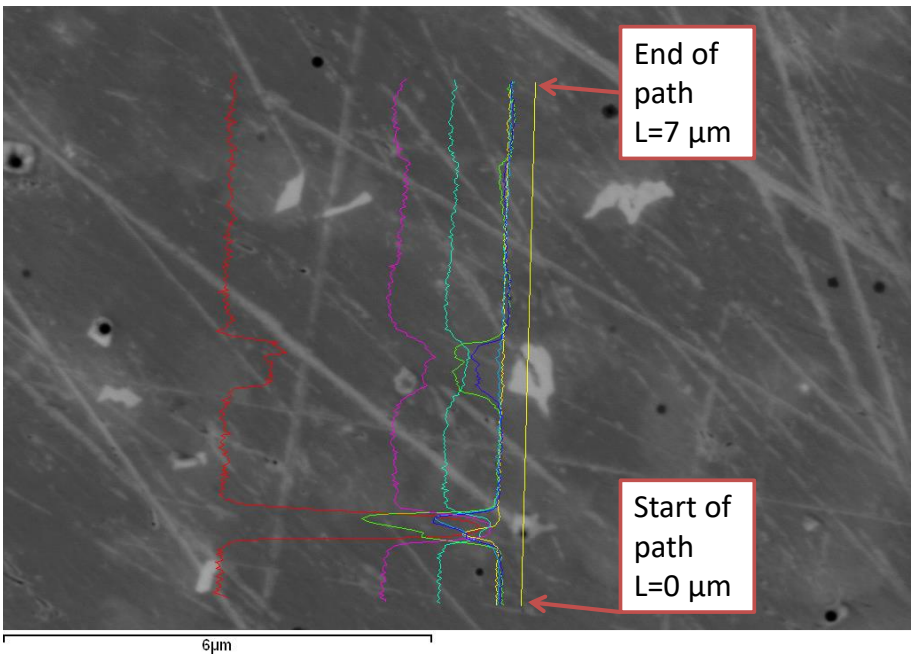

(a)

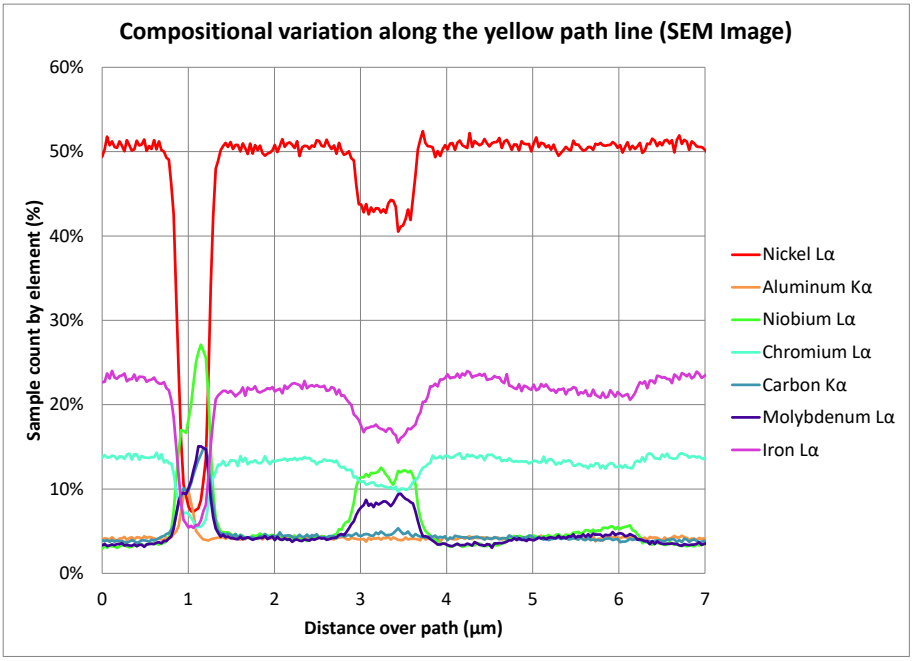

(b)

Figure II.30. Quantitative compositional analysis by line sweep at the level of detail of a section of INCO718 alloy manufactured by the Laser Cladding additive manufacturing process from the SEM image of the (Fig. II.29); (a) chemical composition measurement path, (b) compositional variation for different elements along the path.

The analysis by elements (Fig. II.30) shows that the matrix preserves the composition of the base INCO718, although with a certain difference that is attributed to the overlapping of spectrum lines (for example, in the case of Nb and Mo, whose lines are very close and overlap).

At the coordinate near the 1 µm distance, the graph in (Fig. II.30) shows a composition change that is typical for Niobium carbides. In the same figure (approximately at the 3.25 µm coordinate), again there is a change in the chemical composition of the alloy, which is similar to that of one of the Laves phase.

The scheme of the thermal treatment of the alloy in the TTT diagram for INCO718 (Fig. II.31), shows that the main objective of the alloy double aging is the maximum formation of phases γ, γ' and γ'', and avoiding as far as possible the appearance of the δ phase (within a reasonable aging time).

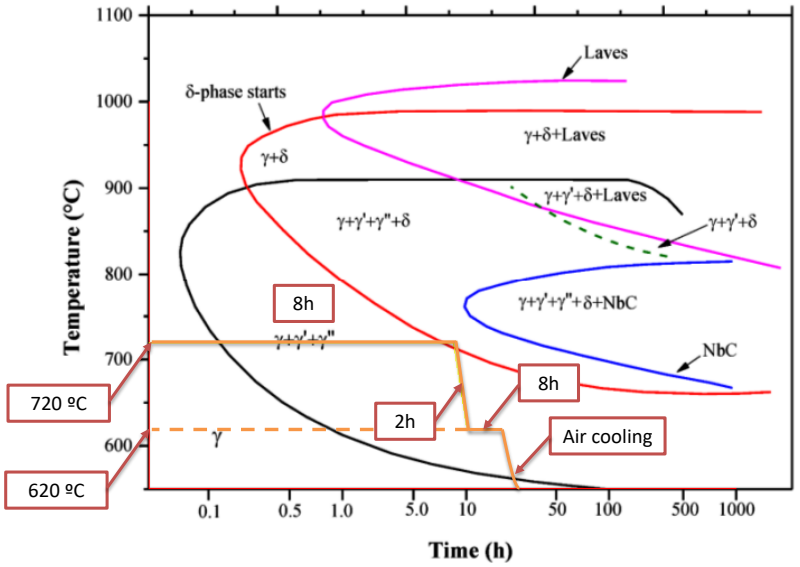

Figure II.31. INCO718 TTT diagram (Petkov, 2018), indicating the standard heat treatment for the super-alloy material manufactured through the Laser Cladding process.

The heat treatment allows the complete dissolution of the delta phase within the material, but not that of the Laves phases (intragranular). For this reason, it is interesting to look for a suitable heat treatment for the Laser Cladding process, since the starting material obtained from the "as-cast" condition is not the same as that produced by a traditional manufacturing process (compare (Fig. II.10) with (Fig. II.28)).

II.5.4 Mechanical Properties

The results of Uniaxial Tensile tests are shown in (Table II.7) and (Fig. II.32). The characteristics of yield, tensile strengths and Young's modulus are similar to the specifications for IN718 of the AMS 5662M standard whatever the number of recycling or the position of the sample within the clad builds.

Table II.7: Mechanical properties of the builds clad with new powder (P0 samples) and recycled powders (P1 to P4 for one to four reuses). Samples referenced PX-1 are located at the bottom of the build and PX-4 at the top.

Sample reference	Rupture strain (%) ± SD	Young's modulus (GPa) ± SD	Yield strength (MPa) ± SD	Tensile strength (MPa) ± SD
IN718 (AMS 5662M)	12.0		1034.0	1276.0
P0-1 P0-2	7.6 ± 3 11.2 ± 3	176.5 ± 6.3 184.0 ± 6.3	1209 ± 46 1235 ± 46	1368 ± 39 1403 ± 39

P0-3	13.8 ± 3	191.6 ± 6.3	1271 ± 46	1451 ± 39
P0-4	14.0 ± 3	181.3 ± 6.3	1162 ± 46	1372 ± 39
P1-1	8.8 ± 3	175.6 ± 5.1	1202 ± 19	1368 ± 31
P1-2	10.1 ± 3	182.0 ± 5.1	1226 ± 19	1401 ± 31
P1-3	13.2 ± 3	182.7 ± 5.1	1241 ± 19	1430 ± 31
P1-4	14.5 ± 3	188.1 ± 5.1	1244 ± 19	1435 ± 31
P2-1	8.8 ± 3	183.4 ± 3.1	1222 ± 17	1388 ± 29
P2-2	11.1 ± 3	185.7 ± 3.1	1257 ± 17	1450 ± 29
P2-3	13.5 ± 3	190.4 ± 3.1	1256 ± 17	1448 ± 29
P2-4	14.6 ± 3	184.4 ± 3.1	1236 ± 17	1428 ± 29
P3-1	8.0 ± 2	186.6 ± 7	1219 ± 12	1391 ± 21
P3-2	9.5 ± 2	172.3 ± 7	1201 ± 12	1379 ± 21
P3-3	9.6 ± 2	180.0 ± 7	1210 ± 12	1388 ± 21
P3-4	12.0 ± 2	187.2 ± 7	1229 ± 12	1426 ± 21
P4-1	4.6 ± 2	184.0 ± 4.3	1207 ± 18	1335 ± 29
P4-3	7.6 ± 2	192.5 ± 4.3	1214 ± 18	1377 ± 29
P4-4	7.8 ± 2	189.4 ± 4.3	1240 ± 18	1391 ± 29

In the case of the Rupture strain, the values obtained are strongly dependent on the sample position within the build and on the number of reuses of the cleaned powders. The lower value of ultimate tensile stress corresponds to the higher number of reuses of the metal powder, and to the position of the specimen within the base block that served for the construction of the specimens themselves (Fig. II.14). After 2 reuses, the rupture strain also decreases strongly.

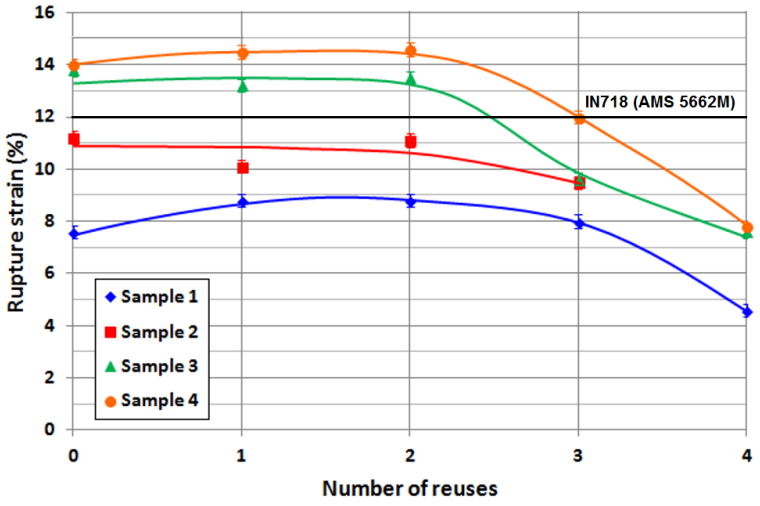

Figure II.32. Evolution of Rupture Strain as a function of the number of reuses and location of the sample within the clad build

II.6 Results and Analysis

The previous results show that the reuse of IN718 powder after the proposed recycling treatment does not modify significantly:

1. The characteristics of the powders since the chemical composition remains the same, the morphology of the particles evolving towards a distribution of their diameter much centred around an average value slightly higher than the initial value, and an aspect ratio value which decreases leading to more spherical particles,
2. The chemical composition of the clad parts in their thickness, and in function of the number of reuses,
3. The precipitates content within the height of the build or with the number of reuses.
4. The Yield and Rupture Strength or the Young's modulus of the fabricated materials.
5. There is significant chemical homogenization in the INCO718 grains generated by the Laser Cladding process after heat treatment. In the SEM images of the thermally treated material, a significant blurring of the chemical elements within the grains is observed.
6. No more secondary phases have been found in a material manufactured by the Laser Cladding process than Niobium Carbides and Laves phases.
7. The Laves phases generated within the deposited material are intragranular, and therefore should not affect the mechanical properties in such a detrimental way as if the mentioned phases were located at the grain boundaries.
8. The heat treatment used as standard in INCO718 is capable of eliminating all the delta phase within the material and matches the phases corresponding to the TTT diagram.

On the other hand, a drop in the rupture strain was pointed out from a third reuse of the recycled powders. This feature was been demonstrated over the thickness of the material, the samples in contact with the substrate exhibiting a lower rupture strain than those situated above.

Two phenomena have thus been pointed out concerning the reduction of the rupture strain, (I) one depending on the height of the clad part, and (II) the other associated with the number of reuse of the powder.

The first phenomenon can be attributed to the conditions of implementation of the process and is independent of the quality of the powders and the second to the characteristics evolution of the reused powders.

During the manufacture of the builds on the DIN C45E steel substrate, the thermal conditions of the process evolve over time due to the difference in thermal conductivity and specific heat between the substrate and the deposited material. When the first layers of IN718 are deposited, the heat flow through the substrate is facilitated due to the better thermal conductivity of the steel. When the thickness of the deposit begins to become large, the heat flow is slowed down by the lower thermal conductivity of IN718. This is reflected, as the EBSD analysis shows, by a modification of the microstructure (Fig. II.20). In the zone close to the substrate and in the median part, in the longitudinal direction, the grains have a columnar growth with an orientation at 125° with respect to the Z axis, reflecting the presence of a heat flow in the Z direction in addition to the principal one in the Y direction. In the upper part of the build, the solidification becomes predominantly equiaxed with a random orientation of the grains. This evolution has been pointed out by Kirka et al. (Kirka et al., 2017) in the case of the electron beam-melting of INCO718.

It is also confirmed using the G_L / R diagram of solidification for IN718 (Kirka et al., 2017) and the model developed in (Chapter III.4), where is showed that the predicted grain sizes are in good agreement with the data of EBDS.

During the tensile tests of samples 1, the loading is carried out in a direction quasi perpendicular to the grains, involving the grain boundaries and the phases present in these zones. This is not the best direction for plastically deforming the material and therefore the rupture strain is affected. It is therefore quite normal to have an increase in ductility between the bottom and the top of the builds. Li et al. (Li et al., 2008) shown, in the case of Ni-Fe alloys, that the strength is independent of grain orientation. However, the plastic strain increased remarkably when the loading axis is parallel to the direction of grain columns, which is due to the enhanced grain boundary and dislocation activities.

When the number of reuses increases, the rupture strain drops rapidly, whatever the position of the samples in the build. This effect is mainly associated with the increase in porosity of the CP3 and CP4 builds. The use of recycled powders with a size distribution highly centred on a higher mean value favours the process stability but also increases

the melt temperature (Kirka et al., 2016). Gas entrapment is favoured but also the epitaxy of the solidified microstructure, leading to a columnar microstructure (oriented at 125 ° with respect to the Z axis), a strong crystallographic orientation (111) and a higher porosity.

CHAPTER III: MODELING OF LASER CLADDING PROCESS AND GRAIN MORPHOLOGY

III.0 Nomenclature and Abbreviations

cdf :	Cumulative distribution function
pdf :	Probability density function
AM:	Additive Manufacturing
CAFE:	Cellular automata finite element
CET:	Columnar to Equiaxed Transition
EBSD:	Electron backscatter diffraction
EL:	End of Layer
LAM:	Laser Additive Manufacturing
LMD:	Laser Metal Deposition
SDAS:	Secondary Dendrite Arm Spacing
SG:	Stray Grain (synonymous of equiaxed grain)
SL:	Start of Layer
SLM:	Selective Laser Melting
SX:	Single-crystal
TEM:	Transverse Electromagnetic Mode
WAAM:	Wire Arc Additive Manufacturing

$A_{\substack{spot \\ laser}}$:	Spot area of laser beam in work plane at $z' = s_n$ (m^2)
a :	Alloy related constant for Gäumann's crystallization model ($K^n . m^{-1}s^{-1}$)
a_1, a_2 :	Distance, auxiliary variable (m)
a_{gr}, b_{gr} :	Alloy related constant for grain size in traditional casting alloy formula (*)
$A_{\substack{mean \\ grain}}$:	Mean area of the projection of set of grains valid for analysis (m^2)
a_o :	Characteristic value of the thickness of the interface for non-equilibrium solidification (m)
B, n_λ :	Alloy related constants for empiric model for microstructure size in rapid solidification

b_1:	Intercept for the equation of the straight line in logarithmic coordinates (-)
C_o:	Powder mass flow rate (Kg.s^{-1})
C^0:	Solute concentration to the initial composition of the alloy (%)
c_p:	Specific heat capacity at constant pressure (J.Kg^{-1}K^{-1})
d_{gr}:	Grain size (m)
d_i:	Diameter, auxiliary variable (m)
D_L:	Thermal diffusivity in liquid phase (m^2.s^{-1})
d_p:	Mean diameter of the powder particles (m)
f_{esc}:	Scaling factor function for the β_G parameter of Gumbel Distribution (-)
$f_{\substack{shape \\ energy}}$:	Radial energy distribution of the laser beam in the $z'=0$ plane (-)
G_L:	Temperature Gradient in liquid isotherm (K.m^{-1})
G_R:	Green's function (m^{-1})
G_S:	Temperature Gradient in solid isotherm (K.m^{-1})
$H(X)$:	Unitary step function (Heaviside) for the domain X (-)
I:	Intensity of laser beam (W.m^{-2})
k:	Thermal conductivity (W.m^{-1}K^{-1})
k_e:	Equilibrium partition coefficient (*)
k_V:	Non-equilibrium partition coefficient (*)
ℓ:	Distance, auxiliary variable (m)
L_f:	Latent heat of fusion (J.Kg^{-1})
$\ell_{\substack{square \\ grain}}$:	Equivalent side length for the area projection by EBSD test (m)
m:	Slope for the equation of the straight line in logarithmic coordinates (-)
m':	Powder feed rate (Kg.s^{-1})
n:	Alloy related constant for Gäumann's crystallization model (-)
N_o:	Number of heterogeneous nucleation sites (m^{-3})
P:	Powder mass flux (Kg.m^{-2}s^{-1})
P_{laser}:	Laser beam power (W)
Q_g:	Gas volumetric flow rate (m^3.s^{-1})
r:	Radial coordinate in the frame of reference of nozzle (m)

R:	Radial auxiliary variable (m)
Re_{p}:	Relative Reynolds number for particles (-)
r_{laser}:	Laser beam radius (m)
r_n:	Centre radius of nozzle outlet (m)
r_o:	Half of the gap distance of nozzle outlet (m)
r_s:	Distance, auxiliary variable (m)
s_n:	Coordinate on the z' axis of the powder consolidation plane (m)
T:	Temperature (K)
t:	Time (s)
Th_{prop}:	Thermophysical properties in the mushy zone melt pool (K)
$\dot{T}$:	Cooling rate (K.s^{-1})
V:	Solidification grow rate (m.s^{-1})
v:	Scanning speed of laser beam (m.s^{-1})
v_g:	Initial carrier gas velocity (m.s^{-1})
V_{int}:	Boundary value on the axis V between the areas of 100% equiaxed grain and 100% columnar grain in a Solidification Map.
v_p:	Mean speed of the particles (m.s^{-1})
$v_{pz'}$:	Component of v_p in the z' direction in the frame of reference of nozzle (m.s^{-1})
$\overline{V}_{\substack{unit \\ cell}}$:	Volume of the equivalent cubic cell grain from grain projection (m^3)
x, y, z:	Coordinate in frame of reference system on semi-infinite substrate (m)
x_o, y_o:	Local coordinates that define the energy density in the surface of substrate (m)
z':	Axial coordinate in the frame of reference of nozzle (m)
z'_{inter}:	Coordinate on the z' axis of start of interaction of centrelines of powder streams with laser beam (m)
α:	Thermal diffusivity (m^2.s^{-1})
α_1, α_2:	Auxiliary variable for deduction of cdf Gumbel's Distribution (*)
α_{vV}:	Angle between the normal direction of the growth solidification interface and the travel direction of scanning the speed of laser beam (-)
β, β_G:	Scale parameter for Gumbel distribution (Generalized Extreme

	Value distribution Type-I) (*)
χ:	Location parameter for the scaling factor function (*)
δ:	Dirac's δ-function (m^{-1})
ε_m:	Peak value of energy density for a given distribution of laser beam ($W.m^{-2}$)
η:	Laser absorptivity of material (-)
ϕ:	Volumetric fraction of equiaxed grains (-)
ϕd_{drop}:	Diameter where the value of the powder mass flow concentration has fallen to a value e^{-2} of the maximum concentration (m)
ϕd_{laser}:	Laser beam diameter (m)
γ:	Angle between the horizontal coordinate axis V and the tangent line to the coordinate V_{int} in a Solidification Map (-)
γ_{suf}:	Surface tension ($N.m^{-1}$)
$\mathrm{H}(T)$:	Enthalpy from the reference temperature T_o ($J.m^{-3}$)
κ:	Numerical counter (integer), auxiliary variable (-)
λ:	Radius, auxiliary variable (m)
λ_{gr}:	Representation of a characteristic of spacing (dimension) in the microstructure (m)
$\ell_{\log}$:	Equation of straight line in logarithmic coordinates for the variable $\log_{10}(G_L)$ (*)
μ_{gas}:	Dynamic viscosity of carrier gas ($kg.s^{-1}m^{-1}$)
μ_{melt}:	Viscosity of the melt pool (Pa.s)
μ, μ_V:	Location parameter for Gumbel distribution (Generalized Extreme Value distribution Type-I) (*)
ρ_p:	Density of a particle within carrier gas ($Kg.m^{-3}$)
θ:	Angle for the equation of the straight line in logarithmic coordinates (-)
ξ:	Variable for the calculation of Gumbel's cdf (-)
ξ_*, ψ_*:	Auxiliary variable for deduction of constant of material n (*)
$\xi_{**}, \psi_{**}, f_{multip}$:	Auxiliary variable for deduction of the scaling factor function for the μ_V location parameter (*)

III.1 Introduction

The additive manufacturing (AM) of metallic components is currently booming with a global growth rate of 25%, both in terms of equipment and applications. Companies such as Renishaw, EOS, DMG MORI, IBARMIA, ADDILAN, ROFIN, TRUMPF, 3D Systems [A-D] ... propose machines based on the different additive manufacturing processes (SLM, LMD, WAAM ...). Sectors such as aeronautics, health, automotive, energy ... are already users of this technology for the production of pieces in small series. Most of these processes are based on the fusion and subsequent solidification of material deposited (normally metals) in the form of powders, wires... (Merklein et al., 2016).

Despite the clear progress made by laser cladding, it has limitations that mean that this technology has not yet been systematically implemented in many industrial sectors. The current limits are due to (i) the peripheral or complementary processes (prior material handling, post-processing, quality control) that in many cases condition its viability, and (ii) the ignorance of how to design products or successfully reorient industrial activities through the integration of these technologies (Bourell et al., 2009). These limitations are certainly not insuperable, and pose challenges for research, technological development and innovation that are being analysed by teams of researchers and companies around the world.

The case for many metallic materials shows that the available variety of alloys is smaller than for the subtractive and / or shaping methods. In addition, the purchase cost is also higher. These problems of availability and cost of the raw material are inherent to the current low volumes of consumption, since there is a vicious circle of low demand, which does not justify the necessary investment in the production of new materials and the unit cost that discourages the increase of consumption (PNAS, 2012). The current problems concern:

- The surface quality of the parts and the productivity: these aspects are associated, since the productivity influences the finish quality of the surface.

- The quality of the product and the repetitiveness of the process: some AM technologies have problems of processing capacity and repetitiveness, that is, they cannot guarantee the dimensional precision with which one part and the next will be manufactured. In the same way, the stability of the physical

properties of the product (hardness, elasticity, resistance to traction and fatigue, metallurgy ...), is a critical aspect for the qualification of parts and processes in certain sectors (automotive, aeronautics, medical ...), (Gibson et al., 2010). It is currently the main problem to relate the microstructure of the component obtained by AM with the parameters of the process and after with the mechanical and physical properties of the product.

- The limited size of the components: the maximum volume of the part that can be done today is limited, although there is an AM process that improves this aspect (WAAM ...).

- The cost of the equipment: this is a problem similar to the cost of the raw material, and due to the current limited market, the cost of the equipment is a brake on the development of the technology.

Although majority of AM processes are currently well controlled from a manufacturing strategy point of view and allow producing healthy components with a low or non-existent porosity level, the microstructure of the parts obtained by these techniques is far from being understood and controlled. In metals the grain size and orientation are essential factors for the control of the properties, especially the mechanical properties. The type of solidification (columnar or equiaxed) and the grain size depend on the local solidification conditions (thermal gradient G_L and solidification growth rate V), while the grain orientation is strongly conditioned by epitaxy phenomena based on the current orientation of the substrate microstructure. Therefore, it is common to find stray grains of several sizes (normally from microns to mm) oriented in a completely random directions. This leads to traction and/or thermal fatigue properties that may be low compared to the characteristics of the base material, because when the constituents needed for grain boundary strengthening are eliminated the high-temperature creep resistance and thermal fatigue behaviour of SX by example in nickel-based superalloys is improved (Liu and Qi, 2014).

It is therefore very important to be able to model the behaviour of the metal during its solidification and to be able to predict what type of solidification will occur and what size of grain will be obtained.

This contribution presents an analytical model of crystallization, growth and morphology for Inconel 718 during the manufacture or repair of components by laser cladding.

The objective is to correlate the main parameters of this additive manufacturing process with the microstructure generated by them and relate them to the mechanical properties obtained from samples. Emphasis is placed on maintaining the simplicity of the model with the aim of enabling the influence of each of the parameters and their effects to be clarified factor by factor.

III.2 State of Art

Laser cladding has a lot of similarity with the welding processes because in both a small melted area is generated (in this case created via high power laser), where particles of powder or filler wire are incorporated.

Although there are some publications on solidification conditions in the case of laser cladding (Fayazfar et al., 2018; Ma et al., 2017; Toyserkani et al., 2005; Zhong and Liu, 2010), the available literature can be extended using, in this case, the analogue process of welding (Anderson et al., 2010; Park et al., 2003; Pinkerton and Li, 2004; Vitek et al., 2012).

These processes can have a detrimental effect on the properties of the material, especially in the molten zone, where both the composition (with the cladding material) and the microstructure change. In particular, the formation of a completely columnar grain structure in the molten zone results in a very low resistance of that zone at room temperature (Villaret et al., 2013a). It is possible, however, under certain conditions, to modify the morphology of the grains in the molten zone from a columnar to equiaxed structure (Flemings, 1974; Greer et al., 2003).

This type of microstructure significantly improves the ductility of the melted zones (Petersen, 1973) and lowers the transition temperature (Lakshminarayanan et al., 2009), especially if the grain obtained is small (Bayraktar et al., 2006). This transition from columnar grains to equiaxed grains, called CET (Columnar to Equiaxed Transition) depends on the temperature field and its evolution in the solidification area. Two parameters have a particular importance in the solidification morphology: the thermal gradient G_L in the liquid isotherm solidification front and the growth speed V of this front. It is generally accepted that a decrease in the G_L/V ratio promotes CET (Kurz and

Fisher, 1998), normally associated with an increase in the constitutional supercooling (Anderson et al., 2010).

The dominant theory to explain CET involves the nucleation and growth of new equiaxed grains in the subcooled liquid near the solidification front that blocks the growth of the columnar grain, by mechanical interaction (Kurz et al., 2001), or by solutal interaction (Martorano et al., 2003). The cooling conditions that promote a high subcooling in the liquid near the solidification front, that is a low G_L/V ratio, favours the nucleation of new equiaxed grains and, consequently, the CET. In laser cladding or welding, an increase in the displacement speed, can decrease the G_L/V ratio, therefore, facilitate the appearance of equiaxed grains and improve the ductility of the melted zone (Bayraktar et al., 2006).

However, the number of nuclei that give equiaxed grains, formed in the subcooled liquid, is controlled mainly by the composition of the molten zone, and especially by the content in some elements that favour the formation of nucleation sites.

Titanium, for example, has a very active role in the morphology of solidification grains for many alloys (Ostrowski and Langer, 1979). In the case of ferritic stainless steels, it has been shown that titanium forms intermetallic compounds in the liquid alloy that provide heterogeneous nucleation sites for equiaxed grains (Villaret et al., 2013b) (Fig. III.1). The exact nature of these compounds is not always identified, and seems to vary according to the composition and cooling conditions (Villafuerte and Kerr, 1990; Villafuerte et al., 1995).

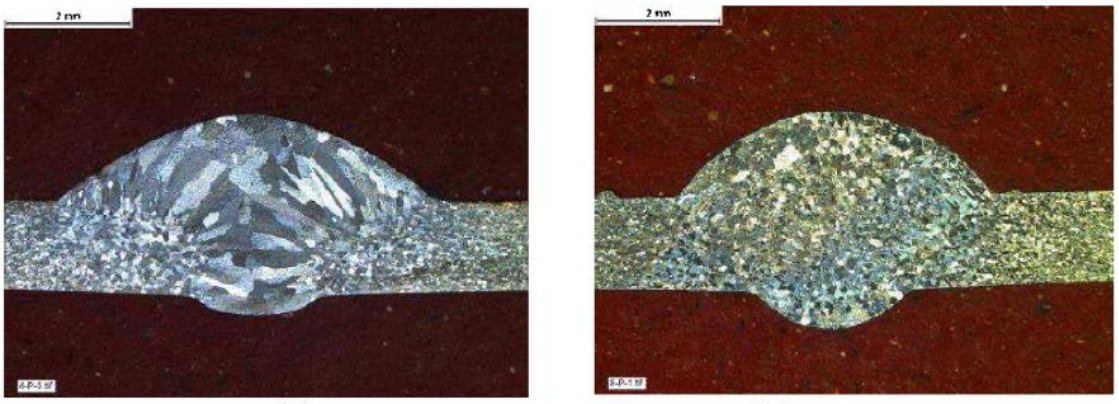

Figure III.1. Morphology of the melted zone microstructure for a ferritic stainless steel with 0.07% Ti (a), and 0.15%Ti (b), (Villaret et al., 2013b).

As the grain structure formed in the fusion zone is of paramount importance in the mechanical properties of that area, some models have been developed to try to predict the microstructure formed after welding or laser cladding process.

Models based on cellular automation, generally coupled to the finite element method (CAFE), have been used to predict with fairly good precision the grain structure formed during solidification of ingots (Carozzani et al., 2012; Rappaz et al., 1996), or for the solidification of welds (Chiocca et al., 2015), but it needs a quite long computing time.

By contrast, classical models based on Hunt's theory (Hunt, 1984) are simpler methods to predict whether CET occurs or not during solidification (Kurz et al., 2001), but require the preliminary determination of the number of heterogeneous nucleation sites N_o, which is not predictable by the model, and which may change, depending on the cooling rate (Gäumann et al., 1997).

In the Hunt's model of unidirectional steady-state solidification (Hunt, 1984), a decrease in nucleation subcooling ΔT_N or an increase in the number of heterogeneous nucleation sites N_o facilitates blockage of columnar grains and, consequently, the appearance of CET. Likewise, the incorporation of inoculants into the alloys allows the CET to occur earlier compared with alloys without inoculants, confirming the predictions of the Hunt's model (Martorano et al., 2003; Sturz et al., 2005).

The final equation of the Hunt model indicates that the CET occurs when the following condition is achieved (Eq. III.1):

$$G_L < 0.617 N_o^{1/3} \Delta T_t \left(1 - \left(\frac{\Delta T_N}{\Delta T_t} \right)^3 \right) \qquad \textit{Eq. III.1}$$

It is assumed that a certain number of equiaxed grains per unit volume N_o nucleates instantaneously ahead of the columnar front when the liquid reaches a subcooling of $\Delta T_N = T_L(C^o) - T_N$, where $T_L(C^o)$ is the temperature of liquidus corresponding to the initial composition of the alloy (C^o) and T_N is the nucleation temperature. The subcooling temperature of the columnar tips is $\Delta T_t = T_L(C^o) - T_t$, where T_t is the temperature in the columnar tips, which is calculated from an empirical relation as a function of the speed of the isotherm.

Gäumann (Gäumann et al., 2001) and Kurz (Kurz et al., 2001) have improved the Hunt's model using a dendrite growth model that explains the effects of rapid solidification to predict CET in processes with large temperature gradients and growth solidification rates.

As shown in (Fig. III.2) (Gäumann et al., 1999), the speed of the isotherms V depends on the location and is linked to the velocity of the heat source v. Along the centre line, V increases rapidly from zero at the bottom of the clad to a value close to v at the surface. The temperature gradient G_L is higher in the lower part of the clad and decreases as it approaches the surface. Unlike castings, where solidification is generally controlled by nucleation and growth processes, laser coatings which are very similar to welding exhibit primarily an epitaxial growth of the adjacent molten substrate. Therefore, the initial metal solidification assumes a crystallographic orientation identical to that of the contiguous solid in the melting line.

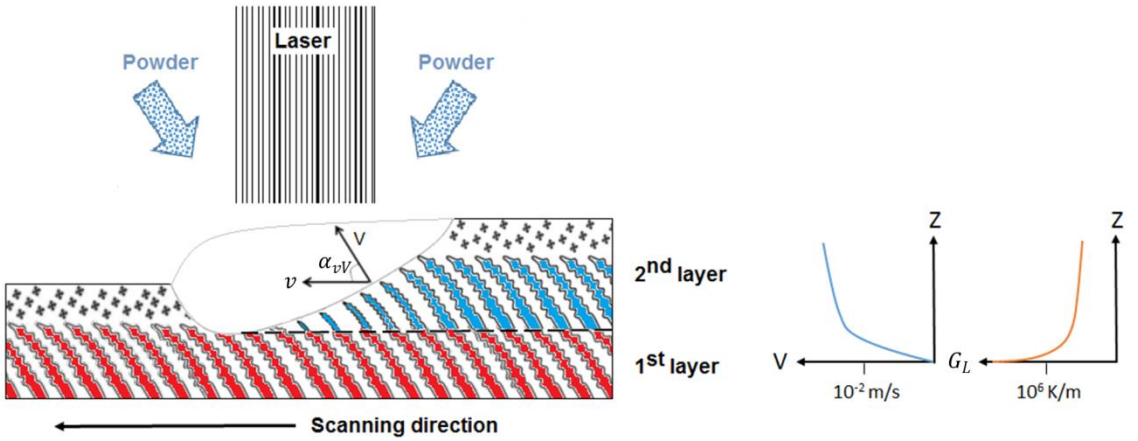

Figure III.2. Diagram of the longitudinal section along the central line of the clad during the laser cladding process and evolution of the solidification velocity V and the temperature gradient G_L along the solid / liquid interface (Gäumann et al., 1999).

For the first layer, the columnar grains begin to grow epitaxially from the substrate and their growth is blocked by the formation of equiaxed grains in the upper part of the layer. The columnar grains in the second layer also grow epitaxially from the columnar grains of the upper part of the first layer since the equiaxed grains have been remelted. There is a competitive growth of grains with different orientations and those closely aligned with the flow direction of maximum heat in the solid/liquid interface obtain a preferential growth. However, equiaxed grains are also formed in the upper part of the second layer. Similar processes of grain growth take place during the deposition of subsequent layers (Renderos et al., 2017).

The Gäumann's model is a generalization of the Hunt's model for multicomponent alloys, adapted to laser cladding process. This model starts from the temperature gradient conditions in the liquid inside the boundary of the molten bath G_L, the growth velocity V, the number of nucleation sites N_o, the volumetric fraction of equiaxed grains ϕ and a pair of constants of the material a and n. It has a validity range for processes of the order of V ~ 0.01 m.s^{-1} and G_L ~ 10^6 K.m^{-1}. The model defines that the CET (columnar to equiaxed) occurs when (Eq. III.2):

$$\frac{G_L^{\,n}}{V} < a\left[\sqrt[3]{\frac{-4\pi N_o}{3\ln(1-\phi)}}\,\frac{1}{n+1}\right]^n \qquad \textit{Eq. III.2}$$

Kobryn et al. (Kobryn and Semiatin, 2003) have developed columnar/equiaxed transition maps for the Ti-6Al-4V alloy for various castings and laser glazes processes that allow determining the morphology of the microstructure as a function of the solidification velocity V and the thermal gradient G_L (Fig. III.3).

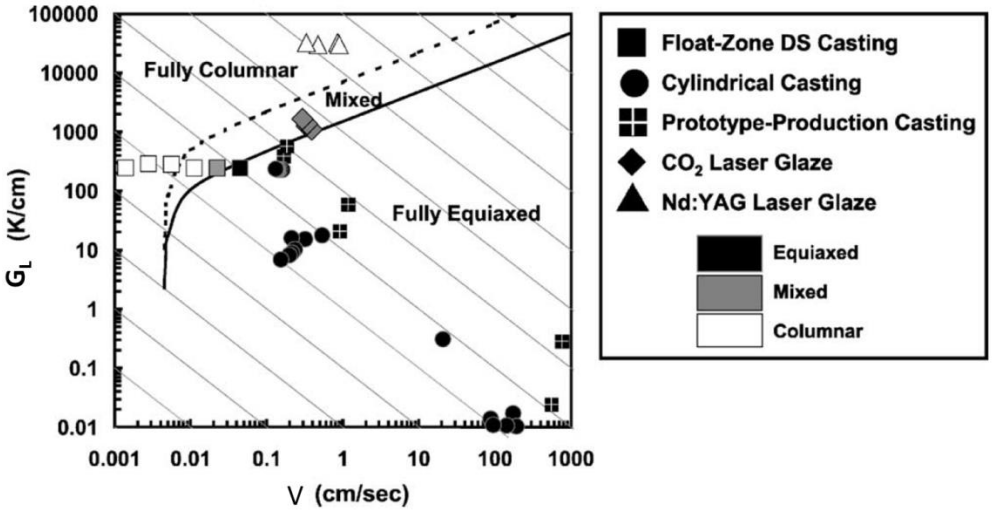

Figure III.3. The Ti–6Al–4V solidification map showing both the measured/predicted values of G_L and V, and the observed macrostructures for various castings and laser glazes (Kobryn and Semiatin, 2003).

These maps are actually a three-dimensional surfaces with the volume fraction of the equiaxed phase (ϕ) on the third axis. The representation proposed by Kobryn et al. is a projection in the V / G_L plane of a 3D evolution of the fraction ϕ.

This contribution focuses on the development of a model applied to the cladding laser process, which takes into account the specificity of this additive manufacturing process,

and which allows predicting the type of structure that will be obtained during the solidification of the clad material.

III.3 Modelling of Laser Cladding Process

The laser cladding process is based on the injection of material (usually metallic powder or wire), into a previously melted pool over the substrate material. The surface of the part where the material is being deposited is melted via a high power laser and the filler external material is deposited and melted together with the base material (Toyserkani et al., 2005).

The solidification conditions are obtained from the model based on an analytical heat source (3D) of general type in quasi-stable state, moving over a semi-infinite substrate, which allows applying specific boundary conditions to the heat source (as the effect of powder attenuation) and the effect of the same on the substrate. A code has been programmed that allows obtaining from the solidification conditions the steady state variations of the temperature gradient (G_L) and the solidification growth velocity (V).

The model is divided into the following steps or sub-models:

i. Attenuation of the laser beam by powder.
ii. Energy balance on the surface of the substrate.
iii. Application of energy balance to obtain temperature field by means of a heat source.
iv. Obtaining the local solidification conditions.
v. Solidification model CET based on the standard cumulative distribution function of Gumbel (cdf) or Extreme Value Type I Distribution.
vi. Observation of the effect in the variation of process parameters in the microstructure of added material.
vii. Experimental validation.
viii. Proposal of a method for obtaining constants of material for a CET model.

It is assumed:

- *Assumption 1:* Particles are considered perfectly spherical, and their distribution in size is taken on basis of a weighted average of the diameter distribution.
- *Assumption 2:* It has been assumed steady state, with constant properties of drag gas for the powder (isothermal).

- *Assumption 3:* Only those particles that come in contact with the melt pool created by laser beam adhere to the substrate.
- *Assumption 4:* The size of the melt pool is approximately the same of the area of incidence of laser beam over the substrate (in the focal plane of work).
- *Assumption 5:* The working fluid for deposition and drag of material in the laser cladding process is considered to be a two-phase compound. A continuous phase that serves as a carrier medium (it is usually a noble gas), and a disperse phase that consists of solid particles (powder). Physical parameters both phases (velocity, temperature, density, etc.), will be described by average values.
- *Assumption 6:* The velocity of drag gas flow determines the behaviour of the dragged powder (both speeds are coupled, but are not necessarily the same).
- *Assumption 7:* A Gaussian distribution of powder concentration in the working plane of consolidation is assumed.
- *Assumption 8:* The density of the particles is high in relation to the amount of volume that they occupy, i.e. they do not shadow each other (they do not interact during the travel nozzle-melt pool).

To develop the experimental part of this model a Nickel Base superalloy (Inconel 718) is used and emphasis is placed on maintaining the simplicity of the model in order to weigh the influence of each process parameter.

III.3.1 Attenuation of Laser Beam on Substrate by Effect of the Powder Shadow

The attenuation model for a coaxial nozzle developed by Pinkerton (Pinkerton, 2007) has been used as basis with certain modifications (Fig. III.4).

The velocity conditions of powder and gas are assumed as steady state at the output of nozzle and the powder velocity remains constant until the substrate is reached. However, the powder velocity is not considered the same as the gas velocity. There is a so-called "sliding velocity" between the two speed values.

The gas velocity is defined as (Eq. III.3):

$$v_g = \frac{Q_g}{4\pi r_n r_o} \qquad \textit{Eq. III.3}$$

It is very difficult to estimate the final velocity of the particles by the effect of the speed of the drag gas stream. In general, the geometry of a coaxial nozzle involves a tortuous path for the powder particles in order to guide them as precisely as possible to the working area (the concentration area below the nozzle which is usually the focal point of the laser beam). In addition the carrier gas shares the same working space in the area of the nozzle tip with the protective gas (at different velocity). In this model it is assumed that most of the particles velocity component is due to the carrier gas inside the nozzle, and not by the protective stream gas. This simplification is valid when the ratio between the velocity of the protective gas and carrier gas is close to 0.8 with low speeds, which are the most suitable for laser cladding process (Arrizubieta et al., 2014).

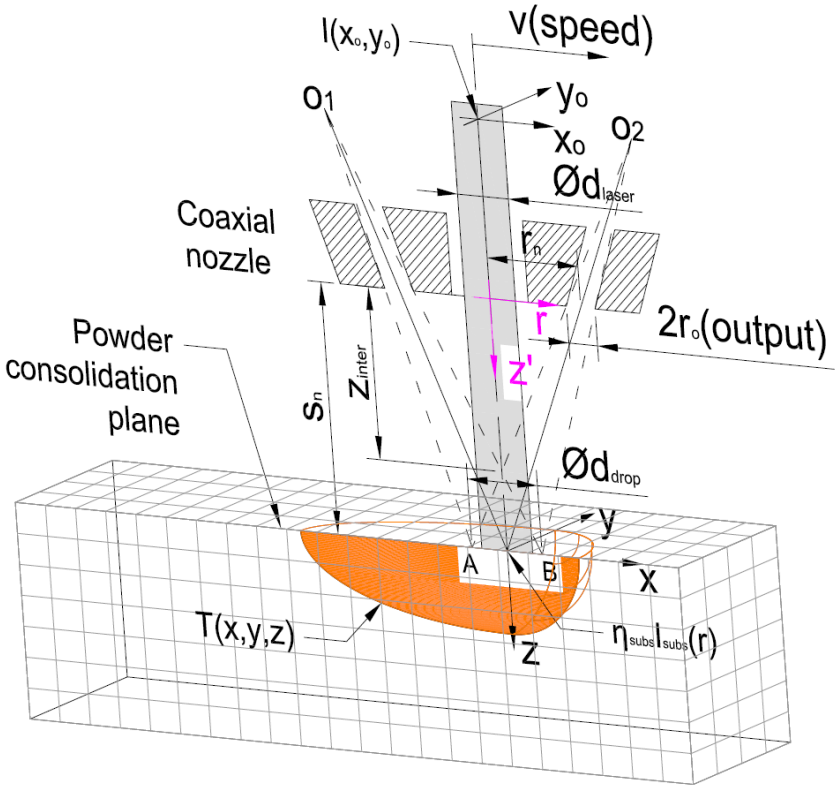

Figure III.4. Schematic powder stream diagram of a coaxial Laser Cladding deposition nozzle, and its interaction with laser beam and substrate (Pinkerton, 2007).

The use of a ratio factor between particle velocity and carrier gas velocity is to model that the net losses in powder velocity due to its multiple collisions within the nozzle must be somehow compensated for by the entraining effect of the carrier gas velocity. As a reference value (Agarwal, 2005) has established that the ratio between particle velocity and drag velocity is about 0.8.

Experimentally, empirical equations have been developed for powder flows dragged by gas under different conditions. One of the most popular is the Hinkle ratio (Hinkle, 1953)

for horizontal tubes, in which the sliding velocity of solid particles with respect to the gas velocity stream by which it is drawn can be defined as (Eq. III.4):

$$\frac{v_p}{v_g} = 1 - 0.044 d_p^{\,0.3} \rho_p^{\,0.5} \qquad \textit{Eq. III.4}$$

This correlation allows obtaining approximate values of sliding velocities according to the results of (Agarwal, 2005), as function of factors relatively simple to quantify: the mean diameter of the particles and their density. For that reason, the Hinkle ratio has been chosen for this model. Therefore, the velocity of the particle in steady state will be (Eq. III.5):

$$v_p = \frac{Q_g (250 - 11 d_p^{\,0.3} \rho_p^{\,0.5})}{1000 \pi r_n r_o} \qquad \textit{Eq. III.5}$$

This equation will be valid while the biphasic flow regime is laminar ($\mathrm{Re_p}$ <1000), therefore it is necessary to check this condition using (Tabernero et al., 2010), calculated by (Eq. III.6):

$$Re_p = \frac{\rho_p d_p \left| v_g - v_p \right|}{\mu_{gas}} \qquad \textit{Eq. III.6}$$

In the case of $Re_p \geq 1000$ the velocity of the powder particles will be taken as directly coupled to the velocity of the carrier gas $v_p = v_g$ (Pinkerton et al., 2007). From (Pinkerton, 2007) it is assumed that the main direction of velocity that attenuates the laser beam is the vertical component (in z' direction), where it is calculated as (Eq. III.7):

$$v_{pz'} = \frac{v_p s_n}{\sqrt{s_n^2 + r_n^2}} \qquad \textit{Eq. III.7}$$

The relative Reynolds number should be calculated for each point (with its respective local velocities) in the space between the nozzle and the substrate where the $\mathrm{powder{+}gas}$ interaction exists. However, taking into account only the velocities in the z' direction (Eq. III.7) and according to *Assumption 5*, the values of v_g, v_p and $v_{pz'}$ will be taken as representative of the entire biphasic stream.

In (Fig. III.4), the points A-B define the diameter where the value of the powder mass flow concentration (*Assumption 7*) has fallen to a value e^{-2} of the maximum concentration value and this fall allows delimiting the part of the powder stream that effectively intervenes in the attenuation of the laser beam.

In practical mode, the value of distances A-B and s_n can be obtained from the study of images of the nozzle (in this case coaxial), as long as that it is fulfilled that the dispersion of the powder jet from its tip is approximately linear (as it is shown by the lines drawn in (Fig. III.5).

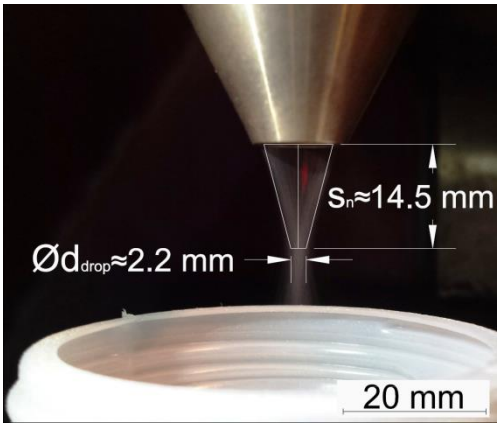

Figure III.5. Example of photography with image processing from which it is possible to obtain an estimate value of the distances A-B and s_n.

From (Fig. III.4), the z-coordinate according to the $[r, z']$ coordinate frame of reference where the powder attenuation start, can be deduced and this is given by (Eq. III.8):

$$z'_{inter} = \frac{s_n(d_i - \phi d_{laser})}{\phi d_{drop} + d_i} \qquad \textit{Eq. III.8}$$

Where $d_i = 2(r_n - r_o)$

From (Pinkerton, 2007) it is known that the powder flow, assumed with a Gaussian density as a function of r coordinate (symmetrical to the z' axis), is variable up to a consolidation plane. This plane, parallel to the r axis, it is located in the $z' = s_n$ coordinate, as seen in the (Fig. III.4). The following relation gives the powder mass flow concentration (Eq. III.9):

$$P(z', r) = \frac{C_o}{\pi r_s^2}\left[Exp\left(-\frac{2a_1^2}{r_s^2}\right) + Exp\left(-\frac{2a_2^2}{r_s^2}\right)\right] \qquad \textit{Eq. III.9}$$

Where $a_1 = \left| \left(\frac{s_n - z'}{s_n} \right) r_n - r \right|$, $a_2 = \left| \left(\frac{s_n - z'}{s_n} \right) r_n + r \right|$ and $r_s = r_o + \frac{z'(\phi d_{drop} - 2r_o)}{2s_n}$

It is necessary to establish the value of C_o, since the peak concentration value (expressed by $P(z', r)$) is variable as the powder mass concentration is consolidated until reaching the working plane (Arrizubieta et al., 2014; Tabernero et al., 2010). This can be calculated by considering a mass balance for different planes before reaching the work plane in $z' = s_n$.

For a plane at distance $z' = \text{constant}$, the total mass flow (m') must be the same ($m' = \text{constant} \ \forall \ z'_{plane}$), therefore the density in powder flux is only a function of r (Fig. III.4). Thus $P = P(r)_{z_{\text{constant}}}$ and from the Cylinder Method (Leithold, 1996) the total mass flow of powder will be (Eq. III.10):

$$m' = 2\pi \int_0^{\ell_{catch}} r * P(r) dr = 2\pi \int_0^{\ell_{catch}} r \left\{ \frac{C_o}{\pi r_s^2} \left[Exp\left(-\frac{2a_1^2}{r_s^2} \right) + Exp\left(-\frac{2a_2^2}{r_s^2} \right) \right] \right\} dr \qquad \textit{Eq. III.10}$$

Where $\ell_{catch} = r_n + 2r_o$

The upper limit of integral (ℓ_{catch}) has been defined in such a way that it encompasses the entire space of powder outlet from the nozzle, then integrating (Eq. III.10) and clearing C_o (Eq. III.11):

$$C_o = \frac{-2m'Exp(b_1)\cdot b_2}{\left\{ Exp\left(\frac{16\cdot\phi d_{drop} {r_n}^2 s_n}{{b_3}^2 b_2}\right)\cdot\left[\sum_{j=0}^{1} Exp\left(\frac{32 r_n s_n\cdot c_j}{{b_2}^{(j+1)} b_3}\right) - 2Exp\left(\frac{8 s_n \ell_{catch}\left(2r_n z' b_3 + s_n\left(\sum_{k=0}^{1} c_k(2r_n-(2k-1)\ell_{catch})\right)\right)}{b_3 {b_2}^2}\right)\right] b_2 + 2\sqrt{2}\sqrt{\pi} r_n Exp(b_1)\cdot(z'-s_n)\left[\sum_{i=-1}^{1}(3|i|-2)*erf\left(\frac{2\sqrt{2}\cdot c_i)}{b_2}\right)\right]\right\}}$$

Eq. III.11

Where:

$$c_i = r_n z' - r_s s_n + i s_n \ell_{catch}$$

$$c_j = (1-j)\ell_{catch} + j\cdot\phi d_{drop}$$

$$c_k = \phi d_{drop}(1-k) + 2kr_o$$

$$b_1 = \frac{8s_n(2r_n\ell_{catch}z'(\phi d_{drop}-2r_o)^2 + s_n(\phi {d_{drop}}^2({r_n}^2 + 2r_n\ell_{catch} + {\ell_{catch}}^2) - 4\cdot\phi d_{drop} r_o {\ell_{catch}}^2 - 4{r_o}^2\ell_{catch}(2r_n-\ell_{catch})))}{(\phi d_{drop}-2r_o)^2\cdot(z'(\phi d_{drop}-2r_o)+2r_o s_n)^2}$$

$$b_2 = z'(\phi d_{drop}-2r_o) + 2r_o s_n$$

$$b_3 = (\phi d_{drop}-2r_o)$$

The effect of the variable C_o in powder flux as it consolidates on the working plane is shown in (Fig. III.6) for both powder mass flow and a nozzle dimensions of arbitrary values.

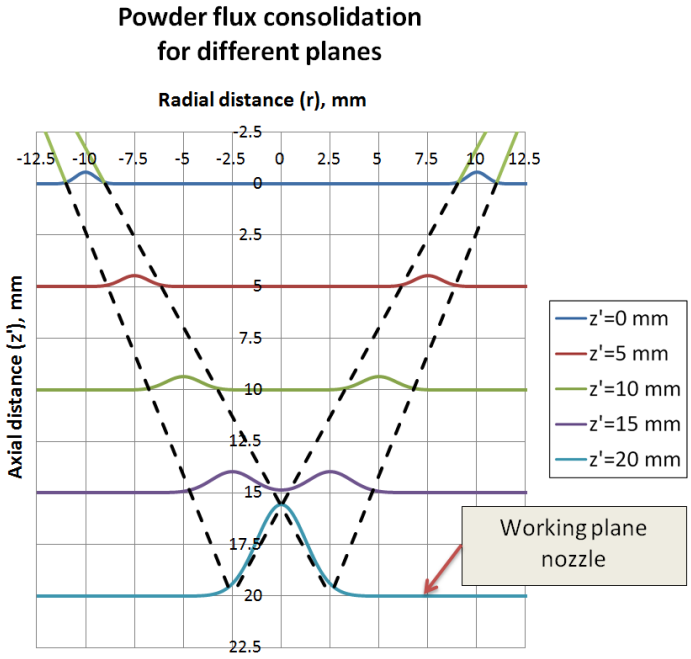

Figure III.6. Effect of value C_o over the powder flux concentration for a nozzle with arbitrary powder mass flow and fixed dimensions: $\phi d_{drop} = 5$, $r_o = 1$, $s_n = 20$ and $r_n = 10$. All dimensions in mm.

III.3.2 Energy and Mass Balance on the Substrate Surface by Interaction of Powder and Laser Beam

From (Pinkerton, 2007) the intensity of the laser beam taking into account the total attenuation due to the "shadow accumulated" as result of the powder flow for different z' planes (from coordinate z'_{inter} to s_n) for any distribution with cylindrical symmetry (respect to the z' axis), is given by (Eq. III.12):

$$I_{att}(z',r) = \varepsilon_m * f_{\substack{shape \\ energy}}(0,r) * \left(1 - \frac{3}{2v_{pz}, d_p \rho_p} \int_{z'_{inter}}^{s_n} P dz'\right) \qquad \textit{Eq. III.12}$$

Where ε_m models the maximum value of energy density for a given distribution as a function of P_{laser} and ϕd_{laser}. In (Eq. III.12) $f_{\substack{shape \\ energy}}$ determines the radial distribution of the laser beam energy in the $z' = 0$ plane (before interaction with powder) for any value

of r coordinate. The (Table III.1) presents the formulas of $f_{\substack{shape \\ energy}}$ and ε_m for the Cylindrical, Gaussian and TEM01 energy distributions (Eq. III.13) to (Eq. III.15).

Table III.1: Energy density distributions for different types of laser beams with circular symmetry.

Cylindrical:

$$f_{\substack{shape \\ \text{cylindrical}}}(0,r) = \frac{1}{2} - \frac{\text{sgn}(2|r| - \phi d_{laser})}{2} \qquad \textit{Eq. III.13}$$

With $\varepsilon_{m\_\text{cylindrical}} = \frac{4P_{laser}}{\pi \cdot \phi d_{laser}{}^2}$, boundary condition $P_{laser}(r \mid r > \phi d_{laser}/2) = 0$

Gaussian:

$$f_{\substack{shape \\ \text{gaussian}}}(0,r) = Exp\left(\frac{-8r^2}{\phi d_{laser}{}^2}\right) \qquad \textit{Eq. III.14}$$

With $\varepsilon_{m\_\text{gaussian}} = \frac{8P_{laser}}{\pi \cdot \phi d_{laser}{}^2}$, boundary condition $P_{laser}(r \mid r = \phi d_{laser}/2) = \varepsilon_{m\_\text{gaussian}} e^{-2}$

TEM01:

$$f_{\substack{shape \\ TEM\,01}}(0,r) = \frac{r^6 Exp\left(\frac{-32r^2}{\phi d_{laser}{}^2}\right)}{\phi d_{laser}{}^6} \qquad \textit{Eq. III.15}$$

With $\varepsilon_{m\_TEM\,01} = \frac{524288e^8 P_{laser}}{\pi \cdot \phi d_{laser}{}^2 (3e^8 - 379)}$, boundary condition

$P_{laser}(r \mid r = \phi d_{laser}/2) = \varepsilon_{m\_TEM\,01}(512/27)e^{-5}$

III.3.3 Energy Quantification for Powder Temperature by use of Negative Enthalpy

In addition to the net effect of the shadow of particles as a whole in the attenuation of energy available from the laser beam to form the melt pool in the substrate area, the powder itself absorbs part of energy. This "powder energy" (expressed as high temperature of itself) is not all useful, since a part of the stream of particles falls out of the useful area of work (determined by ϕd_{laser}, where it is assumed that all the material that hits the zone adheres). The quantification of this energy is expressed as a set of temperatures of the particles that reach the substrate (T_{powder}). Depending on the local value for temperature of powder particles when it reaches the substrate, it is possible that there is a contribution or a decrease of the local energy for the melt pool formation.

This enthalpy can be positive or negative, or both for different locations, depending of process parameters and position of hitting of powder particles within melt pool. The power value of laser beam that increases the powder temperature by interaction with it will be taken as the one that would be reached without effects of attenuation by shadow of other powder particles above. This effect occurs while the powder reaching the consolidation in the working plane coordinates ($z' = s_n$). Therefore the power useful in the heating of powder particles will be the intensity (I_{laser}) corresponding to the ($z' = 0, r$) coordinate, that is $f_{\substack{shape \\ energy}}(s_n, r) = f_{\substack{shape \\ energy}}(0, r)$. For a small spherical particle the energy balance is expressed as (Pinkerton et al., 2007), by (Eq. III.16):

$$\eta_{powder} * \varepsilon_m * f_{\substack{shape \\ energy}}(0, r) * \left(\frac{\pi d_p^{\,2}}{4} \right) \Delta t = \frac{\pi d_p^{\,3} \rho_p c_p \Delta T}{6} \qquad \textit{Eq. III.16}$$

For simplification the powder temperature will be taken as the average of the temperatures in the limit conditions of its trajectories (Pinkerton et al., 2007), that is to say the temperature of the particles that reach the middle zone of laser beam diameter $T_{powder}(s_n, 0)$ and that of the end in the zone of interaction $T_{powder}(s_n, \pm \phi d_{laser} / 2)$.

Thus clearing the value of ΔT and calculating the value of Δt as the time of interaction $\Delta t = \Delta \ell_{\substack{interaction \\ laser\_beam}} / v_{pz'}$, from Eq. 16 is obtained, (Eq. III.17):

$$T_{powder}(s_n, 0) = \frac{3 \eta_{powder} \varepsilon_m f_{\substack{shape \\ energy}}(s_n, 0)}{2 d_p v_{pz'} \rho_p c_p} * \ell_{\substack{powder\_center \\ laser\_beam}} + T_{o\_powder} \qquad \textit{Eq. III.17}$$

Where $\ell_{\substack{powder\_center \\ laser\_beam}}$ is the interaction length for the radius $r = 0$ in the coordinate $z' = s_n$ from focus O_1 or O_2 (according to each case), which from (Fig. III.4) is given by (Eq. III.18):

$$\ell_{\substack{powder\_center \\ laser\_beam}} = \frac{\phi d_{laser} \sqrt{(r_n^2 + s_n^2)}}{2 r_n} \qquad \textit{Eq. III.18}$$

In the case of $T_{powder}(s_n, \pm \phi d_{laser} / 2)$ the temperature is given by (Eq. III.19):

$$T_{powder}(s_n, \phi d_{laser}/2) = \frac{3\eta_{powder}\varepsilon_m f_{shape}^{energy}(s_n, \phi d_{laser}/2)}{2d_p v_{pz} \rho_p c_p} * \ell_{\substack{powder\_edge \\ laser\_beam}} + T_{o\_powder} \qquad \textit{Eq. III.19}$$

Where $\ell_{\substack{powder\_edge \\ laser\_beam}}$ is the interaction length from focus O_1 or O_2 (according to each case), to the coordinate $r = \pm\phi d_{laser}/2$ (+ for stream from vertex O_1 and – for stream from focus O_2) in the $z' = s_n$ plane. From (Fig. III.4) $\ell_{\substack{powder\_edge \\ laser\_beam}}$ is given by (Eq. III.20):

$$\ell_{\substack{powder\_edge \\ laser\_beam}} = \frac{1}{2}\left(\frac{\phi d_{laser}\sqrt{(\phi d_{drop}{}^2 + 4\cdot\phi d_{drop}(r_n - r_o) + 4(r_n^2 - 2r_n r_o + r_o^2 + s_n^2))}}{\phi d_{drop} + 2(r_n - r_o)} \right) \qquad \textit{Eq. III.20}$$

Where the ½ factor before the parenthesis in (Eq. III.20) represents an average that must be interpreted in that way: when observing (Fig. III.4) a particle of powder starting from $O_1 \rightarrow A$ will suffer a zero heating (in no time it touches the laser beam), compared with a particle with $O_1 \rightarrow B$ trajectory that passes completely through laser beam. By symmetry the same can be said of the particles leaving the powder focus O_2 and therefore only the positive coordinate $r = \phi d_{laser}/2$ for the calculation of temperature will be taken and the factor ½ is added.

The mass flows for the same coordinates of powder temperature ($r = 0$ and $r = \phi d_{laser}/2$ in $z' = s_n$ plane) can be calculated from (Eq. III.9) and is given by (Eq. III.21) and (Eq. III.22):

$$P(s_n, 0) = \frac{8m'}{\pi \cdot \phi d_{drop}{}^2} \qquad \textit{Eq. III.21}$$

$$P(s_n, \phi d_{laser}/2) = \frac{8m'}{\pi \cdot \phi d_{drop}{}^2} Exp\left(-2\frac{\phi d_{laser}{}^2}{\phi d_{drop}{}^2} \right) \qquad \textit{Eq. III.22}$$

From (Pinkerton et al., 2007) the total energy flow that is carried by the powder will be, (Eq. III.23):

$$I_{powder}(s_n, r \mid r \le d_{laser}/2) = c_p * P(s_n, r) * \left(T_{\substack{melt \\ powder}} - T(s_n, 0) \right) Exp\left(\frac{r^2}{2\lambda_{powder}{}^2} \right) \qquad \textit{Eq. III.23}$$

Where $\lambda_{powder} = \frac{\sqrt{2} \cdot \phi d_{laser}}{4 \ln\left(\frac{P(s_n, \phi d_{laser}/2) * [T(s_n, \phi d_{laser}/2) - T_{melt}]}{P(s_n, 0) * [T(s_n, 0) - T_{melt}]}\right)}$

It is assumed that no powder falling out of $A_{\substack{spot \\ laser}} = \frac{\pi}{4} \cdot \phi d_{laser}^{\ 2}$ area adheres to the substrate, therefore all energy acquired by this powder steam when heated by the laser beam is lost, thus (Eq. III.24):

$$I_{powder}(s_n, r \mid r > \phi d_{laser}/2 \ \wedge \ r < -\phi d_{laser}/2) = 0 \qquad \textit{Eq. III.24}$$

This energy flow (I_{powder}) can be interpreted as a function of the melting temperatures of powder particles (T_{melt}) and the temperatures of boundary zones in the interaction zone of the melt pool with the substrate $T(s_n, 0)$ and $T(s_n, d_{laser}/2)$. This means actually how much energy is expressed in the form of a negative enthalpy (subtraction of energy from the substrate by impacting of the powder “half melt” against it). The subtraction of that energy will be necessary to achieve the complete liquefaction of the powder particles.

Finally the energy balance on the surface of the substrate in the working plane $z' = s_n$, expressed as intensity I_{subs} is equal to (Eq. III.25):

$$I_{subs} = I(s_n, r) = I_{att}(s_n, r) - I_{powder}(s_n, r \mid r \le \phi d_{laser}/2) \qquad \textit{Eq. III.25}$$

The first term on the right side of (Eq. III.25) is a purely geometric factor, and it is independent of the temperature conditions of powder particles (except in the case that the particles melt, which would cause them to lose their spherical shape). However, due to the effect of surface tension, the particles will tend to maintain their spherical shape even though they are melted.

On the other hand the second term of (Eq. III.25) depends very much on the relative difference between temperatures $T(s_n, r) - T_{melt}$. This is important since the greater the difference between these two values, less energy intensity will reach the substrate. Therefore, it is necessary to establish as precisely as possible the powder temperature to correctly quantify the amount of energy available.

III.3.4 Modelling of Phase Change for Inconel 718 and Temperature-Dependent Thermal Properties

Assuming temperature-independent properties in a process that involves temperatures can lead to a large error when modelling values of characteristics of the medium (by example the thermal field itself). The properties of materials are in general temperature-dependent.

A phase change is an important problem, as it leads to a discontinuity in the values of thermal properties. One way of solving this is to make use of modified properties via a corrector that takes into account the latent fusion heat (ΔL_f), as in the case of specific heat in the solidification range (Peyre et al., 2008). The same can be done for the enthalpies associated with this phase change for the different temperature ranges (Kamara et al., 2011). Thus from (Bandyopadhyay et al., 2002; Kamara et al., 2011; Mishra and Yadava, 2013), and the (Eq. III.26) to (Eq. III.28) for each range of temperature in the material it is possible to elaborate the table of properties for Inconel 718 over a wide temperature range, (Table III.2). The reference temperature for the properties is $T_o = 298K$.

For the range: $T \leq T_S$ $$\mathrm{H}(T) = \rho \int_{T_o}^{T} c_p dT$$ *Eq. III.26*

For the range: $T_S < T \leq T_L$ $$\mathrm{H}(T) = \rho \int_{T_o}^{T_S} c_p dT + \rho L_f \left(\frac{T - T_S}{T_L - T_S} \right)$$ *Eq. III.27*

For the range: $T > T_L$ $$\mathrm{H}(T) = \rho \int_{T_o}^{T_S} c_p dT + \rho L_f + \rho \int_{T_L}^{T} c_p dT$$ *Eq. III.28*

Table III.2: Properties of Inconel 718 as function of temperature.

Temperature (K)	Density (kg/m^3)	Enthalpy (J/m^3)	Specific heat (J/(kg.K))	Thermal conductivity (W/(m.K))	Thermal diffusivity (m^2/s)*10^{-6}
298	8240	0	439	10.3	2.85
373	8221	2.73E+08	454	11.5	3.08
473	8193	6.51E+08	473	13.2	3.41
573	8162	1.05E+09	493	15	3.73
673	8130	1.46E+09	512	16.9	4.06
773	8095	1.88E+09	532	18.8	4.37
873	8058	2.33E+09	551	20.9	4.71
973	8019	2.79E+09	582	22.8	4.89
1073	7978	3.26E+09	604	23.8	4.94
1173	7934	3.75E+09	626	25.8	5.19
1273	7889	4.25E+09	648	28	5.48
1373	7841	4.77E+09	670	30.2	5.75
1473	7792	5.30E+09	692	32.4	6.01
1533 (S)	7761	5.63E+09	710	33.7	6.12
1617 (L)	7579	7.34E+09	769	26.8	4.60
1723	7483	8.00E+09	736	28.2	5.12
1800	7414	8.36E+09	712	29.4	5.57
1973	7258	9.83E+09	659	31.7	6.63
2100	7143	9.90E+09	619	33.5	7.57

(S) Solidus temperature (L) Liquidus temperature

The thermophysical properties of the liquid phase are different from those of the solid alloy (for example thermal conductivity and thermal diffusivity). The values of the thermophysical properties in the “mushy zone” will depend on the amount of liquid and solid fraction. The solid fraction differs with the cooling rate, then the thermophysical ratios and temperature ratios also differ with the cooling rate (Mills, 2002). As a simplification to this model and in order to avoid discontinuities of the thermal properties values within the “mushy zone”, a linear behaviour is assumed, and is given by (Eq. III.29):

$$Th_{prop}(T_{\underset{zone}{mushy}}) = \frac{Th_{prop}(T = T_L) * (T_{\underset{zone}{mushy}} - T_S) + Th_{prop}(T = T_S) * (T_L - T_{\underset{zone}{mushy}})}{\Delta T_{Liq\_Sol}} \qquad \textit{Eq. III.29}$$

For the range: $T_S < T < T_L$

III.3.5 Determination of Powder Temperature as Function of Laser Beam Power and Thermal Properties of Material

The method consists in establishing an iterative loop between the material properties (starting from a given temperature), and the temperature obtained with the properties from that initial temperature until a balance of energy is established.

If the temperature of the material does not coincide within a certain range with the calculated temperature based on the thermal properties, an average of the values of both temperatures (material and thermal properties) is calculated and the loop is reinitiated with the new “average temperature”.

The convergence of the iteration cycle (based on the difference between the powder temperature and that calculated in the previous cycle on the basis of thermal properties), is less than a certain threshold, and the final value of temperature get from loop will be the used as the “good value” of both temperature material and thermal properties for that material. The scheme of loop is shown in (Fig. III.7). It should be taken into account that a basic idea of the model is that each powder particle has essentially the same instantaneous temperature in its entire volume (Biot number << 1). For Laser Cladding process this Biot number of powder particles is in the order of $d_p/6$, so a "lumped" model for the temperature of particles is justified (Ibarra-Medina and Pinkerton, 2010; Zohdi, 2015).

Temperature changes by laser-powder interaction are important because although the powder interaction time in the laser beam is very short (Meriaudeau et al., 1997) the high powers involved (in the order of 10^7~10^8 W/m^2) can result in a phase change (Solidus-Liquidus), or a change of the energy carried by the powder depending on its sensible temperature (enthalpy). For this specific model, it is established that the $\Delta T_{\text{setpoint}} = \left| T_{powder} - T_i \right| \leq 1K$.

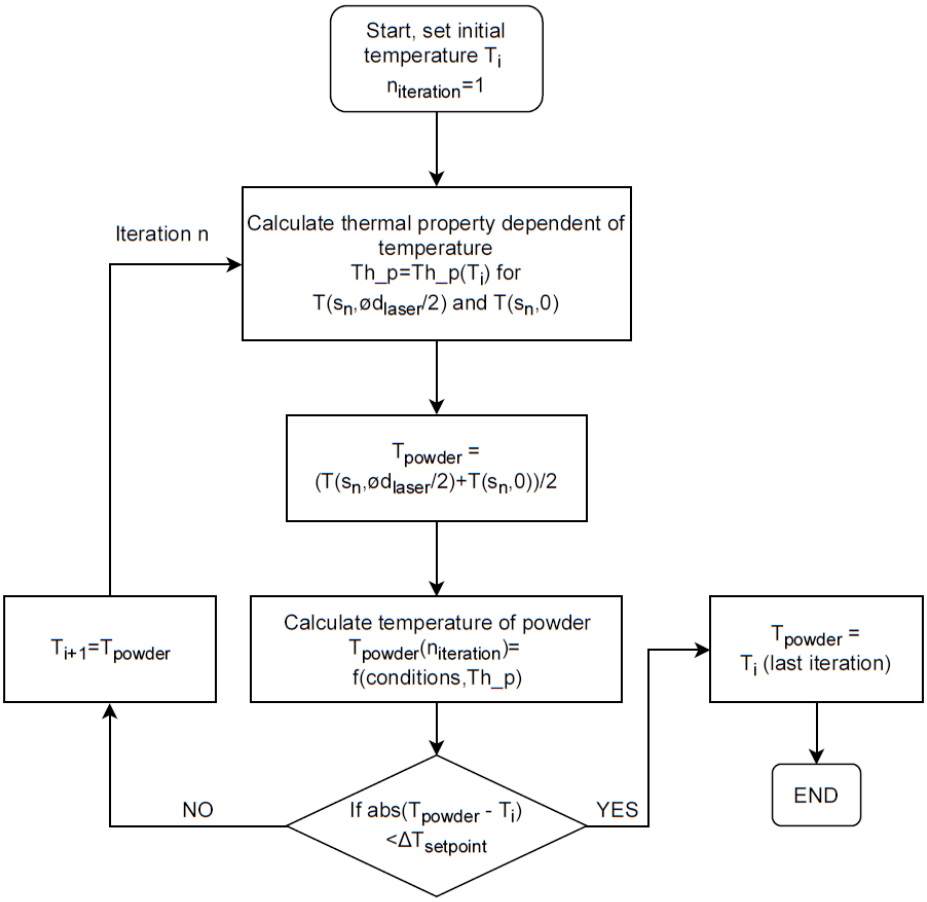

Figure III.7. Iteration scheme to find the actual temperature of powder reaching the substrate taken account the temperature-dependent properties of the material.

III.3.6 Effect of Change in Values of the Main Variables for Powder Attenuation over the Available Laser Beam Power for Substrate

The effect of parameters interaction will be tested for a constant nozzle geometry ($[r_n, r_o, s_n] = \text{constant}$), and for some material and process variables staying constants ($\left[Q_g, \mu_{gas}, \rho_p, \phi d_{drop}, \eta_{powder}\right] = \text{constant}$).

Instead we will vary $d_{p(mean)}$ = [60, 120] μm, m' = [10, 15, 20] gr/min, and P_{laser} = [200, 600] W (ϕd_{laser} = 1mm, with cylindrical power distribution). The results are shown in (Fig. III.8) to (Fig. III.11).

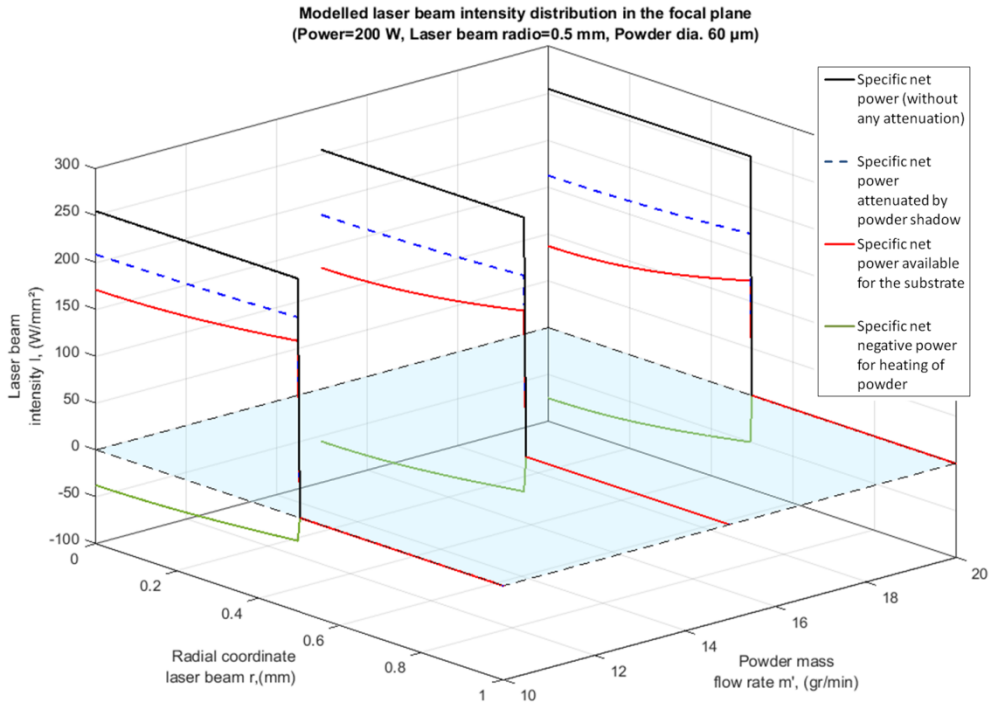

Figure III.8. Effect on the net power available for melt pool formation on the substrate by interaction of laser beam with powder for a given nozzle geometry and with variation of the powder flux ($P_{laser} = 200W$, $d_{p(mean)} = 60\mu m$).

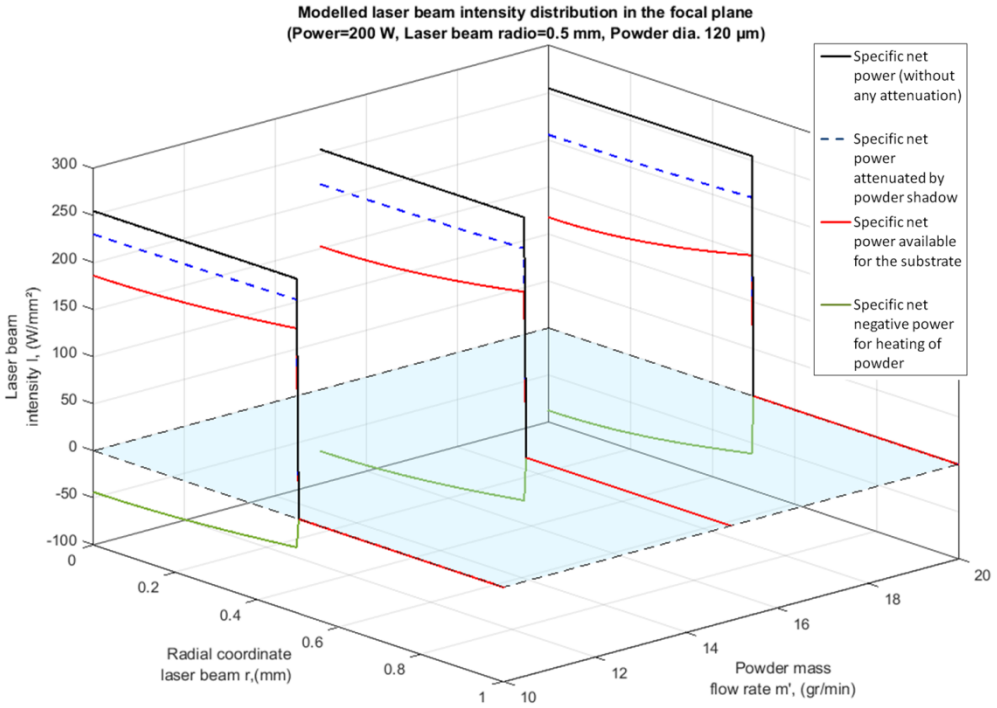

Figure III.9. Effect on the net power available for melt pool formation on the substrate by interaction of laser beam with powder for a given nozzle geometry and with variation of the powder flux ($P_{laser} = 200W$, $d_{p(mean)} = 120\mu m$).

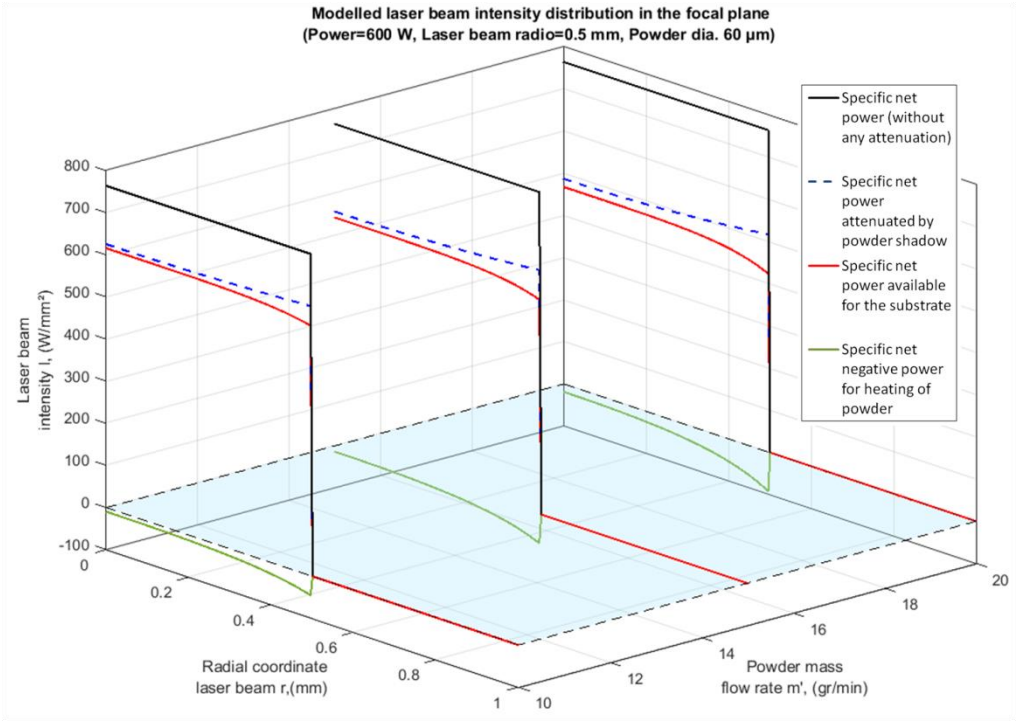

Figure III.10. Effect on the net power available for melt pool formation on the substrate by interaction of laser beam with powder for a given nozzle geometry and with variation of the powder flux ($P_{laser} = 600W$, $d_{p(mean)} = 60\mu m$).

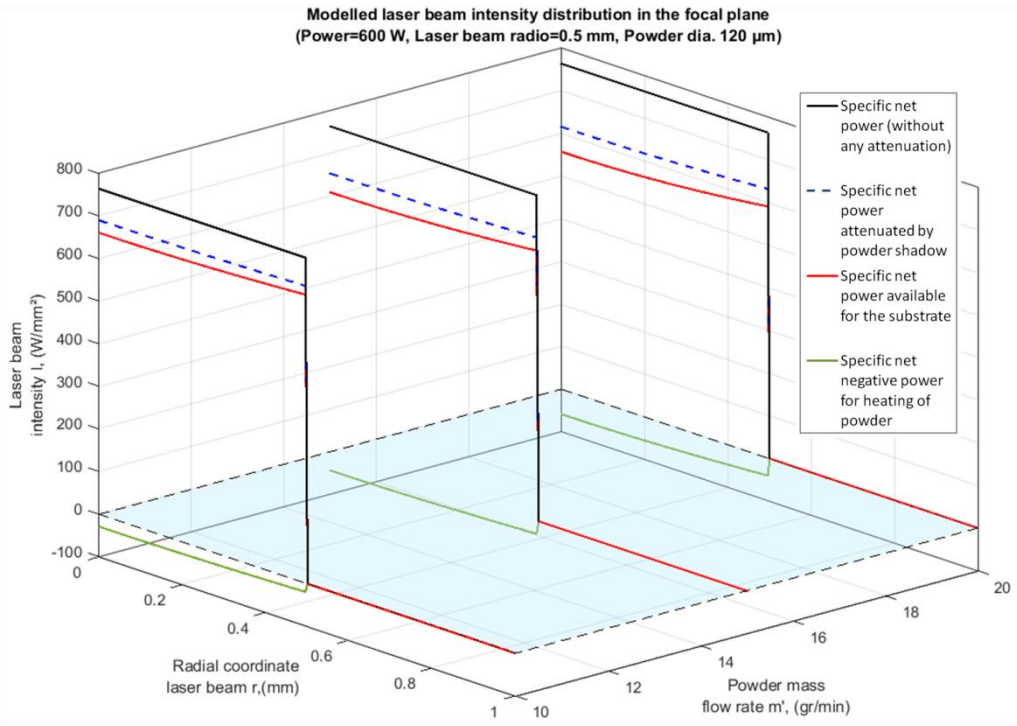

Figure III.11. Effect on the net power available for melt pool formation on the substrate by interaction of laser beam with powder for a given nozzle geometry and with variation of the powder flux ($P_{laser} = 600W$, $d_{p(mean)} = 120\mu m$

III.3.7 Application of Energy Balance by Means of a General Type Heat Source on the Substrate to Obtain the Temperature Field

Analytical heat sources are very useful in describing the temperature field in areas both inside and outside the melt pool. Some examples of analytical heat sources of various types can be found in these references (Darmadi et al., 2011; Peyre et al., 2008; Pinkerton and Li, 2004; Van Elsen et al., 2007). In the case of this model, the solution obtained by Levin (Levin, 2008) will be used as base because it has the following advantages:

- Its formulation is general, that is to say the surface energy density can have any shape necessary on the substrate and not limited to "classic" energy distributions like the Gaussian, Top Hat, Point Source, Cylindrical, etc. This is important due to the fact that, for example in the case of Point Source energy distribution, singularities are generated within the melt pool (such as infinite temperatures), giving rise to unrealistic thermal fields (Darmadi et al., 2011). In our case the attenuation of powder results to a non-standard laser beam energy distribution that the Levin's Analytical Solution is capable of handling.
- The heat source formulation when the differential equation is solved (in steady state), takes into account the particular contour conditions generated due to a heat source moving in a mobile frame of reference. The use of a moving frame of reference for solving the heat equation is because analytical solutions are either too complicated to implement by time dependence or because is inconsistent with the character of source intensity, which supposed to be constant in time and symmetric along axis of moving direction. Using proposed exponential transformation of moving coordinates (Levin's analytical solution), one can express the fundamental solution of the problem as the generalization of the Poisson's equation solution (Levin, 2008). This result in the fact that the cooling rates reached after the solidification of the melt pool can be modelled by this formulation, but not by simpler ones. The advantage of this is that, for example, the formation of martensitic structures at relatively high scanning speeds of laser beam in the substrate can be explained with a relatively simple model.

For a heat source type heat flux with intensity $I = I(x_o, y_o)$ [W/m^2] in local coordinates of frame of reference (x_o, y_o), constant in time, moving at velocity v over the surface of a semi-infinite solid ($z \geq 0$), with z pointing towards to the interior of a homogeneous and

isotropic solid in Cartesian coordinates $[x, y, z]$ in solidarity with the frame of reference of the heat source according to (Fig. III.4), the following mathematical formulation can be applied (Eq. III.30):

$$\frac{\partial^2 T}{\partial x^2}+\frac{\partial^2 T}{\partial y^2}+\frac{\partial^2 T}{\partial z^2}+\frac{v}{\alpha}\frac{\partial T}{\partial x}=-\frac{I\left(x_o, y_o\right)}{k}\delta(z) \qquad \textit{Eq. III.30}$$

Under the boundary condition $T|_{(x^2+y^2+z^2)\to\infty}=0$. The solution for (Eq. III.30) is expressed by (Eq. III.31):

$$T(x,y,z)=2\int_{-\infty}^{\infty}\int_{-\infty}^{\infty} G_R\begin{pmatrix} x, y, z, \\ x_o, y_o, 0\end{pmatrix}\frac{I\left(x_o, y_o\right)}{k}dx_o dy_o \qquad \textit{Eq. III.31}$$

Where $R=\sqrt{(y-y_o)^2+z^2}$ is a radial coordinate, and

$$G_R\begin{pmatrix} x, y, z \\ x_o, y_o, 0\end{pmatrix}=$$

$$\frac{vExp\left(-\frac{v(x-x_o)}{\alpha}\right)}{4\pi\alpha}\left[\begin{array}{l}\left(\left(1-Exp\left(-\frac{v(x-x_o)}{\alpha}\right)\right)^2+\left(\frac{Rv}{\alpha}Exp\left(-\frac{v(x-x_o)}{\alpha}\right)\right)^2\right)^{-\frac{1}{2}} \\ -\left(\left(1+Exp\left(-\frac{v(x-x_o)}{\alpha}\right)\right)^2+\left(\frac{Rv}{\alpha}Exp\left(-\frac{v(x-x_o)}{\alpha}\right)\right)^2\right)^{-\frac{1}{2}}\end{array}\right]$$

The previous expression is the principal part of the Green's function, associated with Laplacian operator and boundary conditions for analytical solution of (Eq. III.30).

The (x_o, y_o) coordinates that define the energy density in the surface plane of the substrate that according to (Fig. III.4) lie in the same coordinate of powder consolidation plane and working distance of the nozzle ($z'=s_n$), therefore the heat flux $I\left(x_o, y_o\right)=I_{subs}$.

First, a transformation of coordinates is necessary to apply the (Eq. III.31) from I_{subs} (Eq. III.25) to $I\left(x_o, y_o\right)$. The I_{subs} is defined solely as a function of r in the working plane $z'=s_n$, therefore $I_{subs}=I(s_n, r)$ becomes only $I_{subs}=I_{subs}(r)$. In addition, and since the heat source moves exclusively on the surface of the solid, $(z=0)$ and the z' axis of the nozzle is in the same direction as that of the substrate (z), the transformation of coordinates for (Eq. III.31) is given by the radial coordinate $r=f(x_o, y_o)$, (Eq. III.32):

$$r = \sqrt{x_o^2 + y_o^2} \qquad \textit{Eq. III.32}$$

Finally taking into account the absorptivity of the substrate η_{subs} and the coordinate transformation, the temperature field in the melt pool is given by (Eq. III.33):

$$T(x,y,z) = 2\int_{-\infty}^{\infty}\int_{-\infty}^{\infty} G_R \begin{pmatrix} x, y, z, \\ x_o, y_o, 0 \end{pmatrix} \frac{\eta_{subs} I_{subs}(r)}{k} dx_o dy_o \qquad \textit{Eq. III.33}$$

It is important to remember that the thermal properties over time (not space) remain constant.

III.3.8 Determination of Melt Pool Temperatures as Function of Attenuated Laser Beam and Thermal Properties of Material

In the same way that temperature-dependent thermal properties values $Th_{prop}(T)$ have been used for calculate powder temperatures, and in turn it has been used to calculate the temperature of particles (assumed as uniform) through a iterative loop, it is possible to establish an analogous procedure to determine the thermal field from the incident energy of the laser beam in the substrate ($\eta_{subs} I_{subs}(r)$).

Unlike the procedure for calculating the temperature of the powder (which assumes a uniform temperature in the volume of itself), the substrate size is much larger (assumed to be semi-infinite), and therefore it is not possible to assign to the same in its entire dimension (and especially to the melt pool that is formed), values of temperature-dependent thermal properties uniform. The reason for this last is that each point within the (x, y, z) coordinate system in the domain of the substrate may, in general, have a different value of temperature.

Another important difference is the phase change. In the case of powder heating the melting of the particle is an undesirable effect (it is simpler for powder particles to lose its spherical shape and complicate a lot the modelling of the heating of them). In the case of substrate, the melt pool formation is essential to carry out the cladding process. The Temperature Gradient (G_L) and solidification growth velocity (V) values are very dependent on local properties, and it is necessary to take this effect into account in some way for a better precision of the model.

In order to solve the problem of assigning values to the thermal temperature-dependent properties in the substrate, it has been chosen an approximate solution. The analytical

heat source of Levin (Eq. III.33), allows to calculate temperatures in discrete points considering the thermal properties of material as constant and the thermal field only a function of the relative position of the heat source energy distribution $(x_o, y_o \mid z' = s_n)$ with respect to a substrate coordinate system (x, y, z).

When a thermal property is defined as constant within a volume it is the same as saying that a temperature has been "chosen" for all the thermal properties of the work volume (substrate). The natural question is: what is the temperature that best represents the phenomenon of the thermal field via the values of temperature-dependent properties?

The method is proposed to solve the previous question and overcome this limitation inherent to an analytical resolution method. It consists of establishing an "approximate temperature function" within the melt pool and taking the temperature-dependent properties as a function of that set of "representative temperatures" especially in its nearby area (in the zone of influence of the laser beam).

The method is summarized in the following steps:

- First is necessary to define a working domain in two dimensions of discrete points (centre in the heat source origin $x_o = 0, y_o = 0$); with low step density in its plane of symmetry (xz plane) (Fig. III.4). It is necessary to divide the substrate domain into small sections characterized by their length (called steps), in order to implement the mathematical solution (step length in x and z axes). A convenient dimension to use as a base is the radio of the laser beam. This is because the higher temperature gradients will be found near the melt pool, which is defined by the variable ϕd_{laser} (Assumption 4). In high power density energy sources (10^7~10^9 W/m^2), the most abrupt change in the thermal field is in the vicinity of the heat source reference system (in this case an attenuated modified laser beam) (Araya and Gutierrez, 2006; Pinkerton, 2007; Van Elsen et al., 2007). Therefore all the step sizes for discretization of domain (and the domain size itself) will be a function of the $r_{laser} = \phi d_{laser} / 2$ value. Another phenomenon to take into account is that normally analytical heat sources are symmetrical (Darmadi et al., 2011; Fassani and Trevisan, 2003; Picasso et al., 1994; Trujillo Guillen, 2005), and this allows simplifying the calculation of the number of nodes to calculate the temperature field.
- Second, the proposed domain dimensions are (based on the observation that the greatest change in the temperature gradient occurs around the area of incidence

of the laser beam): domain length along the x axis (in the xz plane) of $-3r_{laser} \leq x \leq 3r_{laser}$, with step $\Delta x = r_{laser}/4$. For the z axis the length of the domain is defined as $0 \leq z \leq 2r_{laser}$, with $\Delta z = r_{laser}/5$. The dimension in the z domain is justified by the fact that for analytical solutions the high-power heat sources are assumed to be of a superficial nature (Araya and Gutierrez, 2006; Trujillo Guillen, 2005), and that the effects towards the interior of the substrate are rapidly attenuated with depth.

- Third, within the domain created in substrate in the second step (xz plane), the iteration scheme of (Fig. III.12) is applied with a similar principle to that used for the thermal temperature-dependent properties of powder. The difference is that it is not possible “respect to the properties” assume the temperature within the melt pool as uniform (as lumped system for powder). Instead of an “unvarying temperature” (referred to a constant value for thermal properties), a representative "set" of them inside the melt pool will be established, and with it, a set of representative thermal temperature-dependent properties via functions $Th_{prop}(T)$ for each point on the domain in the proximity of the origin of coordinates of heat source (that is approximately the same area of the melt pool).
- Fourth, once the corresponding $Th_{prop}(T)$ properties are calculated, they will be used in the calculation of thermal field via the analytical solution of (Eq. III.33). The approximate thermal properties are calculated by layers for different z values along x local coordinates for each z coordinate, thus the thermal properties will become of the $Th_{prop}(T_{aprox}(z))$ shape.

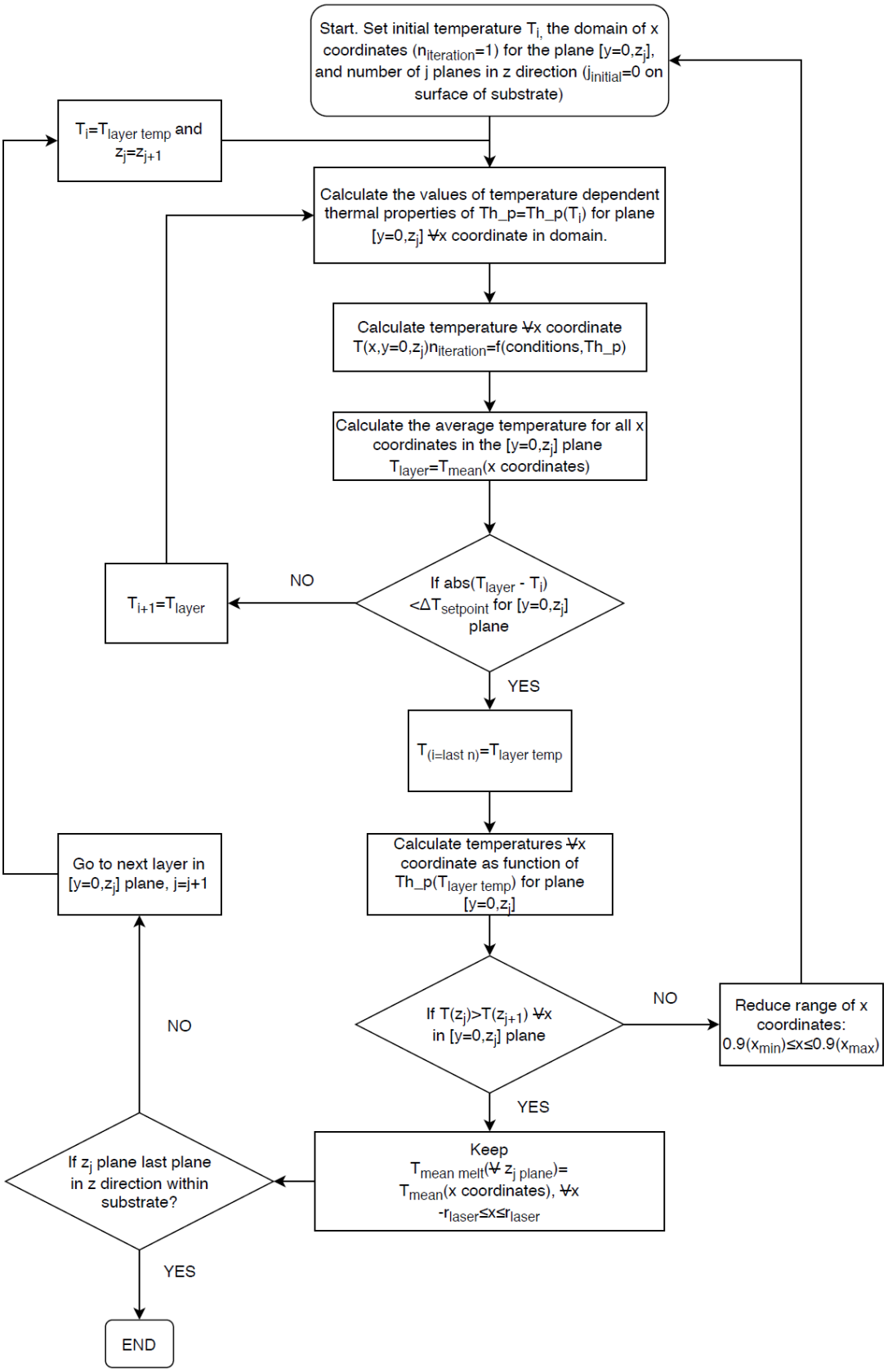

Figure III.12. Interaction scheme to determine thermal properties as function of approximate temperatures for the melt pool volume and nearby zones.

In the case of temperature profiles that are calculated using the algorithm showed in Fig. 12 and applied to specific case for $r_{laser} = 0.5\ mm$ (plane xz of (Fig. III.4)), it is important to note that a possible problem can occur at the domain ends ($-3r_{laser} \le x \le 3r_{laser}$), (Fig. III.14).

Near of domain ends the temperature profiles have almost crossed one over another (overlap), which is at level of thermal field physically impossible. If that case occurs it means that there is something wrong in the convergence criterion (via algorithm) for the mathematical solution for the temperature field. The proximity of the lines for temperature profiles for different substrate depths is much less in the central region for each one of z planes (near of x axis origin). This is because in that zone a higher temperature gradient for different z planes is found. Because it has not been possible to find data for thermal properties of alloy Inconel 718 for very high temperatures it has been decided to use the average temperature over a certain domain of the x coordinate to avoid extrapolate thermal properties in a range beyond that defined in (Table III.2). This range has been defined as $-r_{laser} \le x \le r_{laser}$, and can be modified according to the scheme of (Fig. III.12) to achieve the convergence of the solution by algorithm.

The scheme of (Fig. III.7) and (Fig. III.12) will be applied to a specific case with the following parameters (Table III.3).

Table III.3: Example parameters for application of thermal field model for a specific Laser Cladding Process.

$Q_{g(\text{normalized})} = 4.33*10^{-5}\ \text{m}^3/\text{s}$	$\phi \text{d}_{\text{drop}} = 2.2\ \text{mm}$
μ_{gas}=2.125*10^{-5} kg/(m.s) [Argon]	$\phi \text{d}_{\text{laser}}$=1 mm
r_{n}=5.275 mm	m'=1.463*10^{-4} kg/s
2r_{o}=0.45 mm	P_{laser}(cylindrical)=571 W
$s_n = 14.5\ \text{mm}$	$\eta_{\text{powder}} = \eta_{\text{subs}}$=0.4
$\rho_p = \rho_{\text{subs}}$=8240 kg/m^3	v=8.7 mm/s
$d_{p(mean)} = 80\ \mu\text{m}$	

Applying (Eq. III.3) to (Eq. III.29) for powder heating, the data of (Table III.2), and the algorithm of (Fig. III.7), the quantification of energies for the interaction of the laser beam with powder (Eq. III.25), is shown in (Fig. III.13).

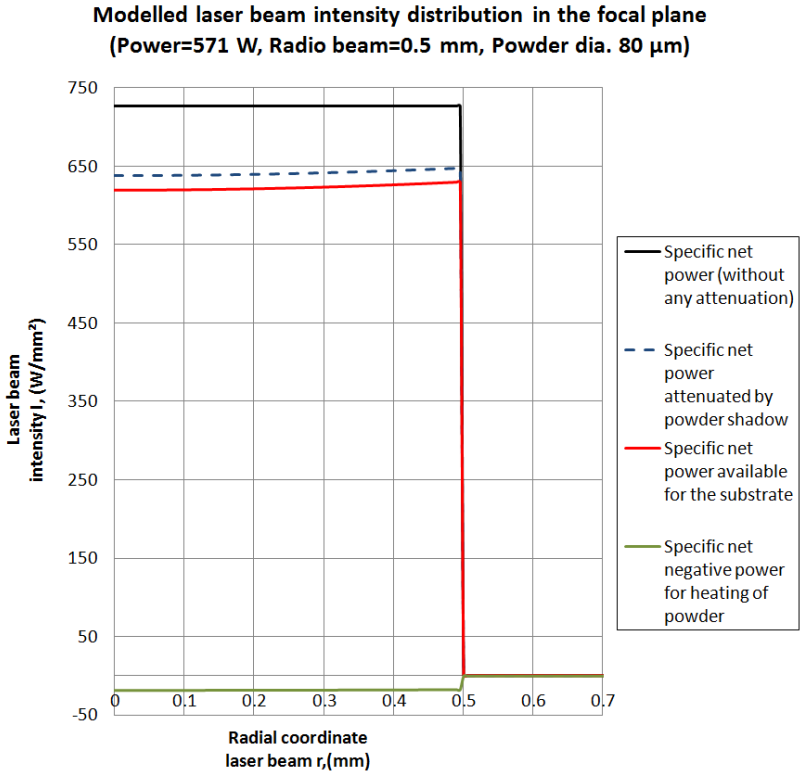

Figure III.13. Total specific energy available for substrate as function of parameters in (Table III.3) at the focal plane of laser beam (red line). The figure takes account the quantification of the effects on power by the interaction between laser beam and powder (Eq. III.25)

The approximate temperature profiles in the melt pool for different distances (planes) from the surface of the substrate ($z=0$) for the xz plane of (Fig. III.4) are calculated from the specific power available for substrate. This power is obtained from the interaction of laser beam-powder showed on (Fig. III.13) and the (Eq. III.33). The resulting temperature profiles are shown in (Fig. III.14).

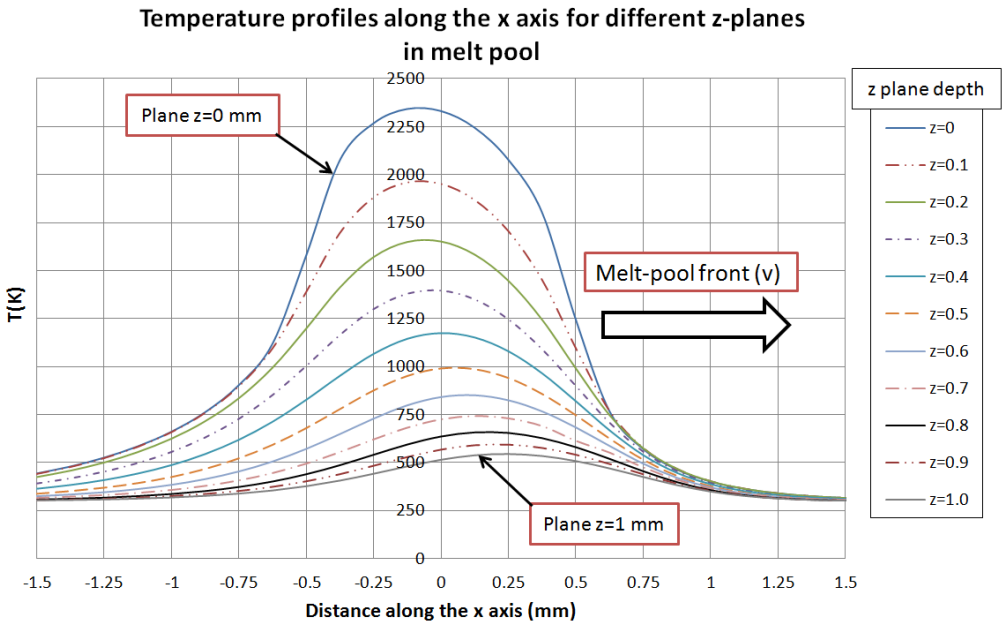

Figure III.14. Approximate temperatures profiles for different z planes of reference (surface $z=0$) to determine the approximate thermal properties of the melt pool in the vicinity of the origin of x axis (origin of the heat source) (Fig. III.4).

From (Fig. III.14), in the $z=0$ coordinate for the approximate value x=0, $T \approx 2300$ K. On the other hand from (Table III.2), the temperature-dependent thermal properties ($Th_{prop}(T)$) are not defined for those specific conditions. The maximum values available for thermal properties are defined up to the temperature of $T = 2100$ K The algorithm of (Fig. III.12) foresees this problem, and what it does to solve it is to average the temperature values that are too high for specific x values over a x range, which is initially taken as $-r_{laser} \leq x \leq r_{laser}$ (point values of temperature are replaced by the average of the values around that specific x coordinate).

In the case of (Fig. III.14), the average temperatures for $z_{surf} = 0 \leq z \leq z_{max} = 1\,(\mathrm{mm})$ allow defining an approximate temperature function within the melt pool in the diameter range of the laser beam source ($d \leq \phi d_{laser}$), as function of the z coordinate in substrate. The range of this function ($d \leq \phi d_{laser}$), can be different depending on the range that has been defined to calculate the average temperatures within the melt pool that is to say $\phi \mathrm{d}_{\mathrm{laser}} = [-r_{laser}, r_{laser}]$ in length. This function $T(x) = f(T_{mean})$ is obtained from the average temperature values instead of the point values according to the x-coordinate for each z plane in consideration.

This approach is useful because it allows the temperature-dependent thermal properties to be calculated quickly in the solidification volume inside the melt pool at relatively low

computational cost. By applying the numerical method described in (Fig. III.12), it is possible to overcome one of the major limitations of an analytical solution, which is that the thermal properties remain constant as a function of a single temperature, along with the difficulty of determining the "good" temperature that models the phenomenon without making an excessive error.

When applying the verification condition for convergence according to the solution algorithm of (Fig. III.12), where for each value of temperature within the substrate (at a specific value of x), the temperature profiles do not "cross" each other as in (Fig. III.14) for different z planes, the average calculated values of temperature can be used to assign values to the thermal properties (again according to the z coordinate).

The idea is to extend the concept of a temperature-dependent thermal property to a position-dependent thermal property when the temperature in different positions is known. Using thermal properties that are variable in the melt pool space is more accurate than simply choosing a fixed temperature as “good value” for the whole volume of molten zone.

For example, by combining the $\mathrm{T}_{\mathrm{mean}}$ data from (Fig. III.14) over $-r_{laser} \le x \le r_{laser}$ for different z planes with (Table III.2) (in the case of thermal conductivity k), a $\mathrm{k}(\mathrm{T}_{\mathrm{mean}}(z))$ composite function can be obtained (Fig. III.15).

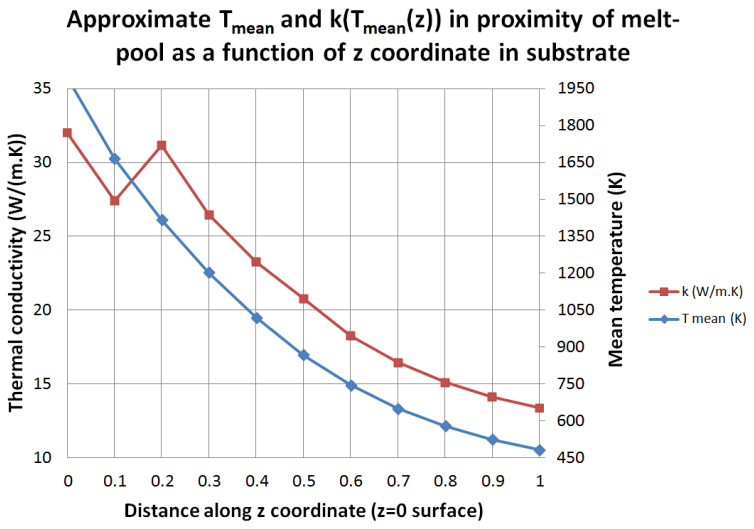

Figure III.15. Approximate temperature in the melt pool zone as a function of the z coordinate to define its inner thermal properties in the range of the laser beam ($-r_{laser} \le x \le r_{laser}$). It also shows the application of $\mathrm{T}_{\mathrm{mean}}(z)$ to a specific temperature-dependent thermal property (thermal conductivity) to define the $\mathrm{k}(\mathrm{T}_{\mathrm{mean}}(z))$ function.

When thermal properties have been approximately estimated as a function of the z coordinate in the substrate, the next step is to define a division of the domain in it (mesh) for the calculation of the thermal gradients (in other words the step for each coordinate-dependent temperature calculation within the x, y, z coordinates in the substrate), to apply the (Eq. III.33).

It is not appropriate to apply a time-dependent convergence criterion such as the one used for the numerical method of finite differences to solve the thermal field (in discrete x, y, z coordinates), since (Eq. III.30) does not depend on it. Therefore, a discretization by coordinates in the domain will be chosen finely enough to have a "good resolution" within the volume of the melt pool (Peyre et al., 2008).

For simplicity the pitch of the domain discretization that has been defined to obtain the temperatures within the melt pool will be a function of the radius of the laser beam. Thus the size of mesh pitch for the x, y, z coordinates will be (Eq. III.34):

$$\Delta x = \Delta y = \Delta z = \frac{r_{laser}}{25} \qquad \textit{Eq. III.34}$$

It is not necessary to establish the same range size for the calculation of the thermal gradients and for the approximate temperature-dependent thermal properties ($-3r_{laser} \leq x \leq 3r_{laser}$). From the Assumption 3 of this model, the size of the melt pool is given approximately by $\phi d_{laser} = 2r_{laser}$, and therefore (and to ensure a sufficient domain size for gradient calculation), the maximum and minimum range coordinates for x and y will be defined as (Eq. III.35):

$$x_{\min} = y_{\min} = -1.5r_{laser} \;\wedge\; x_{\max} = y_{\max} = 1.5r_{laser} \qquad \textit{Eq. III.35}$$

From the data and parameters of (Table III.2) and (Table III.3), applying the algorithms of (Fig. III.7) and (Fig. III.12) and (Eq. III.33) with the range and domain pitch density of (Eq. III.34) and (Eq. III.35), the corresponding surface isotherms for the temperatures $T_{Liquidus}$ and $T_{Solidus}$ (this has been calculated with of a programming code made in Matlab (R)) for $T \;\forall\; (x, y, z)$ in discrete domain points, are shown in (Fig. III.16).

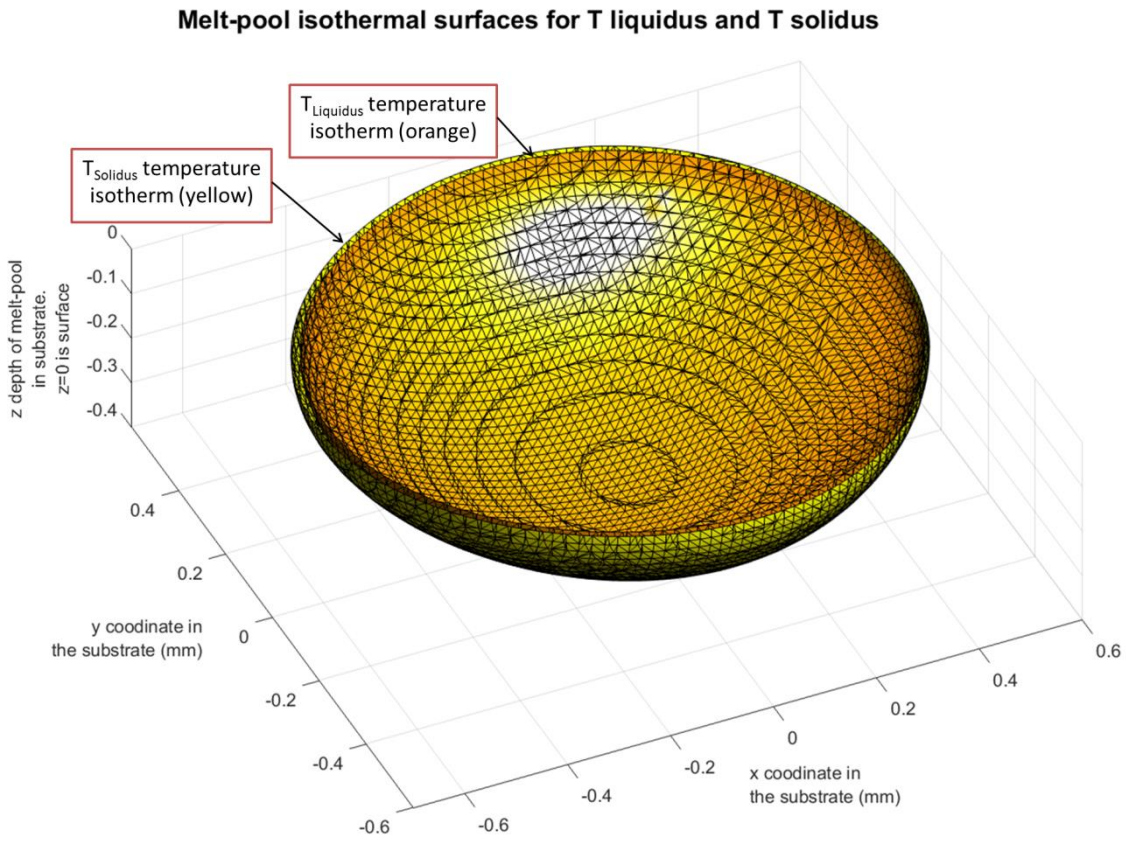

Figure III.16. Isothermal surfaces for the calculation of temperature gradients at the $T_{Liquidus}$ *and* $T_{Solidus}$ *boundary. In this figure the origin of the coordinate system* $(x_o = 0, y_o = 0, z_o = 0)$ *coincides with that of the semi-infinite substrate of (Fig. III.4). The positive* x *coordinates coincide with the direction of advance (*v*) of the laser beam.*

III.3.9 Calculation of Temperature Gradient (G_L) for Liquid Isotherm and the Grow Rate (V) in the Melt Pool

For the calculation of temperature gradients within the data set, the Method of Central Difference is used. For the edges in the same data set, the Single-Sided Differences Method is used (LeVeque, 2007). A unique temperature gradient value (G_L and G_S) must be established for each coordinate within the thermal field based on the reference frame of (Fig. III.4).

The solidification in the melt pool (taking into account its symmetry), is given in the rear part of the same (with respect to the direction of movement of the laser beam), specifically from the plane that is located in the lower z coordinate of the solidus temperature $T_{Solidus}$ over the surface in the isotherm that is the boundary of the melt pool, (Fig. III.17).

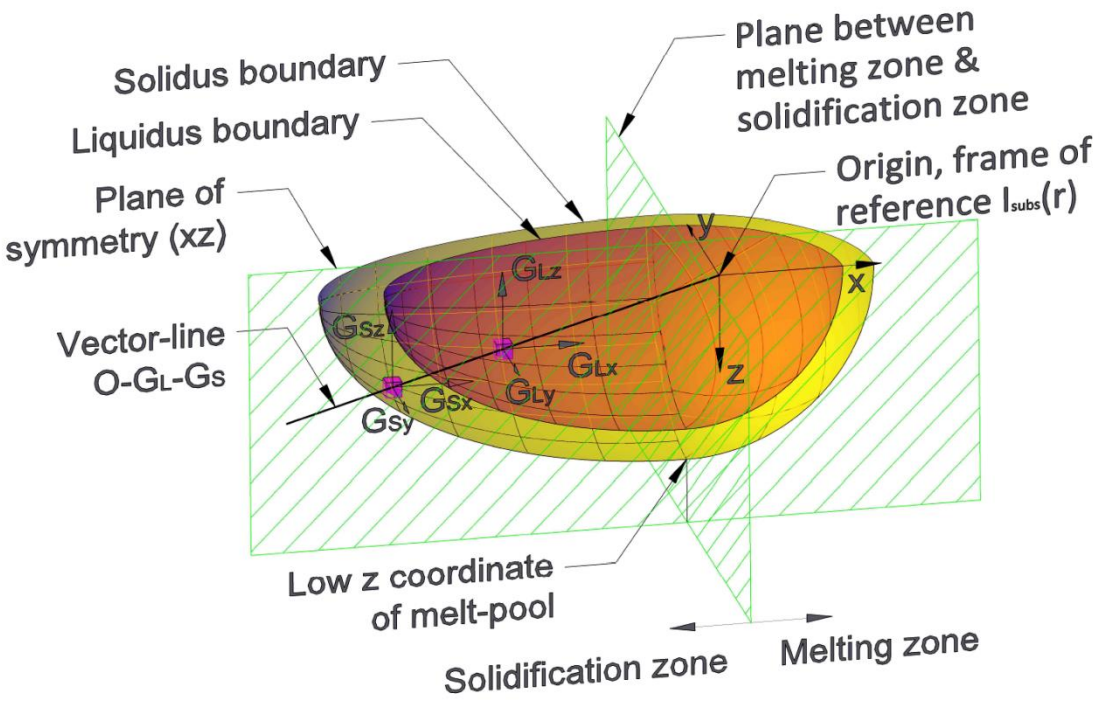

Figure III.17. Scheme for the calculation of temperature gradients G_L and G_S in melt pool. Note that the lowest z coordinate within the melt pool over the surface of isotherm does not coincide with the origin of the frame of reference for the vectors-lines to define the coordinates for the simultaneous calculation of G_L and G_S.

The criterion for establishing a unique value of G_L and G_S is that every point in the surfaces of the isotherms must be crossed by the same vector-line starting from the origin of the frame of reference of the laser beam. As the mesh in the melt pool domain is regular (and defined for an $[x, y, z]$ orthogonal system), and the volume of the melt pool in mushy state is relatively small (Fig. III.16), the projection line $Origin - G_L$ to a specific coordinate $(x_{G_L}, y_{G_L}, z_{G_L})$, automatically defines the G_S coordinate by its extrapolation $(x_{G_S}, y_{G_S}, z_{G_S})$. The use of this approach allows practically the same coordinate density as that of the isotherm of Liquidus temperature.

Once the gradients have been calculated for each domain coordinate in the corresponding conditions for both Liquidus (G_{Lx}, G_{Ly} and G_{Lz}) and Solidus (G_{Sx}, G_{Sy} and G_{Sz}) boundaries, the modules of the same will be calculated (Eq. III.36) and (Eq. III.37):

$$|G_L| = \sqrt{G_{Lx}^2 + G_{Ly}^2 + G_{Lz}^2} \qquad \textit{Eq. III.36}$$

$$|G_S| = \sqrt{G_{Sx}^2 + G_{Sy}^2 + G_{Sz}^2} \qquad \textit{Eq. III.37}$$

When the temperature gradients have been calculated it is necessary to use solidification theory to determine an extra parameter needed to define the grain

morphology originated by the local conditions of solidification (for example with the use of a Solidification Map for a certain alloy). This extra parameter is V the growth velocity of the solidification front of during the change of phase Liquid to Solid.

The temperature gradients across the solid-liquid interface are assumed in steady state and are a function of an energy balance that remains in equilibrium (that to say, there is no change in the interface velocity with time) (Flemings, 1974) since (Eq. III.33) is itself a representation of a steady state. It is possible to make such energy balance between the Liquidus and Solidus boundaries based in the observation of (Fig. III.16), where the distance between Liquidus and Solidus boundaries in the melt pool isotherms are very close. This is because the temperature gradient in the Laser Cladding process is very high (Levin, 2008) and it that in turn leads to a rapid solidification.

Assuming that the distance between Liquidus and Solidus boundaries is small, the energy balance for the growth front of grains can be assumed as that of a plane front. Applying the method for plane growing of grains (Flemings, 1974) which formulation is presented in (Eq. III.38), it is possible to estimate the value of V from G_L and G_S, and the temperature-dependent thermal properties of (Table III.2), thus:

$$k_S G_S - k_L G_L = \rho_S L_f V \qquad \textit{Eq. III.38}$$

Where the properties k_S, ρ_S are referred to the values of thermal properties at $T_{Solidus}$ temperature, and k_L to the values at $T_{Liquidus}$ temperature. Clearing V and reordering (Eq. III.38), the growth velocity V can be estimated as (Eq. III.39):

$$V = \frac{G_S k_S - G_L k_L}{L_f \rho_S} \qquad \textit{Eq. III.39}$$

The (Eq. III.39) indicates that the growth velocity is not directly dependent on the temperature gradient, but on the difference $G_S k_S - G_L k_L$. Since k_S, ρ_S, k_L and L_f are properties of the material (fixed values), the gradient in the Liquidus phase (G_L) will be directly proportional to the heat flow at the Liquidus-Solidus interface. It should be noted that (Eq. III.39) is of a general formulation and does not take into account sub-cooling phenomena or composition gradients.

Furthermore (Eq. III.39) it does not indicate anything about the final morphology after grain solidification. To overcome the latter (and establish a way to estimate the grain morphology based on the Laser Cladding process parameters), it is necessary to use the

model described later in this document. To justify the use of a CET model, it is necessary first to understand the particular metallurgical characteristics of the laser cladding process.

III.3.10 Metallurgy of Laser Cladding Process

Metallurgy refers to the science and technology of metals. The subject area can be considered as a combination of chemistry, physics and mechanics with special reference to metals.

There are two types of metallurgy, Physical Metallurgy is related to physical properties, where these are a function of the phases present in the alloy (or the transformation of them), and the Chemical Metallurgy that is related to the reduction/oxidation of metals (corrosion) (Seetharaman, 2005). This document will be mainly focused on the concepts associated with Physical Metallurgy.

The concept of metallurgy in coatings processes that use lasers as source of energy to the process itself (the case of Laser Cladding), is associated with the guarantee of the quality of the bond between the clad and the substrate materials.

The union is by fusion (and not a union by diffusion), of a small portion of the surface (melt pool), together with the added material (Vuoristo et al., 2005). This union by fusion is much localized, since the source of energy used to create this small foundry (the laser source), is generally of a small size and a very high energy density. The existence of a high energy density (in the order of MW/m^2), is one of the main factors to determine the magnitude of the heat flow (through the value of G_L), which together with the shape and characteristics of the melt pool are key to determining the microstructure that will form when the molten material solidifies.

Along with the reduced size of the melt pool of the process itself (in the scale of millimetres), other important differences with the traditional casting processes are:

- The high cooling rate (because the change of phase liquid/solid takes place on a substrate that it is in general many times larger than the melt pool generated on it and acts as a thermal sink).
- The highly directional conduction of the heat flow (this is general for all LAM processes, that resulting in columnar grain epitaxially growth from the substrate

when the feeding material is similar to the base). However, under certain circumstances, equiaxed grain growth will also be possible (Ma et al., 2017).

Regarding raw materials, it is most common to use filler material consisting of the same type of alloy as the substrate, although it is nevertheless possible to mix different kinds of metal powder if the application requires it. The use of different types of metal powders makes it possible for both physical and chemical metallurgical reactions to occur when the melt is formed (Zhong and Liu, 2010), since materials with very different physical properties (melting points, thermal conductivities, coefficients of thermal expansion, etc.) can be used. A very interesting study of different combinations for both substrate and powder materials are presented in (Toyserkani et al., 2005), which mentions the importance of convection as phenomenon inside the melt pool (which allows the homogenization of components that makes up it), and that can be characterized by the "tension number" (S), (Eq. III.40), which is much related to the laser cladding process and thermal properties of the material:

$$S = \frac{|d\gamma_{suf} / dT| \phi d_{laser} \eta P}{A_{\substack{spot \\ laser}} \mu_{melt} v k} \qquad \textit{Eq. III.40}$$

This equation allows characterizing the convection within the melt pool itself, as a function of several parameters of the same process and of the thermal properties of the material itself. It is established that for values lower than 45000, the convection is negligible (Almeida et al., 2001). However, this strong convection within the liquid phase of the material acts for a very short time, since the solidification is in turn very fast. The balance between the processes of melting, mixing and solidification is very complex, and depends on, among other things, the size of the laser spot, the speed of laser beam respect to the substrate, the amount of powder flow, the absorptivity of the laser beam by the materials during the laser cladding process itself, the kind of protection gas and its flow (Zhong and Liu, 2010).

However, even if a good metallurgical union is reached (apparently), its behaviour may not be satisfactory because the high temperatures and energies involved give rise to that some of the components within the melt pool itself may reacting and forming insoluble phases with very high melting point, such as for example in Al-Nb systems, which can form intermetallic Al_3Nb (Almeida et al., 2001). Some of these phases are very hard and fragile, and therefore their appearance must be avoided as they can generate

cracks or fragile starting points of rupture within the cladded material itself or within the metallurgical union.

Due to large temperature gradients, solid solubility limits for solutes are much higher than expected from equilibrium phase diagrams, plus considerable increases in phase transformation temperatures (Kar and Mazumder, 1989; Zhong and Liu, 2010). This leads to the formation of metastable alloys with extended solid solubility (Agrawal et al., 1993). An excellent study for Laser Cladding applied to eutectic and isomorphic binary alloys can be found in (Toyserkani et al., 2005). There are special cases that make it difficult to obtain a homogeneous alloy during the formation of the clad. This is the case with multi-component alloys, where there are the difficulty by the formation of intermediate compounds between the powder and the substrate during the formation of the melt pool (due to the high temperatures involved), giving rise to problems of crack formation or low quality of substrate/clad union usually due to the formation of brittle or intermetallic phases (Cárcel et al., 2014).

For single phase alloys, such as 316L stainless steel, many of the physical properties will depend on the grain size. Some classic relationships used in traditional type casting are applicable to the Laser Cladding process for these cases (Ma et al., 2017). For example the one that expresses the grain size as a function of the cooling rate ($\dot{T}$), (Eq. III.41):

$$d_{gr} = a_{gr} + \frac{b_{gr}}{\sqrt{\dot{T}}} \qquad \textit{Eq. III.41}$$

Another special feature of Laser Cladding metallurgy is the creation of very fine grain microstructure within the clad material (with very small primary and secondary dendritic distances), in addition to the associated increase in dislocations density, and the distortion of the lattice structure (Zhong and Liu, 2010), this last is a consequence of rapid solidification.

The refinement of the microstructure is explained by the phenomenon of constitutional supercooling. In (Toyserkani et al., 2005) the phenomenon is explained qualitatively for a eutectic alloy (Fig. III.18), where in steady state conditions it is assumed that the interface in the solidification zone remains at constant temperature, the solidification front is flat and moves at constant speed, the solid diffusion effects are neglected due to the high solidification rates, the convection in the melt pool (mixture), is limited to a mass transport by diffusion of the solute in the liquid phase, and the partition coefficient (k_e) can be determined from the equilibrium phase diagram of the alloy.

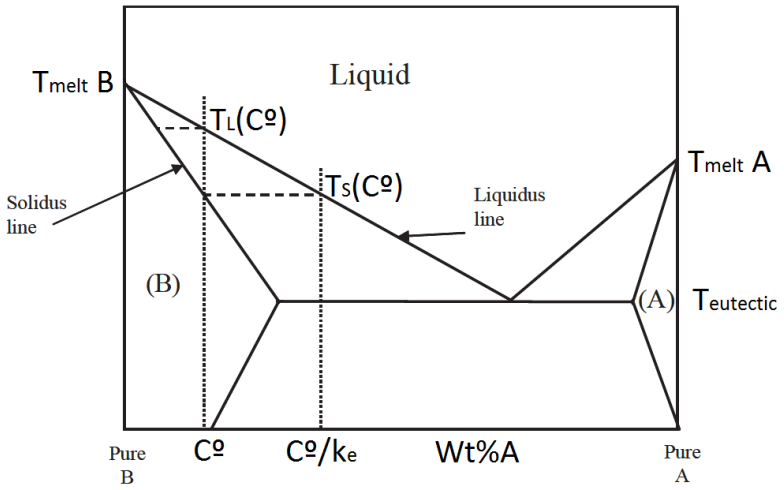

Figure III.18. A schematic of a hypothetical phase diagram indicating steady-state solidification conditions (Toyserkani et al., 2005).

The result is a concentration profile through the solid/liquid interface similar to (Fig. III.19), where the Liquidus Temperature is determined by the composition of the liquid itself that experiences a part of the solidification front (when there is a high proportion of solute). This zone experiences a "real" temperature (given by the gradient G_{Lr}), which is below the solidification temperature determined by the gross composition of the alloy. This phenomenon is called constitutional supercooling.

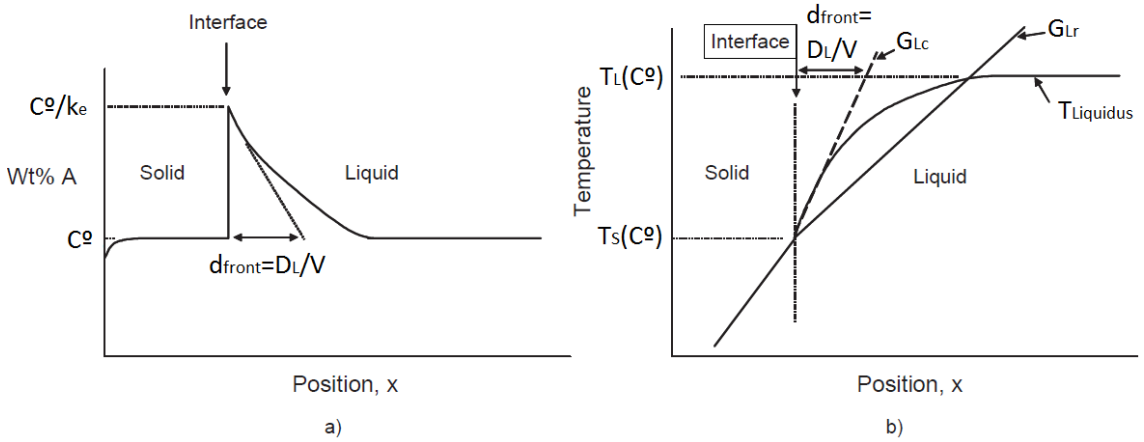

Figure III.19. a) Compositional gradient, b) temperature gradient at the solid/liquid interface during steady-state solidification (Toyserkani et al., 2005).

The critical temperature gradient (G_{Lc}) for the establishment of stable solidification conditions is defined in (Eq. III.42). Above this value no constitutional supercooling will occur, and the solidification front will remain flat.

$$G_{Lc} > \frac{\Delta T(C^o)}{D_L/V} \qquad \textit{Eq. III.42}$$

The alloys used in engineering practice have in general a significant solidification range, therefore they are prone to solidify with a dendritic structure and i.e. it is very difficult to fulfil a small $\Delta T(C^o)$ that can originate a flat solidification interface. Therefore, as the solid grows, the solidification front needs to reject more solute at the front of the solid/liquid interface.

For a binary alloy solidifying at high speed, the solute trapping phenomenon is generated, where the partition coefficient becomes dependent of the solidification velocity (k_V) (Wang et al., 1997) (Eq. III.43):

$$k_V = \frac{k_e + a_o V / D_L}{1 + a_o V / D_L} \qquad \textit{Eq. III.43}$$

The morphology of microstructures due to growth in unstable state is very sensitive to disturbances, and the whole phenomenon is not well understood, although it is believed to be related to the waves on the solidification front that produce instability. On a practical level empirical relations are used in the form of power, equation (Eq. III.44), in which λ_{gr} represents a characteristic of spacing in the microstructure after solidification (Srivatsan and Sudarshan, 1993).

$$\lambda_{gr} = B(\partial T / \partial t)^{-n_\lambda} \qquad \textit{Eq. III.44}$$

Finally, the refinement of the microstructure finally comes from the fact that the most efficient way to generate the concentration gradient by rejection of the solute (related to k_V as a first approximation), is by reducing the dendritic radius tip or through the creation of a cellular-type solidification structure (thus generating more surface for rejection), and therefore originating a refinement over the entire microstructure volume of the clad material. Because the solidification rate varies within the height of melt pool, it is expected that the microstructure of the clad should also be refined across the same (Toyserkani et al., 2005).

Recently (Liang et al., 2017, 2016a, 2016b) have established models for Nickel SX base alloys to estimate: microsegregation for rapid solidification multicomponent alloys, processing-microstructure maps and primary dendritic arm spacing respectively.

The general conclusion of the above text is that the modelling of the crystallization process (including CET), in Laser Cladding process is very complicated, mainly due to phenomena of high cooling rates that can greatly deviate the conditions of solidification from equilibrium.

The conditions of instability have their origin in the particularities of the process itself. However, it is not advisable to avoid the use of this technology due to the great advantages that it offers; especially to its metallurgy particularities (it is possible to precisely control the resulting microstructure).

To overcome this limitation there is experimental information about solidification conditions and structure generated through experimental solidification maps for complex alloys that are available as a function of V and G_L. It should be remembered that solidification maps for alloys illustrate the effect of temperature gradient and solidification rate on the morphology and scale of solidification structures (Blecher et al., 2014).

III.4 Crystallization Model

III.4.1 Relationship between a Solidification Map and Gäumann's Crystallization Model

There are basically two ways of predicting CET for a given multicomponent alloy during a solidification process. One is by means of a mathematical model such as Gäumann's, (Gäumann et al., 1999) and another by the use of solidification maps of experimental type.

By means of mathematical models as for example the deterministic one in (Eq. III.46), (knowing the values of N_o, a and n for a given alloy), ϕ will express the fraction of equiaxial grain ($\phi \to 1$) or columnar grain ($\phi \to 0$) that will originate under certain conditions in a solidification process knowing the local values of V and G_L. The CET models can be classified as stochastic or deterministic (Martorano et al., 2003), we use in this document a deterministic one.

Another way to predict the behaviour of the resulting microstructure after solidification is by means of Solidification Maps (Fig. III.3). These maps are of experimental type (Hunt, 1984; Nastac et al., 2001), and in them it is possible to plot for the local conditions of solidification V and G_L as coordinates and get, not only the morphology of the microstructure, but (depending of the information available in the experimental map), other characteristics such as SDAS and porosity. For this document only information related to the CET from these maps will be taken into account.

In summary, a solidification model is an approximation, by means of a mathematical adjustment (based on physical constants), of the behaviour observed in an experimental solidification map.

The model of Gäumann (Gäumann et al., 2001) is defined as (Eq. III.45):

$$\frac{{G_L}^n}{V} = a\left[\sqrt[3]{\frac{-4\pi N_o}{3\ln(1-\phi)}}\frac{1}{n+1}\right]^n \qquad \textit{Eq. III.45}$$

Clearing ϕ, assuming $[V, a, n, N_o] = \text{constant}$, and replacing in (Eq. III.45) results in:

$$\phi = 1 - Exp\left[-\frac{4\pi N_o({G_L}^n/(Va))^{-3/n}}{3(n+1)^3}\right] = 1 - Exp\left(-a_1 {G_L}^{-3}\right) \qquad \textit{Eq. III.46}$$

Where: $a_1 = f(V) = \dfrac{4\pi N_o (Va)^{3/n}}{3(n+1)^3}$

As G_L normally is expressed for a logarithmic scale coordinate system, for a space in linear coordinates the appropriate change of variables is defined as $\log_{10}(G_L) = G_L'$. Then clearing G_L, and replacing in (Eq. III.46), results in (Eq. III.47):

$$\phi = 1 - Exp\left(-a_1 {G_L}^{-3}\right) = 1 - Exp\left[-a_1\left(Exp(-a_2 G_L')\right)\right] \qquad \textit{Eq. III.47}$$

Where $a_2 = 3\ln(10)$

The graphical representation of (Eq. III.46) expressed as a three-dimensional surface of the form $\phi = f(G_L, V)$ for the specific case of the model of CMSX-4 alloy based on the constants of (Anderson et al., 2010), ($N_o = 2x10^{15}\ (m^{-3})$, $a = 1.25x10^6\ (K^n m^{-1} s^{-1})$ and n=3.4), results in the following graph (Fig. III.20).

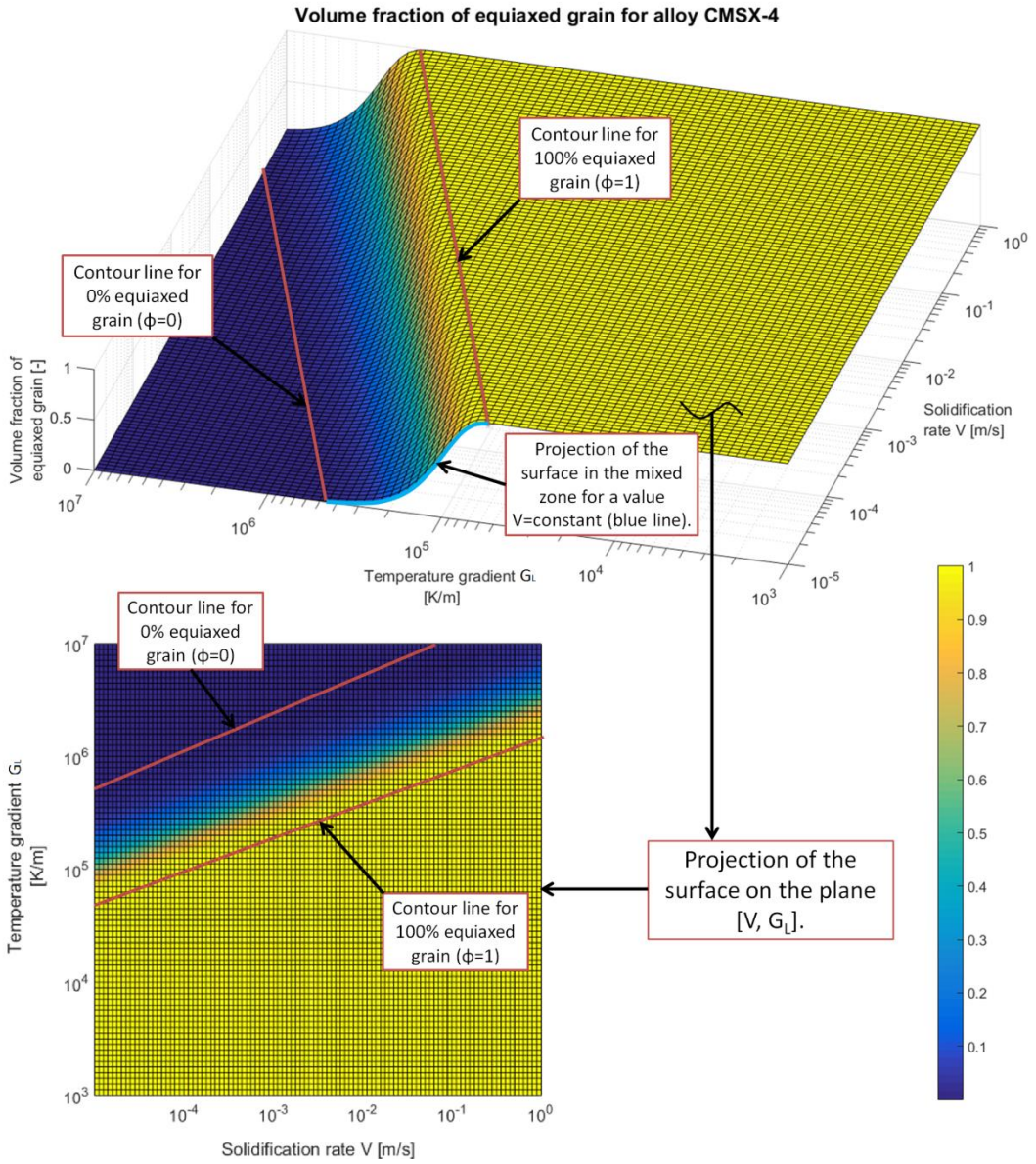

Figure III.20. Representation of equation of the volumetric fraction of equiaxed grains of Gäumann's model (Gäumann et al., 2001) for CMSX-4 alloy.

The experimental solidification map for the same alloy is presented in (Fig. III.21), where two graph of contour line (the lines are the same as the one in the lower left graph of (Fig. III.20), for the mathematical model of Gäumann for $\phi = 0$ and $\phi = 1$ have been superimposed (red lines). The graph shows that the mathematical model correctly describes the CET behaviour of the alloy for conditions with solidification velocities greater than approximately 10^{-2} m/s. In the case V of less than 10^{-2} m/s the model quickly loses accuracy (the real boundary between the equiaxial and columnar grain morphology is delimited by the thick-curved black line).

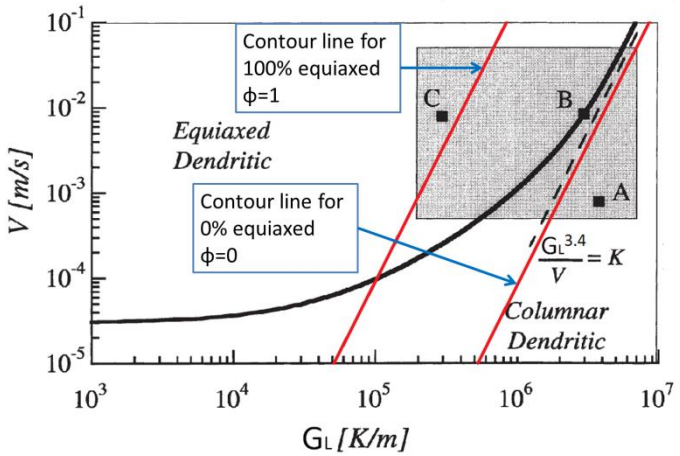

Figure III.21. Microstructure selection map for superalloy CMSX-4 under the experimental conditions described in the text (Gäumann et al., 2001), showing the expected solidification morphology as a function of temperature gradient, (G_L), and solidification velocity, (V).

The alloy constants for (Fig. III.20) obtained from (Anderson et al., 2010) are not calculated uniquely. The procedure for obtaining the constants used in the representation of (Fig. III.20) requires the use of numerical methods to adjust the shape of the mathematical curve, although this method makes no physical sense. For example, a second set of constants for the Gäumann model for CMSX-4 alloy can be (Table III.4):

Table III.4: The original and optimized parameters for the calculation of SG volume fraction (Anderson et al., 2010).

	Original	Optimized
N_o (m^{-3})	$2x10^{15}$	$1.18x10^{15}$
a ($K^n.m^{-1}.s^{-1}$)	$1.25x10^{6}$	$2.03x10^{6}$
n	3.4	5.3

There is nothing to guarantee that the numerical method will converge, nor that the values of the constants obtained are optimal ones.

There are excellent mathematical models such as (Gäumann et al., 2001; Martorano and Biscuola, 2009), but they have the same limitations in their range of application and do not clearly describe the behaviour in the columnar/equiaxial transition. To “describe” the behaviour in the mixed zone means to establish with certain accuracy the percentage of equiaxed or columnar grain formation within the zone. Later on it will be demonstrated that, for example, for a value V=constant, a value of G_L found at the mean distance between the isocurves $\phi = 0$ and $\phi = 1$ will not have an equiaxial grain formation percentage of 50%. Later it will be shown that the crystallization model within the mixed

zone is asymmetric, and that their behaviour is adjusted to a special type of statistical distribution.

On the other hand solidification maps such as those in (Gäumann et al., 2001; Kobryn and Semiatin, 2003; Martorano et al., 2003; Nastac et al., 2001) are not sufficiently exploited, because it is not easy to adapt them to a useful form for use by example in a computer program as it is possible in mathematical models. A very useful idea would be to take the data from a given solidification map and convert it into a formula based on some key data or easily transform the information contained in a solidification map into the constants necessary for a model such as that of Gäumann (with unique values and with some physical sense that allows verifying the numerical fitting by means of key data). Another difficult with experimental Solidification Maps is to model the behaviour in areas of mixed columnar/equiaxed when the CET transition occurs only using graphics as (Fig. III.3). The Solidification Maps have in general well-defined CET boundaries, but they do not give information about the behaviour in the mixed zone. For this document the model of (Gäumann et al., 2001) will be used as basis.

III.4.2 Objectives of the Crystallization Model

1. Describe the mathematical structure under which Gäumann's CET model is based, and use them to create an extended deterministic mathematical model for steady-state in unidirectional solidification.
2. Based on the above objective, accurately and intuitively establish the behaviour of the mixed zone in the columnar/equiaxed transition $\phi = f(V, G_L)$.
3. Extend the application range of Gäumann's model for low solidification speeds V.
4. Establish a methodology to determine both the constants for the model to be proposed in this document and for the Gäumann's model, based on experimental Solidification Maps. The aim is a method of searching for constants that result in a unique set of them that make physical sense. At the same time, this will avoid the use of numerical methods that can result in multiple sets of values for the constants (without physical sense).
5. Establish a practical method for calculating the value of the constant N_o based on EBSD test images, and based on that the constant a for, by example, to use it in the Gäumann's model.

III.4.3 Model of Crystallization Based on Gäumann's Model as a Probability Distribution

It will be shown that Gäumann's model has the same mathematic basic structure as a probability distribution of Extreme Value Type I, and from this fact the necessary constants will be deduced to extend the range of use of the original model through a deterministic mathematical model for steady-state in unidirectional solidification.

If in (Eq. III.47) $\xi = G_L$' and $a_1 = a_2 = 1$ (only for clarification), the resulting expression is equivalent in canonical shape to the formulation of the minimum standard cumulative distribution function (cdf) of Gumbel or Extreme Value Type I Distribution (NIST/SEMATECH, 2012), that is defined in (Eq. III.48):

$$\mathrm{cdf}_{\mathrm{Gumbel}} = 1 - Exp\left[-Exp\left(\xi\right)\right] \qquad \textit{Eq. III.48}$$

From the comparison of (Eq. III.48) with (Eq. III.47), it is observed that both share the same basic structure, that is to say the same canonical shape, from which it can be deduced that the behaviour of Gäumann's model can be represented by a specific cdf (Gumbel).

Both the pdf (probability density function) and cdf (cumulative distribution function) of Gumbel's function are biased in terms of the probabilities calculated from them (for different values of ξ) (NIST/SEMATECH, 2012). Therefore they do not follow the pattern of the Normal Distribution (symmetry for both pdf and cdf). Thus by analogy, the Gäumann's model will present this phenomenon of asymmetry when is used to calculate the volume fraction of equiaxed grains (ϕ) as function of G_L and V especially in the mixed zone of CET (Fig. III.20) and (Fig. III.22).

III.4.4 Deduction of the Crystallization Model Based on the cdf of Gumbel

Since it has been demonstrated by means of (Eq. III.47) and (Eq. III.48) that the Gäumann equation is of the Gumbel's cdf type, the next step is to adapt a general form of it to a surface similar to that shown in (Fig. III.20). The general equation of the cdf of the Gumbel Distribution is represented by the (Eq. III.49):

$$\phi_{Gum} = 1 - Exp\left(-Exp\left(\frac{\xi - \mu}{\beta}\right)\right) \qquad \textit{Eq. III.49}$$

Where μ is the location parameter and β is the scale parameter.

The objective is to obtain, on the basis of relatively easy to get key data from graphs similar to those in (Fig. III.3), the constants μ and β, as a function of G_L and V.

III.4.4.1 Equivalence of ξ for the Crystallization Model Based on cdf of Gumbel

The variable ξ has a precise meaning within the crystallization model based on Gumbel. It is the statistical equivalent of the "location parameter" (i.e. the position of the cfd curve over a coordinate axis). The effect of varying such a parameter can be understood visually by observing the behaviour of the variable ϕ (in a 2d graph), when the coefficients $[N_o, a]$ are taken as constants. In this example the values of (Gäumann et al., 2001), will be used as a typical value. With the above it is possible plotting the (Eq. III.46) as a function $\phi = f(G_L)$. For the alloy CMSX-4 (Fig. III.20) and by taking of specific values for V from $V = 1\text{x}10^{-4}$ to $V = 1\text{x}10^{-2}$ it is possible obtain a figure that represent the projection of the “surface” (2D graph), of probability for the formation of equiaxed grains as function of G_L for different V, (Fig. III.22). The values of V are taken in that range because they are in the middle of the experimental graph of the CMSX4 alloy, and therefore are representative of all the range of work of such alloy (Fig. III.21).

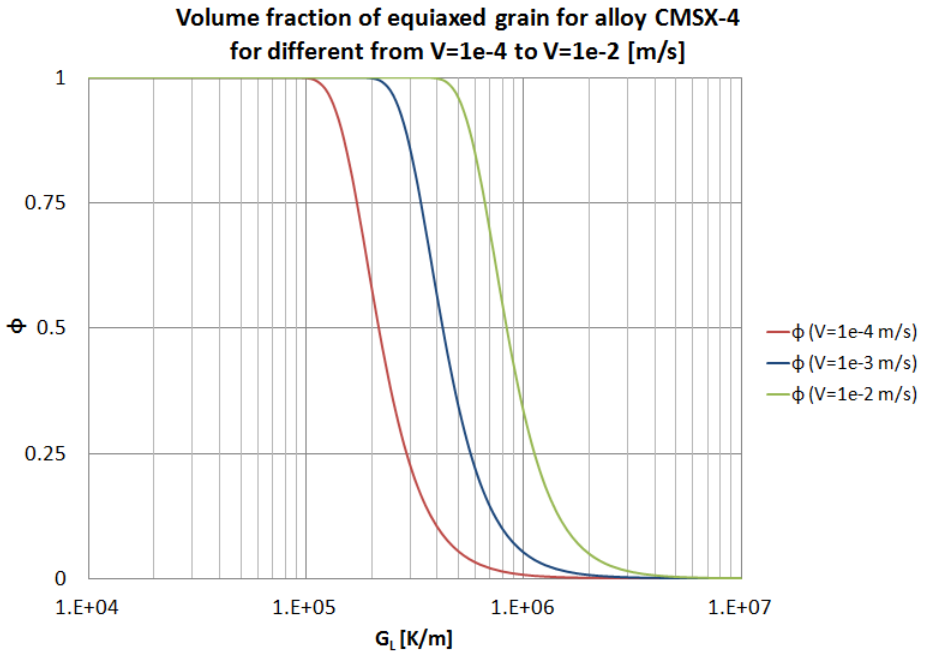

Figure III.22. Volume fraction of equiaxed grains formation for alloy CMSX-4 for different V from $V = 1\text{x}10^{-4}$ to $V = 1\text{x}10^{-2}$ (m/s) as function of G_L (K/m).

From the analysis of (Fig. III.22), it can be seen easily that in logarithmic scale coordinates the plotting of $\phi = f(G_L)$ for a given V is equivalent to the value of $\phi = f(\xi)$ for the (Eq. III.49) and by applying the appropriate change of base (from logarithmic scale to linear scale), results in (Eq. III.50):

$$\xi = \log_{10}(G_L) \qquad \textit{Eq. III.50}$$

III.4.4.2 Deduction of Parameters μ and β for the Crystallization Model Based on cdf of Gumbel

III.4.4.2.1 Particularities of Solidification Maps

The next step is to deduce relationships that allow, from visual analysis and (through simple calculations over graphs similar to the one in (Fig. III.3)), obtain the values of μ and β for (Eq. III.49).

The effect of the scale parameter is to stretch out the graph (NIST/SEMATECH, 2012), as the probability distribution of the (Eq. III.49). From the analysis of (Fig. III.22), it is observed that the shape (stretch) of the function $\phi = f(G_L)$ remains constant in "shape" for different values of V, and therefore β (the scale parameter), must remain constant.

Other observations (from graph as the one of (Fig. III.3)), which allow us to obtain the above parameters (μ and β) are:

- The graphs of solidification maps for alloys such as the one in (Fig. III.3) normally present boundary lines that limit the areas for the regions of 100% equiaxed grain ($\phi = 1$) and fully columnar morphology ($\phi = 0$).
- The relative distance between the boundary line where the grain volume is 100% equiaxed and 100% columnar remains constant for a typical solidification map like that of (Fig. III.3) (for the zone where the slope of both lines are linear and constant).
- The (Eq. III.46) is able to represent that behaviour (relative distance between $\phi = 0$ and $\phi = 1$ constant). This is demonstrated from (Fig. III.22), where a change with the same delta value of V (on the logarithmic scale), produces probability curves that are at the same relative distance from one another.

Therefore if the scale parameter β is kept constant for different values of V (or what is the same, for different location parameters μ); it should be possible to establish a relationship between the relative distances only as a function of $\log_{10}(G_L)$.

III.4.4.2.2 Proposed Method for the Deduction of β Based on the Solidification Map Parameter G_L

As mentioned earlier the effect of the scale parameter (β) is to stretch out the graph. The idea is to establish β in such a way that it is able to represent the projection of the surface graph for a given alloy (for a model of crystallization), for a value of V=constant, as shown in (Fig. III.20) in the detail marked as "Projection of the surface in the mixed zone for a value V=constant (blue line)".

The following method is proposed to derive the variable β based on the Solidification Map Parameter G_L (starting from (Eq. III.46)), when the volumetric grain fraction takes the value of $\phi=0$, $\phi=1/2$ and $\phi=1$ for certain a, V and N_o that remain constant. The scale parameter (β) can be deduced as a function of these values of ϕ, taking them as values of probability that fit in the Gumbel function located on the axis $\log_{10}(G_L)$ in an arbitrary position, that is to say $\mu=f(V)$.

On the one hand (Eq. III.45) is not defined for $\phi=0$ and $\phi=1$, since the evaluation at either values of ϕ is indeterminate or ∞. To solve the problem of indetermination for (Eq. III.45) when $\phi=0$ and $\phi=1$, it has been decided to use as methodology numerical limits near those values with the desired precision. For convenience of numerical management, we have chosen values related to the exponential number to replace the values of ϕ near zero and one by (Eq. III.51) and (Eq. III.52):

$$\phi\approx 0=\frac{1}{e^{\kappa}} \qquad \textit{Eq. III.51}$$

$$\phi\approx 1=1-\frac{1}{e^{\kappa}} \qquad \textit{Eq. III.52}$$

Where κ is an integer. Replacing the values of (Eq. III.51) and (Eq. III.52) in (Eq. III.45), clearing out $G_{L(\phi\approx 0)}$ y $G_{L(\phi\approx 1)}$, and applying logarithm to base 10, result in (Eq. III.53) and (Eq. III.54):

$$\log_{10}(G_{L(\phi\approx 0)}) = \frac{3\ln\left(\left(Va\left(\frac{(n+1)^3(\kappa-\ln(e^{\kappa}-1))}{N_o}\right)^{-n/3}\right)^{1/n}\right)+\ln\left(\frac{4\pi}{3}\right)}{3\ln(10)} \quad \textit{Eq. III.53}$$

$$\log_{10}(G_{L(\phi\approx 1)}) = \frac{3\ln\left(\left(Va\left(\frac{\kappa(n+1)^3}{N_o}\right)^{-n/3}\right)^{1/n}\right)+\ln\left(\frac{4\pi}{3}\right)}{3\ln(10)} \quad \textit{Eq. III.54}$$

For the case of $\phi = 1/2$, and repeating the same procedure as in the (Eq. III.53) and (Eq. III.54), results in (Eq. III.55):

$$\log_{10}(G_{L(\phi=1/2)}) = \frac{3\ln\left(\left(Va\left(\frac{(n+1)^3}{N_o}\right)^{-n/3}\right)^{1/n}\right)-\ln\left(\frac{3\ln(2)}{4\pi}\right)}{3\ln(10)} \quad \textit{Eq. III.55}$$

Then calculating the ratio between the relative distances over the horizontal axis of the logarithms ($\log_{10}(G_L)$) for the different values of ϕ (from $\phi = 1/2$ to $\phi \approx 1$ and from $\phi \approx 0$ to $\phi \approx 1$), (Eq. III.56):

$$Ratio_{\log_{10}(G_L)} = \frac{\log_{10}(G_{L(\phi=1/2)})-\log_{10}(G_{L(\phi\approx 1)})}{\log_{10}(G_{L(\phi\approx 0)})-\log_{10}(G_{L(\phi\approx 1)})} = \frac{\ln\left(\frac{\ln(2)}{\kappa}\right)}{\ln\left(\frac{\kappa-\ln(e^{\kappa}-1)}{\kappa}\right)} \quad \textit{Eq. III.56}$$

The value of $Ratio_{\log_{10}(G_L)}$ depends solely on κ (for convenience defined as an integer $\kappa > 1$). The (Table III.5) shows the result of evaluating the function for different κ along with the relative error difference for the term $\kappa+1$. We have defined the criterion that the value of κ shall be taken from the last term whose difference between its last four consecutive evaluations is not greater than 1%.

Table III.5: Evaluation of the function $Ratio_{\log_{10}(G_L)} = f(\kappa)$ for different values of κ, along with the relative error rate for the term $\kappa+1$.

κ	$Ratio_{\log 10(G_L)} = f(\kappa)$	Relative error (%) $\frac{f(\kappa+1)-f(\kappa)}{f(\kappa)}$	Relative difference in % of error	Convergence condition
2	0.404	11.0%	1.64%	No
3	0.360	9.4%	1.13%	No
4	0.326	8.2%	0.86%	No
5	0.299	7.4%	0.69%	No

6	0.277	6.7%	0.57%	No
7	0.259	6.1%	0.48%	No
8	0.243	5.6%	0.40%	< 1% in the last four terms

From (Table III.5), $\kappa = 8$ and substituting in (Eq. III.56), results in (Eq. III.57):

$$Ratio_{\log_{10}(G_L)} = \frac{\log_{10}(G_{L(\phi=1/2)}) - \log_{10}(G_{L(\phi\approx1)})}{\log_{10}(G_{L(\phi\approx0)}) - \log_{10}(G_{L(\phi\approx1)})} = \frac{\ln\left(\frac{\ln(2)}{8}\right)}{\ln\left(\frac{8-\ln(e^8-1)}{8}\right)} \qquad \textit{Eq. III.57}$$

Finally, the value of β can be obtained from the following reasoning:

- The (Eq. III.46) can be interpreted as a probability of volumetric equiaxed grain formation, with a value always between 0 and 1, that is to say a probability function. It has been demonstrated that its representation is consistent with that of a Gumbel's cdf .
- It is known that there is a relationship for the equiaxed grain volume fraction between the values of $\phi \approx 0$, $\phi = 1/2$ and $\phi \approx 1$ as $f(\log_{10} G_L)$ (Eq. III.57), this relation is shown in (Fig. III.23).

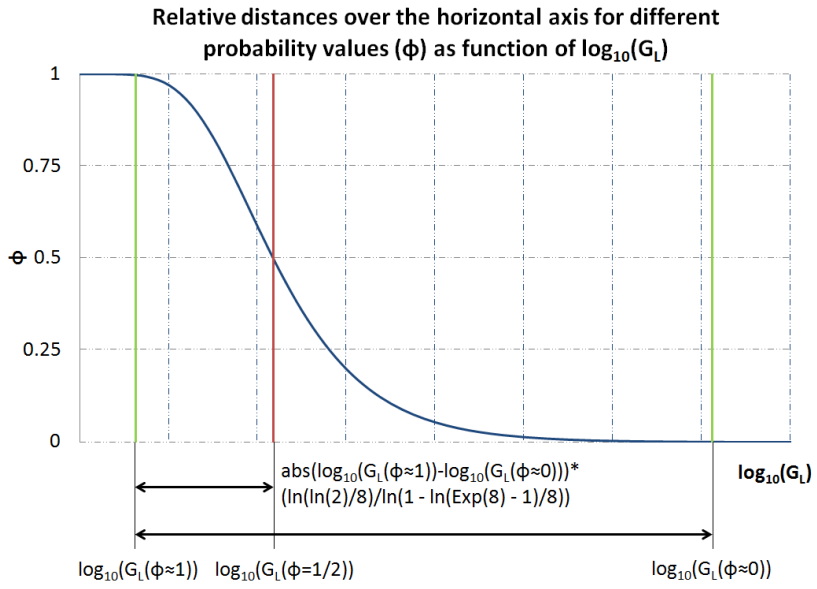

Figure III.23. Relative distance over the horizontal axis for the coordinate $\log_{10}(G_{L(\phi\approx1)})$ *for a volumetric equiaxed grain fraction* ϕ*=½ as function of* $|\log_{10}(G_{L(\phi\approx0)}) - \log_{10}(G_{L(\phi\approx1)})|$.

- From the previous paragraphs it is therefore possible to know the value of β, from (Eq. III.49), clearing the value of μ, and then resolving β for the two known conditions (the distance ratio of (Eq. III.57)).

Clearing μ from (Eq. III.49), rename μ as μ_V (because $\mu = f(V)$) and applying the above proposed method, results in (Eq. III.58):

$$\mu_V = \beta \ln(-\ln(1-\phi_{Gum})) + \xi \qquad \textit{Eq. III.58}$$

The conditions to be replaced in (Eq. III.58) will be those corresponding to (Eq. III.59) and (Eq. III.60).

- Condition 1:

$$\left(\xi_1 = \log_{10}(G_{L(\phi\approx 1)}),\ \phi_{Gum} \approx 1 = 1 - 1/e^8\right) \qquad \textit{Eq. III.59}$$

- Condition 2:

$$\left(\xi_2 = \log_{10}(G_{L(\phi\approx 1)}) + \left|\log_{10}(G_{L(\phi\approx 1)}) - \log_{10}(G_{L(\phi\approx 0)})\right| * Ratio_{\log_{10}(G_L)},\ \phi_{Gum} = 1/2\right) \qquad \textit{Eq. III.60}$$

Operating and clearing β for the above conditions (1 & 2), results in (Eq. III.61):

$$\beta = -\frac{\left|\log_{10}(G_{L(\phi\approx 1)}) - \log_{10}(G_{L(\phi\approx 0)})\right|}{\ln\left(1 - \frac{\ln(e^8 - 1)}{8}\right)} \qquad \textit{Eq. III.61}$$

Where: $V_{(\phi\approx 1)} = V_{(\phi\approx 0)} = V_\phi \ \forall\ G_{L(\phi\approx 1)} \wedge G_{L(\phi\approx 0)}$, see (Fig. III.24) for details about the coordinates associated with (Eq. III.61).

Different tests have been done using (Eq. III.61) to estimate the value of β in the zone where the lines of constant slope for the volumetric fractions (ϕ close to 0 and 1), for graphs similar as the one shown in (Fig. III.3).

A phenomenon has been observed. Between the visual estimation of what mathematically is $\phi \approx 0$ and $\phi \approx 1$, and the real mathematical calculation, there is an underestimation of the value of β close to a factor of 1.7, whose origin is the definition of the limits of ϕ that have been applied to (Eq. III.45).

The volumetric equiaxed grain fraction is derived from an “approximation” of $\phi = 0$ or $\phi = 1$ by itself (Eq. III.51) and (Eq. III.52). This "almost" ϕ value of 0 or 1 makes the value chosen in the ξ variable defined according to (Eq. III.50) very sensitive, as well as

the β value that derives from (Eq. III.61), which means that a correction factor needs to be established for β, from now on defined as β_G (because $\beta = f(G_L)$), therefore (Eq. III.61) is transformed with the respective correction into (Eq. III.62):

$$\beta = \beta_G = -\frac{1.7\left|\log_{10}(G_{L(\phi\approx 1)}) - \log_{10}(G_{L(\phi\approx 0)})\right|}{\ln\left(1-\frac{\ln(e^8-1)}{8}\right)} \qquad \textit{Eq. III.62}$$

Having obtained the parameter β_G, the next one (the location parameter μ_V) shall be calculated.

III.4.4.2.3 Proposed Method for the Deduction of μ Based on the Solidification Map Parameter V

The effect of location parameter (μ), is shifts the graph left or right over an axis (NIST/SEMATECH, 2012). For this model, μ will be the parameter responsible for shift the projected curve defined by β_G over the axis of coordinates V.

In the graph of (Fig. III.20), if the projection indicated by the detail “Projection of the surface in the mixed zone for a value V=constant (blue line)” is “anchored” to one of the contour lines (either for $\phi = 0$ or $\phi = 1$), then it is possible to define the parameter μ (that will move the projection creating the surface of the model of crystallization), as a function of V, since any of the contour lines to “anchor” will be a function of V and in turn $\mu = f(\ell_{\log})$.

Therefore the first step will be to deduce the line of projection in logarithmic scale that represents one of the contour curves, that is to say $\ell_{\log} = f(V)$, in this document for the case where $\phi = 1$.

From the analysis of (Fig. III.3), it is observed that in the area where the slope of the lines for $\phi \approx 0$ and $\phi \approx 1$ are constant in the logarithmic graph, it is possible that their representation can be made by a straight-line function in logarithmic coordinates (Eq. III.63):

$$F(\xi) = \xi^m 10^{b_1} \qquad \textit{Eq. III.63}$$

Where $F(\xi) = G_L$ and $\xi = V$.

Replacing and applying logarithm to base 10:

$$\log_{10}(G_L) = m\log_{10}(V) + b_1 \qquad \textit{Eq. III.64}$$

For the graph of (Fig. III.20), where the value of contour line is $\phi = 1$ (straight line), and applying the concept of point-slope equation in logarithmic coordinates ($\ell_{\log}$) it is possible to determine for (Eq. III.64) the constants m and b_1 (Eq. III.65):

$$\ell_{\log} = \log_{10}(G_L) = \frac{\ln(G_{L(\phi\approx1)}) + m\left(\ln(V) - \ln(V_{(\phi\approx1)})\right)}{\ln(10)} \qquad \textit{Eq. III.65}$$

Where:

$$m = \tan\theta = \frac{1}{n} = \frac{\ln\left(\frac{G_{La(\phi\approx1)}}{G_{Lb(\phi\approx1)}}\right)}{\ln\left(\frac{V_{\phi a}}{V_{\phi b}}\right)} \qquad \textit{Eq. III.66}$$

The associated coordinates related to the (Fig. III.3) for (Eq. III.65) and (Eq. III.66) are shown in (Fig. III.24).

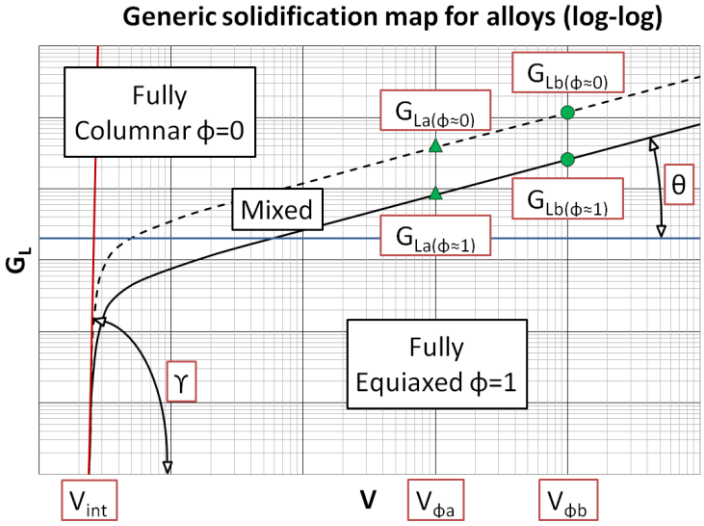

Figure III.24. Coordinates associated to the calculation of coefficients for the model of volumetric fraction of equiaxed grain for a generic Solidification Map $\phi = f(G_L, V)$.

III.4.4.2.4 Physical Meaning of the Material Constant n with Respect to an Experimental Solidification Map

In this model that the slope of an equation of a straight line in logarithmic coordinates being $m = 1/n$ (where n is a constant of material) for the (Eq. III.45) is very useful, because it allows the usage of bibliography data from (Gäumann et al., 2001; Kobryn and

Semiatin, 2003; Martorano et al., 2003; Nastac et al., 2001), or in other words its deduction from graphs like that of (Fig. III.3) or by (Eq. III.66). The validity of the above argument is demonstrated from (Eq. III.45), clearing G_L (Eq. III.67):

$$G_L = \frac{6^{2/3}\pi^{1/3}\left[Va\left(\frac{(-N_o/\ln(1-\phi))^{1/3}}{n+1}\right)^n\right]^{(1/n)}}{3} \qquad \textit{Eq. III.67}$$

If $N_o = \text{constant}$ (it is assumed that the number of heterogeneous nucleation sites is constant for a given solidification process like Laser Cladding), and applying logarithm to base 10 (to use the same base as in the graph of (Fig. III.3)), results in (Eq. III.68):

$$\log_{10}(G_L) = \log_{10}\left(\frac{6^{2/3}\pi^{1/3}}{3}\right) + \frac{1}{n}\left[\log_{10}(V) + \log_{10}\left(a\left(\frac{(-N_o/\ln(1-\phi))^{1/3}}{n+1}\right)^n\right)\right] \qquad \textit{Eq. III.68}$$

The (Eq. III.68) presents the generic shape of a straight line in logarithmic space such as (Eq. III.64). Therefore its slope can be found by defining the auxiliary variables $\psi_* = \log_{10}(G_L)$ and $\xi_* = \log_{10}(V)$, and deriving respect to ψ_* knowing that $d\psi_*/d\xi_* = \tan\theta$, thus (Eq. III.69):

$$\frac{d}{d\xi_*}\left(\log_{10}\left(\frac{6^{2/3}\pi^{1/3}}{3}\right) + \frac{1}{n}\left[\xi_* + \log_{10}\left(a\left(\frac{(-N_o/\ln(1-\phi))^{1/3}}{n+1}\right)^n\right)\right]\right) = \frac{1}{n} \qquad \textit{Eq. III.69}$$

And this results in (Eq. III.70):

$$m = \tan\theta = \frac{1}{n} \qquad \textit{Eq. III.70}$$

In (Eq. III.70) it is shown that the material constant n for the Gäumann's model is equivalent to the inverse of the slope of the boundary line that define the zones for CET in an experimental solidification map for a given alloy (in the zones where the lines have linear behaviour), expressed in logarithmic coordinates.

III.4.4.3 Modification of Parameters to Model the Volumetric Fraction ϕ for Low Solidification Speeds

Preliminarily, the value of the model coefficient $\mu = \mu_V$ in (Eq. III.49) for a logarithmic base coordinate system can be defined as the sum of (Eq. III.65) (the line that defines the fully equiaxed grain volume boundary of (Fig. III.3) where the slope is linear and

constant), plus the ratio deduced in Eq. 57 multiplied by the distance $\left|\log_{10}(G_{L(\phi\approx 0)}) - \log_{10}(G_{L(\phi\approx 1)})\right|$, that is to say (Eq. III.71a) and (Eq. III.71b):

$$\mu_V = \frac{\ln(G_{L(\phi\approx 1)}) + m\left(\ln(V) - \ln(V_{(\phi\approx 1)})\right)}{\ln(10)} + \frac{\left|\log_{10}(G_{L(\phi\approx 0)}) - \log_{10}(G_{L(\phi\approx 1)})\right| \ln\left(\frac{\ln(2)}{8}\right)}{\ln\left(\frac{8-\ln(e^8-1)}{8}\right)} \quad \textit{Eq. III.71a}$$

$$\mu_V = \ell_{\log} + \frac{\left|\log_{10}(G_{L(\phi\approx 0)}) - \log_{10}(G_{L(\phi\approx 1)})\right| \ln\left(\frac{\ln(2)}{8}\right)}{\ln\left(\frac{8-\ln(e^8-1)}{8}\right)} \quad \textit{Eq. III.71b}$$

Representing ϕ_{Gum} (Eq. III.49) in conjunction with (Eq. III.62) and (Eq. III.71), the result will be similar to the generic shape of the surface of Gäumann's model (Eq. III.46) or graphics similar to the one of (Fig. III.20). For a complete representation of the volumetric fraction of equiaxed grains at low solidification rates V, it is necessary to modify (Eq. III.49), specifically the set $(\xi - \mu)/\beta$ by means of an appropriate "scale factor".

The adjustment of the representation via an equation of scale will be made in two stages. The first step is to define a scale function over the logarithmic straight line of (Eq. III.65). It is necessary to establish a scale function in the same domain as the variable V (via multiplication factor), over (Eq. III.65). The effect on (Eq. III.65) will be to minimize the function and establishing the "cut" boundary V_{int} as shown in (Fig. III.24). The boundary V_{int} is a border value defined between the morphology zone of the 100% equiaxed grain and the 100% columnar grain.

The general idea of this "scaling factor function" is shown in (Fig. III.25), where the scale same will always have a range between 0 and 1.

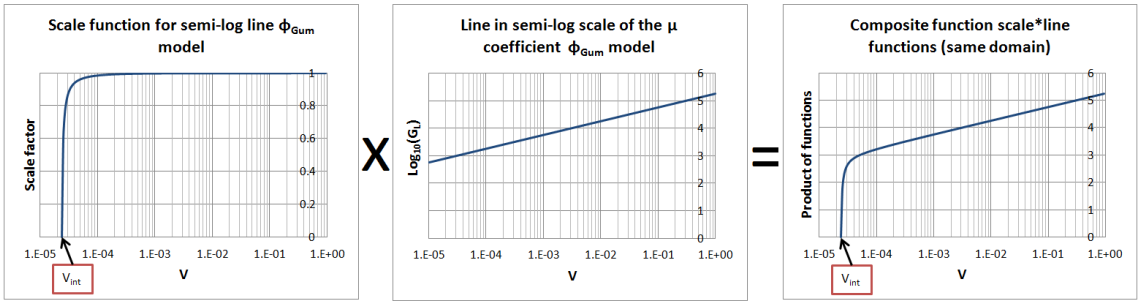

Figure III.25. Scheme of the effect of the "scaling factor function" over the μ_V location parameter function in semi-log coordinates for the same V domain. Left: scale function, middle: straight line representing the behaviour of the preliminary model for the logarithmic straight lines with constant slope, and right: product of both functions on the same domain.

The scale function must have the next desirable characteristics:

- The maximum value within the range of the "scale function" must be 1, and it must be maintained at that value asymptotically regardless of the value of the domain, in this case when $V \to +\infty$.
- The fall in the value "created" by the scale function ($f(V \to V_{\text{int}}) = 0$) within the range of V the must be very abrupt, and must reflect in the V_{int} coordinate value an asymptotic, monotonic and strictly decreasing behaviour.
- It is preferable that the associated function to the scale factor will be in some way related to exponential functions, since ϕ_{Gum} is defined in those terms.

For convenience the scale function ψ_{**} (scale factor for the vertical axis) in the same domain of axis V (through the auxiliary variable ξ_{**}), has been chosen as follows:

$$\psi_{**} = \frac{(n_1 - \coth(\xi_{**} + \chi) + 1)}{n_1} \qquad \textit{Eq. III.72}$$

Where χ is a location parameter of the function itself, and n_1 is a parameter that relates the slope of the function ψ_{**} over the coordinate axis V to the value V_{int}.

This function (Eq. III.72), will be defined in the domain $0 < (\xi_{**} + \chi) < +\infty$, where it is asymptotic in $\psi_{**} = 1$. It is possible to deduce the constant n_1 from an analysis of the left-hand graph of (Fig. III.25). At the coordinate $\xi{**} = \log_{10}(V)$, if it is assumed that the temperature gradient is equal to zero ($G_L = \psi{**} = 0$), it is possible first to determine the value of $\xi{**}$, and then that of n_1 (Eq. III.73):

$$G_L = 0 = \frac{(n_1 - \coth(\xi_{**} + \chi) + 1)}{n_1} \qquad \textit{Eq. III.73}$$

And clearing ξ_{**}:

$$\xi_{**} = \frac{\ln\left(\frac{n_1 + 2}{n_1}\right)}{2} + \chi \qquad \textit{Eq. III.74}$$

Derivation of (Eq. III.73), and equalling it to the tangent of the angle $\tan\gamma$, at the coordinate $(V_{\text{int}}, G_L = 0)$ as shown in (Fig. III.24) results in (Eq. III.75) and (Eq. III.76):

$$n_1 = \tan\gamma - 2,\ V < 90^{\text{o}} \qquad \textit{Eq. III.75}$$

$$\chi = \frac{\ln\left(\frac{\sin\gamma}{\sin\gamma - 2\cos\gamma}\right)}{2} - \log_{10}(V_{\text{int}}) \qquad \textit{Eq. III.76}$$

To restrict the fact that the (Eq. III.72) is also defined for values of $(\xi_{**} - \chi) < 0$, a unitary step function (Heaviside step function) will be used to restrict its range, so (Eq. III.72) will be transformed into (Eq. III.77):

$$\psi_{**} = \left[\frac{(n_1 - \coth(\log_{10}(V) + \chi) + 1)}{n_1}\right] H(V - V_{\text{int}}) \qquad \textit{Eq. III.77}$$

Where V_{int} is the boundary value on the axis V between the CET areas in a Solidification Map, and $H(V - V_{\text{int}})$ is the unitary step function (Heaviside), for the domain $V \geq V_{\text{int}}$.

From (Fig. III.22), it has previously been shown that the value of the variable scale factor β of (Eq. III.49) should remain constant, that is to say "the width" of the S - shape graph of the probability function (ϕ) does not vary as the value of V variable changes.

The latter is valid for a model like the one shown in (Fig. III.20), where the "relative distance" between the isocurves for $\phi \approx 1$ and $\phi \approx 0$ remains constant. However, for alloys solidification maps typically found in the literature such as that of (Fig. III.3), and remembering that $\beta = \beta_G$ (Eq. III.62), there must be a variation (that is to say a change in width for the S - shape curve of the probability function), in the vicinity of V_{int}, as shown in (Fig. III.26).

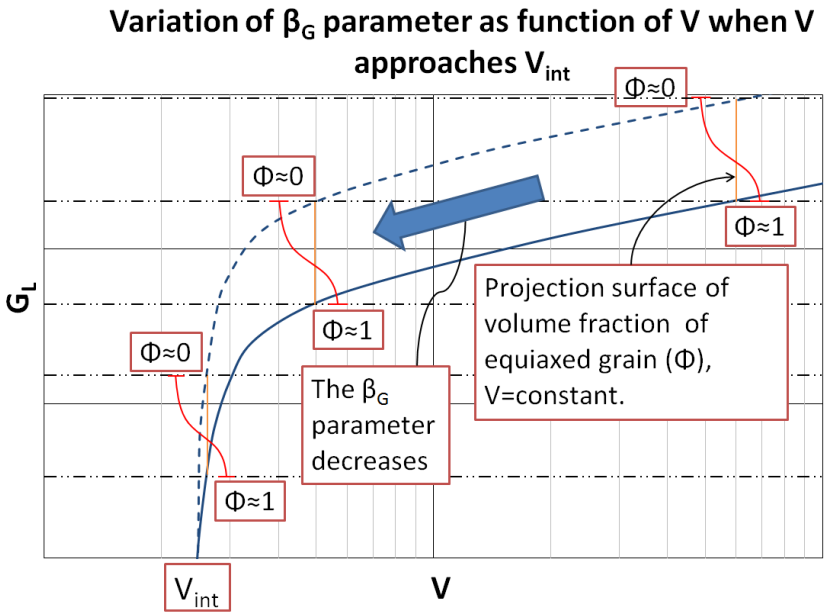

Figure III.26. Variation of the location parameter (β_G) with the consequent narrowing in the projection (S-shape graph orange line) over the width of the equiaxed grain fraction function near of the V_{int} coordinate.

The variation in width of β_G is very small except in the coordinates very close to V_{int}. It is therefore necessary to include in (Eq. III.49) a factor that directly affects β_G, and therefore model its change as seen in (Fig. III.26), as shown in (Eq. III.78):

$$\phi = 1 - Exp\left[-Exp\left(-f_{esc}\left(\frac{\xi-\mu}{\beta}\right)\right)\right] \qquad \textit{Eq. III.78}$$

Where f_{esc} is a scaling factor for $\beta = \beta_G$.

An equation is proposed based on (Eq. III.77), such that $f_{esc} \to \infty \ \ \forall \ \ V \to V_{int}$, or the same $\beta = \beta_G \to 0$. On the one hand, it must be taken into account the condition that for a relatively little change on the value of the coordinate when the V value grows moving away from V_{int}, the value $f_{esc} \to 1$ that is to say $\beta = \beta_G \to \text{constant}$.

The slope of the γ angle of (Fig. III.24) is also taken into account as a parameter to measure of the "abrupt fall" of β_G value when $V \to V_{int}$. Therefore of the above, the scaling factor proposed is:

$$f_{esc} = \beta_G\left(e^{7}\left(1-\psi_{**}^{\frac{1}{\tan\gamma}}\right)\right)+1 \qquad \textit{Eq. III.79}$$

The (Eq. III.79) completes the determination of all parameters necessary for use in (Eq. III.49) as a model to establish the volumetric fraction of equiaxed grains in the form of a mathematical equation of form $\phi = f(G_L, V)$.

III.4.5 Summary of the Crystallization Model and Associated Parameters

Rearranging the Eq. III.[49, 62, 65, 66, 77, 78 and 79], and renaming the variables $\psi_{**} = f_{\text{multip}}$, $\mu = \mu_V$ and $\beta = \beta_G$, the (Table III.6) is presented as the summary of the model:

Table III.6: Summary of constitutive equations of the equiaxed grain volume fraction model (ϕ) based on solidification maps for alloys. The associated coordinates to the model are referred to (Fig. III.24).

$\phi(G_L,V) = \left[1 - Exp\left(-G_L^{-\left(\frac{f_{esc}}{\beta_G \ln(10)}\right)} \cdot Exp\left(\frac{f_{esc}\mu_V}{\beta_G}\right)\right)\right] \cdot H(V - V_{\text{int}})$	Eq. III.80
$\beta_G = -\frac{1.7\left\lvert \log_{10}(G_{L(\phi\approx 0)}) - \log_{10}(G_{L(\phi\approx 1)})\right\rvert}{\ln\left(1 - \frac{\ln(e^8 - 1)}{8}\right)}$	Eq. III.81
$\mu_V = \left[\ell_{\log} + \frac{\left\lvert \log_{10}(G_{L(\phi\approx 0)}) - \log_{10}(G_{L(\phi\approx 1)})\right\rvert \ln\left(\frac{\ln(2)}{8}\right)}{\ln\left(\frac{8 - \ln(e^8 - 1)}{8}\right)}\right] \cdot f_{\text{multip}}$	Eq. III.82
$f_{esc} = \beta_G(e^7(1 - f_{\text{multip}}^{\frac{1}{\tan\gamma}})) + 1$	Eq. III.83
$\ell_{\log} = \frac{\ln(G_{L(\phi\approx 1)}) + m\left(\ln(V) - \ln(V_{(\phi\approx 1)})\right)}{\ln(10)}$	Eq. III.84
$f_{\text{multip}} = \left(\frac{\sin\gamma(V^{\frac{2}{\ln(10)}} - V_{\text{int}}^{\frac{2}{\ln(10)}})(2\cos\gamma - \sin\gamma)}{V^{\frac{2}{\ln(10)}}\sin\gamma(2\cos\gamma - \sin\gamma) + V_{\text{int}}^{\frac{2}{\ln(10)}}(3\cos^2\gamma - 4\sin\gamma\cos\gamma + 1)}\right) H(V - V_{\text{int}})$	Eq. III.85
$m = \tan\theta = \frac{1}{n} = \frac{\ln\left(\frac{G_{La(\phi\approx 1)}}{G_{Lb(\phi\approx 1)}}\right)}{\ln\left(\frac{V_{\phi a}}{V_{\phi b}}\right)}$	Eq. III.86

III.4.6 Example of Application of the Model for the Experimental Solidification Map of Inconel 718

The model will be applied to (Fig. III.27), specifically for the case of the solidification map of the INCONEL 718 alloy (Nastac et al., 2001). Inconel 718 alloy has been chosen for the reason that it will be used in the experimental validation of this model.

First, the image will be pre-processed to place the coordinates of G_L and V (Fig. III.27) in the same scale of (1:1) for the horizontal and vertical axis. Once this is done, the key values to be introduced in (Eq. III.80) to (Eq. III.86) according to the references of (Fig. III.24) will be obtained.

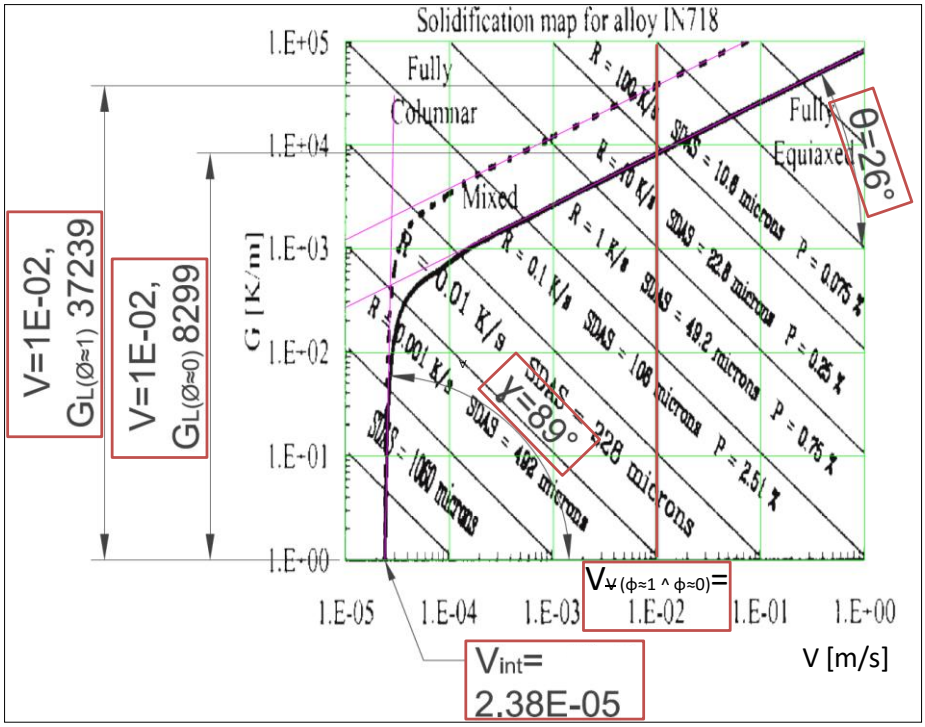

Figure III.27. Solidification map of INCONEL718 with the horizontal and vertical axis scaling at same size to obtain the value of coefficients for the equiaxed grain volume fraction model (ϕ).

The results are summarized in (Table III.7):

Table III.7: Coefficients calculated for the application of the (Table III.6) model from the solidification map for the alloy INCONEL 718 (Fig. III.27).

$V_{int} = 2.38*10^{-5}$ (m.s^{-1})	$\theta = 26.3^{o} \rightarrow \tan\theta = m = 0.495$
$V_{\forall(\phi\approx0 \wedge \phi\approx1)} = 1*10^{-2}$ (m.s^{-1})	$\gamma = 89^{o}$
$G_{L(\phi\approx0)} \approx 10^{3.919} = 8299$ (K.m^{-1})	$G_{L(\phi\approx1)} \approx 10^{4.571} = 37239$ (K.m^{-1})

For simplicity, we have applied the model through a contour graph for the volume of equiaxed grain formation $\phi = 0.01$, $\phi = 0.5$ and $\phi = 0.99$ (Fig. III.28), adjacent with the original solidification map for the INCONEL 718 alloy for the purpose of comparison.

(a)

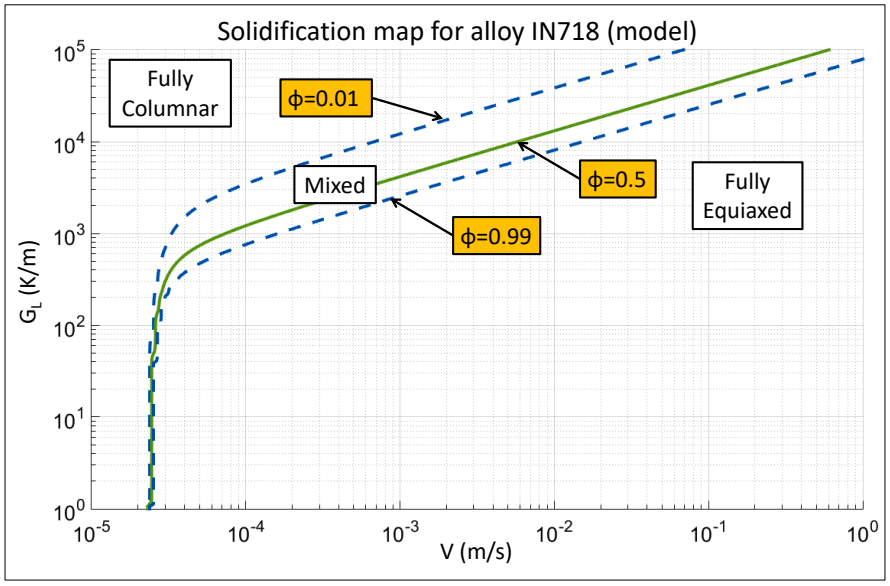

(b)

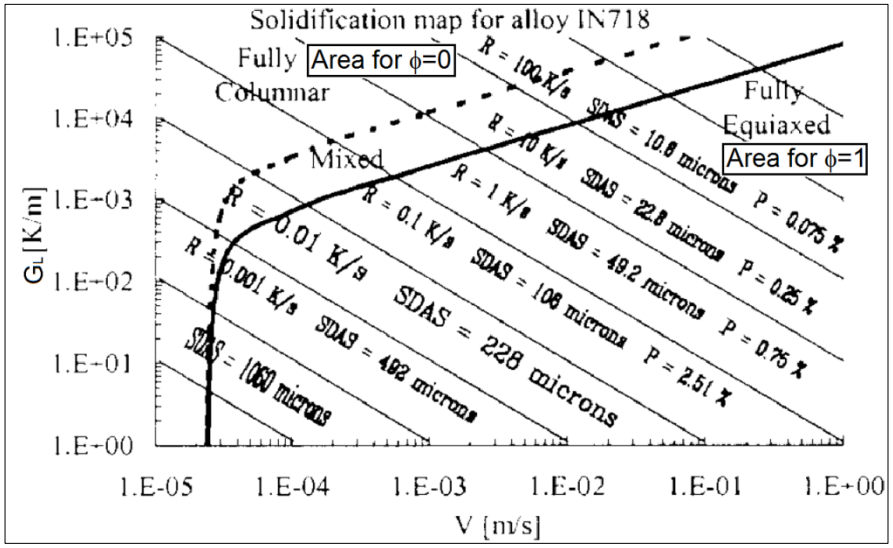

Figure III.28. (a) Comparison between the solidification map generated from the proposed model by means of the isocurves $\phi = 0.01$, $\phi = 0.5$ y $\phi = 0.99$ (blue and green lines), versus (b) the experimental solidification map for the alloy Inconel 718 (Nastac et al., 2001).

The fit in (Fig. III.28) is very good. A very important detail is that the fraction of the equiaxed grain formation volume is not symmetrical in the "mixed morphology" grain zone. This is observed in the relative distance between the fractions $\phi = 0.01$ to $\phi = 0.5$, and from $\phi = 0.5$ to $\phi = 0.99$ which is not equidistant (Fig. III.28a). On the other hand

the model of (Table III.6) reflects very well the asymptotic behaviour at low solidification rates and low temperature gradients.

III.5 Application of the Model for a Metal Powder Reconditioning Method

III.5.1 Experimental Setup

A series of probes has been manufactured based on the optimized parameters of (Renderos et al., 2017). The original objective of that research was to develop a method of reconditioning the INCONEL 718 to take advantage (reuse) the metallic powder not adhered to the substrate. The methodology consisted in the manufacture of specimens from new powder to which an evaluation of mechanical and metallurgical properties would be made.

These specimens generate during their manufacture a waste of unadhered powder, which once collected and reconditioned, would be used as raw material to manufacture a new series of samples, which in turn must generate more unadhered powder and so on (up to a total of 4 times) without adding "fresh" (new) metallic powder.

Due to the heating of the powder as it passes through the laser beam, a certain amount of it oxidizes superficially changing the original absorptivity of laser beam with respect to the new powder, that is, the amount of energy absorbed by the powder itself is greater as it is more opaque (Sainte-Catherine et al., 1991); in addition, a change in the distribution of the mean size of the powder was originated. The continuous repetition of that cycle (collection of unadhered powder and production of samples with the same) according to the number of reuses of powder was increasing, is the origin in the modification of the process parameters. The consecutive reuse of the powder modifies the properties of the surface itself, which makes it necessary to modify the working conditions in the system through the process parameters.

Along with the evolution on the physical properties (surface properties and average powder size), an effect of heat accumulation on the substrate was observed during the sample manufacturing. The first layers deposited were processed on a "cold" substrate (assumed at room temperature, $T_{o(\,first\ layers)} \approx 298\ \mathrm{K}$); on the other hand, the layers manufactured in the final stages of the samples with reconditioned powder were raised on a "hot" substrate (approximately of $T_{o(last\ layers)} \approx 573\ \mathrm{K}$).

The summary that will serve as the basis to establish the local coordinate conditions for their application in both the model for Laser Cladding process and the proposed model for equiaxed grain volumetric fraction (ϕ) applied to the INCONEL 718 alloy (and obtain the variation in the local conditions of G_L and V), is presented in (Table III.8):

Table III.8: Evolution in raw material properties and process variables for sample manufacturing in research about reconditioning of metallic powder for Laser Cladding process on INCONEL 718 (Renderos et al., 2017).

Condition 1: - State of powder: New - Equivalent powder mean diameter: 68.1 μm - Surface condition powder: shiny (not oxidized), $\eta_{powder} = 0.3$ - $T_{o\ (\text{first layers})} \approx 298\ \text{K}$ (not preheating) - Surface condition substrate: shiny (not oxidized), $\eta_{subs} = 0.3$	Condition 2: - State of powder: New - Equivalent powder mean diameter: 68.1 μm - Surface condition powder: shiny (not oxidized), $\eta_{powder} = 0.3$ - $T_{o\ (\text{last layers})} \approx 523\ \text{K}$ (preheating) - Surface condition substrate: opaque (oxidized), $\eta_{subs} = 0.59$
Condition 3: - State of powder: Used (4 times) - Equivalent mean diameter: 81.1 μm - Surface condition powder: opaque (oxidized), $\eta_{powder} = 0.4$ - $T_{o\ (\text{first layers})} \approx 298\ \text{K}$ (not preheating) - Surface condition substrate: shiny (not oxidized), $\eta_{subs} = 0.3$	Condition 4: - State of powder: Used (4 times) - Equivalent mean diameter: 81.1 μm - Surface condition powder: opaque (oxidized), $\eta_{powder} = 0.4$ - $T_{o\ (\text{last layers})} \approx 573\ \text{K}$ (preheating) - Surface condition substrate: opaque (oxidized), $\eta_{subs} = 0.61$

The rest of the parameters (which remain constant), for the application of both the analytical model during the manufacturing of the probes in (Renderos et al., 2017) by means of Laser Cladding process, and that for the proposed model for volumetric fraction of equiaxed grain (ϕ), is presented in (Table III.9):

Table III.9: Constant parameters for verification of Laser Cladding model and application of the proposed volumetric fraction of equiaxed grain model. This table is complementary for (Table III.8).

$Q_{g(\text{normalized})} = 2.6$ (l.min^{-1})
μ_{gas}=2.125*10^{-5} (kg.m^{-1}s^{-1}) [Argon]
r_n=5.275*10^{-3} (m)
$2r_o$=0.45*10^{-3} (m)
$s_n = 14.5*10^{-3}$ (m)
$\rho_p = \rho_{subs}$=8240 (kg.m^{-3})
$\phi d_{drop} = 2.2*10^{-3}$ (m)
ϕd_{laser}=1*10^{-3} (m)
m'=1.463*10^{-4} (Kg.s^{-1})=8.78 (gr.min^{-1})
P_{laser}(cylindrical energy distribution)=571 W
v=8.7*10^{-3} (m.s^{-1})=522 (mm.min^{-1})

III.5.2 Results of the model

The evaluation and verification of the Laser Cladding model (Eq. III.3) to (Eq. III.29) and (Eq. III.31) to (Eq. III.39), and of the volumetric fraction of equiaxed grain (Table III.6), is presented in (Fig. III.29). This graph describes the summary of test results in which a series of specimens manufactured under the conditions of (Table III.8) and (Table III.9) have been submitted for an EBSD examination.

The EBSD test technique has allowed to characterize the distribution in size and geometry of the grains generated during solidification based on the average local conditions of V and G_L. It is desired to verify the following:

-First, if the equiaxed fraction model is capable of correctly describing the morphology of the grain generated during solidification.

-Second, if the Laser Cladding model as function of the input process parameters itself has been capable of generating sufficiently precise local values of V and G_L.

Finally, the EBSD images together with the related points associated with the local conditions of solidification were superimposed on the proposed crystallization model graph (it is a probability surface in two variables V and G_L), for the different process conditions of (Table III.8) and (Table III.9) as shown in (Fig. III.29).

EBSD images have been taken at the bottom and top of the specimen samples for both new powder and reconditioned powder (Renderos et al., 2017). The results shown in (Fig. III.29) indicate grain morphology strongly dependent on local solidification conditions with the tendency of equiaxed grain formation in the upper part in the blocks of alloy manufactured by means of Laser Cladding process.

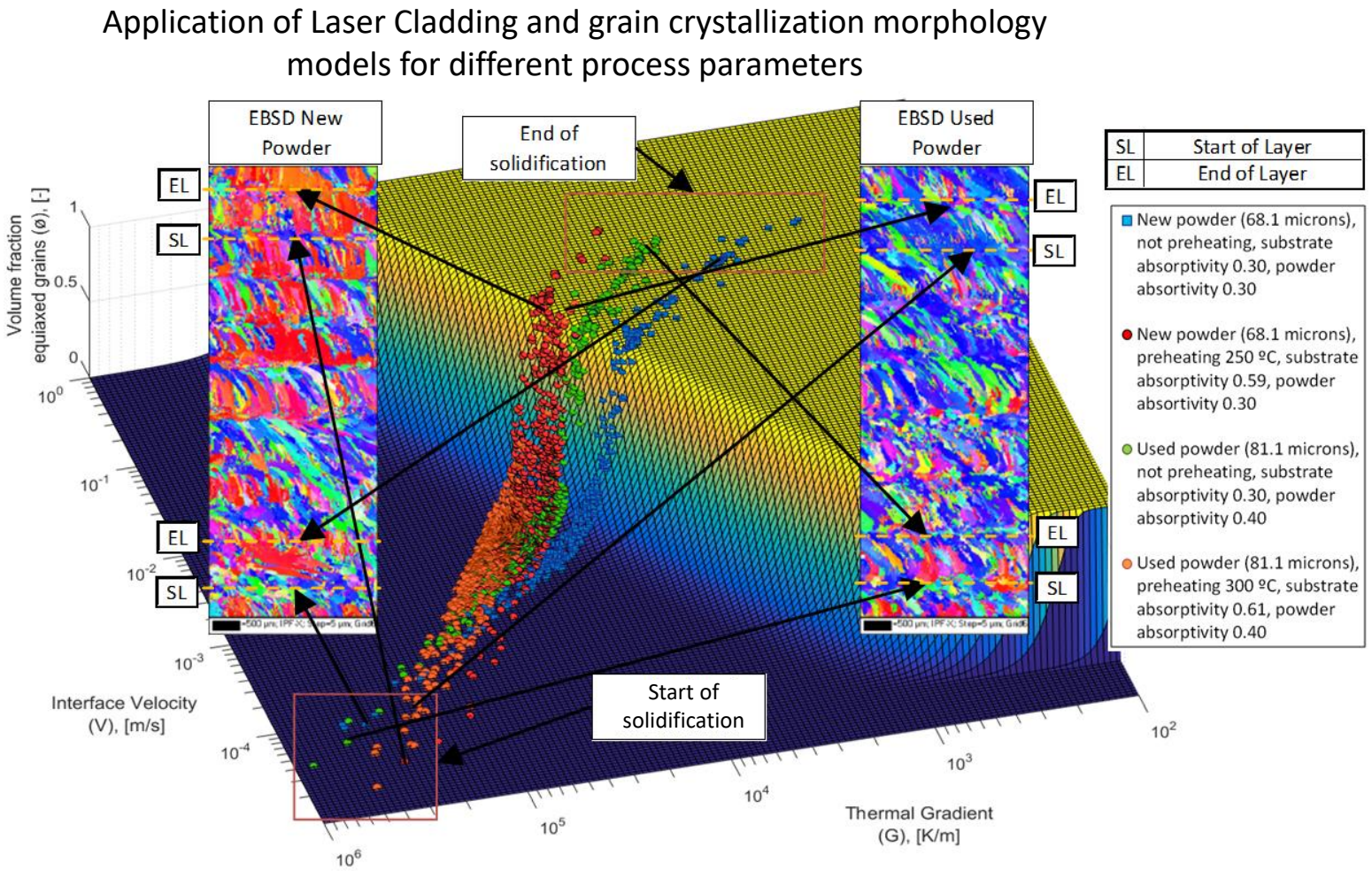

Figure III.29. Representation of the solidification model of the equiaxed grain fraction for the alloy INCONEL 718 for the laser cladding processes based on the parameters of the (Table III.8) and (Table III.9).

III.5.3 Discussion of the Results

The (Fig. III.29) indicates the beginning and end of the melt pool hardening process (beginning and end of solidification), for each set of Laser Cladding process (Conditions 1 to 4, (Tables III.8) and (Tables III.9). In the graph (EBSD map), this is indicated by dotted lines in orange with the abbreviation SL (start of layer) and EL (end of layer). With black arrows, the coordinates of the different stages for the manufacturing of the blocks from which the test probes were made, are indicated on the EBSD figure of the crystallization model. It is also indicated with red line boxes on the graph itself, the beginning and the end of each of the cat layers (the labels “Start of solidification” and “End of solidification”).

Each layer in the substrate always starts with solidification in columnar morphology (indicated by the arrow pointing to the bottom of each cladding layer in the EBSD graph), which is dependent on the maximum gradient of temperature (the cladded material in direct contact with the substrate conducts the temperature better). It is also observable that the solidification concludes with morphology of mixed grain or completely equiaxed (again depending on the local conditions of cladding and temperature gradient). It should also be noted that with each layer of material that is deposited, part of the equiaxed fraction on the previous layer is remelting by the next one, this effect is most evident in the upper layers.

A very particular phenomenon has been observed in (Fig. III.29) while examining the interface between layers: when one layer adheres consecutively to the other, the amount (depth) of remelting depends on the difference between the temperature of the melt pool and the initial temperature of the previous layer (T_o). The above is deduced from the process conditions shown in (Tables III.8) and (Tables III.9). For different process conditions, the initial average temperature (T_o) at the top of the blocks for the manufacturing of the samples always were higher.

In a solidification map for alloys such as that of (Fig. III.28), low temperature gradients tend to generate equiaxed grain morphology (this is an effect of the substrate being hot, since the temperature difference between two points within the sample will be smaller). However, in a hot substrate the amount of melt pool will penetrate a greater distance into the substrate since the laser beam does not have to use a lot of energy to "heat" the base (substrate) where the material is deposited.

The evidence with EBSD indicates that at least for the experimental conditions used in the verification of this model, the second effect (the melting of a part of the surface in the previous substrate with the tendency to create grain with columnar morphology), has been more important than the tendency of the temperature gradients to form grain with equiaxed morphology structure (governed by the local conditions V and G_L of solidification and described by the experimental solidification map of the alloy).

All the previous comments have been well reflected in (Fig. III.29) both by the Laser Cladding model (which serves as the basis for obtaining the average local conditions of V and G_L), and by the grain crystallization morphology model (to know the fraction of equiaxed grain for each local condition $\phi = f(G_L, V)$). Therefore, both models are considered valid.

III.6 Method for Deduction of Number of Nucleation Sites per Unit of Volume (N_0) for Laser Cladding Process

III.6.1 Importance of the Constant N_0 and its Relation to the Material Constant a for Crystallization Models

As mentioned before, one of the limitations in the use of a crystallization model is the availability of experimental data. In this section we will explain the deduction of the number of homogeneous nucleation sites (N_o) for the Gäumann model (Gäumann et al., 2001), and its subsequent application for the deduction of the constant of material "a" (Eq. III.45). Once this value is deduced, it is possible to extrapolate the calculation for the model deduced in this chapter since the value for this material constant is the same for both.

On the other hand (Gäumann et al., 1997), shows that the influence of the number of nucleation sites on CET is important in the higher velocity growth region (V), because once nucleation occurs, the volume of fraction of equiaxed grains is mainly is linked to the number of nucleation sites. Thus if the number of nucleation sites is reduced, then the columnar microstructure is stabilized. The above together with the undercooling are parameters that are specific to the equiaxed grains and for the control of the formation of nuclei.

Therefore, a good estimate of the material constant N_o is important for the prediction and control of the microstructure during a solidification process.

III.6.2 Proposed Method for the Deduction of N_0 Based on EBSD Images

Clearing a from (Eq. III.46) results in (Eq. III.87):

$$a = \frac{G_L^n \left(\frac{4\pi}{3}\right)^{-n/3} \left(\frac{\left(-\frac{N_o}{\ln(1-\emptyset)}\right)^{\frac{1}{3}}}{n+1}\right)^{-n}}{V} \qquad \textit{Eq. III.87}$$

Since it is possible to evaluate the volumetric fraction of equiaxed grain (ϕ) by means of an image analysis of the EBSD test as proposed (Gäumann et al., 2001), the method to deduce N_o will follow an analogous procedure.

It basically consists in counting the number of grains per unit of volume by means of the analysis of the projection of the number of grains per unit of area from images, obtained through an EBSD test, from two different directions of the same volume to analyse. The methodology is the same used by (Brahme et al., 2006), where the images with the projection of the grains from the EBSD test from two different directions were taken perpendicularly at 90 degrees to each other.

In this case, instead of proposing the strict use of images taken at 90 degrees, it will be taken as a criterion if the image is able to show the change of texture in the microstructure.

Or in other words, if is possible to characterize the microstructure of the grains taking into account the variable morphology of the same for different directions. This is important because the Laser Cladding process is highly directional (Hu et al., 2012).

In (Fig. III.30), where the projection of the grains by EBSD images corresponding to two different classes of powder (new and reconditioned) is shown, the morphology of solidification is in the advance direction, that is to say the cut view section is parallel to the direction of movement of the laser beam.

The morphology of grain for an image taken in a perpendicular direction (transversal to the direction of the laser beam movement) however presents a different grain characteristic. Or in other words, it is possible to distinguish, for example, a section view of an image of the longitudinal direction (L) from a transverse one (T), as shown in (Fig. III.30).

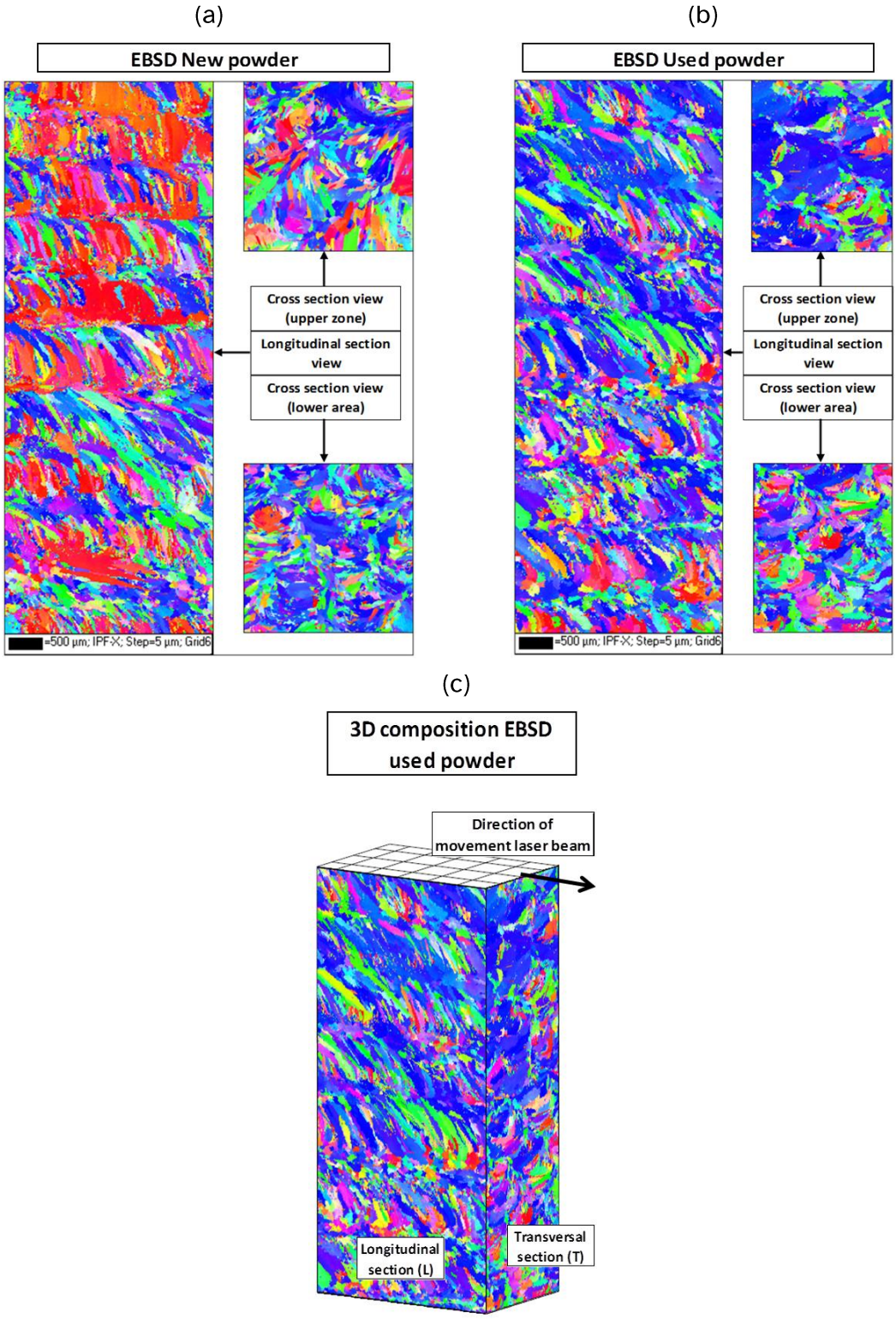

Figure III.30. Morphological distribution of microstructure of grain from images based on EBSD tests (a) for new and (b) reconditioned powder in the longitudinal (L) and transversal (T) directions, respect to (c) the laser beam path (used powder).

The grain size distribution for an EBSD image can be done with specialized and even free software, such as MTEX (Nolze and Hielscher, 2016). By example, for the longitudinal

section view of used powder (discounting the grains at the periphery of the image for being incomplete), the grains “valid” for the calculation of their density per unit area are shown in (Fig. III.31).

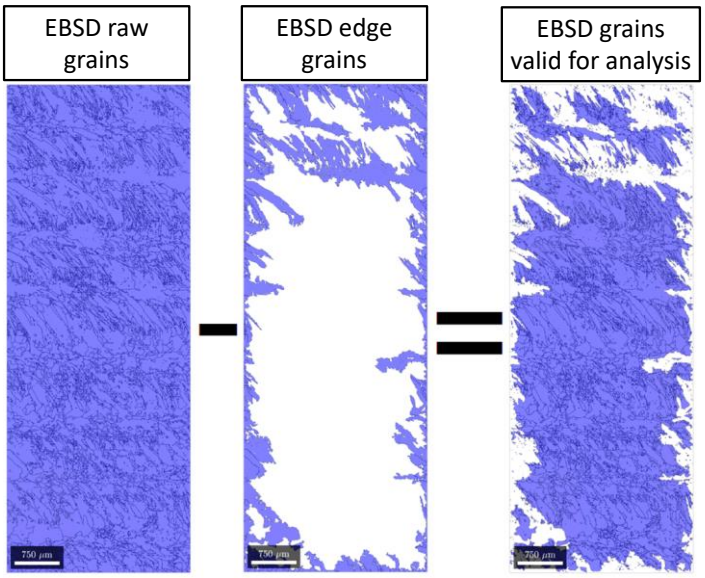

Figure III.31. Grains filtering in an EBSD image to calculate the number of heterogeneous grain growth sites (N_o) based in view sections, in this case for reconditioned powder (longitudinal section).

From the selection of “valid” grains it is possible to obtain the total area of the grains and the number of then, as well as varied statistics to characterize their size distribution. (Table III.10) presents the results for the cross-sectional and longitudinal areas for new and reconditioned powder (Fig. III.30) and (Fig. III.31).

Table III.10: Grain size statistics for transversal (T) and longitudinal (L) sections views for new and used powder based in process parameters described in (Table III.8) and (Table III.9).

		Transversal (T)		Longitudinal (L)	
		New powder	Used powder	New powder	Used powder
Mean	(μm²)	1358.2	1409.5	1094.8	1341.4
Median		75	75	75	75
Mode		25	25	25	25
Standard deviation		7421.6	10138.9	12960.5	10378.1
Minimum		25	25	25	25
Maximum		257800	450800	1562300	675375
Total area of grains		8931400	9027925	30633950	18359125
Kurtosis	-	457.3	1036.0	7974.2	1592.5
Number of grains	-	6576	6405	27981	13687

From the statistics of (Table III.10), it is observed that there is a great data dispersion, which does not allow to use the assumption that the grains can be approximated by ellipsoids homogeneous as in (Brahme et al., 2006), (where it is postulated that their size is approximately uniform). As our assumption, we will admit that the projected sections of the "valid" grains (those not found on the periphery of the EBSD image) are squares. The reason for this assumption will be explained later.

The next step is to calculate an equivalent side length for each "square" type grain according to its corresponding area projection (in this case for L and T views), as shown in (Eq. III.88):

$$\ell_{\substack{square \\ grain}} = \sqrt{A_{\substack{mean \\ grain}}} = \sqrt{A_{\substack{grains \\ projection}} / n_{grains}} \qquad \textit{Eq. III.88}$$

The volume of the equivalent cubic cell grain will be assumed as the product of the equivalent length of the grain projection in the longitudinal (L) and transverse (T) directions by the average of both previous lengths for the third direction.

The use of the average of the grain lengths (in the L and T directions), to estimate the value in the third dimension, is the reason why cubic-shaped cells have been chosen (it

is a simple geometric shape that allows to estimate the missing dimension to calculate the volume of each cell). The above is calculated through (Eq. III.89):

$$V_{\substack{unit \\ cell}} = \frac{\ell_{\substack{square \\ grain(L)}} * \ell_{\substack{square \\ grain(T)}} * \left(\ell_{\substack{square \\ grain(L)}} + \ell_{\substack{square \\ grain(T)}} \right)}{2} \qquad \textit{Eq. III.89}$$

III.6.3 Application of Method for the Deduction of N_0, Results and Discussion

The results from (Eq. III.88) and (Eq. III.89) and from the data of (Table III.10) are presented in (Table III.11), and together with them, the number of heterogeneous nucleation sites for each kind of powder. The number of heterogeneous nucleation sites is defined as the inverse of the volume of the equivalent cubic cell grain in appropriate units.

Table III.11: Calculation of the equivalent cubic cell grain volume and number of heterogeneous nucleation sites for a Laser Cladding process with two different types of clad material (new and used metallic powder).

		New powder		Used powder	
		Transversal (T)	Longitudinal (L)	Transversal (T)	Longitudinal (L)
Length of grain side in equivalent cubic shape $\left(\ell_{\substack{square \\ grain}} \right)$	(μm)	36.9	33.1	37.5	36.6
Length mean value		35.0		37.1	
Volume unit cell	(μm^3)	42643.6		50990.9	
Volume unit cell	(m^3)	4.26E-14		5.10E-14	
Number of heterogeneous nucleation sites (N_o)	(m^{-3})	2.35E+13		1.96E+13	

From (Table III.11), it should be noted that the value of N_o is very uniform even for different Laser Cladding process parameters, but it is very sensitive and dependent of the solidification process, where for example in the case of (Pautrat, 2013), the density of germination sites for the same alloy but for a different solidification process is in the order of 8.10^7 [m^{-3}].

Between the factors that have the greatest effect on the number of nucleation sites, the temperature gradient is one of the most important (in general, for a smaller temperature gradient larger grain size) (Nastac et al., 2001). In the case of the Laser Cladding process, since the gradients are very high, the effect will be a small grain size (or a high N_o value).

Finally, from (Table III.11) the value of N_o suitable for the Laser Cladding process will be chosen to replace it in (Eq. III.87), and deduce the a alloy related constant needed to complete the data availability for any model. In this document two cases have been presented as an example (with new and used powder), and the N_o adequate should mean the one that best represents the process to be controlled.

III.7 Conclusions

- An analytical model for the laser cladding process has been proposed. The model takes into account the main parameters, and “develops” the effect of each of them independently so that it is possible to separate the consequences of each parameter separately.
- The model takes into account the attenuation of the energy supplied by the laser beam on the surface due to the shadow effect of the powder (delivered by a coaxial nozzle), taking into account the effect of drag velocity because of the protective gas.
- An iterative methodology has been proposed to define the temperature-dependent properties for the energy balance in the metallic powder interacting with the laser beam, and thus obtain a more accurate energy balance for the substrate (via negative enthalpy).
- In the application of the laser cladding model for the calculation of the thermal field in the substrate, a general solution in a steady stable state was used. In the calculation of the thermal field a methodology has been proposed to be able to make the solution “dependent” on the thermal properties of the material, which helped to calculate accurately the temperature values within the melt pool, taking into account the change of phase, and therefore to calculate the values of temperature to determine the thermal gradient.
- The calculation of the thermal gradient together with the growth velocity in the solidification front was used as input variables to determine the CET behaviour of an alloy. To model the CET behaviour of an alloy, the use of a solidification model

based on experimental Solidification Maps combined with the behaviour of a Gumbel's probability distribution is proposed.

- The use of a deterministic model for columnar/equiaxed grain formation is justified by the difficulty of modelling the behaviour of a multicomponent alloy.
- The relationship between the CET-model and the experimental-type solidification maps that served as basis has been established.
- The proposed model: extends the range of application of the base model to values of low solidification speeds, intuitively explains the CET behaviour in the mixed zone (the behaviour is modelled based on a well-known probability distribution), and determines in a unique way with a physical sense the constants of material for other models, taking advantage of the information contained in experimental solidification maps.
- A method is included to obtain an estimate for the number of nucleation sites per unit volume, and it is concluded that this value is highly dependent on the solidification process involved. For laser cladding process, its value is very high compared to traditional casting processes, due mainly to temperature gradients.
- The model was tested by means of an experimental essay where different types of raw material (new metallic powder and reconditioned metallic powder to be recycled again) are used to build specimens that were analysed by means of EBSD images. The results of the powder solidification CET morphology are compared with both the proposed model for laser cladding and proposed model for CET crystallization, with good correlation between the predictions and the experimental results.

CHAPTER IV: APPLICATION TO THE REPAIR OF COATED PROBES TO OBTAIN MECHANICAL PROPERTIES IN CLADDING MATERIAL.

IV.0 Nomenclature and Abbreviations

AM:	Additive Manufacturing
AR:	Aspect Ratio
CC:	Spiral-spiral deposition strategy
DCM:	Director Cosine Matrix
DV:	Dang Van
HCF:	High Cycle Fatigue
LCF:	Low Cycle Fatigue
LZ:	Longitudinal Zig-Zig deposition strategy
LZZ:	Longitudinal Zig-Zag deposition strategy
MP:	Generic Mechanical Property
PSB:	Persistent Slip Bands
SCL:	Stress Classification Line
SEM:	Scanning Electron Microscope
SL:	Endurance Limit
VEG:	Virtual Extensometer gauge
ZC:	Longitudinal Zig-Zig + Spiral deposition strategy
ZZC:	Longitudinal Zig-Zag + Spiral deposition strategy

$A_{:}$	Generic area (m^2)
A_{clad}:	Coated cross-sectional area on the neck of a probe (m^2)
A_{grain}:	Grain surface area (m^2)
A_{probe}:	Coated cross-sectional area in the test zone of a probe (m^2)
A_{test}:	Coated cross-sectional area on the neck of a probe (m^2)
c_1, c_2:	Coefficients of polynomial normal stress function for the preform [($N.m^{-4}$), ($N.m^{-2}$)]

d_1, d_2 :	Coefficients of polynomial normal stress function for the clad [(N.m^{-4}), (N.m^{-2})]
D_G :	Fractal dimension boundaries for network of grains (-)
d_{grain} :	Grain size equivalent diameter (m)
D_l :	Fractal dimension of the grain size (-)
D_m :	Fractal dimension of crystallographic orientation of grains (-)
D_R :	Fractal dimension of perimeter-area of grains (-)
D_S :	Fractal dimension of aspect ratio of grains (-)
Dil_{ml} :	Dilution in a multiple bead (-)
d_{test} :	Diameter of test probe (m)
E :	Young modulus uniaxial tensile test general, (N.m^{-2})
E_{clad} :	Young modulus of clad material (N.m^{-2})
E_{comp} :	Young modulus of clad material for the composite specimen (N.m^{-2})
$\%E$:	Tensile elongation at fracture (-)
E_{test} :	Young modulus of elasticity for complete test probe (N.m^{-2})
F :	Load (N)
f :	Volume fraction (-)
HV :	Hardness Vickers (N.m^{-2})
k_{tx} :	Stress concentration factor (-)
L :	Generic length (m)
l :	Grain size length (m)
M :	Bending moment (N.m)
m :	Schmid factor (-)
$m_{\substack{Weibull \\ \phi\_shape}}$:	Weibull dimension for grain geometric texture orientation (-)
N_f :	Number of fatigue test cycles (-)
P :	Cumulative distribution function (-)
q :	Fatigue notch sensitivity (-)

R:	Stress ratio (-)
R_{test}:	Radius of curvature in probes with continuous radius between ends (m)
$sd(x)$:	Standard deviation for x variable
S:	Surface (m^2)
S':	Entropy ($J.K^{-1}$)
t:	Time (s)
t_{clad}:	Thickness of cladding material (m)
$\mathcal{V}$:	Volume (m^3)
Wt, w:	Weight factor of a variable (-)
α:	Dang Van Parameter (-)
β:	Dang Van Parameter (-)
ε:	Proportional deformation (-)
ϕ_{grain}:	Grain geometric orientation (°)
ν:	Poisson modulus (-)
$\boldsymbol{\rho}$:	Stabilized residual stress tensor ($N.m^{-2}$)
σ:	Normal tensile stress in uniaxial test ($N.m^{-2}$)
$\boldsymbol{\Sigma}$:	Macroscopic Cauchy stress tensor ($N.m^{-2}$)
σ_0:	Endurance fatigue limit for R=0 ($N.m^{-2}$)
σ_{-1}:	Endurance fatigue limit for R=-1 ($N.m^{-2}$)
σ_{clad}:	Normal tensile stress inside of the cladded test probe ($N.m^{-2}$)
σ_H:	Hydrostatic stress ($N.m^{-2}$)
σ_n':	Bending fatigue limit ($N.m^{-2}$)
σ_{nom}:	Nominal (average), normal tensile stress in the test probe ($N.m^{-2}$)
σ_n:	Axial fatigue limit ($N.m^{-2}$)
σ_{pre}:	Normal tensile stress inside the preform of test probe ($N.m^{-2}$)
σ_{test}:	Normal tensile stress in the test probe ($N.m^{-2}$)
σ_{UT}:	Ultimate tensile strength ($N.m^{-2}$)
σ_{VM}:	Von Mises Stress ($N.m^{-2}$)

$\sigma_{x\max}$:	Maximum normal tensile stress in the probe in direction x_1 ($N.m^{-2}$)
σ_Y :	Yield strength ($N.m^{-2}$)
τ :	Shear stress ($N.m^{-2}$)
τ_{nd} :	Resolved shear stress ($N.m^{-2}$)

IV.1 Application of Optimal Input Parameters to the Manufacturing of Coated Specimens to Characterize Mechanical Properties in Cladded Material

IV.1.1 Introduction

The laser cladding process produces a material with special mechanical characteristics. To determine the mechanical characteristics (properties), the use of coated specimens is necessary.

With regard to mechanical properties, there are different standards to characterize the properties of materials, specifically metallic materials. There are no specifications for mechanical properties of coated specimens.

On the other hand, there is an enormous amount of prior information about metallic materials that should be taken advantage of in some way. Taking into account the previous paragraph, a proposal will be made for the use of coated specimens considering the following:

- As a point of comparison with respect to the properties of material added during a Laser Cladding process, it will be assumed that the material considered to be of the “base” type (that is, a material manufactured under specifications), will be of better quality than the one deposited. In this work, that "base" material is considered the substrate material.
- The specimens used to characterize the properties of the material, which is a mixture of base + deposition, must be in some way comparable with the existing standards (ASTM Subcommittee E08.05, 2015; ASTM Subcommittee E28.04, 2016; Committee ISO/TC 164/SC 4, 2017, 2010). However, there are no regulations for metallic coated specimens. The only associated standard that has been found is (ASTM Subcommittee F04.15, 2017), which refers to mechanical properties of coatings for medical use on metal specimens.
- We will seek to characterize the mechanical properties of material resulting from cladding process with laser, not the effect that defects have on it, such as pores,

cracks, foreign phases (for example, intermetallic with brittle behaviour), and stress concentrators (this will be explained later).

- The deposition with laser cladding process generates material with directional material properties (Niederhauser and Karlsson, 2005). Different deposition strategies generate different microstructural morphologies, and therefore, it is important to investigate their effect on mechanical properties.
- It should be sought that the coated specimens activate as many defects as possible within the cladded material. In other words, the stress in the test area must be as uniform as possible, and it must cover the largest possible volume of the specimen, so that the behaviour for the material to be evaluated will be representative.

IV.1.2 State of Art. Standard Specimens for Evaluation of Mechanical Properties for Laser Cladded Materials

Different morphologies of standard specimen have been used to characterize the cladded material for coated probes:

- “Dog bone long” in the case of (Lourenço et al., 2016; Walker et al., 2016), where the effect on the fatigue life of a repairment has been simulated by means of laser deposition in an artificial groove on steel specimens. The tests have been carried out in a tension-tension regime.
- “Dog bone short” in the case of (Koehler et al., 2012), with a modification which enabled the specimens to be tested in a 4-point bending test to characterize fatigue endurance by means of a pure bending moment.
- Rotary cylinders with an artificial crack start generator (notch) (Hutasoit et al., 2015). In this work, the effect of the thickness of the cladded layer on the fatigue behaviour over the specimen for different types of coatings has been investigated. In addition, other important factors such as residual stresses within the material itself were also investigated.

The drawings for the three types of standard specimens mentioned in the previous paragraph are presented in (Fig. IV.1), where special emphasis is placed on the ratio between the total area and the cladded area.

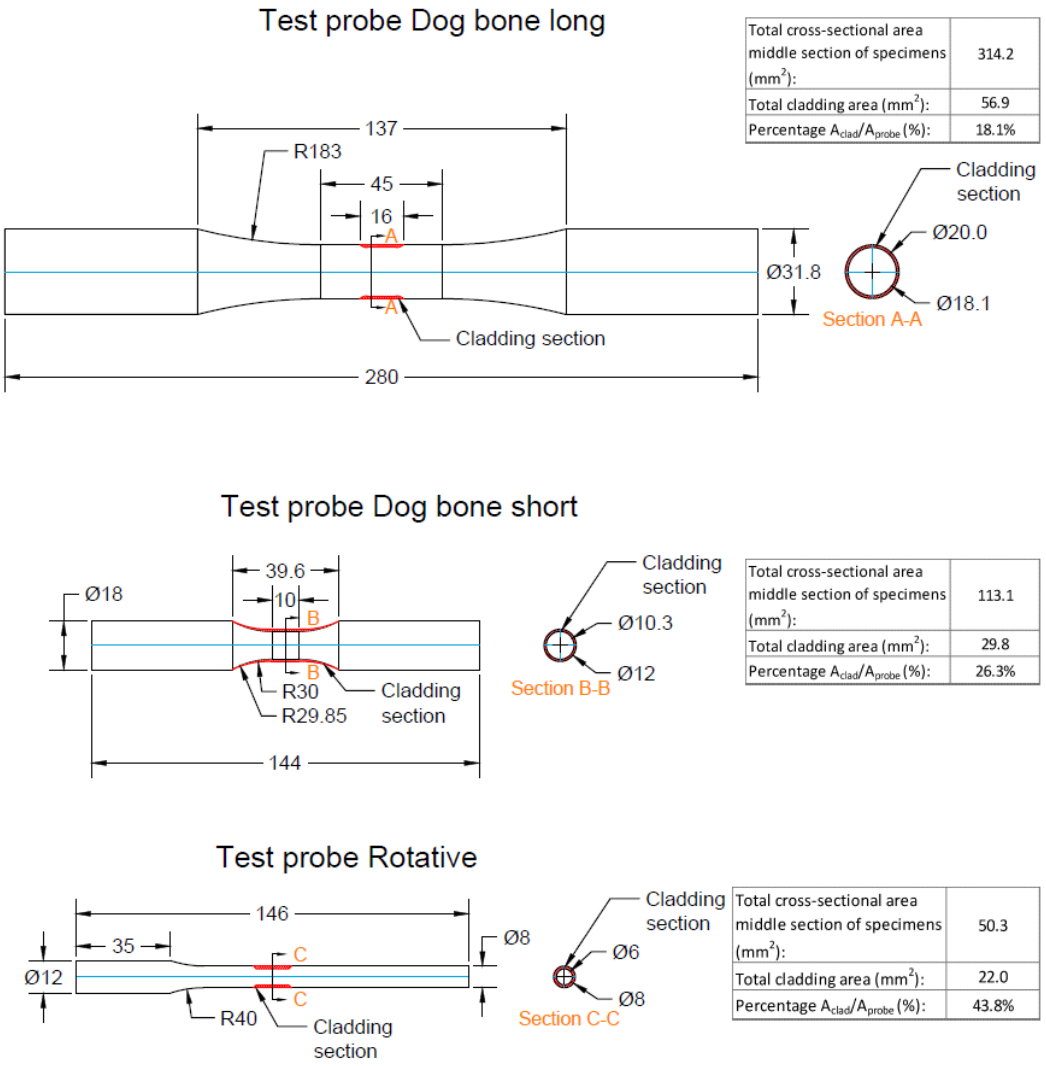

Figure IV.1. Drawings with the main dimensions of standardized specimens applied to characterize mechanical properties of cladded material made by laser cladding process. The ratio of the total area to the cladded area is included, with all of test probes on same scale for comparison purposes (all dimensions in mm).

The advantage of this type of test probes is that when using specimens with standardized shapes it is possible to compare the results with existing literature. The drawback with the previous specimen geometry is that it leads to the material failing in a very small volume of all the material supplied, with the risk of not activating a significant number of defects within the volume of material that has been added.

The reason for notching or using flexural testing for fatigue testing is the tendency to failure due to stress concentrators at the proximity of junction of the cladded material with the substrate.

Figure IV.2 shows the result of finite element analysis (FEM) of the three types of specimens aforementioned ("Dog bone long", "Dog bone short", and rotary cylinder). The geometry for each of the specimens is described in the respective articles. For comparison purposes, the load (P), or bending moment value (M), has been adjusted on the specimen in the finite element program in such a way that the maximum equivalent von Mises stress is approximately 1 MPa (σ_{vm} = 1 MPa).

The material properties (Inconel 718 for both, the base and the supplied material), will be assumed as indicated in Table IV.1.

Table IV.1: Material properties for simulation by finite elements model (FEM), of the standardized specimen geometries "Dog bone long", "Dog bone short", and Rotating specimen.

	Cladding material, deposition strategy=helix (CC)	Base material, min. prop. (AMS 5662M)
Ultimate Strength (MPa)	1284.5 ± 8.5	1276
Yield Strength (yield point) ε=0.2% (MPa)	1028.3 ± 17.5	1034
Percentage elongation after fracture (%)	10.7 ± 1.3	12
Modulus of elasticity (GPa)	197.4 ± 3.2	200

The values of these material properties have been obtained as a result of a tensile test according to (ASTM Subcommittee E28.04, 2016), for specimens with a helix-type layer deposition strategy, similar to the process used by (Hutasoit et al., 2015; Lourenço et al., 2016). It is important to note that in the previous "virtual test", no distinction is made between the mechanical properties of base and cladded material, but the characteristics of, for example, Modulus of Elasticity is the sum of the behaviour of the base material + coating simultaneously.

Later on, it will be necessary to distinguish between different values of Modulus of Elasticity; one for the filler material (E_{clad}), and another for the coated specimen as a whole (E_{test}), but for a preliminary analysis, the value obtained directly from the uniaxial stress test data base + deposition is going to be considered.

IV.1.3 Von Mises Stress Distribution on Coated Specimens for Different Configurations

First it is necessary to make a clarification. An equivalent stress has nothing to do with fatigue; it is a merely calculation number to estimate the onset of yielding on macro scale in a multiaxial stress situation. Fatigue damage is propagating perpendicular to the largest principal stress range; therefore, this stress range determines the fatigue behaviour. Principal stresses in the other directions have hardly any influence on the crack growth. These stresses do not affect the shear stress in the activated slip planes (2D stress state). The best approach would be the "Critical Plane Approach", i.e. analysing different crack growth directions (planes) and using for each plane the stress components perpendicular to that plane (Homan, 2018).

The use of von Mises's criterion aims at visualizing the stresses inside the probes in an intuitive way by means of an equivalent stress. An appropriate criterion will be used in the section dedicated to fatigue life properties.

In (Fig. IV.2), the von Mises equivalent maximum stress area is indicated with the label Max, (all are in the red area, with values of σ_{VM} close to 1).

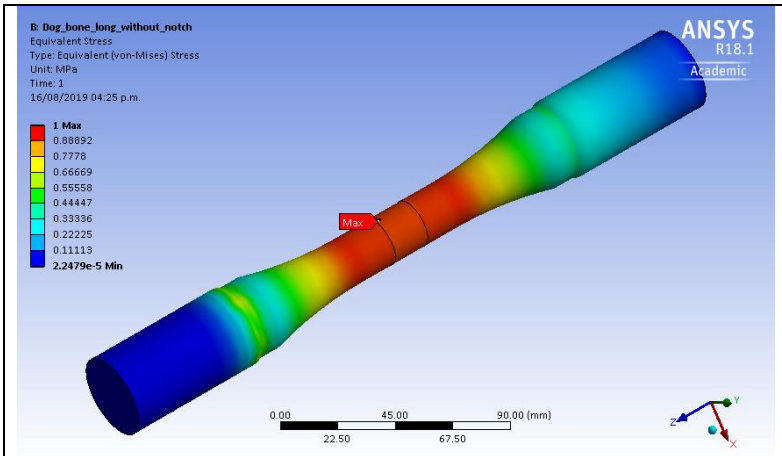

(a)
"Dog bone long" configuration test sample (the added material is included in the model). The maximum equivalent stress value is found in the fillet radius at the

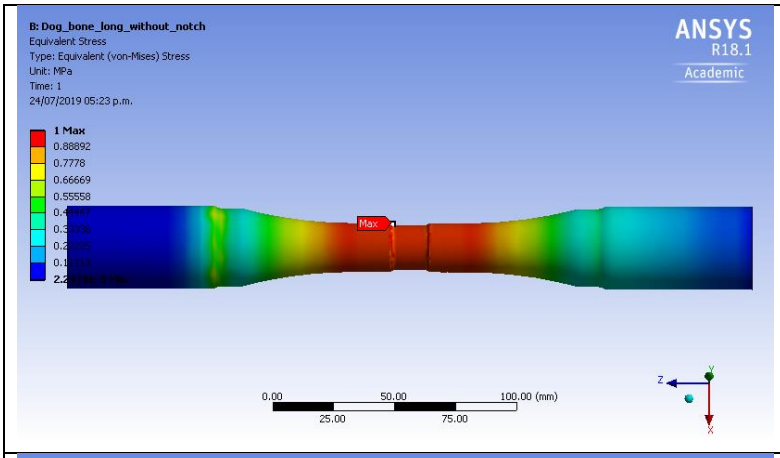

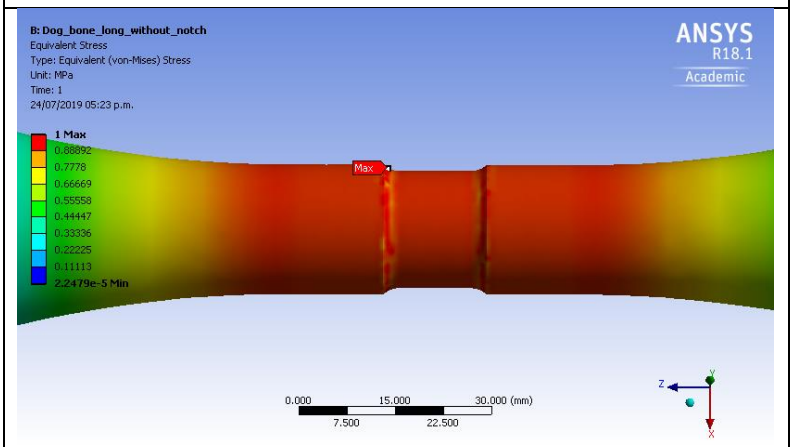

interface area between the base material and the cladded material. The material corresponding to the cladding has been "removed" to expose the area with the maximum equivalent load. The stress concentrator exerts its effect despite the existence of "clad material" to "recover" the original geometry of the specimen.

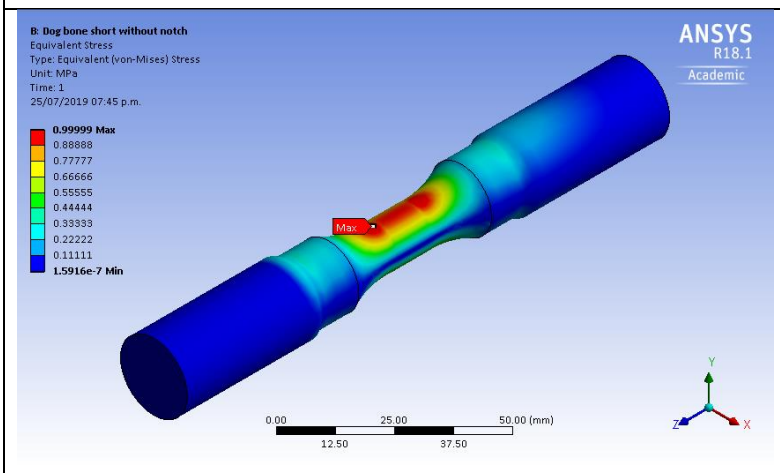

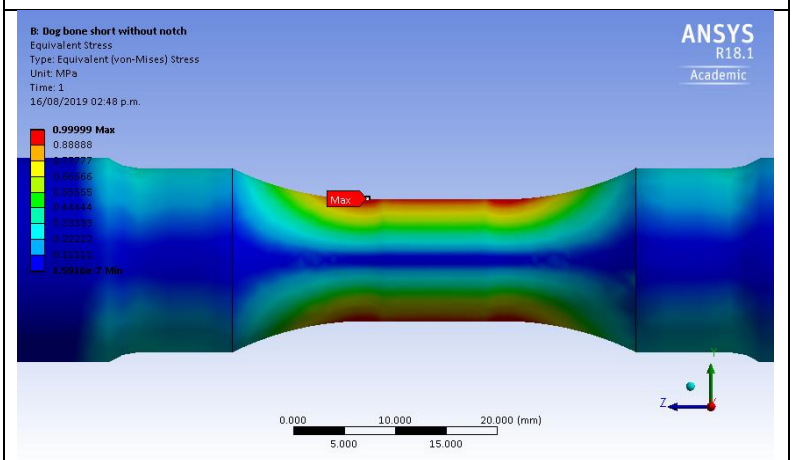

(b)

"Dog bone short" configuration specimen. The maximum stress value for test conditions of this specimen is in the connecting radius, on the surface at the where the union of the substrate with the added material begins. The volume subjected to the maximum equivalent von Mises stress is limited by the load condition on the specimen (bending load), that is, the volume subjected to loads close to the value of σ_{VM} = 1 is low,

	and therefore, activating a low number of defects.
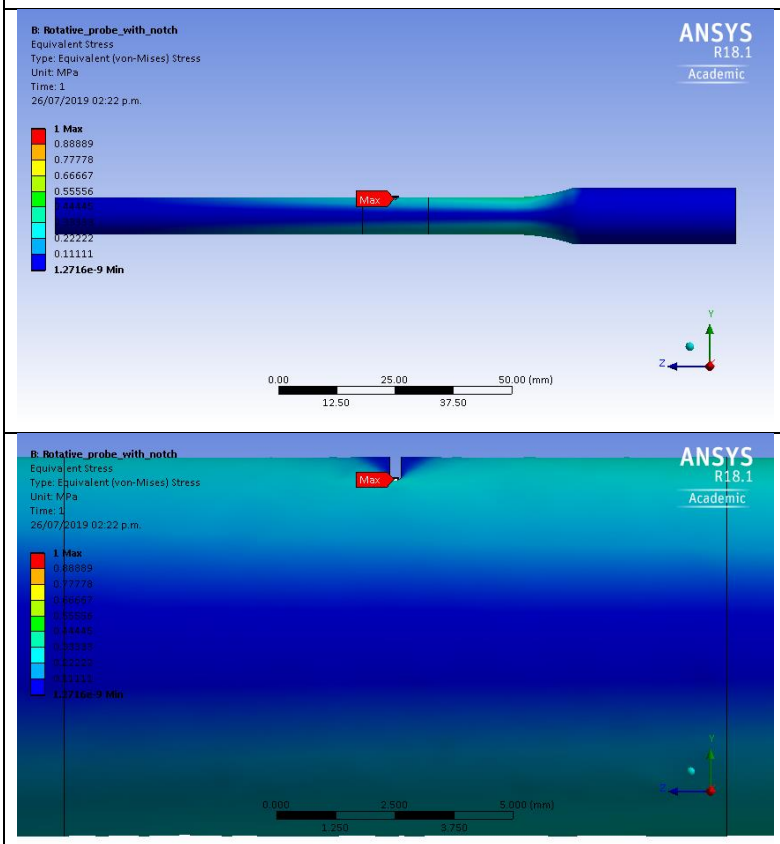	(c) Rotating specimen with notch in the middle of the cladded material. The stress concentrator forces the specimen to fail at the bottom of the same, limiting the volume of material with stresses closed to σ_{VM} = 1 only to the vicinity of the crack, resulting in a low volume for activation of failures within the cladded material.

Figure IV.2. Results of finite element analysis for three models of standardized specimens coated with laser cladding process under different load conditions: (a) "Dog bone long" in tension-tension test (Lourenço et al., 2016), (b) "Dog bone short" under pure bending test (Koehler et al., 2012), and (c) Rotating cylinder with artificial notch (Hutasoit et al., 2015). The zones where the "Max" label appears are within the volume of the body that represents the cladded material.

From the previous FEM results it can be concluded that:

- The maximum stress is not always found on the surface of specimen, but in the interface area between the base material and the added material. In the first drawing of (Fig. IV.2), section (a), it is presented within the filler coating.
- The location of the maximum stress is function of the relative difference between the properties between the base and cladded materials (as it will be seen later), and also of the stress concentrators that are generated by the "grooving" of the specimens with the objective of adding material that simulates the repairment for the same, (Fig. IV.2), section (a).

- For the (Fig. IV.2), section (a), despite the tendency of this type of geometry to fail in the area of the stress concentrator, it has the advantage that it activates a relatively large volume of defects in the cladded material and in the base material, allowing conditions close to reality to be replicated.
- When trying to avoid an increase in stress due to its concentrators, the type of load applied to the specimen can be changed to eliminate them, as in (Fig. IV.2), section (b). However, the drawback in this case is a very little volume of material that will be stressed to the maximum value, which may become a problem. The problem is that the material to be evaluated is very likely to contain a high number of defects, and therefore, it is necessary to evaluate a large volume of material for the test to be representative (Chapter IV.1.6.1).
- Finally, for (Fig. IV.2), section (c), the use of groove (as a stress concentrator) is justified by the fact that this type of specimen will tend to fail in the zone of the change of specimen section (Fig. IV.3), and not in the area of interest for the study of it (that of the cladded material). With the use of a stress concentrator on the surface, it will always be possible to "force" the material to fail in a certain work volume, but with the disadvantage that this volume will be small (note that in Figure IV.2, section (c), the area with von Mises equivalent forces close to 1, will be very small and restricted to the plane of symmetry of the “U” groove).

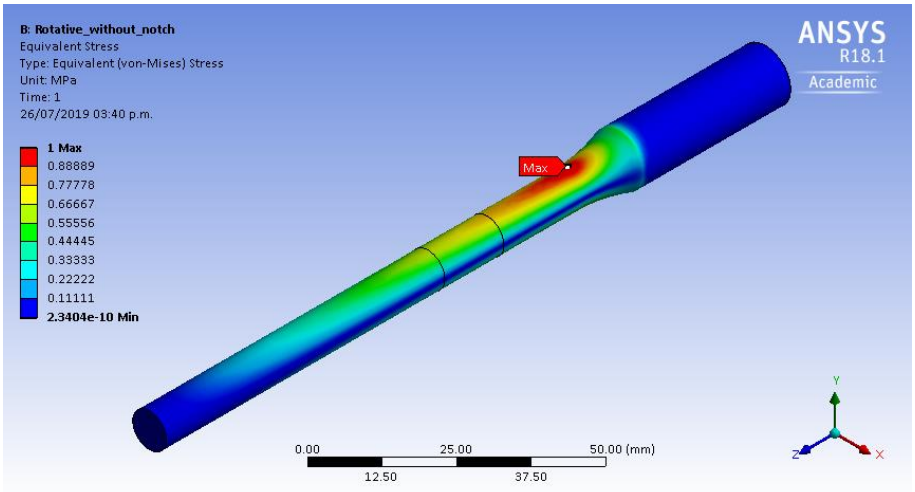

Figure IV.3. Location for maximum equivalent of von Mises stress in specimen with the same load configuration as indicated in (Fig. IV.2), section (c), without the use of a stress concentrator. Note that the maximum stress tends not to be concentrated in the zone representing the laser cladding repairment (delimited by the black lines, centre of test probe).

IV.1.4 Use of Specially Shaped Specimens for the Evaluation of Mechanical Properties of Laser Cladded Materials

First, some authors make use of non-standard test probes in the traditional sense. Its use is limited to specific applications:

- For the evaluation of the resistance to wear and fracture due to buckling mechanism with a vertical load in railway material, (Meng et al., 2019), have used test pieces manufactured directly from railway rail sections (rectangular blocks of 100 x 7.5 x 5 mm), which have been subjected to a three-point bending test. Their objective was to compare different methodologies for the deposition of a hard material by means of laser. The basic configuration of the test for evaluating the mechanical properties of the coating is presented in (Fig. IV.4).

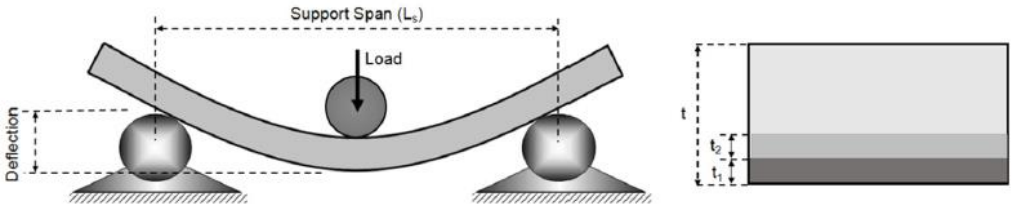

Figure IV.4. Schematic diagram of the three-point bending tests (Meng et al., 2019).

- In the case of (Z. Zhang et al., 2019), composite specimens with a standardized shape have been used, which morphology is 50% of base material and 50% of clad material (on its thickness). The objective is to compare it with the base material as a reference. For both cases, the effect of heat treatment and the use of HIP have also been examined. The objective in this research was to evaluate the feasibility of repairing gas turbines made of an alloy with poor weldability. There has been no emphasis on examining the properties of the added material "per-se", but the metallurgical bond of with the base material was evaluated. ASTM 8E standard (ASTM Subcommittee E28.04, 2016), has been used as basis for the geometry of the specimens. The scheme for the test specimens is shown in (Fig. IV.5).

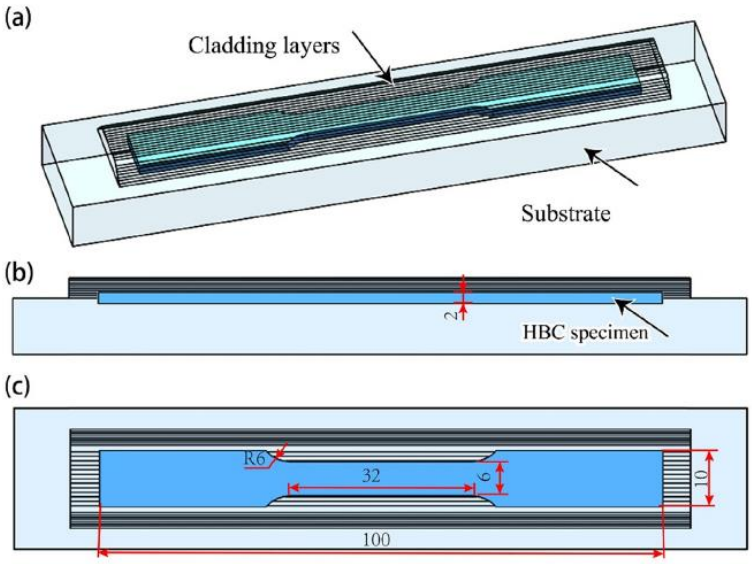

Figure IV.5. Tensile specimens: (a) 3D diagram; (b) longitudinal section; (c) vertical view (Units: mm), (Z. Zhang et al., 2019).

- Other specimen configurations (Chew et al., 2017), have been designed to evaluate the variation of the mechanical properties due to the addition of a clad layer in different ways (in this case, fatigue behaviour). This research has been based on the use of standardized specimens according to ASTM E466-07, with the difference that part of the specimen geometry cannot be considered as flat (there are filler material protrusions in the centre of the specimens). In (Fig. IV.6), the specimens used in this investigation are shown.

  An important detail when performing the mechanical tests (Fig. IV.6, top), is the fact that the failure has not been generated in the desired test area (clad region), but at the beginning (joining edge), of the clad beads, indicating a significant stress concentration effect. In the case of (Fig. IV.6, bottom), the tendency for initiation of cracks has been in the interface between the clad layer and the base material (the author explains it as a function of the difference in hardness between the materials).

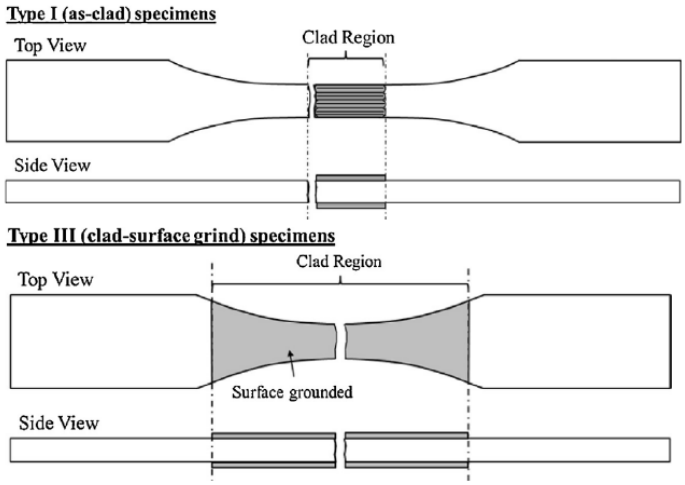

Figure IV.6. Top fatigue specimen with laser deposition "as-clad"; bottom, specimen with extended clad surface and rectified outer surface (Chew et al., 2017).

- Another article with the same approach is the one presented by (Sun et al., 2014), where an extensive study was made on the causes of the decrease in mechanical properties (static and fatigue), of specimens in which an artificial groove has been generated in order to simulate a repairment by means of laser cladding process. Although a metallographic study was carried out in the fracture zone, it is difficult to draw conclusions due to the fact that the specimens are not symmetrical in terms of the material that is added (a buckling effect may occur due to combine materials with different properties). In (Fig. IV.7), the arrangement of the specimens used in the research is shown.

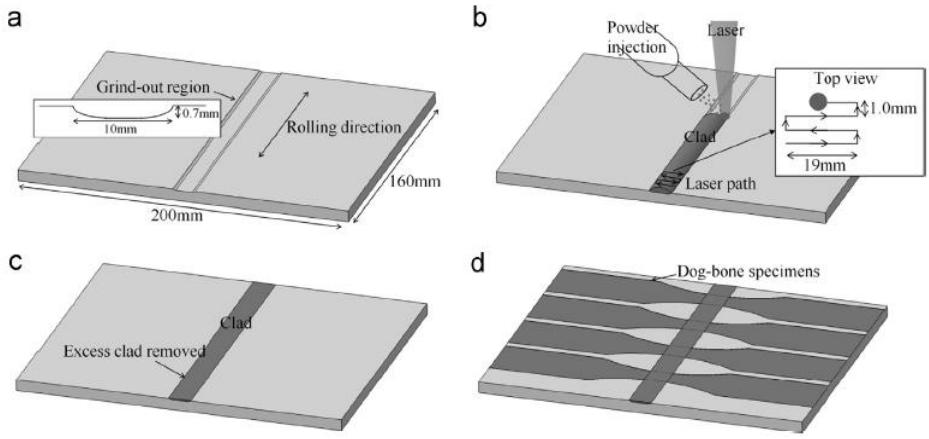

Figure IV.7. Schematic representation of the experimental procedure for the mechanical testing of AISI 4340 steel: (a) 0.7mm grind-out depth along the direction of rolling, (b) multi-track cladding using the optimum processing parameters to fill the grind-out area, (c) excess clad layer removed by a CNC machine for a flat surface finish and (d) individual dog-bone specimens machined by wire-cutting, (Sun et al., 2014).

- In some occasions, direct use of the section of the components is made to evaluate the feasibility of Laser Cladding process as a means of repairing them (Koehler et al., 2011). This research investigates how laser deposition influences the fatigue life of worn crankshafts, which have been repaired with the previous mentioned process. The results in general show a decrease in the fatigue life, with the characteristic (despite the different shape of the "specimens"), that the failure of the repaired components has occurred either in the stress concentrators, or at the joining edges between the clad material and the base material. The general configuration of the test is shown in (Fig. IV.8).

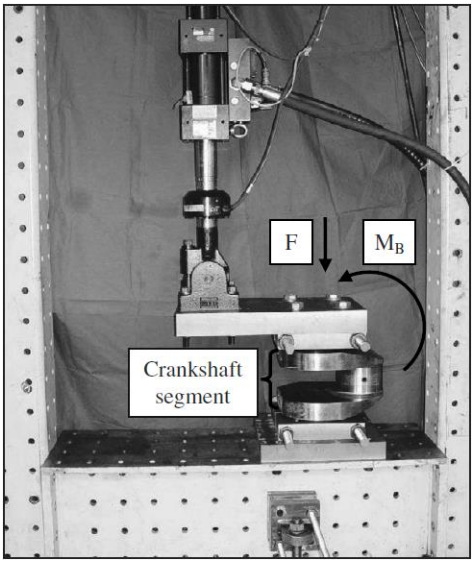

Figure IV.8. Set-up for fatigue testing of crankshaft segments (Koehler et al., 2011).

- Other configurations and shapes of specimens for investigation of the mechanical properties of Laser Cladding process can be found in the articles of (Walker et al., 2016), with an emphasis on modelling the mechanics of fracture; and in the articles by (Alam et al., 2013), where special attention is paid to describe the effect of defects within the added material as crack initiation generators in the specimens coated by Laser Cladding. It is mentioned that the specimens are not standardized, and their load form is working in bending presenting the limitation of generating a relatively small volume at maximum stresses over the total of the specimen. The size and layout of the test is shown in (Fig. IV.9).

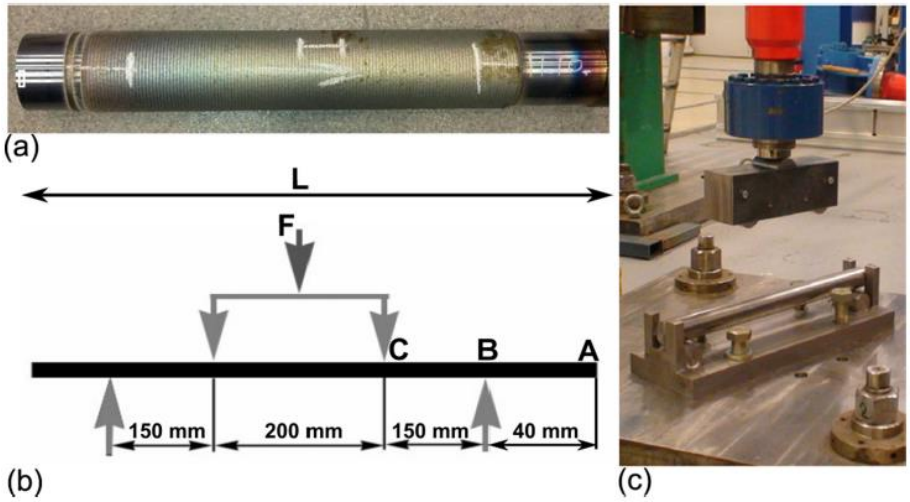

Figure IV.9. Fatigue testing set-up: (a) rod after laser cladding, (b) four-point bending geometry, and (c) fatigue test rig; (Alam et al., 2013).

IV.1.5 Proposal for the Development of Coated Specimens to Characterize the Mechanical Properties of a Coating Made by Laser Cladding Process

IV.1.5.1 Premises for the development of coated specimens

Once the limitations of different types of specimens have been studied in the evaluation of the mechanical properties, a proposal is going to be made on how to evaluate the mechanical properties of coated material through specimens with special geometric characteristics.

The aim of this approach is to isolate the effect produced by the coating on the mechanical properties of the substrate, so the substrate-clad region is set as a whole for its evaluation. For this, the following assumptions will be established:

- The performance in the mechanical resistance of the material will be a direct function of the absence of defects within it. This will apply both for static properties (uniaxial tensile test), as well as to dynamic properties (fatigue test).
- The cladded and the substrate materials have different mechanical properties. Despite being the same alloy, their behavior is different. This can be justified by the fact that a material deposited with laser derives from a manufacturing method that is generally very different from the substrate material. In addition, in the laser cladding process, there are high temperature gradients, fast solidification, high directionality, etc., leading to microstructures that can be very

different from that of the base material (directly related to its mechanical properties).

- The mechanical properties are a function of the material deposition strategy used. This is justified by the directionality (epitaxy), of the material deposited by laser (Tabernero et al., 2011).
- The properties of the base material (related to mechanical properties) are barely affected by the addition of a filler material. A low thermal impact is considered due to the low dilution (Dil_{ml}), that is generally generated during the deposition process. This is especially accurate in multiline-multilayer processes.
- The set of optimal parameters obtained from an optimization process (for a specific material deposition strategy), is applicable to different deposition strategies. Once a set of optimal parameters has been found, it can be used without much variation for a different strategy (versatility of the optimization solution).
- The substrate and the added material act together to resist the stresses to which they are subjected during specimen testing. The bond between the two materials behaves like a perfect metallurgical bond. Although their mechanical properties may differ, the two parts (substrate + coating), "coordinate" and undergo the same deformation.
- The geometric shape of specimens will minimise the effect of stress concentrators, so that the mechanical properties of the 'substrate + coating' material are studied as a single property, instead of the 'substrate + coating + stress concentration' configuration.
- The volume subjected to values close to the maximum stress during a test will be designed to be as large as possible, so that the amount of activated defects within the sample volume will also be as large as possible, meaning that it will represent a real situation.

For the previous mentioned reasons, the “Hourglass” type fatigue tests specimens have been chosen. In the case of static tensile tests, another type of test sample which can be manufactured easier, such as the “Dog-bone long” can be chosen. The justification for the use of each type of test samples will be explained in the following sections.

IV.1.6 Use of “Dog-bone long” Type Coated Specimens in Uniaxial Tensile Test to determine the “Real” Modulus of Elasticity of Cladded Material from “Compound Modulus of Elasticity”

The stress-strain curves that have been obtained for specimens in different scientific articles in (Section IV.6.3), have the disadvantage of not discriminating the behaviour of base material from the cladded material. Although it is desirable for the cladded material to have characteristics similar to those of the base material, in the articles mentioned in (Section IV.6.3), a decrease in the strength of the composite specimens was observed. Therefore, it can be deduce that the material that has been added does not have the same mechanical properties as the base material.

Little information has been found regarding specimens of “composite” metallic material (with more than one well-defined phase), and the effect that each of these phases would have on the mechanical behaviour of the material as a whole. Among the few examples found, (Karolczuk et al., 2013), have investigated the mechanical properties for flat bimetallic specimens subjected to load cycles in fatigue regime for low and high number of cycles (LCF and HCF). The interesting fact about this research is that they make an in-depth study of the stress field for a flat specimen taking into account the difference in Modulus of Elasticity of each material separately, but combining them to model the behaviour of the specimen as a whole. In this research, the approach is different. It is desired to use a common mechanical properties (from the base material and the coated specimen as a whole), and from there, deduce the properties for the coating material (the properties of base material being obtained directly from separate test).

The use of “Dog-bone long” type cylindrical specimens is justified by the fact that rectangular cross section specimens generate stresses at the corners, an effect that is undesirable to characterize the behaviour of the added material due to local plasticity effects.

Regarding the distribution of the stress field, this may be different depending on the characteristics of the materials which are part of the specimen. An example of stress field variation is shown in (Fig. IV.10), for the case of two sections of test pieces subjected to uniaxial tension for constant cross section when they are formed by two different materials or by just one. The stress field in the middle section of each probe (away from the change of cross section of the end), remains constant.

Later on, it will be seen that the use of test pieces with constant cross section ("Dog-bone long" type), is convenient to deduce the mechanical properties (in this case, modulus of elasticity for the cladded material), for a coated test piece. The filler material may present anisotropic behaviour in terms of its mechanical properties, an effect that will be taken into account when discriminating (in this case), the modulus of elasticity of each component of the coated specimen.

The use of cylindrical specimens is useful in the sense that the cladding material is completely symmetrical, and it is possible to compensate for effects such as buckling of the specimen when stressed in the longitudinal direction by the same difference in Modulus of Elasticity.

In literature, during the quantification of the mechanical properties of coated specimens, the characteristics such as the ratio between the volumes of material deposited to the total volume of the specimen or, in other words, the ratio between the cross sections A_{clad} / A_{probe}, (Fig. IV.1), is not taken into account, although there are exceptions such as (Hutasoit et al., 2015). This is a limitation, because there is no clear idea of which is the effect of the coated thickness. Therefore, in this section the thickness of the added material (t_{clad}), will be taken into account.

In (Fig. IV.10, left), the section $\Phi Substrate + t_{clad}$, it is assumed that the deformation is similar for both sections and the base material (in the centre), has better mechanical properties (in this case, higher Modulus of Elasticity). The base material section will support a higher stress value than that the coating layer (there will be a discontinuity in the internal value of the stress field). For a single material with homogeneous mechanical properties, the stress field will be uniform (Fig. IV.10, right).

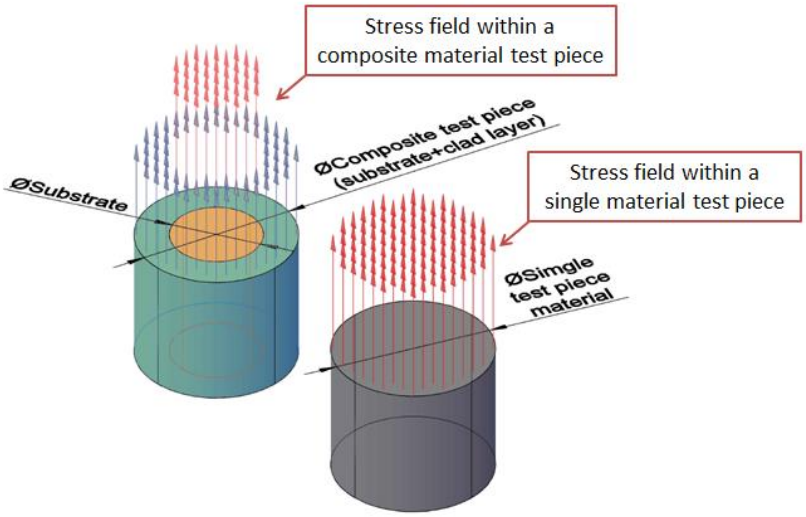

Figure IV.10. Stress field for specimens with uniform cross-section. It is considered that in the case of the composite test probe (left), both materials show joint behaviour, i.e. the same deformation.

IV.1.6.1 Determination of the Modulus of Elasticity of a Coating Material by Means of Test Probes.

In terms of stress, one of the key studies to be carried out is the ability to accurately calculate the behaviour of the mechanical property that defines the stiffness of the material (modulus of elasticity for the composite specimen (E_{comp})), from the modulus of elasticity of the region of added material (E_{clad}).

As mentioned previously, the uniaxial tensile test of "Dog-bone long" type specimens is the most appropriate, since the normal stress field is uniform in the central zone of the probe (not necessarily constant), and allows the evaluation of the value of this (σ_{test}), simply as F / A, as shown in (Fig. IV.11). Using a force balance, the total load on a cross section of the specimen will be defined as (Eq. IV.1):

$$F_{test} = F_{pre} + F_{clad} \qquad \textit{Eq. IV.1}$$

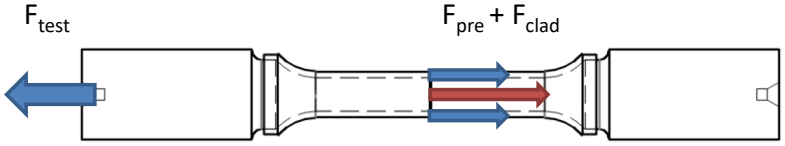

Figure IV.11. Load balance for a coated specimen. A constant cross-section specimen is used so that the stress within the specimen remains uniform.

If the deformation for the base material and the coating material is the same (it is assumed that both materials deform together), then the linear elastic regime during the first stages of deformation, Hooke's law, is fulfilled, (Eq. IV.2):

$$\sigma = \varepsilon.E \qquad \textit{Eq. IV.2}$$

For this type of specimen (in the uniaxial tensile test the deformation-stress data is taken as a whole), the stress is (Eq. IV.3):

$$\sigma_{test} = F_{test} / A_{test} \qquad \textit{Eq. IV.3}$$

Since the unitary deformation for the specimen as well as for the clad and substrate materials as a whole are assumed to be the same, (Eq. IV.4):

$$\varepsilon_{clad} = \varepsilon_{pre} = \varepsilon_{test} \qquad \textit{Eq. IV.4}$$

Substituting (Eq. IV.4) and (Eq. IV.2) in (Eq. IV.1), and taking into account:

$A_{test} = \frac{\pi}{4} {d_{test}}^2$, $A_{pre} = \frac{\pi}{4}\left({d_{test}}^2 - 2t_{clad}\right)$, $A_{clad} = A_{test} - A_{pre}$; The Young's Modulus of the cladded material as a function of those of the base material and that obtained from the uniaxial tensile test curve of the composite probe will be given by (Eq. IV.5):

$$E_{clad} = \frac{E_{pre}(d_{test} - 2t_{clad})^2 - E_{test}{d_{test}}^2}{4t_{clad}(t_{clad} - d_{test})} \qquad \textit{Eq. IV.5}$$

In (Eq. IV.5), it is assumed that both the cladded material and the base material have well differentiated mechanical properties. This is based on a very low value of (Dil_{ml}) as mentioned previously (low degradation due thermal damage). In addition, a defect-free specimen in the base-cladding joint is assumed.

The quality of the metallurgical joint is very important. An example of specimen with poor quality joint is shown in (Fig. IV.12); the effect, in general, will be fracture of the coated specimens in the area of change section on the base material (neck), where the contribution of the added material during the tensile test can be neglected. (Eq. IV.5) is valid as long as there are no low-quality metallurgical bonding phenomena, and when the base and the cladded material undergo the same deformation.

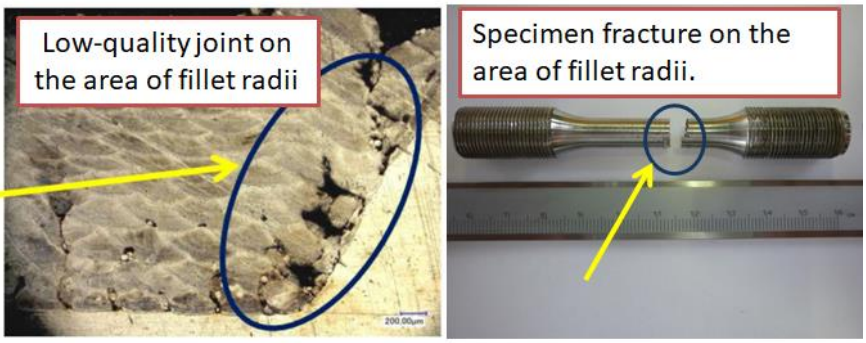

Figure IV.12. Left, cross-section detail in the area of the fillet radius showing a low-quality joint of base material + cladding material. Right, effect of low-quality joint on the tensile test result of the sample; the fracture has occurred in an undesired area of the probe (neck); with negligible participation in the strength of the coated material.

According to the standard (ASTM Subcommittee E28.04, 2016), the specimen rupture should occur in the central area of the probe (Gage Length), as can be seen in (Fig. IV.13). The Design of the coated specimens and the conditions for the coating process have been optimised for this purpose. Detailed drawings of the specimens and their dimensions are given in (APPENDIX, PROBE DRAWINGS).

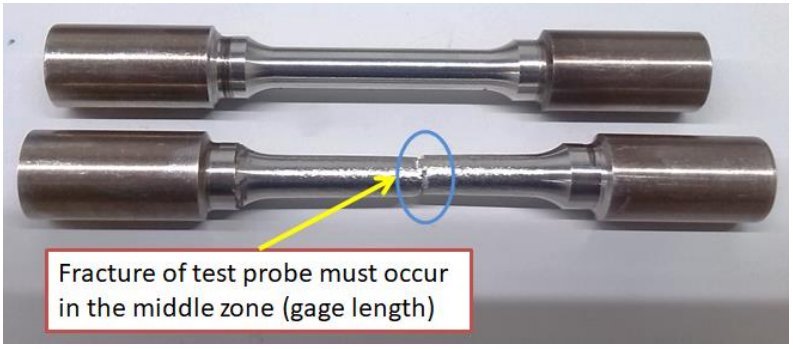

Figure IV.13. Top; coated specimen prior to uniaxial tensile test. Bottom; specimen after test. The rupture has occurred in the middle zone of the specimen, within the calibrated zone designed to calculate the deformation of the probe at fracture.

IV.1.7 Coating Strategies Used in Test Probes to Obtain Mechanical Properties from a Uniaxial Tensile Test.

There are tool paths in Laser Cladding processes that are commonly used for flat substrates (Alvarez et al., 2018; Toyserkani et al., 2005). Among all, three strategies have been chosen, which will be adapted to the geometries of cylindrically symmetrical specimens:

- Helical strategy: The material deposition follows a helix-shaped path along the axis of symmetry of the specimen. This strategy will represent a perpendicular

deposition direction when compared to the main direction of stress during the uniaxial tensile test of the specimen.

- Longitudinal in Zig-Zag: the deposition of the material for the same layer follows a bidirectional strategy in the direction of the axis of symmetry of the specimen. The sequence will be: Start (switch on and deposition of material with the laser), Return and offset (the laser returns to the starting point with a lateral offset movement and the sequence is repeated).
- Longitudinal in Zig-Zig: the deposition of the material for the same layer follows a unidirectional strategy in the direction of the axis of symmetry of the specimen. The sequence will be: Start (switch on and deposition of material with the laser), End (switch off the laser), Return and offset (it returns to the starting point with a lateral offset movement and the sequence is repeated).

The use of various strategies (path tool), in the deposition of the coating on the specimens has been carried out on the basis that a texture difference is generated in the microstructure of the deposited material, and thus in its mechanical properties (Dinda et al., 2012; Parimi et al., 2014; X. Zhang et al., 2019).

The fundamental difference at the level of the coated specimens regarding to the use of the three previous deposition strategies lies in the direction of deposition compared to the symmetry axis of the specimen. In order to enhance the effect of the deposition strategy on the mechanical properties (and to keep the number of specimens to be manufactured into a reasonable number), in addition to the three previous strategies, the following combinations (2 layers, one for each strategy) have been realised:

- Longitudinal Sequence in Zig-Zag + Helix.
- Longitudinal Sequence in Zig-Zig + Helix.

A summary of the strategies used on the specimens for the deposition of the coating material in this research is presented in (Fig. IV.14):

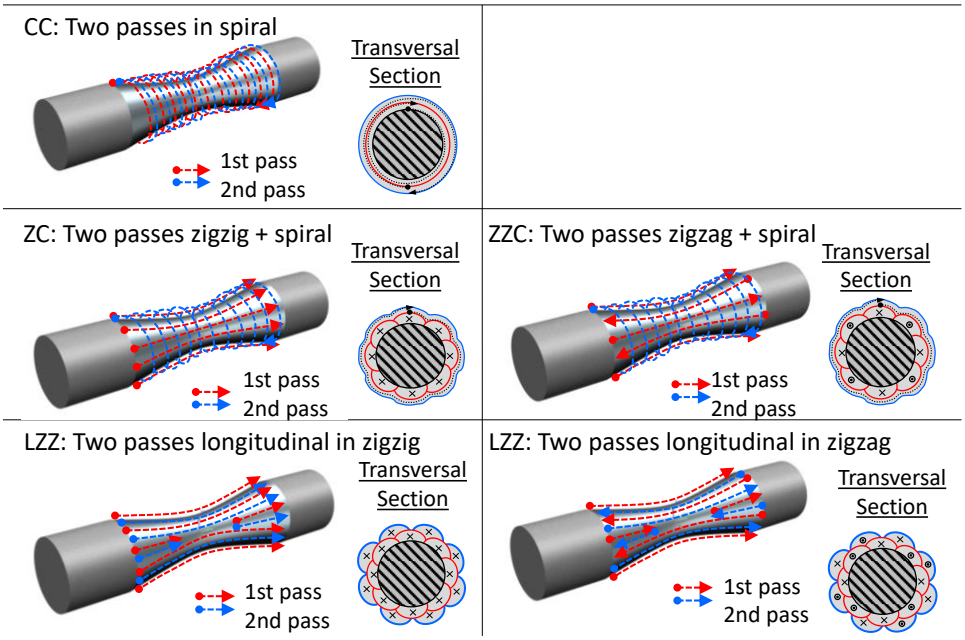

Figure IV.14. Coating strategies used in the preparation for uniaxial tensile test specimens. The number of coating strategies and the number of coating layers have been limited to isolate the effect of each configuration on the microstructure and mechanical properties.

These previous strategies have been chosen as a way to calculate the mechanical properties at static level by using uniaxial tensile tests, and to obtain the values of E_{clad} for each of the strategies shown in (Fig. IV.14).

The texture change generated in each deposition strategy is significant. For example, an extra specimen of each type of probe was cut and metallurgically prepared (with Kalling's reagent number 2), according to (ASTM Subcommittee E04.01, 2015), to verify the change in the type of microstructure generated in the coating. A detail of the cross-section between the structures generated by the CC-type (left) and LZ-type (right) strategies is shown in (Fig. IV.15).

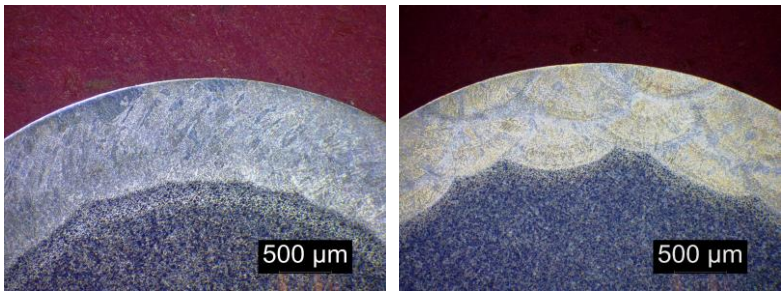

Figure IV.15. Cross-sectional micrographs of two specimens showing the change in microstructure generated by the deposition strategy (tool path), used in the laser cladding process. On the left, a CC type strategy and on the right an LZ type strategy.

It should be taken into account that all the specimens have been manufactured and coated with INCO718 alloy. Furthermore, all of them have been subjected to the thermal heat treatment shown in (Fig. IV.16). For most applications, INCO718 alloy resistance is based on solution annealing and precipitation hardening. The alloy hardens by the precipitation of secondary phases (for example, "gamma prime" and "gamma double-prime"), in the metallic matrix. The precipitation of these nickel phases (combined with aluminium, titanium, niobium), is induced by heat treatment in the temperature range of 600 to 815 ° C (Special Metals, 2007).

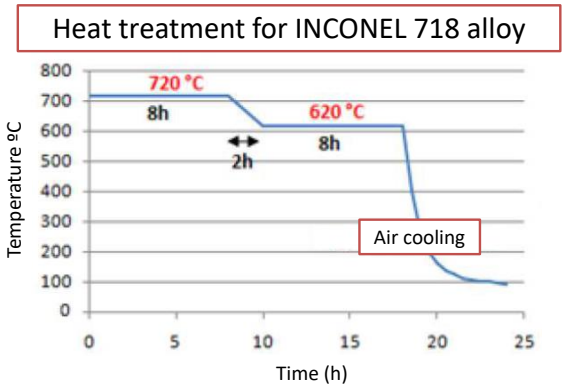

Figure IV.16. Heat treatment applied to coated specimens made from INCO718 alloy.

For more details of the phases found in the cladded material layer, the composition of the base material substrate and the metal powder used in the cladding process, see (Chapter II.5.3).

Other considerations to be taken into account for the correct manufacturing of the coating layer of the coated specimens are the following:

- Maintain the perpendicularity of the "deposition nozzle + laser beam" set with respect to the substrate surface. The latter will depend on the versatility of the CAM solution used to program the tool-path trajectory and the accuracy of the machinery to implement the code. In (Fig. IV.17), the simulation of a helix-type tool-path trajectory for a coated hourglass-type specimen via a self-developed code is depicted, along with a sequence photographs of its physical implementation on a laser-equipped CNC machine.

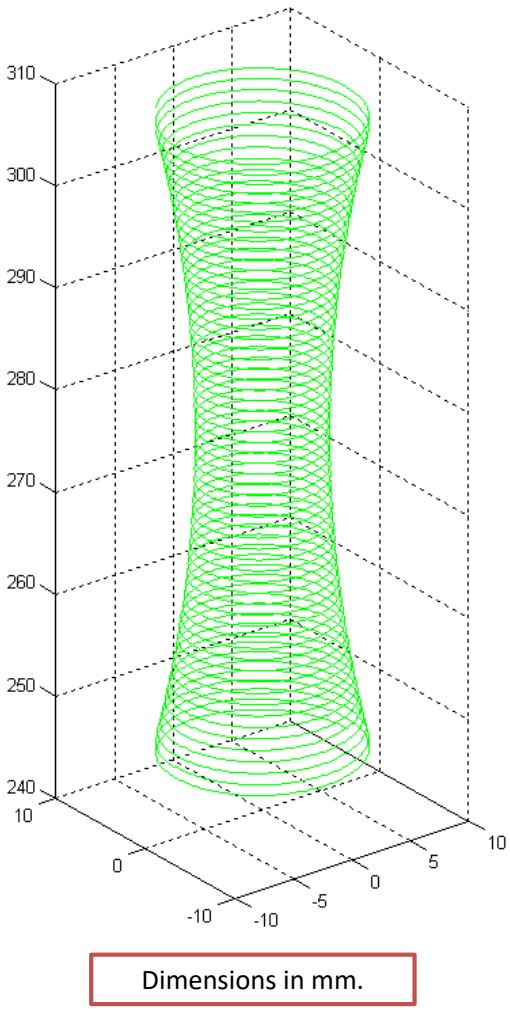

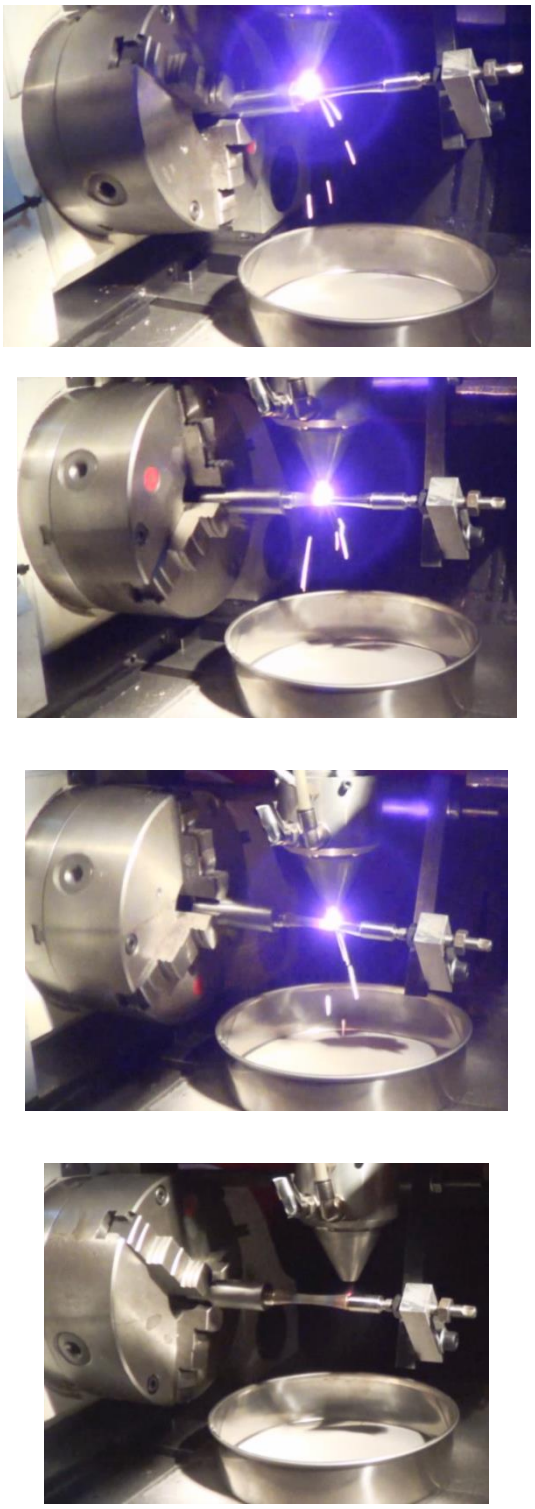

Figure IV.17. Left, drawing of Helix path on CAM code coordinates for a coated hourglass-type specimen. Right, photographs of the sequence (from top to bottom), of the implementation of the code on a CNC machine equipped with Laser Cladding AM process. It should be taken into account that the kinematic elements of the CNC machine allow the nozzle to be perpendicular as possible to the substrate surface as far as possible during material deposition (as shown in the photographic sequence).

- Maintenance of a uniform HAZ throughout the Laser Cladding process. It is advisable to maintain the thickness of the HAZ (usually by power regulation), to avoid deviations from optimum conditions and to maintain a uniform microstructure throughout the coating. The relative size of the substrate compared to the amount of energy introduced into the substrate makes the HAZ highly variable. Two examples are shown in (Fig. IV.18). In the upper left (A), the HAZ variation is shown on a small cylindrical substrate that has been spiral coated without any control of the energy delivered. On the bottom right (B), is shown the HAZ of a coated specimen of variable cross-section with power moderation. The effect of the power control is that overheating and significant variation in the width of the HAZ has been avoided.

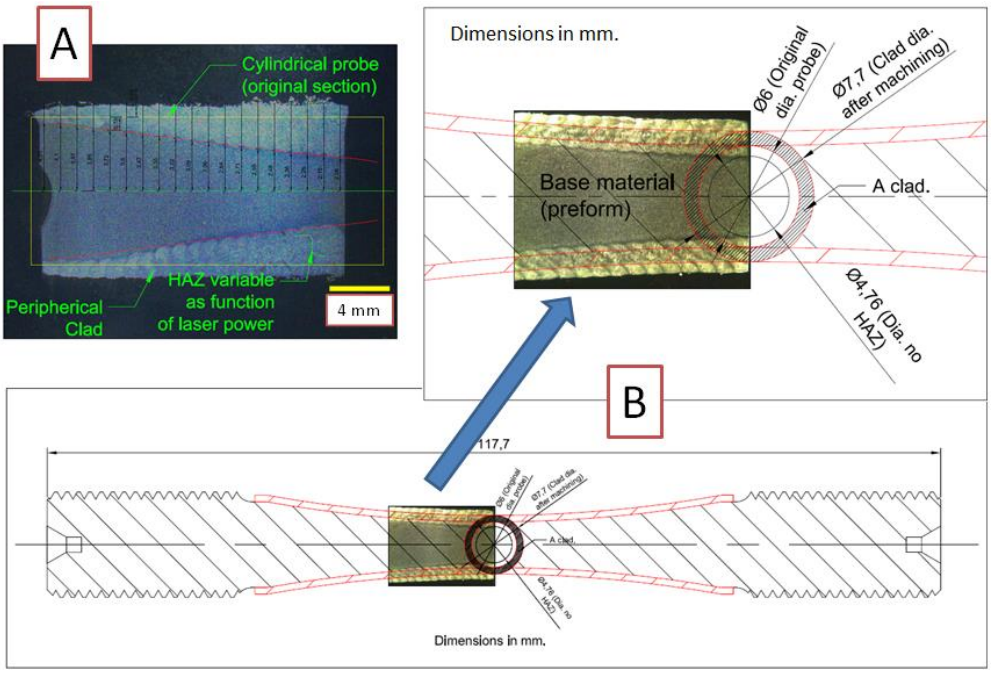

Figure IV.18. (A), cross-section of a helical material deposition on a straight cylindrical section specimen without laser beam power control; a significant HAZ variation is observed. (B), specimen coated in helix strategy (the area that was coated is indicated with a red border), and a detail of the probe showing the preservation (as far as possible), of the HAZ thickness.

- An excess in deposition of cladding material on the coating of the specimens must be ensured to ensure that there is sufficient material for machining, and to meet the dimensional specifications given in the design. The objective is that during subsequent machining and polishing of the specimens, the dimensional requirement with respect to a standard is fulfilled. The finish machining of the coated specimens (usually mirror finish), will allow see the defects left by the lack

of material through the surface roughness derived from the Laser Cladding process itself. An example of the initial dimensions of an specimen before and after Laser Cladding process is shown in (Fig. IV.19, left). The same figure (Fig IV. 19, right), shows a machined and polished specimen in its final state. The sample dimensions have been based on (ASTM Subcommittee E08.05, 2015).

Figure IV.19. Left, coated specimen in different manufacturing stages (a) preform, (b) coated specimen with longitudinal strategy respect to its axis, (c) coated specimen with helix strategy. Right, machined and polished coated specimen. Note the excess material that has been added in each type of strategy to ensure that there is enough material to machining the specimen to the final dimension according to the standard specifications.

IV.2 Static Mechanical Properties of Specimens Coated by Laser Cladding Process (Uniaxial Tensile Test).

IV.2.1 Mechanical Properties. Results of Tests on Coated Specimens.

IV.2.1.1 Uniaxial Tensile Test.

For the uniaxial tensile test, a UMI ES-100 series machine with a capacity of 100 kN was used in combination with a UMA25 extensometer to measure the strain. The extensometer has an initial length of 25 mm. The strain rate was 0.5 mm/mm/min as indicated in the specification (ASTM Subcommittee E28.04, 2016). Five specimens of each type of probe have been tested according to the deposition strategies shown on (Fig. IV.14).

Stress-Strain graph for tests on coated samples is shown in (Fig. IV.20). The (Fig. IV.20), shows the behaviour of the base material + coating, and should not be used directly in the calculation of the mechanical properties for the coating.

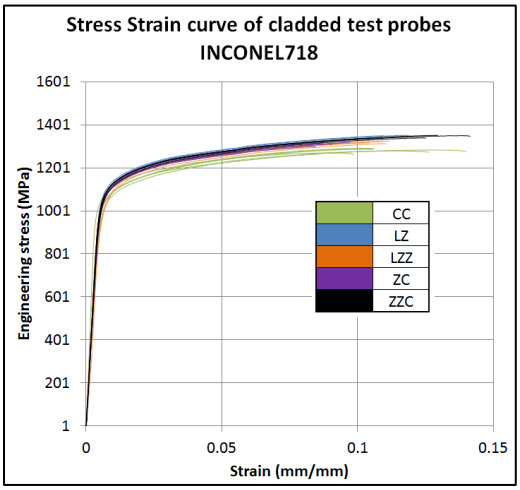

Graph IV.20. Stress-strain graph for test on coated samples for the 5 strategies shown in (Fig. IV.14). The base material and the coating of the specimens are INCO718.

The (Fig. IV.21), shows the summary of the mechanical properties for all tensile tests. The (Fig. IV.21), shows (for comparison), the minimum mechanical property requirements for INCO718 alloy according to (SAE AMS5662M, 2009).

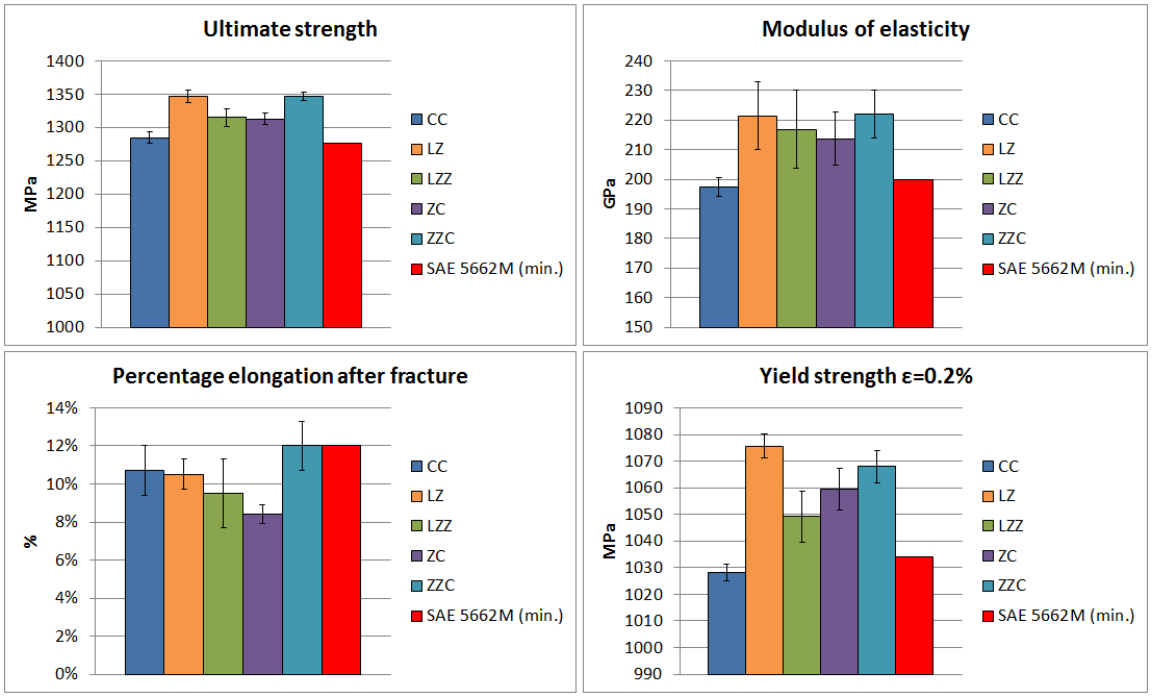

Figure IV.21. Summary graph of the mechanical properties of the tensile test for coated specimens and comparison of the results with the standard values for the material INCO718 according to ASTM.

IV.2.1.2 Micro Hardness Test.

Hardness values have measured for different simple deposition strategies, as shown in (Fig. I.V.14), (this is done only for strategies CC, LZ & LZZ, not combinations of them). It

has been decided to perform the hardness test in isolation on substrates larger than the specimen size, in order to obtain more data for this property for each deposition strategy. The reason for the use of large substrates is that, despite using a "Microhardness" type test method, few indentations can be made along the thickness of the coating (few data was obtained).

A Struders (EMCOTEST), model A300 with a test weight of 0.3 kgf and a retention time (dwell time), of 15 seconds was used for the analysis.

In (Fig. IV.22), an example of data collected from a sample coated with the LZ deposition strategy is shown (Fig. IV.22, left). The same figure (Fig. IV.22, right), shows the graphs of the test results for different types of deposition strategies. In each result graph, three different behaviours (zones) can be distinguished.

First is the coated zone, where an increase (with high variability) in the hardness value is seen for all deposition strategies, each starting from the surface and moving inwards into the substrate.

Second, the transition zone in the HAZ is observed, where in general, the value of hardness shows the tendency to increase, and finally the area of substrate, where in all cases (regardless of the type of deposition strategy that has been used), the hardness values are similar and show less variability.

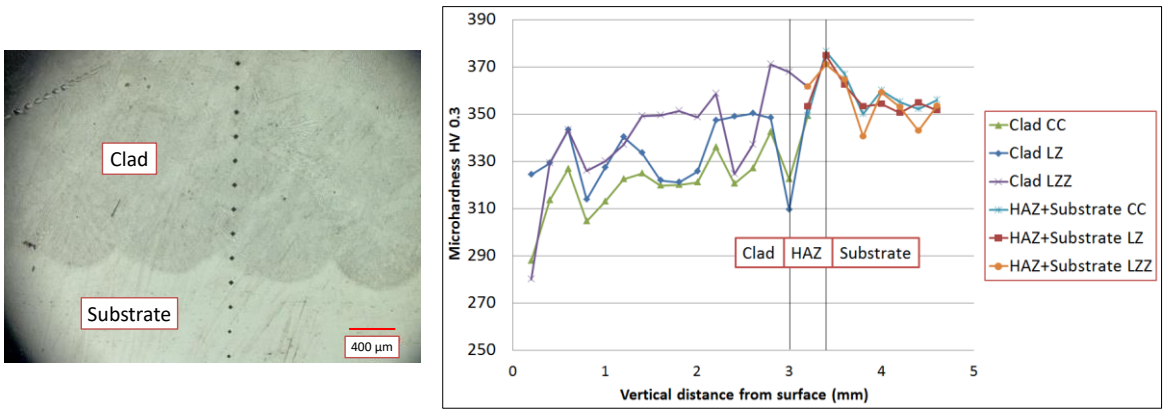

Figure IV.22. Left, example of data collection for an HV microhardness test at 0.3 kgf. The hardness test was performed on a larger substrate to collect more information regarding to the hardness associated with each deposition strategy. Right, graph of the hardness test results for different deposition strategies, where the variability of data is appreciated as a function of the coordinate within the substrate + coating set.

The (Fig. IV.23) shows the average hardness values measured for each deposition strategy. For comparison, the average hardness value for a sample of INCO718 taken as

a base material is shown. The same heat treatment was used for the coated samples and base material.

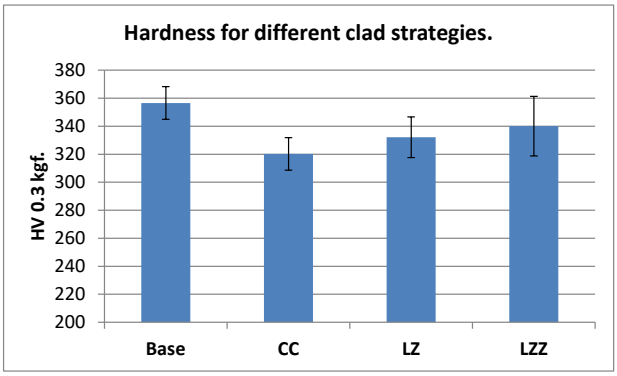

Figure IV.23. Mean value of micro hardness (HV 0.3 kgf test), for simple strategies used to manufacture the coated specimens. For comparison, the average value of a sample of base material (INCO 718) is shown.

The microhardness value for the base material tends to be approximately 5-10% higher than for any of the other strategies. In the case of the LZZ strategy, the hardness values are similar compared to the base material. However, the LZZ strategy has the highest standard deviation of all hardness test values.

IV.2.1.3 Analysis of Fracture Surfaces of Specimens (Tensile Test).

The analysis of the fracture zones in the coated samples is important to verify the ductility of the material, which plays an important role for the calculation of the mechanical properties of the whole assembly (coating + substrate). A ductile behaviour allows the combination of substrate + coating material to work together for a long time in elastic deformation regime (which serves as the basis for the Modulus of Elasticity). A good bond (coating + substrate), also helps to meet one of the conditions listed in (Section IV.1.6), which states that it is necessary to ensure that the substrate and the coating work together to resist axial tension during the uniaxial tensile test.

The analysis followed is based on observations of the fracture surface with a digital optical microscope. An example of micrographs of these different fracture surfaces is shown in (Fig. IV.24).

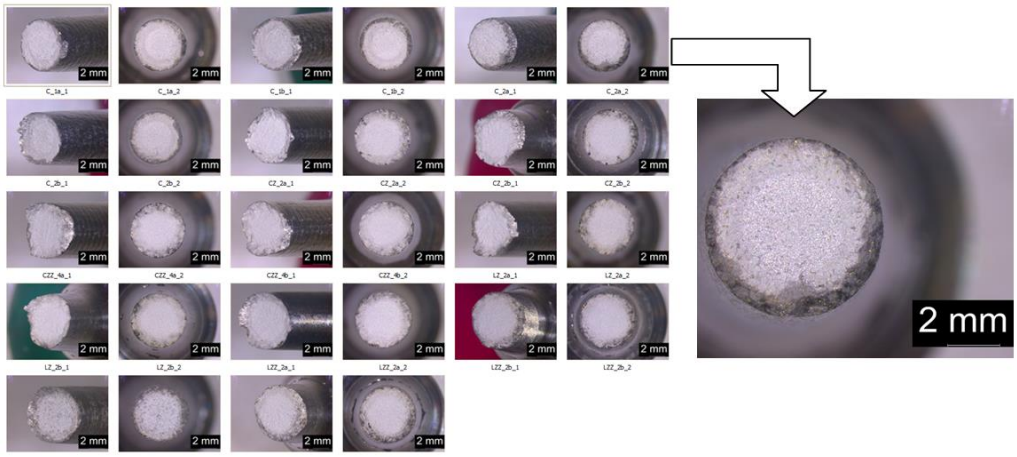

Figure IV.24. Micrographs of the fracture zones of coated specimens for different strategies after the uniaxial tension test.

The micrographs are not only presented in a perpendicular view to the fracture area, but with a certain twist to give perspective of it. All have a ductile cup appearance. According to (Ipohorski and Acuña, 1988), when the tensile stress in a test piece is longitudinal (and the maximum shear stresses act on planes oriented at 45 ° from the traction axis), the shear stresses are responsible for the process of plastic deformation of the metal. Therefore, a component of ductile material under tension will begin to fracture along these planes, resulting in a rough surface, and a 45 ° ductile edge near the free surface. In contrast, with a brittle material, the overload fracture produces a rupture perpendicular to the stress with little plastic deformation (Fig. IV.25).

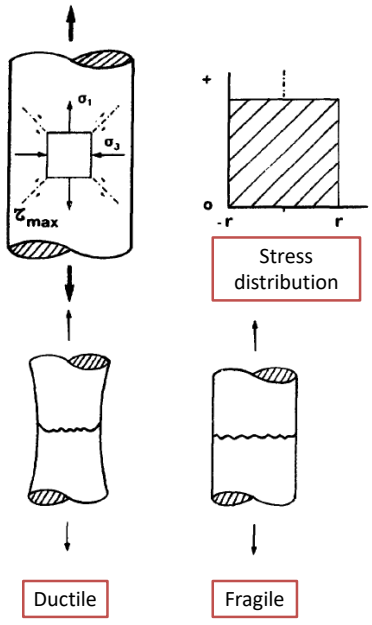

Figure IV.25. Stress distribution (top), and appearance of the fracture zone according to (Ipohorski and Acuña, 1988), for a specimen subjected to a uniaxial tensile test with ductile behaviour (left, bottom), and brittle (right, bottom).

At a higher level of detail, SEM micrographs have been taken in the area of the coating fracture of the samples. An example of them is presented at different amplifications for one of the samples for the LZ strategy (Fig. IV.26). Magnifications are sequential from (1) to (4). A series of "holes" in the surface are observed as a detail which origin is the microcavities that are initiated by the decohesion and creep of the material around the inclusions, second-phase particles or any discontinuity that produces a concentration of stresses and an increase in the plastic flow. As the deformation process progresses, the existing microcavities grow under the stress conditions at the end of the crack, until they are very close to each other. Finally, the walls or ligaments that separate them break, resulting in a fracture surface characterized by hemispherical or semi-ellipsoidal depressions that are simply "cavities" or "dimples". When the fracture occurs by simple traction, the cavities are equiaxed (Ipohorski and Acuña, 1988). All the previous characteristics that have been mentioned, that are typical of ductile fractures; has been observed in all the SEM photographs that have been taken from different specimens. Therefore, the coated specimens that have been tested have deformed and broken under the ductile behaviour regime.

INCONEL 718 is by itself a material that has a ductile behaviour at room temperature, since it can be modelled by the von Mises failure criterion (Gil, 1998). Therefore, the objective of all these previous analyses is to ensure if those characteristic have been preserved in the clad material of the coated specimens.

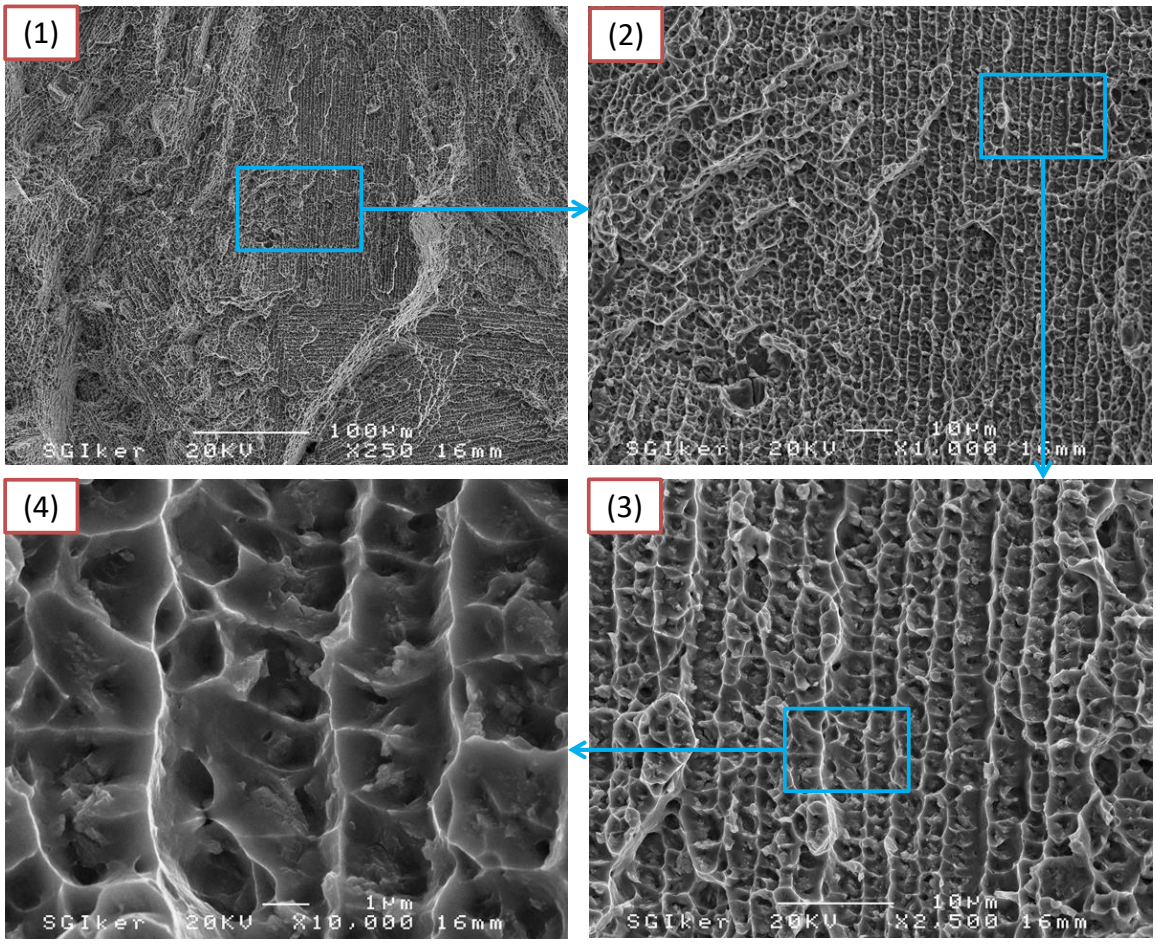

Figure IV.26. Sequence of SEM images of a cladding section of a coated specimen for the LZ deposition strategy in order of magnification from (1) to (4). The characteristics of the fracture correspond to those of a rupture of ductile material.

IV.2.1.4 Determination of the Modulus of Elasticity and Yield Strength for the Cladding Material Based on the Results of Uniaxial Tensile Tests of Coated Specimens.

The (Table IV.2) shows the tensile test results for the coated specimens for the different coating strategies of the (Fig. IV.14), and the results of the calculation of the Modulus of Elasticity for the coating (E_{clad}). As a necessary complement to deduce E_{clad}, uniaxial tensile tests have also been carried out with standardized specimens of base material (E_{pre}), of same dimensions as those of the coated specimens. The results in the mechanical properties of these previous tests (base material), will replace the reference values shown in (Fig. IV.21), taken from (SAE AMS5662M, 2009).

Applying (Eq. IV.5) to the results of Modulus of Elasticity of (Table IV.2), and for the values of E_{pre} = 205.1 GPa, d_{test} = 8 mm and t_{clad} = 1 mm as constants values for all the

coated tensile test specimens according to the design of (Annexes, Drawings of test probes), the values of E_{clad} are calculated in the bottom row of (Table IV.2), together with the relative value E_{clad} / E_{comp} (%).

Table IV.2: Results of uniaxial tensile tests for the different cladding strategies on coated specimens of base material; and the calculated value of E_{clad} as a function of the mechanical properties of E_{pre}, E_{test} and the geometric dimensions of the specimen and its coating.

	Two passes in spiral (CC)	Two passes longitudinal in zigzig (LZ)	Two passes longitudinal in zigzag (LZZ)	Two passes: zigzig + spiral (ZC)	Two passes: zigzag + spiral (ZZC)	Base material
Ultimate strength (MPa)	1284.5 ± 8.5	1346.3 ± 9.4	1315.2 ± 13.2	1312.9 ± 8.4	1346.7 ± 6.7	1287.0 ± 9.1
Percentage elongation after fracture	10.7% ± 1.3%	10.5% ± 0.8%	9.5% ± 1.8%	8.4% ± 0.5%	12.0% ± 1.3%	15.0% ± 1.1%
Yield strength (yield point) ε=0.2% (MPa)	1028.3 ± 17.05	1075.68 ± 4.47	1049.2 ± 9.475	1059.48 ± 7.65	1068.05 ± 6.04	1094 ± 8.9
Compound modulus of elasticity (GPa), E_test	197.4 ± 3.2	221.5 ± 11.4	216.9 ± 13.1	213.8 ± 9.1	222.0 ± 8.0	205.1 ± 8.5
Modulus of elasticity of coating (GPa), E_clad	**187.5**	**242.6**	**232.1**	**225.0**	**243.7**	
E_clad / E_test (%)	**95.0%**	**109.5%**	**107.0%**	**105.2%**	**109.8%**	

The values of E_{clad} are 5% lower in the case of CC, and up to almost 10% in the case of LZZ. The combined effect of the variables E_{test} and t_{clad} on the value of E_{clad} is shown in (Fig. IV.27).

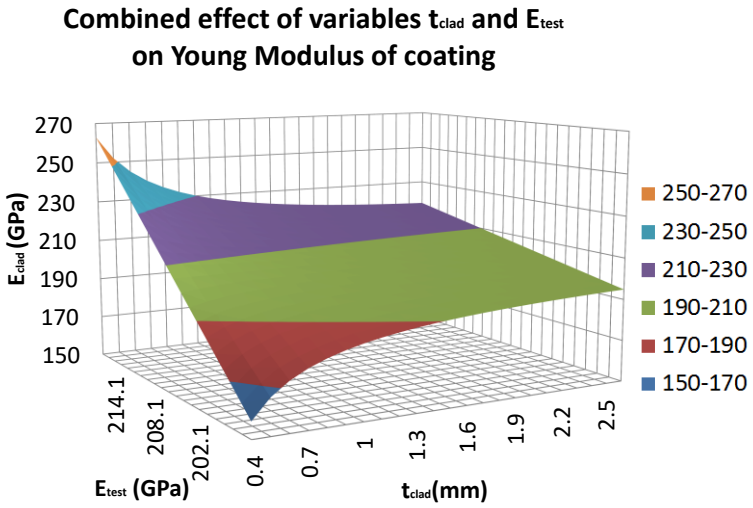

Figure IV.27. Combined effect of variation of E_{test} and t_{clad} over the calculated value of E_{clad} keeping the values of E_{pre} and d_{test} constant.

The figure shows that a thin coating thickness of the specimen will have the greatest effect on E_{clad} over a wide range on uniaxial tensile test results of the coated specimen. Therefore, the thickness of the coating is a fundamental factor for the characterisation of the mechanical properties of the coated specimens, and in the dispersion on the values calculated as a result of the uniaxial tensile tests.

The application of (Eq. IV.5), allows to indirectly characterizing the isotropic properties that depend on the cladding strategy. In all the coated specimens, the same optimized deposition parameters have been maintained as far as possible. Therefore, most of the variation in mechanical properties measured from the tensile tests is due to the change of orientation of the microstructure due to the use of different deposition strategies (tool path).

Being able to accurately characterise the mechanical properties of materials manufactured by additive manufacturing (AM), would allow reducing the uncertainty in their values of mechanical properties with respect to the base materials as seen in (Fig. IV.28) (Gorsse et al., 2017). This part of the research aims to understand the behaviour of materials "working" together in the case of coated samples.

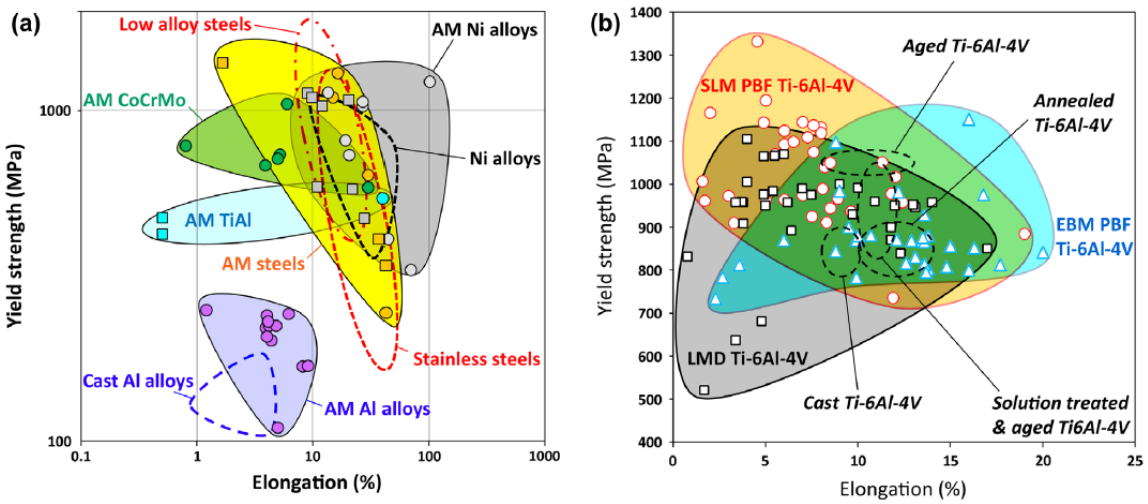

Figure IV.28. Materials property space for room temperature yield strength vs. elongation of additively manufactured alloys and conventionally manufactured alloys (dashed lines), including (a) steels, Ni alloys, Al alloys, TiAl and CoCrMo, and in (b) Ti-6Al-4V alloys (Gorsse et al., 2017).

The value of σ_{Yclad} can be estimated from the Law of mixtures, used in micro-mechanics to estimate properties of composite materials based on their individual component mechanical properties. This approach can be applied to the elastic constants (Modulus

of Elasticity, Kirchhoff and Poisson's ratio), to the coefficient of thermal expansion and the stress values corresponding to the Elastic Limit and the Yield Strength.

The Law of Mixtures is defined as (Eq. IV.6):

$$\sigma_{Ytest} = f_{clad}\sigma_{Yclad} + f_{pre}\sigma_{Ypre} \qquad \textit{Eq. IV.6}$$

The volumetric fractions f_{clad} and f_{pre} (Eq. IV.7), are defined on length of the coated specimen, therefore, $L_{test} = L_{pre} = L_{clad}$:

$$f_{clad} = \frac{V_{clad}}{V_{test}} = \frac{L_{clad}A_{clad}}{L_{test}A_{test}} = \frac{A_{clad}}{A_{test}} \qquad \textit{Eq. IV.7}$$

Given that the specimen is only composed of "two different materials" (in the sense that both materials composing the specimen have different mechanical characteristics), then (Eq. IV.8):

$$f_{pre} = 1 - f_{clad} \qquad \textit{Eq. IV.8}$$

Rearranging (Eq. IV.6), and taking:

$A_{test} = \frac{\pi}{4}{d_{test}}^2$, $A_{pre} = \frac{\pi}{4}\left({d_{test}}^2 - 2t_{clad}\right)$, $A_{clad} = A_{test} - A_{pre}$, the value of σ_{Yclad} is calculated as (Eq. IV.9):

$$\sigma_{Yclad} = \frac{{d_{test}}^2\sigma_{Ytest} - 4d_{test}t_{clad}\sigma_{Ypre} + 4{t_{clad}}^2\sigma_{Ypre}}{\left(d_{test} - 2t_{clad}\right)^2} \qquad \textit{Eq. IV.9}$$

By applying (Eq. IV.9) to the values in (Table IV.2), the estimated yield strength values of the coating can be calculated and compared for each deposition strategy with respect to that of the coated samples, as shown in (Table IV.3):

Table IV.3: Determination of the Yield Strength for cladded material in coated specimens based on Law of mixtures of composite materials and the data of mechanical properties of base material and the coated specimens.

	Two passes in spiral (CC)	Two passes longitudinal in zigzig (LZ)	Two passes longitudinal in zigzag (LZZ)	Two passes: zigzig + spiral (ZC)	Two passes: zigzag + spiral (ZZC)	Base material
Yield strength (yield point) clad material ε=0.2% (MPa), σ_{Yclad}	977.2	1061.4	1014.4	1032.6	1047.9	
σ_{Yclad} / σ_{Ytest} (%)	95.0%	98.7%	96.7%	97.5%	98.1%	

The difference in the values of Yield Strength calculated previously for σ_{Yclad} is not too big respect to σ_{Ytest} (5% smaller in the case of the CC strategy), but it is always a lower value than the base material regardless of the strategy used (Table IV.2).

The importance of previous calculation lies in the fact that it will serve as a basis to establish a criterion for the manufacturing of coated specimens according to different deposition strategies for fatigue tests. The Law of Mixtures will not be used to estimate Ultimate Strength values or the percentage of elongation after fracture, since this law is only valid in the elastic range of the material. It is also known that the anisotropy of the material has an influence on the precision of the Mixtures Law (the law is so simple that it does not take anisotropy into account), but as a first approximation to a better description of the mechanical properties of the coating material of the specimens, will be considered as sufficient.

IV2.2 Criteria for Manufacturing of Coated Specimens to be used in Fatigue Test

It is necessary to establish criteria for defining the design of coated specimens used for fatigue tests.

IV.2.2.1 Basic Background on Fatigue Life for High Number of Cycles in Metallic Materials.

First of all, it is necessary to establish a general background for the fatigue life of polycrystalline metallic materials in order to clarify some factors that will be very important in the design of coated specimens for fatigue testing:

- Fatigue will be defined as: “the process of progressive localized permanent structural change occurring in a material subjected to conditions that produces fluctuating stresses and strains at some point or points that may culminate in cracks or complete fracture after a sufficient number of fluctuations" (ASTM Subcommittee E08.02, 2020).
- Fatigue damage originates from cracks that present three well differentiated stages: initiation or nucleation, propagation and final fracture. The stage of crack growth defines the morphology of the crack zone itself. The morphology of the rupture zone is also a function of the microstructure. In the initial propagation stage of cracks, the source of material damage is due to shear stress.

- The origin of the cracks are defects within the material at microstructure level (pores, inclusions, foreign phases, etc.), which in turn lead to a slippage of crystalline planes within the metal itself (shear displacement), with respect to the adjacent material.
- If the variable loading provides sufficient strain energy, new dislocations will occur within the material, to the point where several of them will coalesce and the grain where it has coalesced will fracture. The initial growth of this crack can be stopped if it "collides" with the edge of another grain (an interference is generated).
- The loading cycles can continue to the point where several of these transgranular cracks grow (microscopic at first), interlock with each other and propagate until the effective cross-section of the material is insufficient to withstand the stress. A sudden rupture will then occur, based on phenomena related to Fracture Mechanics (these aspects will not be touched upon in this research). At this stage, the final failure is due to normal stress in tension. The sequence of the previous stages is illustrated in (Fig. IV.29), where the phenomenon of fatigue damage at the microcrack level (left), evolves to the macrocrack level (right), (Avilés, 2005).

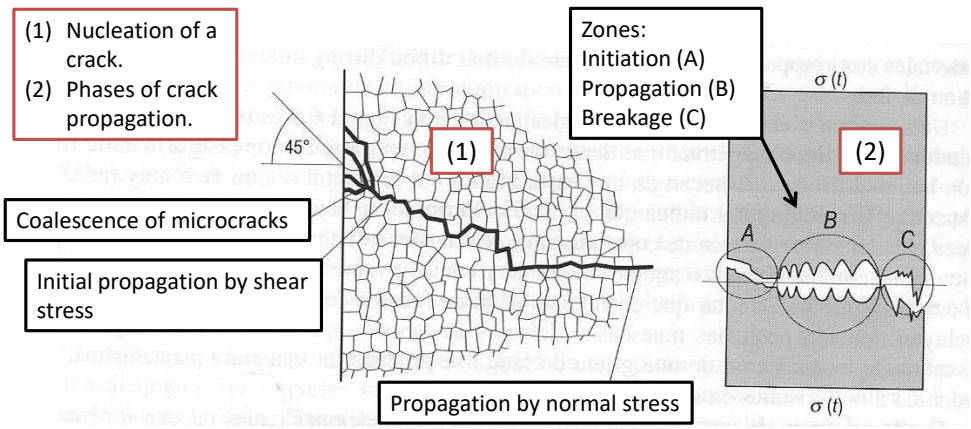

Figure IV.29. Schematic of the initiation, propagation and growth zones up to crack fracture in a polycrystalline metallic material (Avilés, 2005).

- The study on material fatigue life is normally carried out at fracture of the piece, and in this research the fatigue of low cycles (N_f up to 10^3 cycles), intermediate life fatigue (N_f from 10^3 up to 10^5 cycles) will not be considered. Fatigue life will only be considered for high number of cycles (more than 10^5 cycles), in a polycrystalline metallic material at room temperature. For this research, the

stopping criterion for the testing on coated specimens (where samples will be considered that an infinite life has been reached), is for $N_f \geq 10^6$ cycles.

Regarding the behaviour of metallic polycrystalline materials, the effect of some mechanical properties obtained from the uniaxial tensile test and the hardness test on fatigue life has been investigated. Some information has been found relating the aforementioned properties with the leaning in the fatigue life behaviour for steels, and almost nothing specifically for Nickel-based alloys, except in the case of (Avilés, 2005). In any case, the literature mentions the following:

- Effect of σ_Y: this value is theoretically of particular importance, but there is not much information on its direct effect on fatigue life. Theoretically, it is assumed that the activation of slip planes (which can lead to crack initiation in grains), should be strongly related to the Yield Strength of the material. However, for fatigue of high number of cycles, the stress threshold for crack propagation is the Fatigue Limit for rotating specimen (σ_n), which in this research, will be taken as the ideal comparison value (Pang et al., 2014). In (Martinez et al., 2010), some correlations are found for estimating fatigue life as a function of σ_Y but in combination with other mechanical properties of the material (applied to steels in this case). In general, it has been documented that the higher the Yield Strength, higher the endurance limit.
- Effect of σ_{UT}: In this case, the trend found for a large number of steels is that for higher ultimate tensile strength, higher fatigue endurance limit (up to a threshold of approximately 1800 MPa), (Campbell, 2008; Pang et al., 2014). The explanation for the phenomenon of increased fatigue endurance limit has been described as an association between high opposition to microstrength and crack growth, with a low strain ratios within the material in HCF. The tendency for low strain ratios will be reflected as a high macro value of σ_{UT} (Li et al., 2013).
- Effect of Young's modulus (E): According to (Antunes et al., 2019), this mechanical property is directly related to the fatigue crack growth rate (LCF). The reason for the previous is that Young's Modulus affects the overall deformation of

the component, which influences both the plastic deformation and the hardening of the material at the crack tip. The effective fatigue threshold is reported to correlate with this mechanical property for a wide range of metallic and composite materials (Wasén and Heier, 1998). In high cycle fatigue life (HFC), Young's modulus will be considered of little importance, but not in the calculation of the stress within the specimens, because when the material works in the elastic region, different values of E will define the stiffness for different materials within the coated specimens.

- Effect of hardness (HV): this mechanical property is one of the simplest to obtain from a test, and has been tried to be used to estimate one of the most complicated mechanical properties (fatigue endurance limit). The relationship between hardness and fatigue endurance limit has only been investigated for a few ferrous materials (Casagrande et al., 2011; Pang et al., 2014). The general trend is that the higher the hardness, up to a certain limit, higher the fatigue endurance limit (relationships are not always linear). No information has been found on the combined effect of two hardnesses of different values on the fatigue endurance limit for a cladding material (e.g. that of base material + coating together). The hardness data obtained from the coating material samples in this research will be used in the selection of strategies (tool path), for the elaboration of coated specimens to evaluate the fatigue life.
- Elongation at fracture effect ($\%E$): it will be taken into account because it allows quantifying the defects inherent to the Laser Cladding process (micropores, inclusions, etc.). A higher presence of these imperfections is associated with a lower value of elongation in coated materials with respect to the base material (Fayazfar et al., 2018). Furthermore, it will be assumed as a principle that for higher the number of defects, higher the possibility of crack nucleation.

In high cycle fatigue life, the number of defects (pores, cracks, unmelted metal powder, foreign phases, etc.), will be of great importance, as crack nucleation will be accelerated due to the presence of any of them. It is worth remembering that in HCF, most of the

fatigue endurance life of a part is "wasted" in the crack nucleation stage (Shamsaei et al., 2015), as shown in (Fig. IV.30).

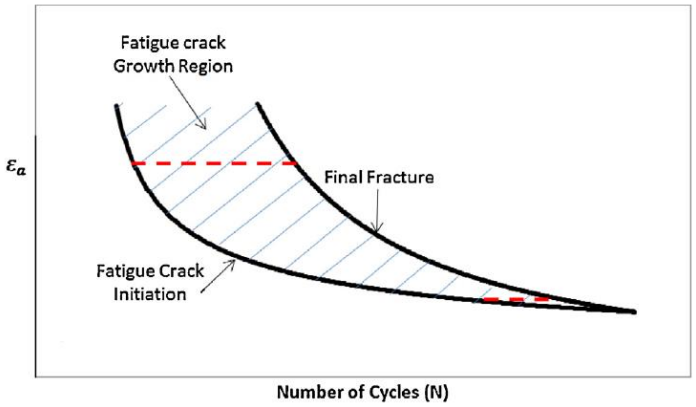

Figure IV.30. Strain life schematic of crack nucleation, growth, and final fracture (Shamsaei et al., 2015).

IV.2.2.2 Classification of different coating material deposition strategies based on a mechanical property weighting system to define the strategies to be used in the manufacturing of coated fatigue specimens.

In the previous section of this document, the influence of (σ_Y, σ_{UT}, E, HV and $\%E$) on the fatigue endurance life for a polycrystalline metallic material has been described.

The quantitative mode of influence on fatigue life (a kind of weighting system), for each of the test values mentioned previously, is not quantified for ferrous materials (which are the vast majority of the available research).

No research is available for the influence on fatigue life for a material manufactured by a laser cladding process of a nickel-based alloy. Therefore, a classification of the influence of the mechanical properties obtained from static tensile test (plus hardness) will be proposed for the fatigue life of a material manufactured by the Laser Cladding process. The proposed classification of the influence of static properties on dynamic properties (fatigue) will take into account the following parameters: Ultimate Tensile Strength (σ_{UT}), Yield Strength (σ_Y), Modulus of elasticity (E_{clad}), Hardness (HV) and Percentage of elongation at fracture ($\%E$). The previous mechanical properties will be referred to as "static mechanical properties".

The system of relative weights proposed for each mechanical property is based on the importance found in the literature for each of them, with the intention of establishing a

relationship between the following concepts: “High quality in certain static mechanical properties is equivalent to long fatigue life”.

The relative weights of the static mechanical properties applied to fatigue life for a high number of cycles are as follows:

- w_{UT} = 0.25: there is relative agreement that it is important for fatigue life, and many correlations that allow its effect to be isolated.
- w_{Y} = 0.20: it is considered important, but there is not much literature which obtain clear conclusions on how to use it to estimate the fatigue life.
- $w_{\%E}$ = 0.20: it is a value that will allow to indirectly estimating the number of defects within the supplied material.
- $w_{E(clad)}$ = 0.175: less important in HCF than in LCF. In our case, it is basic to describe the stress field inside a coated specimen and therefore, it is necessary to take it into account.
- w_{HV} = 0.175: it is together with the ultimate tensile strength limit one of the properties of which there are the greatest amount of correlations, but it has the disadvantage that its relationship with the fatigue life presents greater uncertainty.

The total sum of the weights assigned to each of the variables will add up to 1. For a better estimation of the effect of each mechanical property for the different cladding strategies, normalized variables will be used, each one with respect to their maximum value, thus (Eq. IV.10):

$$MP_{norm\_i} = \frac{MP_{i-data}}{\max[MP_{i...n-data}]} \qquad \textit{Eq. IV.10}$$

Then, for each set of values for each contribution strategy, the weighted arithmetic mean function will be applied, as shown in (Eq. IV.11):

$$W_{strat} = \frac{\sum_{i=1}^{n\_data} w_i MP_{norm\_i}}{\sum_{i=1}^{n\_data} w_i} = \frac{\sum_{i=1}^{n\_data} w_i MP_{norm\_i}}{\sum_{i=1}^{n\_data} w_i = 1} = \sum_{i=1}^{n\_data} w_i MP_{norm\_i} \qquad \textit{Eq. IV.11}$$

The use of (Eq. IV.10) and (Eq. IV.11) has the advantage of associating the final calculus for each cladding strategy and their easy comparison with each other, as all values will

always be reduced to a relative scale between 0 and 1. (Table IV.4) presents the summary of all calculations from the original mechanical properties data.

Table IV.4: Summary of calculations for the classification of cladding strategies according to their mechanical properties (static mechanical properties), for the manufacturing of coated specimens for fatigue testing.

						Weights					
						0.25	0.2	0.2	0.175	0.175	
	Mechanical property					Normalized mechanical property					
Strategy	σ_{UT} (MPa)	σ_{Y} (MPa)	%E (%)	E_{clad} (GPa)	HV 0.3 kgf (-)	σ_{UT_norm}	σ_{Y_norm}	$\%E_{norm}$	E_{clad_norm}	HV 0.3_{norm}	W_{strat}
CC	1284.5	977.2	10.7	187.5	320.2	0.9538	0.8932	0.713	0.7693	0.8981	**0.8516**
LZ	1346.3	1061.4	10.5	242.6	332.1	0.9997	0.9702	0.700	0.9953	0.9313	**0.9211**
LZZ	1315.2	1014.4	9.5	232.1	340.1	0.9766	0.9272	0.633	0.9522	0.9537	**0.8898**
ZC	1312.9	1032.6	8.4	225.0	326.2 *	0.9749	0.9439	0.560	0.9231	0.9147	**0.8661**
ZZC	1346.7	1047.9	12.0	243.7	330.1 **	1	0.9579	0.800	1	0.9259	**0.9386**
Base mat.	1287.0	1094.0	15.0	205.1	356.6	0.9557	1	1	0.8415	1	**0.9612**
Max. Value	1346.7	1094.0	15.0	243.7	356.6						
* Calculated by the average of CC and LZ											
** Calculated by the average of CC and LZZ											

The hardness values for the ZC and ZZC strategies (combination of simple strategies), have been obtained as the average of those obtained from the “pure” deposition strategies CC, LZ and LZZ.

The results of (Table IV.4) show that the normalised value of the static mechanical properties of the base material obtained the highest value in the proposed variable weight system (W_{strat}). From the remaining strategies, only the weighted ZZC values show some similarity with those obtained for the base material. The worst "quality" according to the previous classification (based on static mechanical properties), has been the CC strategy, but with only 11.4% less than the base material.

It is not known whether the proposed quantification for each deposition strategy at the level of static mechanical properties test level will have an analogue in the fatigue life behaviour of the coated samples. Does a higher value at the level of certain static properties equate to a higher fatigue life?

To investigate if there is any relationship mentioned in the previous paragraph, an experimental methodology will be proposed which shall consist on taking the worst, the intermediate and the best of the results from the classification of the strategies (Table IV.4).

Therefore, for the manufacturing of fatigue-coated specimens, the strategies (from worst to best) that will be used, are CC, LZZ and ZZC, and will be compared with the results of fatigue tests obtained with similar size specimens made only from base material.

IV.2.3 Geometry of Coated Specimens for Fatigue Life Testing.

At the beginning of this chapter, a number of particular characteristics for the evaluation of the mechanical properties of a cladded material by the use of coated specimen tests were stated:

- The base material shall be taken as a point of comparison to evaluate the mechanical property performance of a coated material.
- The geometrical shape of the coated specimens shall be similar to that defined by a specific standard.
- The coating material of the specimens should be, as far as possible, free from defects and, in addition, little affected by the effects of stress concentrations that depend on the specimen geometry.
- The test results should reflect the isotropy of mechanical properties inherent in the Laser Cladding deposition process.
- The number of activated defects in the coated specimens should be maximised to resemble the behaviour of a real component.

A series of proposals for fatigue test coated specimens have also been analysed to evaluate endurance fatigue limit (Fig. IV.2). A number of preliminary conclusions have been drawn from these design proposals:

- The test loading configuration and specimen geometry is varied: three types of standardised specimens tested in three different regimes (rotational, uniaxial tension, 4-point bending).
- The test configuration produces non-compliance with some of the desirable characteristics for the evaluation of the life fatigue endurance of the coating, such as: isolating or will minimise the influence of stress concentrations,
- Activating the largest possible volume of defects during the test and taking into account anisotropy of the deposited material.

Taking into account what was described in the previous paragraph, the use of “Hourglass” type coated specimen design with a large continuous radius of curvature between the grip ends is proposed. Based on (ASTM Subcommittee E08.05, 2015), section 5.2.1.2., a choice of parameters will be made to meet the geometric requirements of the previous standard and to overcome the deficiencies in specimen geometry that have been studied in (Fig. IV.2); the comparison is shown in (Table IV.5):

Table IV.5: General recommendations for establish the shape of coated specimens to evaluate the fatigue life for materials manufactured by the Laser Cladding Process.

Rule from ASTM E8 / E8M – 16a Standard Test Methods for Tension Testing of Metallic Materials	**Proposal based on the rule in the first column of this table**	**Justification for the proposal of geometric shape**
The specimens can have both a flat design (plane symmetry) and full axial symmetry (circumferential).	Specimens with full circumferential axial symmetry shall be used. The use of flat specimens is ruled out although it is possible to manufacture them with plane symmetry, see (Fig. IV.6).	The cladding material on specimen must retain some symmetry with respect to some geometrical characteristic. It has been mentioned that the cladding material will have different mechanical properties than the base material. Therefore, lack of symmetry in the placement of the coating with respect to the substrate material will cause buckling during the test. Flat symmetric specimens shall not be used due to the sharp edges at the corners of the specimen, which would lead to undesirable stress concentration at the edge (Fig. IV.31).
The design of full symmetry (circumferential), specimens can be applied to both the rotating type test configuration and the axial type load.	The load regime used will be axial type with stresses ratios of $R \approx 0$ and $R = -1$ (the minus sign in R will be explained later in this document).	The design of the coated specimens shall be such that the volume stressed to 90% of the maximum value is maximised for each section of the coated specimen (base and coated material). A rotating type specimen test configuration prevents that volume subjected to fatigue damage from being maximised (due to the way the stress is distributed). A detailed analysis of the stress within the specimens will be carried out later in this chapter. The use of two different “stress ratios” (R) will allow the results to be evaluated by means of an adequate fatigue criterion, taking into account the texture of the deposited material according to the strategies to be used according to [SECTION DONDE ESTÁ LAS ESTRATEGIAS A FATIGA ESCOGIDAS ¿6.10.2?].
The radius of curvature	A radius of curvature of at	A very large radius of curvature will effectively minimise the effect of stress

between the “grip” areas should not be less than 8 times the minimum diameter of the specimen.	least 20 times (and not more than 30 times) of the minimum diameter of the sample between the end gripping areas is proposed.	concentration due to the continuous change of the specimen cross-section (low k_{tx}). A radius of curvature greater than 30 times the minimum sample diameter is not recommended, as it may result in excessively slender samples, prone to buckling.
The standard (ASTM Subcommittee E08.02, 2020), does not apply to coated specimens. From another standard not applicable to metallic specimens (ASTM Subcommittee F04.15, 2017), it is recommended that the coating is designed to fail at the reduced section of the coated specimen. In general, the thickness of the coating applied to the substrate depends on the objectives of the investigation.	The thickness of the coating must be constant along the reduced section of the specimen, and the recommended proportion at the minimum cross-sectional areas is $A_{clad} / A_{probe} \leq 40\%$.	The cladding material thickness depends on: -The optimal deposition process parameters for the material (optimal conditions define a single thickness depending on the coating strategy on the substrate). -The research objectives (thickness has a strong influence on the overall mechanical strength of the sample (Fig. IV.27), and can be used as an independent variable). -The relative dimensions of the substrate in order to avoid an excessive Dilution (Dil), value that can decrease the performance of the base material due to excessive thermal damage (HAZ), (Fig. IV.18). - The capability of the technological solution (degrees of movement of the machine, numerical control, CNC, etc.), available to manufacturing the specimen design (Fig. IV.17). Inconsistent coating thickness can lead to uneven stress distribution. A detailed analysis of the stress inside the specimens will be made later.

The rest of the recommendations of the ASTM standard for metallic specimens on: machining, surface finish, specimen alignment, etc., are maintained in accordance with the (ASTM Subcommittee E08.02, 2020), The aim is to ensure as much compatibility as possible with previously performed specimen tests in order to be able to compare results.

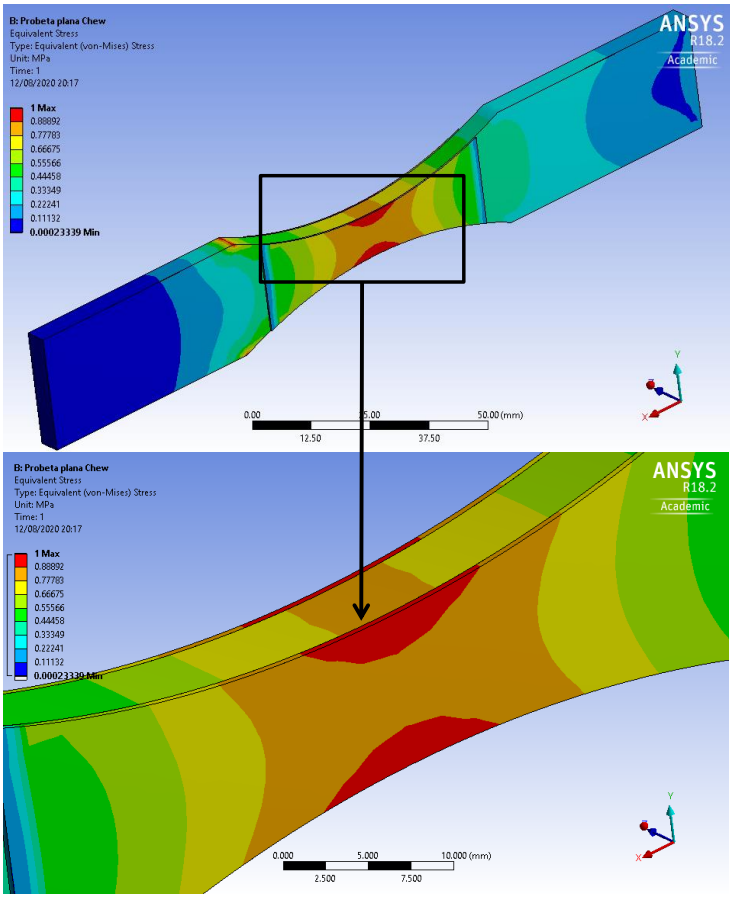

Figure IV.31. Equivalent von Mises stress distribution (normalized to 1 MPa), for a specimen with plane symmetry with the arrangement proposed by (Chew et al., 2017). The bottom detail on the figure shows that high concentration of stress is generated at the edges of the coated material. The coating material properties used are taken from (Table IV.4), from the ZZC cladding strategy.

IV.2.3.1 Comparative Stress Analysis in FEM Models of Coated Specimens to Clarify the Proposed Criteria for the Design of Cladding Specimens for Fatigue Test.

In (Section IV.1.3), (Fig. IV.2); shows the stress field tensor calculated by means of the finite element method for different types of specimens subjected to an Equivalent von Mises stress. It has been explained that at test fatigue level, the previous criterion does not make much sense, and the objective has only been to intuitively “visualize” the

existence of stresses within the material (nothing is established regarding fatigue life). There are ways to use the von Mises criterion with certain modifications to include the effect of the material's load spectrum (through modifying coefficients), so its application to fatigue, although not being direct, is possible (Engin and Coker, 2017; Ion et al., 2011).

A derivation of the tensor stress obtained from the FEM analysis method is the so-called Stress Linearization. It consists of approximating a general tensor field in 3D by means of a tension on a line-path for certain applications, among which it is included in fatigue analysis of welds (Sönnerlind, 2017). The previous line-pat is called SCL, and it is basically a coordinate system on which the tensor field is locally measured (Mackenzie, 2017). The advantage of stress linearization is that it allows analysis of stress fields that deviate from linear behaviour near stress concentrators.

The application of Stress Linearization (for this research), will consist on placing different SCLs inside virtual models of coated specimens, and modelling the 3D tensor stress to an equivalent line stress to "visualise" the magnitude of the local tensor stress over a trajectory in key areas of the specimens (the Equivalent von Mises stress will again be used). The aim of the previous process is to create a kind of "virtual stress gauges" within each test specimen.

The stresses within the coated specimens that will be analysed to justify the validity of the design recommendations in (Table IV.5), will be one of the probe designs in (Fig. IV.2), specifically the one corresponding to (Koehler et al., 2012), and a proposed design that adheres to the recommendations in the table mentioned previously. The specific dimensions of the proposed coated specimens can be found in (APPENDIX, DRAWINGS OF PROBES).

The specific location of the virtual strain gauges shall be in the plane passing through the centre of each specimen in the direction of its axis of symmetry, with an origin indicating the “start” of the specimen. Some of these virtual gauges share the same origin and, where possible, the symmetry of the specimens shall be used to plot the equivalent stress values.

The position of the SCLs for the two specimen designs to be compared is shown in (Fig. IV.32).

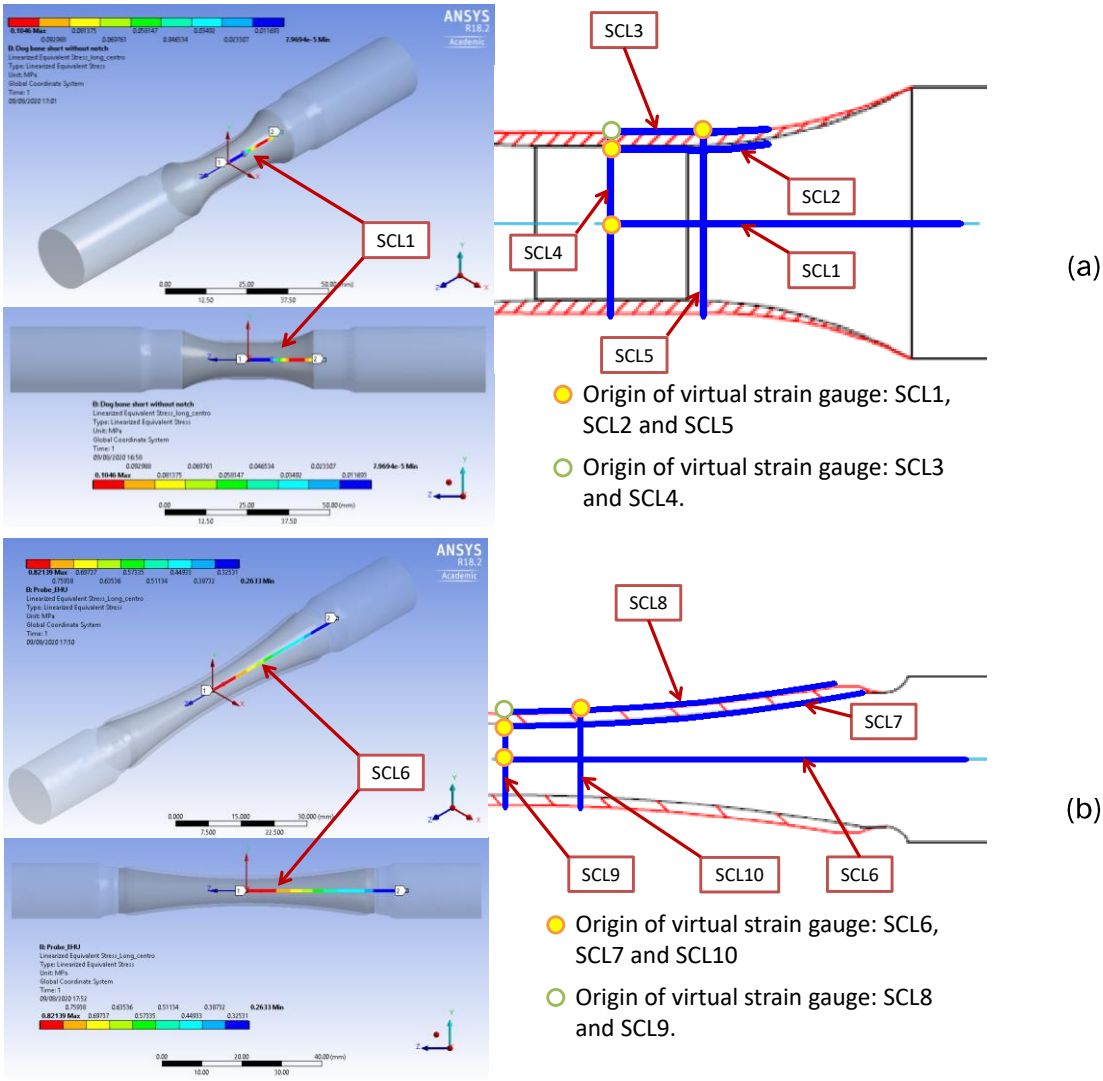

Figure IV.32. Position of the SCLs acting as virtual strain gauges to determine the equivalent linearized von Mises stress inside the coated specimens for: (a) the design proposed by (Koehler et al., 2012) and (b) the design according to the recommendations in (Table IV.5).

From the previous figure, SCL 4 and 9 are in the plane of transverse symmetry in the middle part of each type of specimen. The drawings of each specimen design on the left of each SCL positioning diagram are for reference only (the largest SCL on each specimen type is shown for clarity of position). The distance between SCL4-SCL5 and SCL9-SCL10 is 6mm.

The graphs with the linearized stresses are shown in (Fig. IV.33). The origin of each graph coincides with that indicated in the design of each sample in (Fig. IV.32). The distances in graph are measured in a coordinate system associated with each SCL (therefore, the graphs are not symmetrical). For comparison purposes, all stresses shown in the graphs are scaled to a range of values between zero and one. The mechanical

properties for the substrate and the coating material (ZZC strategy), for FEM analysis were taken from (Table IV.4).

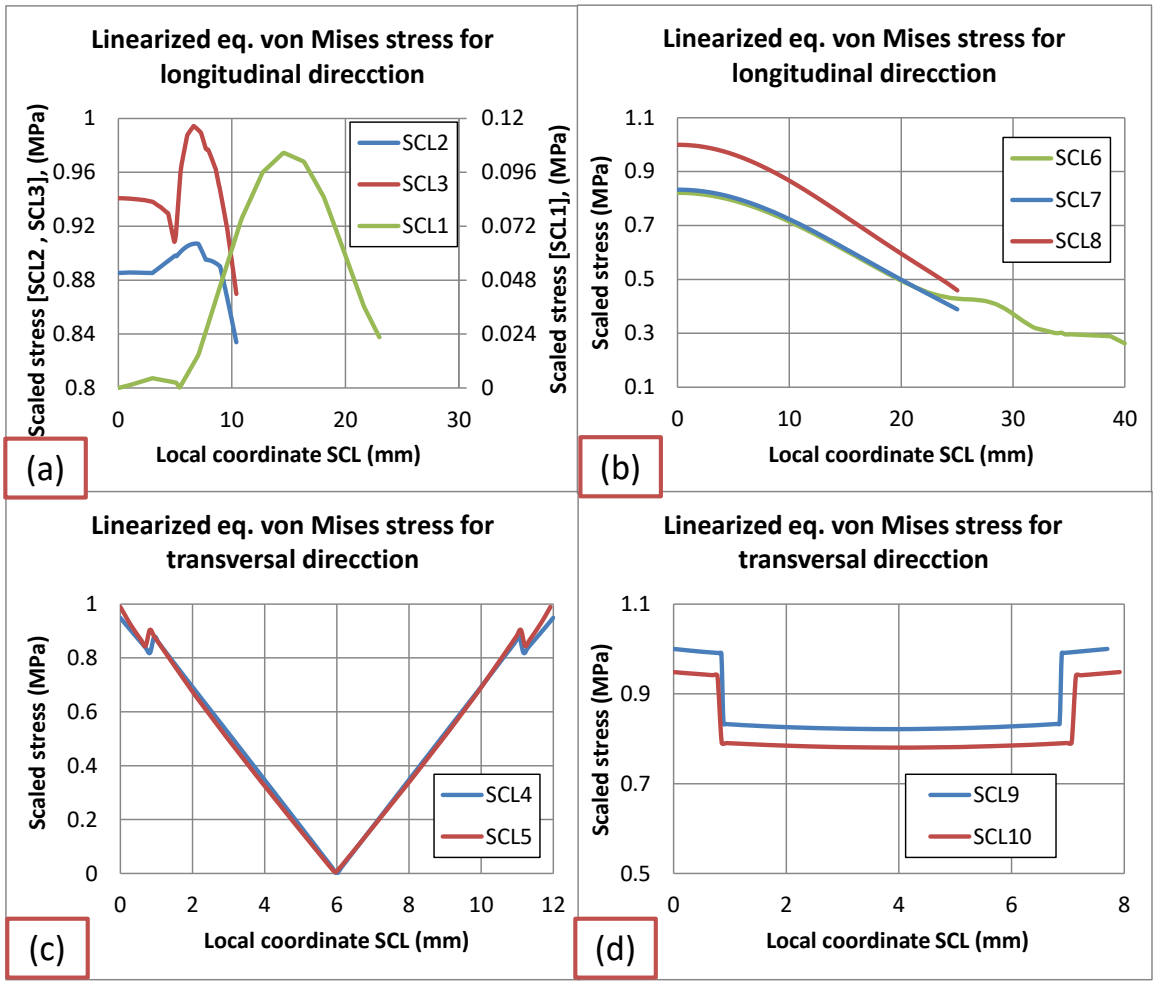

Figure IV.33. Equivalent linearised von Mises stresses in the longitudinal and transverse directions of the SCLs of (Fig. IV.32) for the specimens according to the recommended design of (Koehler et al., 2012), (a) and (c); and based on the design recommendations of (Table IV.5), (b) and (d).

The characteristics of the linearized stresses at analogue positions for SCL pairs will be compared according to their relative location (Fig. IV.32). The comparison of the characteristics mentioned previously is presented in (Table IV.6).

Table IV.6: Comparison of the results obtained on the equivalent linearized stress values of the SCL of (Figs. IV.32 and IV.33). The aim of the comparison is to investigate whether the design parameters of coated specimens of (Table IV.5) allow to meet the requirements recommended by (ASTM Subcommittee E08.05, 2015).

Analogous SCLs according to the relative position in each coated specimen design.	**Comparative behaviour of linearized stress.**	**Comment on the objective of this SCL in the characterisation of stresses in coated specimens and the comparison of linearized stresses for each case.**
SCL1 and SCL6: on the axis of symmetry of each substrate in each specimen, with the origin at the geometric centre of each specimen.	SCL1: shows stress close to zero, but variable along the coordinates of the SCL. There are two exceptions to the trend of the value close to zero: in the area near the beginning of the fillet radius and at the end of this of curvature in the preform. Values near zero are to be expected in a rotating specimen test regime. The behaviour of the previous stress tends to be slightly erratic, although it is not too important because it is close to zero. SCL6: the value of stress is always strictly decreasing even in the areas close to the section change from the area with constant curvature of the substrate to the clamping area. The stress within the material has a "smooth" behaviour along the SCL coordinates.	The aim of these SCLs is to investigate the behaviour of stresses within the substrate, right on the axial symmetry axis of the specimen. It is observed that SCL6 has much smoother stress value transition behaviour from its origin than SCL1. The proposed coated specimen design has the effect of exposing a larger volume of the substrate to a large stress.
SCL2 and SCL7: on the surface of the substrate of each specimen, just below	SCL2: presents a uniform stress value close to its origin, but as the local SCL coordinate advances, there is an increase in stress (which can be	The aim of these SCLs is to investigate how stresses behave in the area of the substrate surface just below the coating. It is observed that:

the base-coating interface, and with origin in the transverse plane of symmetry of the specimen.	attributed to the stress concentrator of the fillet radius), and subsequently a drop in its value. The stress concentration due to the presence of the fillet radius on the substrate has a noticeable effect on the stress distribution over the substrate surface. SCL7: the stress value is not uniform starting from the origin of the SCL from the centre of symmetry of the specimen, but it decreases very slowly in a strictly decreasing and "smooth" way. The effect of the stress concentrator due to the fillet radius of the preform is slight.	SCL2 has the advantage of a uniform stress value near the origin, but is affected by the fillet radius stress concentrator. Specimens with design of constant area centre section and slot with coated material have this characteristic (sensitivity to stress concentrators), and are therefore prone to failure in that area near to fillet radius, and not in the centre as recommended by the standard (Fig. IV.13). SCL7 shows non-uniform stress values (due to the continuous radius of curvature between the "grips" of the substrate), but always close to the maximum value at the centre of the sample over a certain distance from the origin of the SCL (90% of the maximum stress at a distance of approximately d_{test}).
SCL3 and SCL8: on the surface of the coating of each specimen, and with coordinate origin in the transverse plane of symmetry of the specimen.	SCL3: presents a uniform linearized stress value close at its origin, but this uniform value is of short-range and next follows a very sharp drop in it. As one moves up the local SCL coordinate, there is an increase in stress that can be attributed to the fillet radius by the stress concentrator (with a sharp peak in the value of the equivalent stress), and then a sharp drop in the value of the equivalent stress. The stress concentration due to the presence of the fillet radius on the substrate has a very noticeable effect on the stress distribution on the surface of the coating. The peak in stress value can also be partly attributed to the effect that the coating	The aim of these SCLs is to investigate how the stresses behave in the surface area of the coating and their interaction with the inner substrate. It is observed that: SCL3 exhibits a uniform stress value near its origin but a very short distance, and then is very quickly affected by the radius of curvature stress concentrator (fillet radius) and possibly by the non-uniform coating thickness. The variation in coating thickness (which is characteristic of specimens with a constant area centre section type design and a groove repaired with coated material), causes the stress value inside to have a complex behaviour, (Fig. IV.33). The stress behaviour measured by SCL3 is apparently a magnification of the stress measured with SCL2.

	does not have a uniform thickness and less material "can" resist the load. SCL8: the stress value is not uniform starting from the origin of SCL (from the plane of symmetry of the centre of the specimen), but the stress decreases very slowly in a strictly decreasing and "smooth" way.	SCL8 shows non-uniform stress values (due to the continuous radius of curvature of the substrate), but close to the maximum stress value on the centre of the sample over a certain distance in the SCL coordinate system (90% at about d_{test} distance). The effect of the stress concentrator due to the continuous radius of curvature of the preform is smooth and there is no overlap with the equivalent SCL7 stress values. In summary, the effect of (k_{tx}) is small.
SCL4 and SCL9: pass through the substrate and the coating in the plane of transverse symmetry in the centre of the sample.	SCL4: shows an abrupt drop in the value of the linearized equivalent stress from the surface (where the maximum value is found), towards the inside of the specimen (where the stress reaches zero). The tendency in the stress behaviour according to the graph of SCL4 is linear. There is complete symmetry in the graph with respect to the centre of the specimen. There is a “break” in the line that describing the stress values in the substrate-cladding material interface, due to the different mechanical properties at the joint of the two materials. SCL9: the trend observed in the equivalent linearized stress value is to remain constant for the coating, then a discontinuity at the edge with the substrate, and finally a change in the stress value to a different one from that of the coating. It is observed that in both cases (substrate and	The purpose of these SCLs is to investigate the behaviour of the equivalent linearized stress value over the transversal entire cross-section of the central zone of the coated sample. It is observed that: SCL4 presents stress values with the typical behaviour of a rotating type fatigue test specimen, i.e. maximum stresses at the surface with zero values at the centre (axis of symmetry). Since a von Mises criterion has been used, the graph for SCL4 is completely symmetrical, but in reality it should be approximately a continuous straight line. The disadvantage of using a rotating sample test setup is that only the surface stress is maximum and inward decreases rapidly (there is less chance of defect activation in a large volume on specimen). The advantage of this type of configuration (rotating probe); is that the magnitude function of the stress value is relatively easy to calculate with classical beam theory. SCL9 here, the equivalent linearized stress value shows an

	coating); the values are different but maintain the characteristic of remaining approximately constant along the SCL.	approximately constant behaviour (typical for the axial type test setup). The material throughout the coating thickness is subjected to relatively high stress, which increases the probability of activating defects in the coating, and the same is true for the substrate material. The disadvantage is that the value of this "approximately constant" stress magnitude function within each section of this type of variable cross-section coated specimen is much more complicated to calculate than that of a constant area cross-section specimen.
SCL5 and SCL10: pass through the substrate and coating parallel to the plane of transverse symmetry in the centre of the specimen, at a distance of 6 mm from the centre of the probe.	SCL5 and SCL4 exhibit completely analogous behaviours. The comment for SCL4 is valid for SCL5. SCL10 and SCL9 exhibit completely analogous behaviours. The comment for SCL10 is valid for SCL9.	The objective of these SCLs is to investigate the behaviour of the equivalent linearized stress value across the entire cross section of the coated specimen when it moves away from the plane of symmetry (d = 6 mm in this case). It is observed that the behaviour described for SCL4 and SCL9 is preserved.

From the analysis of (Table IV.6) it can be concluded that the parameters recommended in (Table IV.5) are a good option for the design of coated specimens for fatigue resistance at a high number of cycles and maximisation of compatibility with the standard used as a basis in this research for the development of the coated specimens: ASTM E466-15.

IV.2.4 Deduction of the Magnitude of the Normal Stress Field in an "Hourglass" Coated Specimen.

The magnitude of the tensile field in the axial direction measured transversely in an “Hourglass” coated specimen type has a different behaviour in the central area (the stress is maximum in the substrate), as it is observed by the measure of the SCL in the (Fig. IV.33, d). Regarding the case of (Fig. IV.33, d) the magnitude of the stress field is function of the difference in mechanical properties between the coating and the substrate material, (specifically of the modulus of elasticity E_{pre} and E_{clad}), which can present several cases of behaviour. If $E_{clad} > E_{pre}$, the magnitude of the stress is greater in the coating than in the substrate. The reverse is also true, if $E_{clad} < E_{pre}$ the magnitude of stress will be greater in the substrate than in the coating.

Thus, the function derived for the magnitude of the stress inside the "Hourglass" coated specimen should be able to model both the maximum and minimum normal stress values (tension and compression for the different "stress ratio" (R) that will be used in the tests), as well as their position inside the specimen itself, depending on the mechanical properties of the substrate and the coating.

After the analysis of (Fig. IV.33, d), it is observed that the magnitude of the stress field is not uniform; this is because the specimen does not have a constant cross section along its axis of symmetry, unlike a “Dog Bone” type specimen (Fig. IV.13).

If the magnitude of the stress inside a coated specimen type “Dog bone” with constant cross section can be assumed to be uniform (but with a different value depending on whether it is evaluated in the substrate or in the coating), then the magnitude of the stress inside of a “Hourglass” type specimen with continuous radius of curvature can be assumed to be of parabolic type (Fig. IV.33, d).

Due to the narrowing in the neck of an “Hourglass” type specimen, the magnitude of the stress will be maximum in this “neck” area and therefore, objective will be to model the stress field in that section of the specimen.

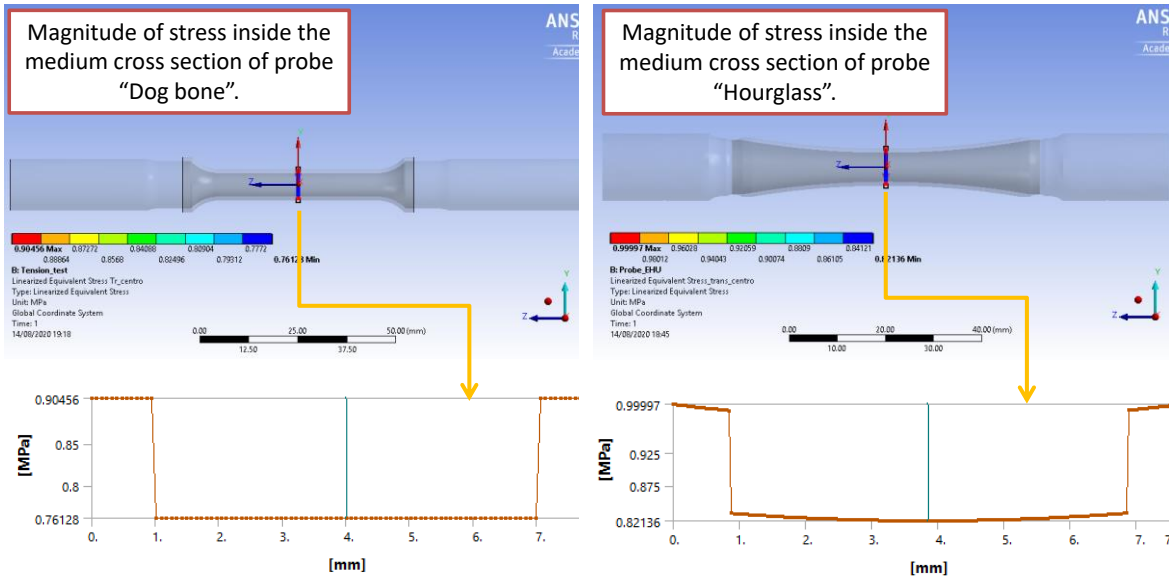

Figure IV.34. Left, the magnitude of the stress within a "Dog bone" type sample. The uniform stress value at the bottom left of the graph corresponds to the coating; the value in the middle of the graph corresponds to the substrate. Right, stress magnitude within an “Hourglass” sample. The stress value at the right bottom of the graph is not uniform either at the ends (cladding) or in the middle of the graph (substrate). For the previous graph, the shape of the functions for the substrate and for the coating shall be assumed as parabolas.

Let the parabolic functions of (Eq. IV.12) and (Eq. IV.13) be those corresponding to the magnitude of the stress in the preform (σ_{pre}) and the coating (σ_{clad}), of the “Hourglass” type specimen:

$$\sigma_{pre}(x_1) = c_1 x_1^{\,2} + c_2, \text{ with domain in } x_1 = \left\{0, \frac{d_{test}}{2} - t_{clad}\right\} \qquad \textit{Eq. IV.12}$$

$$\sigma_{clad}(x_1) = d_1 x_1^{\,2} + d_2, \text{ with domain in } x_1 = \left\{\frac{d_{test}}{2} - t_{clad}, \frac{d_{test}}{2}\right\} \qquad \textit{Eq. IV.13}$$

The coordinate system of (Eq. IV.12) and (Eq. IV.13) will be set as shown in (Fig. IV.35). The origin of the coordinate system will be located in the centre of symmetry of the specimen, in the narrowest area of the neck.

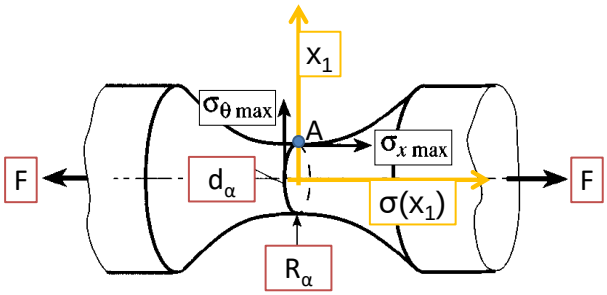

Figure IV.35. Reference framework for parabolic functions (Eq. IV.12) and (Eq. IV.13) for the magnitude of the stresses in a "Hourglass" specimen type; $\{x_1, \sigma(x_1)\}$.

To derive the constants $[c_1, c_2]$ and $[d_1, d_2]$ for the equations (Eq. IV.12) and (Eq. IV.13) respectively, first it is necessary to calculate the value of stress concentration factor at point "A" on the surface of the "Hourglass" type specimen in (Fig. IV.35).

The value of k_{tx} can be calculated from (Pilkey, 1997), where for the corresponding equivalent equation (Eq. IV.14), a change of nomenclature has been made with respect to the original equation to the nomenclature of this document:

$$k_{tx} = \frac{\sigma_{x\max}}{\sigma_{nom}} \frac{\sqrt{2}(2R_\alpha(\nu+1)+d_\alpha)\sqrt{\frac{k_\alpha}{R_\alpha}}+4R_\alpha(\nu+1)+d_\alpha(2\nu+1)}{2\left(2\sqrt{2}R_\alpha\nu\sqrt{\frac{k_\alpha}{R_\alpha}}+4R_\alpha+d_\alpha\right)} \qquad \textit{Eq. IV.14}$$

where $k_\alpha = 2R_\alpha + d_\alpha$.

The stress concentration factor of (Eq. IV.14) will be assumed to be valid both outside the substrate and outside the coating, as they will be calculated as two surfaces that would independently correspond to the "surface" of the specimen.

The values of R_α and d_α will be assigned according to the part of the specimen that is being analysed to determine the corresponding $k_{\substack{tx \\ pre}}$ and $k_{\substack{tx \\ clad}}$.

For the substrate of the coated specimen ($k_{\substack{tx \\ pre}}$), the substitution of variables will be:

$R_\alpha = R_{pre} = R_{test} + t_{clad}$ and $d_\alpha = d_{pre} = d_{test} - 2t_{clad}$.

For the cladding of the coated specimen ($k_{\substack{tx \\ clad}}$), the substitution of variables will be:

$R_\alpha = R_{test}$ and $d_\alpha = d_{test}$.

The value of $k_{t\theta}$ associated with $\sigma_{\theta\max}$ at point "A" of the neck of the specimen in (Fig. IV.35) will not be taken into account because its value for the geometry of specimens designed according to (Table IV.5) is negligible (Pilkey, 1997).

To determine the forces inside each section within the coated specimen, the use of (Eq. IV.1) allows dividing the load that each section supports:

$$F_{test} = F_{pre} + F_{clad} \qquad \textit{Eq. IV.1 (repeated)}$$

If the parabolic functions $\sigma_{pre}(x_1) = c_1 x_1^{\,2} + c_2$ and $\sigma_{clad}(x_1) = d_1 x_1^{\,2} + d_2$ are integrated over the ranges corresponding to the preform and the cladding using the Method of Cylindrical Shells, F_{pre} F_{clad} and can be deduced as (Eq. IV.15) and (Eq. IV.16):

$$F_{pre} = 2\pi \int_0^{d_{test}/2 - t_{clad}} x_1 (c_1 x_1^{\,2} + c_2) dx_1 \qquad \textit{Eq. IV.15}$$

$$F_{clad} = 2\pi \int_{d_{test}/2 - t_{clad}}^{d_{test}/2} x_1 (d_1 x_1^{\,2} + d_2) dx_1 \qquad \textit{Eq. IV.16}$$

The nominal forces $\sigma_{nom} = F / A$ for each section of the specimen are defined as (Eq. IV .17) and (Eq. IV.18):

$$\sigma_{\substack{nom \\ pre}} = \frac{F_{pre}}{A_{pre}} = \frac{4F_{pre}}{\pi d_{pre}^{\,2}} \qquad \textit{Eq. IV.17}$$

$$\sigma_{\substack{nom \\ clad}} = \frac{F_{clad}}{A_{clad}} = \frac{4F_{clad}}{\pi (d_{test}^{\,2} - d_{pre}^{\,2})} \qquad \textit{Eq. IV.18}$$

If the longitudinal deformation within the sample is assumed to be equal for the substrate and the coating, taking (Eq. IV.4):

$$\varepsilon_{clad} = \varepsilon_{pre} = \varepsilon_{test} \qquad \textit{Eq. IV.4 (repeated)}$$

For the linear elastic range at macroscopic level of the nominal normal stress inside the specimen it is known that (Eq. IV.2):

$$\sigma = \varepsilon.E \qquad \textit{Eq. IV.2 (repeated)}$$

Combining (Eq. IV.2), (Eq. IV.4), (Eq. IV.17) and (Eq. IV.18), and manipulating the mathematical expressions, we obtain (Eq. IV.19):

$$\frac{E_{pre}}{E_{clad}} = \frac{F_{pre}({d_{test}}^2 - {d_{pre}}^2)}{F_{clad}{d_{pre}}^2} \qquad \textit{Eq. IV.19}$$

The (Eq. IV.19) in combination with (Eq. IV.1) allows to calculate the value of shown in (Eq. IV.20) and (Eq. IV.21), solely as a function of the modulus of elasticity corresponding to the substrate and the coating (enhancing the importance of differentiating the mechanical properties of the different “parts” of the coated specimen).

$$F_{pre} = \frac{E_{pre}F{d_{pre}}^2}{E_{pre}{d_{pre}}^2 - E_{clad}({d_{pre}}^2 - {d_{test}}^2)} \qquad \textit{Eq. IV.20}$$

$$F_{clad} = \frac{E_{clad}F({d_{pre}}^2 - {d_{test}}^2)}{E_{clad}({d_{pre}}^2 - {d_{test}}^2) - E_{pre}{d_{pre}}^2} \qquad \textit{Eq. IV.21}$$

Using the previous equations of this section of the document; the constants $[c_1, c_2]$ and $[d_1, d_2]$ for the parabolic stress functions in the substrate and coating can be obtained as follows.

The (Eq. IV.15) and (Eq. IV.26), and the constants c_2 and d_2 are solved, resulting respectively in (Eq. IV.22) and (Eq. IV.23):

$$c_2 = \frac{32F_{pre} - \pi c_1(d_{test} - 2t_{clad})^4}{8\pi(d_{test} - 2t_{clad})^2} \qquad \textit{Eq. IV.22}$$

$$d_2 = \frac{4F_{clad} - \pi d_1 t_{clad}({d_{test}}^3 - 3{d_{test}}^2 t_{clad} + 4d_{test}{t_{clad}}^2 - 2{t_{clad}}^3)}{4\pi t_{clad}(d_{test} - t_{clad})} \qquad \textit{Eq. IV.23}$$

From the (Eq. IV.22) and (Eq. IV.23) we can obtain the extra boundary condition necessary for the proposed parabolic function. By knowing the nominal stresses and the stress concentration factor, it is possible to establish the stress value in an extra coordinate (the surface), of the reference frame in (Fig. IV.35).

By substituting the coordinates $\sigma_{pre}(d_{test}/2-t_{clad}) = \underset{pre}{\sigma_{nom}}\underset{pre}{k_{tx}} = c_1(d_{test}/2-t_{clad})^2 + c_2$ together with $\sigma_{clad}(d_{test}/2) = \underset{clad}{\sigma_{nom}}\underset{clad}{k_{tx}} = d_1(d_{test}/2-t_{clad})^2 + d_2$, and clearing the constants c_2 and d_2, we obtained respectively (Eq. IV.24) and (Eq. IV.25):

$$c_2 = \underset{pre}{k_{tx}}\ \underset{pre}{\sigma_{nom}} - c_1(d_{test}/2-t_{clad})^2 \qquad \textit{Eq. IV.24}$$

$$d_2 = \underset{clad}{k_{tx}}\ \underset{clad}{\sigma_{nom}} - \frac{d_1 {d_{test}}^2}{4} \qquad \textit{Eq. IV.25}$$

By matching (Eq. IV.22) with (Eq. IV.24), and (Eq. IV.23) with (Eq. IV.25), the constants c_1 and d_1 are derived as a function of known variables, as shown in (Eq. IV.26) and (Eq. IV.27) respectively:

$$c_1 = \frac{8(\pi \underset{pre}{k_{tx}}\ \underset{pre}{\sigma_{nom}}(d_{test}-2t_{clad})^2 - 4F_{pre})}{\pi(d_{test}-2t_{clad})^4} \qquad \textit{Eq. IV.26}$$

$$d_1 = \frac{2(\pi \underset{clad}{k_{tx}}\ t_{clad}\underset{clad}{\sigma_{nom}}(d_{test}-t_{clad}) - F_{clad})}{\pi {t_{clad}}^2 (d_{test}-t_{clad})^2} \qquad \textit{Eq. IV.27}$$

Substituting (Eq. IV.26) in (Eq. IV.24) and (Eq. IV.27) in (Eq. IV.25) deduces both constants c_2 and d_2 as a function of known variables, as shown in (Eq. IV.28) and (Eq. IV.29) respectively:

$$c_2 = \frac{8F_{pre} - \pi \underset{pre}{k_{tx}}\ \underset{pre}{\sigma_{nom}}(d_{test}-2t_{clad})^2}{\pi(d_{test}-2t_{clad})^2} \qquad \textit{Eq. IV.28}$$

$$d_2 = \frac{F_{clad}{d_{test}}^2 + \pi \underset{clad}{k_{tx}}\ t_{clad}\underset{clad}{\sigma_{nom}}({d_{test}}^2 - 2d_{test}t_{clad} + 2{t_{clad}}^2)(t_{clad}-d_{test})}{2\pi {t_{clad}}^2 (d_{test}-t_{clad})^2} \qquad \textit{Eq. IV.29}$$

The coefficients from (Eq. IV.26) to (Eq. IV.29) must be substituted in (Eq. IV.22) and (Eq. IV.23).

IV.2.5 Validation of the Analytical Model of the Stress Field Magnitude for a Coated Specimen.

To compare the precision of the previous mathematical model of the (Eq. IV.12) and (Eq. IV.13) (with their respective coefficients), a specific test case for a specimen with dimensions according to the recommendations of (Table IV.5), was modelled by the FEM technique. The mechanical and dimensional properties used in both models (FEM and analytical) are shown in (Table IV.7).

Table IV.7: Mechanical properties and dimensions assigned to the FEM and analytical models for the purpose of validating the latter. The mechanical properties are taken from (Table IV.4).

Characteristic	Value assigned in the FEM and analytical models.
E_{clad} (GPa)=	243.7 (ZZC strategy)
E_{pre} (GPa)=	205.1
ν (-)=	0.3
d_{test} (mm)=	7.7
t_{clad} (mm)=	0.85
R_{test} (mm)=	170.15
F (N)=	1000

The results of the FEM model are shown in (Fig. IV.36). The Principal Maximum Linearized Stress has been used as a comparison criterion. The reason for using linearized stress (different from the equivalent stress case like von Mises), is that the calculation will show the stress sign; where a positive magnitude indicates tension on the coated specimen and a negative magnitude indicates compression of the specimen.

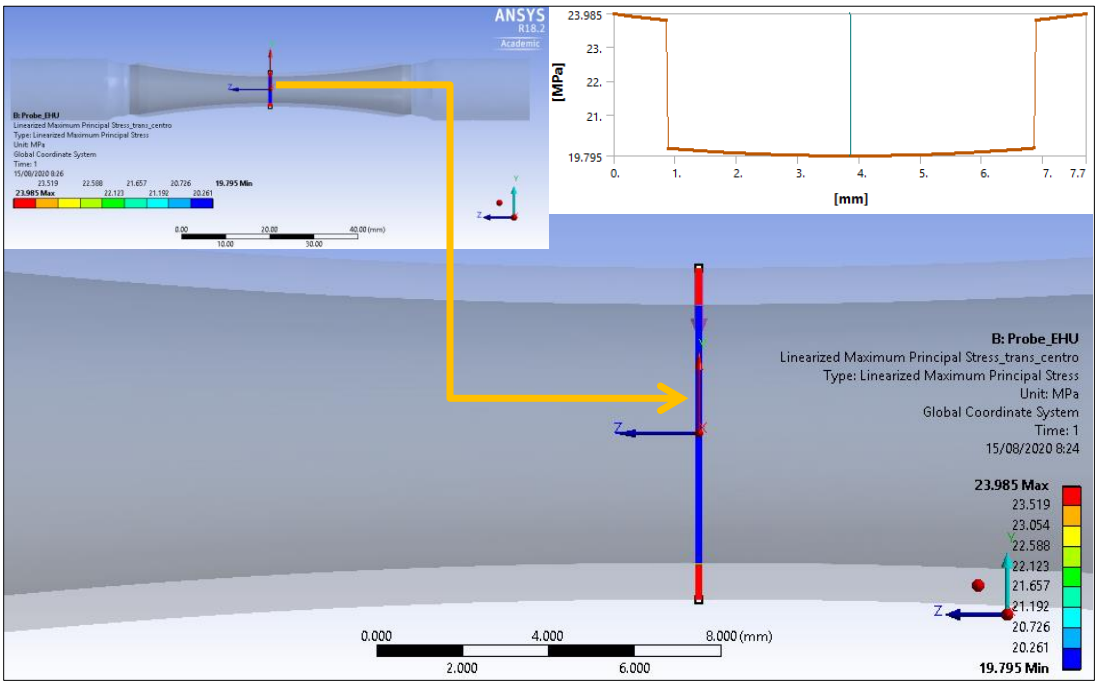

Figure IV.36. Result of the FEM calculation of a coated specimen for the parameters of (Table IV.7). The colour code in the figure (bottom right area), indicates that the maximum normal stress at the centre of the cross-section of the specimen is located in the coating. The top-right graph shows the set of values calculated by the programme, with discontinuity in the stress values at the substrate-coating interface.

By using the analytical model defined by the equations from (Eq. IV.12) to (Eq. IV.29), and using the parameters of (Table IV.7), the coefficients of (Table IV.8) are calculated:

Table IV.8: Coefficients and some of the intermediate values for the analytical model of the stress magnitude in coated specimens defined between equations (Eq. IV.12) to (Eq. IV.29).

$k_{tx\ pre}$ (-)	$k_{tx\ clad}$ (-)	F_{pre} (N)	F_{clad} (N)	$\sigma_{nom\ pre}$ (MPa)
1.00774	1.00998	565.39	434.61	19.996
$\sigma_{nom\ clad}$ (MPa)	c_1 (N/mm^4)	c_2 (N/mm^2)	d_1 (N/mm^4)	d_2 (N/mm^2)
23.76	0.03440	19.84169	0.08142	22.79001

The (Fig. IV.37) shows the superposition of the graphs from the calculations of FEM and analytical models on the same domain (the set of coordinates on the frame of reference is defined in (Fig. IV.35); at central cross-section of the coated specimen). The relative error between both models is also shown; the FEM model is taken as more accurate.

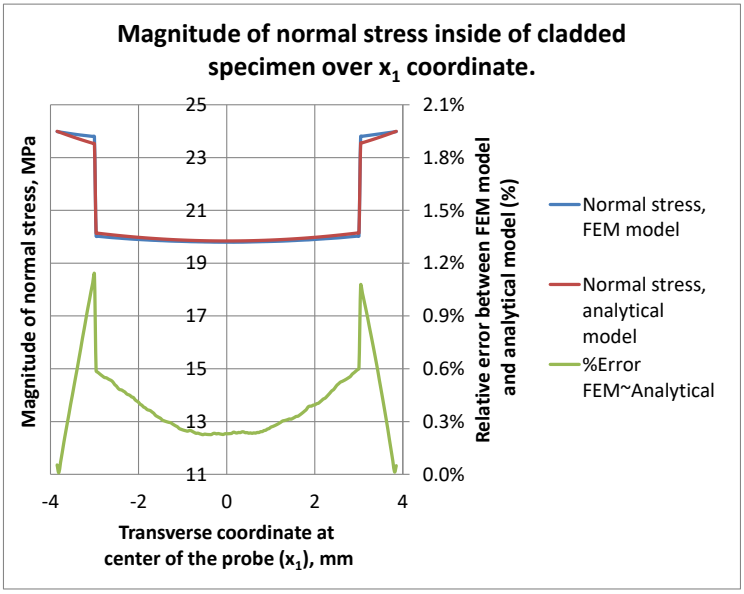

Figure IV.37. Graph for comparison between the FEM results and the analytical model for calculating the magnitude of the normal stress within a coated sample. On the auxiliary axis (right on the graph), the relative magnitude of error between the two models is scaled. It has been assumed that the FEM model is more accurate as base for calculating the relative error.

If the parameters E_{clad}, E_{pre}, ν, d_{test}, t_{clad} and R_{test} of (Table IV.7) are kept constant, and $F(t) = -1000\cos(\omega t)$ [N] is defined in such a way as to change its value (over half a cycle of the cosine function for convenience), it is possible to verify by a graphing the magnitude and sing of normal stress as a function of t ($\sigma(t)$). The result is shown in (Fig. IV.38).

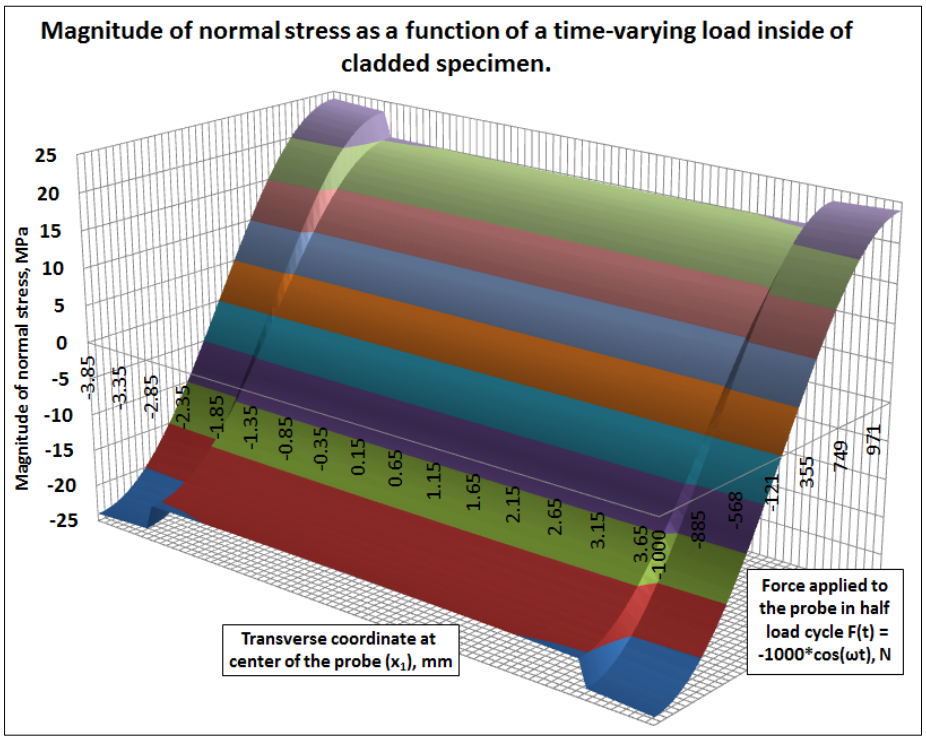

Figure IV.38. Surface graph showing the variation in the magnitude of normal stress within a coated specimen as a function of a time-varying force (half cycle has been plotted for clarity). The analytical model accurately describes the change in the magnitude of the stress (and its sign), as the applied load also changes its sign (it goes from negative to positive, passing through zero symmetrically as the force F does).

It is possible to use the FEM simulation to perform all the calculations described in this section of the report, but the computational cost is excessive.

The summary of the analytical model is shown in (Table IV.9), where all the equations have been simplified so as to start from the minimum number of geometric parameters of the coated specimen and mechanical properties.

As this model will be used to describe the fatigue behaviour in specimens for a cladding material (fluctuating load variable in time), the load parameter on the specimen will be considered fluctuating in time, as follows: $F = f(t) \therefore [c_1, c_2, d_1, d_2] = f(t)$.

Table IV.9: Summary of the equations of the analytical model to calculate the magnitude of the normal stress in the neck area of an "Hourglass" coated specimen with fluctuating load over time $F = f(t)$.

$$\sigma_{pre}(x_1) = c_1 x_1^{\,2} + c_2$$

$$\sigma_{clad}(x_1) = d_1 x_1^{\,2} + d_2$$

$$c_1 = -F(t)\frac{16E_{pre}\left(\sqrt{2}(2R_{test}(\nu-1)-d_{test}+2t_{clad}\nu)k_1+4R_{test}(1-\nu)+k_3-2\nu d_{test}\right)}{\pi(d_{test}-2t_{clad})^2 k_5}$$

$$c_2 = F(t)\frac{2E_{pre}\left(\sqrt{2}(2R_{test}(3\nu-1)-d_{test}+6t_{clad}\nu)k_1+4R_{test}(3-\nu)+3k_3-2\nu d_{test}\right)}{\pi k_5}$$

$$d_1 = F(t)\frac{4E_{clad}\left(\sqrt{2}(2R_{test}(\nu-1)-d_{test})k_2+4R_{test}(1-\nu)+d_{test}(1-2\nu)\right)}{\pi t_{clad}(t_{clad}-d_{test})k_6}$$

$$d_2 = F(t)\frac{E_{clad}\left[\sqrt{2}\left(2R_{test}({d_{test}}^2(\nu-1)+(\nu+1)k_7)-d_{test}({d_{test}}^2-k_7)\right)k_2-\ldots\right.}{\left.4R_{test}\left({d_{test}}^2(\nu-1)-k_7(\nu+1)\right)-d_{test}\left({d_{test}}^2(2\nu-1)-(2\nu+1)k_7\right)\right]}{\pi t_{clad}(d_{test}-t_{clad})k_6}$$

, with auxiliary variables:

$$k_1 = \sqrt{\frac{2R_{test}+d_{test}}{R_{test}+t_{clad}}}$$

$$k_2 = \sqrt{\frac{2R_{test}+d_{test}}{R_{test}}}$$

$$k_3 = d_{test}+2t_{clad}$$

$$k_4 = {2t_{clad}}^2-2d_{test}t_{clad}$$

$$k_5 = \left(4E_{clad}t_{clad}(d_{test}-t_{clad})+E_{pre}(d_{test}-2t_{clad})^2\right)\left(2\sqrt{2}\nu(R_{test}+t_{clad})k_1+4R_{test}+k_3\right)$$

$$k_6 = \left(4E_{clad}t_{clad}(d_{test}-t_{clad})+E_{pre}(d_{test}-2t_{clad})^2\right)\left(2\sqrt{2}R_{test}\nu k_2+4R_{test}+d_{test}\right)$$

$$k_7 = 2d_{test}t_{clad}-{2t_{clad}}^2$$

Based on the results shown in (Fig. IV.37) and (Fig. IV.38); it is concluded that the analytical model is accurate and suitable for calculating the magnitude of stresses within a coated hourglass specimen.

IV.3 Mechanical properties of coated material in fatigue tested specimens.

IV.3.1 Proposal of a Methodology to Determine the Fatigue Life of Specimens Coated by the Laser Cladding Process.

A methodology is proposed to calculate the fatigue life of specimens coated by the Laser Cladding process, taking into account the texture of their microstructure.

IV.3.1.1 Background

It has been documented in (Section IV.2.2.1), that the failure process of a material under fatigue loading has three well-defined stages:

- Nucleation of microcracks within the material.
- Microcracks propagation phase (initial growth by shear stress and later by normal stress).
- Coalescence of microcracks in macrocracks until material failure due to tensile test behaviour.

A detailed reading of the stages of fatigue life previously mentioned allows for some interpretations:

1. The three phases of fatigue failure are highly dependent on the crystalline microstructure. Therefore, the proposed approach to modelling the fatigue life behaviour of the material must take this into account. It is not valid to apply the assumption of a homogeneous solid without any substructure. If the textural characteristics of the material are not taken into account and "nominal" type criterion values are used, significant errors are possible in the determination of the fatigue stress within the material in the case of coated specimens.
2. The need to consider the microstructure within the material in some way "forces" the internal stresses in the material to interact in different directions. Subsequently, it will be shown that the directional variation is related to the crystallographic orientation within the material itself (in the case of a multicrystalline solid). Therefore, it will be necessary to use and adapt a criterion that takes into account the crystallographic orientation of the material (in our case a metallic alloy).
3. The design of coated specimens in the previous section of this document is for use in uniaxial fatigue testing. The test setup for determining fatigue mechanical properties must take into account and provide useful information on the crystallographic orientation of the specimen grains using the uniaxial test setup.

Taking into account the 3 previous numerals, it is proposed:

- To use a multiaxial fatigue life criterion as a basis for determining the fatigue life of a coated material: depending on the criteria, both the crystallographic

orientation of the material's grains and the behaviour at the non-homogeneous microstructure level are taken into account.

- The multiaxial criterion must be one related to the so-called "Critical Plane Methods". The main hypothesis in Critical Plane Methods" is that the behaviour of a material under fatigue at a point P whose stress tensor is $\boldsymbol{\Sigma}(t)$, is defined by the most solicited plane (Π), which passes through that point P (Avilés, 2012). It is possible to associate this plane Π with a specific crystalline system and take into account the texture of the material. Generally, these criteria are expressed mathematically as a linear combination of values related to a normal stress and a shear stress in the plane Π.
- The proposed multiaxial criterion is the Dang Van criterion (Carpinteri et al., 2003), which is expressed as (Eq. IV.30):

$$\max\left[\left|\tau_{nd}(t)\right| + \alpha \cdot \sigma_H(t)\right] \leq \beta \qquad \textit{Eq. IV.30}$$

The reason for using this criterion is that it is based on an approximation in two different size scales for the stresses within a material (one at the microscopic level and the other at the macroscopic level). In this criterion, both types of stresses are related (micro-macro), through the Lin-Taylor hypothesis (Deng et al., 2014). At detailed level, in a metallic material, PSBs (microscopic) will be responsible for crack initiation (by shear stress), and their growth will be related to hydrostatic stress (by normal stress). The criterion at microscale level (in the Π-plane), can be expressed by (Eq. IV.31):

$$\tau(t)_{micro} + \alpha\sigma_{H\_micro}(t) \leq \beta_{micro} \qquad \textit{Eq. IV.31}$$

The relationship with the macroscopic stress level (test specimen), is given by the tensor relationship (Eq. IV.32):

$$\boldsymbol{\sigma}(t)_{micro} = \boldsymbol{\Sigma}(t) + dev\boldsymbol{\rho}_s \qquad \textit{Eq. IV.32}$$

The tensor $\boldsymbol{\rho}_s$ in the proportional load regime (when the principal stresses remains proportional to each other all the time: $\sigma_2(t)/\sigma_1(t) = \lambda_1, \sigma_3(t)/\sigma_1(t) = \lambda_2$ (Avilés, 2012)), can be determined from the average of the extreme values of the macroscopic stress at the instants t_1 and t_2 (that is, the times when the two calculated values of the tensor $\boldsymbol{\Sigma}(t)$ are at their extreme ends), (Eq. IV.33):

$$\boldsymbol{\rho}_s = -\frac{1}{2}\left(\boldsymbol{\Sigma}(t_1) + \boldsymbol{\Sigma}(t_2)\right) \qquad \textit{Eq. IV.33}$$

With (Eq. IV.33) it is possible to justify the use of the stress ratios (R), which have been proposed in (Table IV.5), since in a uniaxial test specimen for the cases of pulsating and alternate fatigue limit stress ($R = 0,\ R = -1$), the constants α and β of the (Eq. IV.30) can be deduced, and will be calculated as (Eq. IV.34) and (Eq. IV.35):

$$\alpha = \frac{3(\sigma_0 - \sigma_{-1})}{2(\sigma_{-1} - 2\sigma_0)} \qquad \textit{Eq. IV.34}$$

$$\beta = \frac{\sigma_{-1} \cdot \sigma_0}{2(2\sigma_0 - \sigma_{-1})} \qquad \textit{Eq. IV.35}$$

For details of the deduction for $\boldsymbol{\rho}_s$, α and β see (Kouhia, 2019).

The criterion of Dang Van (Eq. IV.30), consists of two parts: $|\tau_{nd}(t)|$ that refers to the shear stress in the plane Π under study, and the normal stress $\sigma_H(t)$.

The hydrostatic stress is defined as the normal stress acting on any octahedral plane (Eq. IV.36):

$$\sigma_H = \frac{1}{3}\left(\sigma_1 + \sigma_2 + \sigma_3\right) = \frac{1}{3}\left(\Sigma'_{xx} + \Sigma'_{yy} + \Sigma'_{zz}\right) \qquad \textit{Eq. IV.36}$$

The (Eq. IV.36) is defined for a coordinate system on axes that coincide with the principal stresses (Fig. IV.39).

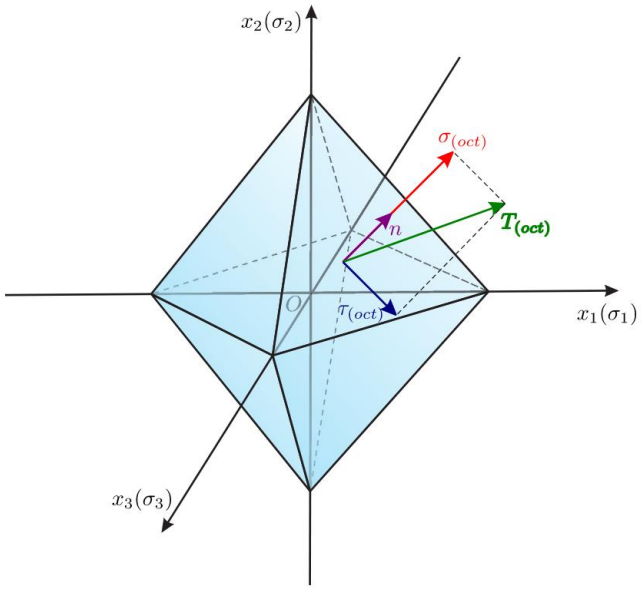

Figure IV.39. A plane whose normal vector makes equal angles to the axes of the principal stresses is called octahedral plane. There are eight such planes that form a regular octahedron. The normal and shear stresses that act on these planes are called octahedral stresses (RockMechs, 2020).

As the hydrostatic stress is an invariant (Eq. IV.37), the transformation to another coordinate system allows to use it independently of the orientation of the coordinate system used (Avilés, 2012).

$$\sigma_H = \frac{1}{3} tr(\boldsymbol{\Sigma}) = \frac{1}{3} tr(I_1) \qquad \textit{Eq. IV.37}$$

The shear stress in the Π-plane will be related to the microstructure of the material, specifically to its crystallographic orientation. Therefore, a brief review of the crystalline systems present in the INCO718 alloy will be necessary.

- The main crystallographic phase of this alloy is the Gamma phase (γ). Being essentially a compound of nickel with other chemical elements in substitution (Chapter II.2.2.2). The alloy has the same crystal structure as pure, face-centred cubic (FCC) nickel, and a mesh parameter a = 0.3608 nm. The proportion of this phase varies between more than 98% (by weight), for a material obtained under special solidification conditions, to around 80% after some special heat treatments (Pautrat, 2013).
- For the study of the microstructure of the INCO718 alloy by means of SEM through the EBSD technique, only the gamma phase is taken as the basis of the

crystallographic orientation of all the material (γ). The way to obtain the crystallographic orientation of the material is the study of diffracted electrons via Kikuchi patterns (Boehlert et al., 2010; Wang and Chou, 2017).

- For a nickel-based alloy, sliding in a crystal (which results in crack nucleation and thus the initiation of fatigue failure), often occurs in high atomic density planes in compact directions. The four octahedral planes corresponding to the high-density planes for an FCC-type crystal (such as in the matrix phase of INCO178) are shown in (Fig. IV.40). The four octahedral slip planes have three primary slip directions (with easy slip), resulting in 12 independent primary slip systems <110> {111}. In addition, in the four octahedral slip planes there are also three secondary slip directions resulting in another 12 independent secondary slip systems <112> {111}. Thus, there are 12 primary and 12 secondary slip systems associated with the four octahedral planes.

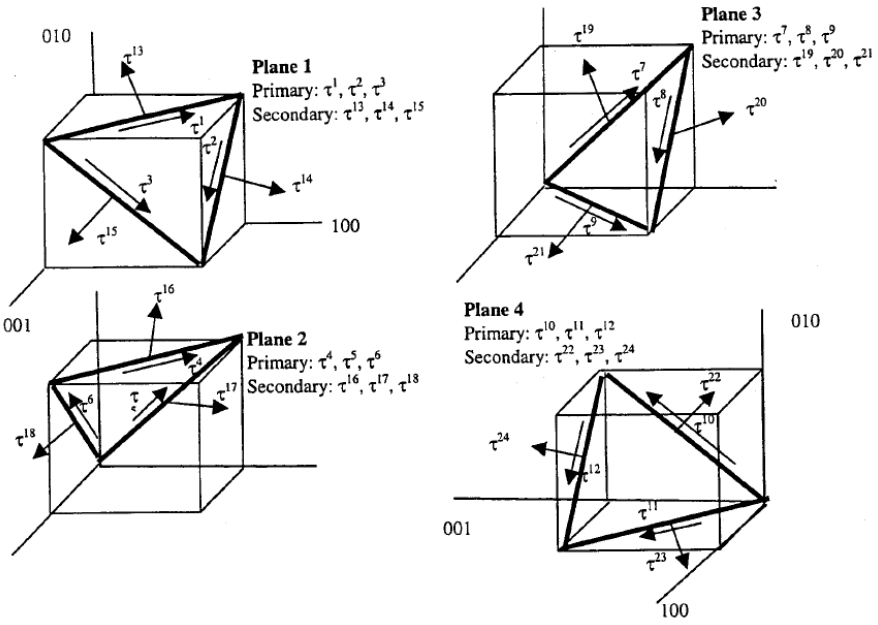

Figure IV.40. Primary close-packed and secondary non-close packed slip directions on the octahedral planes for a FCC crystal (Arakere and Swanson, 2002).

In addition, there are three cubic-type sliding planes that have each two sliding additional directions, resulting in six independent cubic-type sliding systems <110> {100}, as shown in (Fig. IV.41).

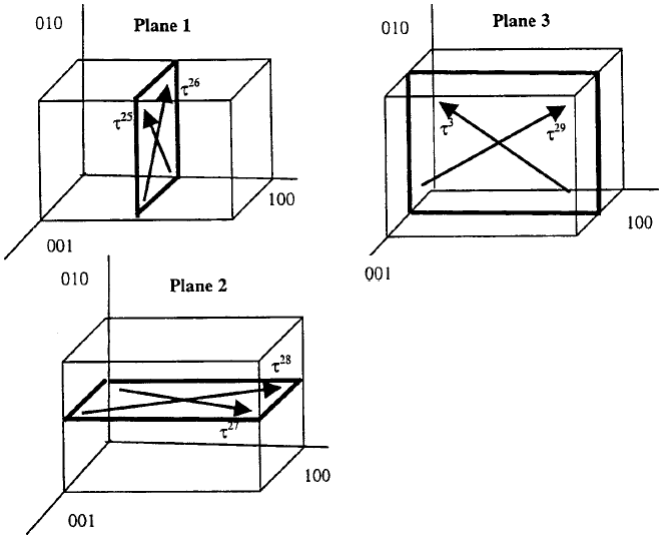

Figure IV.41. Cube slip planes and slip directions for a FCC crystal (Arakere and Swanson, 2002).

In nickel-based alloys (Arakere and Swanson, 2002) mentions that of all the previous slip mechanisms (both primary and secondary for octahedral and cubic planes), the activation tendency of slip systems at room temperature is only for the <110> {111} combination. Therefore, this investigation will focus on the sliding systems shown in (Table IV.10).

Table IV.10: Preferential planes and sliding directions for Nickel-based FCC alloys. The index "n" will indicate the direction of the vector normal to the octahedral plane, and the index "d" the direction of movement in that plane.

Slip system directions (d)			Octaedral planes (n)
$[1\,\bar{1}\,0]$	$[1\,0\,\bar{1}]$	$[0\,\bar{1}\,1]$	$(1\,1\,1)$
$[\bar{1}\,0\,1]$	$[\bar{1}\,1\,0]$	$[0\,1\,\bar{1}]$	$(1\,\bar{1}\,1)$
$[1\,1\,0]$	$[\bar{1}\,\bar{1}\,0]$	$[0\,1\,1]$	$(1\,1\,\bar{1})$
$[0\,\bar{1}\,\bar{1}]$	$[1\,0\,1]$	$[\bar{1}\,0\,\bar{1}]$	$(\bar{1}\,1\,1)$

From the analysis of (Table IV.10), it can be deduced that depending on the orientation of a specific FCC cell, there are $(n=4)\cdot(d=12)=48$ possible combinations of sliding initiation system for the planes of a crystal.

- Choosing the appropriate sliding system and applying it to solve shear stress in the plane Π will be determined by Schmid's Law which postulates that: when “a crystal” is subjected to a load, the sliding within it begins when a critical value is reached often called “critical resolved shear stress”. The sliding in the crystal will begin in the first system which plane-direction combination reaches the critical

shear stress value regardless of the uniaxial tensile stress or other type of normal stress in the plane of the lattice plane (Arminjon, 1991). The generalized Schmid's law to resolve the shear stress (τ_{nd}) in a material subjected to uniaxial stress (as in the design of coated specimens that has been proposed in this research), is shown in (Eq. IV.38). The use of the prime symbol (‘), in the macroscopic stress components (Σ) will be explained later.

$$\pm\tau_{nd} = \ell_{nx}\ell_{dx}\Sigma'_{xx} + \ell_{ny}\ell_{dy}\Sigma'_{yy} + \ell_{nz}\ell_{dz}\Sigma'_{zz} + \ldots \\ (\ell_{ny}\ell_{dx} + \ell_{nx}\ell_{dy})\Sigma'_{xy} + (\ell_{nz}\ell_{dy} + \ell_{ny}\ell_{dz})\Sigma'_{yz} + (\ell_{nx}\ell_{dz} + \ell_{nz}\ell_{dx})\Sigma'_{xz} \qquad \textit{Eq. IV.38}$$

Where (Eq. IV.39):

$$\ell_{\left[\begin{matrix}plane(n)\vee \\ direction(d)\end{matrix}\ \begin{matrix}respect\ to \\ [x\vee y\vee z]\ axis \\ sample\ ref.\ system\end{matrix}\right]} = \\ \frac{\left(h_{[n\vee d]}\right)\left(h_{[x\vee y\vee z]}\right)+\left(k_{[n\vee d]}\right)\left(k_{[x\vee y\vee z]}\right)+\left(l_{[n\vee d]}\right)\left(l_{[x\vee y\vee z]}\right)}{\sqrt{\left(h_{[n\vee d]}{}^2+k_{[n\vee d]}{}^2+l_{[n\vee d]}{}^2\right)\left(h_{[x\vee y\vee z]}{}^2+k_{[x\vee y\vee z]}{}^2+l_{[x\vee y\vee z]}{}^2\right)}} \qquad \textit{Eq. IV.39}$$

For example, in the case of a tensile stress in the direction $x=[1\,0\,0]$ on the plane $n=(11\bar{1})$ and in the direction of sliding $d=[101]$, the combination of direction cosines ℓ_{dx} and ℓ_{nx} will be:

$$\forall\sigma=[100],\begin{cases}h_x=1\\k_x=0\\l_x=0\end{cases}$$

$$\forall n=(11\bar{1}),\begin{cases}h_n=1\\k_n=1\\l_n=-1\end{cases}$$

$$\forall d=[101],\begin{cases}h_d=1\\k_d=0\\l_d=1\end{cases}$$

$$\ell_{dx}=\frac{1\cdot1+0\cdot0+1\cdot0}{\sqrt{(1^2+0^2+1^2)(1^2+0^2+0^2)}}=\frac{1}{\sqrt{2}}$$

$$\ell_{nx}=\frac{1\cdot1+1\cdot0+(-1\cdot0)}{\sqrt{(1^2+1^2+(-1)^2)(1^2+0^2+0^2)}}=\frac{1}{\sqrt{3}}$$

Based on (Eq. IV.38) it is possible to calculate the resolved shear stress in any direction for all possible combinations of direction-plane from (Table IV.10).

Regarding the microstructure in a polycrystalline material, it can be assumed that when a crystal is untextured, it can be treated as an isotropic material. A material that has been deposited by the Laser Cladding process is not isotropic, as it has a texture depending on the process parameters, although it normally does not have a complete orientation. In polycrystals, it is not possible to activate a single sliding direction, as this is incompatible with the different grain orientation directions. When a crystal is surrounded by other crystals with different crystallographic orientation, its deformation "may" not start with one of the primary systems, but as documented (Boehlert et al., 2010), for the INCO718 alloy the tendency for activation of the primary slip systems is maintained as described in (Table IV.10).

To solve for the shear stress to be applied according to the fatigue criterion of (Eq. IV.30) (for the case of a coated specimen subjected to uniaxial tension), it is necessary to transform the macroscopic stress of the specimens to the crystal frame of reference. The (Eq. IV.38) is given for the local frame of reference of an FCC crystal cell as shown in the octahedral plane of (Fig. IV.42).

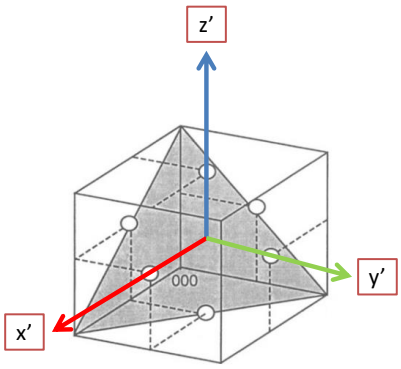

Figure IV.42. Local frame of reference of a FCC cubic crystalline cell system. Plane (111) is shown shaded for reference.

The frame of reference associated with the coated specimen is shown in (Fig. IV.43).

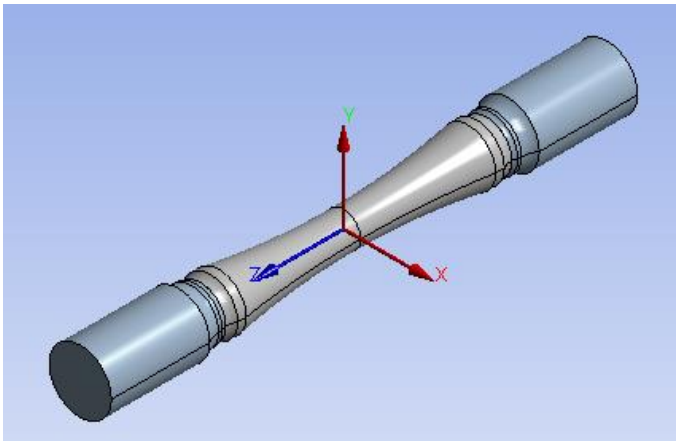

Figure IV.43. Reference frame for the coated sample. The direction of the axial stress is on the z-axis, on the axis of symmetry of the specimen.

The stress tensor inside the coated specimen (macroscopic), for a time variable load with behaviour as sinusoidal function in proportional load regime for stress ratios $R=-1$ and $R=0$ is given by (Eq. IV.40):

$$\boldsymbol{\Sigma}(t)_R=\begin{bmatrix}0&0&0\\0&0&0\\0&0&\Sigma_{test}\end{bmatrix}\left[-(2R+1)\cos\left((2R+1)\frac{2\pi}{T}t+\frac{\pi R}{2}\right)+R+1\right] \qquad \textit{Eq. IV.40}$$

$$\forall\ [R=-1, R=0]$$

Where $\Sigma_{test}=\Sigma_{zz}$ is obtained from (Eq. IV.41):

$$\Sigma_{test}(x_1)=\Sigma_{zz}(x_1)=\begin{cases}c_1{x_1}^2+c_2, \forall\ \ 0\le x_1\le (d_{test}/2-t_{clad})\\ d_1{x_1}^2+d_2, \forall\ \ (d_{test}/2-t_{clad})<x_1\le (d_{test}/2)\end{cases} \qquad \textit{Eq. IV.41}$$

The (Eq. IV.40) will give a different stress tensor depending on whether is used the stress ratio R = -1 or R = 0.

The coordinates $[x_1,\sigma(x_1)]$ of (Eq. IV.41) are referred to the local frame of reference of the specimen in (Fig. IV.35). The (Eq. IV.41) uses the coefficients $[c_1,c_2,d_1,d_2]$ of (Table IV.9), which are dependent on the geometry of the coated specimen, the material properties of both the coating and the substrate, and the load $F=f(t)$.

As the variable t is already included in the tensor equation (Eq. IV.40), the value of $F=f(t)$ will no longer be considered fluctuating over time and a fixed value will be assigned to it, which will be substituted in the coefficients of (Table IV.9). The value for $F=f(t)$ that would allow to load reach at $t\to\infty$ is equivalent to the value of the amplitude of the nominal load obtained for the limit of fatigue for infinite life (endurance

limit) [σ_{0a}, σ_{-1a}] of the coated specimen. $F = f(t) = F_a$ is calculated from (Eq. 72), according to the “stress ratio” being used.

The value of $F = f(t)$ that the load could reach at $t \to \infty$, is equivalent to the value of the nominal load amplitude obtained for the limit on infinite life at fatigue (endurance limit, [σ_{0a}, σ_{-1a}]); of the coated specimen. Therefore, $F = f(t) = F_a$ is calculated from (Eq. IV.42), according to the "stress ratio" used.

$$F(\infty) = F_a = \begin{cases} (\sigma_{0a}) A_{test} \forall R = 0 \\ (\sigma_{-1a}) A_{test} \forall R = -1 \end{cases} \qquad \textit{Eq. IV.42}$$

Substituting the previous F_a according to the fatigue limit corresponding to the infinite life for pulsating and alternating stress in (Table IV.9), allows the calculation for each crystal (according to its radial coordinate x_1), of the Dang Van criterion.

A preliminary step is necessary before evaluating the previous mentioned criterion for each crystal. The tensor defined from the value of the uniaxial load F_a (in the frame of reference of the specimen), must be transformed to the crystallographic orientation system of each grain.

The change of system coordinates from the frame of reference system of the coated specimen (Fig. IV.43) to that of the crystal (Fig. IV.42) will be carried out by means of a director cosine transformation matrix (DCM). The relationship between both coordinate systems is shown in (Table IV.11):

Table IV.11: Relationship variables between the frames of reference of the crystal with respect to the frame of reference of the coated specimen.

DCM=		Sample reference system		
		x	y	z
Crystal reference system	x'	A_{11}	A_{12}	A_{13}
	y'	A_{21}	A_{22}	A_{23}
	z'	A_{31}	A_{32}	A_{33}

The frame of reference transformation matrix will be defined as (Eq. IV.43), and its graphical interpretation is shown in (Fig. IV.44).

$$\mathbf{DCM} = \begin{bmatrix} \cos(\theta_{x'x}) = A_{11} & \cos(\theta_{x'y}) = A_{12} & \cos(\theta_{x'z}) = A_{13} \\ \cos(\theta_{x'y}) = A_{21} & \cos(\theta_{y'y}) = A_{22} & \cos(\theta_{y'z}) = A_{23} \\ \cos(\theta_{x'z}) = A_{31} & \cos(\theta_{y'z}) = A_{32} & \cos(\theta_{z'z}) = A_{33} \end{bmatrix} \qquad \textit{Eq. IV.43}$$

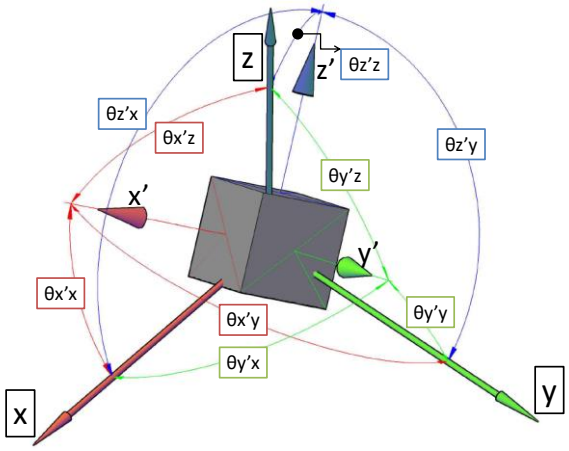

Figure IV.44. Graphical interpretation of the DCM coefficients of the (Eq. IV.43).

Therefore, the equivalent tensor in the uniaxial stress to the crystal frame of reference will be (Eq. IV.44):

$$\boldsymbol{\Sigma}'(t) = \mathbf{DCM} \cdot \boldsymbol{\Sigma}(t)_R \cdot \mathbf{DCM}^{\mathrm{T}} = \begin{bmatrix} \Sigma'_{xx} & \Sigma'_{xy} & \Sigma'_{xz} \\ \Sigma'_{xy} & \Sigma'_{yy} & \Sigma'_{yz} \\ \Sigma'_{xz} & \Sigma'_{yz} & \Sigma'_{zz} \end{bmatrix} \qquad \textit{Eq. IV.44}$$

IV.3.2 Procedure to Evaluate the Dang Van Criterion for FCC Crystals of INCO718 alloy crystals in a Specimen Coated by the Laser Cladding Process.

The procedure for evaluating the Dang Van criterion on each crystal for the cross-section of interest (middle section), in coated specimens will be as follows:

1. Determine the fatigue life limit of two sets of coated specimens of similar dimensions for stress ratios of R = -1 and R = 0.
2. Calculate the strength F_a according to (Eq. IV.42) for the stress ratios that have been previous mentioned.
3. Determine for each grain under study the tensor in the crystallographic coordinate system according to its position x_1 within the coated specimen for time t where the macroscopic uniaxial stresses reach their extreme values, (Eq. IV.40) and (Eq. IV.41).

4. Obtain the maximum shear stress value with (Eq. IV.38) using all the possible plane-system combinations of (Table IV.12) for each grain under study.
5. Calculate the hydrostatic stress according to (Eq. IV.66) for each grain of material corresponding to that of step (4).
6. Determine the constants of the Dang Van criterion with (Eq. IV.34) and (Eq. IV.35).
7. Apply the Dang Van criterion to each crystal of the material according to (Eq. IV.30).

Table IV.12: Plane-sliding system combinations for the resolution of the maximum shear stress for an FCC crystal of INCO718 alloy.

Combination plane-system	Octahedral Plane (n)	Slip system direction (d)	Combination plane-system	Octahedral Plane (n)	Slip system direction (d)
1	(1 1 1)	[1 -1 0]	25	(-1 -1 -1)	[1 -1 0]
2	(1 1 1)	[1 0 -1]	26	(-1 -1 -1)	[1 0 -1]
3	(1 1 1)	[0 -1 1]	27	(-1 -1 -1)	[0 -1 1]
4	(1 1 1)	[-1 0 1]	28	(-1 -1 -1)	[-1 0 1]
5	(1 1 1)	[-1 1 0]	29	(-1 -1 -1)	[-1 1 0]
6	(1 1 1)	[0 1 -1]	30	(-1 -1 -1)	[0 1 -1]
7	(1 -1 1)	[1 1 0]	31	(-1 1 -1)	[1 1 0]
8	(1 -1 1)	[-1 -1 0]	32	(-1 1 -1)	[-1 -1 0]
9	(1 -1 1)	[0 1 1]	33	(-1 1 -1)	[0 1 1]
10	(1 -1 1)	[0 -1 -1]	34	(-1 1 -1)	[0 -1 -1]
11	(1 -1 1)	[1 0 -1]	35	(-1 1 -1)	[1 0 -1]
12	(1 -1 1)	[-1 0 1]	36	(-1 1 -1)	[-1 0 1]
13	(1 1 -1)	[1 -1 0]	37	(-1 -1 1)	[1 -1 0]
14	(1 1 -1)	[-1 1 0]	38	(-1 -1 1)	[-1 1 0]
15	(1 1 -1)	[1 0 1]	39	(-1 -1 1)	[1 0 1]
16	(1 1 -1)	[-1 0 -1]	40	(-1 -1 1)	[-1 0 -1]
17	(1 1 -1)	[0 -1 -1]	41	(-1 -1 1)	[0 -1 -1]
18	(1 1 -1)	[0 1 1]	42	(-1 -1 1)	[0 1 1]
19	(-1 1 0)	[1 1 0]	43	(1 -1 -1)	[1 1 0]
20	(-1 1 0)	[-1 -1 0]	44	(1 -1 -1)	[-1 -1 0]

21	(-1	1	0)	[1	0	1]
22	(-1	1	0)	[-1	0	-1]
23	(-1	1	0)	[0	1	-1]
24	(-1	1	0)	[0	-1	1]
45	(1	-1	-1)	[1	0	1]
46	(1	-1	-1)	[-1	0	-1]
47	(1	-1	-1)	[0	1	-1]
48	(1	-1	-1)	[0	-1	1]

IV.3.3 Experimental Tests.

Tests were carried out on several series of specimens under constant amplitude axial force regime in a Vibrophore Amsler 422/464 series resonance machine. The tests were performed at room temperature, using stress ratios of R = -1 and R = 0.1. The resonance frequencies were approximately 125 Hz, with a sinusoidal waveform function. The tests were carried out under the conditions indicated in (ASTM Subcommittee E08.02, 2020).

The numbers of tests for each cladding strategy that was selected for the fatigue specimens plus those for the base material (Table IV.4), were 20 specimens. Each set of tests was carried out at different stress levels in order to determine the endurance limits for infinite life (endurance limit for $(R=-1,\sigma_{-1})$ and $(R=0.1,\sigma_{0.1})$). The use of the stress ratio of R = 0.1 instead of R = 0 is due to the technical difficulty of maintaining a zero-order load in the valley of the sinusoidal cycle (F_{min}) for the specimens. The transformation by means of linear interpolation equation knowing two values of stress ratio and the respective limits of endurance limit for $(R=-1,\sigma_{-1})$ and $(R=0.1,\sigma_{0.1})$, are calculated by (Eq. IV.45):

$$\sigma_0 = \frac{11\sigma_{-1}\sigma_{0.1}}{9\sigma_{-1}+2\sigma_{0.1}} \qquad \textit{Eq. IV.45}$$

The graph with the test results is shown in (Fig. IV.45).

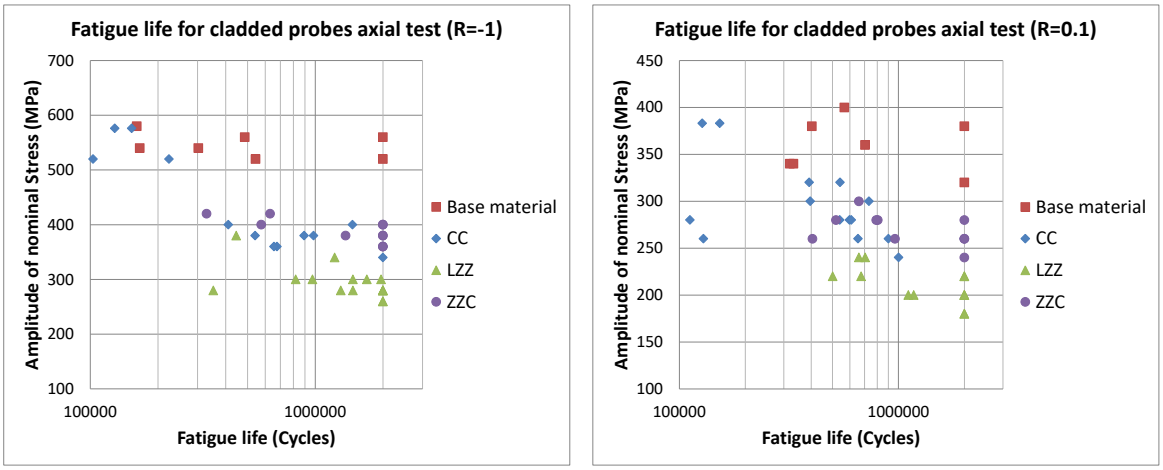

Figure IV.45. S-N graph with the results of the fatigue tests on coated specimens for constant amplitude axial load regime with stress ratios of R = 0.1 and R = -1. The tests were carried out at room temperature and are considered as infinite life $2*10^6$ *cycles.*

In the statistical treatment of the data obtained from the fatigue test was used the method of maximum likelihood (Martín-Meizoso et al., 2009), choosing as the nucleus for the fitting a Weibull cumulative distribution function, because it is considered the most appropriate when the number of trials is limited (Weibull, 1961). The results for the endurance limits (infinite life σ_{-1} and $\sigma_{0.1}$) are shown in (Table IV.13).

Table IV.13: Endurance limits for infinite life for the CC, LZZ and ZZC strategies in specimens coated by the laser cladding process. Results also include specimens made only of base material. The value of σ_0 *is obtained as a quantity derived from* σ_{-1} *and* $\sigma_{0.1}$ *(Eq. IV.45).*

	Endurance Limit (Stress Amplitude)					
Strategy	σ_{-1} (MPa)		$\sigma_{0.1}$ (MPa)		σ_0 (MPa), derived from (Eq. IV.45).	
Base material	550.67	+/- 20.67	338.36	+/- 3.94	363.87	+/- 4.07
CC	361.13	+/- 2.32	258.22	+/- 10.34	272.33	+/- 9.41
LZZ	280.67	+/- 2.33	219.74	+/- 11.89	228.77	+/- 10.55
ZZC	404.40	+/- 28.88	271.41	+/- 14.25	288.67	+/- 13.46

IV.3.3.1 Microscopic Analysis by SEM Using EBSD Technique to determine the texture for Strategies Used in Coated Specimens.

For each strategy that was used in the manufacture of coated specimens and for specimens made only of base material, samples were prepared to be analysed by means of the Electron Backscatter Diffraction (EBSD) technique. The samples consist of cylinder sections that were manufactured under the same process parameters as the coated specimens, in such a way that the microstructure generated is the same. All samples are circular cross sections of diameter $d_\alpha = d_{test}$ (Fig. IV.35).

The cross-sectional surface of each circular specimen was polished according to (ASTM Subcommittee E04.01, 2015). The analysis was carried out on a Schottky-type field emission scanning electron microscope (JEOL JSM-7000F) equipped with an EBSD Nordlys II HKL premium detector for crystallographic information in the Sgiker facilities

(EHU, Leioa). The acceleration voltage for the electron source was 20 KV, with data being collected on a regular grid with a resolution of 10 μm.

The images with the texture of the grains for each cladding strategy plus that of the base material are shown in (Fig. IV.46).

Base material

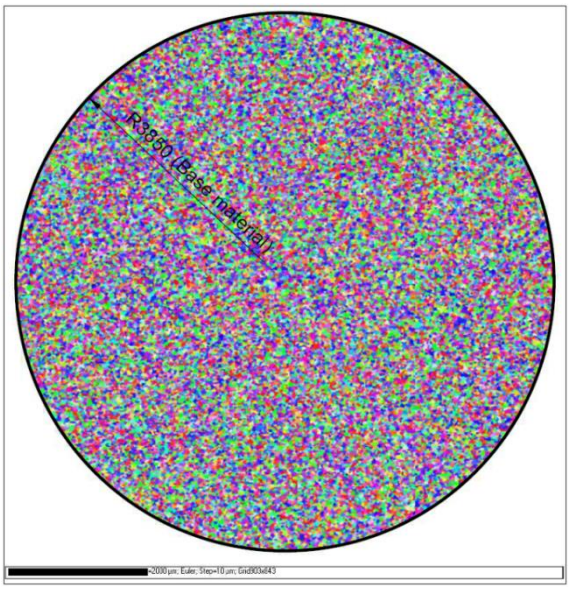

CC

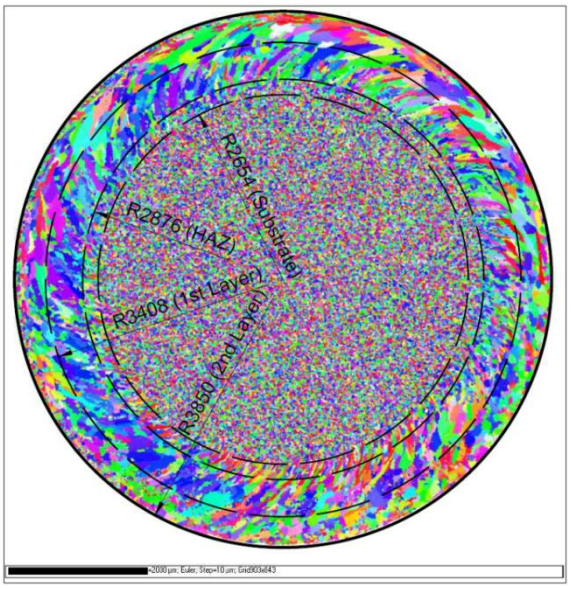

LZ

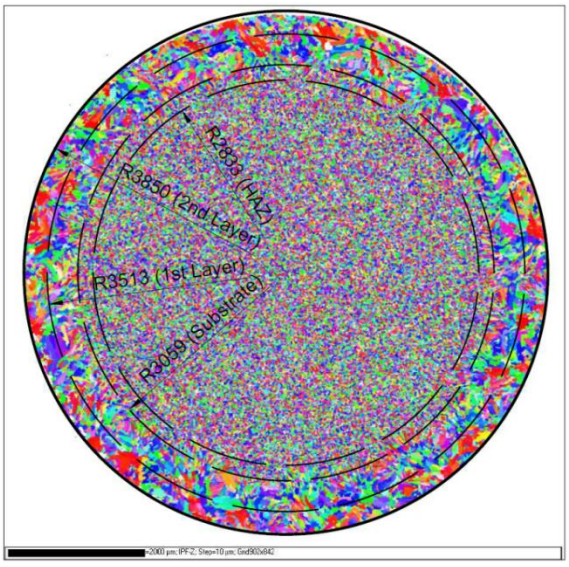

LZZ

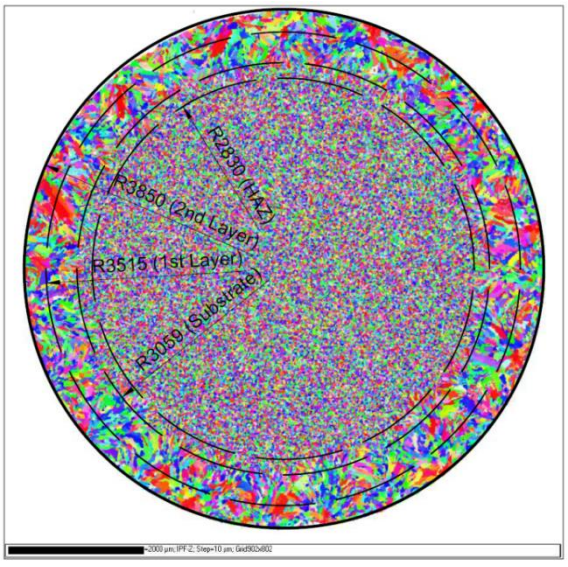

ZC

ZZC

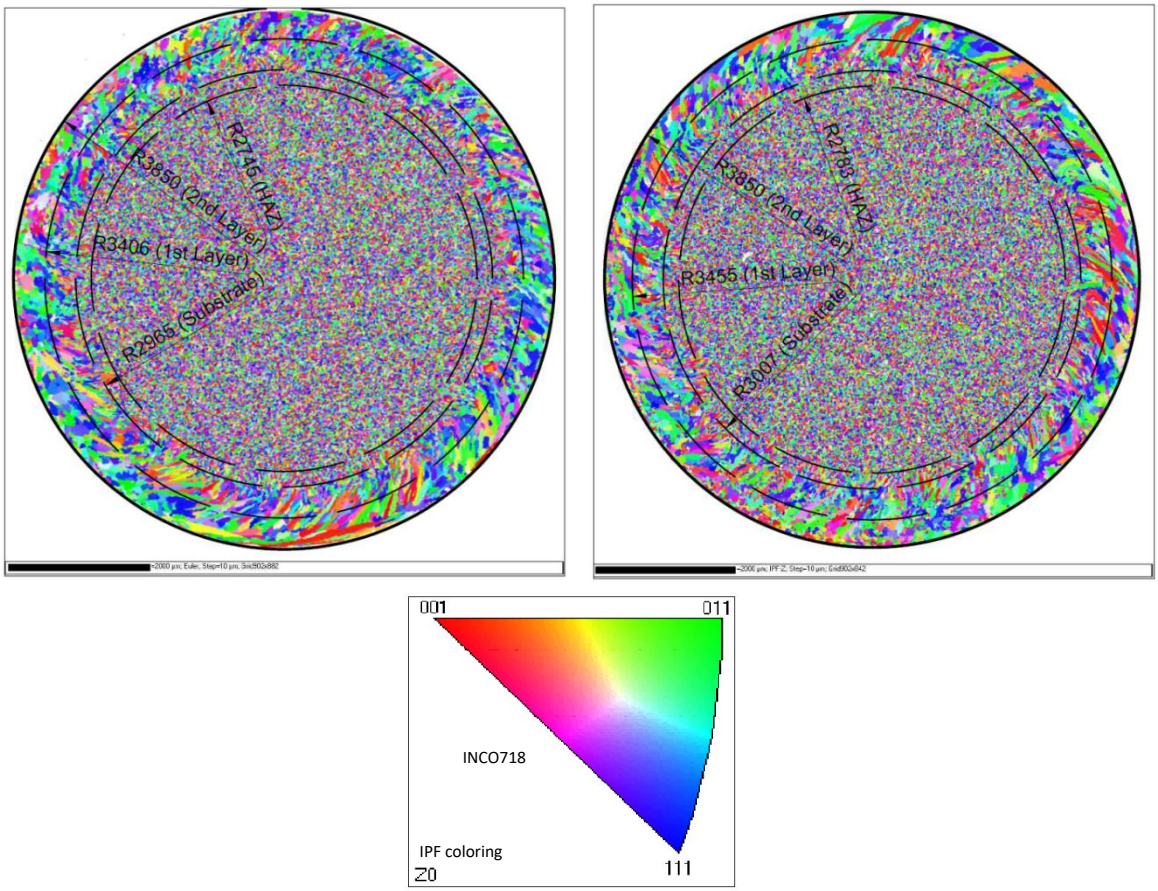

Figure IV.46. Texture of grains in the cross-section for samples prepared with the different strategies in coated specimens. The sample in the cross section for the base material is also included. In the orientation reference triangle of the stereographic projection, the direction [001] coincides with the Z axis of the frame of reference in the specimen (Fig. IV.43).

The microstructures in (Fig. IV.46) show a significant difference depending on the deposition strategy used. A trend of directionality of the texture is observed depending on the predominant strategy that was used. On the one, the CC texture shows a tendency of crystal growth from the substrate similar to that of a helix. On the other hand, the longitudinal strategies (LZ and LZZ) show solidification patterns similar to cross-sectional sections of the melt pool in (Fig. IV.15, right). The mixed deposition strategies (ZC and ZZC), resemble a combination of CC textures with LZ and LZZ.

The pole figures of the different strategies are shown in (Fig. IV.47). For each deposition strategy (plus the base material), there will be three pole figures showing information from three sets of zones: internal (substrate), external (coating), and complete section (substrate + coating).

There is a great variety of sizes and shapes of grains in the coating area. On the other hand, in the substrate area all the grains are small (compared to the majority of coating grains), equiaxed and with an apparently random distribution in the crystallographic orientation.

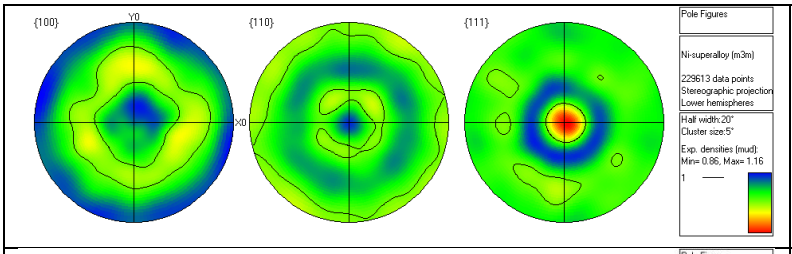	Complete transversal section	Base Material
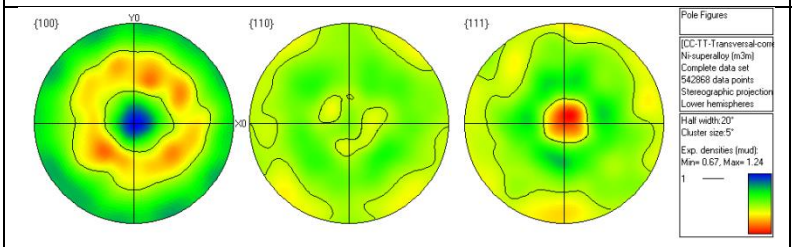	Complete transversal section	CC
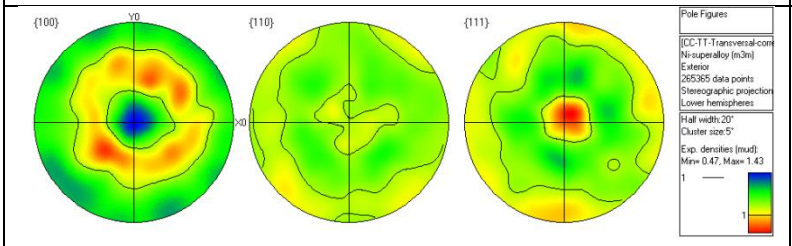	Exterior transversal section	
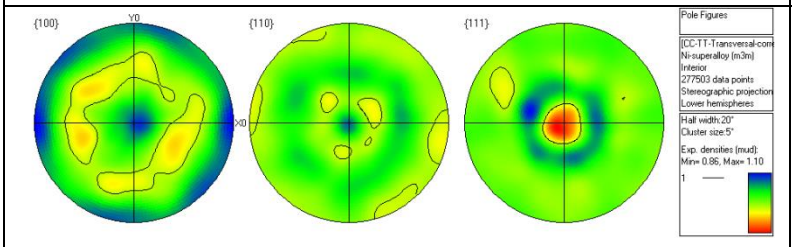	Interior transversal section	
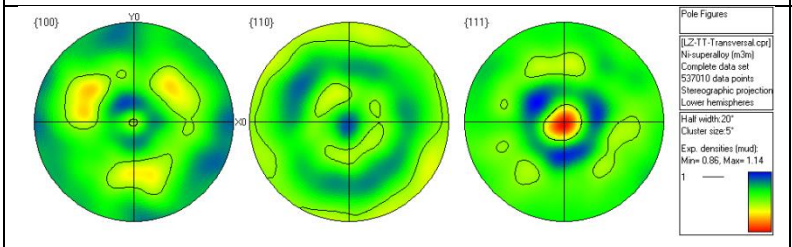	Complete transversal section	LZ
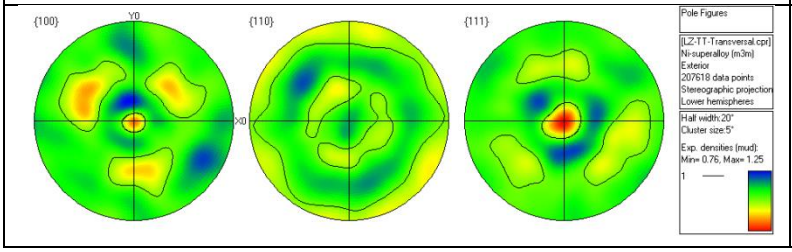	Exterior transversal section	

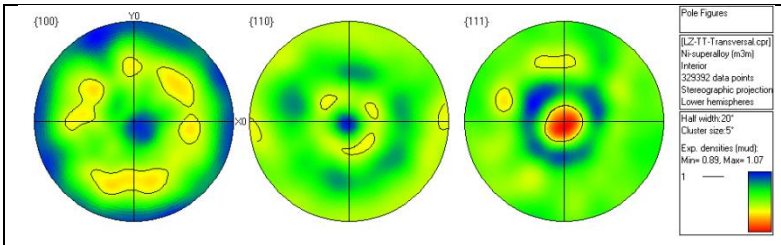	Interior transversal section	
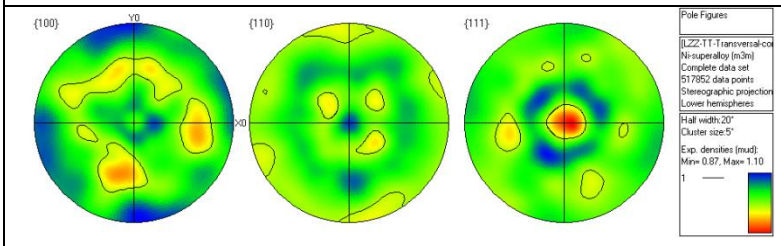	Complete transversal section	LZZ
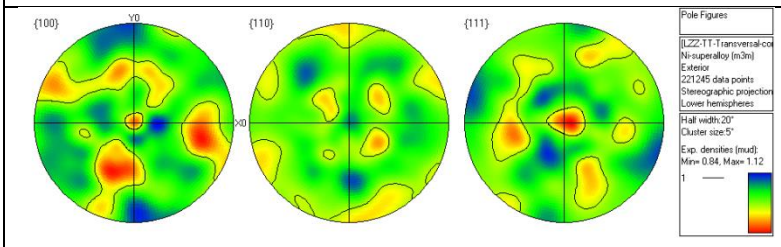	Exterior transversal section	
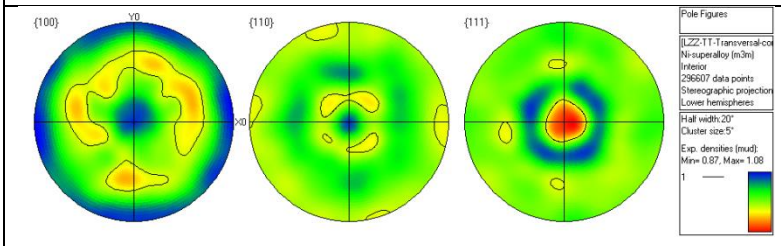	Interior transversal section	
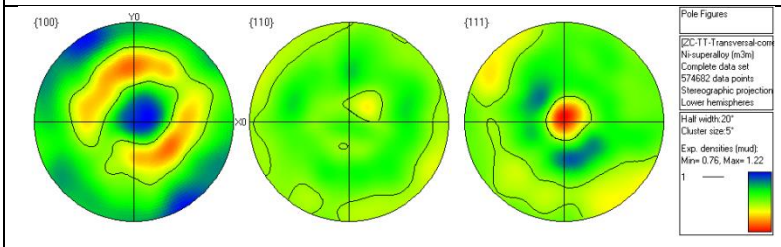	Complete transversal section	ZC
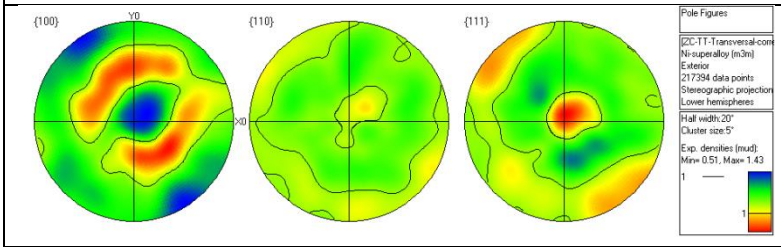	Exterior transversal section	
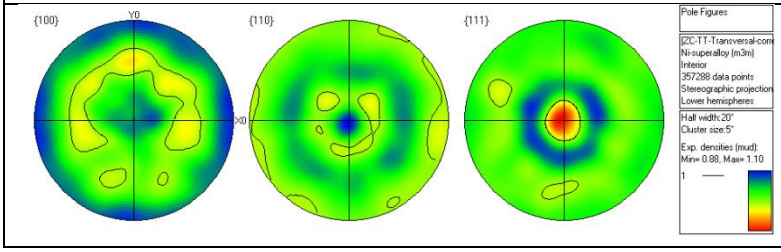	Interior transversal section	

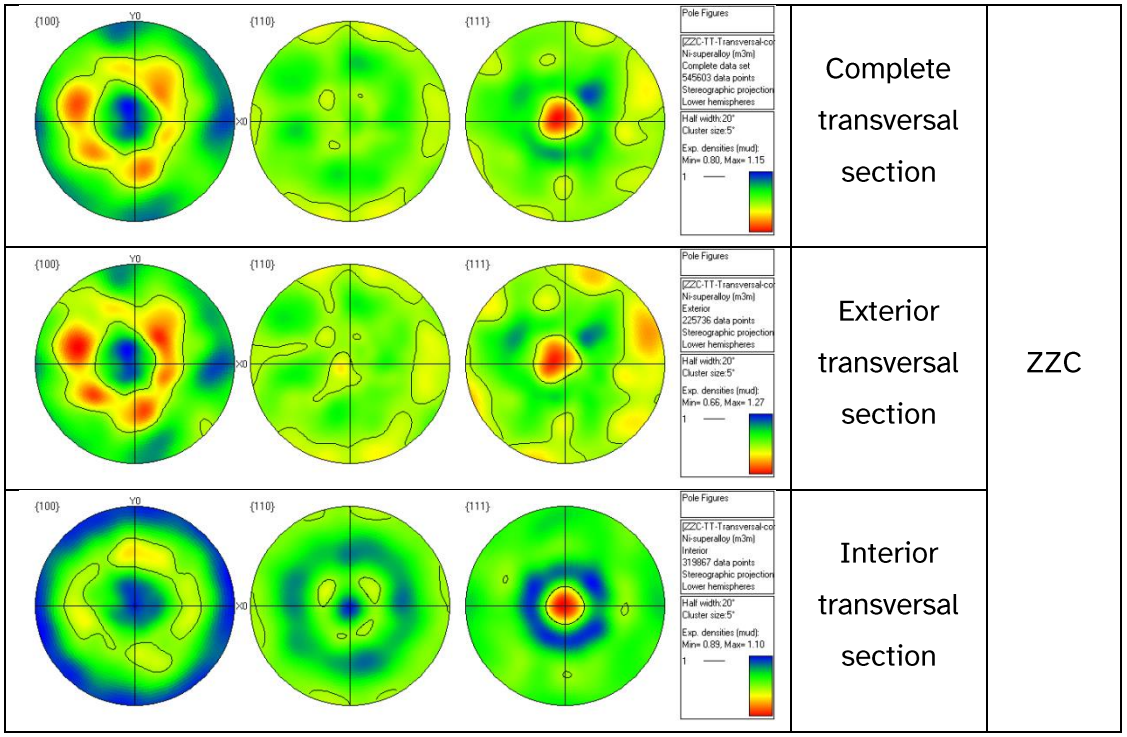

Figure IV.47. Pole figures for the different deposition strategies of coated specimens. Three sets of images are displayed: full cross section, outer zone (coating) and inner zone (substrate). The pole figure of the base material is also shown.

The pole figures show through a stereographic projection the distribution of the poles (normal to specific crystalline planes), using the frame of reference of sample axes as reference axes (Godec and Jenko, 2000). The texture of the base material is completely isotropic, since all the poles according to the orientation colour code are uniformly distributed in the projection. The same isotropy phenomenon is also observed in the interior cross sections of all the deposition strategies (substrate), which is expected for they are formed by the same material as the base.

For the external areas, a different orientation trend is observed at the poles according to the deposition strategy used:

- CC: there is a slight trend in the appearance of the family of planes {111}.
- LZ and LZZ: are observed a slight relative abundance of families {100} and {111}.
- ZC and ZZC: are observed a slight relative abundance of the families {110} and {111}.

It is interesting to note that the relative abundance of the families of crystallographic planes according to some “simple” deposition strategy (CC, LZ and LZZ), is not reflected in the “combined” deposition strategies (ZC and ZZC). Therefore, it is not considered

adequate to ensure that knowledge of the textures of simple strategies can predict the texture of the more complexes (composite deposition strategies).

IV.3.4 Application of the Dang Van Criterion to Coated Specimens.

The microscopic analysis by means of SEM using the EBSD technique in conjunction with a computer code programmed in Matlab (R) plus the auxiliary computer application for analysis and modelling of crystallographic textures MTEX (Nolze and Hielscher, 2016), have allowed to calculate the spatial crystallography orientation of each grain both in the substrate (only base material specimens are included here), as well as in the grains of the coating for each cladding strategy.

The orientation for each grain is shown graphically in (Fig. IV.46). The limits of fatigue endurance limit of (Table IV.13) allow to calculate the corresponding F_a (Eq. IV.42), which are shown in (Table IV.14). The dimensions of the coated fatigue test specimens are shown in (Chapter Annexes).

Table IV.14: Amplitude of nominal load corresponding to the duration for infinite fatigue life of the different deposition strategies in coated specimens and specimens of only made of base material for fatigue tests.

	Force Endurance Limit (Force Amplitude)	
Strategy	$F_{-1a} = (\sigma_{-1a}) A_{test}$ (N)	$F_{0a} = (\sigma_{0a}) A_{test}$ (N)
Base material	25642.6	16944.1
CC	16816.5	12681.4
LZZ	13069.8	10653.0
ZZC	18831.4	13442.3

Substituting the data of F_a for each cladding strategy from (Table IV.14) in the model on (Table IV.9), in addition with the calculation by (Eq. IV.30) to (Eq. IV.44), and applying the procedure described in (Section IV.3.2) a set of graphs are obtained for three specific cases (CC, LZZ and ZZC) + base material, as shown in (Fig. IV.48):

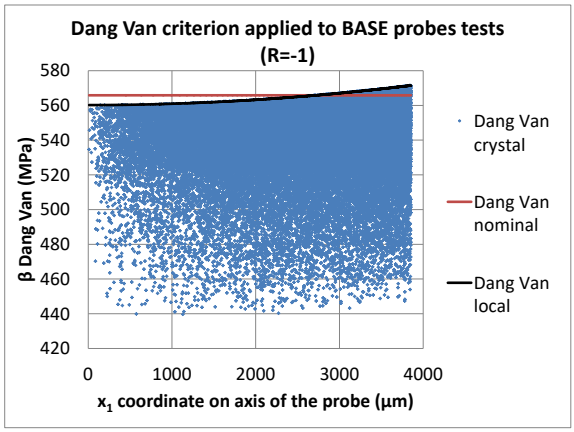
Dang Van criterion applied to BASE probes tests
(R=-1)
β Dang Van (MPa)
580
560
540
520
500
480
460
440
420
0
1000
2000
3000
4000
x1 coordinate on axis of the probe (µm)
Dang Van crystal
Dang Van nominal
Dang Van local

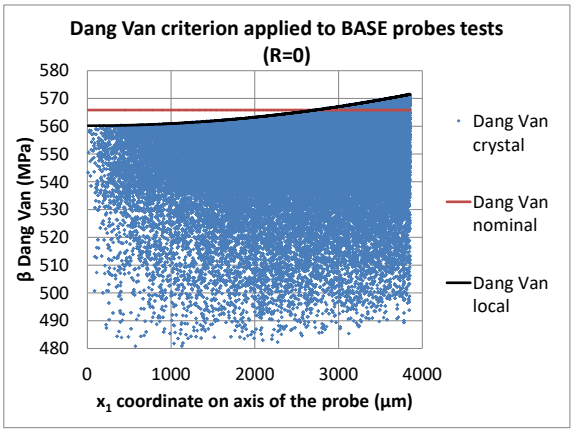
Dang Van criterion applied to BASE probes tests
(R=0)
β Dang Van (MPa)
580
570
560
550
540
530
520
510
500
490
480
0
1000
2000
3000
4000
x1 coordinate on axis of the probe (µm)
Dang Van crystal
Dang Van nominal
Dang Van local

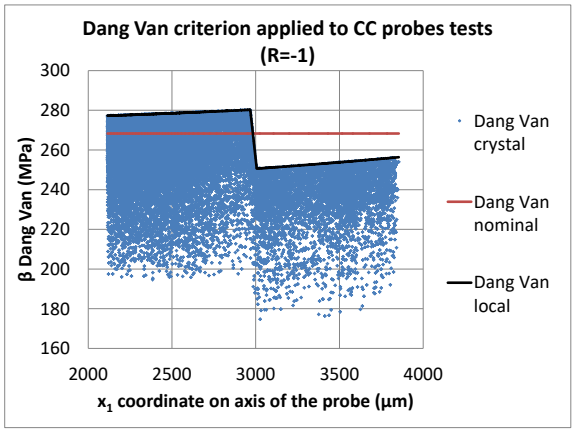
Dang Van criterion applied to CC probes tests
(R=-1)
β Dang Van (MPa)
300
280
260
240
220
200
180
160
2000
2500
3000
3500
4000
x1 coordinate on axis of the probe (µm)
Dang Van crystal
Dang Van nominal
Dang Van local

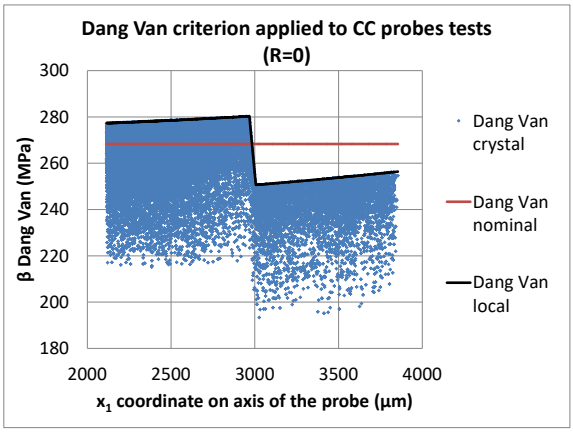
Dang Van criterion applied to CC probes tests
(R=0)
β Dang Van (MPa)
300
280
260
240
220
200
180
2000
2500
3000
3500
4000
x1 coordinate on axis of the probe (µm)
Dang Van crystal
Dang Van nominal
Dang Van local

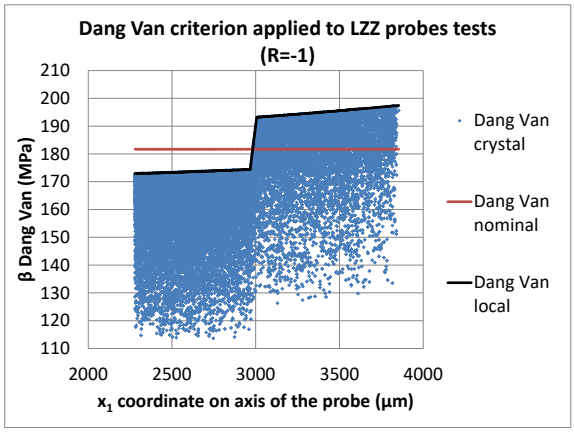
Dang Van criterion applied to LZZ probes tests
(R=-1)
β Dang Van (MPa)
210
200
190
180
170
160
150
140
130
120
110
2000
2500
3000
3500
4000
x1 coordinate on axis of the probe (µm)
Dang Van crystal
Dang Van nominal
Dang Van local

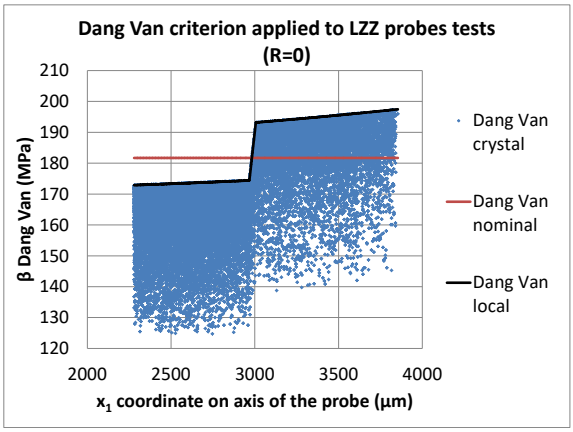
Dang Van criterion applied to LZZ probes tests
(R=0)
β Dang Van (MPa)
210
200
190
180
170
160
150
140
130
120
2000
2500
3000
3500
4000
x1 coordinate on axis of the probe (µm)
Dang Van crystal
Dang Van nominal
Dang Van local

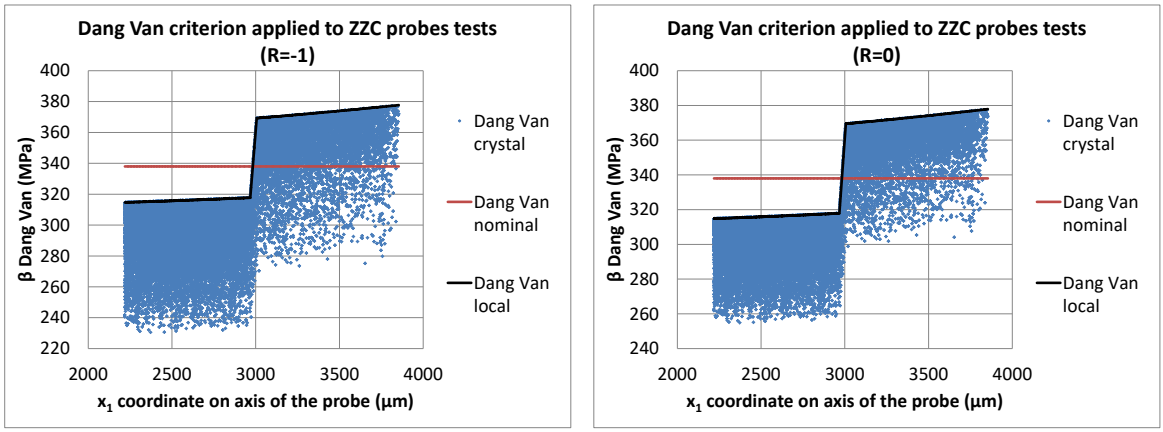

Figure IV.48. Graphical results of the Dang Van criterion applied to specimens made of only base material and coated specimens. Three approaches are shown: DV criterion applied to the grain according to its crystallographic orientation (point cloud), local DV criterion according to the coordinate within the specimen (black line), and nominal DV criterion (red line).

The explanation of each set of graphics is as follows:

- Dang Van Criterion at the level of each crystal. It is represented by a cloud of points, where each of them indicates the response of the material to the level of fatigue stress for infinite life according to the crystallographic orientation of the grain within the coated specimen. The Dang Van criterion was graphed as a function of the coordinate of the referenced system shown in (Fig. IV.35). As only base material is found inside the specimen, as shown in (Fig. IV.46), and there is radial symmetry in the value of internal stress in the specimen (Fig. IV.33), the DV criterion has not been calculated for all the crystals of the substrate, but only for those in the outer zone of the coated specimen, plus a small section within the substrate. The step-shaped jump on the values of $\beta = \beta_{DV}$ (values of the DV criterion) is notorious by the change of the substrate-coating material (the step is due to the variation of the internal stress inside the coated specimen).
- Dang Van criterion at local level according to the coordinate x_1 of the internal frame of reference for the stress in coated specimen. It is represented by the black line in the graphs of (Fig. IV.48). It is interpreted as the extreme limit that the DV criterion "can" reach when the crystallographic orientation of the grain is totally favourable for the initiation of fatigue damage (start of sliding within the

grain planes due to shear). A totally favourable grain orientation is equivalent to the shear stress in the study plane Π in the grain reaches the value of Tresca failure criterion: $\max|\tau_{nd}(t)| = \tau_{\max}(t) = \max[(\sigma_1(t) - \sigma_3(t)) \vee (\sigma_3(t) - \sigma_1(t))]/2$. The use of the local DV criterion is useful if the crystallographic orientation of the material is not to be taken into account and the worst case crystallographic orientation is assumed, or if an upper limit is to be set to compare how close to failure a grain is depending on its crystallographic orientation.

- Nominal Dang Van criterion. It is represented by the red line in (Fig. IV.48). The red line should be interpreted as the direct application of DV criteria without taking into account the variation in the distribution of the uniaxial stress within the coated specimen. It is calculated by applying only (Eq. IV.34) and (Eq. IV.35) to calculate a global $\beta = \beta_{DV}$. The use of this criterion is not considered as an adequate option, since by ignoring the internal "structure" of the coated specimen (that is, the variation in the stress distribution along with the difference in the mechanical properties). Nominal Dang Van criterion underestimates or overestimates the stresses within the specimen (the red line in the graph crosses the black line, which represents the limit case of the DV criterion).

The calculated $\alpha = \alpha_{DV}$ and $\beta = \beta_{DV}$ values for the cases of (Fig. IV.48) are shown in (Table IV.15).

Table IV.15: Calculated values of $\alpha = \alpha_{DV}$ and $\beta = \beta_{DV}$ for the cases of application of the Dang Van criterion to specimens made of only base material and coated specimens of (Fig. IV.48).

	Base material	CC	LZZ	ZZC
α_{DV}	1.5825	0.7258	0.4402	1.004
β_{DV}	565.8	268.3	181.7	338.0

IV.3.5 Sensitivity of the Microstructure to the Dang Van Failure Criterion.

Microstructure sensitivity shall be defined as a parameter that quantifies the difference in behaviour of the calculated values of the DV fatigue criterion for the difference in

mechanical properties and texture within the coated specimen relative to a specimen that does not take into account either microstructure or mechanical properties. The criterion to be used for comparison purposes only is the nominal DV criterion.

The difference between the values of the nominal DV criterion and the dots values of the crystal DV criterion for each coordinate is not uniform, and is utilized as an way that allows calculate the sensitivity of the different type of microstructure generated (Hor et al., 2013).

For the nominal DV criterion (represented by $\beta = \beta_{DV}$, (Table IV.15)), the number of grains with a certain crystallographic orientation which are in the "unsafe" zone is different depending on the deposition strategy. All points above the nominal DV curve are considered as “unsafe” only for the purpose of comparison of the sensitivity of the microstructure.

Sensitivity will not only be reflected by the average values that these crystal DV point data deviate from the nominal DV limit, but also in the number of them.

The data for microstructure sensitivity analysis of coated specimens are calculated by (Eq. IV.46):

$$\delta\beta_{\substack{DV_{crystal} \\ nom}} = abs\left(\beta_{DV_{crystal}} - \beta_{DV_{nom}}\right) \forall x_1 = \left\{d_{test}/2 - t_{clad}, d_{test}/2\right\} \qquad \textit{Eq. IV.46}$$

In the zone of the substrate of coated specimens, only data with a linear trend distribution would be observed because the microstructure is completely isotropic, and the same would be expected for specimens made only of base material.

For the case of specimens made only of base material, the data for microstructure sensitivity analysis is calculated by (Eq. IV.47):

$$\delta\beta_{\substack{DV_{crystal} \\ nom}} = \left(\beta_{DV_{crystal}} - \beta_{DV_{nom}}\right) \forall x_1 / \left\{\beta_{DV_{crystal}} > \beta_{DV_{nom}}\right\} \qquad \textit{Eq. IV.47}$$

The graphs results for the microstructure sensitivity calculation are shown in (Fig. IV.49). Where is applicable, the statistical fitting curves are included.

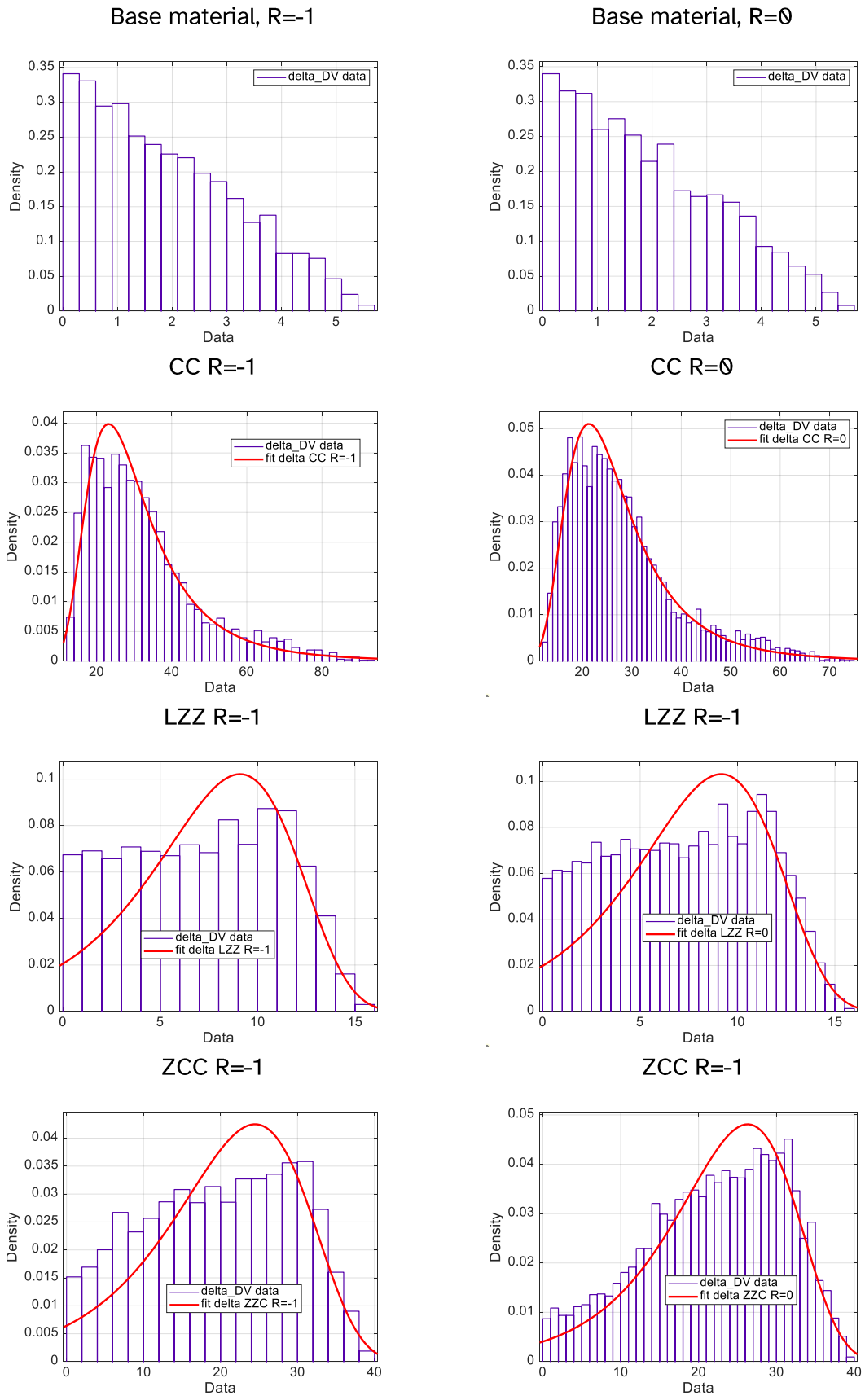

Figure IV.49. Graphs of the values with the distribution of the microstructure sensitivity for specimens made of base material only and coated specimens. In the case of coated

specimens, the graphs of the probability distributions that best fits the histograms generated from the sensitivity data are included. In the case of specimens made of base material only, a linear trend in the sensitivity values is observed due to the isotropy of the microstructure. All probability fits have been performed using the maximum likelihood method (Martín-Meizoso et al., 2009).

The fit distributions and their corresponding statistics are shown in (Table IV.16).

Table IV.16: Fits distributions and statistics associated with the graphs of the (Fig. IV.49).

CC R=-1	LZZ R=-1	ZZC R=-1
Distribution: Generalized Extreme Value Log likelihood: -22850 Domain: -Inf < y < Inf Mean: 32.635 Variance: 298.12 Mode: 23.1927 Parameter Estimate Std. Err. k 0.201783 0.0134928 sigma 9.40192 0.117886 mu 24.8892 0.146085	Distribution: Extreme Value Log likelihood: -15072.1 Domain: -Inf < y < Inf Mean: 7.01601 Variance: 21.3359 Mode(mu): 9.09484 Parameter Estimate Std. Err. mu 9.09484 0.0522469 sigma 3.60148 0.0380227	Distribution: Extreme Value Log likelihood: -24471.6 Domain: -Inf < y < Inf Mean: 19.4953 Variance: 123.3 Mode(mu): 24.4927 Parameter Estimate Std. Err. mu 24.4927 0.112825 sigma 8.6578 0.082769
CC R=0	**LZZ R=0**	**ZZC R=0**
Distribution: Generalized Extreme Value Log likelihood: -21309.6 Domain: -Inf < y < Inf Mean: 28.2553 Variance: 160.582 Mode: 21.3322 Parameter Estimate Std. Err. k 0.17649 0.0128683 sigma 7.31197 0.0895274 mu 22.5038 0.112573	Distribution: Extreme Value Log likelihood: -17643.9 Domain: -Inf < y < Inf Mean: 7.1094 Variance: 20.906 Mode(mu): 9.16719 Parameter Estimate Std. Err. mu 9.16719 0.0477137 sigma 3.56502 0.0347206	Distribution: Extreme Value Log likelihood: -26502 Domain: -Inf < y < Inf Mean: 21.8914 Variance: 96.2028 Mode(mu): 26.3057 Parameter Estimate Std. Err. mu 26.3057 0.094126 sigma 7.6475 0.0696734

The statistical data of the mode from (Table IV.16) shows that there is greater microstructure sensitivity in the CC and ZZC deposition strategies compared to the LZZ deposition strategy, (Fig. IV.50).

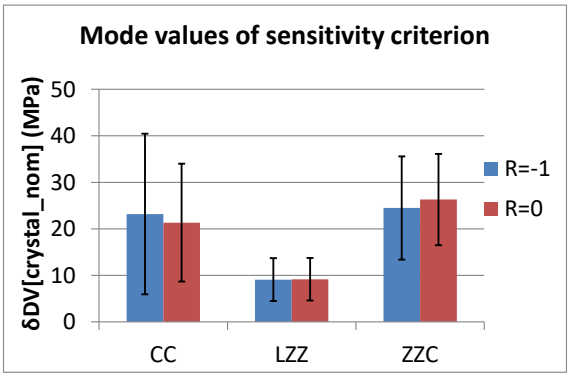

Figure IV.50. Graph with the values of the statistical mode of the sensitivity criterion $\delta\beta_{DV_{crystal}^{nom}}$ *for the strategies used in the coated specimens. The corresponding standard deviation is indicated with the error bars.*

Interestingly, the sensitivity of the microstructure generated in the coating of the cladding samples does not seem to depend on a specific crystallographic grain orientation, but rather on a set of families of planes. The frequency of occurrence of all combinations [plane + direction] in (Table IV.12), of the main slip systems used in the calculation of the Dang Van criterion (Eq. IV.30) was analysed. Counting the frequency of occurrence of the systems that maximise the resolved critical shear stress, a clear trend of occurrence of two specific systems is observed:

- System #9: (1 1 1) [0 1 1]
- System #46: (1 -1 -1) [-1 0 -1]

The occurrence of these two systems is practically independent of the deposition strategy used, as shown in (Fig. IV.51). Therefore, there must be some other characteristic associated with the microstructure that explains the differences both in the sensitivity of the microstructure and in the mechanical behaviour of the fatigue-coated specimens.

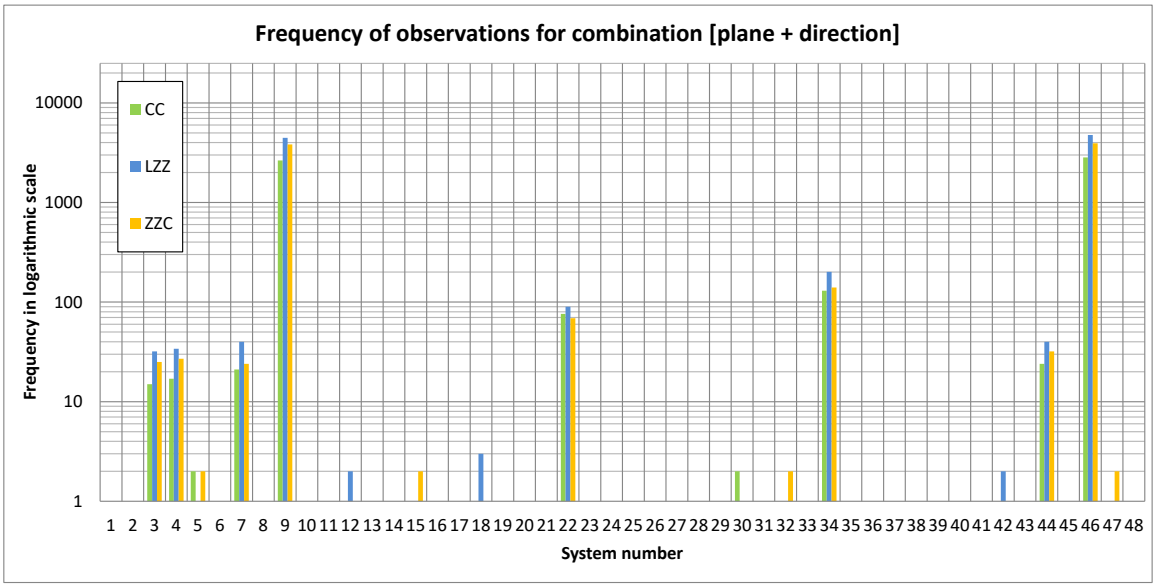

Figure IV.51. Graph with the observed frequency of the combinations [plane + sliding system] for the coating area in cladded specimens.

IV.3.6 Comparison of the Strength Properties of Coated Specimens Respect to Probes Made of Base Material.

The comparison between the nominal values of the fatigue endurance limit for R = -1 and R = 0 of (Table IV.13) must be made with some nuances. At the nominal stress level, it will be sufficient to perform the quotient between the different results of the fatigue strength limit for the coating strategies with respect to that of the base material (the base material is taken as a reference), (Eq. 78):

The comparison between the nominal values of the fatigue endurance limit for R = -1 and R = 0 of (Table IV.13) must be made with some nuance. At nominal stress level, it will be enough to make the quotient between the different results of the fatigue endurance limit of the strategies (CC, LZZ and ZZC), with respect to that of the base material (the base material is taken as a reference), (Eq. IV.48):

$$\%R_{nom} = \frac{\{\sigma_0, \sigma_{-1}\}^{\text{strategy}}_{\text{nom}}}{\{\sigma_0, \sigma_{-1}\}^{base}_{nom}} \qquad \textit{Eq. IV.48}$$

If the variation in the distribution of normal stresses within the specimen related to crystallographic orientation and mechanical properties are taken into account for each deposition strategy, as shown in (Fig. IV.48), the most unfavourable case for the coating will be taken in which the crystallographic orientation of the grains are the most

damaging (when the conditions of the local type DV criterion are met); and where the values of the stress inside the specimen are maximum (outer zone of the coating).

When the stress distribution within the specimen is taken into account, the corresponding stress concentration factor (Eq. IV.14) must be applied, at the nominal value of (Table IV.13) only for the case of specimens made of base material. The value of k_{tx} will not be substituted for that of k_{fx} (fatigue stress concentration), because the notch sensitivity value data for the INCO718 material provided by the Laser Cladding process is unknown. However, (Pilkey, 1997) suggests that k_{tx} can be used safely if information is not available regarding to q (a problem that generally occurs with "news materials").

When the stress distribution inside the specimen is taken into account, the comparison between endurance limits respect to the base material will be (Eq. IV.49):

$$\%R_{real} = \frac{\sigma_{clad}(d_{test}/2)_{\text{strategy}}}{k_{tx}\{\sigma_0, \sigma_{-1}\}^{base}_{nom}} \forall F = \{F_{-1a}, F_{0a}\} \qquad \textit{Eq. IV.49}$$

For the data in (Table IV.13), the relationship between the fatigue endurance limits applying (Eq. IV.48) and (Eq. IV.49) is shown in (Table IV.17).

Table IV.17: Comparison of fatigue endurance limits of specimens coated by Laser Cladding process with respect to specimens of the same dimensions made only base material.

	Fatigue limit (Nominal) [MPa]				Fatigue limit (local value) [MPa]			
	R=-1		R=0		R=-1		R=0	
Base	550.67	%R respect to base material	363.87	%R respect to base material	556.16 with k_{tx}	%R respect to base material	367.50 with k_{tx}	%R respect to base material
CC	361.13	65.6%	272.33	74.8%	345.51	62.1%	260.55	70.9%
LZZ	280.67	51.0%	228.77	62.9%	305.31	54.9%	248.87	67.7%
ZZC	404.40	73.4%	288.67	79.3%	452.52	81.4%	323.15	87.9%

Table 54 shows that the coating material of the ZZC strategy specimens has a better limit of endurance to fatigue when comparing to those of the CC and LZZ strategies. It is interesting to note that the classification of strategies based on the uniaxial stress test in (Table IV.4) does not coincide with the results of the fatigue tests. According to the table proposal mentioned previously, the best fatigue-resistant strategies should be

in this order: ZZC, LZZ and CC, but the evidence given by the fatigue life limits shows the sequence: ZZC, CC and LZZ.

The only weighted factor in (Table IV.4) that follows the same order sequence as the fatigue limits in (Table IV.13) is $\%E$ (percent elongation at fracture).

IV.3.6.1 Residual Stresses in Specimens.

Regarding residual stresses, it is known that they have an unfavourable effect on the fatigue life of metallic materials (Flavenot et al., 1983; Hutasoit et al., 2015). The trend for specimens coated by the Laser Cladding process is always a decrease in the fatigue life of the specimens (Koehler et al., 2012), sometimes up to 70% with respect to the substrate material. The thermal cycles of the laser cladding process are responsible for the most part of the residual stress (Shamsaei et al., 2015), along with differences in the mechanical and thermal properties of the substrate and coating materials. Materials with high Modulus of Elasticity and Ultimate Strength (such as INCO718), tend to produce residual stresses even up to the order of 75% of Yield Strength (Rangaswamy et al., 2005).

Samples of all deposition strategies (and base material) were prepared in the configuration shown in (Fig. IV.18, A). The samples consist of cylindrical sections which were fabricated with the same parameters as the test specimens itself to generate a similar microstructure, and which have subsequently been cut in half.

The specimens were cut longitudinally with the intention of calculating the stresses inside the specimens. The machining of the test parts was carried out by EDM with the aim of introducing the least amount of extra residual stresses than by conventional machining. Subsequently, the flat surface of the semi-cylinder was polished similar to a metallographic preparation according to (ASTM Subcommittee E04.01, 2015).

An X-ray diffractometer Panalytical X'Pert PRO for polycrystalline sample with theta-theta geometry, wavelength Cr-Ka1, 2θ =128.13°, was used to measure residual stresses. The material properties for comparison were: Modulus of Elasticity=183.4 GPa, Poisson's Ratio=0.29 and Biaxial + Shear as stress evaluation mode. The residual stress sampling area was a circumference of 1mm diameter and 4 tests were carried out in different zones of the semi-cylinder section, as shown in (Fig. IV.52).

- (a): plane zone at the edge.

- (b): plane zone at middle distance from the edge.
- (c): plane zone in the centre, on the axis of symmetry of the sample.
- (d): random in the outer convex area.

The resulting measured residual stresses were expressed in the following three directions with respect to the axis of the sample, as shown in (Fig. IV.52):

- $\sigma_1(T)$: transverse direction, perpendicular to the axis of symmetry.
- $\sigma_2(L)$: longitudinal direction, parallel to the axis of symmetry of the sample.
- $\sigma_\phi(45)$: 45° with respect to the longitudinal axis of symmetry of the half cylinder.

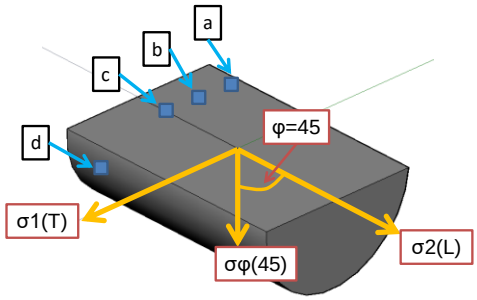

Figure IV.52. Location of test areas for data collection of residual stresses in samples representatives of the deposition strategies of coated specimens and base material probes (substrate).

The graphs with the results of the residual stress tests are shown in the (Fig. IV.53).

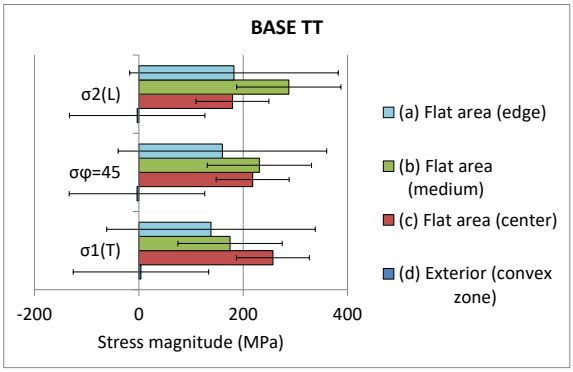

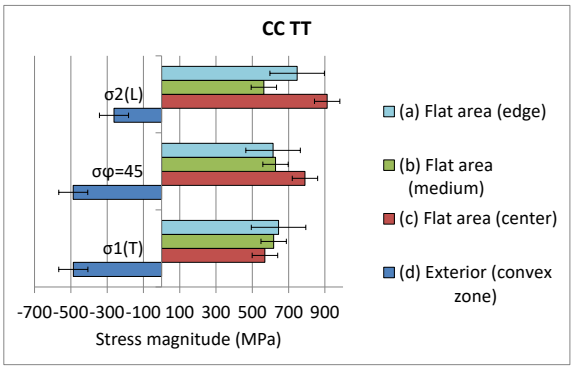

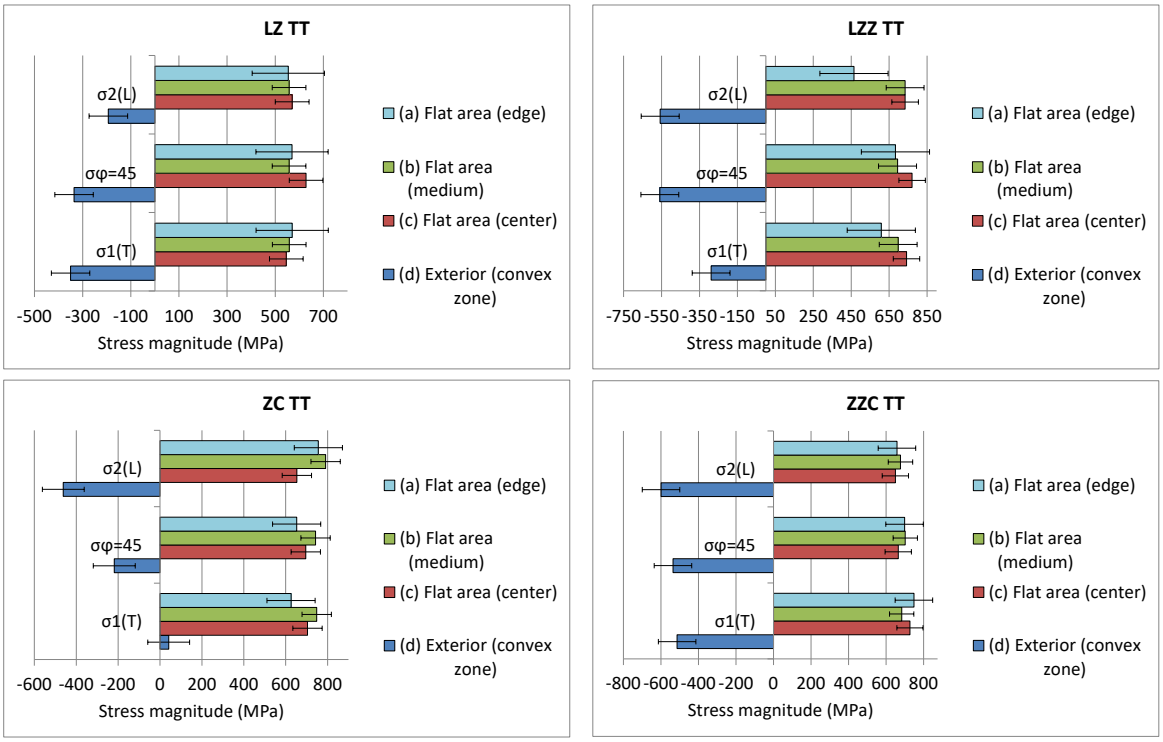

Figure IV.53. Graphs showing the results of residual stress tests on representative samples of the strategies used on coated specimens and for the base material. Positive sign indicates stress in tension, negative in compression.

Residual stresses show very different values depending on the measurement area, with compression in the outer area (convex zone of the sample), and tensional stress in the interior (plane zone of the half cylinder).

The measured values of the residual stresses tests are very high compared to the Yield Strength of (Table IV.2) and the change in sign between the sampling zone (a) and (d) on (Fig. IV.52) is not consistent because two very close zones have a very high difference regarding their values. This can be attributed to the size of the analysed area (1 mm diameter), which is quite big in relation to the deposited layers thickness (0.5 mm).

The measuring device did not allow precise measurements for each deposited layer. Consequently, the transition between compressive and tensile stresses (coating to base), cannot be precisely identified.

Residual stresses are multiaxial and are internally balanced, so there is generally a very high gradient near the surface. Due to stresses during work (loads), the magnitude of residual stresses decreases over time, this is known as "relaxation". Gradient, multi-axiality and relaxation mean that residual stresses cannot be considered as average stresses in addition to those produced by working loads (Avilés, 2005).

Because of the previous paragraph and the fact that the residual stress test data will not be considered with sufficient accuracy to be used in calculations within this investigation, only the trend of values in compression in the area corresponding to the outside of the cladding and tensile stress inside the specimens will be taken as useful data.

IV.4 Microstructure/Mechanical Properties Correlation Model for Coated Specimens.

IV.4.1 Descriptive Statistics of the Geometric Characteristics of the Microstructure in the Cladding Zone and the Substrate of Coated Specimens.

To optimize the structure and properties of alloys, it is necessary to take into account the organization of the microstructure within them. In the case of materials manufactured by means of the Laser Cladding process, there is an important variation in the texture of the microstructure generated (Fig. IV.46), which is mainly dependent on the deposition strategy used (Fig. IV.14), since the rest of the process parameters have been kept constant for this research.

The difference in texture is significant in strength performance according to the results of the mechanical properties tests (Table IV.2) and (Table IV.13).

At the geometrical level, two parameters were studied from the EBSD images of the cross sections of the coated samples (Fig. IV.46): the cross-sectional area of the grains and their aspect ratio.

The use of these two previous parameters shall serve as convenient bases to define correlations between microstructure and mechanical properties (Chapter IV.4.4). The explanation on the use of these two parameters will be explained later.

The areas and AR of the grains in the coated zone and inside the specimens (base material) have been calculated using ImageJ(R) software, open source image analysis software. From the generated database, the corresponding histograms for both the area and the AR were plotted. To quantify the data in the histograms, they were adjusted to probability distribution functions using the maximum likelihood method (Martín-Meizoso et al., 2009). The results are shown in (Fig. IV.54).

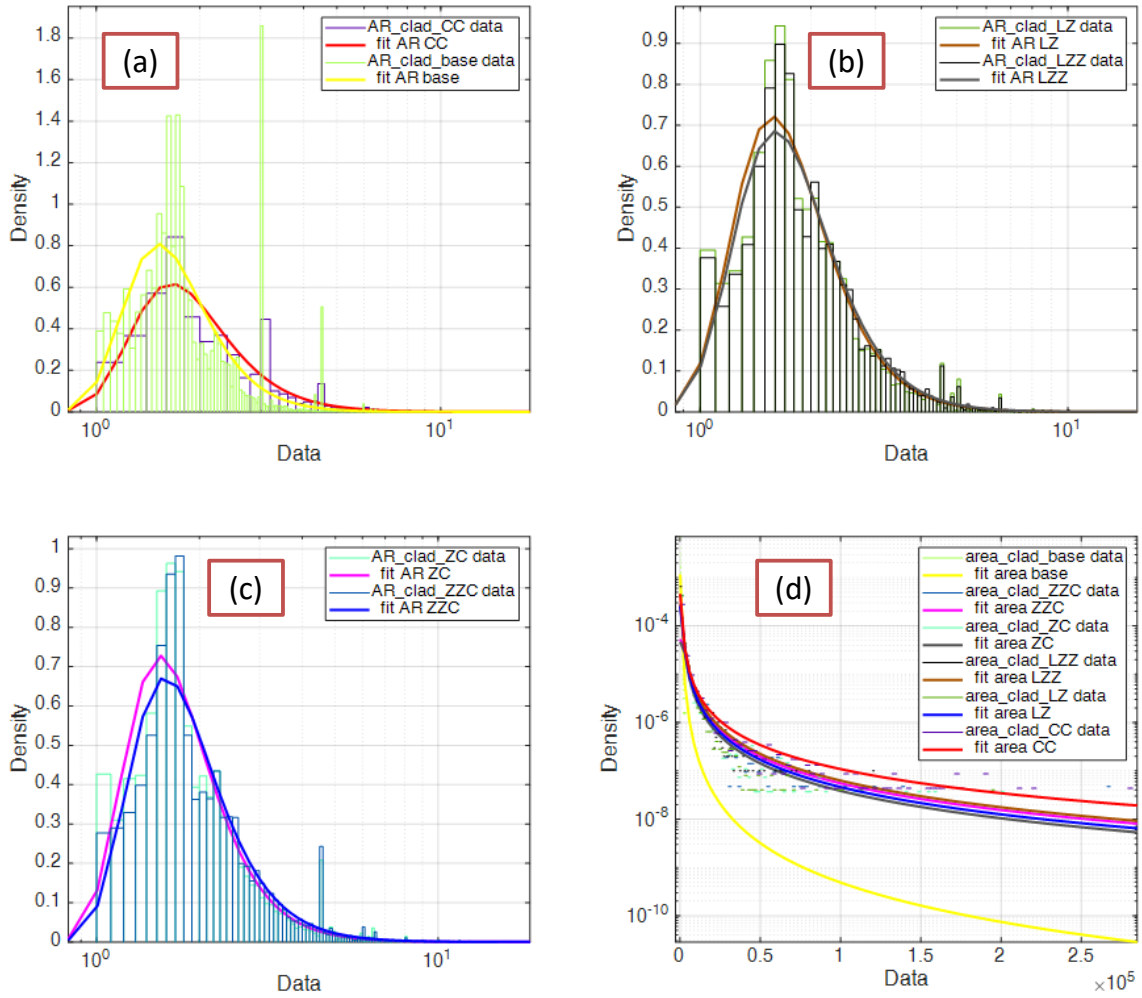

Figure IV.54. Histograms from the data obtained of the image analysis of (Fig. IV.46); together with the corresponding fitting curves of the probability distributions (all of the "Generalized Extreme Value Distribution" type). (a) AR for base material and CC, (b) AR for LZ and LZZ, (c) AR for ZC and ZZC (d) grain area for all deposition strategies and base material. Some axes are shown in logarithmic scale due to the great dispersion on values of the data.

The objective of the graphs in (Fig. IV.54) is to demonstrate the differences between the area and AR values for the different deposition strategies and the base material. As it can be seen in the previous figure, the difference is not appreciable, but the statistics associated with the probability distributions functions (Table IV.18) shown a significant variation in the parameters that characterize the probability distribution functions for each set of data.

Table IV.18: Estimated parameters for the probability distributions functions of the histograms in (Fig. IV.54). The location (mu), scale (sigma) and shape (k) values characteristic of each curve were highlighted in order to show the differences between the parametric descriptors for each deposition strategy and the base material (substrate).

Area of grains in the clad ($\mu m)^2$	AR of grains in the clad (-)
CC	
Distribution: Generalized Extreme Value Log likelihood: -62541.3 Parameter Estimate Std. Err. k 1.4993 0.0232403 sigma 320.019 7.43448 mu 286.409 4.46354	Distribution: Generalized Extreme Value Log likelihood: -9677.54 Parameter Estimate Std. Err. k 0.286116 0.0106043 sigma 0.618129 0.0068127 mu 1.80108 0.00812712
LZ	
Distribution: Generalized Extreme Value Log likelihood: -97967.4 Parameter Estimate Std. Err. k 1.13317 0.0143839 sigma 295.711 4.43522 mu 315.556 3.16794	Distribution: Generalized Extreme Value Log likelihood: -13245.4 Parameter Estimate Std. Err. k 0.235908 0.00753622 sigma 0.522981 0.0043131 mu 1.67939 0.00532716
LZZ	
Distribution: Generalized Extreme Value Log likelihood: -81213.8 Parameter Estimate Std. Err. k 1.19144 0.0165632 sigma 352.119 6.07357 mu 348.598 4.20652	Distribution: Generalized Extreme Value Log likelihood: -11270 Parameter Estimate Std. Err. k 0.241933 0.00861318 sigma 0.551255 0.00510444 mu 1.71696 0.00627002
ZC	
Distribution: Generalized Extreme Value Log likelihood: -105639 Parameter Estimate Std. Err. k 1.12367 0.0131172 sigma 248.638 3.50605	Distribution: Generalized Extreme Value Log likelihood: -14942.9 Parameter Estimate Std. Err. k 0.278458 0.00740949 sigma 0.523665 0.00422967

mu 288.347 2.49574	mu 1.65814 0.0050931
ZZC	
Distribution: Generalized Extreme Value Log likelihood: -84213.7 Parameter Estimate Std. Err.	Distribution: Generalized Extreme Value Log likelihood: -12609.1 Parameter Estimate Std. Err.
k 1.1889 0.0152405 sigma 303.984 5.05186 mu 322.162 3.45642	k 0.303388 0.00868467 sigma 0.569685 0.00533724 mu 1.73524 0.00631583
BASE MATERIAL	
Distribution: Generalized Extreme Value Log likelihood: -215072 Parameter Estimate Std. Err.	Distribution: Generalized Extreme Value Log likelihood: -29864.1 Parameter Estimate Std. Err.
k 0.584893 0.00830927 sigma 128.366 0.90726 mu 209.58 0.916868	k 0.217155 0.00490385 sigma 0.464834 0.00239622 mu 1.6038 0.00298032

IV.4.2 Background on Microstructure/Mechanical Properties Correlations in Materials with Highly Variable Texture.

In rapid solidification processes (such as DED processes, including Laser Cladding), which give rise to non-equilibrium processes (Chapter Introduction, section 2), an important part of the self-organisation of the microstructure generated during the solidification of the material can be "apparently" very disordered (Carpinteri, 1994), i.e. a great variety of grain shapes and sizes. The explanation for this apparent disorder must be sought in synergetic theory (action of two or more causes which effect is greater than the sum of the individual effects).

Synergetic theory considers self-organising processes and the properties of a decay process as inherent to any open system, whether organic or inorganic in nature. Biological, chemical, physical and other non-equilibrium processes tend to undergo transformations from the corresponding non-equilibrium phase to a “bifurcation”.

The driving force of this self-organisation mentioned above is the tendency of open systems to minimise entropy production. This follows from the Glansdorf-Prigogin and

Klimontowich theorem. For open systems that exchange energy and matter with the environment, an entropy change consists of two parts (Eq. IV.50):

$$dS' = d_iS' - d_eS' \qquad \textit{Eq. IV.50}$$

Where d_eS' takes into account the energy transfer across the system contours, and d_iS' the entropy change inside the system. Therefore, the entropy production will be (Eq. IV.51):

$$d_iS'/dt = p \qquad \textit{Eq. IV.51}$$

The minimisation of the (Eq. IV.50) function favours the emergence of "dissipative" type structures. Dissipative structures consist of highly ordered self-organised formations in systems far from thermodynamic equilibrium, which exhibit specific “shapes” and typical space-temporal dimensions. Thus, the apparent “disorder” of the non-equilibrium states is simply the synergetics of the system minimising entropy production. The most important features of these “dissipative structures” are:

- Characteristic 1: their duration (they exist only if energy is supplied continuously).
- Characteristic 2: its focus on a localized region.
- Characteristic 3: the existence of a fractal dimension that describes them (these structures have fractal properties).

At the level of the relationship between microstructural and mechanical properties, it has been found that the phenomenon is controlled not only by the initial structure (static structure at equilibrium), but also by the dynamic (dissipative) structure at the bifurcation points (Ivanova et al., 1998).

Laser Cladding process meets all the requirements to generate structures that can be characterized by fractal-like properties:

- The material addition process will last as long as the laser beam supplies energy to the system (high energy in a given time span).
- Spatial focusing of the process (basically the whole system is concentrated in the area of the melt pool).
- Non-equilibrium (the laser beam generates high temperature gradients that thermodynamically drive the process away from equilibrium).

- Synergy is one reason why the microstructure generated in the laser cladding process is different depending on the strategy used (path), even using the same process parameters (the texture varies both in size and in the morphology of the grains).

In view of the previous statements, it is proposed that the relationship between microstructure and mechanical properties of a laser-added material will be fractal in behaviour.

IV.4.3 Fractals and Their use in the Characterisation of Mechanical Properties of Textured Materials.

Fractal geometry has its origins in the studies of (Mandelbrot, 1975), which resulted in the development of a new branch of mathematics, called fractal geometry. It is based on the concept of self-similarity, the use of fractional dimensions and algorithms.

In conventional materials science, elements of microstructure are described using Euclidean dimensions (d). For point defects (e.g., vacancies and interstitial atoms), d = 0; for linear defects (such as dislocations), d = 1; for planar defects (twins), d = 2; and for three-dimensional formations (crystal structure), d = 3. The Euclidean dimension cannot be used to describe structural elements that differ from the standard (e.g., points or straight lines).

It is known that the grain boundaries (the most important elements on the microstructure) are curvilinear. This shape can be described by the fractal dimension ($D_{fractal}$) corresponding to $1 \leq D_{fractal} \leq 2$. Surface defects can also be described using the "fine dimension", corresponding to the range $2 \leq D_{fractal} \leq 3$ (Ivanova et al., 1998).

Some of the applications in which fractal geometry has been used are:

- Fractal nature of metal fracture surfaces (Mandelbrot et al., 1984).
- The use of fractals in the analysis of metal microstructures (Hornbogen, 1989).
- Fragmentation resistance of brittle materials (Xu et al., 2016).
- The mechanical behaviour of minerals and refractory materials (Terzić et al., 2015).
- Strength in rocks as function of fractal dimension of grain size and shape (He et al., 2019).

- Fractal analysis of the dendritic microstructure of an aluminium alloy (Hinojosa et al., 2000).
- Solid mechanics with a frame of reference in fractal structures (Balankin, 2015).

Self-similarity in scale (a morphology that remains similar for magnifications in a wide range of sizes), is applicable to the case of specimens coated by the Laser Cladding process. An example of 3 grains of elongated geometry from the EBSD image of (Fig. IV.46, CC strategy) is shown in (Fig. IV.55), of approximately the same AR but a scale difference of 1: 100.

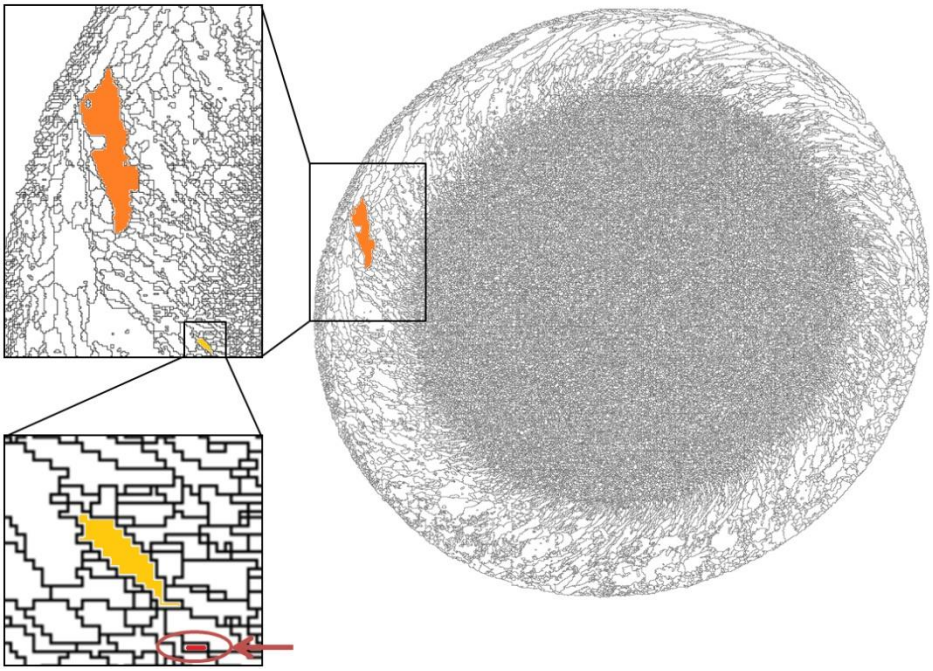

Figure IV.55. Example of self-similarity in grain morphology for an EBSD image of the CC deposition strategy on a coated specimen. The scale of the self-similarity will be limited in this case by the resolution of the image used in the fractal geometry analysis (the resolution in the EBSD image is 10 microns, the diameter of the cross-section shown is approximately 7.7 mm).

IV.4.4 Fractal Model for the Characterisation of the Mechanical Properties of Specimens Coated by Laser Cladding Process.

The most common relationship between microstructure and mechanical properties applied to INCO718 alloy is one of the Hall-Petch type (Eq. IV.52), (Wang et al., 2012):

$$\sigma_y = \sigma_{o\_HP} + K_g d_{grain}^{-1/2} \qquad \textit{Eq. IV.52}$$

The application range of (Eq. IV.52) is approximately $1 \leq d_{grain} \leq 1120 \ \mu m$. The (Eq. IV.52) has the restriction that the grain size is assumed to be approximately uniform (d_{grain} refers to a grain of equiaxial morphology), a requirement that is not fulfilled in the coating microstructures shown in the EBSD images of the cross sections of the specimens in (Fig. IV.46).

To overcome the problem on the description of complex and irregular geometries (variable d_{grain}), typical of alloys and metals, fractal geometry is adequate and has been applied previously to characterize zinc alloys (Streitenberger et al., 1995).

Therefore, an alternative will be proposed to correlate the microstructure generated by the laser cladding process based on the publications of (He et al., 2019) and (Kobayashi et al., 2016).

In the work of (He et al., 2019), the Ultimate Strength of rocks is quantified as a function of the fractal characteristics of the projected areas of the grains using two geometric descriptors: grain size and is AR. Grain size is assumed to originate from the projection of a circular area, in such a way that a grain length l_i can be calculated from the 2D area analysis of EBSD images (obtaining the area), and defining l_i as (Eq. IV.53):

$$l_i = \sqrt{\frac{4A_{i\_grain}}{\pi}} \qquad \textit{Eq. IV.53}$$

The fractal dimension of the grains (D_l), requires the use of a cumulative distribution function to describe the dispersion in their size, and thus solve the restriction regarding grain morphology of (Eq. IV.52). The cumulative distribution function in (He et al., 2019) is defined as (Eq. IV.54):

$$1 - P_{li} = \left(\frac{l_{\min}}{l_i} \right)^{D_l} \qquad \textit{Eq. IV.54}$$

The shape of the grains will also be considered as an important characteristic to describe the mechanical behaviour of the material, as it will be related to the variation in the grain morphology of the microstructure and therefore the mechanical properties that dependent on it. To describe the variation in grain geometry, the parameter “Aspect Ratio” will be used, because it is a simple way to quantify the variety of elongated grain shapes by means of a single quantity. In (Fig. IV.46) a wide variation of both parameters

is shown, especially in the CC deposition strategy, which shows grains of many different sizes, as well as highly varied AR.

The fractal corresponding to the AR of the grains (D_S), associated to the cumulative probability function necessary to calculate it, has its origin in the work of (He et al., 2019), and is shown in (Eq. IV.55):

$$1 - P_{ARi} = AR_i^{-D_S} \qquad \textit{Eq. IV.55}$$

Another fractal dimension that is used in modelling the microstructure of metals is the grain surface dimension fractal (D_R) (Streitenberger et al., 1995). This fractal is used as a means to indirectly examine the area-volume relationship of a grain, and is calculated by means of (Eq. IV.56):

$$P_{grain}^{\,1/D_R} = \kappa_{grain} A_{grain}^{\,1/2} \qquad \textit{Eq. IV.56}$$

The slope on the fit line for the graph $\ln(P_{grain\_i})$ versus $\ln(A_{grain\_i})$ for a set of grains, will allow obtaining the value $D_R/2$. The perimeter of the grains is usually modelled as that of an ellipse with semi-axes [a, b] (MTEX, 2020), as shown in (Fig. IV.56).

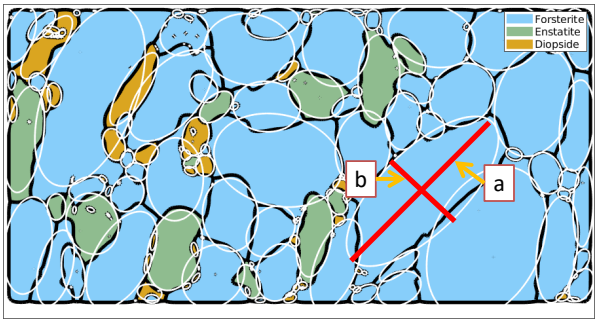

Figure IV.56. Example of grain modelling through ellipses to estimate the value of P_{grain} necessary for calculating the grain surface dimension fractal (MTEX, 2020).

The previous fractal (D_R) has the limitation that the value of the slope $D_R/2$ can have different interpretations (Streitenberger et al., 1995):

a. The set consists of self-similar fractal objects.
b. The set consists of geometrically dissimilar Euclidean objects.

In case (a), an exhaustive verification of the set will be required by means of imaging tests at different scales to verify the "fractality" of the dimension.

In case (b) the object is not fractal and D_R only describes the average geometry of the grain size.

For the reasons described previously, the grain surface dimension fractal should be used with some caution. The application of the method from (Eq. IV.53) to (Eq. IV.56) to the area, aspect ratio and grain perimeter data (modelled as ellipses), obtained for the different cladding strategies is shown in (Fig. IV.57).

Fractal analysis of entire cross-section area of CC strategy.

D_l D_S $D_R / 2$

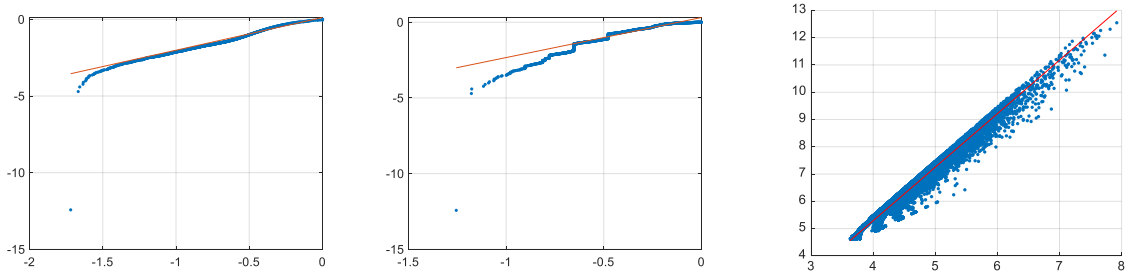

Fractal analysis of entire cross-section area of LZ strategy.

D_l D_S $D_R / 2$

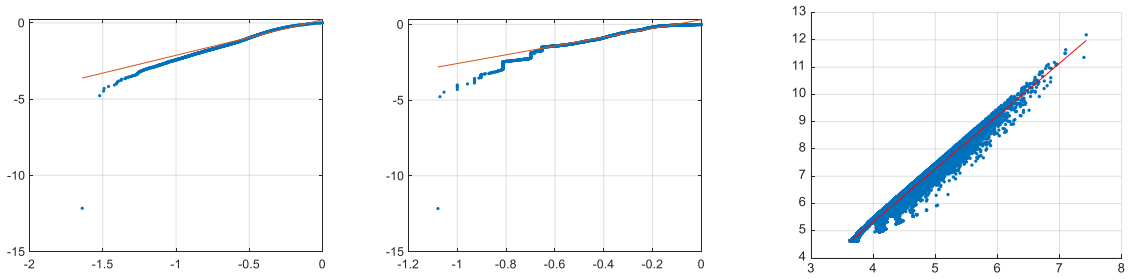

Fractal analysis of entire cross-section area of LZZ strategy.

D_l D_S $D_R / 2$

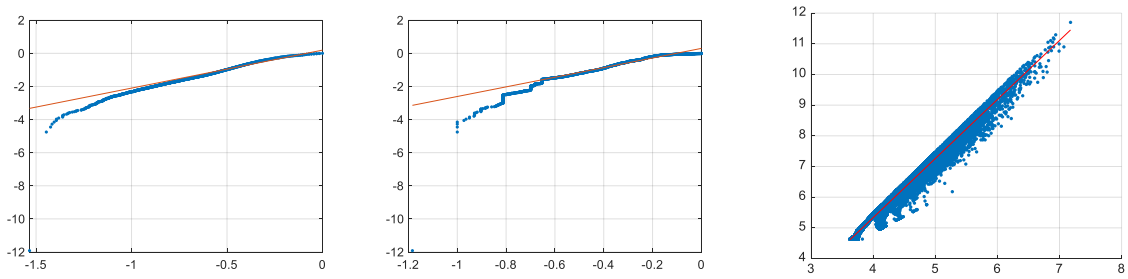

Fractal analysis of entire cross-section area of ZC strategy.

D_l D_S $D_R / 2$

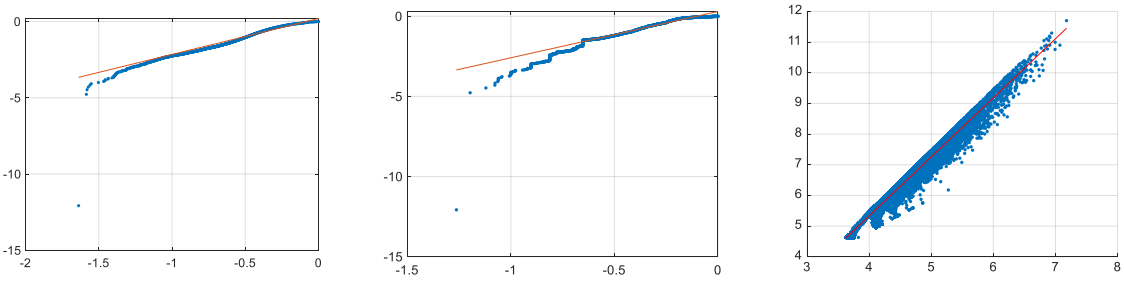

Fractal analysis of entire cross-section area of ZZC strategy.

D_l D_S $D_R / 2$

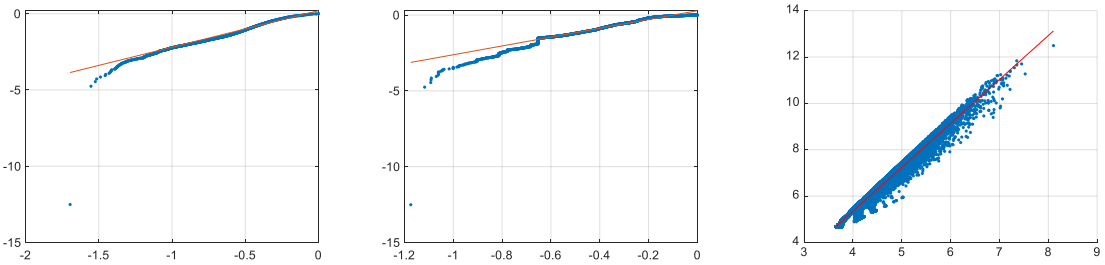

Graph IV.57. Evaluation of different types of fractal dimension for the deposition strategies of specimens coated by the Laser Cladding process. The red line is the least squares method fit to a linear function for the fractal dimension calculation, the blue cloud of points corresponding to the data obtained from the EBSD images (Fig. IV.46).

The values of the fractals dimension corresponding to (Fig. IV.57) are shown in (Table IV.19).

Table IV.19: Fractal values corresponding to the graphs in (Fig. IV.57). The coefficient of determination R^2 is appended to each fractal dimension set of data.

Material	D_l	R^2	D_S	R^2	D_R	R^2
Base material	2.7911	0.8635	3.0308	0.9105	3.9450	0.9507
CC	2.1320	0.9540	2.6452	0.9106	3.9240	0.9583
LZ	2.3354	0.9484	2.8962	0.9250	3.8770	0.9609
LZZ	2.2932	0.9546	2.9060	0.9233	3.8492	0.9646
ZC	2.3520	0.9535	2.8867	0.9340	3.8286	0.9604
ZZC	2.3913	0.9601	2.9064	0.9360	3.7889	0.9613

In the work of (Kobayashi et al., 2016), the use of the method of boundaries fractal dimension between grains (D_G) is proposed as a way to evaluate the tendency to

intergranular corrosion. In this research, this last approach will be changed, and the use of the fractal dimension of the grain edges will aim to evaluate the synergy of the material, which in turn is associated with the dissipation-bifurcations for non-equilibrium states, and therefore to the morphology of the microstructure, which as it is known, is the main strength factor for metallic materials.

Grain boundaries play an important role in the fatigue life of metallic materials by acting as a blocker for crack propagation across grains in the crack growth stage and for the interaction of persistent slip bands (Zhang and Wang, 2007).

For this research the use of the “box-counting method” (Gonzato, 1998) is proposed on black and white images of textures for the different strategies of Laser Cladding process plus the base material shown in (Fig. IV.46). The implementation of the box-counting method was carried out through the computer code “boxcount.m” (Moisy, 2020) written in Matlab (R). For example, for the deposition strategy of (Fig. IV.55), the application of the "box-counting method” will generate the graph shown in (Fig. IV.58).

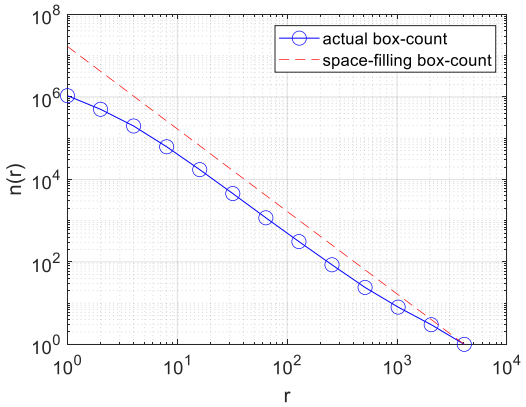

Figure IV.58. Plot of the box-count results for the black and white EBSD figure of the cross-section of a specimen coated with the CC strategy (Fig. IV.55).

The method was used on the entire image of the cross-section of the sample. No discrimination has been made between substrate and clad materials due to the resulting mechanical properties (especially strength), depends on both zones resisting the loads together.

According to (Moisy, 2020), the red dotted line that is drawn in the previous graph shows the scale $N(r) = r^{-2}$ that can serve as comparison as the “expected data” assuming a 2D image that fills the entire space. The discrepancy between the two curves (blue and red) would indicate possible fractal behaviour. For the rest of the strategies, the evaluation graphs are presented in (Fig. IV.59).

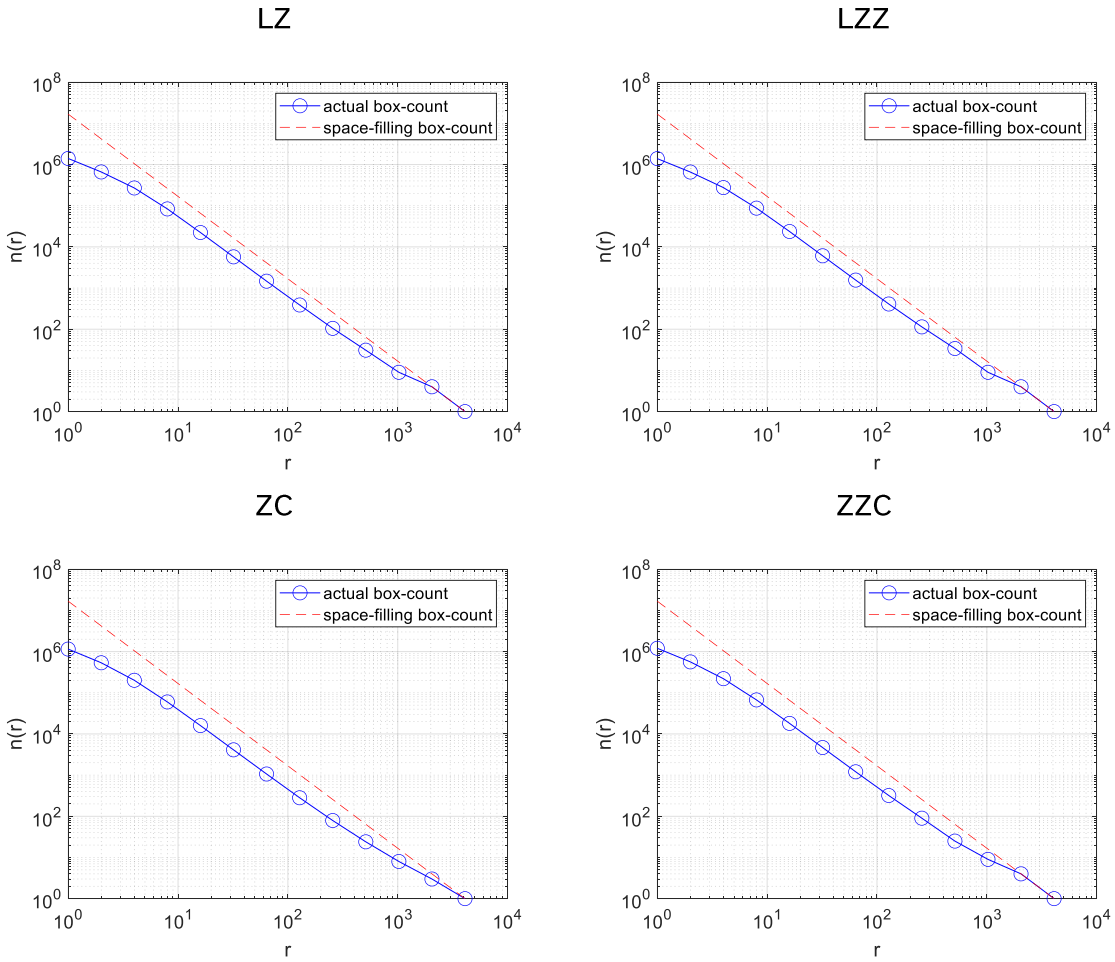

Figure IV.59. Evaluation of the fractal dimension of grain boundaries for different deposition strategies in specimens coated by the Laser Cladding process using the box-count method.

The values of the fractals dimensions corresponding to (Fig. IV.59) are shown in (Table IV.20).

Table IV.20: Fractal dimensions values corresponding to the graphs in (Fig. IV.59). The value of coefficient of determination R^2 is appended to each fractal dimension data.

Material	D_G	R^2
Base material	1.7684	0.9507
CC	1.644	0.9583
LZ	1.6894	0.9609
LZZ	1.6883	0.9646
ZC	1.6523	0.9604
ZZC	1.673	0.9613

IV.4.4.1 Proposal of Fractal Model to Correlate the Crystallographic Orientation of the Grains of a Material with the Mechanical Properties of the Coated Specimens.

In (Section IV.4.2), the importance of the crystallographic orientation of grains in the fatigue endurance of a material was documented.

The way to quantify the tendency to slip within a grain in the crystallographic planes by shear stress was described by means of the Schmid factor (Eq. IV.38), related to the Dang Van fatigue criterion (Eq. IV.30) for specimens in uniaxial tension test. Therefore, it is reasonable to assume that some relationship between the crystallographic orientation associated with the grains and the mechanical properties for a polycrystalline alloy may exist.

Experimental evidence in the engineering field of grain boundary indicates that the fundamentals of fracture processes in polycrystals are strongly influenced by the structure of the grain boundary and its coupling during deformation processes, i.e. the orientation relationship between crystal lattices in adjacent grains (Dingreville et al., 2017).

The structure of the grain boundary is "included" in the fractal model proposed by (Kobayashi et al., 2016), in such a way that the other factor (the crystallographic orientation) must be included in the proposed model correlation for microstructure-mechanical properties.

Some attributes of the crystal lattice of the grains can be considered as initial selection criteria relevant for the proposal of a fractal model of crystallographic orientation. In a metal with an FCC-type microstructure (as is the case of INCO718), two of these attributes can be considered in relation to crack propagation:

- The magnitude of the Schmid factor for primary slip in FCC systems.
- The relationship between Schmid factors for primary and secondary sliding systems, or in other words, which set of the previous mentioned systems will be activated more easily by initiating the sliding within the grains of the material.

In the literature, it was documented that secondary sliding systems are highly dependent on temperature (Arakere and Swanson, 2002), and that for the testing conditions used in

this research, only the primary systems will be responsible for the initiation of the failure within the material.

In the context of failure in metallic materials of FCC crystal structure, it is appropriate to use a representation of the crystal lattice properties using primary Schmid factor contour curves within the inverse pole figure for FCC-type crystals along appropriate reference directions (Dingreville et al., 2017).

All orientations found on the same isoparametric curves can be physically interpreted as orientations having identical lattice properties, that is, the same Schmid factor for different crystallographic orientations. In the case of FCC crystal lattices, the analysis will be performed on a standard stereographic triangle-base, as shown in (Fig. IV.60).

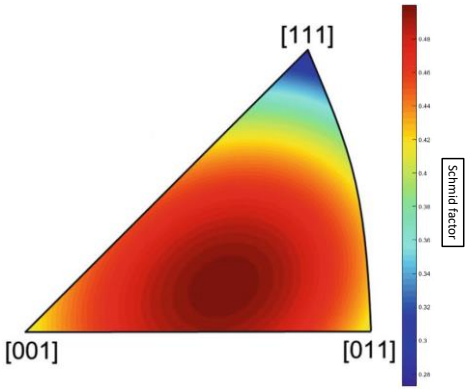

Figure IV.60. Standard stereographic triangle showing the maximum Schmid factor on any ⟨110⟩{111} slip system in a FCC crystal (Dingreville et al., 2017).

The interpolation of the stereographic triangle of crystallographic orientations of the coated specimens (Fig. IV.46), showing the isoparametrics corresponding to the primary Schmid factor is shown in (Fig. IV.61).

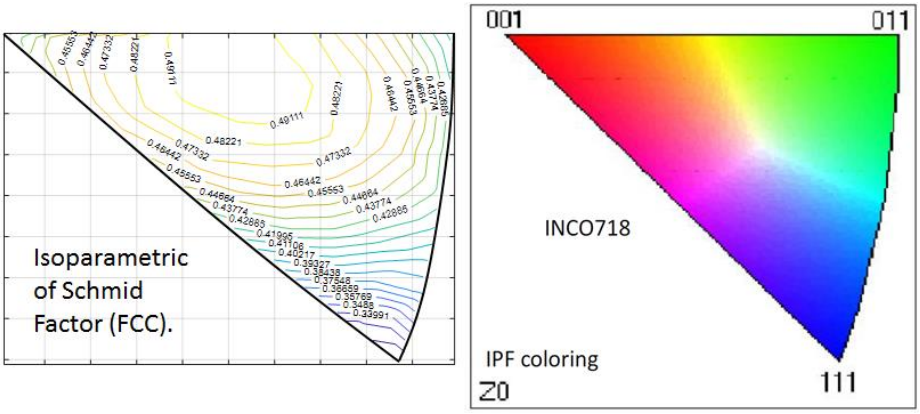

Figure IV.61. Isoparametric of the primary Schmid factors for an FCC crystal system with respect to the triangle of crystallographic orientations of the cladding specimens of (Fig. IV.46).

Based on (Fig. IV.61), it can be stated that at each grain orientation a primary Schmid factor value can be assigned (but not vice versa).

Once the Crystallographic Orientation-Primary Schmid Factor relationship is established in the microstructure, it is necessary to give this relationship a functional fractal shape.

The following is argued:

- The 2D projection of the cross-sections of the grains of the clad specimen samples are representative of the entire 3D microstructure of the material for a sufficient number of grains. This is based on the fractal surface-volume relationship of (Streitenberger et al., 1995), (Eq. IV.57):

$$S^{1/D} = \kappa V^{1/3} \qquad \textit{Eq. IV.57}$$

- The cross-sectional area of the grains in the images of the coated specimen samples presents a fractal behaviour in the case of textures generated by the Laser Cladding process.
- The contribution of a single grain to the overall strength of a material at a given stress will depend not only on its size (small grains are known to favour tensile strength in metals), but will also be affected by a favourable or unfavourable crystallographic orientation (which is related to the Schmid factor, $m_{i\ grain\_orientation}$).

Therefore, the variable that will serve as the basis for the proposed crystallographic orientation fractal model will be formulated as (Eq. IV.58):

$$S_{m\_i} = \left(A_{grain\_i}\right)\left(m_{i\ grain\_orientation}\right) \forall i = \{1...n\_grains\} \qquad \textit{Eq. IV.58}$$

The probability density function for the grain crystallographic orientation fractal (D_m) will be defined as (Eq. IV.59):

$$1 - P_{Sm\_i} = \left(\frac{S_{m\ \min}}{S_{m\_i}}\right)^{D_m} \qquad \textit{Eq. IV.59}$$

The method to determine the proposed fractal dimension of (Eq. IV.59) will follow the same procedure as (Eq. IV.54), since both cumulative distributions functions are similar. The results when using the proposed fractal model in the samples of the clad specimens of (Fig. IV.46), are shown in (Fig. IV.62).

Base material (D_m=3.0812, R^2=0.9876)

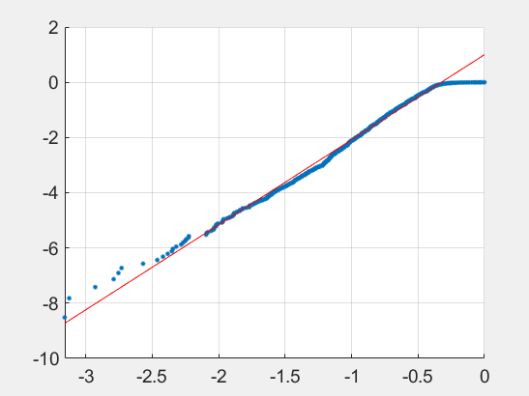

CC (D_m=1.2720, R^2=0.9859)

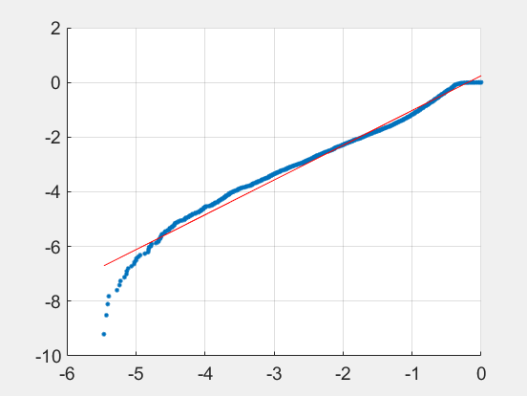

LZ (D_m=1.6144, R^2=0.9953)

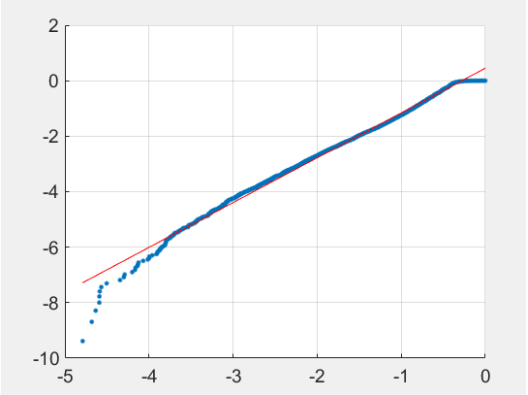

LZZ (D_m=1.5301, R^2=0.9929)

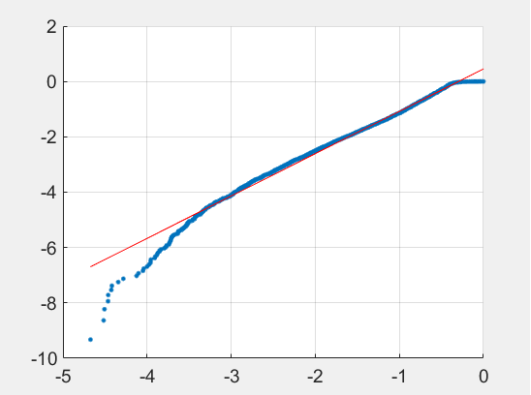

ZC (D_m=1.4560, R^2=0.9837)

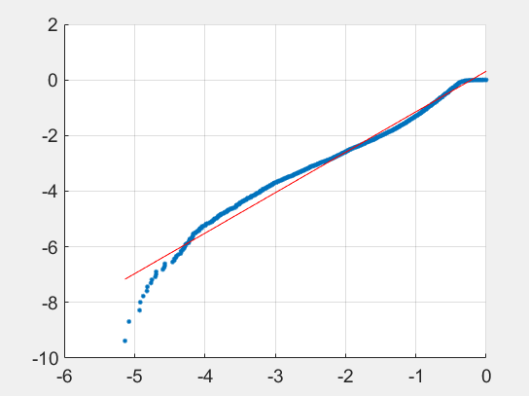

ZZC (D_m=1.4126, R^2=0.9875)

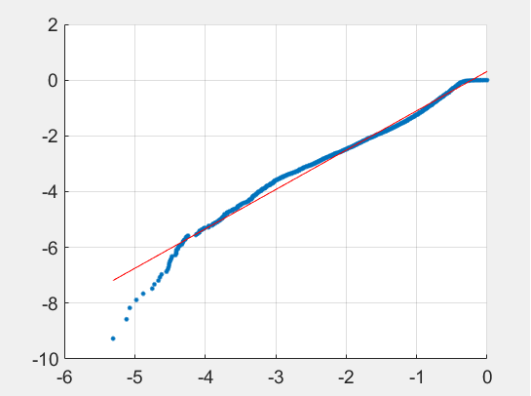

Graph IV.62. Evaluation of the proposed crystallographic fractal dimension (D_m), for different Laser Cladding deposition strategies and the base material (substrate). In red is shown the line for the least squares method fit to a linear function for the fractal dimension calculation, in blue the point cloud corresponding to the data obtained from the EBSD images of (Fig. IV.46).

The fractal D_m presents a good least squares coefficient of determination (R^2), and the difference in fractal values D_m between each deposition strategy and especially regarding the base material is very noticeable.

The application of the proposed fractal (D_m), can serve as an alternative to combine two important aspects of the microstructure in the mechanical properties: crystallographic orientation and grain area (and indirectly the volume of the grain).

4.4.2 Use of the Weibull Distribution as a Means of Characterising the Geometric Orientation of Grains in Coated Specimens.

The use of a statistical distribution is proposed as an alternative to the use of fractals to characterize a parameter of the microstructure which does not present the characteristics of fractal behaviour, the grain orientation.

Let be the geometric orientation of each grain, defined by angle (ϕ_{grain}), in a local frame of reference with fixed orientation with respect to some coordinate axes [x, y], as shown in (Fig. IV.63).

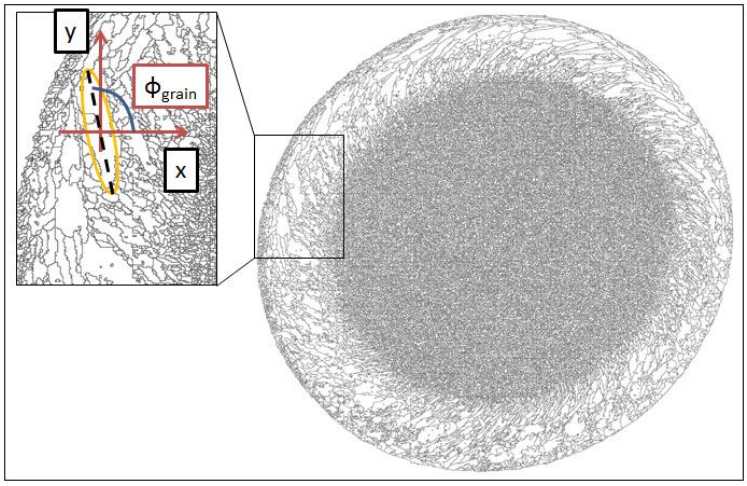

Figure IV.63. Example of geometric orientation of a grain with respect to the local reference frame [x, y] of invariable orientation (the x & y axes in any local grain frame remain parallel). The domain of ϕ_{grain} will be ($0 \leq \phi_{grain} < 180°$).

The distribution of measured values of angle ϕ_{grain} does not have a scaling mode as in the case of grain area or AR, but could be characterised by means of a suitable statistical distribution.

The use of the Weibull distribution (Weibull, 1961) is proposed because of its versatility, which can be used to model a wide variety of behaviours in the distribution of a data set,

with a minimum number of parameters through a relatively simple formulation (Eq. IV.60):

$$P(\phi) = 1 - \exp\left[-\left(\frac{\phi}{\phi_0} \right)^m \right] \qquad \textit{Eq. IV.60}$$

Where ϕ_0 is the angle for which the probability is $P(\phi_0) = 1 - 1/\exp(1) \approx 0.6321$. The coefficient of the "Weibull shape parameter" ($m = m_{\substack{Weibull \\ \phi\_shape}}$), will be the slope by linear fit of the graph described by the function of (Eq. IV.61):

$$\ln\left[\ln\left(\frac{1}{1 - P_i} \right) \right] = m \ln\left(\frac{\phi_i}{\phi_0} \right) \qquad \textit{Eq. IV.61}$$

The results when applying the proposed probability distribution of the geometric grain orientation are shown in (Fig. IV.64).

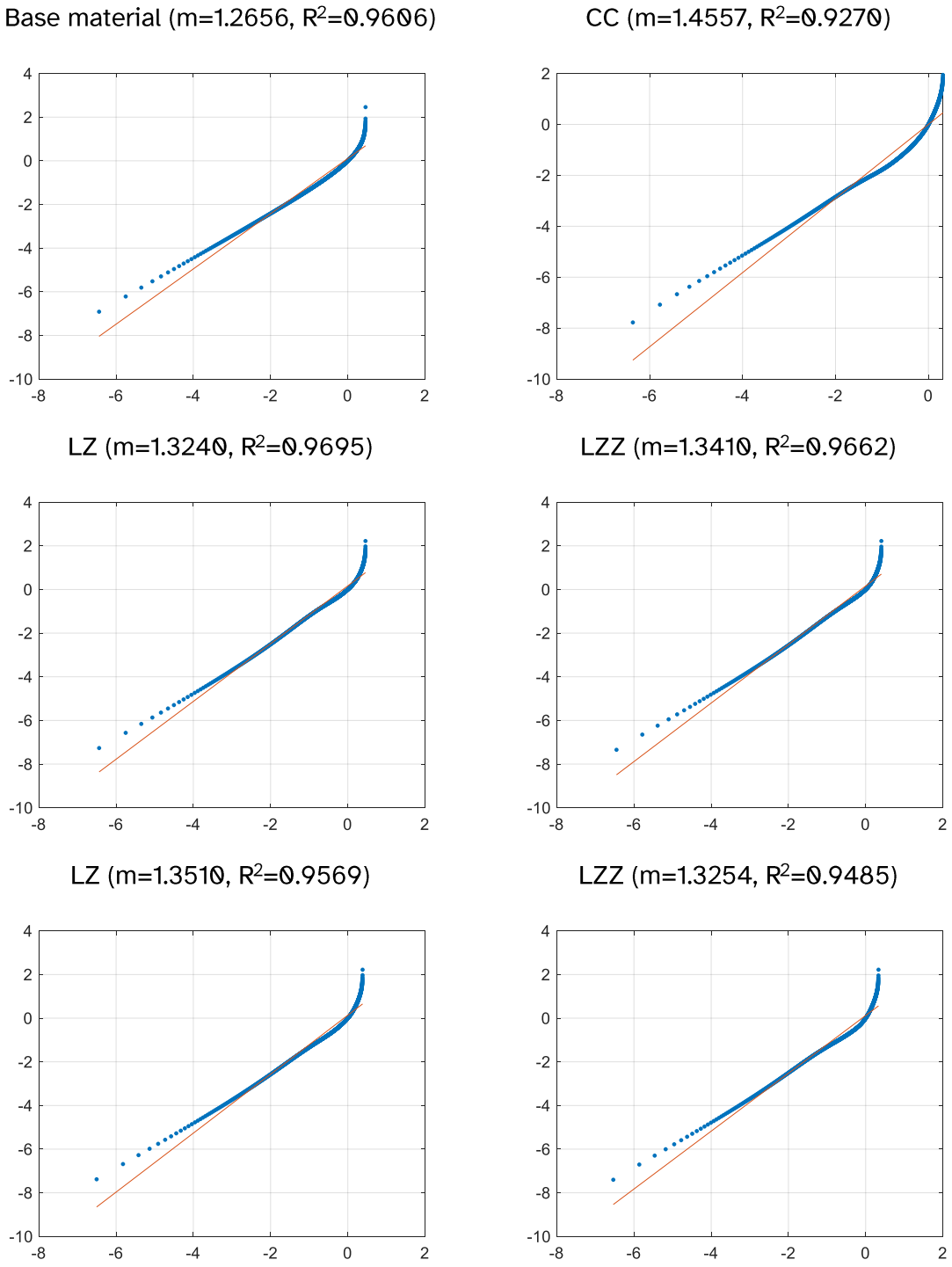

Figure IV.64. Evaluation of the proposed probability distribution $P(\phi)$ for geometric grain orientation for the different Laser Cladding strategies and the base material (substrate). The fit line (by the least squares method to a linear type function, shown in red) is used for the calculation of the "Weibull shape parameter" (m); in blue the point cloud corresponding to the data obtained from the EBSD images of the (Figure IV.46).

IV.4.5 Statistical Correlation of Mechanical Properties with Microstructure for Specimens Coated by the Laser Cladding Process.

Once all the sets of characterization values of the microstructure based on fractals and adjustment by means of Weibull's cumulative function distribution were obtained, an optimization and compromise software will be used to determine the relationships between the microstructure variables of the materials versus mechanical properties.

Similar to the process that has been used in (Chapter I.3.8), the software Lumière (Logiciel à Usage de Modélisation Industrielle Et de Recherche Expérimentale) will be used.

In addition, a set of constraints will be defined for the statistical modelling of the responses (desired mechanical properties), as a function of the inputs (fractal values and $m = m_{\substack{Weibull \\ \phi\_shape}}$ of the material texture).

There is the disadvantage of the limited number of "response" data from tests on specimens.

In the case of mechanical properties measured from the uniaxial tensile test, the available results are shown in (Table IV.21).

Table IV.21: Mechanical properties data obtained from uniaxial tensile tests on coated material and base material (substrate) specimens.

	Mechanical property			
Strategy	σ_{UT} (MPa)	σ_Y (MPa)	%E (%)	E_{clad} (GPa)
CC	1284.5	977.2	10.7	187.5
LZ	1346.3	1061.4	10.5	242.6
LZZ	1315.2	1014.4	9.5	232.1
ZC	1312.9	1032.6	8.4	225.0
ZZC	1346.7	1047.9	12.0	243.7
Base mat.	1287.0	1094.0	15.0	205.1

For coated and base material specimens subjected to uniaxial tensile fatigue testing, the data are shown in (Table IV.13, repeated).

Table IV.13, repeated: Endurance limits for infinite life for the CC, LZZ and ZZC strategies in specimens coated by the laser cladding process. Results also include specimens made only of base material. The value of σ_0 is obtained as a quantity derived from σ_{-1} and $\sigma_{0.1}$ (Eq. IV.45).

	Endurance Limit (Stress Amplitude)					
Strategy	σ_{-1}(MPa)		$\sigma_{0.1}$ (MPa)		σ_0 (MPa), derived from (Eq. IV.45).	
Base material	550.67	+/- 20.67	338.36	+/- 3.94	363.87	+/- 4.07
CC	361.13	+/- 2.32	258.22	+/- 10.34	272.33	+/- 9.41
LZZ	280.67	+/- 2.33	219.74	+/- 11.89	228.77	+/- 10.55
ZZC	404.40	+/- 28.88	271.41	+/- 14.25	288.67	+/- 13.46

For a Multiple Regression analysis, the number of sample data must be greater than or equal to the number of available equations that is required to model the process.

The minimum number of possible linear equations based on the use of all fractal parameters and statistical fitting will be six, as shown in the summary of material characterisation parameters in (Table IV.22).

Table IV.22: Summary of fractal and geometrical parameters to characterise the microstructure of different textures generated during a Laser Cladding process.

Material	D_l	D_S	D_R	D_G	D_m	$m_{Weibull\ \phi\_shape}$
Base material	2.7911	3.0308	3.9450	1.7684	3.0812	1.2656
CC	2.1320	2.6452	3.9240	1.6440	1.2720	1.4557
LZ	2.3354	2.8962	3.8770	1.6894	1.6144	1.3240
LZZ	2.2932	2.9060	3.8492	1.6883	1.5301	1.3410
ZC	2.3520	2.8867	3.8286	1.6523	1.4560	1.3510
ZZC	2.3913	2.9064	3.7889	1.6730	1.4126	1.3254

Due to the low amount of data available for fatigue tests, it was decided to model only the properties of the uniaxial stress test.

Normalized variables will be used in order to avoid the appearance of very high or low numerical correlation coefficients in the results of the linear regressions, in the same way as in (Chapter I.3.8). The normalization of the data will be calculated with the (Eq. IV.62):

$$x_{sv} = \frac{x - \bar{x}}{sd\left(x_{data\ i...n}\right)} \qquad \textit{Eq. IV.62}$$

The summary of the normalized (Table IV.21) and (Table IV.22) data is shown in (Table IV.23).

Table IV.23: Summary of standardized data of the microstructure characteristics and mechanical properties (based on the tension tensile test), in cladded and base material specimens.

Material	D_{l_sv}	D_{S_sv}	D_{G_sv}	$m_{shape\_W\_sv}$	D_{m_sv}	D_{R_sv}	σ_{Y_sv}	σ_{UT_sv}	$\%E_{sv}$	E_{clad_sv}
Base material	1.8615	1.2071	1.8564	-1.2543	2.0111	1.2959	1.2560	-1.0449	1.7352	-0.7889
CC	-1.1412	-1.8501	-0.9428	1.7955	-0.6771	0.9383	-1.5269	-1.1368	-0.1379	-1.5792
LZ	-0.2146	0.1399	0.0788	-0.3174	-0.1684	0.1395	0.4793	1.1344	-0.2251	0.8951
LZZ	-0.4068	0.2176	0.0540	-0.0447	-0.2936	-0.3329	-0.6405	-0.0086	-0.6607	0.4236
ZC	-0.1390	0.0646	-0.7560	0.1158	-0.4037	-0.6830	-0.2069	-0.0931	-1.1399	0.1048
ZZC	0.0401	0.2208	-0.2903	-0.2949	-0.4682	-1.3577	0.6389	1.1491	0.4284	0.9445

The requirements to be fulfilled for the statistical modelling of σ_{Y_sv}, σ_{UT_sv}, $\%E_{sv}$ and E_{clad_sv} will be:

- The confidence level is defined at 95%, with a minimum of 2.5% and a maximum of 97.5%.
- The maximum level of risk for the coefficients will be 10%.
- The correlation coefficient will be set to a minimum of 0.985

IV.4.5.1 Correlation Matrices of Variables and Linear Regression Models of Mechanical Properties.

The summary with the results of the model for the mechanical properties will be presented in different tables according to the modelled property.

The results for the variable σ_{Y_sv} (options 1 and 2) are shown in (Table IV.24) and (Table IV.25). It has not been possible to comply with some of the restrictions that were established in the case of the model for the Yield strength property, and therefore more than one possible fitting option was calculated.

The (Table IV.26) and (Table IV.27) show the results for the variables σ_{UT_sv}, $\%E_{sv}$ and E_{clad_sv}.

Table IV.24: Correlation matrix for the variables to be modelled, with a confidence level of 95% with a range of [2.5% 97.5%], for the Yield strength property.

Multiple Linear Regression

Defined Confidence Level: 95.00 %.

Correlation matrix

Significant correlations at 95.00 %
r = 0.8114 (6 - 2)

	Fra_DS#	mW_fi#	Fra_DG#*Fra_Dm#	mW_fi#*Fra_Dm#
Fra_DS#	1			
mW_fi#	-0.9895	1		
Fra_DG#*Fra_Dm#	0.4619	-0.4848	1	
mW_fi#*Fra_Dm#	-0.1416	0.1714	-0.9394	1

Range of variation of the Factors

Factors to consider	Minimum	Average	Maximum	Standard deviation
Fra_Dl	-1.1412	0	1.8615	1
Fra_DS	-1.8501	0	1.2071	1
Fra_DG	-0.9428	0	1.8564	1
mW_fi	-1.2543	0	1.7955	1
Fra_Dm	-0.6771	0	2.0111	1
Fra_DR	-1.3577	0	1.2959	1

The control statistics for the Multiple Linear Regressions are presented below. In all cases, the correlation coefficient (R) will be assumed to be valid for values> = 0.985, with risks for each variable less than 10% and without the use of “constants” in any of the linear correlations.

Table IV.25: Regression matrices with control statistics for the variables of the Yield strength property from uniaxial tensile tests on cladded specimens.

Regression of σ_Y (option 1)

Individual sample Frac_Dl#

Summary of Coefficients

Table with the residual standard deviation.
Sr = 0.2532 - Nur = 4

Variable	Coefficient	Standard deviation	t Student	Confidence %	Risk %	Centring
Fra_DS#	-1.994	0.7847	-2.541	93.61	6.39	Non
mW_fi#	-2.9037	0.7847	-3.7002	97.92	2.08	Non

Confidence Interval 95%

Variable	Coeff	Mini (2.50 %)	Maxi (97.50 %)
Fra_DS#	-1.994	-4.1727	0.1848
mW_fi#	-2.9037	-5.0824	-0.7249

Decomposition of the sum of squares

Source	Sum of the squares	Ddl	Medium	Fisher	Confidence	Risk %

			Square		%	
Regression	4.7436	2	2.3718	36.9957	99.74	0.26
Residues	0.2564	4	0.0641			
Total	5	6	0.8333			
Correlation coefficient (R):	0.9740					
Residual Standard deviation Sr :	0.2532	Ddl	4			

Analysis of Effects Contributions.

Effects	Contributions	%
Fra_DS#	-8.7665	-175.33
mW_fi#	13.5101	270.2
Residues	0.2564	5.13
Total	5	100

Regression of σ_Y (option 2)

Individual sample Frac_Dl#

Summary of Coefficients

Table with the residual standard deviation.
Sr = 0.4987 - Nur = 4

Variable	Coefficient	Standard deviation	t Student	Confidence %	Risk %	Centring
Fra_DG#*Fra_Dm#	1.7446	0.445	3.9206	98.28	1.72	-

mW_fi#*Fra_Dm#	2.108	0.6033	3.4942	97.5	2.5	-

Confidence Interval 95%

Variable	Coeff	Mini (2.50 %)	Maxi (97.50 %)
Fra_DG#*Fra_Dm#	1.7446	0.5091	2.9801
mW_fi#*Fra_Dm#	2.108	0.433	3.7831

Decomposition of the sum of squares

Source	Sum of the squares	Ddl	Medium Square	Fisher	Confidence %	Risk %
Regression	4.0051	2	2.0026	8.0517	96.04	3.96
Residues	0.9949	4	0.2487			
Total	5	6	0.8333			
Correlation coefficient (R):	0.8950					
Residual Standard deviation Sr :	0.4987	Ddl	4			

Analysis of Effects Contributions.

Effects	Contributions	%
Fra_DG#*Fra_Dm#	6.5283	130.57
mW_fi#*Fra_Dm#	-2.5232	-50.46
Residues	0.9949	19.9
Total	5	100

Table IV.26: Correlation matrix of the variables to be modelled, with a confidence level of 95% with a range of [2.5% 97.5%].

Multiple Linear Regression

Defined Confidence Level: 95.00 %.

Correlation matrix
Significant correlations at 95.00 %
r = 0.8114 (6 - 2)

	Frac_Dl#	Fra_DS#	Fra_DG#	mW_fi#	Fra_Dm#	Frac_DR#
Frac_Dl#	1					
Fra_DS#	0.848	1				
Fra_DG#	0.9172	0.779	1			
mW_fi#	-0.8651	-0.9895	-0.8101	1		
Fra_Dm#	0.9419	0.6927	0.9568	-0.7161	1	
Frac_DR#	0.2975	-0.1137	0.4849	0.0702	0.5913	1

Range of variation of the Factors

Factors to consider	Minimum	Average	Maximum	Stand. deviation
Fra_DL	-1.1412	0	1.8615	1
Fra_DS	-1.8501	0	1.2071	1
Fra_DG	-0.9428	0	1.8564	1
mW_fi	-1.2543	0	1.7955	1
Fra_Dm	-0.6771	0	2.0111	1
Fra_DR	-1.3577	0	1.2959	1

The control statistics for the Multiple Linear Regressions are presented below. In all cases, the correlation coefficient (R) will be assumed to be valid for values> = 0.985, with risks for each variable less than 10% and without the use of “constants” in any of the linear correlations.

Table IV.27: Regression matrices with control statistics for the variables of the mechanical properties from uniaxial tensile tests on cladded specimens.

Regression of σ_{UT}

Individual sample Frac_Dl#

Summary of Coefficients

Table with the residual standard deviation.
Sr = 0.0334 - Nur = 3

Variable	Coefficient	Standard deviation	t Student	Confidence %	Risk %	Centring
Fra_DS#	-2.7352	0.1047	-26.1225	99.99	0.01	Non
mW_fi#	-3.9554	0.1082	-36.5601	100	0	Non
Fra_Dm#	-1.3418	0.0216	-61.9883	100	0	Non

Confidence Interval 95%

Variable	Coeff	Mini (2.50 %)	Maxi (97.50 %)
Fra_DS#	-2.7352	-3.0685	-2.402
mW_fi#	-3.9554	-4.2997	-3.6111
Fra_Dm#	-1.3418	-1.4107	-1.2729

Decomposition of the sum of squares

Source	Sum of the squares	Ddl	Medium Square	Fisher	Confidence %	Risk %
Regression	4.9967	3	1.6656	1496.3736	100	0
Residues	0.0033	3	0.0011			
Total	5	6	0.8333			
Correlation coefficient (R):	0.9997					
Residual Standard deviation Sr :	0.0334	Ddl	3			

Analysis of Effects Contributions.

Effects	Contributions	%
Fra_DS#	-3.4094	-68.19
mW_fi#	5.6948	113.9
Fra_Dm#	2.7112	54.22
Residues	0.0033	0.07
Total	5	100

Regression of %Elongation

Individual sample Frac_Dl#

Summary of Coefficients

Table with the residual standard deviation.

Sr = 0.2581 - Nur = 2

Variable	Coefficient	Standard deviation	t Student	Confidence %	Risk %	Centring
Frac_Dl#	1.0519	0.3466	3.0346	90.64	9.36	Non
Fra_DS#	-2.0678	0.4499	-4.5963	95.58	4.42	Non
Fra_DG#	1.9296	0.498	3.8744	93.94	6.06	Non
Frac_DR#	-0.9828	0.3009	-3.2665	91.77	8.23	Non

Confidence Interval 95%

Variable	Coeff	Mini (2.50 %)	Maxi (97.50 %)
Frac_Dl#	1.0519	-0.4396	2.5434
Fra_DS#	-2.0678	-4.0036	-0.1321
Fra_DG#	1.9296	-0.2133	4.0726
Frac_DR#	-0.9828	-2.2774	0.3118

Decomposition of the sum of squares

Source	Sum of the squares	Ddl	Medium Square	Fisher	Confidence %	Risk %
Regression	4.8668	4	1.2167	18.2637	94.74	5.26
Residues	0.1332	2	0.0666			
Total	5	6	0.8333			
Correlation coefficient (R):	0.9866					
Residual Standard deviation Sr :	0.2581	Ddl	2			

Analysis of Effects Contributions.

Effects	Contributions	%
Frac_Dl#	4.0816	81.63
Fra_DS#	-4.5399	-90.8
Fra_DG#	7.7867	155.73
Frac_DR#	-2.4617	-49.23
Residues	0.1332	2.66
Total	5	100

Regression of E_{clad}

Individual sample Frac_Dl#

Summary of Coefficients

Table with the residual standard deviation.

Sr = 0.1753 - Nur = 4

Variable	Coefficient	Standard deviation	t Student	Confidence %	Risk %	Centring
mW_fi#	-1.3668	0.1123	-12.169	99.97	0.03	Non
Fra_Dm#	-1.2341	0.1123	-10.9875	99.96	0.04	Non

Confidence Interval 95%

Variable	Coeff	Mini (2.50 %)	Maxi (97.50 %)

mW_fi#	-1.3668	-1.6786	-1.055
Fra_Dm#	-1.2341	-1.5459	-0.9223

Decomposition of the sum of squares

Source	Sum of the squares	Ddl	Medium Square	Fisher	Confidence %	Risk %
Regression	4.8771	2	2.4385	79.3464	99.94	0.06
Residues	0.1229	4	0.0307			
Total	5	6	0.8333			
Correlation coefficient (R):	0.9876					
Residual Standard deviation Sr :	0.1753	Ddl	4			

Analysis of Effects Contributions.

Effects	Contributions	%
mW_fi#	3.3014	66.03
Fra_Dm#	1.5757	31.51
Residues	0.1229	2.46
Total	5	100

Not all correlation models comply with all the restrictions that were proposed.

- Correlation 1 for σ_{Y_sv} : presents problems in the level of risk in the Fra_DS variable (D_S), and the correlation coefficient (R) is less than 0.985.
- Correlation 2 for σ_{Y_sv} : presents problems in the correlation coefficient (R), as it is lower than 0.985.
- Correlation for $\%E_{sv}$: presents problems in the risk level of the variables Fra_Dl (D_l), Fra_DG (D_G) and Fra_DR (D_R).

Due to restrictions on the amount of information from available trials, statistically significant correlations cannot be guaranteed with the restrictions that were imposed. However, it is possible to know if the variables that were selected to model the microstructure are adequate, using a normality test for the residues (Mohd Razali and Yap, 2011). The results of the calculation to verify the normality between the error generated by the correlation model of mechanical properties and the experimental data of the uniaxial tensile tests (in the clad and the base material specimens), together with the histograms corresponding to each error of the modelled property, are shown in (Table IV.28).

Table IV.28: Results of the Shapiro and Wilk hypothesis tests for the error between the modelled variables of (Table IV.23) and the data of (Table IV.24) to (Table IV.27).

Adequacy to a Normal Law

CHARACTERISTICS OF THE SAMPLE
Error σ_Y (correlation option 1)

Defined Confidence Level: 95.00%.

Number of observations:	Average:	Standard deviation:	D.D.L.:
6	0	0.2264	5

Normality Test: SHAPIRO AND WILK

Calculated Statistics	Law	Confidence %	Risk (alpha)%
0.9583	Normal Distribution	15.6935	84.3065

The distribution is not significantly different from a normal distribution.

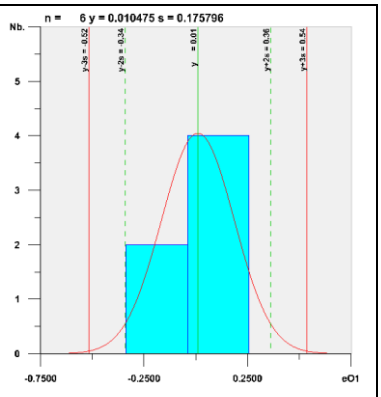

Adequacy to a Normal Law

CHARACTERISTICS OF THE SAMPLE
Error σ_Y (correlation option 2)

Defined Confidence Level: 95.00%.

Number of observations:	Average:	Standard deviation:	D.D.L.:
6	-0.1331	0.4216	5

Normality Test: SHAPIRO AND WILK

Calculated Statistics	Law	Confidence %	Risk (alpha)%
0.9019	Normal Distribution	58.673	41.327

The distribution is not significantly different from a normal distribution.

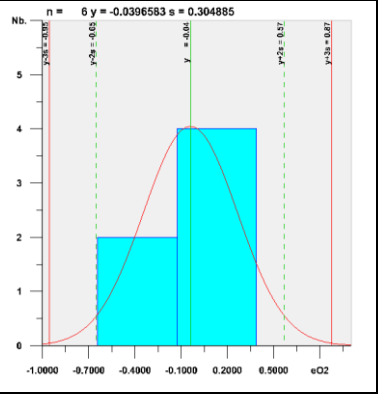

Adequacy to a Normal Law

CHARACTERISTICS OF THE SAMPLE
Error σ_{UT}

Defined Confidence Level: 95.00%.

Number of observations:	Average:	Standard deviation:	D.D.L.:
6	0	0.0258	5

Normality Test: SHAPIRO AND WILK

Calculated Statistics	Law	Confidence %	Risk (alpha)%
0.9319	Normal Distribution	35.8933	64.1067

The distribution is not significantly different from a normal distribution.

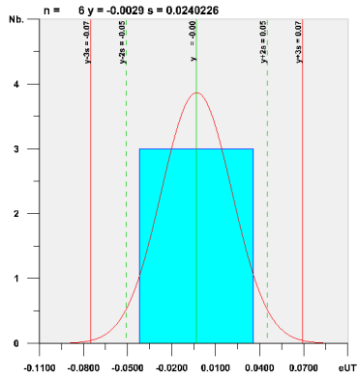

Adequacy to a Normal Law

CHARACTERISTICS OF THE SAMPLE
Error %Elongation

Defined Confidence Level: 95.00%.

Number of observations:	Average:	Standard deviation:	D.D.L.:
6	0	0.1632	5

Normality Test: SHAPIRO AND WILK

Calculated Statistics	Law	Confidence %	Risk (alpha)%
0.9271	Normal Distribution	39.7357	60.2643

The distribution is not significantly different from a normal distribution.

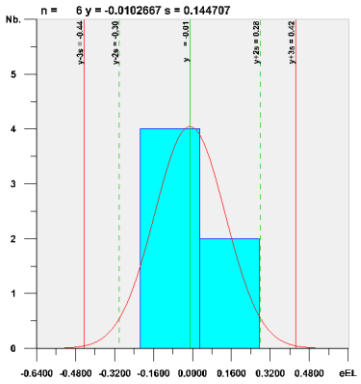

Adequacy to a Normal Law

CHARACTERISTICS OF THE SAMPLE
Error E_{clad}

Defined Confidence Level: 95.00%.

Number of observations:	Average:	Standard deviation:	D.D.L.:
6	0	0.1568	5

Normality Test: SHAPIRO AND WILK

Calculated Statistics	Law	Confidence %	Risk (alpha)%
0.8922	Normal Distribution	64.9114	35.0886

The distribution is not significantly different from a normal distribution.

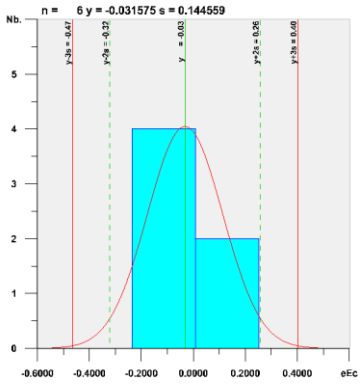

The results in (Table IV.28) indicate that all variables for characterising the microstructure and predicting the mechanical behaviour of a coating material are significant.

IV.4.6 Analysis of Results and Conclusions from the Correlations found Between Microstructure and Mechanical Properties in a material Deposited by Laser Cladding Process.

Some conclusions based on multiple regression models found that relate the fractal and Weibull dimension characteristics of the coated and base material specimens to the mechanical properties obtained from uniaxial tensile tests are:

- Some variables model the microstructure more frequently than others. Not all fractal or Weibull dimensions appear with the same frequency in the statistical correlations, as shown in (Fig. IV.65).

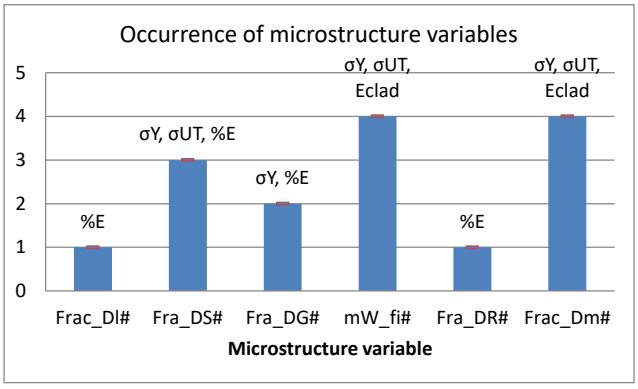

Figure IV.65. Frequency of occurrence of variables in models of the mechanical properties of a cladding material. Each variable frequency bar indicates the mechanical property where it is used in the statistical correlation models.

- The mechanical properties of a cladding material that can be best correlated with the microstructure through the fractal dimension and Weibull distribution are σ_{UT} and E_{clad}. At the intermediate level is σ_Y, and the most difficult to model is $\%E$.
- The mechanical properties that best correlate with the microstructure (through modelling using fractal dimensions and Weibull distribution) are important in fatigue life (Section IV.2.2.1 Basic Background on Fatigue Life for High Number of Cycles in Metallic Materials). Therefore, the use of fractal dimensions and Weibull distribution can be a viable alternative in the modelling of fatigue-related properties in Laser Cladding materials.
- Fractal dimension D_m and Weibull dimension $m_{\substack{Weibull \\ \phi\_shape}}$ are the statistical correlation variables with the highest frequency of occurrence. Therefore, their usefulness as a way to characterise the microstructure of the material deposited by the Laser Cladding process is demonstrated.

IV.4.7 Qualitative Verification of the Methodology for Characterising the Fatigue Life of Specimens Coated by the Laser Cladding Process.

The number of combinations of different deposition strategies for the coated specimens (including also the base material), used in the fatigue tests, has not provided sufficient data to create a statistical model that correlates the microstructure characteristics with the fatigue strength life.

Only 8 fatigue strength endurance limit values are available, all obtained from a series of specimens, as shown in (Table IV.13). However, it is possible to use the proposed base variable of the fractal dimension of crystallographic orientation S_{m_i}, (Eq. IV.58), as a method to indirectly verify the model to evaluate the fatigue endurance limit of coated specimens using the Dang Van criterion (Section IV.4).

The proposed qualitative method is based on image comparison and will consist of:

- Calculate the data for a set of grains (with (Eq. IV.58)), for Schmid factors for the primary slip systems for FCC crystals in the range 0.48 to 0.5. The range mentioned previously is considered as critical unfavourable values.
- Draw on the grain microstructure obtained from the EBSD images of the cross sections of the coated specimen samples (Figure IV.46), the grains with critical S_{m_i} fractal value (in an appropriate and standardised colour scale).
- Compare the fractographs of the specimens subjected to fatigue test with that of the previous mentioned critical grain structure (according to the data calculated from S_{m_i}). The objective is to determine by visual inspection if there is any similarity between the crack propagation zones on the coated specimens, with those predicted as a whole by the model of (IV.4 Microstructure/Mechanical Properties Correlation Model for Coated Specimens).

The idea is to compare the “high stress” zones at grain level according to the Dang Van criterion versus “the base variable” for the fractal dimension of crystallographic orientation (S_{m_i}). That means superimposing the magnitude of the "maximum stress" for a certain area within the grain structure, with the tendency of the grains to slip based on data calculated from the fractal variable S_{m_i}.

The (Fig. IV.66) shows the areas with the highest “stress” according to the Dang Van criterion at the grain level (left column). The representation of the grains with S_{m_i} fractal value close to the critical one according to the fractal of crystallographic orientation is shown in the centre and on the right a pair of typical photomicrographs of the fracture cross-section of the cladding specimens testing in fatigue.

Because the variation in the stress inside the cladded specimen (according to the model of IV.2.5 Validation of the Analytical Model of the Stress Field Magnitude for a Coated Specimen) is significant only in the zone of the substrate-coating interface. The representation of the critical grains according to the fractal S_{m_i} was been drawn only for the outer area of EBSD images of the cross-sections of the cladding samples.

Comparison of images for the CC strategy. The figures show that the highest stress at the grain level (according to Dang Van's criteria), is found in the inner zone of the coated specimen (left) and the most critical grains in the intermediate zone of the coating. Therefore, the failure is expected to start in the inner zone of the coating, near the interface with the substrate. The images to the right show two examples of fractographs of specimens coated with CC strategy. Circles in red indicate the area from which the crack has propagated.

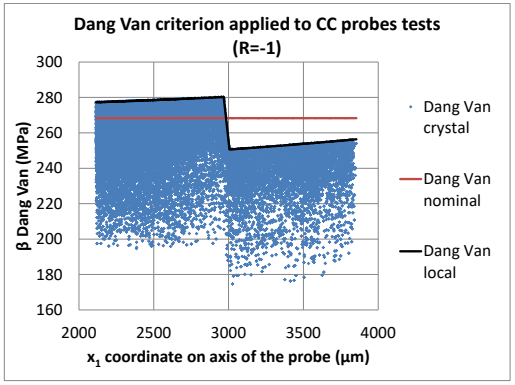

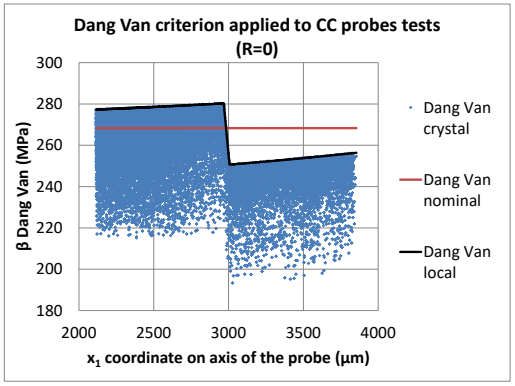

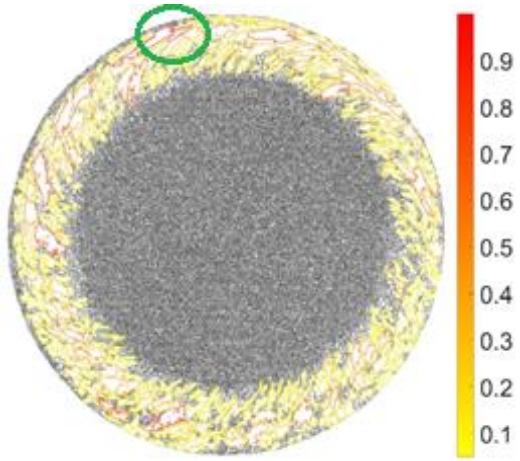

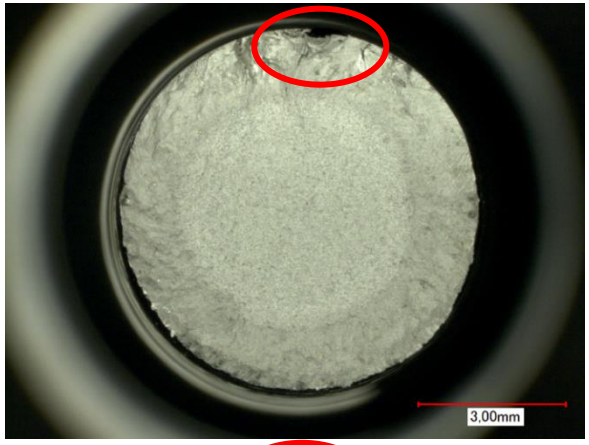

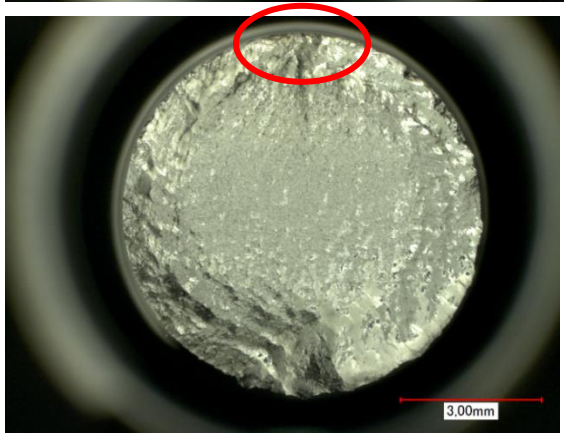

Image comparison for the LZZ strategy. The figures show that the highest stress at the grain level (according to Dang Van's criteria) is found in the outer zone of the coated specimen (left) and the most critical grains in the intermediate zone of the coating. Therefore, the failure is expected to start in the outer region of the coating, near the surface of the coating. The images to the right show two examples of fractographs of specimens coated with the LZZ strategy. Circles in red indicate the area from which the crack has propagated.

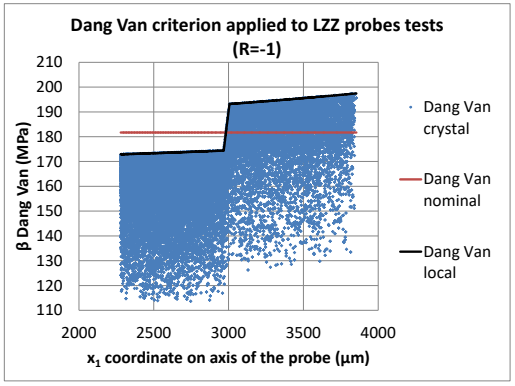

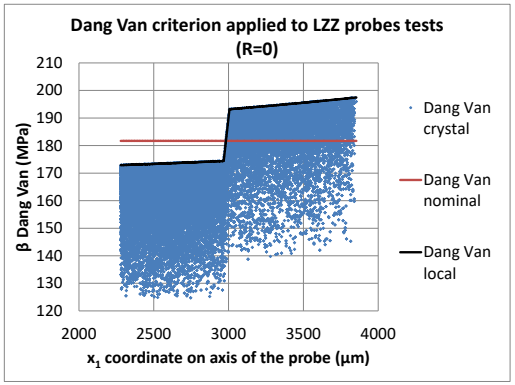

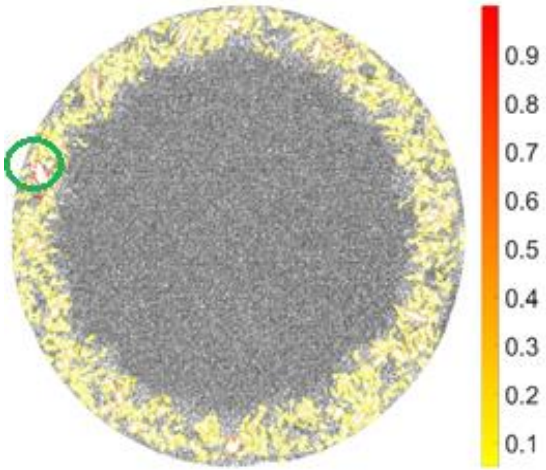

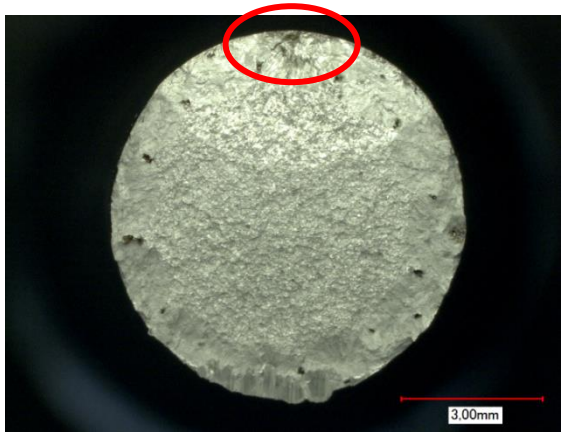

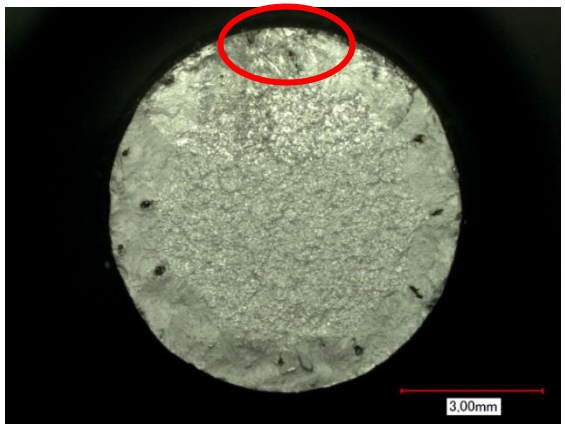

Comparison of images for the ZZC strategy. The figures show that the highest stress at the grain level (according to Dang Van's criteria), is found in the outer area of the coated specimen (left) and the most critical grains in the outer area of the coating. Therefore, it is expected

that the failure begins in the outer zone of the coating, on the surface of the coating. The images to the right show two examples of fractographs of specimens coated with the ZZC strategy. Circles in red indicate the area from which the crack has propagated.

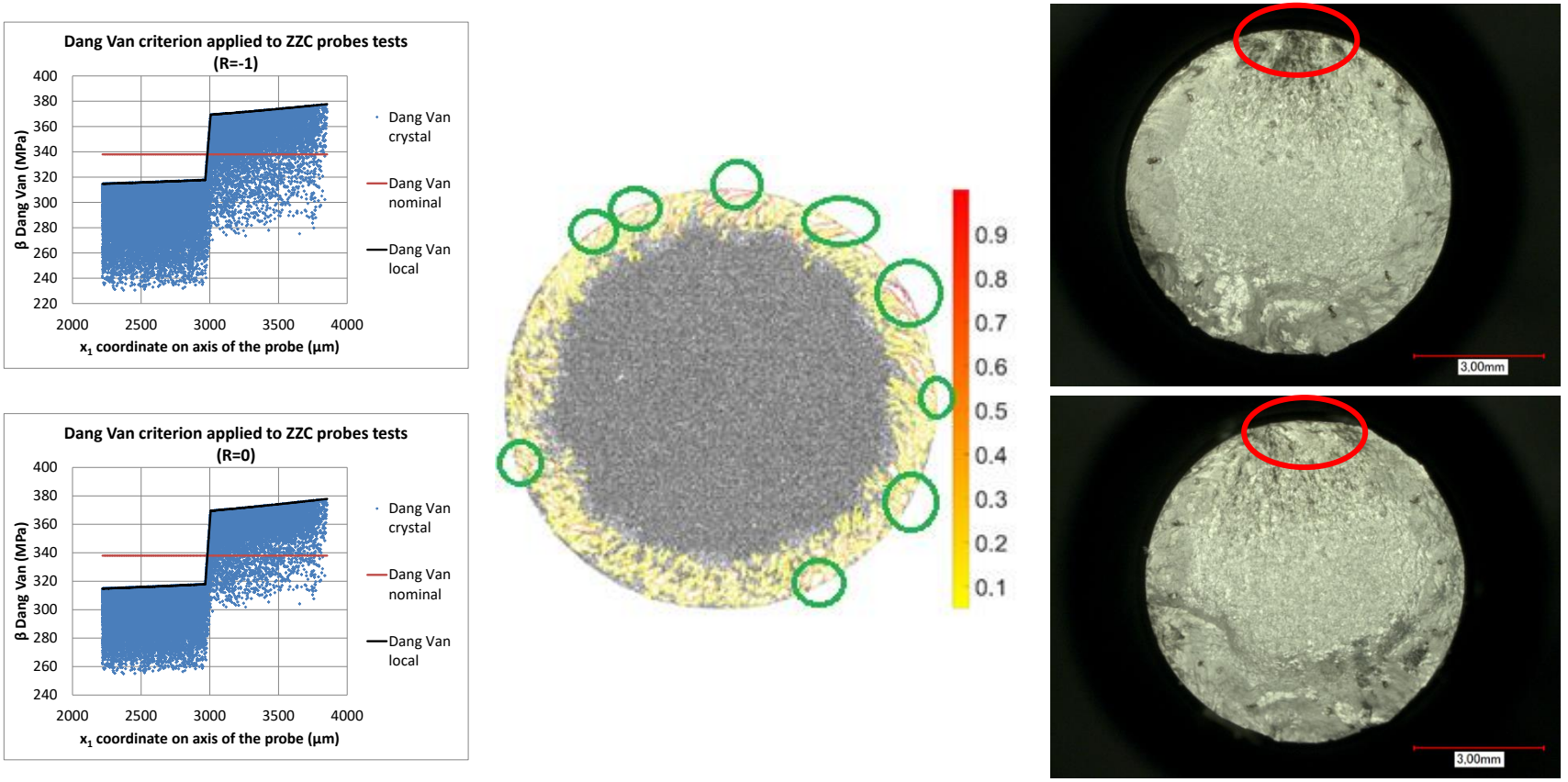

Figure IV.66. Graphics to qualitatively verify the validity of the Dang Van criteria (at the level of crystal), and the fractal model for crystallographic orientation in samples coated by the Laser Cladding process. The colour scale in the central images is relative, with the value 1 (red), indicating the grains with the most unfavourable crystallographic orientation fractal dimension.

IV.4.7.1 Results of the Quantitative Evaluation of the Crystallographic Orientation fractal S_{m_i}

- Qualitatively, the evaluation of the fracture in coated specimens as a function of the base variable of the crystallographic orientation fractal (S_{m_i}) has correctly located the zone of crack propagation in the specimens. However, its precision has been affected by the existence of small defects within the coating of the probe, specifically lack of fusion of the metal powder. The origin of the defects is unknown, although it is speculated that it was been a defect in the cladding machine, since not all the specimens have presented pore defects.
- Based on the observation of the fractographs, the shape of crack propagation is different depending on the cladding strategy used; therefore, taking into account the texture of the microstructure is important for predicting the zone most prone to fracture.
- A greater number of tests based on design of experiments is necessary to be able to precisely adjust the fractal method by crystallographic orientation that was proposed.

CHAPTER V: GENERAL CONCLUSIONS

Chapter I: parameter optimization for the laser cladding process.

- The design of experiments is applicable to the additive manufacturing method by laser cladding for the search for optimal process parameters.
- The use of fourth degree polynomials is adequate to describe the geometric shapes of a filler bead.
- The process of optimization of input parameters will be restricted not only by the geometry of the bead, but also by metallurgical considerations, a set of optimal parameters at a geometric level can result in low-quality added material due to the appearance of undesirable phases.
- There is no absolute optimum in the search for parameters of the laser cladding process; sometimes a compromise solution is necessary.
- Basic research in the laser cladding process can be directly applied in finding solutions for industry.

Chapter II: microstructure characterization of new and recycled in718 powder and resulting laser cladding material.

- Some particles react under the influence of the energy source and spinel type oxides appear. However, there are two variables affecting positively the option of recycling the powder: On one hand the scarce amount of non-desirable phases, estimated to be lower than 2% of the recollected powder and, on the other hand the possibility of segregating magnetically these phases from the rest of the powder.
- The chemical composition of the recycled powder is similar to the raw material and complies with the standard specifications for the INCO 718 material. Two parameters can limit the reuse of recycled powders: oxygen and niobium content. The recycled powder size distribution is mainly centred on a slightly high mean value.
- The builds show no difference in chemical composition or in the different phases depending on the number of reuse. On the other hand, the microstructure evolves towards a columnar structure with a very marked crystallographic orientation (111). The static properties of the recycled builds are similar to those of the new

powder builds for a limited reuse number (2). Beyond this value, the breaking strain decreases sharply and becomes a limiting factor.

- It should be remarked that in this process of reusing the powder, there is no need of adding new material to obtain good quality samples but at the difference with other additive manufacturing processes (EBM or SLM), the reuse of the recycled powder is limited to 2 reuses. The implementation of this step of removing non-desirable phases allows the improvement of the final efficiency, reducing costs and decreasing the hazardous powder amount.

Chapter III: modelling of laser cladding process and grain morphology.

- An analytical model for the Laser Cladding process has been proposed. The model takes into account the main parameters, and “develops” the effect of each of them independently so that it is possible to separate the consequences of each parameter separately.
- The model takes into account the attenuation of the energy supplied by the laser beam on the surface due to the shadow effect of the powder (delivered by a coaxial nozzle), taking into account the effect of drag velocity because the protective gas.
- An iterative methodology has been proposed to define the temperature dependent properties for the energy balance in the metallic powder interacting with the laser beam, and thus obtain a more accurate energy balance for the substrate (via negative enthalpy).
- In the application of the Laser Cladding model for the calculation of the thermal field in the substrate, a general solution in a steady stable state was used. In the calculation of the thermal field a methodology has been proposed to be able to make the solution “dependent” on the thermal properties of the material, which helped to calculate accurately the temperature values within the melt pool, taking into account the change of phase, and therefore to calculate the values of temperature to determine the thermal gradient.
- The calculation of the thermal gradient together with the growth velocity in the solidification front was used as input variables to determine the CET behaviour of an alloy. To model the CET behaviour of an alloy, it is proposed the use of a solidification model based on experimental Solidification Maps combined with the behaviour of a Gumbel’s probability distribution.

- The use of a deterministic model for columnar/equiaxed grain formation is justified by the difficulty of modelling the behaviour of a multicomponent alloy. The relationship between the CET-model and the experimental-type solidification maps that served as basis has been established.
- The proposed model allows: extend the range of application of the base model to values of low solidification speeds, intuitively explain the CET behaviour in the mixed zone (the behaviour is modelled based on a well-known probability distribution), and determine in a unique way with a physical sense the constants of material for other models taking advantage of the information contained in experimental solidification maps.
- A method is included to obtain an estimate for the number of nucleation sites per unit volume, and it is concluded that this value is highly dependent on the solidification process involved. For Laser Cladding process, its value is very high compared to traditional casting processes, due mainly to temperature gradients.
- The model was tested by means of an experimental essay where different types of raw material (new metallic powder and reconditioned metallic powder to be recycled again), are used to build specimens that were analysed by means of EBSD images. The results of the powder solidification CET morphology are compared with both the proposed model for Laser Cladding and proposed model for CET crystallization, with good correlation between the predictions and the experimental results.

Chapter IV: application to the repair of coated probes to obtain mechanical properties in cladding material.

- There is a wide variety of configurations for the design of coated specimens; however, most proposals do not take into account the variation in mechanical properties of the material added in the laser cladding process.
- There is no direct relationship between mechanical properties obtained from a uniaxial tensile test and the properties of resistance to fatigue in the case of coated specimens.
- Not all coated specimen designs are equally valid for evaluating mechanical properties observed in cladded material.
- The use of specimens with normalized geometry is possible for the evaluation of the mechanical properties of a material added by laser cladding, in addition to allowing the comparison of results with previous tests.

- The field of tension inside coated specimens has a great influence on the evaluation of mechanical properties.
- Dang Van's fatigue criterion is a suitable tool to model the behaviour of a material added by laser cladding taking into account the microstructure.
- Different material deposition strategies have different sensitivity to fatigue failure.
- The use of fractals is a suitable method to characterize the microstructure of specimens coated by the laser cladding process.
- Of various types of fractals available to characterize microstructure, those that take crystallographic orientation into account appear most frequently in correlations between microstructure and mechanical properties in the case of material added by the laser cladding process.
- Statistical distributions are a useful tool for relating microstructure to mechanical properties in laser cladding process.

ANNEXES

1. Drawing of coated specimen for uniaxial tensile test

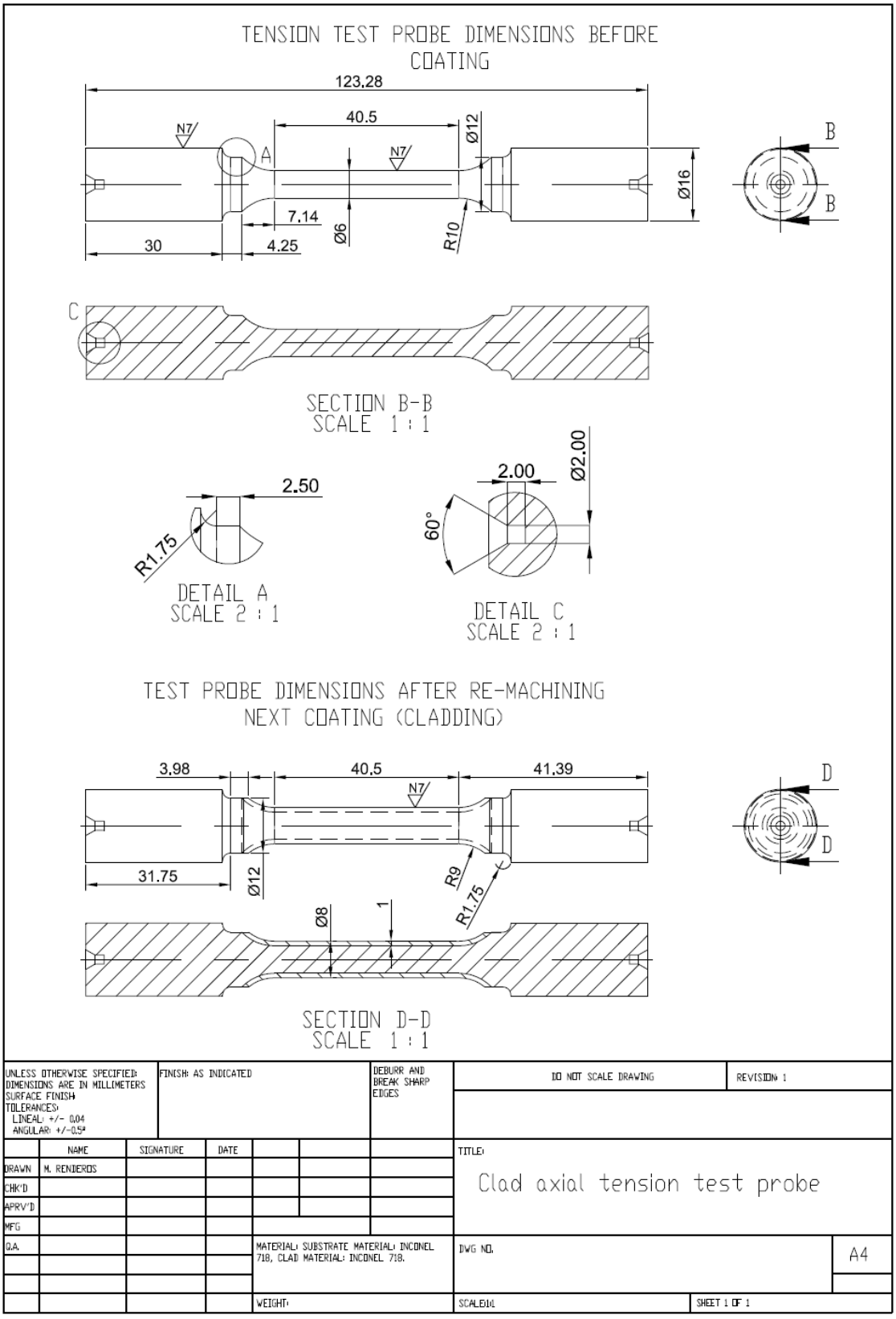

2. Drawing of coated specimen for fatigue testing

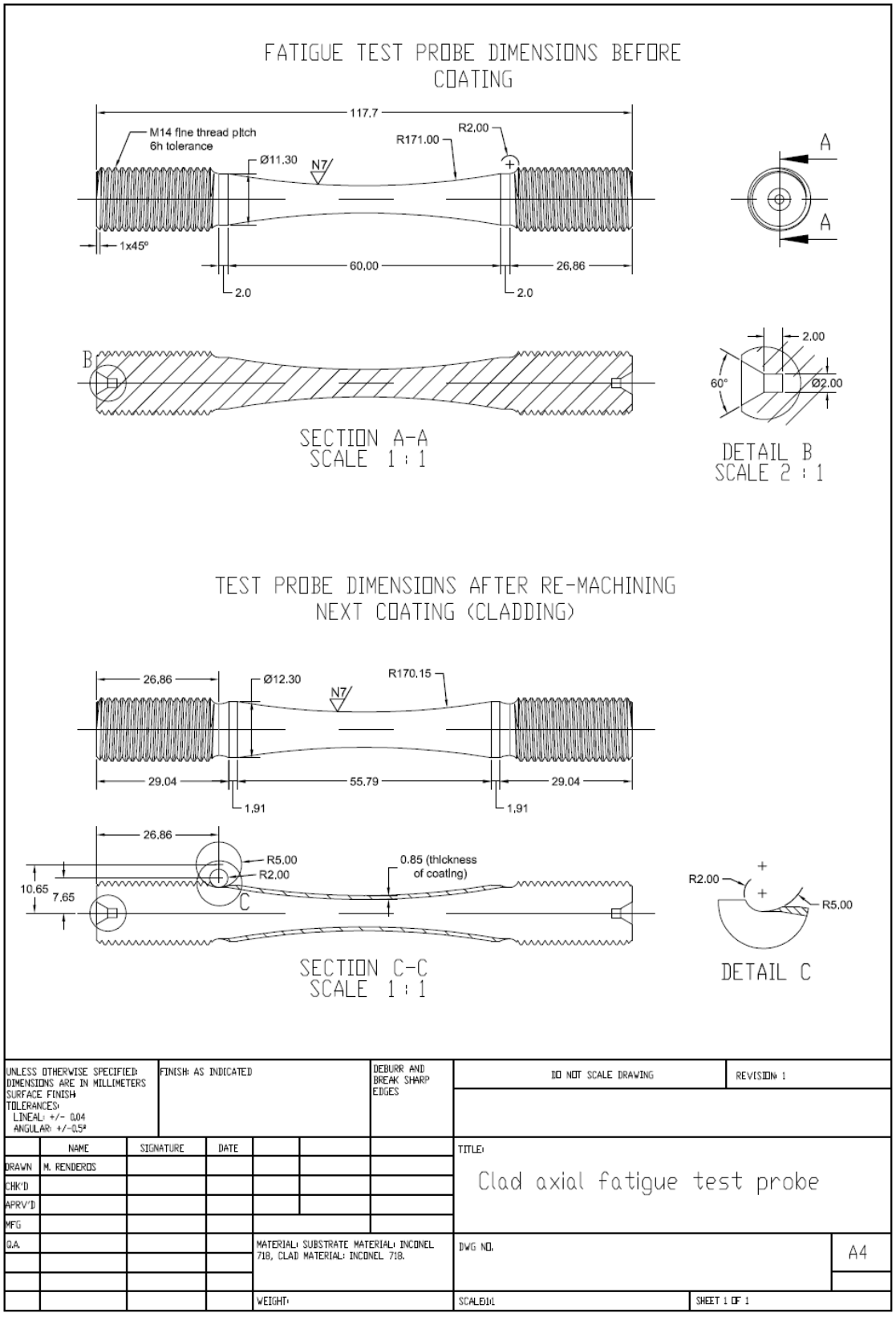

REFERENCES

3D SYSTEMS, 2018. Metal Additive Manufacturing Software: A Critical Element for Successful and Profitable Metal 3D Printing, Technical eBook. 3D SYSTEMS, https://www.3dsystems.com/metal-additive-manufacturing-software-critical-element-successful-and-profitable-metal-3d-printing.

Agarwal, A.T., 2005. Theory and design of dilute phase pneumatic conveying systems. Powder Handl. Proc 17, 18–22.

Agrawal, G., Kar, A., Mazumder, J., 1993. Theoretical studies on extended solid solubility and nonequilibrium phase diagram for Nb-Al alloy formed during laser cladding. Scr. Metall. Mater. 28, 1453–1458. https://doi.org/10.1016/0956-716X(93)90498-H

Akca, E., Gursel, A., 2015. A Review on Superalloys and IN718 Nickel-Based INCONEL Superalloy. Period. Eng. Nat. Sci. 1. https://doi.org/10.21533/pen.v3i1.43

Alam, M.M., Powell, J., Kaplan, A.F.H., Tuominen, J., Vuoristo, P., Miettinen, J., Poutala, J., Näkki, J., Junkala, J., Peltola, T., 2013. Surface pore initiated fatigue failure in laser clad components. J. Laser Appl. 25, 032004. https://doi.org/10.2351/1.4793794

Almeida, A., Petrov, P., Nogueira, I., Vilar, R., 2001. Structure and properties of Al-Nb alloys produced by laser surface alloying. Mater. Sci. Eng. A 303, 273–280. https://doi.org/10.1016/S0921-5093(00)01838-4

Alvarez, P., Montealegre, M.Á., Pulido-Jiménez, J.F., Arrizubieta, J.I., 2018. Analysis of the Process Parameter Influence in Laser Cladding of 316L Stainless Steel. J. Manuf. Mater. Process. 2, 55. https://doi.org/10.3390/jmmp2030055

Anderson, T.D., DuPont, J.N., DebRoy, T., 2010. Origin of stray grain formation in single-crystal superalloy weld pools from heat transfer and fluid flow modeling. Acta Mater. 58, 1441–1454. https://doi.org/10.1016/j.actamat.2009.10.051

Ansari, M., Shoja Razavi, R., Barekat, M., 2016. An empirical-statistical model for coaxial laser cladding of NiCrAlY powder on Inconel 738 superalloy. Opt. Laser Technol. 86, 136–144. https://doi.org/10.1016/j.optlastec.2016.06.014

Antunes, F.V., Borges, M.F., Prates, P., Branco, R., Oliveira, M., 2019. Effect of yield stress on fatigue crack growth. Frat. Ed Integrità Strutt. 13, 9–19. https://doi.org/10.3221/IGF-ESIS.50.02

Arakere, N.K., Swanson, G., 2002. Effect of Crystal Orientation on Fatigue Failure of Single Crystal Nickel Base Turbine Blade Superalloys. J. Eng. Gas Turbines Power 124, 161–176. https://doi.org/10.1115/1.1413767

Araya, G., Gutierrez, G., 2006. Analytical solution for a transient, three-dimensional temperature distribution due to a moving laser beam. Int. J. Heat Mass Transf. 49, 4124–4131. https://doi.org/10.1016/j.ijheatmasstransfer.2006.03.026

Ardila, L.C., Garciandia, F., González-Díaz, J.B., Álvarez, P., Echeverria, A., Petite, M.M., Deffley, R., Ochoa, J., 2014. Effect of IN718 Recycled Powder Reuse on Properties of Parts Manufactured by Means of Selective Laser Melting. Phys. Procedia, 8th International Conference on Laser Assisted Net Shape Engineering LANE 2014 56, 99–107. https://doi.org/10.1016/j.phpro.2014.08.152

Arminjon, M., 1991. A Regular Form of the Schmid Law. Application to the Ambiguity Problem [WWW Document]. Textures Microstruct. https://doi.org/10.1155/TSM.14-18.1121

Arrizubieta, J.I., Tabernero, I., Ruiz, J.E., Lamikiz, A., Martinez, S., Ukar, E., 2014. Continuous Coaxial Nozzle Design for LMD based on Numerical Simulation. Phys. Procedia 56, 429–438. https://doi.org/10.1016/j.phpro.2014.08.146

ASM Handbook, 1985. Metals Handbook, Volume 9, 9th ed. American Society for Metals.

ASTM Subcommittee E04.01, 2015. ASTM E407 - 07(2015)e1 Standard Practice for Microetching Metals and Alloys. ASTM International, West Conshohocken, PA. https://doi.org/10.1520/E0407-07R15E01

ASTM Subcommittee E08.02, 2020. ASTM E1823 - 20a Terminology Relating to Fatigue and Fracture Testing. ASTM International, West Conshohocken, PA. https://doi.org/10.1520/E1823-20A

ASTM Subcommittee E08.05, 2015. ASTM E466 - 15 Standard Practice for Conducting Force Controlled Constant Amplitude Axial Fatigue Tests of Metallic Materials. ASTM International. https://doi.org/10.1520/E0466-15

ASTM Subcommittee E28.04, 2016. ASTM E8 / E8M - 16a Standard Test Methods for Tension Testing of Metallic Materials. ASTM International. https://doi.org/10.1520/E0008_E0008M-16A

ASTM Subcommittee F04.15, 2017. ASTM F1160 - 14(2017)e1 Standard Test Method for Shear and Bending Fatigue Testing of Calcium Phosphate and Metallic Medical and Composite Calcium Phosphate/Metallic Coatings. ASTM International. https://doi.org/10.1520/F1160-14R17E01

Aumund-Kopp, C., Riou, A., 2019. Introduction to additive manufacturing technology. A guide for Designers and Engineers (Technical report No. 2.1 Edition Reprinted 2018). European Powder Metallurgy Association (EPMA), United Kingdom.

Avilés, R., 2012. Notas sobre análisis de fatiga en máquinas: métodos avanzados de análisis de fatiga. Publicaciones, Escuela Técnica Superior de Ingeniería, Bilbao.

Avilés, R., 2005. Análisis de fatiga en máquinas, Edición: 1. ed. Ediciones Paraninfo, S.A.

Azam, F.I., Rani, A.M.A., Altaf, K., Rao, T.V.V.L.N., Zaharin, H.A., 2018. An In-Depth Review on Direct Additive Manufacturing of Metals. IOP Conf. Ser. Mater. Sci. Eng. 328, 012005. https://doi.org/10.1088/1757-899X/328/1/012005

Balankin, A.S., 2015. A continuum framework for mechanics of fractal materials I: from fractional space to continuum with fractal metric. Eur. Phys. J. B 88, 90. https://doi.org/10.1140/epjb/e2015-60189-y

Bandyopadhyay, S., Sundar, J.K.S., Sundararajan, G., Joshi, S. V, 2002. Geometrical Features and Metallurgical Characteristics of {N}d:{YAG} Laser Drilled Holes in Thick {IN}718 and {T}i-6{A}1-4{V} Sheets. J. Mater. Process. Technol. 127, 83–95.

Bayraktar, E., Moiron, J., Kaplan, D., 2006. Effect of welding conditions on the formability characteristics of thin sheet steels: Mechanical and metallurgical effects. J. Mater. Process. Technol., Achievements in Mechanical & Materials Engineering 175, 20–26. https://doi.org/10.1016/j.jmatprotec.2005.04.007

Benson, J.M., 2012. Safety consideration when handling metal powders. J. South. Afr. Inst. Min. Metall. 7A, 563–575.

Berkmanns, J., Faerber, M., 2010. Laser basics. LASERLINE® Technical. (Technical report No. GAS/309700/APUK/1108), Laser basics. Linde AG. BOC Group Limited, Manchester.

Bhadeshia, H.K.D.H., 2020. Nickel Based Superalloys [WWW Document]. Nickel Based Superalloys. URL http://www.phase-trans.msm.cam.ac.uk/2003/Superalloys/superalloys.html (accessed 11.23.20).

Blecher, J.J., Palmer, T.A., Debroy, T., 2014. Solidification map of a nickel-base alloy, in: Metallurgical and Materials Transactions A: Physical Metallurgy and Materials Science. pp. 2142–2151. https://doi.org/10.1007/s11661-013-2149-1

Boehlert, C.J., Li, H., Wang, L., Bartha, B., 2010. Slip System Characterization of Inconel 718 Using In-Situ Scanning Electron Microscopy. Adv. Mater. Process. 168, 41–45.

Bourell, D.L., Leu, M.C., Rosen, D.W., 2009. Roadmap for Additive Manufacturing Identifying the Future of Freeform Processing.

Brahme, A., Alvi, M.H., Saylor, D., Fridy, J., Rollett, A.D., 2006. 3D reconstruction of microstructure in a commercial purity aluminum. Scr. Mater. 55, 75–80. https://doi.org/10.1016/J.SCRIPTAMAT.2006.02.017

Campbell, F.C., 2008. Elements of Metallurgy and Engineering Alloys - ASM International, Materials Properties and Performance, Chapter 14. 9639 Kinsman Road Materials Park, OH.

Cao, J., Liu, F., Lin, X., Huang, C., Chen, J., Huang, W., 2013. Effect of overlap rate on recrystallization behaviors of Laser Solid Formed Inconel 718 superalloy. Opt. Laser Technol. 45, 228–235. https://doi.org/10.1016/j.optlastec.2012.06.043

Cárcel, B., Serrano, A., Zambrano, J., Amigó, V., Cárcel, A.C., 2014. Laser Cladding of TiAl Intermetallic Alloy on Ti6Al4V -Process Optimization and Properties. Phys. Procedia 56, 284–293. https://doi.org/10.1016/J.PHPRO.2014.08.173

Carozzani, T., Digonnet, H., Bellet, M., Gandin, C.-A., 2012. 3D CAFE simulation of a macrosegregation benchmark experiment, in: IOP Conference Series: Materials Science and Engineering. p. 012087. https://doi.org/10.1088/1757-899X/33/1/012087

Carpene, E., Höche, D., Schaaf, P., 2010. Fundamentals of Laser-Material Interactions, in: Schaaf, P. (Ed.), Laser Processing of Materials: Fundamentals, Applications and Developments, Springer Series in Materials Science. Springer, Berlin, Heidelberg, pp. 21–47. https://doi.org/10.1007/978-3-642-13281-0_3

Carpinteri, A., 1994. Fractal nature of material microstructure and size effects on apparent mechanical properties. Mech. Mater., Special Issue on Microstructure and Strain Localization in Geomaterials 18, 89–101. https://doi.org/10.1016/0167-6636(94)00008-5

Carpinteri, A., Freitas, M. de, Spagnoli, A., 2003. Biaxial/Multiaxial Fatigue and Fracture, Volume 31, 1st ed. Elsevier, Amsterdam.

Carroll, P.A., Pinkerton, A.J., Allen, J., Syed, W.U.H., Sezer, H.K., Brown, P., Ng, G., Scudamore, R., Li, L., 2006. The effect of powder recycling in direct metal laser deposition on powder and manufactured part characteristics, in: Proceedings of AVT-139 Specialists Meeting on Cost Effective Manufacture via Net Shape Processing: NATO Research and Technology Organisation.

Casagrande, A., Cammarota, G.P., Micele, L., 2011. Relationship between fatigue limit and Vickers hardness in steels. Mater. Sci. Eng. A 528, 3468–3473. https://doi.org/10.1016/j.msea.2011.01.040

Chen, C., Lian, G., Jiang, J., Wang, Q., 2018. Simplification and experimental investigation of geometrical surface smoothness model for multi-track laser cladding processes. J. Manuf. Process. 36, 621–628. https://doi.org/10.1016/j.jmapro.2018.11.004

Chew, Y., Pang, J.H.L., Bi, G., Song, B., 2017. Effects of laser cladding on fatigue performance of AISI 4340 steel in the as-clad and machine treated conditions. J. Mater. Process. Technol. 243, 246–257. https://doi.org/10.1016/j.jmatprotec.2016.12.020

Chiocca, A., Soulie, F., Bordreuil, C., Deschaux-Beaume, F.F., 2015. Microstructure generation during CuNi bead on plate: comparison of experimental results and CA prediction.

Committee ISO/TC 164/SC 4, 2017. ISO 1099:2017 Metallic materials -- Fatigue testing -- Axial force-controlled method (ICS: 77.040.10 Mechanical testing of metals).

Committee ISO/TC 164/SC 4, 2010. ISO 1143:2010 Metallic materials -- Rotating bar bending fatigue testing (ICS： 77.040.10 Mechanical testing of metals).

Darmadi, D., Norrish, J., Tieu, A., 2011. Analytic and Finite Element Solutions for Temperature Profiles in Welding using Varied Heat Source Models. Fac. Eng. - Pap. Arch.

DebRoy, T., Wei, H.L., Zuback, J.S., Mukherjee, T., Elmer, J.W., Milewski, J.O., Beese, A.M., Wilson-Heid, A., De, A., Zhang, W., 2018. Additive manufacturing of metallic components – Process, structure and properties. Prog. Mater. Sci. 92, 112–224. https://doi.org/10.1016/j.pmatsci.2017.10.001

Deng, G.J., Tu, S.T., Zhang, X.C., Wang, Q.Q., Xuan, F.Z., 2014. Small fatigue crack initiation mechanisms and growth behavior of 304 stainless steel at room temperature, in: Ye, L. (Ed.), Recent Advances in Structural Integrity Analysis - Proceedings of the International Congress (APCF/SIF-2014). Woodhead Publishing, Oxford, pp. 142–146. https://doi.org/10.1533/9780081002254.142

DeVore, J.L., 2011. Probability and Statistics for Engineering and the Sciences, Edición: 008. ed. Cengage Learning, Inc, Boston, MA.

Dinda, G.P., Dasgupta, A.K., Mazumder, J., 2012. Texture control during laser deposition of nickel-based superalloy. Scr. Mater. 67, 503–506. https://doi.org/10.1016/j.scriptamat.2012.06.014

Ding, R.G., Huang, Z.W., Li, H.Y., Mitchell, I., Baxter, G., Bowen, P., 2015. Electron microscopy study of direct laser deposited IN718. Mater. Charact. 106, 324–337. https://doi.org/10.1016/j.matchar.2015.06.017

Dingreville, R., Aksoy, D., Spearot, D., 2017. A primer on selecting grain boundary sets for comparison of interfacial fracture properties in molecular dynamics simulations. Sci. Rep. 7. https://doi.org/10.1038/s41598-017-08637-z

Engin, Z., Coker, D., 2017. Comparison of Equivalent Stress Methods with Critical Plane Approaches for Multiaxial High Cycle Fatigue Assessment. Procedia Struct. Integr., 2nd International Conference on Structural Integrity, ICSI 2017, 4-7

September 2017, Funchal, Madeira, Portugal 5, 1229–1236. https://doi.org/10.1016/j.prostr.2017.07.049

Ensor, K.B., Glynn, P.W., 1997. Stochastic Optimization via Grid Search. Lect. Appl. Math.-Am. 33, 89–100.

Fassani, R.N.S., Trevisan, O. V., 2003. Analytical modeling of multipass welding process with distributed heat source. J. Braz. Soc. Mech. Sci. Eng. 25, 302–305. https://doi.org/10.1590/S1678-58782003000300013

Fatoba, O., Adesina, O., Farotade, G., Adediran, A., 2017. Modelling and Optimization of Laser Alloyed AISI 422 Stainless Steel using Taguchi Approach and Response Surface Model (RSM). BJAST 23. https://doi.org/10.9734/CJAST/2017/24512

Fayazfar, H., Salarian, M., Rogalsky, A., Sarker, D., Russo, P., Paserin, V., Toyserkani, E., 2018. A critical review of powder-based additive manufacturing of ferrous alloys: Process parameters, microstructure and mechanical properties. Mater. Des. 144, 98–128. https://doi.org/10.1016/j.matdes.2018.02.018

Flavenot, J.F., Skalli, N., Le Maître, F., 1983. Fatigue Strength Estimation Incorporating Residual Stresses. CIRP Ann. 32, 475–479. https://doi.org/10.1016/S0007-8506(07)63443-X

Flemings, M.C., 1974. Solidification Processing, in: Materials Science and Technology. Wiley-VCH Verlag GmbH & Co. KGaA, Weinheim, Germany. https://doi.org/10.1002/9783527603978.mst0173

Frazier, W.E., 2014. Metal Additive Manufacturing: A Review. J. Mater. Eng. Perform. 23, 1917–1928. https://doi.org/10.1007/s11665-014-0958-z

Garcia, C., Lis, A.K., Loria, E.A., Deardo, A., 1992. Thermomechanical Processing and Continuous Cooling Transformation Behavior of IN-718. https://doi.org/10.7449/1992/Superalloys_1992_527_536

Gäumann, M., Bezençon, C., Canalis, P., Kurz, W., 2001. Single-crystal laser deposition of superalloys: processing–microstructure maps. Acta Mater. 49, 1051–1062. https://doi.org/10.1016/S1359-6454(00)00367-0

Gäumann, M., Henry, S., Cléton, F., Wagnière, J.-D., Kurz, W., 1999. Epitaxial laser metal forming: analysis of microstructure formation. Mater. Sci. Eng. A 271, 232–241. https://doi.org/10.1016/S0921-5093(99)00202-6

Gäumann, M., Trivedi, R., Kurz, W., 1997. Nucleation ahead of the advancing interface in directional solidification. Mater. Sci. Eng. A 226–228, 763–769. https://doi.org/10.1016/S0921-5093(97)80081-0

Ghosal, P., Majumder, M.C., Chattopadhyay, A., 2018. Study on direct laser metal deposition. Mater. Today Proc., International Conference on Materials Manufacturing and Modelling, ICMMM - 2017, 9 - 11, March 2017 5, 12509–12518. https://doi.org/10.1016/j.matpr.2018.02.232

Gibson, I., Rosen, D.W., Stucker, B., 2010. Additive manufacturing technologies: Rapid prototyping to direct digital manufacturing. Springer US, Boston, MA. https://doi.org/10.1007/978-1-4419-1120-9

Gil, C.M.L., 1998. Determination of Yield in Inconel 718 for Axial-Torsional Loading at Temperatures up to 649 C.

Godec, M., Jenko, M., 2000. Presentation methods of texture measurements. Mater Manuf Technol 34, 359–364.

Gong, X., Zhang, Y., Liu, M., 2013. Powder transport model for laser cladding by lateral powder feeding: I. Powder flow field with cylindrical distribution. Int. J. Adv. Manuf. Technol. 67, 2501–2509. https://doi.org/10.1007/s00170-012-4667-1

Gonzato, G., 1998. A practical implementation of the box counting algorithm. Comput. Geosci. 24, 95–100.

Gorsse, S., Hutchinson, C., Gouné, M., Banerjee, R., 2017. Additive manufacturing of metals: a brief review of the characteristic microstructures and properties of steels, Ti-6Al-4V and high-entropy alloys. Sci. Technol. Adv. Mater. 18, 584–610. https://doi.org/10.1080/14686996.2017.1361305

Graybill, B., Li, M., Malawey, D., Ma, C., Alvarado Orozco, J., Martinez Franco, E., 2018. Additive Manufacturing of Nickel-Based Superalloys. https://doi.org/10.1115/MSEC2018-6666

Greer, A.L., Cooper, P.S., Meredith, M.W., Schneider, W., Schumacher, P., Spittle, J.A., Tronche, A., 2003. Grain Refinement of Aluminium Alloys by Inoculation. Adv. Eng. Mater. 5, 81–91. https://doi.org/10.1002/adem.200390013

Han, L., Phatak, K.M., Liou, F.W., 2004. Modeling of laser cladding with powder injection. Metall. Mater. Trans. B 35, 1139–1150. https://doi.org/10.1007/s11663-004-0070-0

Hassan, B., Corney, J., 2017. Grain boundary precipitation in Inconel 718 and ATI 718Plus. Mater. Sci. Technol. 33, 1879–1889. https://doi.org/10.1080/02670836.2017.1333222

He, W., Hayatdavoudi, A., Shi, H., Sawant, K., Huang, P., 2019. A Preliminary Fractal Interpretation of Effects of Grain Size and Grain Shape on Rock Strength. Rock Mech. Rock Eng. 52, 1745–1765. https://doi.org/10.1007/s00603-018-1645-4

Hinkle, B.L., 1953. Acceleration of particles and pressure drops encountered in horizontal pneumatic conveying. Georgia Institute of Technology.

Hinojosa, M., Montelongo, O., Ortíz, U., 2000. Análisis fractal de la microestructura dendrítica en una aleación de aluminio. Ingenierias III, 13.

Hofmann, D.C., Roberts, S., Otis, R., Kolodziejska, J., Dillon, R.P., Suh, J., Shapiro, A.A., Liu, Z.-K., Borgonia, J.-P., 2014. Developing Gradient Metal Alloys through Radial Deposition Additive Manufacturing. Sci. Rep. 4, 5357. https://doi.org/10.1038/srep05357

Homan, J., 2018. Principal Stresses vs. Equivalent Stresses in Fatigue. Fatec Eng. URL https://www.fatec-engineering.com/2018/10/19/principal-stresses-vs-equivalent-stresses-in-fatigue/ (accessed 8.13.20).

Hor, A., Saintier, N., Robert, C., Palin-Luc, T., Morel, F., 2013. Analysis of the mesoscopic high cycle multiaxial fatigue strength of fcc metals with crystal plasticity and generalized extreme values probability. Presented at the The Tenth International Conference on Multiaxial Fatigue & Fracture (ICMFF10), pp. 1–8.

Hornbogen, E., 1989. Fractals in microstructure of metals. Int. Mater. Rev. 34, 277–296. https://doi.org/10.1179/imr.1989.34.1.277

Hu, B., Hu, F.Y., Huang, X.R., 2012. Directionally Solidified Laser Cladding. Adv. Mater. Res. 557–559, 1708–1711. https://doi.org/10.4028/www.scientific.net/AMR.557-559.1708

Hunt, J.D., 1984. Steady state columnar and equiaxed growth of dendrites and eutectic. Mater. Sci. Eng. 65, 75–83. https://doi.org/10.1016/0025-5416(84)90201-5

Hutasoit, N., Luzin, V., Blicblau, A., Yan, W., Brandt, M., Cottam, R., 2015. Fatigue life of laser clad hardfacing alloys on AISI 4130 steel under rotary bending fatigue test. Int. J. Fatigue 72, 42–52. https://doi.org/10.1016/j.ijfatigue.2014.11.001

Ibarra-Medina, J., Pinkerton, A.J., 2010. A CFD model of the laser, coaxial powder stream and substrate interaction in laser cladding. Phys. Procedia 5, 337–346. https://doi.org/10.1016/j.phpro.2010.08.060

Ion, D., Lorand, Kun, Mircea, D., Karoly, M., 2011. The equivalent stress concept in multiaxial fatigue. J. Eng. Stud. Res. 17, No 2, Pag. 53-62.

IPG Photonics, 2019. Industrial Fiber Lasers for Materials Processing, catalogue R29 11/19. https://www.ipgphotonics.com/en/647/Widget/Industrial+Fiber+Lasers+for+Materials+Processing+2019.pdf.

Ipohorski, M., Acuña, R.J., 1988. Fractogrfía. Aplicaciones al Análisis de Fallas (No. CNEA 490). Comisión Nacional de Energía Atómica, Buenos Aires, Argentina.

Ivanova, V.S., Bunin, I.J., Nosenko, V.I., 1998. Fractal material science: A new direction in materials science. JOM 50, 52–54. https://doi.org/10.1007/s11837-998-0068-1

Kamara, A.M., Marimuthu, S., Li, L., 2014. Finite Element Modeling of Microstructure in Laser-Deposited Multiple Layer Inconel 718 Parts. Mater. Manuf. Process. 29, 1245–1252. https://doi.org/10.1080/10426914.2014.930963

Kamara, A.M., Wang, W., Marimuthu, S., Li, L., 2011. Modelling of the melt pool geometry in the laser deposition of nickel alloys using the anisotropic enhanced thermal conductivity approach. Proc. Inst. Mech. Eng. Part B J. Eng. Manuf. 225, 87–99. https://doi.org/10.1177/09544054JEM2129

Kar, A., Mazumder, J., 1989. Extended solid solution and nonequilibrium phase diagram for Ni-Al alloy formed during laser cladding. Metall. Trans. A 20, 363–371. https://doi.org/10.1007/BF02653915

Karolczuk, A., Kowalski, M., BaDski, R., Zok, F.D.A., 2013. Fatigue phenomena in explosively welded steel-titanium clad components subjected to push-pull loading. Int. J. Fatigue 48, 101–108.

Kear, B.H., Breinan, E.M., Greenwald, L.E., 1979. Laser glazing – a new process for production and control of rapidly chilled metallurgical microstructures. Met. Technol. 6, 121–129. https://doi.org/10.1179/030716979803276796

Keiser, D.D., Brown, H.L., 1976. Review of the physical metallurgy of Alloy 718 (Materials No. TID-4500, R63). AEROJET NUCLEAR COMPANY, IDAHO OPERATIONS OFFICE.

Kirka, M.M., Medina, F., Dehoff, R., Okello, A., 2017. Mechanical behavior of post-processed Inconel 718 manufactured through the electron beam melting process. Mater. Sci. Eng. A 680, 338–346. https://doi.org/10.1016/j.msea.2016.10.069

Kirka, M.M., Unocic, K.A., Raghavan, N., Medina, F., Dehoff, R.R., Babu, S.S., 2016. Microstructure Development in Electron Beam-Melted Inconel 718 and Associated Tensile Properties. JOM 68, 1012–1020. https://doi.org/10.1007/s11837-016-1812-6

Kobayashi, S., Tsurekawa, S., Watanabe, T., 2016. A new approach to grain boundary engineering for nanocrystalline materials. Beilstein J. Nanotechnol. 7, 1829–1849. https://doi.org/10.3762/bjnano.7.176

Kobryn, P.A.A., Semiatin, S.L.L., 2003. Microstructure and texture evolution during solidification processing of Ti-6A1-4V. J. Mater. Process. Technol. 135, 330–339. https://doi.org/10.1016/S0924-0136(02)00865-8

Koehler, H., Partes, K., Seefeld, T., Vollertsen, F., 2011. Influence of Laser Reconditioning on Fatigue Properties of Crankshafts. Phys. Procedia, Lasers in Manufacturing 2011 - Proceedings of the Sixth International WLT Conference on Lasers in Manufacturing 12, 512–518. https://doi.org/10.1016/j.phpro.2011.03.063

Koehler, H., Schumacher, J., Schuischel, K., Partes, K., Bomas, H., Jablonski, F., Vollertsen, F., Kienzler, R., 2012. An approach to calculate fatigue properties of laser cladded components. Prod. Eng. Res. Dev. 6, 137–148. https://doi.org/10.1007/s11740-012-0369-7

Kouhia, R., 2019. Fatigue (Chapter 6). Course implementations - TAU RAK-33060 2019-01, http://www.tut.fi/rakmek/rak_33060/harj/fatigue_models.pdf.

Krakow, R., Johnstone, D.N., Eggeman, A.S., Hünert, D., Hardy, M.C., Rae, C.M.F., Midgley, P.A., 2017. On the crystallography and composition of topologically close-packed phases in ATI 718Plus®. Acta Mater. 130, 271–280. https://doi.org/10.1016/j.actamat.2017.03.038

Kurz, W., Bezençon, C., Gäumann, M., 2001. Columnar to equiaxed transition in solidification processing. Sci. Technol. Adv. Mater. 2, 185–191. https://doi.org/10.1016/S1468-6996(01)00047-X

Kurz, W., Fisher, D.J., 1998. Fundamentals of Solidification, 4th edition. ed. CRC Press, Uetikon-Zuerich, Switzerland ; Enfield, N.H.

Lakshminarayanan, A., Shanmugam, K., Balasubramanian, V., 2009. Effect of Autogenous Arc Welding Processes on Tensile and Impact Properties of Ferritic Stainless Steel Joints. J. Iron Steel Res. Int. 16, 62–16. https://doi.org/10.1016/S1006-706X(09)60012-1

Lambarri, J., Leunda, J., García Navas, V., Soriano, C., Sanz, C., 2013. Microstructural and tensile characterization of Inconel 718 laser coatings for aeronautic components. Opt. Lasers Eng. 51, 813–821. https://doi.org/10.1016/j.optlaseng.2013.01.011

Leithold, L., 1996. The calculus 7. HarperCollins College Pub.

LeVeque, R.J., 2007. Finite difference methods for ordinary and partial differential equations : steady-state and time-dependent problems. Society for Industrial and Applied Mathematics.

Levin, P., 2008. A general solution of 3-D quasi-steady-state problem of a moving heat source on a semi-infinite solid. Mech. Res. Commun. 35, 151–157. https://doi.org/10.1016/j.mechrescom.2007.09.003

Li, H., Liaw, P.K., Choo, H., Misra, A., 2008. Effect of grain orientation on ductility in a nanocrystalline Ni–Fe alloy. Appl. Phys. Lett. 93, 051907. https://doi.org/10.1063/1.2968662

Li, Y., Ma, J., 1997. Study on overlapping in the laser cladding process. Surf. Coat. Technol. 90, 1–5. https://doi.org/10.1016/S0257-8972(96)03022-8

Li, Z., Tian, X., Tang, H., Wang, H., 2013. Low cycle fatigue behavior of laser melting deposited TC18 titanium alloy. Trans. Nonferrous Met. Soc. China 23, 2591–2597. https://doi.org/10.1016/S1003-6326(13)62772-7

Liang, Y.-J., Cheng, X., Li, J., Wang, H.-M., 2017. Microstructural control during laser additive manufacturing of single-crystal nickel-base superalloys: New processing–microstructure maps involving powder feeding. Mater. Des. 130, 197–207. https://doi.org/10.1016/j.matdes.2017.05.066

Liang, Y.-J., Cheng, X., Wang, H.-M., 2016a. A new microsegregation model for rapid solidification multicomponent alloys and its application to single-crystal nickel-base superalloys of laser rapid directional solidification. Acta Mater. 118, 17–27. https://doi.org/10.1016/j.actamat.2016.07.008

Liang, Y.-J., Li, A., Cheng, X., Pang, X.-T., Wang, H.-M., 2016b. Prediction of primary dendritic arm spacing during laser rapid directional solidification of single-crystal nickel-base superalloys. J. Alloys Compd. 688, 133–142. https://doi.org/10.1016/j.jallcom.2016.06.289

Lilliefors, H.W., 1967. On the Kolmogorov-Smirnov Test for Normality with Mean and Variance Unknown. J. Am. Stat. Assoc. 62, 399–402. https://doi.org/10.2307/2283970

Ling, L.-S.-B., Yin, Z., Hu, Z., Liang, J.-H., Wang, Z.-Y., Wang, J., Sun, B.-D., 2020. Effects of the γ″-Ni3Nb Phase on Mechanical Properties of Inconel 718 Superalloys with Different Heat Treatments. Materials 13, 151. https://doi.org/10.3390/ma13010151

Liu, Z., Qi, H., 2014. Mathematical Modeling of Crystal Growth and Microstructure Formation in Multi-layer and Multi-track Laser Powder Deposition of Single-crystal Superalloy. Phys. Procedia 56, 411–420. https://doi.org/10.1016/J.PHPRO.2014.08.144

Lourenço, J.M., Sun, S.D., Sharp, K., Luzin, V., Klein, A.N., Wang, C.H., Brandt, M., 2016. Fatigue and fracture behavior of laser clad repair of AerMet® 100 ultra-high strength steel. Int. J. Fatigue 85, 18–30. https://doi.org/10.1016/j.ijfatigue.2015.11.021

LPW TECHNOLOGY LTD, 2016. LPW Technology case study 05: powder degradation (Technical report No. 5), Case studies. LPW Technology Ltd., United Kingdom.

Ma, M., Wang, Z., Zeng, X., 2017. A comparison on metallurgical behaviors of 316L stainless steel by selective laser melting and laser cladding deposition. Mater. Sci. Eng. A 685, 265–273. https://doi.org/10.1016/j.msea.2016.12.112

Mackenzie, D., 2017. Stress Linearization Concepts and Restrictions in Elastic Design by Analysis. Presented at the ASME 2017 Pressure Vessels and Piping Conference, American Society of Mechanical Engineers Digital Collection. https://doi.org/10.1115/PVP2017-65678

Mahadevan, S., Nalawade, S., Singh, J.B., Verma, A., Paul, B., Ramaswamy, K., 2010. Evolution of δ Phase Microstructure in Alloy 718, in: Superalloy 718 and Derivatives. John Wiley & Sons, Ltd, pp. 737–750. https://doi.org/10.1002/9781118495223.ch57

Majumdar, J.D., Manna, I., 2011. Laser material processing. Int. Mater. Rev. 56, 341–388. https://doi.org/10.1179/1743280411Y.0000000003

Mandelbrot, B., 1975. Les objets fractals - forme, hasard et dimension. Flammarion, Paris.

Mandelbrot, B.B., Passoja, D.E., Paullay, A.J., 1984. Fractal character of fracture surfaces of metals. Nature 308, 721–722. https://doi.org/10.1038/308721a0

Manikandan, S.G.K., Sivakumar, D., Prasad Rao, K., Kamaraj, M., 2015. Laves phase in alloy 718 fusion zone — microscopic and calorimetric studies. Mater. Charact. 100, 192–206. https://doi.org/10.1016/j.matchar.2014.11.035

Martín-Meizoso, A., Martínez-Esnaola, J.M., Gil Sevillano, J., 2009. Cálculo del límite de fatiga mediante el método de máxima verosimilitud, in: Anales de Mecánica de la Fractura 26. pp. 406–410.

Martorano, M.A., Beckermann, C., Gandin, C.A., 2003. A solutal interaction mechanism for the columnar-to-equiaxed transition in alloy solidification. Metall. Mater. Trans. Phys. Metall. Mater. Sci. 34 A, 1657–1674. https://doi.org/10.1007/s11661-003-0311-x

Martorano, M.A., Biscuola, V.B., 2009. Predicting the columnar-to-equiaxed transition for a distribution of nucleation undercoolings. Acta Mater. 57, 607–615. https://doi.org/10.1016/J.ACTAMAT.2008.10.001

Meng, L., Zeng, X., Hou, K., Hu, Q., Wang, D., 2019. Effect of laser cladding and laser-induction hybrid cladding coatings on the bending properties and fracture behavior of rails. Surf. Coat. Technol. 374, 1038–1050. https://doi.org/10.1016/j.surfcoat.2019.06.051

Meriaudeau, F., Truchetet, F., Grevey, D., Vannes, A.B., 1997. Laser Cladding process and image processing. J. Laser Eng. 6, 161–187. https://doi.org/10.1101/gr.133546.111

Merino Casals, M.C., 2012. Diagramas y transformaciones de fase 3. Soluciones sólidas, in: Serie Química de Materiales. pp. 96–122.

Merklein, M., Junker, D., Schaub, A., Neubauer, F., 2016. Hybrid Additive Manufacturing Technologies – An Analysis Regarding Potentials and Applications. Phys. Procedia, Laser Assisted Net Shape Engineering 9 International Conference on Photonic Technologies Proceedings of the LANE 2016 September 19-22, 2016 Fürth, Germany 83, 549–559. https://doi.org/10.1016/j.phpro.2016.08.057

Miller, M.K., Burke, M.G., 1991. Precipitation in Alloy 718: A combined AEM and APFIM investigation, in: The Minerals, Metals & Materials Society. Edited by Edward A. Loria, Pittsburgh, PA, pp. 337–350.

Mills, K.C., 2002. Recommended values of thermophysical properties for selected commercial alloys. Woodhead.

Mishra, S., Yadava, V., 2013. Modeling and optimization of laser beam percussion drilling of nickel-based superalloy sheet using Nd: YAG laser. Opt. Lasers Eng. 51, 681–695. https://doi.org/10.1016/j.optlaseng.2013.01.006

Mohd Razali, N., Yap, B., 2011. Power Comparisons of Shapiro-Wilk, Kolmogorov-Smirnov, Lilliefors and Anderson-Darling Tests. J Stat Model Anal. 2.

Moisy, F., 2020. boxcount [WWW Document]. URL https://www.mathworks.com/matlabcentral/fileexchange/13063-boxcount (accessed 8.26.20).

Mondal, S., Bandyopadhyay, A., Pal, P.K., 2014. Application of artificial neural network for the prediction of laser cladding process characteristics at Taguchi-based optimized condition. Int. J. Adv. Manuf. Technol. 70, 2151–2158. https://doi.org/10.1007/s00170-013-5393-z

Mondal, S., Bandyopadhyay, A., Pal, P.K., 2011. Ni-Cr-Mo Cladding on Mild Steel Surface using CO 2 Laser and Process Modeling with Response Surface Methodology (RSM). Int. J. Eng. Sci. Technol. 3.

MTEX, 2020. Ellipse Based Shape Parameters | MTEX [WWW Document]. URL https://mtex-toolbox.github.io/EllipseBasedParameters.html (accessed 8.26.20).

Nabhani, M., Razavi, R.S., Barekat, M., 2018. An empirical-statistical model for laser cladding of Ti-6Al-4V powder on Ti-6Al-4V substrate. Opt. Laser Technol. 100, 265–271. https://doi.org/10.1016/j.optlastec.2017.10.015

Najmon, J.C., Raeisi, S., Tovar, A., 2019. 2 - Review of additive manufacturing technologies and applications in the aerospace industry, in: Froes, F., Boyer, R. (Eds.), Additive Manufacturing for the Aerospace Industry. Elsevier, pp. 7–31. https://doi.org/10.1016/B978-0-12-814062-8.00002-9

Nandwana, P., Peter, W.H., Dehoff, R.R., Lowe, L.E., Kirka, M.M., Medina, F., Babu, S.S., 2016. Recyclability Study on Inconel 718 and Ti-6Al-4V Powders for Use in Electron Beam Melting. Metall. Mater. Trans. B 47, 754–762. https://doi.org/10.1007/s11663-015-0477-9

Nastac, L., Valencia, J.J., Tims, M.L., Dax, F.R., 2001. Advances in the Solidification of IN718 and RS5 Alloys, in: Superalloys 718, 625, 706 and Various Derivatives (2001). TMS, pp. 103–112. https://doi.org/10.7449/2001/Superalloys_2001_103_112

Ngo, T.D., Kashani, A., Imbalzano, G., Nguyen, K.T.Q., Hui, D., 2018. Additive manufacturing (3D printing): A review of materials, methods, applications and challenges. Compos. Part B Eng. 143, 172–196. https://doi.org/10.1016/j.compositesb.2018.02.012

Nguejio, J., Szmytka, F., Hallais, S., Tanguy, A., Nardone, S., Godino Martinez, M., 2019. Comparison of microstructure features and mechanical properties for additive manufactured and wrought nickel alloys 625. Mater. Sci. Eng. A 764, 138214. https://doi.org/10.1016/j.msea.2019.138214

Niederhauser, S., Karlsson, B., 2005. Fatigue behaviour of Co–Cr laser cladded steel plates for railway applications. Wear, Contact Mechanics and Wear of Rail/Wheel Systems 258, 1156–1164. https://doi.org/10.1016/j.wear.2004.03.026

Niñerola, R., Petrovic, V., 2015. Powder recyclability in electron beam melting for aeronautical use. Aircr. Eng. Aerosp. Technol. 87, 147–155. https://doi.org/10.1108/AEAT-11-2013-0212

NIST/SEMATECH, 2012. e-Handbook of Statistical Methods [WWW Document]. Probab. Distrib. URL https://www.itl.nist.gov/div898/handbook/eda/section3/eda366g.htm (accessed 10.24.18).

Nolze, G., Hielscher, R., 2016. Nolze and Hielscher · Orientations-perfectly colored research papers. J Appl Cryst 49, 1786–1802. https://doi.org/10.1107/S1600576716012942

Nowotny, St., Scharek, S., Kempe, F., Beyer, E., 2003. COAXn: Modular system of powder nozzles for laser beam build-up welding. Int. Congr. Appl. Lasers Electro-Opt. 2003, P519. https://doi.org/10.2351/1.5060160

Ocelík, V., de Oliveira, U., de Boer, M., de Hosson, J.Th.M., 2007. Thick Co-based coating on cast iron by side laser cladding: Analysis of processing conditions and coating properties. Surf. Coat. Technol. 201, 5875–5883. https://doi.org/10.1016/j.surfcoat.2006.10.044

Ocelík, V., Nenadl, O., Palavra, A., De Hosson, J.Th.M., 2014. On the geometry of coating layers formed by overlap. Surf. Coat. Technol. 242, 54–61. https://doi.org/10.1016/j.surfcoat.2014.01.018

Oliveira de, U., Ocelík, V., De Hosson, J.Th.M., 2005. Analysis of coaxial laser cladding processing conditions. Surf. Coat. Technol. 197, 127–136. https://doi.org/10.1016/j.surfcoat.2004.06.029

Ostrowski, A., Langer, E.W., 1979. PRECIPITATION OF TITANIUM CARBONITRIDES IN AS-CAST 17% CHROMIUM STAINLESS STEELS.

Pang, J.C., Li, S.X., Wang, Z.G., Zhang, Z.F., 2014. Relations between fatigue strength and other mechanical properties of metallic materials. Fatigue Fract. Eng. Mater. Struct. 37, 958–976. https://doi.org/10.1111/ffe.12158

Pardoe, I., 2020. 7.5 - Tests for Error Normality | STAT 501 [WWW Document]. PennState Stat. Online Courses. URL https://online.stat.psu.edu/stat501/lesson/7/7.5 (accessed 5.27.20).

Parimi, L.L., A., R.G., Clark, D., Attallah, M.M., 2014. Microstructural and texture development in direct laser fabricated IN718. Mater. Charact. 89, 102–111. https://doi.org/10.1016/j.matchar.2013.12.012

Park, J.-W., Babu, S.S., Vitek, J.M., Kenik, E.A., David, S.A., 2003. Stray grain formation in single crystal Ni-base superalloy welds. J. Appl. Phys. 94, 4203–4209. https://doi.org/10.1063/1.1602950

Pautrat, A., 2013. Étude expérimentale quantitative de la solidification de l'inconel 718 en fonderie. ParisTech, l'École nationale supérieure des mines de Paris.

Petersen, W.A., 1973. Fine Grained Weld Structures, in: 53rd AWS Annual Meeting. WELDING RESEARCH SUPPLEMENT, Detroit, pp. 74–79.

Petkov, V.I., 2018. Alloy 718 manufactured by AM Selective Laser Melting : Evaluation of microstructure and weldability (Student thesis, https://www.diva-portal.org/smash/record.jsf?pid=diva2%3A1236176&dswid=9655).

Peyre, P., Aubry, P., Fabbro, R., Neveu, R., Longuet, A., 2008. Analytical and numerical modelling of the direct metal deposition laser process. J. Phys. Appl. Phys. 41. https://doi.org/10.1088/0022-3727/41/2/025403

Picasso, M., Marsden, C.F., Wagniere, J.D., Frenk, A., Rappaz, M., 1994. A simple but realistic model for laser cladding. Metall. Mater. Trans. B 25, 281–291. https://doi.org/10.1007/BF02665211

Pilkey, W.D., 1997. Peterson's Stress Concentration Factors, 2nd Edition. John Wiley & Sons, New York.

Pinkerton, A.J., 2014. Advances in the modeling of laser direct metal deposition. J. Laser Appl. 27, S15001. https://doi.org/10.2351/1.4815992

Pinkerton, A.J., 2007. An analytical model of beam attenuation and powder heating during coaxial laser direct metal deposition. J. Phys. Appl. Phys. 40, 7323–7334. https://doi.org/10.1088/0022-3727/40/23/012

Pinkerton, A.J., Li, L., 2004. An analytical model of energy distribution in laser direct metal deposition, in: Proceedings of the Institution of Mechanical Engineers, Part B: Journal of Engineering Manufacture. SAGE PublicationsSage UK: London, England, pp. 363–374. https://doi.org/10.1243/095440504323055498

Pinkerton, A.J., Moat, R., Shah, K., Li, L., Preuss, M., Withers, P.J., 2007. A verified model of laser direct metal deposition using an analytical enthalpy balance method. Int. Congr. Appl. Lasers Electro-Opt. 2007, 1806. https://doi.org/10.2351/1.5061038

PNAS, N.A. of S., 2012. Frontiers of Engineering: Reports on Leading-Edge Engineering from the 2011 Symposium. The National Academies Press, Washington, DC. https://doi.org/10.17226/13274

Ram, G.D.J., Reddy, A.V., Rao, K.P., Reddy, G.M., 2004. Control of Laves phase in Inconel 718 GTA welds with current pulsing. Sci. Technol. Weld. Join. 9, 390–398. https://doi.org/10.1179/136217104225021788

Rangaswamy, P., Griffith, M.L., Prime, M.B., Holden, T.M., Rogge, R.B., Edwards, J.M., Sebring, R.J., 2005. Residual stresses in LENS® components using neutron diffraction and contour method. Mater. Sci. Eng. A, Measurement and Interpretation of Internal/Residual Stresses 399, 72–83. https://doi.org/10.1016/j.msea.2005.02.019

Rao, G.A., Srinivas, M., Sarma, D.S., 2006. Effect of oxygen content of powder on microstructure and mechanical properties of hot isostatically pressed superalloy Inconel 718. Mater. Sci. Eng. A 435–436, 84–99. https://doi.org/10.1016/j.msea.2006.07.053

Rappaz, M., Gandin, C.A., Desbiolles, J.L., Thévoz, Ph., 1996. Prediction of grain structures in various solidification processes. Metall. Mater. Trans. A 27, 695–705. https://doi.org/10.1007/BF02648956

Redwood, B., 2021. Additive manufacturing technologies: An overview [WWW Document]. Addit. Manuf. Technol. Overv. URL https://www.3dhubs.com/knowledge-base/additive-manufacturing-technologies-overview/ (accessed 2.4.21).

Reed, R., 2007. Physical Metallurgy and Microstructure of Superalloys, Materials and Technology. The Minerals, Metals & Materials Society (TMS), Pittsburgh, PA.

Renderos, M., Torregaray, A., Gutierrez-Orrantia, M.E., Lamikiz, A., Saintier, N., Girot, F., 2017. Microstructure characterization of recycled IN718 powder and resulting laser clad material. Mater. Charact. 134, 103–113. https://doi.org/10.1016/J.MATCHAR.2017.09.029

RockMechs, 2020. Octahedral stresses. RockMechs Rock Mech. Eng. URL https://www.rockmechs.com/octahedral-stresses/ (accessed 8.19.20).

SAE AMS5662M, 2009. AMS5662M: Nickel Alloy, Corrosion and Heat Resistant, Bars, Forgings, and Rings 52.5Ni 19Cr 3.0Mo 5.1Cb 0.90Ti 0.50Al 18Fe, Consumable Electrode or Vacuum Induction Melted 1775°F (968°C) Solution Heat Treated, Precipitation Hardenable - SAE International (No. AMS5662M). AMS F Corrosion Heat Resistant Alloys Committee.

Sainte-Catherine, C., Jeandin, M., Kechemair, D., Ricaud, J.-P., Sabatier, L., 1991. Study of dynamic absorptivity at 10.6 µm (CO2) and 1.06 µm (ND-YAG) wavelengths as a function of temperature. J. Phys. IV 01, C7-151-C7-157. https://doi.org/10.1051/jp4:1991741

Sames, W.J., List, F.A., Pannala, S., Dehoff, R.R., Babu, S.S., 2016. The metallurgy and processing science of metal additive manufacturing. Int. Mater. Rev. 61, 315–360. https://doi.org/10.1080/09506608.2015.1116649

Saqib, S., Urbanic, R.J., Aggarwal, K., 2014. Analysis of Laser Cladding Bead Morphology for Developing Additive Manufacturing Travel Paths. Procedia CIRP, Variety Management in Manufacturing 17, 824–829. https://doi.org/10.1016/j.procir.2014.01.098

Schirra, J.J., Caless, R.H., Hatala, R., 1991. The Effect of Laves Phase on the Mechanical Properties of Wrought and Cast + HIP Inconel 718. https://doi.org/10.7449/1991/SUPERALLOYS_1991_375_388

Sealy, M.P., Madireddy, G., Williams, R.E., Rao, P., Toursangsaraki, M., 2018. Hybrid Processes in Additive Manufacturing. J. Manuf. Sci. Eng. 140. https://doi.org/10.1115/1.4038644

Seetharaman, Seshadri., 2005. Fundamentals of metallurgy. Woodhead Pub. and Maney Pub. on behalf of the Institute of Materials, Minerals and Mining.

Seow, C.E., Coules, H.E., Wu, G., Khan, R.H.U., Xu, X., Williams, S., 2019. Wire + Arc Additively Manufactured Inconel 718: Effect of post-deposition heat treatments on microstructure and tensile properties. Mater. Des. 183, 108157. https://doi.org/10.1016/j.matdes.2019.108157

Shamsaei, N., Yadollahi, A., Bian, L., Thompson, S.M., 2015. An overview of Direct Laser Deposition for additive manufacturing; Part II: Mechanical behavior, process parameter optimization and control. Addit. Manuf. 8, 12–35. https://doi.org/10.1016/j.addma.2015.07.002

Slotwinski, J., Garboczi, E., Stutzman, P., Ferraris, C., Watson, S., Peltz, M., 2014. Characterization of Metal Powders Used for Additive Manufacturing. J. Res. Natl. Inst. Stand. Technol. 119, 460–493. https://doi.org/10.6028/jres.119.018

Sohrabi, M.J., Mirzadeh, H., Rafiei, M., 2018. Solidification behavior and Laves phase dissolution during homogenization heat treatment of Inconel 718 superalloy. Vacuum 154, 235–243. https://doi.org/10.1016/j.vacuum.2018.05.019

Sönnerlind, H., 2017. Introduction to Modeling Stress Linearization in COMSOL Multiphysics®. COMSOL Multiphysics. URL https://www.comsol.com/blogs/introduction-to-modeling-stress-linearization-in-comsol-multiphysics/ (accessed 8.13.20).

Special Metals, 2007. Special Metals INCONEL® alloy 718 (No. Publication Number SMC-045). https://www.specialmetals.com/assets/smc/documents/inconel_alloy_718.pdf, Huntington, WV.

Srivatsan, T.S., Sudarshan, T.S., 1993. Rapid solidification technology: an engineering guide. Technomic Pub.

Stavropoulos, P., Foteinopoulos, P., Papacharalampopoulos, A., Bikas, H., 2018. Addressing the challenges for the industrial application of additive manufacturing: Towards a hybrid solution. Int. J. Lightweight Mater. Manuf. 1, 157–168. https://doi.org/10.1016/j.ijlmm.2018.07.002

Streitenberger, P., Förster, D., Kolbe, G., Veit, P., 1995. The fractal geometry of grain boundaries in deformed and recovered zinc. Scr. Metall. Mater. 33, 541–546. https://doi.org/10.1016/0956-716X(95)00265-W

Strondl, A., Lyckfeldt, O., Brodin, H., Ackelid, U., 2015. Characterization and Control of Powder Properties for Additive Manufacturing. JOM 67, 549–554. https://doi.org/10.1007/s11837-015-1304-0

Sturz, L., Drevermann, A., Pickmann, C., Zimmermann, G., 2005. Influence of grain refinement on the columnar-to-equiaxed transition in binary Al alloys. Mater. Sci. Eng. A 413–414, 379–383. https://doi.org/10.1016/j.msea.2005.08.199

Sun, S.D., Liu, Q., Brandt, M., Luzin, V., Cottam, R., Janardhana, M., Clark, G., 2014. Effect of laser clad repair on the fatigue behaviour of ultra-high strength AISI 4340 steel. Mater. Sci. Eng. A 606, 46–57. https://doi.org/10.1016/j.msea.2014.03.077

Sundararaman, M., Banerjee, S., Mori, H., 2001. The Stability of γ" and γ' Phases in Alloy 718 Under Electron Irradiation. https://doi.org/10.7449/2001/Superalloys_2001_379_387

Szymczyk-Ziółkowska, P., Smolina, I., Rusińska, M., Woźna, A., Tomassetti, A., Chlebus, E., 2019. Logistical Aspects of Transition from Traditional to Additive Manufacturing. pp. 752–760. https://doi.org/10.1007/978-3-319-97490-3_71

Tabernero, I., Calleja, A., Lamikiz, A., López de Lacalle, L.N., 2013. Optimal Parameters for 5-axis Laser Cladding. Procedia Eng., The Manufacturing Engineering Society International Conference, MESIC 2013 63, 45–52. https://doi.org/10.1016/j.proeng.2013.08.229

Tabernero, I., Lamikiz, A., Martínez, S., Ukar, E., Figueras, J., 2011. Evaluation of the mechanical properties of Inconel 718 components built by laser cladding. Int. J. Mach. Tools Manuf. 51, 465–470. https://doi.org/10.1016/j.ijmachtools.2011.02.003

Tabernero, I., Lamikiz, A., Martínez, S., Ukar, E., López de Lacalle, L.N., 2012. Modelling of energy attenuation due to powder flow-laser beam interaction during laser cladding process. J. Mater. Process. Technol. 212, 516–522. https://doi.org/10.1016/j.jmatprotec.2011.10.019

Tabernero, I., Lamikiz, A., Ukar, E., López De Lacalle, L.N., Angulo, C., Urbikain, G., 2010. Numerical simulation and experimental validation of powder flux distribution in coaxial laser cladding. J. Mater. Process. Technol. 210, 2125–2134. https://doi.org/10.1016/j.jmatprotec.2010.07.036

Terzić, A., Mitić, V.V., Kocić, L., Radojević, Z., Pašalić, S., 2015. Mechanical properties and microstructure fractal analysis of refractory bauxite concrete. Sci. Sinter. 47, 331–346. https://doi.org/10.2298/SOS1503331T

Thode, H.C., 2002. Testing For Normality, 1 edition. ed. CRC Press, New York.

Thomas, A., 2005. Estudio del comportamiento en caliente del Inconel 718. Projecte/Treball Final de Carrera. UPC, Escola Tècnica Superior d'Enginyeria Industrial de Barcelona, Departament de Ciència dels Materials i Enginyeria Metallúrgica, http://hdl.handle.net/2099.1/2774.

Tian, Y., McAllister, D., Colijn, H., Mills, M., Farson, D., Nordin, M., Babu, S., 2014. Rationalization of Microstructure Heterogeneity in INCONEL 718 Builds Made by the Direct Laser Additive Manufacturing Process. Metall. Mater. Trans. A 45, 4470–4483. https://doi.org/10.1007/s11661-014-2370-6

Tofail, S.A.M., Koumoulos, E.P., Bandyopadhyay, A., Bose, S., O'Donoghue, L., Charitidis, C., 2018. Additive manufacturing: scientific and technological challenges, market uptake and opportunities. Mater. Today 21, 22–37. https://doi.org/10.1016/j.mattod.2017.07.001

Toyserkani, E., Corbin, S., Khajepour, A., 2005. Laser Cladding. CRC Press.

Trujillo Guillen, M., 2005. Función de Green para la ecuación hiperbólica de transmisión del calor. Riunet. Universitat Politècnica de València, Valencia (Spain). https://doi.org/10.4995/Thesis/10251/1905

Van Elsen, M., Baelmans, M., Mercelis, P., Kruth, J.-P., 2007. Solutions for modelling moving heat sources in a semi-infinite medium and applications to laser material processing. Int. J. Heat Mass Transf. 50, 4872–4882. https://doi.org/10.1016/J.IJHEATMASSTRANSFER.2007.02.044

Villafuerte, J., Kerr, H., 1990. Grain structures in gas tungsten-arc welds of austenitic stainless steels with ferrite primary phase. https://doi.org/10.1007/BF02656582

Villafuerte, J.C., Kerr, H.W., David, S.A., 1995. Mechanisms of equiaxed grain formation in ferritic stainless steel gas tungsten arc welds. Mater. Sci. Eng. A 194, 187–191. https://doi.org/10.1016/0921-5093(94)09656-2

Villaret, V., Deschaux-Beaume, F., Bordreuil, C., Fras, G., Chovet, C., Petit, B., Faivre, L., 2013a. Characterization of Gas Metal Arc Welding welds obtained with new high Cr-Mo ferritic stainless steel filler wires. Mater. Des. 51, 474–483. https://doi.org/10.1016/j.matdes.2013.04.054

Villaret, V., Deschaux-Beaume, F., Bordreuil, C., Rouquette, S., Chovet, C., 2013b. Influence of filler wire composition on weld microstructures of a 444 ferritic stainless steel grade. J. Mater. Process. Technol. 213, 1538–1547. https://doi.org/10.1016/j.jmatprotec.2013.03.026

Vitek, J.M., Babu, S.S., Park, J.-W., David, S.A., 2012. Analysis of Stray Grain Formation in Single-Crystal Nickel-Based Superalloy Welds. pp. 459–465. https://doi.org/10.7449/2004/superalloys_2004_459_465

Vuoristo, P., Tuominen, J., Nurminen, J., 2005. Laser coating and thermal spraying - process basics and coating properties. Therm. Spray 2005 Therm. Spray Connects Explore Its Surf. Potential DVS-ASM 1270–1277.

Walker, K., Lourenço, J.M., Sun, S., Brandt, M., Wang, C., 2016. Quantitative fractography and modelling of fatigue crack propagation in high strength AerMet®100 steel repaired with a laser cladding process. Int. J. Fatigue 94. https://doi.org/10.1016/j.ijfatigue.2016.06.031

Wang, G.X., Prasad, V., Matthys, E.F., 1997. Solute distribution during rapid solidification into an undercooled melt. J. Cryst. Growth 174, 35–40. https://doi.org/10.1016/S0022-0248(96)01058-5

Wang, W., Pinkerton, A.J., Wee, L.M., Li, L., 2007. Component Repair Using Laser Direct Metal Deposition, in: Hinduja, S., Fan, K.-C. (Eds.), Proceedings of the 35th International MATADOR Conference. Springer London, pp. 345–350.

Wang, X., Chou, K., 2017. Electron Backscatter Diffraction Analysis of Inconel 718 Parts Fabricated by Selective Laser Melting Additive Manufacturing. JOM 69, 402–408. https://doi.org/10.1007/s11837-016-2198-1

Wang, Z., Zhou, D., Deng, Q., Chen, G., Xie, W., 2012. The Microstructure and Mechanical Properties of Inconel 718 Fine Grain Ring Forging, in: Superalloy 718 and Derivatives. John Wiley & Sons, Ltd, pp. 343–349. https://doi.org/10.1002/9781118495223.ch26

Wasén, J., Heier, E., 1998. Fatigue crack growth thresholds—the influence of Young's modulus and fracture surface roughness. Int. J. Fatigue 20, 737–742. https://doi.org/10.1016/S0142-1123(98)00034-6

Weibull, W., 1961. Fatigue Testing and Analysis of Results, 1st ed. Pergamon, ISBN 978-1-4831-5416-9.

Wiberg, A., Persson, J., Ölvander, J., 2019. Design for additive manufacturing – a review of available design methods and software. Rapid Prototyp. J. 25, 1080–1094. https://doi.org/10.1108/RPJ-10-2018-0262

Wong, K.V., Hernandez, A., 2012. A Review of Additive Manufacturing [WWW Document]. ISRN Mech. Eng. https://doi.org/10.5402/2012/208760

Xiao, H., Li, S.M., Xiao, W.J., Li, Y.Q., Cha, L.M., Mazumder, J., Song, L.J., 2017. Effects of laser modes on Nb segregation and Laves phase formation during laser additive manufacturing of nickel-based superalloy. Mater. Lett. 188, 260–262. https://doi.org/10.1016/j.matlet.2016.10.118

Xu, Y., Song, D., Chu, F., 2016. Approach to the Weibull modulus based on fractal fragmentation of particles. Powder Technol. 292, 99–107. https://doi.org/10.1016/j.powtec.2016.01.021

Zhang, H.Y., Zhang, S.H., Li, Z.X., Cheng, M., 2010. Hot die forging process optimization of superalloy IN718 turbine disc using processing map and finite element method. Proc. Inst. Mech. Eng. Part B J. Eng. Manuf. 224, 103–110. https://doi.org/10.1243/09544054JEM1571

Zhang, X., Cui, W., Li, W., Liou, F., 2019. Effects of tool path in remanufacturing cylindrical components by laser metal deposition. Int. J. Adv. Manuf. Technol. 100, 1607–1617. https://doi.org/10.1007/s00170-018-2786-z

Zhang, Z., Zhao, Y., Shan, J., Wu, A., Gu, H., Tang, X., 2019. Influence of heat treatment on microstructures and mechanical properties of K447A cladding layers obtained by

laser solid forming. J. Alloys Compd. 790, 703–715. https://doi.org/10.1016/j.jallcom.2019.03.136

Zhang, Z.F., Wang, Z.G., 2007. Grain boundary effects on fatigue damage and material properties: Macro- and micro-considerations, in: Sih, G.C. (Ed.), Multiscaling in Molecular and Continuum Mechanics: Interaction of Time and Size from Macro to Nano: Application to Biology, Physics, Material Science, Mechanics, Structural and Processing Engineering. Springer Netherlands, Dordrecht, pp. 389–438. https://doi.org/10.1007/978-1-4020-5062-6_17

Zhao, Y., Hao, L., Xiong, W., 2020. Phase Transformations During Continuous Cooling in Inconel 718 Alloys Manufactured by Laser Powder Bed Fusion and Suction Casting. ArXiv200601737 Cond-Mat Physicsphysics.

Zhong, M., Liu, W., 2010. Laser surface cladding: The state of the art and challenges. Proc. Inst. Mech. Eng. Part C J. Mech. Eng. Sci. 224, 1041–1060. https://doi.org/10.1243/09544062JMES1782

Zohdi, T.I., 2015. On the thermal response of a surface deposited laser-irradiated powder particle. CIRP J. Manuf. Sci. Technol. 10, 77–83. https://doi.org/10.1016/j.cirpj.2015.05.001

Zwinkels, J., 2015. Light, Electromagnetic Spectrum. pp. 1–8. https://doi.org/10.1007/978-3-642-27851-8_204-1